031103

AMC PAMPHLET **AMCP 706-181**

AD A038817

ENGINEERING DESIGN HANDBOOK

EXPLOSIONS IN AIR

PART ONE

DDC
RECEIVED
JAN 28 1975
D

Reproduced by
NATIONAL TECHNICAL
INFORMATION SERVICE
US Department of Commerce
Springfield, VA. 22151

HEADQUARTERS, U S ARMY MATERIEL COMMAND

DISTRIBUTION STATEMENT A
Approved for public release;
Distribution Unlimited

DEPARTMENT OF THE ARMY
HEADQUARTERS UNITED STATES ARMY MATERIEL COMMAND
5001 Eisenhower Ave, Alexandria, VA 22333

AMC PAMPHLET
No. 706-181

15 July 1974

ENGINEERING DESIGN HANDBOOK
EXPLOSIONS IN AIR, PART ONE

TABLE OF CONTENTS

Paragraph		*Page*
	LIST OF ILLUSTRATIONS	viii
	LIST OF TABLES	xv
	PREFACE	xvii
	CHAPTER 1. GENERAL PHENOMENOLOGY	
1–0	List of Symbols	1–1
1–1	Definition of Explosion	1–2
1–2	Blast Wave Characteristics	1–2
1–3	"Ideal" Blast Waves in Free Air	1–2
1–3.1	Measured Primary Shock Characteristics	1–2
1–3.2	Functional Forms of Primary Shock Characteristics	1–3
1–3.2.1	Pressure-Time History	1–3
1–3.2.1.1	Positive Phase	1–3
1–3.2.1.2	Negative Phase	1–4
1–3.2.2	Particle Velocity and Other Parameters	1–5
1–3.3	Secondary and Tertiary Shock Characteristics	1–5
1–4	"Nonideal" Blast Waves	1–5
1–4.1	In Free Air	1–5
1–4.2	Ground Effects	1–6
1–5	Reflection and Diffraction of Blast Waves	1–7
1–5.1	Reflection of a Plane Wave	1–7
1–5.1.1	Types of Reflection	1–7
1–5.1.1.1	Normal Reflection	1–7
1–5.1.1.2	Regular Oblique Reflection	1–8
1–5.1.1.3	Mach Reflection	1–9
1–5.1.2	Reflection Process	1–10
1–5.1.2.1	Strong Shock Waves	1–10
1–5.1.2.2	Weak Shock Waves	1–11

DDC
RECEIVED
JAN 28 1975

DISTRIBUTION STATEMENT A
Approved for public release;
Distribution Unlimited

TABLE OF CONTENTS (Con't.)

Paragraph		*Page*
1–5.2	Diffraction of a Plane Wave	1–11
1–5.2.1	Two-dimensional Rigid Thick Wall	1–12
1–5.2.2	Three-dimensional Block	1–13
1–5.2.3	Circular Cylinder	1–14
1–6	Effects on Blast Waves	1–16
1–6.1	Shape or Asymmetry of Source on Blast Waves	1–16
1–6.1.1	Common Shapes	1–16
1–6.1.1.1	Straight Line Charge	1–17
1–6.1.1.2	Muzzle Blast	1–17
1–6.1.1.3	Large Plane Charge	1–17
1–6.1.2	Distance Effect	1–17
1–6.2	Long-range Focusing	1–18
1–6.2.1	Homogeneous Medium	1–18
1–6.2.2	Inhomogeneous Medium	1–18
1–6.2.2.1	Theory	1–19
1–6.2.2.2	Practice	1–20
1–6.3	Variation of Types of Energy Source	1–21
1–6.3.1	Chemical Explosives	1–21
1–6.3.2	Nuclear Explosives	1–22
1–6.3.3	Other Sources	1–23
	References	1–24

CHAPTER 2. AIR BLAST THEORY

2–0	List of Symbols	2–1
2–1	General	2–2
2–2	Basic Equations	2–3
2–2.1	Coordinate Systems	2–3
2–2.2	Forms of Equations	2–3
2–2.2.1	Lagrangian	2–3
2–2.2.2	Eulerian	2–4
2–2.3	Rankine-Hugoniot Conditions	2–4
2–2.4	Single Spatial Variable Cases	2–5
2–2.4.1	Linear Flow	2–5
2–2.4.2	Spherically Symmetric Flow	2–5
2–2.4.3	Cylindrically Symmetric Flow	2–5
2–2.4.4	Application	2–6
2–3	Analytic Solutions to Equations	2–6
2–3.1	Taylor's Similarity Solution for Spherically Symmetric Blast Waves	2–6
2–3.2	Initial Conditions for Solutions	2–9
2–3.2.1	Initial Isothermal Spherical Detonation Front	2–9
2–3.2.2	Other Initial Conditions	2–10
2–3.3	Mach Shock Reflection	2–10
2–3.4	Some Recent Theories	2–14
2–3.4.1	Weak Shock Regime of a Blast Wave	2–14
2–3.4.2	Intermediate and Strong Shock Strengths	2–16

TABLE OF CONTENTS (Con't.)

Paragraph		*Page*
2–3.5	Theilheimer's Solution for the "Time Constant" of an Air Blast Wave	2–19
2–4	Summary of Pertinent Equations	2–20
2–4.1	Basic Equations of Motion	2–21
2–4.2	Rankine-Hugoniot Conditions	2–21
2–4.3	Basic Equations for Spherically Symmetric Flow	2–21
2–4.4	Taylor's Similarity Solution	2–21
2–4.5	Theilheimer's Solution for Initial Decay of a Shock	2–21
	References	2–22
	CHAPTER 3. BLAST SCALING	
3–0	List of Symbols	3–1
3–1	Introduction	3–2
3–2	Scaling Laws for Blast Parameters	3–2
3–2.1	Hopkinson Scaling	3–2
3–2.1.1	Definition	3–2
3–2.1.2	Experimental Verification	3–3
3–2.1.3	Implications	3–5
3–2.1.4	Model Analysis	3–7
3–2.2	Sachs' Scaling	3–9
3–2.2.1	Assumptions	3–11
3–2.2.2	Model Analysis	3–11
3–2.2.3	Experimental Verification	3–13
3–2.2.4	Application	3–13
3–2.3	Other Scaling Laws for Blast Parameters	3–15
3–2.3.1	Additional Blast Source Parameter	3–15
3–2.3.2	Small Scaled Distances	3–17
3–2.3.3	Wecken's Laws	3–18
3–3	Scaling Laws for Interaction With Structures	3–20
3–3.1	"Replica" Scaling	3–20
3–3.2	Scaling for Impulsive Loading	3–21
3–3.3	Missile Response to Air Blast	3–23
3–4	Limitations of Scaling Laws	3–23
	References	3–24
	CHAPTER 4. COMPUTATIONAL METHODS	
4–0	List of Symbols	4–1
4–1	General	4–2
4–2	Methods With Discontinuous Shock Fronts	4–2
4–2.1	Kirkwood and Brinkley Method	4–2
4–2.2	Gränstrom Method	4–5
4–2.3	Method of Characteristics	4–6
4–3	Methods With Fictitious Viscosity	4–8

TABLE OF CONTENTS (Con't.)

Paragraph		*Page*
4–3.1	Brode's Method	4–9
4–3.2	WUNDY Code (NOL) and LSZK Equation of State	4–13
4–4	Particle and Force (PAF) Method	4–16
4–4.1	Governing Equations	4–17
4–4.2	The Finite Difference Forms	4–18
4–4.2.1	Neighbors	4–18
4–4.2.2	Forces	4–19
4–4.2.2.1	Nondissipative	4–19
4–4.2.2.2	Dissipative	4–21
4–4.3	Test Cases	4–22
4–4.3.1	Flow Past a Wedge	4–22
4–4.3.2	Flow Past a Blunt Cylinder	4–23
4–4.3.3	Flow Past a Cone	4–23
4–5	Particle-in-cell (PIC) Method	4–24
4–5.1	State Equations	4–24
4–5.2	Two-dimensional Demonstration Problem	4–25
4–5.2.1	Phase 1 of Calculation	4–25
4–5.2.2	Phase 2 of Calculation (The Transport of Material)	4–27
4–5.2.3	Phase 3 of Calculation (Functionals of Motion)	4–27
4–5.3	Other Boundary Conditions	4–27
4–6	Fluid-in-cell (FLIC) Method	4–29
4–6.1	Computing Mesh	4–29
4–6.2	The Difference Equations	4–30
4–6.2.1	Step 1	4–30
4–6.2.2	Step 2	4–31
4–6.2.3	Boundary Conditions and Stability	4–33
4–7	Comparisons of Various Methods	4–34
	References	4–35

CHAPTER 5. AIR BLAST EXPERIMENTATION

5–0	List of Symbols	5–1
5–1	General	5–1
5–2	Units and Dimensions for Blast Data	5–2
5–3	"Free Air" Measurements	5–2
5–4	Measurements for Blast Sources on the Ground	5–5
5–5	Measurements of Mach Waves and Other Obliquely Reflected Waves	5–10
5–6	Measurements of Normally Reflected Waves	5–12
5–7	Measurements Under Real and Simulated Altitude Conditions	5–13
5–8	Measurements for Sequential Explosions	5–16
5–9	Accuracy of Measurement of Blast Parameters	5–18
	References	5–19

TABLE OF CONTENTS (Con't.)

Paragraph		*Page*
	CHAPTER 6. COMPILED AIR BLAST PARAMETERS	
6–0	List of Symbols	6–1
6–1	General	6–2
6–2	Sources of Compiled Data on Air Blast	6–2
6–3	Generation of Tables and Graphs of Air Blast Wave Properties	6–3
6–3.1	Shock-front Parameters	6–4
6–3.1.1	Rankine-Hugoniot Equations	6–4
6–3.1.2	Expressions for Perfect Gas in Terms of Overpressure ($\bar{P}_s \leqslant 3.5$)	6–5
6–3.1.3	Expressions for Perfect Gas in Terms of Shock Velocity ($U \leqslant 2.0$)	6–5
6–3.2	Impulses and Durations	6–9
6–3.3	Time Constant and Initial Decay Rate	6–11
6–3.4	Oblique Reflection Data	6–12
6–3.5	Conversion Factors	6–15
6–4	Example Calculations	6–17
	References	6–21
	CHAPTER 7. AIR BLAST TRANSDUCERS	
7–0	List of Symbols	7–1
7–1	General	7–1
7–2	Pressure Transducers	7–1
7–2.1	Side-on Gages	7–1
7–2.1.1	BRL Side-on Gages	7–2
7–2.1.2	Southwest Research Institute Side-on Gages	7–2
7–2.1.3	Atlantic Research Corporation Side-on Gages	7–4
7–2.1.4	British Side-on Gages	7–4
7–2.1.5	Other Side-on Gages	7–6
7–2.2	Reflected Pressure Gages	7–6
7–2.3	Miniature Pressure Gages	7–7
7–2.3.1	BRL Miniature Transducers	7–8
7–2.3.2	Langley Research Center Miniature Transducers	7–8
7–2.3.3	Other Minature Transducers	7–10
7–3	Arrival-time Gages and Zero-time Markers	7–14
7–4	Total Head Gages and Drag Gages	7–17
7–4.1	Total Head Gages	7–17
7–4.2	Drag Gages	7–17
7–4.2.1	Drag Gage of Johnson and Ewing	7–18
7–4.2.2	NOL Drag Force Gages	7–18
7–4.2.3	SRI Drag Probes	7–18
7–4.2.4	BRL Biaxial Drag Gage	7–19
7–5	Density Gage	7–19
7–6	Impulse Transducers	7–20

TABLE OF CONTENTS (Con't.)

Paragraph		*Page*
7–6.1	Free Plug Transducer	7–20
7–6.2	Sliding Piston Gage	7–21
7–6.3	Spring Piston Gage	7–21
7–7	Various Mechanical Gages	7–21
7–7.1	Deformation Gages	7–21
7–7.2	Peak Pressure Gages	7–22
7–8	Summary	7–26
	References	7–33

CHAPTER 8. INSTRUMENTATION SYSTEMS

8–1	General	8–1
8–2	Ground-based Instrumentation Systems	8–1
8–2.1	Cathode-ray-tube Systems	8–1
8–2.1.1	The BRL CRT Systems	8–2
8–2.1.2	The CEC Type 5-140 CRT System	8–4
8–2.1.3	British CRT Systems	8–4
8–2.1.4	The Denver Research Institute CRT System	8–4
8–2.1.5	The Langley Research Center CRT System	8–6
8–2.1.6	Other CRT Systems	8–6
8–2.2	Magnetic Tape Systems	8–6
8–2.3	Galvanometer Oscillograph Systems	8–9
8–2.4	Transient Recorders	8–10
8–2.5	Instrumentation Problems Associated With Nuclear Blast Tests	8–10
8–2.5.1	TREE	8–11
8–2.5.2	EMP	8–11
8–2.5.2.1	EMP Generation	8–11
8–2.5.2.2	Near Surface Burst	8–11
8–2.5.2.3	Free Air Burst	8–12
8–2.5.2.4	EMP Interaction With Systems	8–12
8–2.5.2.4.1	Gages	8–12
8–2.5.2.4.2	Induction of Currents into Cables	8–12
8–2.5.2.4.3	Recording Systems	8–13
8–3	Portable Systems	8–13
8–3.1	Galvanometer Oscillograph Systems	8–13
8–3.2	Magnetic Tape Recorder Systems	8–14
8–3.2.1	The Leach MTP-1200 Recorder	8–14
8–3.2.2	The Genisco Data 10-110 Recorder	8–14
8–3.2.3	Typical Portable Magnetic Tape Recorder Systems	8–15
8–3.3	Self-recording Gages	8–17
8–3.3.1	Blast Pressure Sensors	8–19
8–3.3.2	Time Base	8–19
8–3.3.3	Initiation Methods	8–20
8–3.3.4	Acceleration Methods	8–20

TABLE OF CONTENTS (Con't.)

Paragraph		*Page*
8–4	Calibration Techniques	8–20
	References	8–25
	CHAPTER 9. PHOTOGRAPHY OF BLAST WAVES	
9–1	General	9–1
9–2	Motion Picture Equipment	9–1
9–2.1	Low-speed Framing Cameras	9–1
9–2.2	High-speed Framing Cameras	9–1
9–2.2.1	Rotating Prism Cameras	9–1
9–2.2.2	Rotating Drum Cameras	9–2
9–2.2.3	Rotating Mirror Cameras	9–3
9–2.2.4	Image Dissector Cameras	9–4
9–3	Streak Photography Equipment	9–6
9–4	Still Photography Equipment	9–7
9–4.1	Conventional Cameras	9–7
9–4.2	Fast Shutter Cameras	9–7
9–4.3	Image Converter Cameras	9–9
9–5	Shadowgraph and Schlieren Equipment	9–13
9–5.1	Shadowgraph Equipment	9–13
9–5.2	Schlieren Equipment	9–14
9–6	Techniques in Photography of Air Blast Waves	9–15
	References	9–22
	CHAPTER 10. DATA REDUCTION METHODS	
10–0	List of Symbols	10–1
10–1	General	10–1
10–2	Reduction of Film and Paper Traces	10–1
10–2.1	Types of Records	10–1
10–2.2	Reading of Records	10–3
10–2.3	Record Correction for Gage Size and Flow Effects	10–4
10–2.4	Reduction of Dynamic Pressure Data	10–5
10–2.5	Determination of Positive Phase Duration	10–7
10–3	Reduction of Magnetic Tape Data	10–9
10–4	Reduction of Data from Self-recording Gages	10–10
10–5	Reduction of Data from Motion or Still Photographs	10–10
10–6	Other Data Reduction	10–12
	References	10–13
	BIBLIOGRAPHY	B–1
	INDEX	I–1

LIST OF ILLUSTRATIONS

Fig. No.	*Title*	*Page*
1–1	Ideal Blast Wave	1–3
1–2	Recorded Pressure-Time Histories of Actual Blast Waves from 1-lb_m Pentolite Explosive Spheres	1–6
1–3	P-T Curves Produced by a Cased Charge	1–7
1–4	Typical Nonideal Pressure Traces Showing Precursor	1–8
1–5	Normal Reflection of a Plane Shock from a Rigid Wall	1–8
1–6	Regular Oblique Reflection of a Plane Shock from a Rigid Wall	1–9
1–7	Mach Reflections from a Rigid Wall	1–10
1–8	Reflection of Strong Shock Waves	1–11
1–9	Geometry of Mach Reflection	1–12
1–10	Reflection of Weak Shock Waves	1–12
1–11	Diffraction of a Shock Front Over a Wall	1–13
1–12	Diffraction of a Shock Front Over a Three-dimensional Block Structure (Plan View)	1–14
1–13	Pressures on a Three-dimensional Block Structure During Diffraction	1–14
1–14	Tracings of Shadowgraphs Showing the Interaction of a Shock Front With a Cylinder	1–15
1–15	Tracings of Shadowgraphs Showing the Interaction of a Shock Front With a Cylinder	1–16
1–16	The Blast Wave from a 7.62 mm Rifle at Three Stages of Expansion	1–17
1–17	Incident Shock Overpressure Ratio vs Scaled Distance	1–18
1–18	Surface Air Blast Pressure vs Range from Detonations on the Surface	1–19
1–19(A)	Typical Sound Velocity Gradient	1–19
1–19(B)	Paths of Sound Rays in the Atmosphere, for Sound Velocity Gradient of Fig. 1–19(A)	1–20
1–20	Various Types of Velocity Gradients To Be Expected and the Increase in Intensity at a Focus for Each Type	1–21
1–21	Shock Wave Distortion by Layered Atmospheric Temperature and Wind Structure	1–22
1–22	Typical Explosion Ray Paths	1–23
1–23	Variation of Peak Overpressure Ratios P_s With Shock Radius λ_s for Various Explosions	1–24
2–1	Mach Shock Reflection	2–11
2–2	Diffraction of a Shock by a Wedge	2–11
2–3	Graph of Chester's Function $K(M_s)$	2–12
2–4	Graph of the Function $\log_{10} f(M_s)$ Given by Eq. (4) in Ref. 14	2–12
2–5	Motion of Triple Point	2–13
2–6	Diffraction on a Cylinder	2–14

LIST OF ILLUSTRATIONS (Con't.)

Fig. No.	*Title*	*Page*
2–7	Variation of Shock Strength ζ vs Dimensionless Shock Radius R_s/R_o for Spherical Blast Waves, $\gamma = 1.4$	2–15
2–8	Spherical Blast Wave	2–18
2–9	Cylindrical Blast Wave	2–18
2–10	Plane Blast Wave	2–19
3–1	Hopkinson Blast Wave Scaling	3–4
3–2	Pressure-distance Curves for Ground-burst Blast of Bare Charges	3–4
3–3	Experimental Positive Impulses vs Distance Curves (on ground) from Various Sources	3–5
3–4	Comparisons of Peak Particle Velocities for Surface Burst TNT Charges	3–6
3–5	Peak Overpressure vs Sachs' Scaled Distance	3–14
3–6	Hopkinson Scaled Impulse vs Scaled Distance	3–15
3–7	Sachs' Scaled Impulse vs Scaled Distance	3–16
3–8	$\bar{p}$ vs $\bar{R}$ for Various Values of ξ, High-$\bar{p}$ Range	3–17
3–9	Comparison of Predicted and Measured Reflected Impulse I_r–Sea Level Conditions	3–18
3–10	Comparison of Predicted and Measured Reflected Impulse I_r – Reduced Pressure Ambient Conditions	3–19
3–11	"Replica" Scaling of Response of Structures to Blast Loading	3–21
3–12	"Replica" Scaling of Elastic Response of Aluminum Cantilevers to Air Blast Waves	3–22
3–13	"Replica" Scaling of Permanent Deformation of Aluminum Cantilevers Under Air Blast Loading	3–22
3–14	Peak Overpressure Ratio vs Scaled Distance	3–24
4–1	Peak Excess Pressure Ratio vs Distance in Charge Radii for Pentolite at a Loading Density of 1.65 g/cm^3	4–5
4–2	Initial Singularity in Method of Characteristics	4–6
4–3	Schematic of Region of Numerical Solution for Method of Characteristics	4–8
4–4	Physical Plane Showing the Main Shock, Contact Surface, and Second Shock	4–9
4–5	Physical Plane (λ-τ) Showing Shock Front, Contact Surface, and Second Shock for Cases With Equal Initial Energy and Equal Initial Mass	4–10
4–6	Pressure as a Function of Lagrange Position R_o for the Point-source Solution at Times Indicated	4–12
4–7	A Comparison of the PAF Detached Bow Wave Positions (Dashed Lines) After Impact With Those Observed in a Shock Tube Experiment Involving a Mach 1.35 Flow Past a Wedge	4–22
4–8	The Steady-state Detached Shock Front Position in a Mach 1.58 Flow Past a Blunt Cylinder	4–23

LIST OF ILLUSTRATIONS (Con't.)

Fig. No.	*Title*	*Page*
4–9	A Comparison of Steady-state PAF Pressures (the Dots) Along the Cone Face With Experimental Values Observed in a Mach 1.41 Flow Past a 75-deg Cone	4–23
4–10	A Late-time PAF Particle Plot (the Dots) Compared to an Experimental Steady-state Bow Wave	4–23
4–11	Configuration of Mass Points at Time t = 12.593 for the Calculation for Nitrogen With M_s = 1.008	4–29
4–12	Configuration of Mass Points at Time t = 6.329 for the Calculation for Nitrogen With M_s = 1.588	4–29
4–13	Measured and Calculated Shock Positions at the Time of First Shock Reflection $M_1 = M_s$ = 3.15	4–33
5–1	Logarithmic Plot of Free-air Pressure vs Scaled Distance for Cast TNT	5–3
5–2	Logarithmic Plot of Positive Impulse vs Scaled Distance in Free Air for Cast TNT	5–3
5–3	Experimental Pressure vs Scaled Distance for Four Types of Charges	5–3
5–4(A)	Side-on and Normally Reflected Pressure vs Scaled Distance	5–4
5–4(B)	Side-on and Normally Reflected Pressure vs Scaled Distance	5–5
5–5	Side-on and Normally Reflected Pressure vs Scaled Distance	5–5
5–6	Side-on and Normally Reflected Duration vs Scaled Distance	5–5
5–7	Radius-time Curves for 1-lb_m Sphere of TNT at Sea Level Conditions	5–6
5–8	Pressure-Distance Curves for Ground Burst Blast of Bare Charges	5–7
5–9	Experimental Positive Impulses vs Distance Curves (on ground) from Various Sources	5–7
5–10	Scaled Arrival Time vs Ground Range	5–8
5–11	Scaled Peak Overpressure vs Ground Range	5–8
5–12	Scaled Positive Duration vs Ground Range	5–8
5–13	Scaled Positive Overpressure Impulse vs Ground Range	5–9
5–14	Comparisons of Peak Particle Velocities for Surface Burst TNT Charges of Various Weights from 60 lb_m to 20,000 lb_m	5–10
5–15	Comparison of the Time Variation of Velocity at a Specific Scaled Distance from Surface Burst TNT Charges from 60 lb_m to 20,000 lb_m	5–26
5–16	x-t Diagram from Particle Velocity and Shock Front Data	5–10

LIST OF ILLUSTRATIONS (Con't.)

Fig. No.	*Title*	*Page*
5–17	Measured Arrival Times for Flat Top I, II, and III Compared With Prediction	5–10
5–18	Measured Positive Duration for Flat Top I, II, and III Compared With Prediction	5–11
5–19	Measured Overpressure for Flat Top I, II, and III Compared With Prediction	5–11
5–20	Measured Positive Overpressure Impulse for Flat Top I, II and III Compared With Prediction	5–11
5–21	Measured Dynamic Pressure for Flat Top I, II, and III Compared With Prediction	5–11
5–22	Paths of Triple Point	5–12
5–23	Typical Time Histories in Mach Reflection Region	5–12
5–24	Triple Point Loci Over Reflecting Surfaces of Hard-packed Dirt and Dry Sand	5–13
5–25	Typical Complex Shock Waves Observed in Reflection Studies	5–13
5–26	Normally Reflected Peak Overpressure vs Scaled Distance	5–14
5–27	Scaled Normally Reflected Positive Impulse vs Scaled Distance	5–14
5–28	Geometrically Scaled Reflected Impulse vs Scaled Distance at Different Atmospheric Pressures	5–15
5–29	Normally Reflected Positive Impulse as a Function of Scaled Distance ($R/W^{1/3}$) and Ambient Pressure p_o	5–16
5–30	Normally Reflected Pressure-Time History, Scaled Distance = 0.10 ft/$lb_m^{1/3}$, 0.1 mm Hg (approx. 210,000-ft altitude)	5–17
5–31	Phenomenon of Blast Wave Coalescence for Two Charges Detonated With Time Delay	5–17
5–32	Scaled Delays Between Shock Fronts from Sequential Explosions	5–18
6–1	Compiled Shock-front Parameters for Incident Air Blast Waves	6–9
6–2	Compiled Shock-front Parameters for Normally Reflected Air Blast Waves	6–11
6–3	Compiled Impulses and Durations	6–13
6–4	Geometry for Regular Reflection	6–14
6–5	Reflected Overpressure Ratio as a Function of Angle of Incidence for Various Side-on Overpressures	6–14
6–6	Typical Reflected Overpressure vs Horizontal Distance for Selected Heights of Burst, 1 lb_m Pentolite at Sea Level	6–17
6–7	Typical Dynamic Pressure vs Distance for Selected Heights of Burst, 1 lb_m Pentolite at Sea Level	6–17
7–1	Schematic of BRL Piezoelectric Side-on Blast Gage	7–3

LISTS OF ILLUSTRATIONS (Con't.)

Fig. No.	Title	Page
7–2	SwRI Side-on Blast Gage	7–3
7–3	Atlantic Research Corp. Pencil Blast Gage, Type LC-13	7–4
7–4	The British H3 Side-on Gage	7–5
7–5	The British H3B Blast Gage	7–5
7–6	The British H3C Blast Gage	7–6
7–7	Side-on Blast Gage Using Small, Flush-diaphragm Transducers	7–6
7–8	Reflected Pressure Gage of Granath and Coulter	7–7
7–9	Exploded View of Half-inch Gage of Granath and Coulter	7–8
7–10	Sectional View of Gage of Baker and Ewing	7–9
7–11	Sectional View of NASA Miniature Transducer of Morton and Patterson	7–10
7–12	Atlantic Research Corp. Miniature Pressure Transducers	7 11
7–13	Kistler Model 603A Quartz Miniature Pressure Transducer	7–12
7–14	Internal Schematic of Kistler Model 603A Pressure Transducer Showing Scheme for Acceleration Compensation	7–12
7–15	Basic Single Coil Variable Impedance Pressure Transducer, Kaman Nuclear	7–12
7–16	Shaevitz-Bytrex Miniature Pressure Transducers	7–13
7–17	Dynisco Pressure Transducer	7–13
7–18	British AWRE MQ20 Pressure Transducer	7–16
7–19	Early Type of Blast Switch	7–16
7–20	BRL Arrival-time Gage of Watson and Wilson	7–16
7–21	Cross Sections of Typical BRL Total Head Gages	7–17
7–22	Comparison of Pressure-Time and Drag-Time Traces for 0 deg and 90 deg to Flow Direction, Gage of Johnson and Ewing	7–18
7–23	SRI Total Drag Probe Assembly, Schematic Cross Section	7–19
7–24	Assembly Drawing of BRL Biaxial Drag Gage	7–19
7–25	Diagram of Density Gage of Dewey and Anson	7–19
7–26	Record from Density Gage of Dewey and Anson	7–20
7–27	Permanent Tip Deflection of 0.051-in. 6061 Aluminum Alloy Beam vs Distance for Spherical Pentolite or TNT	7–23
7–28	Surface Tension Blast Pressure Gage of Muirhead and McMurtry	7–24
7–29	Squirt Blast Pressure Gage of Palmer and Muirhead	7–25
8–1	Block Diagram of CRT Oscilloscope Recording System	8–1
8–2	BRL Four-channel Recording Equipment	8–2

LIST OF ILLUSTRATION (Con't.)

Fig. No.	*Title*	*Page*
8–3	Eight-channel BRL Recorder	8–3
8–4	Drum Camera for Eight-channel BRL Recorder	8–4
8–5	Block Diagram of Eight-channel BRL Recorder	8–5
8–6	CEC Sixteen-channel Oscillograph Recorder	8–6
8–7	NASA Langley Fourteen-channel CRT Recording System	8–7
8–8	Block Diagram of SwRI Magnetic Tape Recorder System	8–8
8–9	Block Diagram of IITRI Record-reproduce Instrumentation	8–8
8–10	Magnetic Tape Recorder System for Air Blast Recording	8–9
8–11	Influence of Ground on Return Conduction Current	8–12
8–12	Typical Pressure Instrumentation System Employing Magnetic Tape Recorder	8–16
8–13	Schematic Diagram of Quasi-static Gage Calibration Apparatus	8–24
8–14	Quasi-static Pressure Calibrator for Field Use	8–24
8–15	Dynamic Pressure Calibrator of Rathke	8–25
9–1	Schematic Diagram of an Intermittent-type Camera	9–1
9–2	Principle of Operation of Rotating Prism Camera	9–2
9–3	Rotating Plane Prism Used in the Eastman High Speed Camera	9–2
9–4	Schematic Diagram of Fastax 8-mm Rotary Prism High-speed Camera	9–3
9–5	Mechanism for Hycam Rotating Prism Cameras	9–4
9–6	Essential Features of a Rotating-mirror Framing Camera	9–5
9–7	Rotating-mirror Framing Camera With Diaphragm	9–5
9–8	Optical System of Sultanoff's High-speed Camera	9–6
9–9	Essential Features of a Streak Camera	9–7
9–10	Typical Rotating-mirror Cameras	9–8
9–11	Test Arrangement Used at BRL for Simultaneous Streak and Kerr Cell Photography of Blast Waves	9–8
9-12	Streak Camera Photographs of Blast from 1-lb Pentolite Spheres	9–9
9–13	Still Photograph of Large Chemical Explosion	9–10
9–14	Backlit Kerr Cell Photographs of Blast Waves from Small Pentolite Spheres	9–11
9–15	Image Tube Diagrammatic	9–11
9–16	Schematic of Image-converter Camera	9–12
9–17	Diagram of Cordin Biplanar Image-converter Camera	9–12
9–18	Sequence of Backlit Image-converter Photographs of Weak Air Shocks	9–13
9–19	Shadowgraph Diagrammatic	9–14

LIST OF ILLUSTRATIONS (Con't.)

Fig. No.	*Title*	*Page*
9–20	Schlieren System Diagrammatic	9–15
9–21	Schlieren Picture of Blast from a Pressurized Glass Sphere	9–16
9–22	Views of Shock Waves from 8-lb_m TNT Spheres Detonated 8 ft Above Concrete	9–18
9–23	View of Shock Wave from 5-ton TNT Ground-burst Hemisphere	9–18
9–24	Schlieren Streak Record of the Collision of Two Unequal Spherical Shock Waves	9–19
9–25	Spark Shadowgraph of the Explosion Generated from a Pressurized Glass Sphere	9–20
9–26	Double Exposure Photograph of Moving Explosive Charge Detonation	9–21
9–27	Block Diagram of Instrumentation for Backlit Photography of Air Shocks	9–21
10-1	Typical Traces from Oscillograph Record Cameras.	10–2
10–2	Typical Traces from Four-channel Blast Recorders.	10–3
10–3	Typical Trace from Eight-channel BRL Blast Recorder	10–4
10–4	Calculated Response of a Gage of Finite Diameter to Linearly Decaying Pressure	10–5
10–5	Method of Extrapolation of Experimental Records	10–5
10–6	Recorded Side-on and Total Head Pressure-Time Histories and Calculated Dynamic Pressure-Time History	10–7 10–7
10–7	Linear Plot of BRL Self-recording Gage Record Obtained at a Ground Range of 334 ft from the 1961 Canadian 100-ton HE Test	10–8
10–8	Semi-logarithmic Plot of Gage Record With Pressure Plotted Against the Logarithmic Scale	10–8
10–9	Semi-logarithmic Plot of Gage Record With Time Plotted Against the Logarithmic Scale	10–9
10–10	Photo-optical Records of Shock Front Profile	10–11
10–11	Velocity Field Setup	10–11

LIST OF TABLES

Table No.	*Title*	*Page*
1–1	Peak Pressure and Positive Impulse Relative to Composition B (The Comparison Being on an Equal Volume Basis)	1–23
2–1	Blast Wave Energy Parameter B for Some Values of Ratios of the Specific Heats	2–16
3–1	List of Physical Parameters for Hopkinson Blast Scaling	3–8
3–2	Sach's Scaling Parameters	3–11
3–3	Blast Scaling Laws Proposed by Wecken	3–19
3–4	Additional Parameters in Wecken's Analysis	3–19
3–5	Dimensionless Products Corresponding to Wecken's Scaling	3–20
3–6	Primary Buckingham π Terms. Blast Loading and Response of High-speed Structure	3–23
4–1	Coefficients of Partial Derivatives in Kirkwood-Brinkley Method	4–5
4–2	Comparison of Detonation Velocities D Calculated for LSZK Substance With Detonation Velocities Determined at Bruceton	4–16
4–3	Input Data for Flow Past a Wedge–PAF Method	4–22
4–4	A Comparison of Methods for Calculating Time Dependent Fluid Dynamics	4–34
6–1	Explosive Properties	6–4
6–2	Sachs' Scaled Nondimensional Blast Parameters	6–5
6–3	Scaled Shock-front Parameters for Incident Blast Waves	6–8
6–4	Scaled Shock-front Parameters for Reflected Blast Waves	6–10
6–5	Scaled Impulses and Durations of Overpressure	6–12
6–6	Time Constant and Initial Decay Rate of $\bar{p}_s$	6–14
6–7	Typical Compiled Data for Strong, Obliquely Reflected Shocks	6–15
6–8	Limit of Regular Reflection $\alpha_{extreme}$ vs Shock Strength	6–16
6–9	Conversion Factors for Scaled Blast Wave Properties	6–18
7–1	Summary of Properties of AWRE Foulness Pattern Standard Piezoelectric Transducers	7–15
7–2	Characteristics of Side-on Pressure Transducers	7–26
7–3	Characteristics of Flush-mounted Pressure Transducers	7–27

LIST OF TABLES (Con't.)

Table No.	*Title*	*Page*
8–1	Characteristics of Leach MTR-1200 Tape Recorder	8–14
8–2	Operating Environmental Specifications for DAQ-PAC	8–17
8–3	DAQ-PAC Specifications	8–18
8–4	General Requirements for Blast Pressure Gage	8–21
8–5	Capabilities of Improved Self-recording Blast Pressure System	8–22

PREFACE

Scientific interest in the processes of generation and transmission through the air of blast waves from explosive sources dates back at least to the latter part of the nineteenth century. The number of reported experimental and analytic studies of air blast phenomenology increased materially during World War II. In spite of the voluminous literature on the subject, there has been no single reference work comprehensive enough to cover both theoretical and experimental aspects of air blast technology. This handbook attempts to remedy this problem.

Explosions in Air, Part One is a general reference handbook on the topic, intended for use by both casual and experienced investigators in air blast theory and experiment. A special feature of the handbook is the inclusion of large-scale graphs of scaled air blast parameters. The literature relating to air blast technology is reviewed thoroughly and an extensive list of reference is included.

This handbook includes chapters on general phenomenology, air blast theory, blast scaling, computational methods, air blast experimentation, compiled blast data, air blast transducers, instrumentation systems, photography of air blast waves, and data reduction methods. It is illustrated by many figures and graphs. Specifically excluded from this handbook are classified aspects of air blast technology, laboratory applications such as shock tubes, and response of structures to blast loading. These topics are presented in *Explosions in Air, Part Two*, AMCP 706-182(S).

This handbook was prepared by the Southwest Research Institute, San Antonio, Texas, for the Engineering Handbook Office of Duke University, prime contractor to the U. S. Army Materiel Command. Dr. Wilfred E. Baker was the author. Technical guidance and coordination were provided by a committee with representatives from the Ballistic Research Laboratories, Picatinny Arsenal, and the U. S. Army Electronics Command. Members of this committee were Charles N. Kingery, Chairman; William J. Taylor; Richard W. Collett; and Charles Goldy.

The Engineering Design Handbooks fall into two basic categories, those approved for release and sale, and those classified for security reasons. The Army Materiel Command policy is to release these Engineering Design Handbooks to other DOD activities and their contractors and other Government agencies in accordance with current Army Regulation 70-31, dated 9 September 1966. It will be noted that the majority of these Handbooks can be obtained from the National Technical Information Service (NTIS). Procedures for acquiring these Handbooks follow:

a. Activities within AMC, DOD agencies, and Government agencies other than DOD having need for the handbooks should direct their request on an official form to:

Commander
Letterkenny Army Depot
ATTN: AMXLE-ATD
Chambersburg, PA 17201

b. Contractors and universities must forward their requests to:

National Technical Information Service
Department of Commerce
Springfield, VA 22151

(Requests for classified documents must be sent, with appropriate "Need to Know" justification, to Letterkenny Army Depot.)

Comments and suggestions on this Handbook are welcome and should be addressed to:

Commander
US Army Materiel Command
ATTN: AMCRD-TV
5001 Eisenhower Avenue
Alexandria, VA 22333

DA Forms 2028 (Recommended Changes to Publications), which are available through normal publications supply channels, may be used for comments/suggestions.

CHAPTER 1

GENERAL PHENOMENOLOGY

1-0 LIST OF SYMBOLS

A = path of triple point

a,b,c,f,g,h = constants

C, C′ = charge center; image center

E = total explosive energy

I = incident wave front

I_s^+ = positive impulse

I_s^- = negative impulse

L = largest characteristic dimension of blast source

M, M′, M″ = locus of Mach stem front

P_r = side-on overpressure of reflected wave

P_0, P_0' = diffracted Mach stems

P_s, P_s^+, P_s^- = side-on overpressure of incident wave, overpressure of positive phase, overpressure of negative phase

$\bar{P}_s$ = dimensionless pressure ratio

p = absolute pressure

p_0 = ambient pressure

q = dynamic pressure

R = reflected wave front, or distance from blast center

r = radial cylindrical coordinate

r_0 = characteristic dimension of blast source

S = slipstream locus

Sf = reflecting surface locus

T = triple point

T^+, T^- = positive phase duration, negative phase duration

t = time

t_a = blast wave arrival time

U = velocity of incident wave

U_r = velocity of reflected wave

u = particle velocity at time t; wind velocity

u_0 = particle velocity in ambient air

u_s = particle velocity at time $t = 0$

u_r = particle velocity of reflected wave

V = total volume

V_1, V_2 = locus of vortices

W = explosive charge mass

z = axial cylindrical coordinate

α,β,ν = constants

α_I, α_R, $\alpha_{I\,crit}$, α' α_{min} = various angles describing geometry of obliquely reflected shocks

γ = ratio of specific heats

$\theta, \theta_s, \theta_r, \theta_0$ = temperature, temperature of incident wave, temperature of reflected wave, temperature of ambient air

λ_s = shock radius

$\rho, \rho_s, \rho_r, \rho_0$ density, density of incident wave, density of reflected wave, density of ambient air

ϕ angle of inclination of A to Sf

1-1 DEFINITION OF EXPLOSION

The word "explosion" is defined by Webster as: "explosion: a large-scale, rapid and spectacular expansion, outbreak, or other upheaval". We will use the word in a somewhat more restrictive context in this handbook, implying a process by which a pressure wave of finite amplitude is generated in air by a rapid release of energy. Some widely different types of energy sources can produce such pressure waves, and thus be classified as "explosives" according to our definition. The stored energy in a compressed gas or vapor, either hot or cold, can be such a source. The failure of a high pressure gas storage vessel or steam boiler, or the muzzle blast from a gun, are, therefore, examples of explosions. Release of electrical energy by discharge in a spark gap, or the rapid vaporization of a fine wire or thin metal film, can produce strong pressure waves in air, and thus can be classified as an explosion source. The more usual energy sources for explosions in air are, however, either chemical or nuclear materials, which are capable of violent reactions when properly initiated.

1-2 BLAST WAVE CHARACTERISTICS

Regardless of the source of the initial finite pressure disturbance, the properties of air as a compressible gas will cause the front of this disturbance to steepen as it passes through the air (colloquially, to "shock-up") until it exhibits nearly discontinuous increases in pressure, density, and temperature. The resulting shock front moves supersonically, i.e., faster than sound speed in the air ahead of it. The air particles are accelerated also by the passage of the shock front, producing a net particle velocity in the direction of travel of the front. These characteristics of the shock or blast wave differ quite markedly from an acoustic wave – the latter involves only infinitesimal pressure changes, produces no finite change in particle velocity, moves at sonic velocity, and does not "shock-up". We can emphasize the differences in other ways. The transmission of blast waves in air is inherently a *nonlinear* process involving nonlinear equations of motion, while acoustic wave propagation can be handled quite adequately by *linear* theory. The processes of reflection and diffraction occur for either type of wave on encountering obstacles, but these processes are markedly different for blast waves and sound waves.

1-3 "IDEAL" BLAST WAVES IN FREE AIR

1-3.1 MEASURED PRIMARY SHOCK CHARACTERISTICS

Let us consider the characteristics of ideal, or classical, blast waves formed in air by one of the sources mentioned in par. 1-2. We will assume that an explosion occurs in a still, homogeneous atmosphere and that the source is spherically symmetric, so that the characteristics of the blast wave are functions only of distance R from the center of the source and time t. Let us further assume that an ideal pressure transducer, which offers no resistance to flow behind the shock front and follows perfectly all variations in pressure, records the time history of absolute pressure at some given fixed distance R. The record that such a gage would produce is shown in Fig. 1-1. For some time after the explosion, the gage records ambient pressure p_0. At arrival time t_a, the pressure rises quite abruptly (discontinuously, in an ideal wave) to a peak value $p_0 + P_s^+$. The pressure then decays to ambient in total time $t_a + T^+$, drops to a partial vacuum of amplitude P_s^- and eventually returns to p_0 in total time $t_a + T^+ + T^-$. The

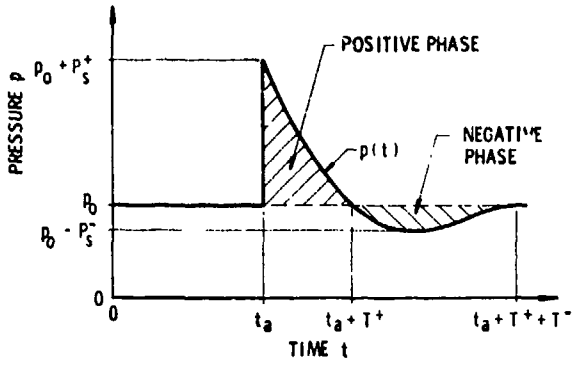


Figure 1-1. Ideal Blast Wave

quantity P_s^+ usually is termed the peak side-on overpressure or merely the peak overpressure. The portion of the time history above initial ambient pressure p_0 is called the positive phase, of duration T^+. That portion below p_0, of amplitude P_s^- and duration T^-, is called the negative phase. Positive and negative impulses, which are defined by the equations

$$I_s^+ = \int_{t_a}^{t_a + T^+} [p(t) - p_0] \, dt \qquad (1\text{-}1)$$

and

$$I_s^- = \int_{t_a + T^+}^{t_a + T^+ + T^-} [p_0 - p(t)] \, dt \qquad (1\text{-}2)$$

are also significant blast wave parameters. Under well-controlled experimental conditions, it is possible to observe the ideal blast wave characteristics*.

1-3.2 FUNCTIONAL FORMS OF PRIMARY SHOCK CHARACTERISTICS

1-3.2.1 PRESSURE-TIME HISTORY

To describe completely the characteristics of the pressure-time history of the "ideal" blast wave, one should specify its form as a function of time. A number of different authors have recommended or used such functional forms, which are based on empirical fitting to measured or theoretically predicted time histories. Primary emphasis has been given to fitting the positive phase.

1-3.2.1.1 POSITIVE PHASE

1. *Two Parameter Form:*

The simplest of these "blast wave shapes" involve only two parameters. Flynn[1]*, in considering blast loading of structures, assumed a linear decay of pressure, given by the equation**

$$p(t) = p_0 + P_s^+ (1 - t/T^+) \qquad (1\text{-}3)$$

where

$$t_a < t \leq t_a + T^+$$

In fitting this form to data, the true value for P_s^+ usually is preserved, and the positive phase duration T^+ is adjusted to maintain true positive impulse I_s^+. One also could adjust the positive phase duration to match the initial decay rate of Eq. 1-3 with that of experimental data, but this would result in an underestimate of the positive impulse. This form is admittedly oversimplified, but it is often adequate for response calculations. Ethridge[2] has shown that a form of the equation

$$p(t) = p_0 + P_s^+ e^{-ct} \qquad (1\text{-}4)$$

where

$$t_a < t \leq t_a + T^+$$

*Where the symbols designating peak pressures, durations, and impulses appear without superscript plus or minus signs later in this handbook, the plus sign indicating positive phase will be implied.

*Superscript numbers refer to References at the end of each chapter.

**In the following equations t_a can be set equal to zero or any other convenient number.

will accurately fit many gage records over most of the positive phase. With this form one also can match the amplitude P_s^+ and the initial decay rate or the amplitude and the positive impulse* with experimental results. Eq. 1-4 is undoubtedly a better representation than the purely linear decay predicted by Eq. 1-3.

2. *Three or More Parameter Form:*

The next more complex formulation involves three parameters. This form, usually termed the "modified Friedlander equation", is

$$p(t) = p_0 + P_s^+ (1 - t/T^+) e^{-bt/T^+} \quad (1\text{-}5)$$

where

$$t_a < t \leq t_a + T^+$$

The additional parameter allows freedom in matching any three of the four blast characteristics P_s^+, T^+, I_s^+, and initial decay rate $\left.\frac{dp}{dt}\right|_{t=0}$.

Ethridge[2] noted that rate of exponential decay in experimental records appeared to decrease with time and he proposed a four-parameter equation to allow still more freedom in matching. This equation is

$$p(t) = p_0 + P_s^+ (1 - t/T^+) e^{-b(1 - ft/T^+)t/T^+} \quad (1\text{-}6)$$

All four of the previously mentioned characteristics could then be fitted, or some additional characteristic introduced in place of one of these four. Brode[3] also has proposed a four-parameter model given by the equation

$$p(t) = p_0 + P_s^+ (1 - t/T^+) e^{-b[1 + g/(1 + ht/T^+)]} \quad (1\text{-}7)$$

to match time histories of positive phase overpressure which he predicted from theoretical calculations of blast waves generated from a point source. The most complex formula to date which has been proposed for fitting positive phase time history data is also due to Brode[4]. This equation, involving five parameters, is

$$p(t) = p_0 + P_s^+ (1 - t/T^+) \left[ae^{-\alpha t/T^+} + (1-a)e^{-\beta t/T^+}\right] \quad (1\text{-}8)$$

Ethridge[2] shows that a very excellent fit of experimental data can be made with this equation.

One can ask the question, "In defining overpressure, which of the Eqs. 1-3 through 1-8 should I use?" No unique answer can be given to this question. All of the equations are strictly empirical. Eqs. 1-3 and 1-4 are simple, but both deviate considerably from some of the observed characteristics of ideal blast waves. The linear decay Eq. 1-3 is inaccurate, and the failure of Eq. 1-4 to return to ambient pressure is inaccurate. Eq. 1-5 is still reasonably simple and allows more accurate matching with observed parameters. Eqs. 1-6 through 1-8 are increasingly complex, but they also allow increasing accuracy in adjusting to experiment or theory. The author feels that one should use the simplest form commensurate with the accuracy he desires for any given analysis. Probably the best compromise is the "modified Friedlander equation", Eq. 1-5, since it does allow adjustment to conform to the most important blast wave properties, and yet it is not too complex.

1-3.2.1.2 NEGATIVE PHASE

The characteristics of the negative phase of the pressure-time history have been ignored almost totally. Probably this is the case because most investigators have felt that the negative phase is relatively unimportant compared to the positive phase, or because they have experienced considerable difficulty in accurately measuring or computing its char-

*Even though the pressure never returns to ambient with this form, I_s^+ is finite.

acteristics. The only proposed functional form for this phase which the author could locate is one due to Brode[3], given by the equation

$$p(t) = p_0 - P_s^- \left[(t/T^-)(1 - t/T^-)\, e^{-4t/T^-}\right] \quad (1\text{-}9)$$

where

$$t_a + T^+ < t < t_a + T^+ + T^-$$

This form is based on Brode's point-source theoretical solution.

1-3.2.2 PARTICLE VELOCITY AND OTHER PARAMETERS

The blast front in its passage through the air not only increases the pressure, but also increases density ρ and temperature θ, and accelerates the air particles to produce a particle velocity u in the direction of travel. If we were to plot time histories of these physical quantities, they would be similar to Fig. 1-1 with the exception that the durations would not necessarily be the same as for pressure-time history.

John Dewey[5] has proposed an empirical equation to fit time histories of particle velocity u for blast waves generated by TNT explosions. This equation, involving four parameters, is

$$u(t) = u_s\,(1 - \beta t)\, e^{-\alpha t} + a\, \ell n\,(1 + \rho t) \quad (1\text{-}10)$$

Dewey notes that the last term in this equation does not agree with theoretical predictions from Brode's theory, but is required to fit experimental data. He attributes the discrepancy to the contribution of afterburning which is not accounted for in Brode's theory.

1-3.3 SECONDARY AND TERTIARY SHOCK CHARACTERISTICS

For any finite explosion source our ideal blast wave also can exhibit numerous repeated shocks of small amplitude occurring at various times after t_a. These are caused by the successive implosion toward the center of rarefaction waves from the contact surface between explosion products and air.* Secondary and tertiary shocks of this nature, sometimes facetiously called "pete" and "repete", have indeed been observed, as can be seen in Fig. 1-2. These later waves have little effect on any of the characteristics of the positive phase of the blast wave with the exception of positive duration T^+. This parameter can be changed quite markedly if a secondary shock happens to arrive just prior to the initial decay reaching p_0. On the other hand, secondary and repeated shocks can markedly affect the negative phase, causing it to be abruptly terminated, or markedly reducing the negative impulse I_s^- or amplitude P_s^-. The only reasonably complete discussion of secondary shocks appears to be that of Rudlin[6] who points out differences in scaled arrival times and overpressures for secondary shocks with type of explosive source and presence or absence of a ground reflecting plane.

1-4 "NONIDEAL" BLAST WAVES

1-4.1 IN FREE AIR

Quite often, the observed characteristics of air blast waves differ in one or more respects from the "ideal" waves which we have just discussed. If the blast source is of low specific energy content, such as a relatively low pressure mass of expanding gas, then the finite pressure pulse generated in the surrounding air may progress some distance before "shocking-up". This phenomenon has been observed by Larson and Olson[7] in measurements of the waves generated by bursting air-filled pressure vessels. The pressure-time histories of waves close to such vessels exhibit rise-times to maximum pressure which are of the same order of magnitude as times for decay back to atmospheric pressure. If the blast source is a cased explo-

*These later shocks for explosions in free air should not be confused with reflected shocks occurring when reflecting boundaries are present.

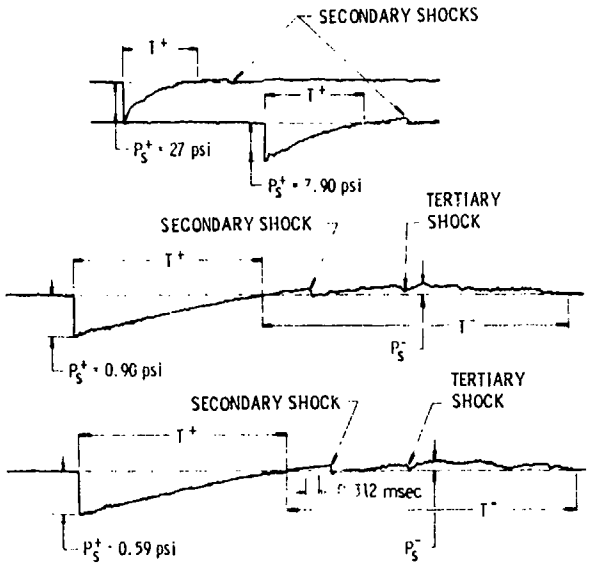


Figure 1-2. Recorded Pressure-Time Histories of Actual Blast Waves from 1-lb$_m$ Pentolite Explosive Spheres

sive charge, recorded time histories of pressure may be quite "trashy" in appearance, that is to say, many small pressure disturbances superimposed on the primary pressure variation of the blast wave. An example is shown in Fig. 1-3. These disturbances are the ballistic shocks generated by fragments of the casing moving at supersonic speed through the air. Because fragment velocities decay less rapidly than blast wave velocity, these fragments outrun the blast wave for some time, and they produce disturbances prior to blast wave arrival*. This effect is shown quite clearly in Fig. 1-3.

Blast waves from sources of shapes other than spherical are affected by the shape of the source. These deviations are, however, quite different from the nonideal effects discussed here. Characteristics of waves from effectively infinite line or plane sources are discussed in par. 1-6 of this handbook, while characteristics of waves from finite sources of various shapes are covered in Chapter 3 of AMCP 706-182, *Explosions in Air, Part Two*[36].

*Eventually the blast wave will catch up to and pass the fragments, because the lower limit for blast wave velocity is sound speed while the lower limit for the velocity of the fragments, which are decelerated by drag, is zero.

1-4.2 GROUND EFFECTS

The character of blast waves from large energy sources detonated near the ground can be modified considerably by certain "ground effects", quite independently of the effects of shock reflection from a relatively rigid surface, which we will discuss later. Thermal radiation from a nuclear weapon may preheat the air near the ground, which causes a severe enough inhomogeneity in the atmosphere near the ground that the subsequent passage of a blast wave is affected seriously. Pressure gages located near the ground then will record decidedly nonideal time histories, as indicated by some typical data reproduced here as Fig. 1-4[8]. The disturbance arriving ahead of the main shock is usually termed a "precursor". In the precursor regime, dynamic pressures** may be much greater than in a region where ideal waves occur. As can be seen from Fig. 1-4, precursor effects tend to disappear, and the blast wave to return to its classical (or ideal) form as the wave moves farther from the blast source. These effects are more pronounced over dusty or heat-absorbing surfaces than over dust-free or heat-reflecting surfaces.

Precursors from a large chemical explosion on the surface of a prairie have been observed by John Dewey[9] to occur along roads compacted in the prairie. He attributed the precursors to strong ground waves, which would have propagated along the compacted roads at greater velocity than through the uncompacted prairie.

The deviations from ideal blast wave characteristics which have been noted are only a few examples of such deviations which can occur. But, small variations in initial sphericity of a shock front, or other small aberration from ideal conditions, usually "smooth out" quite quickly on passage of the blast wave through the air, resulting in relatively ideal blast waves everywhere except close to the blast source. A surprisingly large majority

**Dynamic pressure $q = (1/2)\rho u^2$ where ρ is density and u is a particle velocity.

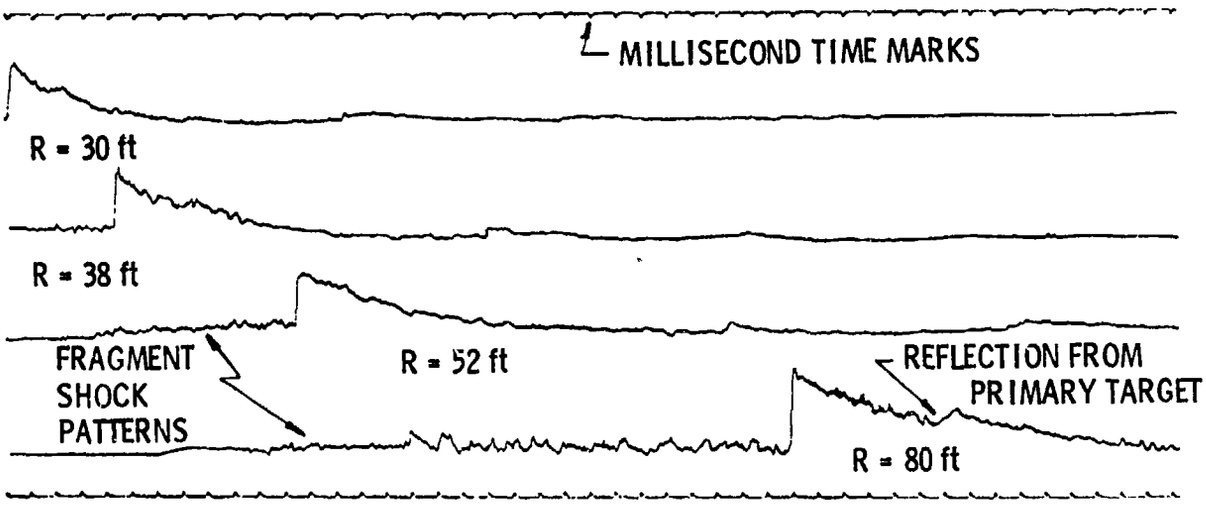


Figure 1-3. P-T Curves Produced by a Cased Charge

of measured blast wave properties agree quite well with those of ideal waves. In other words, the characteristics of the ideal waves discussed earlier are also the characteristics of stable blast waves.

1-5 REFLECTION AND DIFFRACTION OF BLAST WAVES

So far we have considered the properties of air blast waves as they propagate freely through the air. On encountering any solid or dense object, these waves are seriously modified, as they *reflect* from this object and *diffract* around it. Let us now discuss these two phenomena.

1-5.1 REFLECTION OF A PLANE WAVE

1-5.1.1 TYPES OF REFLECTION

1-5.1.1.1 NORMAL REFLECTION

The simplest case of reflection is that of normal reflection of a plane shock wave from a plane, rigid wall. This phenomenon is shown schematically in Fig. 1-5. On the left, the incident wave I is shown just prior to impingement on the wall. It is moving at velocity U into still air whose ambient conditions are designated by the symbols with subscript zero. The conditions immediately behind the shock front are, as indicated, those for the free-air shock wave discussed previously in this chapter. On the right, the front R is shown immediately after reflection from the wall. It is moving away from the wall with a velocity U_r into the flow field and compressed region associated with the incident wave. In the reflection process, the incident particle velocity u_s is arrested ($u = 0$), and the pressure, density, and temperature of the reflected wave are all increased above the values in the incident wave. The overpressure at the wall surface usually is termed the "reflected overpressure", and is designated P_r.* For very weak shocks, $P_s << p_0$, acoustic approximations are valid, and the reflected overpressure is twice the incident overpressure, $P_r = 2P_s$. For stronger incident shocks, the enhancement of reflected pressure is increased. An upper limit often cited in the literature[10] is $P_r = 8P_s$. This limit constitutes a popular misconception and is probably considerably in error, since it is based on the assumption that the air behaves as a perfect gas even at the high pressures and temperatures extant under strong shock conditions. Döering and Burkhardt[11] and Shear and McCane[12] have shown that this ratio can be much greater (perhaps 20 or more) if real gas

*Superscript plus signs for positive phase are implied in this discussion.

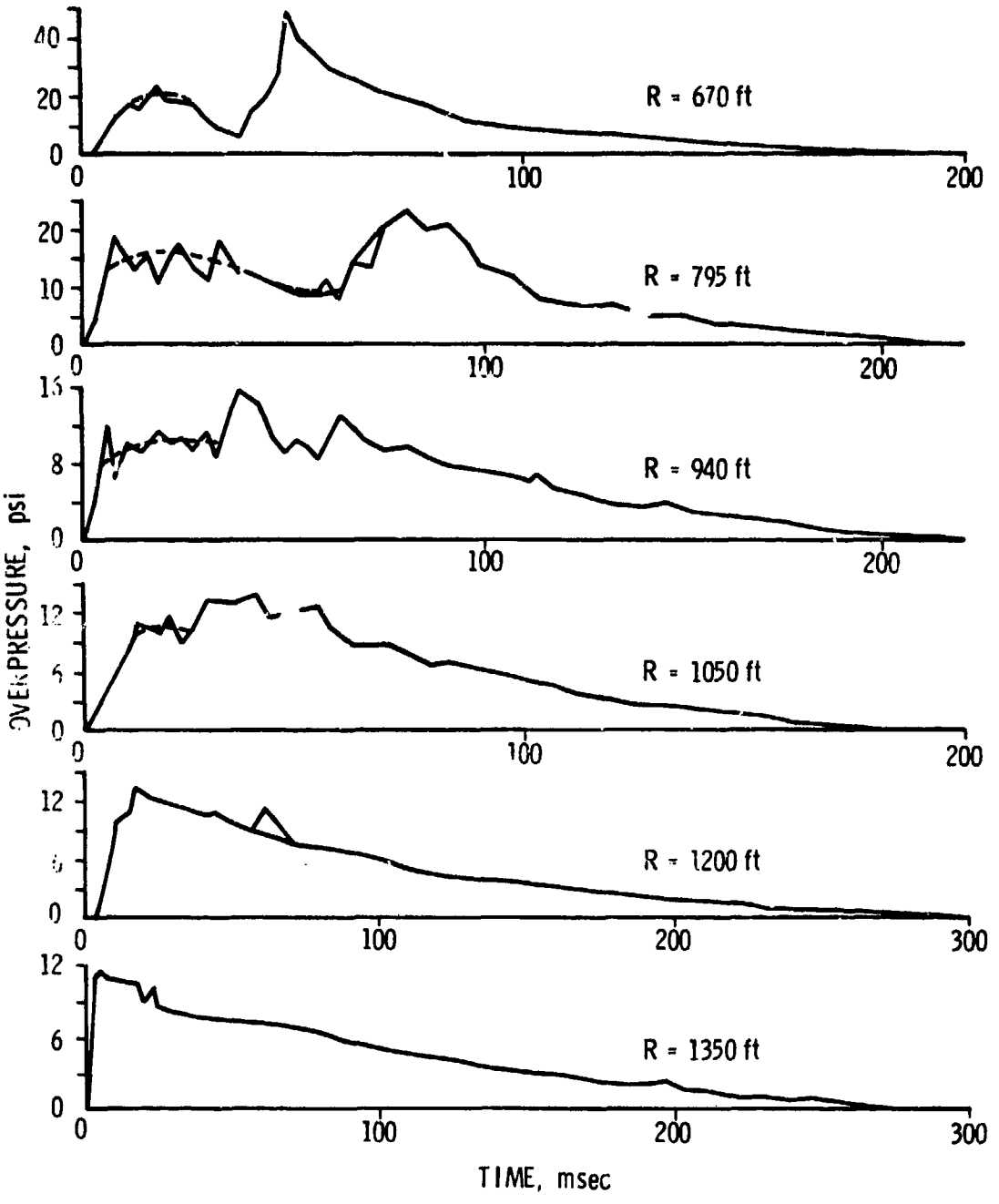


Figure 1-4. Typical Nonideal Pressure Traces Showing Precursor[8]

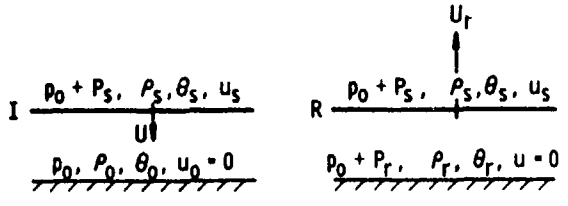


Figure 1-5. Normal Reflection of a Plane Shock from a Rigid Wall

effects such as dissociation and ionization of the air molecules are accounted for.

1-5.1.1.2 REGULAR OBLIQUE REFLECTION

The next case, in order of complexity to the "normal" case of reflection is that of

so-called regular oblique reflection of a plane shock wave from a rigid, plane wall. This phenomenon is illustrated in Fig. 1-6. The incident shock travels into still air (Region ①) at velocity U, with the incident shock front making an angle of incidence α_I with respect to the wall The properties behind this front (Region ②) are those for a free-air shock. On making contact with the wall, the flow behind the incident shock is turned, because the component normal to the wall must be zero, and the shock is reflected from the wall at a reflection angle α_R not necessarily equal to α_I. The symbols in Region ③ indicate the reflected shock properties which are the conditions for that region. A pressure transducer flush-mounted in the wall would record only the ambient and reflected wave pressures (direct jump from conditions of Region ① to those of Region ③) as the wave pattern traveled along the wall, while one mounted at a short distance from the wall would record the ambient pressure, then the incident wave pressure, and finally the reflected wave pressure. Some interesting properties of this regularly reflected shock are:[13]

1. For a given strength of incident shock, there is some critical angle of incidence $\alpha_{I\,crit}$ such that the type of reflection described previously cannot occur for $\alpha_I > \alpha_{I\,crit}$. In the limit of vanishing shock strength, $\alpha_{I\,crit} = 90$ deg; and in the limit of infinite shock strength, $\alpha_{I\,crit} = \mathrm{Sin}^{-1}\ 1/\gamma = 39.97$ deg for air with $\gamma = 1.4$ (see Fig. 54, Ref. 35).

2. For each gaseous medium, there is some angle α' such that for $\alpha_I > \alpha'$ the strength of the reflected shock is greater than it is for head-on reflection. This is given by $\alpha' = (1/2)\ \mathrm{Cos}^{-1}\ (\gamma - 1)/2$. For air (approximated as an ideal gas with $\gamma = 1.40$), $\alpha' = 39.23$. However, it is only for weak or moderate shocks, $p_2/p_1 < 7.02$ in ideal air, that this can occur before regular reflection is forbidden.

3. For a given strength of incident shock, there is some value of the angle of incidence such that for $\alpha_I = \alpha_{min}$ the strength of the reflected shock, P_r/p_0, is a minimum.

4. The angle of reflection α_R is an increasing monotonic function of the angle of incidence α_I.

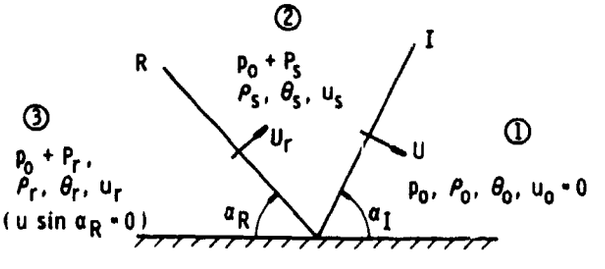


Figure 1-6. Regular Oblique Reflection of a Plane Shock from a Rigid Wall

These properties of oblique shocks – referring respectively to items 1 through 4 for reflected shocks – differ quite markedly from corresponding properties of acoustic waves, which are:

1. Regular reflection occurs for $0 < \alpha_I \leqslant 90$ deg
2. $P_r = 2P_s$ for all values of α
3. $P_r = 2P_s$ for all values of α
4. $\alpha_I = \alpha_R$ for all values of α_R.

1-5.1.1.3 MACH REFLECTION

The next type of reflection, in order of complexity, is Mach reflection of a plane shock wave that is obliquely incident on a plane, rigid wall. As noted in the preceding discussion of regular oblique reflection, there is some critical angle of incidence – dependent on shock strength – greater than at which regular reflection cannot occur. Ernst Mach showed[13], in 1877, that the incident and reflected shocks would coalesce to form a third shock. Because of the geometry of the shock fronts, they are termed "Mach V" or "Mach Y" shock fronts, with the single shock formed by the coalesced incident and reflected shocks normally called the "Mach stem". The geometry of Mach

reflection is shown in Fig. 1-7. In addition to the incident and reflected shocks, I and R, we now have the Mach shock M with the junction T of the three shocks being called the "triple point".* In addition, there is also a "slipstream" S which is a boundary between regions of different particle velocity and different density, but of the same pressure**. When α_I in Fig. 1-6 exceeds $\alpha_{I\,crit}$, the Mach wave M is formed at the wall and grows as the shock systems move along the wall, the locus of the triple point being a straight line AB.

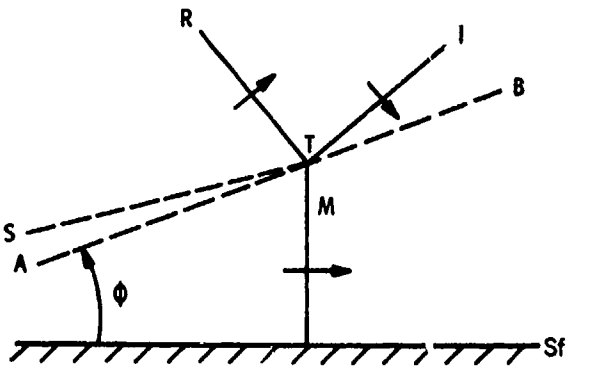


Figure 1-7. Mach Reflections from a Rigid Wall

1-5.1.2 REFLECTION PROCESS

Let us now consider the reflection process for blast waves generated by a finite source and reflected from a rigid, plane wall, using the concepts previously discussed.

1-5.1.2.1 STRONG SHOCK WAVES

In Fig. 1-8 are represented three successive stages in the reflection of strong shocks. The incident wave I_1 resulting from a charge C is first shown just as its front touches the reflecting surface Sf. Normal reflection occurs here, and the pressure above that of the atmosphere on the reflecting surface is more than twice the peak overpressure of the incident wave P_s. The magnitude of the increase of pressure over $2P_s$ is determined by the strength of I_1.

As the incident wave expands to some greater size I_2, the reflected wave R_2 also expands, but the reflected wave is not spherical. The angles at which I_2 and R_2 meet the surface Sf are not equal, as was noted in our discussion of regular reflection. The angle of the reflected shock R_2 is dependent on the strength and angle of incidence of the incident shock.

At some distance from the charge C determined by the distance of C from Sf and by the strength of the incident shock, a new phenomenon occurs. The intersection of *R* and I no longer lies on Sf but lies above it and follows some path A. A new shock front M, the Mach stem, connects the intersection of R and A to the surface. The intersection of R, A, and M is called the triple point T. As the shock system expands further, the Mach stem grows rapidly, tending to swallow up the two-shock system above it. If C is very close to the surface, but not on it, the Mach stem is formed almost directly under C and, in a short time, will grow until most of the shock system becomes a Mach stem and R and A remain distinct in only a small region directly over the charge. If the charge C is on the surface Sf, no separate reflection R is formed, and the entire stock wave can be considered a Mach wave.

A very practical property of the reflection of shocks is that the pressure (and positive impulse) in the neighborhood of the triple point and in the Mach stem itself is considerably greater than that of the incident shock wave I_3, or in the shock which would have been emitted if C were in contact with Sf. That is, if C is a bomb bursting above the ground, represented by Sf, the intensity of the blast in the region M and just above it is greater, for a given horizontal distance from the bomb, than would have been the case if the bomb had been burst in contact with the ground.

*The junction T is in fact a line of intersection of the three shock fronts rather than a point.

**The slipstream should not be confused with a contact surface, defined in Chapter 2. A contact surface is a boundary between regions of different density and/or temperature, but with the same pressure and particle velocity.

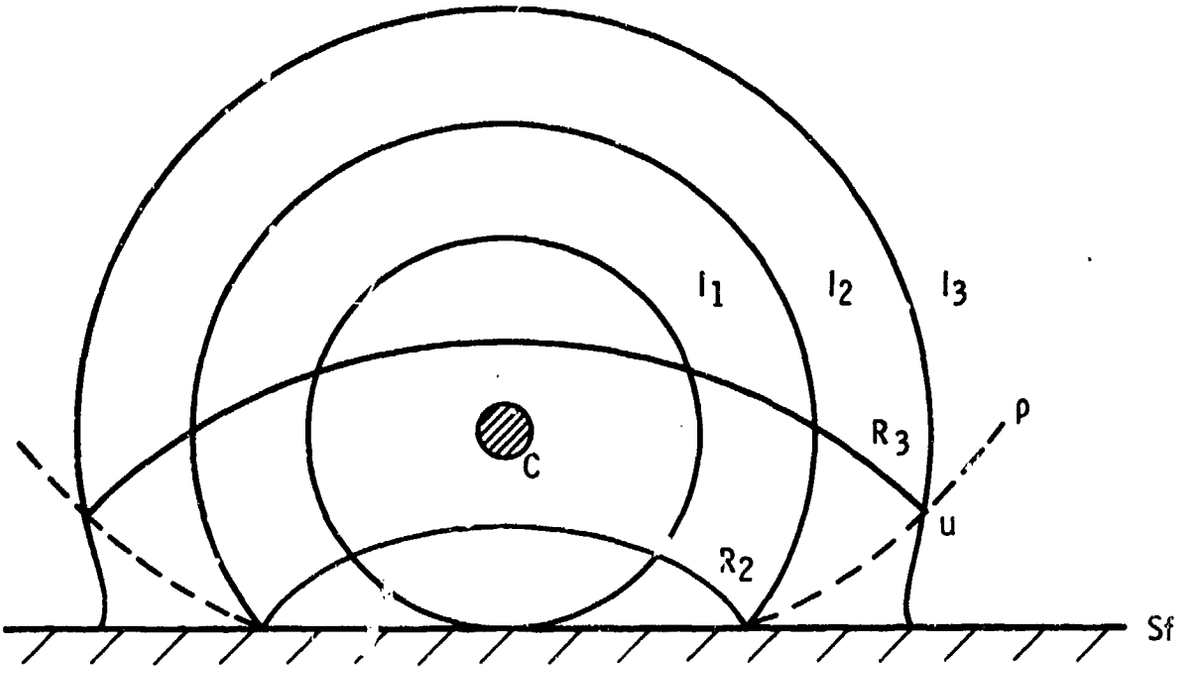


Figure 1-8. Reflection of Strong Shock Waves

In Fig. 1-9 the geometry of the Mach reflection process can be seen in more detail. By comparison with Fig. 1-7, one can see that incident and reflected shocks are both curved, and that the path of the triple point is no longer a straight line. Although the Mach stem is shown as a vertical straight line in Fig. 1-9, this is not always the case in reality.

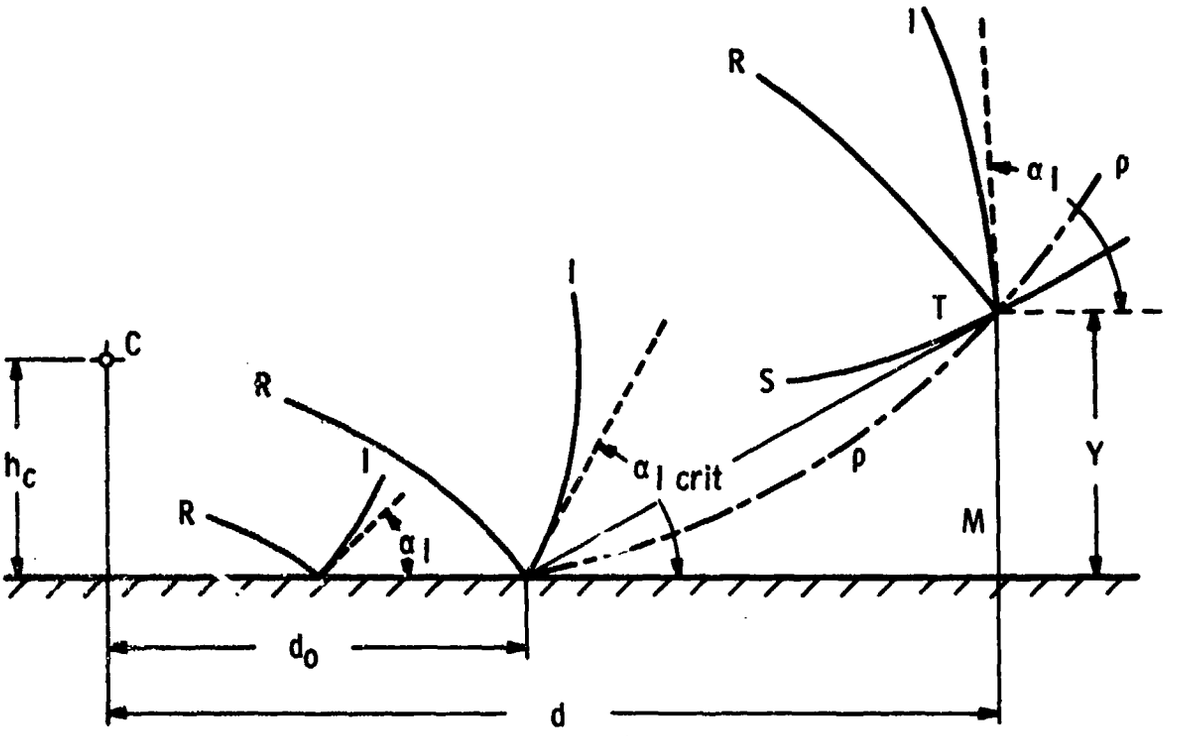
1-5.1.2.2 WEAK SHOCK WAVES

Very weak shock waves, i.e., those of nearly acoustic strength, are reflected from plane surfaces in such a way that a geometrical construction of the wave system can be made very simply. Consider a point source of the shock C (Fig. 1-10) and, some distance from it, a plane reflecting surface Sf. The incident wave I, striking the surface, will be reflected from it in such a way that the reflected wave R may be considered to arise from a second image source C′ which is on the opposite side of the reflecting surface, on a line perpendicular to Sf through the true source, and at a distance from Sf equal to the distance of C from the surface.

Fig. 1-10 shows two successive stages of this reflection process. In the first stage the incident wave I_1 is just tangent to the surface. The excess pressure over that of the atmosphere at the reflecting surface is just double (for very weak shock waves) that of the incident wave where it is not in contact with the surface. At a later stage, the incident wave is represented at I_2 and the reflected wave at R_2, which is imagined to arise from the image source C′. Again, the pressure at the line of contact of I_2, R_2, and the surface Sf is just double that at I_2 where it is not in contact with the surface. The angles at which the shocks I_2 and R_2 meet the surface Sf are equal, and no Mach stem is formed. For most practical cases of interest in air blast technology, shocks are too strong for this acoustic approximation to be applicable, and this simplified geometry cannot be used.

1-5.2 DIFFRACTION OF A PLANE WAVE

When a blast wave encounters a solid object of finite extent, very complicated processes



Y = height of Mach stem

h_c = height of charge above reflecting surface

d_0 = horizontal distance for start of formation of Mach stem

d = any horizontal distance $> d_0$

Figure 1-9. Geometry of Mach Reflection

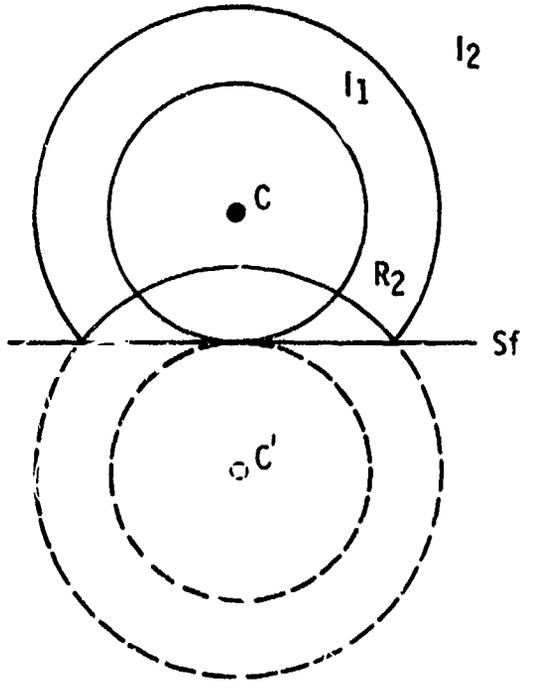


Figure 1-10. Reflection of Weak Shock Waves

ensue. The interaction of the shock front with such obstacles is termed *diffraction.*

The phenomenology to be described indicates the complexity of the diffraction process for even the very simple case of passage of a plane shock wave over obstacles of very regular geometry. For more complex shapes, or for different blast orientations, or for curved shock waves, the processes are even more complicated. Many shock-tube experiments have been conducted to determine diffracted shock configurations and pressures (in fact, the discussion that follows is based on the results of such experiments). The reader is referred to Refs. 15 through 23 for comprehensive studies of the diffraction process.

1-5.2.1 TWO-DIMENSIONAL RIGID THICK WALL

The diffraction process can perhaps best be illustrated by describing the sequence of

events occurring when a plane blast wave traveling over a rigid plane encounters a rigid, thick wall protruding from the plane, as illustrated in Fig. 1-11(A). The geometry is shown in the first sketch of this figure, with the blast front being normally incident on the front face of the wall, and the pressure on all faces on the wall being at ambient pressure p_0. As the incident wave I first encounters the wall, reflection of the portion of the wave striking the front face of the wall occurs; the reflected wave R moves to the left, and the pressure on the front face jumps to $p_0 + P_r$. Above the wall, the incident waves continue on relatively undisturbed.

As the reflected wave moves to the left away from the front face of the wall, a rarefaction front moves down the front face, as shown in Fig. 1-11 (B). A vortex is shed from the upper lefthand corner at the wall. A vortex is a region of air spinning about an axis at a high speed. Low overpressures exist at its center because of the Venturi effect. At the instant depicted in Fig. 1-11 (B), the lower portion of the front face still feels the reflected pressure $p_0 + P_r$, while the upper portion feels a lower pressure quite near the pressure $p_0 + P_s$ in the incident wave. The portion of the top face behind the incident shock I is subjected to pressure $p_0 + P_s$, with the pressure perhaps somewhat reduced below

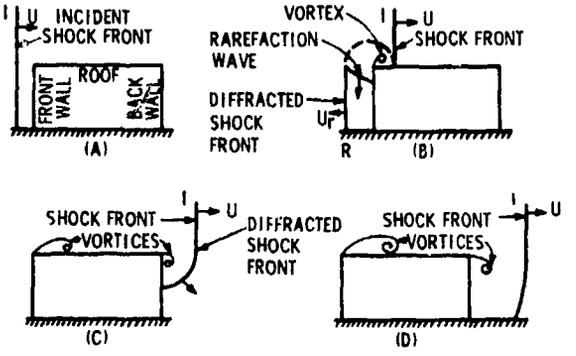


Figure 1-11. Diffraction of a Shock Front Over a Wall[16]

(Reprinted by permission of C. H. Norris, R. J. Hansen, M. J. Holley, Jr., J. M. Biggs, S. Namyet, and J. K. Minami, Structural Design for Dynamic Loads, McGraw-Hill Book Co., N.Y., 1959.)

this value in the vicinity of the vortex. Ahead of the incident shock, the pressure on the top face and on the rear face of the wall is still p_0.

As the incident shock front passes beyond the rear face of the wall, it diffracts around this face, as shown in Fig. 1-11(C). A second vortex is formed at the upper righthand corner of the wall. At the instant shown in Fig. 1-11 (C), the reflected wave from the front face of the wall has been completely attenuated by the rarefaction wave, and the pressure on the front face is $p_0 + q$, where q is dynamic pressure. On the top face the pressure is still nearly equal to $p_0 + P_s$. Behind the diffracted incident wave on the rear face, pressure is somewhat less than $p_0 + P_s$. Ahead of the front I, the pressure is p_0. The maximum back wall pressure develops slowly as a result of vortex phenomena and the time required for the back wall to be enveloped by the blast. In the final stage, the incident wave has passed beyond the wall, the diffraction process is over, and the wall is immersed in the flow field behind the front. For a long-duration blast wave, pressures are nearly those which would be measured in steady-state wind tunnel experiments.

1-5.2.2 THREE-DIMENSIONAL BLOCK

For a three-dimensional block structure, the phenomena described in par. 1-5.2.1 also occur along the sides of the block, so that the preceding discussion also applies to diffraction about the sides of such structures. This process is illustrated in Fig. 1-12. Fig. 1-13 gives recorded pressure-time histories for the front, top, and back faces of a model three-dimensional block structure, as recorded in shock tube at BRL[33]. The pressure-time history for the front face of the block shows reflected pressure (initially P_r) and the effect of the rarefaction wave produced at the front face which causes rapid reduction in reflected pressure. The pressure recorded on the top face of the block shows an initial peak of side-on pressure P_s and a less rapid pressure decay. The pressure recorded at the back face of the block shows a slow rise time of pressure with no real "shocking-up". Detailed

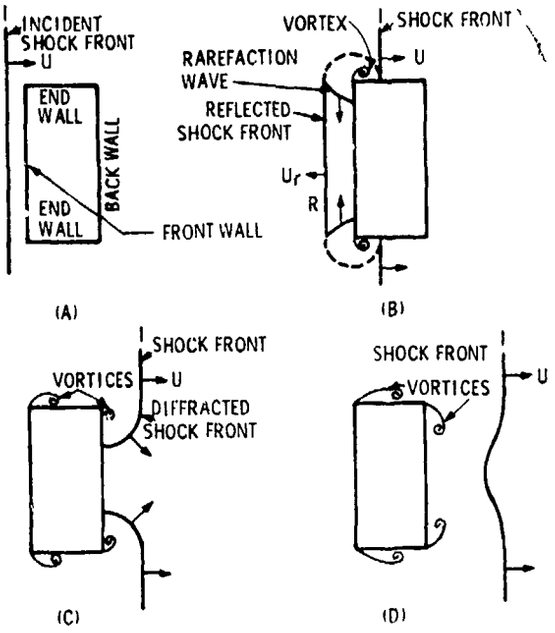


Figure 1-12. Diffraction of a Shock Front Over a Three-dimensional Block Structure (Plan View)[16]

(Reprinted by permission of C. H. Norris, R. J. Hansen, M. J. Holley, Jr., J. M. Biggs, S. Namyet, and J. K. Minami, Structural Design for Dynamic Loads, McGraw-Hill Book Co., N.Y., 1959.)

loading of another three-dimensional structure is given in a report by Janus and Kingery[34].

1-5.2.3 CIRCULAR CYLINDER

In Figs. 1-14 and 1-15 are shown the sequence of events involved in diffraction of a blast wave about a circular cylinder[15]. In these figures the shock fronts are shown as thick lines and their direction of movement by arrows normal to the shock front. In Fig. 1-14(A), the incident shock has collided with the cylinder giving rise to a curved, expanding, reflected shock R. In Fig. 1-14(B), the incident shock I and reflected shock R are now joined to the cylinder surface by a Mach stem M. R is now much weaker than in Fig. 1-14(A) and is omitted in the succeeding parts of the figure.

In this shock configuration a slipstream S has been formed. This slipstream is a line dividing flows of differing densities, but of the same pressure. When a Mach stem is formed on a plane surface the slipstream

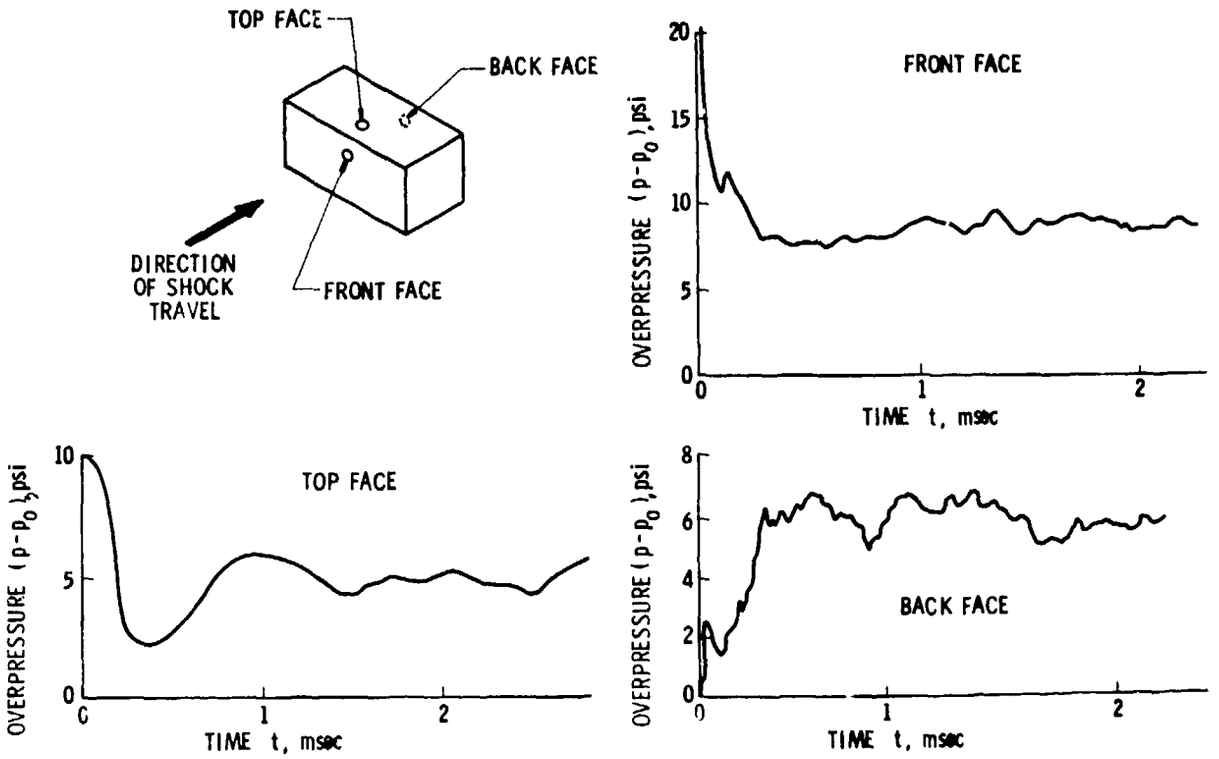


Figure 1-13. Pressures on a Three-dimensional Block Structure During Diffraction[33]

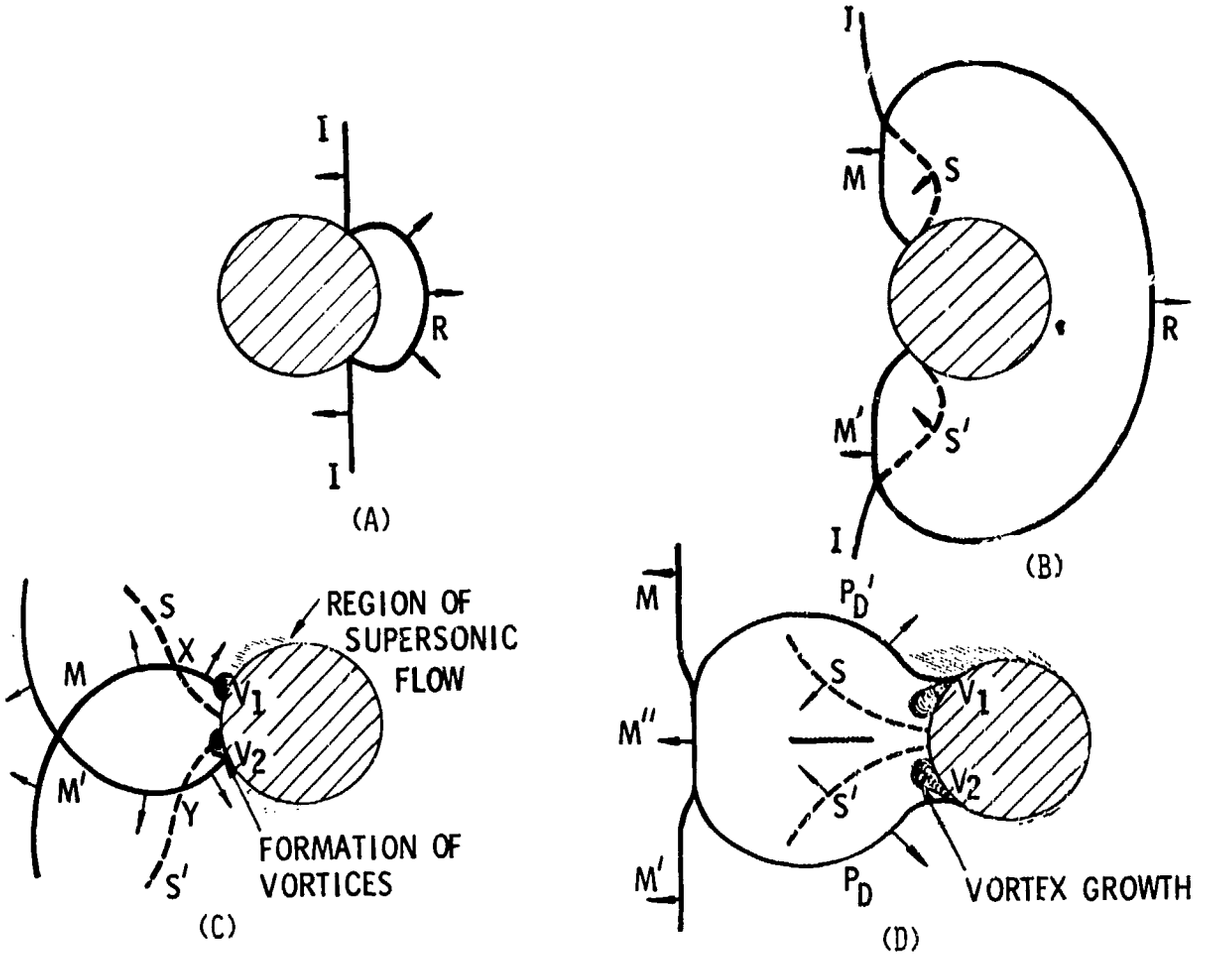


Figure 1-14. Tracings of Shadowgraphs Showing the Interaction of a Shock Front With a Cylinder

extends upstream, slanting down to meet the surface. In the present case, however, the increased flow near the cylinder surface has caused the foot of the slipstream to move nearer to the foot of M. The slipstream, therefore, presents a curved appearance. In Fig. 1-14(C), the feet of the Mach stems have reflected from each other and are now moving on a second circuit of the cylinder. The slipstreams have been swept nearer the rear of the cylinder and now intersect with the diffracted parts of the Mach stems X and Y. The commencement of two vortices is indicated at V_1 and V_2. These are probably induced by the back pressure behind the shocks X and Y interacting with the boundary layer flow at the surface of the cylinder. The shaded portion is due to a localized region of supersonic flow. In Fig. 1-14(D), the Mach stems, M and M′, have moved some way downstream of the cylinder. A Mach stem M″ joins the free air parts of M and M′ with the diffracted parts P_D and P'_D which terminate on the cylinder surface. The growth of the vortices is apparent in this figure. In Figs. 1-15(A) and (B), the foot of P_D has moved further round the cylinder upstream. Notice that the point of flow separation has followed this shock. In Fig. 1-15(C), the vortices, V_1 and V_2, are breaking away from the cylinder; while in Fig. 1-15(D), the vortices are being swept downstream, and the point of flow separation has moved toward the rear of the cylinder again.

The phenomenology described indicates the complexity of the diffraction process for even the very simple case of passage of a plane

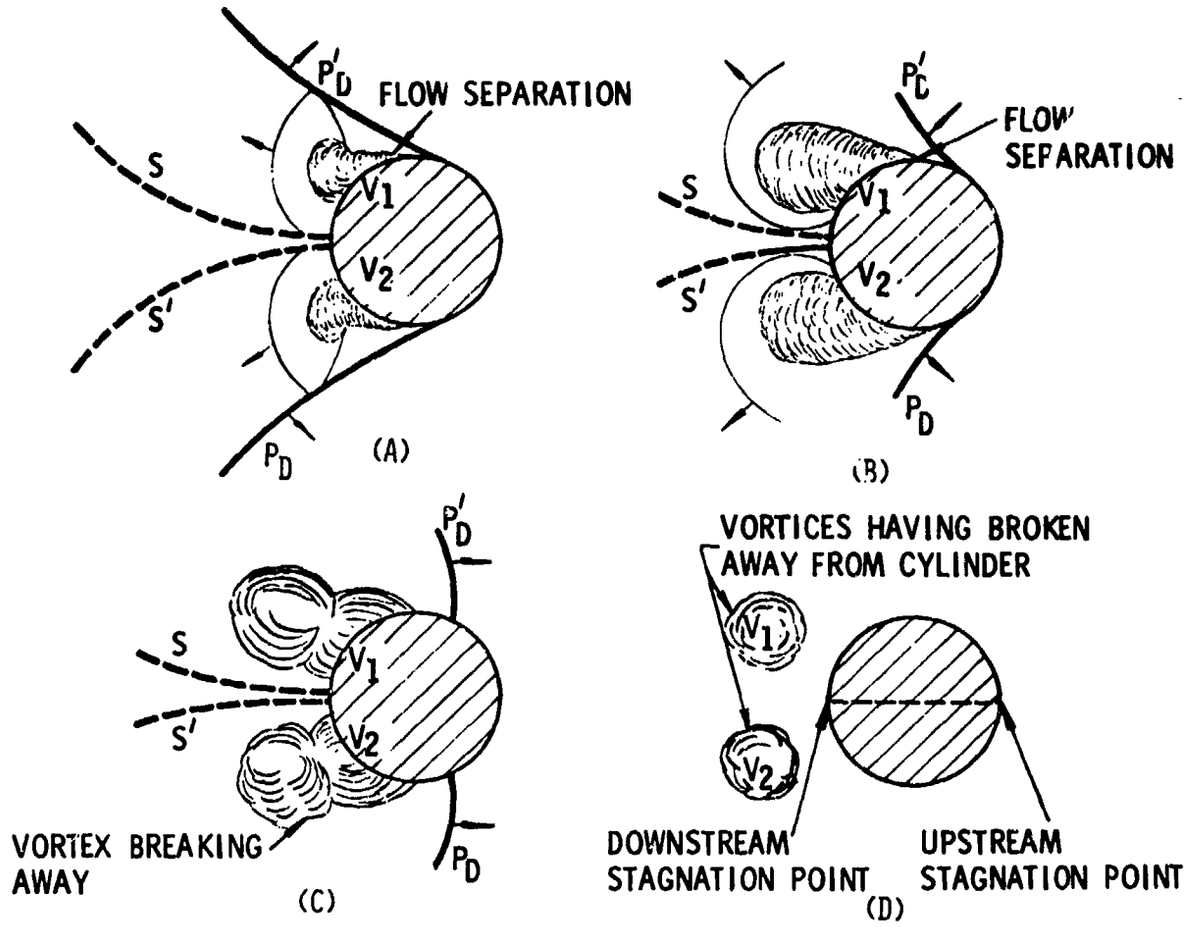


Figure 1-15. Tracings of Shadowgraphs Showing the Interaction of the Shock Front With a Cylinder

shock wave over obstacles of very regular geometry. For more complex shapes, or for different blast orientations, or for curved shock waves, the processes are even more complicated. Many shock-tube experiments have been conducted to determine diffracted shock configurations and pressures (in fact, the discussion is based on the results of such experiments). The reader is referred to Refs. 16 through 23 for comprehensive studies of the diffraction process.

1-6 EFFECTS ON BLAST WAVES

1-6.1 SHAPE OR ASYMMETRY OF SOURCE ON BLAST WAVES

1-6.1.1 COMMON SHAPES

In most air blast theoretical work, the source of blast energy is assumed to be a point or a sphere, so that the blast wave characteristics are a function of one space dimension only, i.e., the radial distance from the center of the source. Similarly, in most air blast experimentation, great pains are taken to make the source as spherical as possible so that comparisons can be made with one-dimensional theory, or to eliminate the effects of shape of source. Many real blast sources, however, are distributed or highly directional. Detonating cord is widely used in explosive operations, and it is essentially a line source rather than spherical. Explosive in the form of thin sheets is also now widely used, and it represents a plane source. The gases released from gun muzzles after exit of projectiles are important sources for blast waves, and they represent axisymmetric but highly directional sources. Let us now discuss some of the effects of shape or asymmetry of the source on blast wave characteristics.

1-6.1.1.1 STRAIGHT LINE CHARGE

For straight line charges which are very long compared to their diameters, Kennedy[13] reports that both theoretical and experimental studies indicate blast waves that are similar in their general characteristics to the waves from spherical or "blocky" sources but which have much less rapid decay of pressure and impulse with distance. In fact, for such line charges, a different scaling law usually is applied than the commonly used Hopkinson blast scaling (see Chapter 3). The peak overpressure P_s is a function of $R/(W/L)^{1/2}$ rather than $R/W^{1/3}$ where distance L is measured normal to the charge axis. Similarly, the scaled positive side-on impulse $I_s/(W/L)^{1/2}$ is a function of $R/(W/L)^{1/2}$, rather than the scaled impulse $I_s/W^{1/3}$ being a function of $R/W^{1/3}$. To explain, the shock front expands cylindrically rather than spherically, but it is still a function of only one space coordinate, provided one considers distances which are short compared with length of the line source, i.e., $R << L$ – where R is the distance from the blast center and L is the larger characteristic dimension of the blast source.

1-6.1.1.2 MUZZLE BLAST

Muzzle blast waves from guns are axisymmetric but not spherically symmetric. They usually consist of a single shock front (see Fig. 1-16), but one which has highly directional properties near the muzzle. The general characteristics at any point in the blast field are nearly similar to those of spherical sources, but the difference is that the muzzle blast field characteristics are a function of two spatial cylindrical coordinates, (r, z) rather than one spherical coordinate R. Divergence is more nearly spherical than for line charges, but it is definitely a function of the two cylindrical coordinates r and z.

1-6.1.1.3 LARGE PLANE CHARGE

Blast waves generated by a large, plane source, such as a thin sheet of explosive or a blanket of woven detonating chord, decay even more slowly with distance from the

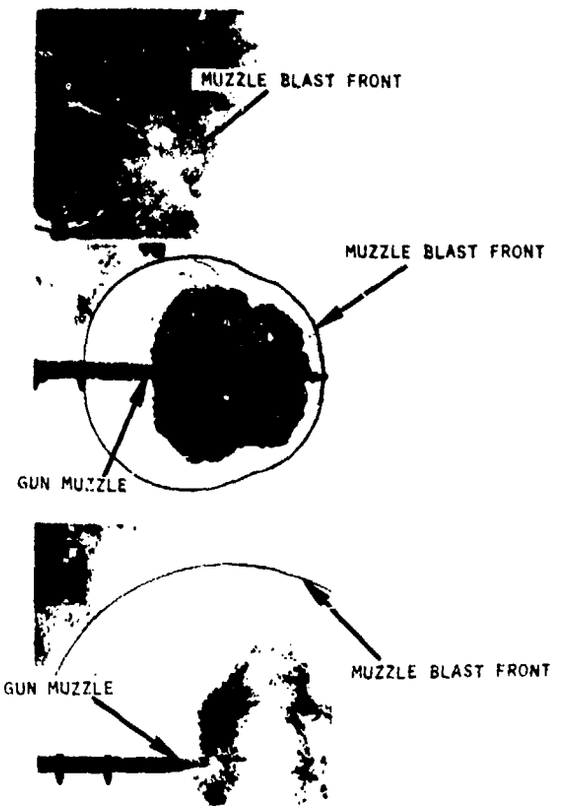


Figure 1-16. The Blast Wave from a 7.62 mm Rifle at Three Stages of Expansion

(Courtesy of Royal Armament Research and Development Establishment)

source than do waves from line sources. Lindberg and Firth[24] have compared theoretically predicted variations in peak overpressure with distance for spherical, infinite cylindrical (line), and infinite plane blast sources (see Fig. 1-17). The scaled distance parameter R/r_o in their plot is based on characteristic dimension r_o which is defined as

$$r_o = E/[p_0 L^{(3-\nu)}]^{1/\nu} \quad (1\text{-}11)$$

where

ν = 1,2,3, respectively, for plane, cylindrical, and spherical blasts
E = total explosive energy.

1-6.1.2 DISTANCE EFFECT

Any real blast source is, of course, finite in extent, so that the idealization of infinite line

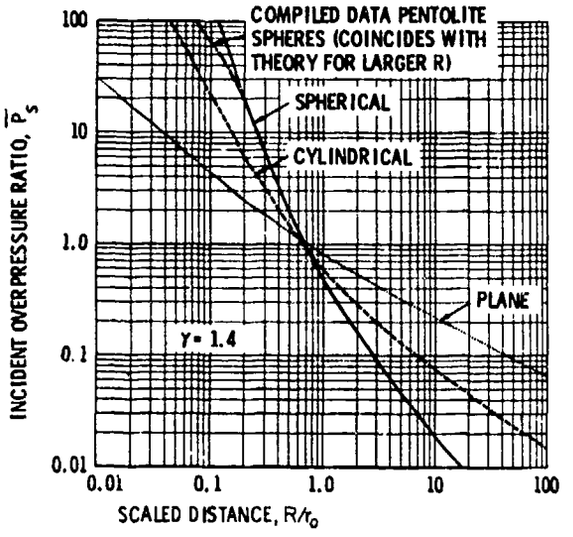


Figure 1-17. Incident Shock Overpressure Ratio vs Scaled Distance[24]

or plane sources only can give reasonable approximations for small distances from the sources. As one moves further from a real, nonspherical source, i.e., for $R >> L$, the blast front tends to more closely approximate that of one which would have emanated from a spherical blast source. All effects of asymmetry of the new spherical source disappear and, for $R >> L$, waves from two sources having the same total energy but very different shapes become indistinguishable.

1-6.2 LONG-RANGE FOCUSING

1-6.2.1 HOMOGENEOUS MEDIUM

As a blast wave is propagated through the air to great distances from its source, it weakens and decreases in shock velocity until it is propagating at essentially the speed of sound. If the air were a homogeneous, still medium, then acoustical laws still apply; the velocity of propagation would be constant, and the pressure in the front would decrease as the inverse of the distance. Because the head of the wave would now be moving at nearly the same velocity as the tail, the duration of the very low magnitude positive overpressure eventually should reach some nearly constant value. In fact, the entire time history should approach essentially a constant functional form, changing only in amplitude as it advances. Such acoustic asymptotes for overpressure, duration, and positive phase impulse are given in Chapter 6.

1-6.2.2 INHOMOGENEOUS MEDIUM

If the orderly behavior described in par. 1-6.2.1 were indeed always observed in the transmission of air blast waves over long distances, then long range focusing of blast waves would be of minor interest. The shock wave characteristics from even very large energy blast sources would decrease rapidly to their acoustic asymptotes; and the amplitudes and durations of the resulting weak pressure waves could be estimated by extrapolation from measured time histories, using the acoustic law for inverse decrease in pressure with increase in distance from the blast source. Such a procedure has been followed by Perkins, et al.[25] in estimating the side-on overpressures at large distances from TNT explosive charges detonated on or near the ground (see Fig. 1-18). Unfortunately, the atmosphere cannot be considered a homogeneous, still medium over any appreciable distance from a given location on the ground; and the variations in meteorological conditions—such as wind velocity, temperature, and perhaps relative humidity—seriously can affect the propagation of air shocks at long distances.

Berning[26] points out that the phenomenon of unusual sound or blast propagation has been known for many years, dating back even to the era prior to the Civil War. Successive zones of audibility and silence along radial lines from the blast centers of severe explosions or artillery fire have been noted by many observers. Complaints of damage from blast waves at long distances from the source have emphasized the fact that some kind of *"constructive"* or *"destructive"* focusing of blast waves can occur at long distances. It is termed "constructive" from the point of view of the blast physicist, who notes that the blast pressure is enhanced; it is termed "destructive" from the point of view of the homeowner, whose windows are shattered or walls are cracked.

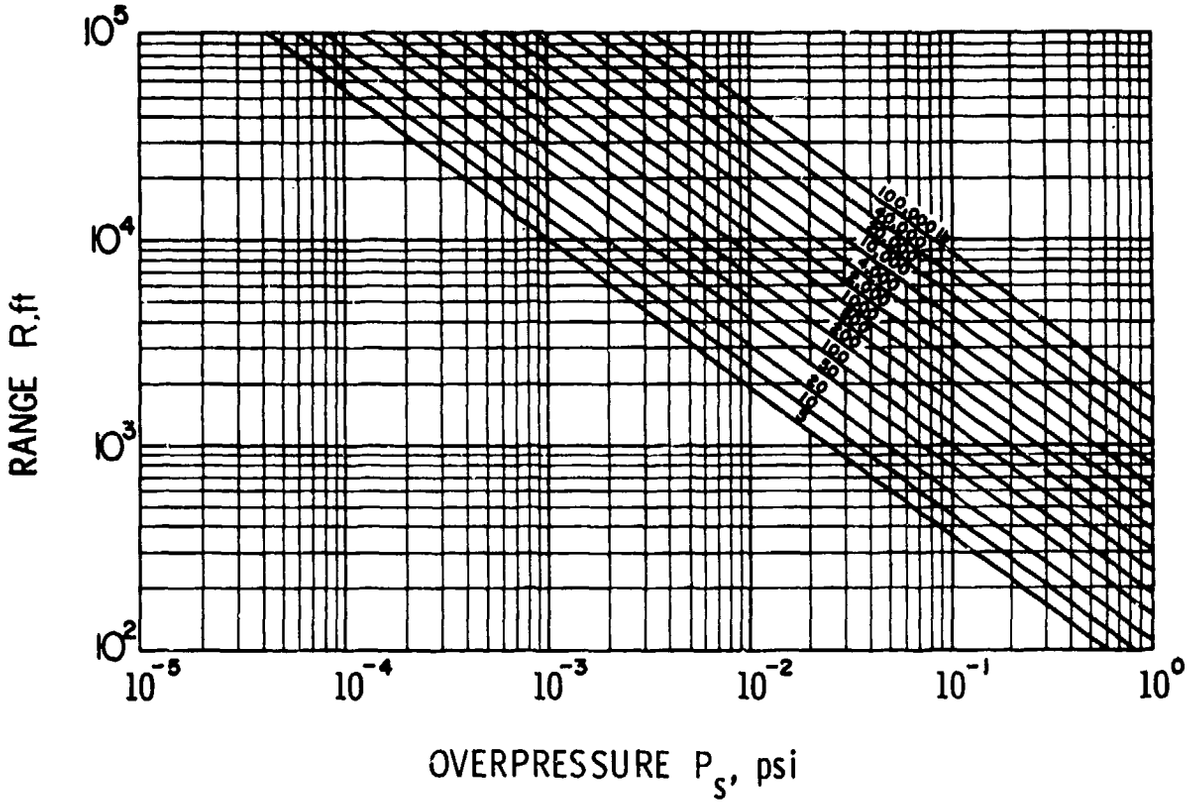


Figure 1-18. Surface Air Blast Pressure vs Range from Detonations on the Surface[25]

1-6.2.2.1 THEORY

A theory for propagation of blast waves over long distances has been developed by Berning[26], under the assumptions that the blast wave can be treated as a sound wave, and that only wind and air temperature have appreciable effect on propagation velocities. This theory, based on earlier work by Fujiwhara[27] and Milne[28], utilizes Lord Rayleigh's concept of "rays of sound" which represent the changing direction of propagation of the sound waves. Equations for these sound rays are given as functions of the gradients in sound velocity with increasing altitude (caused by the variation in temperature and wind shear with altitude) and of the initial angle of inclination of a given sound ray. A typical sound velocity gradient and the corresponding ray paths are shown in Figs. 1-19(A) and (B), respectively. From this theory, one can determine the *location* of areas in which focusing could occur, provided one has accurate data on wind and temperature structure of the atmosphere in the neighborhood of the blast source. One cannot as easily determine the *magnitude* of the increased blast pressure. Some estimates can

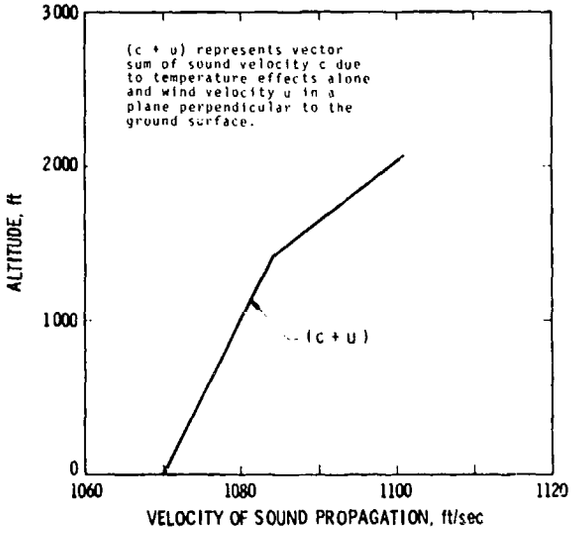


Figure 1-19(A). Typical Sound Velocity Gradient

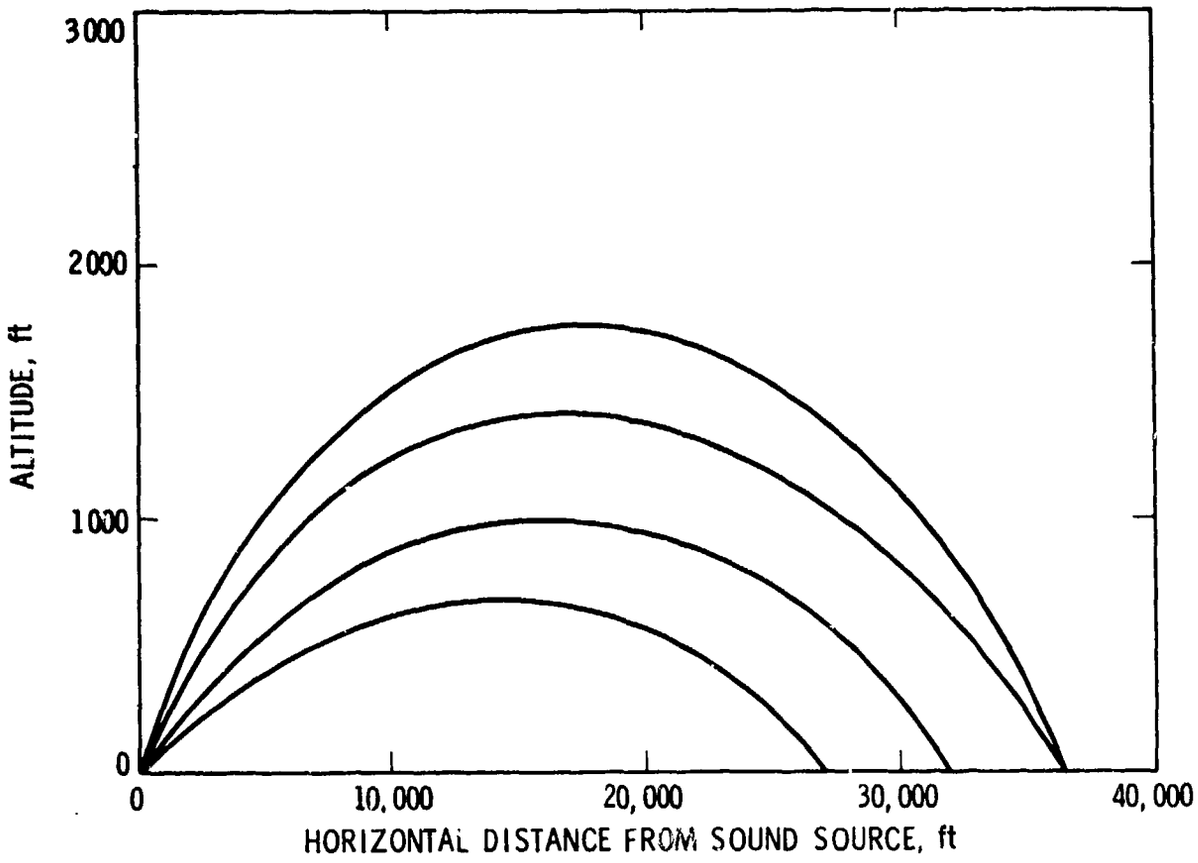


Figure 1-19(B). Paths of Sound Rays in the Atmosphere, for Sound Velocity Gradient of Fig. 1-19(A)

be made based on empirical observations of pressures and damage to light structures or glass. Perkins, et al.[25] have done this, and they have correlated blast strengths with various velocity gradients. They report their estimates in terms of factors which multiply the blast overpressures predicted by the homogeneous atmospheric case (Fig. 1-20). The multiplication factors for various types of gradients are illustrated in that figure.

1-6.2.2.2 PRACTICE

In practice, the application of Berning's relatively simple theory for the prediction of focusing can be quite tedious and time consuming. One must obtain data on the temperature and wind velocity and direction, as a function of altitude up to at least 10,000 ft. These data must be translated into sound velocity gradients along a number of azimuths through the blast source location. The equations must then be solved for each separate azimuth and for a number of sound rays. All of the calculations must be performed quite rapidly so that the meteorological conditions do not change appreciably in the meantime. If much firing is anticipated at a test site, it may prove advisible to automate as much of this procedure as possible. Perkins, et al.[25] report the use of an analog computer for solution of the equations involved, and the acquisition of a library of velocity gradients and corresponding focus predictions at Aberdeen Proving Ground over a period of several years. They found that prediction of focus conditions often could be made with sufficient accuracy by comparing the existing current velocity gradients with those in the library. Using this procedure, and allowing testing to occur only on days when no focus was predicted in inhabited areas, they were able to reduce

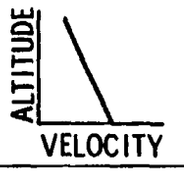
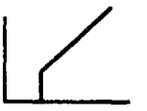
CATEGORY	DESCRIPTION		MULTIPLICATION FACTOR
1	SINGLE NEGATIVE GRADIENT		0
2	SINGLE POSITIVE GRADIENT		5
3	ZERO GRADIENT NEAR SURFACE WITH POSITIVE GRADIENT ABOVE		10
4	WEAK POSITIVE GRADIENT NEAR SURFACE WITH STRONG POSITIVE GRADIENT ABOVE		25
5	NEGATIVE GRADIENT NEAR SURFACE WITH STRONG POSITIVE GRADIENT ABOVE		35

Figure 1-20. Various Types of Velocity Gradients To Be Expected and the Increase in Intensity at a Focus for Each Type

markedly the incidence of complaints and claims of damage from these areas as a result of the firing of large weapons and detonation of large explosive charges.

Procedures similar to those developed by Berning[26] and Perkins, et al.[25] have been employed at a number of other test sites to control the incidence of focusing effects from large blast sources. An excellent general discussion of the overall problem of effects of long-range blast focusing and of the difficulties in obtaining accurate estimates of these effects is given by Reed[29], who was concerned with side effects of cratering with nuclear explosives. Reed also includes an extensive bibliography on the subject in his report. He uses the adjective "caustic" to indicate exceptional disturbances at long ranges. Figs. 1-21 and 1-22 are illustrations of typical vertical sound velocity profiles and resulting distortions and focusing of ray paths[29].

1-6.3 VARIATION OF TYPES OF ENERGY SOURCE

Most of the available experimental data and analyses of blast waves in air are limited to a few types of chemical explosives (usually either TNT or Pentolite) and to nuclear explosives. What are the effects for other explosives or other types of blast sources?

1-6.3.1 CHEMICAL EXPLOSIVES

During World War II, the British and Americans conducted many tests with different types of chemical explosives in attempts to optimize blast damaging effects. They

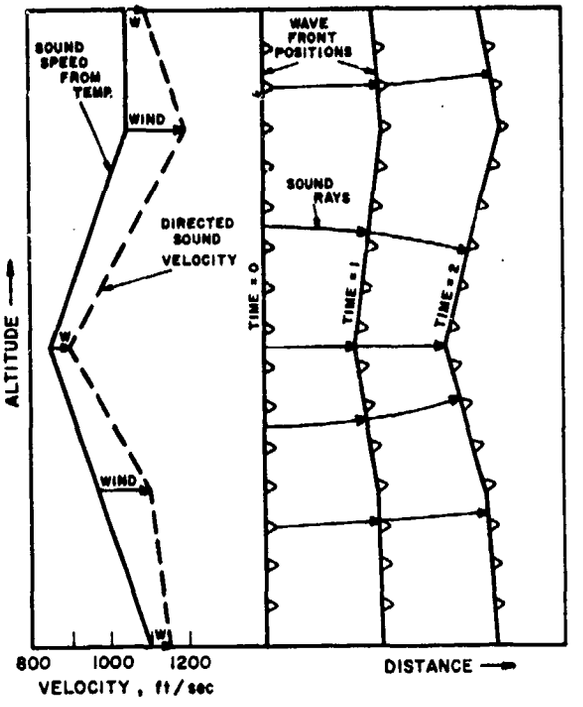


Figure 1-21. Shock Wave Distortion by Layered Atmospheric Temperature and Wind Structure[29]

found that a number of explosives generated blast waves of measurably different peak pressure and impulse from those of a "standard" explosive of their choosing. In particular, those explosives which contained significant quantities of aluminum powder exhibited those differences.* Kennedy[13] has summarized much of this early work, and he has noted that the general characteristics of blast waves from different chemical explosives are quite similar—their relative peak overpressures and impulses being essentially independent of distance from the charge. Results, of measurements over a number of distances, therefore, could be averaged and quoted as ratios applicable over all distances. Such ratios for a number of explosives, relative to Composition B, are shown in Table 1-1[13]. Comparisons for other explosives are given in AMCP 706-182(S), *Explosions in Air, Part Two* (U).

Because the ratios for peak pressure and impulse do not differ greatly, one can approximately equate blast waves from different explosives by using a conversion to an "equivalent weight" or "equivalent energy" of some standard explosive which is usually TNT. This conversion is a multiplier which would cause the blast data for the other explosive to coalesce with TNT data, as nearly as possible. This coefficient for Pentolite is usually assumed to be about 1.1 X TNT. Note that it is not equivalent to the coefficients given in Table 1-1, or their inverses. While not exact, this method offers a way of estimating blast for explosives where limited data exist. Sometimes the conversion coefficient can be estimated from ratios of the heats of detonation for a new explosive to that of TNT, with these heats of detonation being measured in a bomb calorimeter. Note from Table 1-1, that, although blast parameters are *measurably* different for different chemical explosives, the entire range of differences is not great. A maximum coefficient of 1.5 covers the entire range of peak pressures and impulses, for all the explosives compared on an equal volume basis. One, therefore, should view with caution claims for vastly superior chemical explosives for generating air blast.

1-6.3.2 NUCLEAR EXPLOSIVES

Nuclear explosives differ from chemical explosives in their ability to produce air blast waves primarily because of the sheer magnitude of their total energy release, and because of the difference in energy density between the two types of explosive sources. Close to a nuclear weapon burst, the blast overpressure will be greater than that from a scaled chemical explosion of the same effective blast yield. At greater distances, the blast waves will be quite similar[30]. In comparing blasts from TNT and nuclear explosives at sea level, the total yield from the nuclear explosive is often related to the detonation energy of TNT by an effectiveness factor of 0.5 i.e., $Y_{total\ (nuc)} = 0.5\ Y_{total\ (TNT)}$. In the calculations of properties of blast waves from nuclear explosions, the nuclear explosive sources often are assumed to be point sources because of their high energy density.

*The reaction of aluminum with the "oxidizer" present in chemical explosives is more energetic than the decomposition of the chemical explosive by itself.

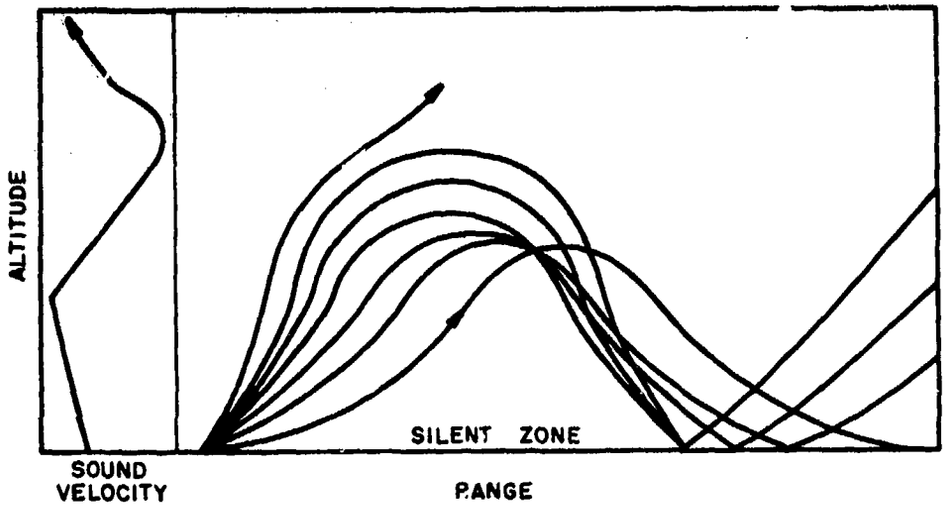


Figure 1-22. Typical Explosion Ray Paths[29]

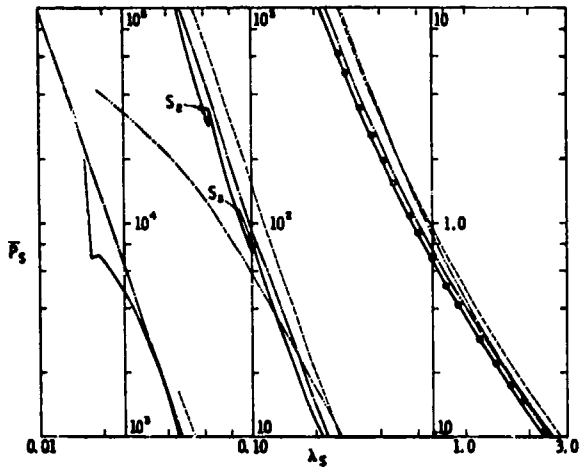
1-6.3.3 OTHER SOURCES

Other types of blast sources often have smaller energy densities than condensed chemical explosives. Such sources include bursting pressure vessels, the muzzle and breech blasts from guns and recoilless weapons, detonable gas mixture, etc. Air blasts generated by such sources will have peak overpressures that are initially less than those from solid chemical explosives, but again, these waves will become essentially similar to those of approximately scaled TNT blasts at sufficiently great distances from the blast center. Larson and Olson[31] show such data for light pressure vessels burst by burning propellant. Brode[3] presents results of calculations showing the differences in peak overpressures for various types of blast sources (see Fig. 1-23). Again, an approximate "TNT equivalent" can be estimated by comparing the ratio of energies available to drive the blast wave from these more diffuse sources to that of the detonation energy of TNT. A method used by Baker, et al.[32], for a compressed gas source, is to estimate blast energy by assuming an isentropic expansion from gas conditions at the instant of pressure release to ambient atmospheric pressure. The change in internal energy of the gas then is assumed to be the relevant input energy for blast. The equation for computing this energy E is

$$E = \frac{p_0 V}{\gamma - 1}\left[\left(\frac{p}{p_0}\right) - \left(\frac{p}{p_0}\right)^{1/\gamma}\right] \qquad (1\text{-}12)$$

TABLE 1-1
PEAK PRESSURE AND POSITIVE IMPULSE RELATIVE TO COMPOSITION B (THE COMPARISON BEING ON AN EQUAL VOLUME BASIS)

Explosive	Relative peak pressure	Relative positive impulse
Torpex (30% Al)	1.13	1.21
Torpex-2	1.12	1.15
Minol-3	1.09	1.13
DBX	1.07	1.11
HBX	1.06	1.11
Tritonal 75/25	1.04	1.10
Minol-2	1.06	1.09
Tritonal 80/20	1.04	1.08
Trialen	1.02	1.06
Baronal	1.00	1.02
Comp. B	(1.00)	(1.00)
Pentolite	0.98	0.97
Ednatol	0.94	0.95
TNT	0.92	0.94
Picratol	0.90	0.90
Amatex	0.88	0.85
Amatol	0.86	0.80



Point Source, Air, (– – – –) Perfect, (— – —) Imperfect; Hot Sphere 2 x 10^4 atm and 3.86 x 10^5 °K (————); TNT (—— ——)

Figure 1-23. Variation of Peak Overpressure Ratios $\bar{P}$ With Shock Radius λ_s for Various Explosions[3]

where

p = initial absolute pressure

V = total volume

p_0 = ambient pressure

γ = ratio of specific heats for the expanding gas

By comparing this energy to the detonation energy of TNT (1000 cal/g = 18.3 X 10^6 in.-lb_f/lb_m), a "TNT equivalent" can be estimated. A sample calculation follows.

Sample Calculation

In the Apollo Service Module, there is a pressure vessel which stores 7 X 10^4 in.^{3} of helium at a pressure of 3500 psia. The NASA Manned Spacecraft Center was concerned about the possible blast effects of rupture of this vessel during vibration testing in their laboratory. What is the TNT equivalent of burst of this vessel?

Input values for Eq. 1-12 are

p_0 = 14.7 psia (ambient pressure at Houston, Texas)

p = 3500 psia

$V = 7 \times 10^4$ in.^{3}

γ = 5/3 (Helium is a monatomic gas.)

From Eq. 1-12,

$$E = \frac{14.7 \times 70{,}000}{\left(\frac{5}{3} - 1\right)} \left[\left(\frac{3500}{14.7}\right) - \left(\frac{3500}{14.7}\right)^{3/5}\right]$$

$$= 1.546 \times 10^6 \left[238 - (238)^{3/5}\right]$$

$E = 3.27 \times 10^8$ in.-lb_f

Using the detonation energy of TNT, we have

$$W_{TNT} = \frac{3.27 \times 10^8}{18.13 \times .0^6}$$

$$= 18.02 \text{ lb}_m \text{ of TNT}$$

REFERENCES

1. P.D. Flynn, *Elastic Response of Simple Structures to Pulse Loading*, BRL Memo. Report No. 525, Aberdeen Proving Ground, Md., November 1950.

2. N. H. Ethridge, *A Procedure for Reading and Smoothing Pressure-Time Data from H. E. and Nuclear Explosions*, BRL Memo. Report 1691, Aberdeen Proving Ground, Md., September 1965.

3. H. L. Brode, "Numerical Solutions of Spherical Blast Waves", Jour. of Appl. Phys. 26, 6, 766-775 (June 1955).

4. H. L. Brode, *The Blast Wave in Air Resulting from a High Temperature, High Pressure Sphere of Air*, RM-1825-AEC, The Rand Corp., Santa Monica, California, December 1956.

5. John M. Dewey, "The Air Velocity in Blast Waves from TNT Explosions", Proc. of the Royal Soc. A, 279, 366-385 (1964).

6. L. Rudlin, Private communication regarding second and secondary airshocks from HE explosions.

7. R. J. Larson and W. Olson, *Measurements of Air Blast Effects from Simulated Nuclear Reactor Core Excursions*, BRL Memorandum Report No. 1102, Aberdeen Proving Ground, Md., September 1957.

8. E. J. Bryant, N. H. Ethridge, and J. H. Keefer, *Operation TEAPOT, Project 1.14b, Measurements of Air-Blast Phenomena with Self-Recording Gages*, WT-1155, July 1965 (AD-617 170).

9. John M. Dewey, "Precursor Shocks Produced by a Large Yield Chemical Explosion", *Nature*, 205, p. 1306.

10. S. Glasstone (Ed.), *The Effects of Nuclear Weapons*, U. S. Government Printing Office, Washington, D. C., p. 124, 1962.

11. W. Döering and G. Burkhardt, *Contributions to the Theory of Detonation*, TR No. F-TS-1227-1A, Wright-Patterson AFB, Ohio, p. 306, May 1949.

12. R. Shear and P. McCane, *Normally Reflected Shock Front Parameters*, BRL Memorandum Report No. 1273, Aberdeen Proving Ground, Maryland, May 1960.

13. W. D. Kennedy, *Effects of Impact and Explosion*, Report of Div. 2, NDRC, Washington, D.C. Vol. I: *Explosions and Explosives in Air*, Chapter 2, Part II, p. 84, 1946.

14. E. Mach and J. Sommer, "Über die Fortpflanzungsgeschwindigkeit von Explosionsschallwellen", *Akademie der Wissenschafter, Sitzangberichte der Wiener*, Vol. 74, 1877.

15. V. J. Bishop, R. D. Rowe, *The Interaction of a Long Duration Friedlander Shaped Blast Wave with an Infinitely Long Right Circular Cylinder. Incident Blast Wave 20.7 psi, Positive Duration 50 ms and a 16 cm Diameter Cylinder*, AWRE Report No. 0-38/67, Atomic Weapons Research Establishment, Alderwaston, Berkshire, England, April 1967.

16. C. H. Norris, R. J. Hansen, M. J. Holley, Jr., J. M. Briggs, S. Namyet, and J. K. Minami, *Structural Design for Dynamic Loads*, McGraw-Hill Book Co., New York, 1959, pp. 249-252.

17. W. Bleakney, *Shock Loading of Rectangular Structures*, Tech. Rept. 11-11, Princeton Univ. Dept. of Physics, Princeton, N. J., January 10, 1952.

18. W. Bleakney, *Rectangular Block, Diffraction of a Shock Wave Around an Obstacle*, Princeton Univ. Dept. of Physics, Princeton, N. J., December 17, 1949.

19. W. Bleakney, *The Diffraction of Shock Waves Around Obstacles and the Transient Loading of Structures*, Tech. Rept. II-3, Princeton Univ. Dept. of Physics, Princeton, N. J., March 16, 1950.

20. D. R. White, D. K. Weimer, and W. Bleakney, *The Diffraction of Shock Waves Around Obstacles and the Transient Loading of Structures*, Tech. Rept. II-6, Princeton Univ. Dept. of Physics, Princeton, N. J., Aug. 1, 1950.

21. R. E. Duff and R. N. Hollyer, *The Effects of Wall Boundary Layer on the Diffrac-*

tion of Shock Waves Around Cylindrical and Rectangular Obstacles, University of Michigan, Ann Arbor, Mich., June 21, 1950.

22. G. Uhlenbeck, *Diffraction of Shock Waves Around Various Obstacles*. University of Michigan, Engineering Research Institute, Ann Arbor, Mich., March 21, 1950.

23. W. Bleakney, D. R. White and W. C. Griffith, "Measurements of Diffraction of Shock Waves and Resulting Loading of Structures", Jour. of Appl. Mech. 17, 1, 439-445 (March 1950).

24. H. E. Lindberg and R. D. Firth, *Structural Response of SPINE Vehicles, Vol. II, Simulation of Transient Surface Loads by Explosive Blast Waves*, Tech. Rept. AFWL-TR 66-163, Vol. II Air Force Weapons Lab., Kirtland AFB, N. Mex., May 1967.

25. B. Perkins, Jr., P. H. Lorrain and W. H. Townsend, *Forecasting the Focus of Air Blasts due to Meteorological Conditions in the Lower Atmosphere*, BRL Report No. 1118, Aberdeen Proving Ground, Maryland, October 1960.

26. W. W. Berning, *Investigations of the Propagation of Blast Waves Over Relatively Large Distances and the Damaging Possibilities of such Propagation*, BRL Report No. 675, Aberdeen Proving Ground, Maryland, November 1948.

27. S. Fujiwhara, Bull. Cent. Meteor. Obs. Japan 2, 1, 1912; and 2, 2, 1916.

28. E. A. Milne, Phil. Mag. and Jour. of Science, 42, 96-114 (1921).

29. J. W. Reed, *Acoustic Wave Effects Project: Airblast Prediction Techniques*, SC-M-69-332, Sandia Laboratories, Albuquerque, N. Mex., May 1969.

30. C. N. Kingery, *Parametric Analysis of Sub-Kiloton Nuclear and High Explosive Blast* [illegible] Report No. 1393, February 1968 (AD-833 698).

31. R. J. Larson and W. Olson, *Measurements of Air Blast Effects from Simulated Nuclear Reactor Core Excursions*, BRL Memorandum Report No. 1102, September 1957.

32. W. E. Baker, S. Silverman, and T. D. Dunham, *Study of Explosions in the NASA-MSC Vibration and Acoustic Test Facility (VATF)*, Final Report on Contract NAS 9-7749, March 1968.

33. G. Beichler, *Records of Air Shock Loading on a Three-Dimensional Model*, BRL Mechanical Note No. 842, APG Maryland, Jan. 1954.

34. R. J. Janus and C. N. Kingery, *Air Blast Loading on a Three-Dimensional Model of a Gabled Shelter*, AFSWP 1054, Jan. 1958.

35. R. Courant and K. O. Friedrichs, *Supersonic Flow And Shock Waves*, Interscience Publishers, New York, N.Y., 1948.

36. AMCP 706-182(S), Engineering Design Handbook, *Explosions in Air, Part Two* (U).

CHAPTER 2

AIR BLAST THEORY

2-0 LIST OF SYMBOLS

a_i = Lagrangian coordinates, i = 1,2,3

$a_J, b_J, c_J, d_J, e_J, h_J, q_J, Q_J$ = parameters in fits to shock trajectories

a_0 = sound velocity in ambient air

A = a constant in Taylor's solution

A_0 = a constant

A_s = area of a "stream tube"

B = a function of γ, a geometric dependent parameter

$C\pm$ = slopes of characteristics in the (α, β) plane

C_T = velocity of triple point

c_p = specific heat at constant pressure

c_v = specific heat at constant volume

D = detonation velocity

e, e_i = internal energy, internal energy at location i

e_{tot} = total energy

E_0 = energy per unit length in a blast source

f = a functional form

F, ψ, Φ = functions in G.I. Taylor's similarity solution

HE = internal (heat) energy

J = the Jacobian

K = a constant

KE = kinetic energy

M_s = U/a_0 = Mach number of a shock front

p, p_i, p_{max} = absolute pressure, absolute pressure at location i, maximum pressure in shock front

$\bar{P}_s = \frac{p_s + p_0}{p_0}$ = scaled peak overpressure

P_s = $p_s - p_0$, peak overpressure

p_0 = ambient pressure

$q(\eta)$ = exponent in a power law

r = radial distance

R = radius of shock front

R_g = universal gas constant for air

R_0 = a characteristic length defined by Jones (Ref. 19)

R_s = shock radius

S = entropy

t = time

t_a = shock front arrival time

T = absolute temperature

= triple point

u_i = particle velocities

U, U_s = shock velocity

$v = 1/\rho$ = specific volume

x_i = Eulerian coordinates, $i = 1,2,3$

α,β = curvilinear coordinates

γ = c_p/c_v = ratio of specific heats for air

δ_i = displacements

ζ = $1/M_s^2$ = shock strength

η = r/R = dimensionless radial position

θ = a function of α and β, also a time constant

λ = an angle

λ_1 = a parameter in Sakurai's approximation

μ_c = a function of shock Mach number

ξ = R_s/R_0 = dimensionless shock radius

ρ, ρ_i = density, density at location i

ρ_I = initial density

ρ_0 = ambient density

τ = time in Lagrangian system

τ^* dimensionless time

χ relative angle

2-1 GENERAL

In this chapter, basic equations which describe the transmission of blast waves through air will be presented together with certain special solutions that can be obtained analytically. The equations are complex enough that only a few "exact" solutions for limiting cases and restricted geometries are possible. One usually must resort to numerical solution by electronic computer to obtain predictions which can be compared with experiment. Computer methods, for numerical solution of the basic equations presented here, will be deferred to Chapter 4.

For anyone involved in theoretical study of blast waves, one particular text is required reading. This text is *Supersonic Flow and Shock Waves*, by R. Courant and K. O. Friedrichs[1]. All of the basic equations for shock transmission through air are presented there with lucid descriptions and with considerable insight into the physics of shock waves and accompanying flow fields. Much of the material in this chapter is based on a study of this excellent book. Another good reference on this topic is a voluminous report by Döering and Burkhardt[2].

In studying air blast theory, one's first step should be to discard any notion that acoustic theory is adequate to describe air blast in all but a limited class of problems. In fact, one should include a state of mind in which one considers an acoustic wave as a degenerate shock wave, rather than the state of mind which considers a shock wave as a strong acoustic wave. One should become accustomed to thinking of waves which move faster than sound (sometimes much faster); which have finite (sometimes large) pressure, density, and temperature changes and finite particle velocities associated with them; and which have fronts across which changes in these various parameters are so rapid that they are usually described by discontinuous "jump". None of these notions are consistent with acoustic theory.

2-2 BASIC EQUATIONS

2-2.1 COORDINATE SYSTEMS

In writing fluid dynamic equations involving large motions and changes in properties, one can employ one of two different forms of these equations, which are named for Lagrange and Euler, respectively. The equations in Lagrangian form are fixed conceptually to particles in the fluid, and describe motion of particles as functions of time and other parameters characterizing each individual particle. In a Cartesian coordinate system,

$$x_i = a_i + \delta_1 (a_1, a_2, a_3, t), i = 1,2 \quad)^*$$

where

x_i = Eulerian coordinates

a_i = Lagrangian coordinates of the particle at some specified initial time

δ_i = displacements

t = time

In the Eulerian form, attention is directed to points fixed in an inertial frame of reference and to what happens at these points in course of time t. A rigidly mounted side-on blast gage would record variation of pressure in an Eulerian system fixed with respect to the ground, for example. Motion in the Eulerian system is described by giving velocity components u_i as a function of x_i and t. Transformation from Eulerian to Lagrangian coordinates is effected by solving the system of ordinary differential equations

$$\frac{\partial x_i}{\partial \tau} = \dot{x}_i = u_i(x_1, x_2, x_3, t) \qquad (2\text{-}2)$$

where

$$x_i = x_i\ (a_1, a_2, a_3, \tau)$$
$$t = \tau$$

*Subscript i will indicate three components throughout this discussion.

and the dot here denotes differentiation with respect to time in a Lagrangian system. Constants of integration can be taken as parameters a_i.

2-2.2 FORMS OF EQUATIONS

2-2.2.1 LAGRANGIAN

In Lagrangian form, considerations of conservation of momentum of moving fluid elements lead to the set of equations

$$\rho \frac{\partial^2 x_i}{\partial \tau^2} + \frac{\partial p}{\partial x_i} = 0 \qquad (2\text{-}3)$$

where

ρ = fluid density

p = absolute pressure*

From considerations of conservation of mass, one obtains the equation

$$J = \frac{\rho_I}{\rho} \qquad (2\text{-}4)$$

where

$$J = \frac{\partial(x_1, x_2, x_3)}{\partial(a_1, a_2, a_3)} \qquad (2\text{-}5)$$

is the Jacobian.

In shock theory, viscosity and heat conduction effects are usually assumed negligible everywhere but in shock fronts. This is expressed by the equation

$$\frac{DS}{Dt} = 0 \qquad (2\text{-}6)$$

where S is entropy of a fluid element.

Finally, an equation of state is required to complete the set of equations. A possible form for such an equation is

$$p = f(\rho, S) \qquad (2\text{-}7)$$

*Gravity and other body forces are assumed negligible.

As noted by Courant and Friedrichs[1], Eqs. 2-3 through 2-7 are deceptively simple, but their expression in terms of the initial Lagrangian coordinates a_i will lead to a number of complicated nonlinear terms. Only when treating special cases involving a single space coordinate can one use this representation with any facility.

2-2.2.2 EULERIAN

In Eulerian coordinates, the Eqs. 2-3, 2-4, 2-6, and 2-7 take the form:

$$\frac{\partial u_i}{\partial t} + \sum_{j=1}^{3} u_j \frac{\partial u_i}{\partial x_j} + \frac{1}{\rho}\frac{\partial p}{\partial x_i} = 0 \qquad (2\text{-}8)$$

(conservation of momentum)

$$\frac{\partial \rho}{\partial t} + \sum_{i=1}^{3} \frac{\partial(\rho u_i)}{\partial x_i} = 0 \qquad (2\text{-}9)$$

(conservation of mass)

$$\frac{\partial S}{\partial t} + \sum_{i=1}^{3} u_i \left(\frac{\partial S}{\partial x_i}\right) = 0 \qquad (2\text{-}10)$$

(adiabatic change of state)

where

$$p = f(\rho, S) \qquad (2\text{-}11)$$

is the form of the equation of state.

An alternative form of Eq. 2-10 is*

$$\rho e_{tot} + \sum_{i=1}^{3} \frac{\partial(p\dot{x}_i)}{\partial x_i} = 0 \qquad (2\text{-}12)$$

where total energy

$$e_{tot} = \frac{1}{2}\sum_{i=1}^{3} \dot{x}_i^2 + e \qquad (2\text{-}13)$$

and e is internal energy.

*See Ref. 1, pp. 15-16.

2-2.3 RANKINE-HUGONIOT CONDITIONS

In the steep gradients within shock fronts, the previously given equations are not valid, because viscosity and heat conduction effects become important. In blast theory, the even more complex equations that take these effects into account are seldom used, but instead they are replaced by a set of equations or "jump" conditions that were first completely formulated by Hugoniot[3], and usually are called the Rankine-Hugoniot conditions. These equations*, for a coordinate system moving with a discontinuity, are given by

$$\left.\begin{aligned} &u_1\,\rho_1 = u_2\,\rho_2 \text{ (conservation of mass)} \\ &p_1 + \rho_1 u_1^2 = p_2 + \rho_2 u_2^2 \\ &\quad \text{(conservation of momentum)} \\ &e_1 + \frac{p_1}{\rho_1} + \frac{1}{2}u_1^2 = e_2 \\ &\quad + \frac{p_2}{\rho_2} + \frac{1}{2}u_2^2 \\ &\quad \text{(conservation of energy)} \end{aligned}\right\} (2\text{-}14)$$

Here, subscripts 1 and 2 denote one side or the other of the discontinuity.

An alternative form of Eqs. 2-14 for an inertial system with the discontinuity moving with velocity U is given by equations

$$\left.\begin{aligned} &\rho_1 (u_1 - U) = \rho_2 (u_2 - U) \\ &p_1 + \rho_1 (u_1 - U)^2 = p_2 \\ &\quad + \rho_2 (u_2 - U)^2 \\ &\rho_1 (u_1^2/2 + e_1)(u_1 - U) + p_1 u_1 \\ &\quad = \rho_2 (u_2^2/2 + e_2) \\ &\quad (u_2 - U) + p_2 u_2 \end{aligned}\right\} (2\text{-}15)$$

As noted by Döering and Burkhardt[2], the Rankine-Hugoniot equations apply for shock fronts of any curvature. A comment by G. I. Taylor[3,2] with regard to these equations and their usefulness in blast technology is quite apropos to a study of air blast, and is quoted

*See Ref. 2, p. 11.

here: "They are so certainly correct in their application to real gases that the only possible explanation of any set of measurements which appears to contradict them is that the observations are wrong."

2-2.4 SINGLE SPATIAL VARIABLE CASES

The general equations for air blast transmission which have been previously given are very difficult to solve, either analytically or numerically, in arbitrary three-dimensional cases. Most of the available solutions are limited to one of the three "one-dimensional" cases, i.e., cases in which the shock and flow fields can be described in terms of a single spatial variable and time. The equations for these three special cases are presented in a number of standard works in fluid dynamics[1,2], but will be repeated here for completeness.

2-2.4.1 LINEAR FLOW

In linear flow, all quantities depend only on time t and one Cartesian coordinate x. The governing equations in Eulerian form are then

$$\frac{\partial u}{\partial t} + u\left(\frac{\partial u}{\partial x}\right) + \frac{1}{\rho}\left(\frac{\partial p}{\partial x}\right) = 0 \qquad (2\text{-}16)$$

(conservation of momentum)

$$\frac{\partial \rho}{\partial t} + u\left(\frac{\partial \rho}{\partial x}\right) + \rho\left(\frac{\partial u}{\partial x}\right) = 0 \qquad (2\text{-}17)$$

(conservation of mass)

$$\frac{\partial S}{\partial t} + u\left(\frac{\partial S}{\partial x}\right) = 0 \qquad (2\text{-}18)$$

(adiabatic changes of state)

The equation of state, Eq. 2-11, is needed to complete the set of equations.

2-2.4.2 SPHERICALLY SYMMETRIC FLOW

If the flow is spherically symmetric, then all quantities depend only on time t and the distance r from the origin of coordinates. All flows are radial, with a single velocity component u. The fundamental equations are

$$\frac{\partial u}{\partial t} + u\left(\frac{\partial u}{\partial r}\right) + \frac{1}{\rho}\left(\frac{\partial p}{\partial r}\right) = 0 \qquad (2\text{-}19)$$

(conservation of momentum)

$$\frac{\partial \rho}{\partial t} + u\left(\frac{\partial \rho}{\partial r}\right) + \rho\left(\frac{\partial u}{\partial r}\right) + \frac{2u\rho}{r} = 0 \qquad (2\text{-}20)$$

(conservation of mass)

$$\frac{\partial S}{\partial t} + u\left(\frac{\partial S}{\partial r}\right) = 0 \qquad (2\text{-}21)$$

(adiabatic changes of state)

where

$$r = (x_1^2 + x_2^2 + x_3^2)^{1/2}$$

In this case again, an equation of state is needed to complete the set of equations.

2-2.4.3 CYLINDRICALLY SYMMETRIC FLOW

The third special case consists of cylindrically symmetric flow. The radial distance from the axis of symmetry is the single spatial coordinate for this system. Here, the basic equations are:

$$\frac{\partial u}{\partial t} + u\left(\frac{\partial u}{\partial r}\right) + \frac{1}{\rho}\left(\frac{\partial p}{\partial r}\right) = 0 \qquad (2\text{-}22)$$

(conservation of momentum)

$$\frac{\partial \rho}{\partial t} + u\left(\frac{\partial \rho}{\partial r}\right) + \rho\left(\frac{\partial u}{\partial r}\right) + \frac{u\rho}{r} = 0 \qquad (2\text{-}23)$$

(conservation of mass)

$$\frac{\partial S}{\partial t} + u\left(\frac{\partial S}{\partial r}\right) = 0 \qquad (2\text{-}24)$$

(adiabatic changes of state)

where

$$r = (x_1^2 + x_2^2)^{1/2}$$

2-2.4.4 APPLICATION

Of these three cases, the one most applicable to blast waves in air is the second, spherically symmetric. This case applies to either a spherical source far from any reflecting surface or to a hemispherical source located on a perfectly rigid reflector, both of which approximate a number of real blast sources. The first (plane wave) case is quite useful for prediction of performance of shock tubes, but shock tubes are not a topic of discussion in this handbook.

2-3 ANALYTIC SOLUTIONS TO EQUATIONS

Eqs. 2-1 through 2-15 constitute all of the general equations that usually are used in air blast theory. To solve specific problems, one must add initial and boundary conditions and must choose specific equations of state. Once equations of state are chosen, Eqs. 2-14 or 2-15 also yield a number of additional interrelations between shock front properties. The remainder of this chapter will be devoted to specific problems and to those analytical solutions which are available in the literature.

Some specific or partial analytic solutions are avaliable for one-dimensional cases. Several of these solutions are used to generate initial conditions for computer code numerical calculations. We will now discuss in some detail a few of these solutions.

2-3.1 TAYLOR'S SIMILARITY SOLUTION FOR SPHERICALLY SYMMETRIC BLAST WAVES

A famous blast wave solution for strong shocks is due to G. I. Tavlor[4] and usually termed "Taylor's similarity solution". It will be given here.

The similarity assumptions* made by Taylor are for pressure

$$p/p_0 = R^{-3}\ F(\eta) \tag{2-25a}$$

for density

$$\rho/\rho_0 = \Psi(\eta) \tag{2-25b}$$

and for radial velocity

$$u = R^{-3/2}\ \Phi(\eta) \tag{2-25c}$$

In Eqs. 2-25, R is the radius of the shock wave forming the outer edge of the disturbance and is a function of time, r is any radial distance from the blast center, and $\eta = r/R$. Also, p_0 and ρ_0 are the pressure and density, respectively, of the ambient air. Eq. 2-19 can now be satisfied. This problem is solved most conveniently by the inverse method of making appropriate choices for velocity of propagation and shock radius. If the velocities U of propagation and shock radius R are given by

$$U = \frac{dR}{dt} = A\,R^{-3/2} \tag{2-26a}$$

$$R = \left(\frac{5}{2}\,At\right)^{2/5} \tag{2-26b}$$

then from Eq. 2-19, the conservation of momentum constraint,

$$-A\left(\frac{3}{2}\,\Phi + \eta\,\Phi'\right) + \Phi\,\Phi' + \frac{p_0}{\rho_0}\,\frac{F'}{\Psi} = 0 \tag{2-27}$$

where A is a constant; the primes denote partial derivatives with respect to $\eta = r/R$; and Φ, F, ψ are functions in Taylor's similarity solution. The continuity equation (Eq. 2-20) yields

$$-A\,\eta\,\Psi' + \Psi'\,\Phi + \Psi\left(\Phi' + \frac{2}{\eta}\,\Phi\right) = 0 \tag{2-28}$$

Further, if a perfect gas is assumed, Eq. 2-11 takes the form

$$p = \rho\,R_g\,T \tag{2-29}$$

*A more general similarity transformation has been employed by Garg and Siekman[5] which contains Taylor's law but also requires the strong shock assumption.

For constant specific heats the entropy[6] is given by

$$S = \frac{\gamma R_g}{(\gamma - 1)} \ln\left(\frac{T}{T_0}\right) - R_g \ln\left(\frac{p}{p_0}\right) =$$

$$\frac{K}{\gamma - 1}\left[\ln\left(p\,\rho^{-\gamma}\right) - \ln\left(p_0\,\rho_0^{-\gamma}\right)\right] \quad (2\text{-}30)$$

where

γ = the ratio of specific heats of air

R_g = gas constant of air.

Substitution of Eq. 2-30 in Eq. 2-21 yields

$$\left(\frac{\partial}{\partial t} + u\,\frac{\partial}{\partial r}\right)\left(p\rho^{-\gamma}\right) = 0 \quad (2\text{-}31)$$

and thus using the similarity laws (Eqs. 2-25) and Eqs. 2-26, Eq. 2-31 becomes

$$A(3F + \eta F') + \frac{\gamma F}{\Psi}\Psi'(-A\eta + \Phi) - \Phi F' = 0 \quad (2\text{-}32)$$

Eqs. 2-27, 2-28, and 2-32 can be reduced to nondimensional form by substitution of

$$f = Fa_0^2/A^2 \quad \therefore F = \frac{A^2}{a_0^2} f \quad (2\text{-}33)$$

$$\phi = \Phi/A \quad \therefore \Phi = A\phi \quad (2\text{-}34)$$

where the velocity of sound in air is given by

$$a_0 = [\gamma p_0/\rho_0]^{1/2} \quad (2\text{-}35)$$

The results of this substitution are the equations

$$\phi'(\eta - \phi) = \frac{1}{\gamma}\left(\frac{f'}{\Psi}\right) - \frac{3}{2}\phi \quad (2\text{-}36)$$

$$\frac{\Psi'}{\Psi} = \frac{\phi' + (2\phi/\eta)}{\eta - \phi} \quad (2\text{-}37)$$

$$3f + \eta f' + \frac{\gamma\Psi'}{\Psi} f(-\eta + \phi) - \phi f' = 0 \quad (2\text{-}38)$$

By elimination of ϕ' and ψ' from Eq. 2-38 using Eqs. 2-36 and 2-37, one obtains the equation for calculating f' when f, ϕ, Ψ, and η are knowns. This equation is

$$f'\left[(\eta - \phi)^2 - (f/\Psi)\right] = f\left[-3\eta + \phi\left(3 + \frac{\gamma}{2}\right) - (2\gamma\phi^2/\eta)\right] \quad (2\text{-}39)$$

Similarly, ϕ', Ψ' can then be expressed in terms of f, ϕ, Ψ, η for simultaneous numerical integrations. A forward spatial method of integration can be used to integrate for f, Ψ, and ϕ at a given layer η if an initial condition is given. In Taylor's solution, a backward spatial integration scheme was used to integrate from the shock front ($\eta = 1$) to the interior.

The Rankine-Hugoniot relations for the case where $\eta = 1$, which is at the shock wave front, can be reduced to the equations (see Ref. 6, Eqs. 4.2, 4.3, 4.5, and 4.6)

$$\frac{\rho_1}{\rho_0} = \frac{\gamma - 1 + (\gamma + 1)\,p_1/p_0}{\gamma + 1 + (\gamma - 1)\,p_1/p_0} \quad (2\text{-}40)$$

$$\frac{U^2}{a_0^2} = \frac{1}{2\gamma}\left[(\gamma - 1) + (\gamma + 1)\,p_1/p_0\right] \quad (2\text{-}41)$$

$$\frac{u_1}{U} = \frac{2[(p_1/p_0) - 1]}{\gamma - 1 + (\gamma + 1)\,p_1/p_0} \quad (2\text{-}42)$$

(It is noted that in Liepmann and Puckett[6], the spatial coordinate is shock-fixed; in the case given here the shock is propagating into a stationary medium; therefore, u_1, $u_2 - u_1$, p_2, p_1 (Ref. 6) may be written U, u_1, p_1, and p_0 here.)

However, Eqs. 2-40 to 2-42 cannot be satisfied consistent with the similarity assumptions represented by Eqs. 2-25. However, when the shock is strong ($p_1 >> p_0$) Eqs. 2-40 through 2-42 become

$$\frac{\rho_1}{\rho_0} \cong \frac{\gamma + 1}{\gamma - 1} \quad (2\text{-}43a)$$

$$\frac{U^2}{a_0^2} \cong \frac{(\gamma+1)}{2\gamma}\frac{p_1}{p_0} \qquad (2\text{-}43b)$$

$$\frac{u_1}{U} \cong \frac{2}{\gamma+1} \qquad (2\text{-}43c)$$

and they are now consistent with the similarity assumptions.

At $\eta = 1$, Eqs. 2-25, 2 26, 2-33, 2-34, and 2-43 yield

$$\Psi = \frac{\gamma+1}{\gamma-1} \qquad (2\text{-}44a)$$

$$f = \frac{2\gamma}{\gamma+1} \qquad (2\text{-}44b)$$

$$\phi = \frac{2}{\gamma+1} \qquad (2\text{-}44c)$$

where $p = p_1$ and $u = u_1$. Eq. 2-39 and similar equations for Ψ' and ϕ' derived from Eqs. 2-36, 2-37, and 2-38 can now be integrated to yield values of f, ϕ, Ψ behind the shock front, i.e., for $\eta < 1$.

To complete the solution one must determine the constant A in Eq. 2-26. To do this we add an additional condition by assuming an instantaneous energy release of amount E, which remains nearly constant for some period of time. This condition is especially well met if Taylor's solution is used only for the brief initial stage of shock expansion to start numerical integrations.

In general, the kinetic energy of the disturbances within a sphere of radius R is

$$KE = 4\pi \int_0^R (1/2)\,\rho\, u^2\, r^2\, dr \qquad (2\text{-}45)$$

The integral energy (or heat energy is

$$HE = 4\pi \int_0^R (\rho c_v T) r^2 dr$$

$$= 4\pi \int_0^R \left(\frac{pr^2}{\gamma-1}\right) dr \qquad (2\text{-}46)$$

The total energy in terms of f, ϕ, Ψ, and η is obtained by Eqs. 2-45 and 2-46 and using Eqs. 2-25, 2-33, and 2-34; one obtains

$$E = 4\pi A^2 \left[(1/2)\,\rho_0 \int_0^1 \Psi\phi^2\eta^2 dn + \frac{p_0}{a_0^2(\gamma-1)} \int_0^1 f\eta^2\, d\eta \right] \qquad (2\text{-}47)$$

Using Eq. 2-35 to eliminate p_0/a_0^2, one finds from Eq. 2-47

$$A^2 = \left(\frac{1}{B}\right)\frac{E}{\rho_0} \qquad (2\text{-}48)$$

where

$$B = 2\pi \int_0^1 \Psi\phi^2\eta^2 d\eta + \frac{4\pi}{\gamma(\gamma-1)} \int_0^1 f\eta^2 d\eta \qquad (2\text{-}49)$$

which is a function of γ only.

Eq. 2-49 can be integrated by quadrature formulas, and discrete values of ϕ, Ψ, and f determined through numerical integration of the three simultaneous ordinary differential Eqs. 2-36, 2-37, 2-39, and the ones for ϕ' and Ψ' derived from Eqs. 2-34, 2-36, and 2-38. The time history and space distribution of p, ρ, and u as well as the location and velocity of the shock, R, U, have now been determined at discrete points. The particle velocity, the pressure, and the density just behind the shock (u_1, p_1, and ρ_1) may be determined from Eqs. 2-26 and 2-43.

For air at not too high a temperature, $\gamma = 1.4$. In this case, Taylor[4] gives the integrated value of B as 5.36; i.e.,

$$E = 5.36\,\rho_0 A^2 \qquad (2\text{-}50)$$

Also at the shock front

$$\left.\begin{aligned} p_{max} &= p_1 = 0.155\, R^{-3}\, E \\ U &= R^{-3/2}\, E^{1/2}\, (B\rho_0)^{-1/2} \\ t_a &= 0.926\, R^{3/2}\, \rho_0^{1/2}\, E^{-1/2} \end{aligned}\right\} \quad (2\text{-}51)$$

where t_a is the arrival time of the shock front at distance R, while ρ_1 and u_1 can be easily calculated by Eqs. 2-43.

For a given time t, Eqs. 2-48 and 2-26b yield

$$R = \left(\frac{5}{2} At\right)^{2/5} \quad (2\text{-}52)$$

$$= \left[\frac{5}{2}\left(E_0^{1/2}\rho_0^{-1/2}/\sqrt{5.36}\right)t\right]^{2/5}$$

since

$$A = E_0^{1/2}\rho_0^{-1/2}/\sqrt{5.36}$$

It is noted that an equally important analogous solution for a cylindrical blast wave was derived by S. C. Lin [7].

Sakurai[21] has extended G.I. Taylor's solution by expanding an expression for the shock radius in an infinite power series of terms in M_s. He considers plane, cylindrical, and spherical waves by including a multiplier of the form $(R_0/R_s)^{\alpha+1}$, where $\alpha = 0, 1, 2$, in the expansion. The basic approach is similar to Taylor's, but higher order approximations can be made and plane and cylindrical shocks are handled in addition to the spherical shocks of Taylor's solution.

2-3.2 INITIAL CONDITIONS FOR SOLUTIONS

2-3.2.1 INITIAL ISOTHERMAL SPHERICAL DETONATION FRONT

A modification to initial conditions is given by Brode[8]. However, the complex physical-chemical processes in an explosion are such that accurate theoretical predictions are a very difficult task, see Oppenheim[9]. Brode's initial condition was either a point source or an isothermal sphere. Some theoretical estimates do exist which can be of value to engineers and physicists. Landau and Stanyukovich (Chapter VII, p. 540, of Ref. 9) have deduced the parameters of the detonation front from the equations of state for highly compressed explosive products*. The basic relations derived for detonation waves are

$$\left.\begin{aligned} p_1 &= \frac{1}{4}\rho_0 D^2 \\ u_1 &= \frac{1}{4} D \\ \rho_1 &= \frac{4}{3}\rho_0 \end{aligned}\right\} \quad (2\text{-}53)$$

which are in agreement with Zeldovich and Kompaneets results[10] derived from minimizing the propagation velocity D of the detonation front. Furthermore, Landau and Stanyukovich derived the equation

$$D = A_D \rho_0 \quad (2\text{-}54)$$

where, for most secondary explosives,

$$A_D \cong 4.5\ (\text{km/sec})/(\text{g/cm}^3) \quad (2\text{-}55)$$

However, the "suitable" general equation of state assumed by Landau and Stanyukovich takes the form

$$p = \Phi(v) + f(v)T \quad (2\text{-}56)$$

where v is the specific volume, instead of the ideal gas form assumed by Taylor. Other equations of state will be given later in Chapter 4.

If the forces of repulsion and attraction between molecules are represented by

$$\Phi(v) = av^{-n} - bv^{-m} \quad (2\text{-}57)$$

and since, for highly heated explosion products, the forces of attraction can be neglected, this equation of state reduces to

$$p = Av^{-n} + f(v)\,T \quad (2\text{-}58)$$

*More complete discussions of equations of state appear in Chapter 4.

Experimental determination of A, n, $f(\nu)$ is required for Eq. 2-58. Some simplification may be achieved by using results of statistical physics[9].

For large ν, f approaches the limit R_g/ν. This is because molecules become very deformed at high pressures, and van der Waal forces do not apply, i.e.,

$$f(\nu) = \frac{B(\nu)}{\nu} \tag{2-59}$$

but $B(\nu)$ is a slowly varying function and approaches R_g as ν goes to ∞.

2-3.2.2 OTHER INITIAL CONDITIONS

If ..ear-field measurements are available, other initial conditions can be used to calculate the far-field properties. For instance, one may specify either p and e_{TOT} at the charge surface or p and $\partial p/\partial r$ at some radial distance r_i (Shear and Wright[11]).

Richards[12] considers a primary shock and an initial rarefaction wave appearing on either side of a contact surface, separated from it by shocked ambient gas (subscript 1) and expanded explosive gases (subscript 2), respectively. Again, subscript 0 will be used for ambient gas ahead of the shock and subscript e for the unexpanded explosive.

These considerations lead to two equations of state in alternate forms

$$e_1 = H_1(p_1, \nu_1) \tag{2-60}$$

$$e_2 = H_2(p_2, \nu_2) \tag{2-61}$$

and four Rankine-Hugoniot equations [cf. Eqs. (55.02), (59.01), (59.02), (59.03), (59.05) of Ref. 1].

$$e_1 = e_0 + (p_1 + p_0)(\nu_0 - \nu_1)/2 \tag{2-62}$$

$$e_2 = e_e + (p_2 + p_e)(\nu_e - \nu_2)/2 \tag{2-63}$$

$$u_1^2 = (p_1 - p_0)(\nu_0 - \nu_1) \tag{2-64}$$

$$(u_2 - u_e)^2 = (p_e - p_2)(\nu_2 - \nu_e) \tag{2-65}$$

For a contact surface, there exist the conditions that the pressure and the normal velocity component be continuous[1], i.e., leading in this case to the equations

$$p_1 = p_2 \tag{2-66}$$

$$u_1 = u_2 \tag{2-67}$$

These conditions are applied throughout the extremely narrow initially disturbed region. There are then eight equations with eight unknowns, e_1, e_2, ν_1, ν_2, p_1, p_2, u_1, u_2, and five parameters e_e, p_e, p_0, ν_0, e_0. If e_e, p_e * are measured and, since p_0, ν_0, e_0, (or p_e, ρ_0, T_0, c_v), are known for undisturbed atmospheric conditions, the initial conditions can be completely determined.

The wave speeds are

$$U' = u_2 + (u_e - u_2)\,\nu_2/(\nu_2 - \nu_e) \tag{2-68}$$

$$U'' = u_1\,\nu_0/(\nu_0 - \nu_1) \tag{2-69}$$

for the initial rarefaction wave and shock wave, respectively.

2-3.3 MACH SHOCK REFLECTION

Some solutions have been obtained for two-dimensional cases, especially for Mach reflection from straight and curved boundaries. They will be discussed here. First, let us consider the physical effect of the simplest boundary condition such as the incidence of the shock wave on a straight element of a rigid wall. If the oblique shock is not too strong, regular reflection occurs which can be calculated with the assistance of an oblique shock chart[6] composed of shock polar curves. However, if the incident wave is very strong, the usual technique would yield an imaginary flow condition[13]. Physically, a "Mach reflec-

*In place of measuring p_e, one may also measure $U = D$ (Eq. 2-59 with $D = U$ for an estimate) and add one more Eq. 2-69 to solve for the above eight unknowns plus p_e.

tion" will occur[13] as shown in Fig. 2-1 with shock-fixed coordinates. For a straight incident shock in such cases, there will be a curved reflected shock plus a normal shock stem near the wall. We have noted before that the point of intersection is called the triple point T, and that there will be a contact surface, called the "slipstream", trailing "downstream" in shock-fixed coordinates. For a strong shock wave moving over a wedge, similarly, Mach reflection occurs as shown in Fig. 2-2 with space-fixed coordinates. Whitham[34] formulated a two-dimensional theory* for shock dynamics over convex or concave walls. He used a set of curvilinear coordinates, (α, β) one parallel and the other perpendicular to the shock front. They are correlated with the time-distance coordinates. The curves with coordinates, $\alpha = a_0 t$ and β = constant, are "rays", which are the discrete trajectories orthogonal to the moving (curved) incident shock. Since the distance measured along a ray β = constant between the shock positions at t, and $t + dt$ is $U\,dt$, it is equal to $M_s\ (\alpha, \beta)\ d\alpha$. The function $M_s = M_s\ (\alpha, \beta)$ is the local Mach number of the shock referred to the sound velocity of the undisturbed medium. Let the corresponding distance across the "quasi-streamtube" bounded by β and $\beta + \Delta\beta$ be $A(\alpha, \beta)\ d\beta$. The geometric relations that are then satisfied are

$$\frac{\partial \theta}{\partial \beta} = \frac{1}{M_s}\left(\frac{\partial A_s}{\partial \alpha}\right), \qquad \frac{\partial \theta}{\partial \alpha} = -\frac{1}{A_s}\left(\frac{\partial M_s}{\partial \beta}\right) \tag{2-70}$$

and

$$\frac{\partial}{\partial \alpha}\left[\frac{1}{M_s}\left(\frac{\partial A_s}{\partial \alpha}\right)\right] + \frac{\partial}{\partial \beta}\left[\frac{1}{A_s}\left(\frac{\partial M_s}{\partial \beta}\right)\right] = 0 \tag{2-71}$$

where A_s is the area of a stream tube (for a derivation see Ref. 34), and $\theta\ (\alpha, \beta)$ is the angle made by a ray with a fixed direction. From considerations of similarity to channel flow,

*A three-dimensional generalization was made by Whitham[14] and will not be discussed here in detail.

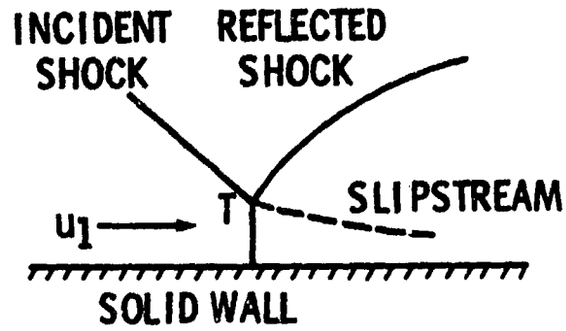


Figure 2-1. Mach Shock Reflection[13]

$$M_s = M_s(A_s) \quad \text{or} \quad A_s = A_s(M_s) \tag{2-72}$$

provided that A_s is a decreasing function of M_s. For a small change of area dA, the corresponding change in Mach number is[33]

$$\frac{dA_s}{A_s} = \frac{-2M_s\ dM_s}{(M_s^2 - 1)\ K(M_s)} \tag{2-73a}$$

where

$$K(M_s) \cong 2\left[\left(1 + \frac{2}{\gamma+1}\,\frac{1-\mu_c^2}{\mu_c}\right) \times \left(2\mu_c + 1 + \frac{1}{M_s^2}\right)\right]^{-1} \tag{2-73b}$$

and

$$\mu_c^2 = \frac{(\gamma - 1)\ M_s^2 + 2}{2\gamma M_s^2 - (\gamma - 1)} \tag{2-73c}$$

and $K(M_s)$ is a slowly varying function of M_s (decreasing from 0.5 at $M_s = 1$ to 0.3941 at

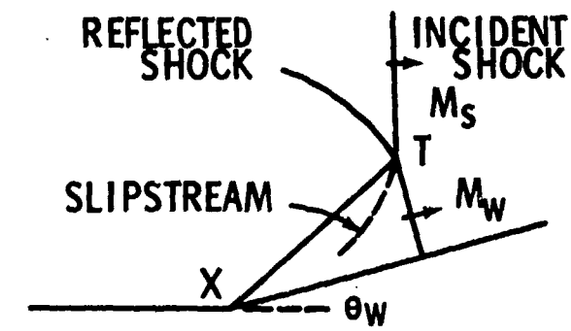


Figure 2-2. Diffraction of a Shock by a Wedge[14]

M_s = 1.4, etc., as M_s goes to ∞ (Ref. 24). Integration of Eq. 2-73a gives a good approximation for a channel of slowly varying cross section.

Integration of Eq. 2-73a yields

$$A_s = K_s(\beta) f(M_s) \tag{2-74}$$

where

$$f(M_s) = \exp\left[-\int \frac{2M_s\, dM_s}{(M_s^2 - 1)\, K(M_s)}\right]$$

$K(M_s)$ and $\log_{10} f(M_s)$ are shown in Figs. 2-3 and 2-4 from Whitham[34]. Eqs. 2-70, 2-72, 2-73, and 2-74 are used to derive the slopes of the local characteristics in the (α, β) plane, i.e.,

$$\left(\frac{\partial}{\partial\alpha} \pm C_\pm \frac{\partial}{\partial\beta}\right)\left(\theta \pm \int \frac{dM_s}{A_s C_\pm}\right) = 0$$

where

$$C_\pm(\alpha,\beta) = \pm\sqrt{\frac{-M_s}{A_s A_s'}} = \pm\left[\frac{(M_s^2-1)}{2} K(M_s)\right]^{1/2}/A_s \tag{2-75}$$

and the prime denotes the partial derivatives with respect to α. The equation

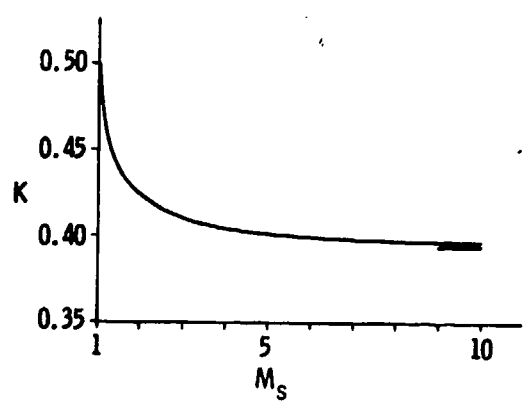


Figure 2-3. Graph of Chester's Function $K(M_S)$ (Ref. 14)

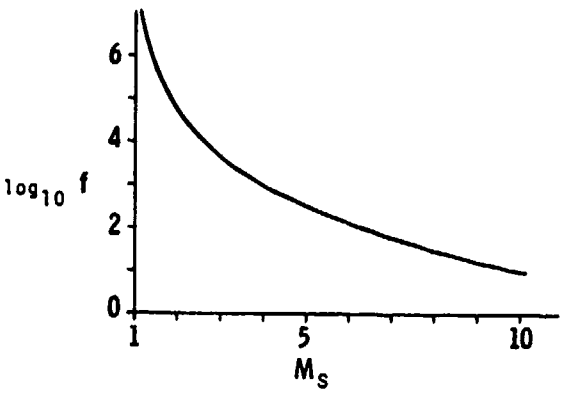


Figure 2-4. Graph of the Function $\log_{10} f(M_S)$ Given by Eq. (4) in Ref. 14

$$\theta\pm\ (\alpha,\beta) = \pm\int_{M_w(\alpha_w,0)}^{M_s(\alpha,\beta)} \frac{dM_s}{A_s C\pm} = \theta_w(\alpha_w, 0) \tag{2-76}$$

is a solution of Eq. 2-75, ("+" and "–" denote $C_\pm$, respectively) where the angle made by the ray β equals a constant with respect to a fixed direction. Curves of $\int_1^{M_s} dM_s/(AC_+)$ are given graphically by Whitman.

To determine the propagation of the triple point T

$$[T(t) = P,\ T(t+\Delta t) = R \text{ in Fig. 2-5}]$$

$$(\overline{PR})^2 = (A_0\Delta\beta)^2 + (M_0\Delta\alpha)^2 = (M_1\Delta\alpha)^2 + (A_1\Delta\beta)^2 \tag{2-77}$$

where

$$M_1 = M_w$$

and where the "trace" of the triple point in the (α, β) plane (α being $a_0 t$), is traveling like a wave front in a one-dimensional flow diagram. The speed of the triple point $C_T = \Delta\beta/\Delta\alpha$ is measured along this trace. Since $\overline{PR}$ is an element of the trace, Eq. 2-77 yields an approximate formula for $C_T(t)$.

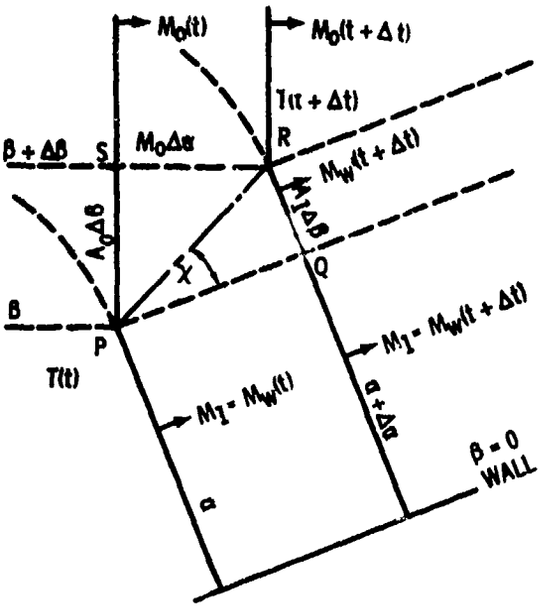


Figure 2-5. Motion of Triple Point[14]

$$C_T = \pm \left(\frac{M_0^2 - M_1^2}{A_1^2 - A_0^2} \right)^{1/2} \qquad (2\text{-}78)$$

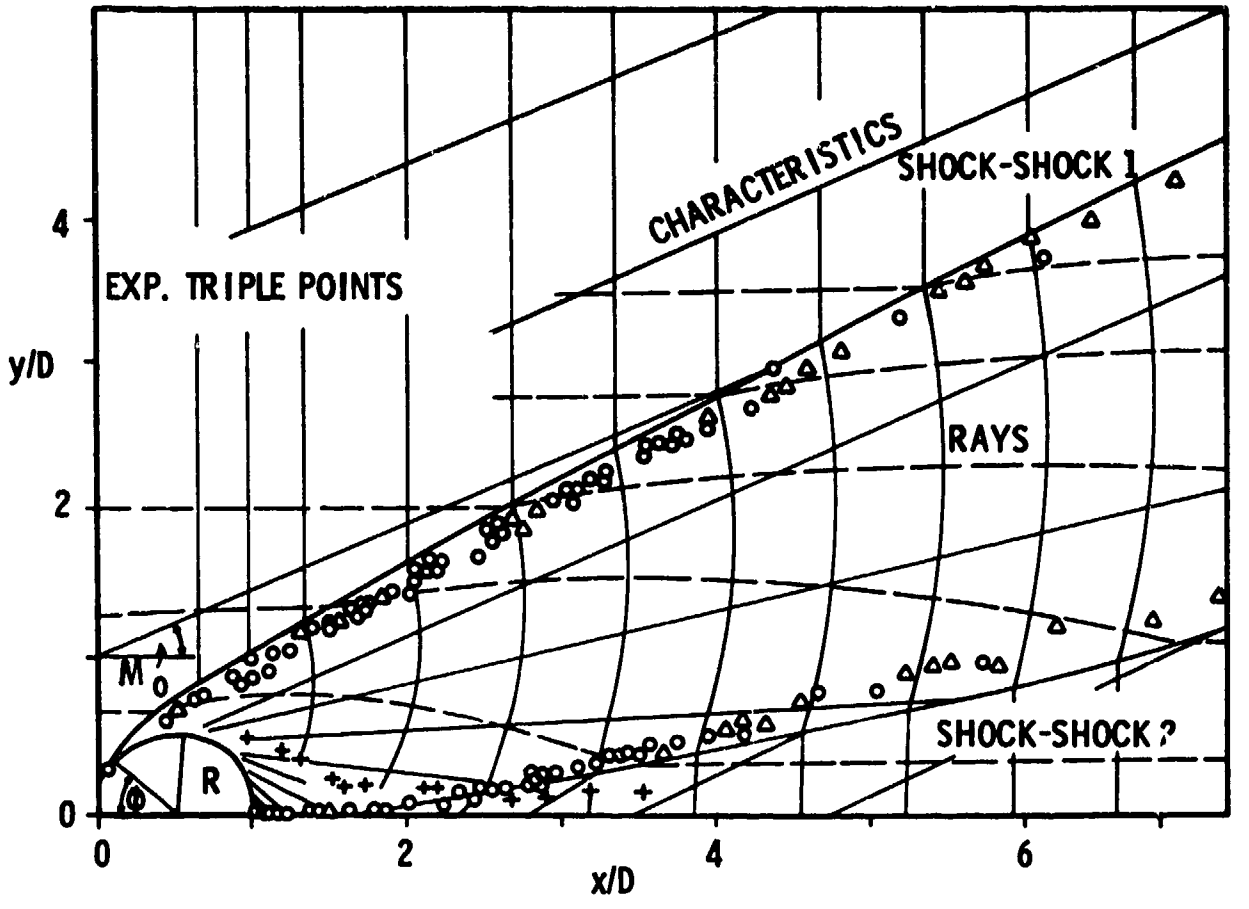
where the sign depends on direction of propagation (it is positive in Fig. 2-2). The relative angle χ and the distance $\overline{PR}$ with respect to the wall are, respectively,

$$\tan\chi = \left(\frac{A_1}{M_1} \right) C_T, \qquad \overline{PR} = \left(M_1^2 + C_T^2 A_1^2 \right)^{1/2} a_0 \Delta t \qquad (2\text{-}79)$$

Shocks of finite strength have trajectories that do not coincide in a flow diagram with the characteristics for weak compression waves in (t, β) or (α, β) plane. Thus, Eq. 2-76 as used by Whitham[34] to calculate the angle QPS (see Fig. 2-5) is only valid for very weak shocks and in such cases regular reflection may occur. If $A_0(t)$, $M_0(t)$, $M_w(t)$ are prescribed at t, then the channel flow approximation between β and $\beta + \Delta\beta$ would determine $M_w(t+\Delta t)$ from Eq. 2-77 and Fig. 2-5, knowing the assumed approximate value of A_1. More accurately, one should use a trial and error procedure by adjusting the location of Q so that $M_w(t+\Delta t)$ calculated from the "quasi-stream tube" bounded by β and $\beta + \Delta\beta$ agrees with that from the "quasi-stream tube" bounded by β and 0.

The advantage of the method lies in a quick estimate in some cases of the locus of the triple point and the conditions just behind the Mach shock. A graphical procedure is required but the assumption of negligible regular reflection possibly limits greatly its practical application. The locus of the triple point for diffraction of incident shock of strength 2.81 over a cylinder is in good agreement with experiments of Bryson and Gross[15], Fig. 2-6; however, there was no direct check on the shock Mach number and the overpressures.

Some discussion of the terminology "shock-shock" introduced by Whitham[34] must be made as it has been employed in related work such as that described by Fig. 2-6, which is in agreement with the measured loci of the triple point of Bryson and Gross. The original descriptions of Whitham appeared very ambiguous and misleading. Serious readers should study his paper very carefully. In his summary, he stated in conclusion of the creation of a "shock-shock" that, "In particular, a shock-shock is the trace of a genuine shock in the flow behind, and thus corresponds to Mach reflection". Since a genuine shock is usually a curve in the two-dimensional case, its trace would be a surface. Then Mach reflection may mean the reflected shock or the complete triple shock. Furthermore, it is not clear whether the "shock-shock" corresponds to Mach reflection or the *trace* corresponds to the Mach reflection. The simple conclusion is that the "shock-shock" is just the locus of the triple point (Figs. 2-1, 2-2) in the physical plane. As another illustration, $\overline{PR}$, in Fig. 2-5, is just an element of the locus of the triple point, i.e., the so-called "shock-shock". In the (t, β) or (α, β) planes the triple point is propagating as a pseudo one-dimensional "wave front". In order to describe the generation of the triple shock and such possible phenomena as the coalescing of compression waves into a new shock, the two-space-dimensional flow



$M_0 = 2.81$, O $Re = 7.79 \times 10^4$, Δ $Re = 0.87 \times 10^4$, + Vortex Loss

Figure 2-6. Diffraction on a Cylinder[15]

diagram as an extension to Rudinger[16] needs to be made; however, such graphical methods are very tedious and subject to possible human errors in every step of application. More modern techniques using high-speed computers will be described in Chapter 4, which replace such graphical methods.

2-3.4 SOME RECENT THEORIES

2-3.4.1 WEAK SHOCK REGIME OF A BLAST WAVE

Bach and Lee[17] presented an approximate analytical method that is valid for very weak shock regimes of a blast wave. This method assumes a power-law density profile behind the blast wave:

$$\frac{\rho(r,t)}{\rho_0} = \Psi(\eta,\zeta) = \Psi(1,\zeta)\ \eta^{q(\zeta)} \tag{2-80}$$

where

$$\eta = \frac{r}{R_s(t)} \tag{2-81a}$$

$$\zeta = (a_0/\dot{R}_s)^2 \tag{2-81b}$$

$$\dot{R}_s = \frac{dR_s}{dt}$$

The exponent of the density profile $q(\zeta)$ is determined for each local shock Mach number from the mass integral. The continuity and momentum equation then determined the particle velocity and the pressure distributions. Analogous to Taylor's theory, the dependence of the shock decay coefficient on

the shock velocity is determined from the energy integral. The solution is in good agreement with known numerical and analytical solutions for low shock strength as shown in Fig. 2-7.

For a weak oblique blast wave encountering a small band along a plane wall, a theory is presented by Srivastava and Chopra[18]. It is assumed that the relative outflow from the reflected shock is supersonic. The solution is

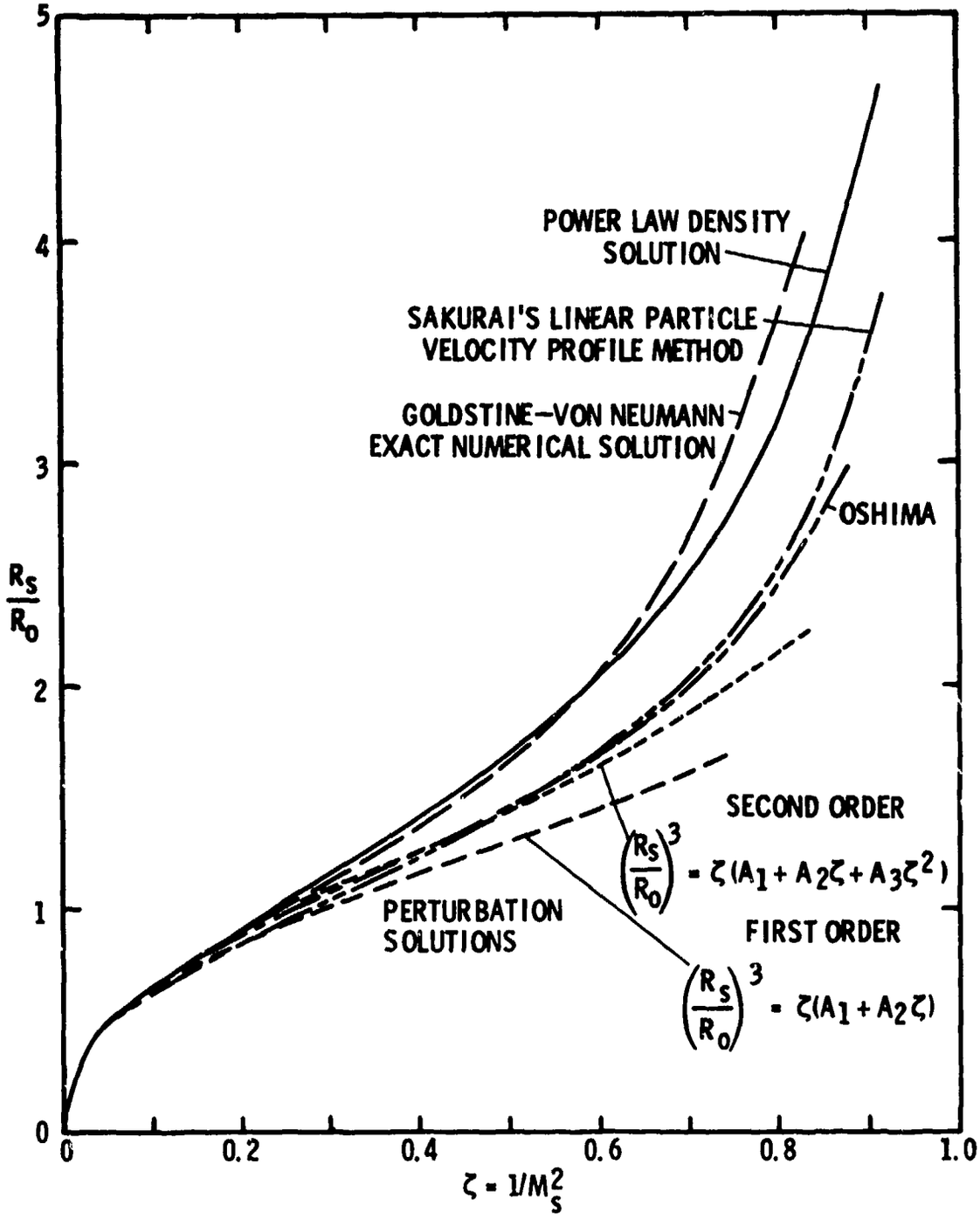


Figure 2-7. The Variation of Shock Strength ζ vs Dimensionless Shock Radius R_s/R_o for Spherical Blast Waves ($\gamma = 1.4$) (Ref. 19)

TABLE 2-1
BLAST WAVE ENERGY PARAMETER *B*
FOR SOME VALUES OF RATIOS OF THE SPECIFIC HEATS[20]

References	Spherical				Cylindrical			Plane		
	$\gamma=$ 5/3	$\gamma=$ 7/5	$\gamma=$ 1/3	$\gamma=$ 6/5	$\gamma=$ 5/3	$\gamma=$ 7/5	$\gamma=$ 6/5	$\gamma=$ 5/3	$\gamma=$ 7/5	$\gamma=$ 6/5
1. Taylor[4]	3.04	5.36	7.28	10.79						
2. Sakurai[21]	3.04	5.35			2.22	3.94		0.678	1.21	
3. Lin[7]						3.85				
4. Rogers[25]		5.36		10.8		4.03	8.10		1.22	2.52
5. Rouse[26]						3.965				
6. Sedov[27]	3.11	5.32	6.94	10.9	2.20	4.00	8.16	0.675	1.22	2.45
7. Jones*[28]	3.08	5.33			2.26	3.94		0.678	1.22	
8. Gerber[29]					2.26	3.94				

*Jones in his Appendix C also gives the numerical procedure to calculate B for a given constant γ for all three cases.

obtained completely with the help of conformal transformations and complex variable techniques. Numerical results were given in their paper for two incident shock strengths, but there were no comparisons with either experiment or other theories.

2-3.4.2 INTERMEDIATE AND STRONG SHOCK STRENGTHS

A more interesting, but not always dependable matching technique, was employed by Jones[19] for intermediate scaled overpressures ($10 > P_s/p_0 > 0.02$). First he assumed the trajectory equation for strong blast[20]

$$\tau^* = \frac{a_0 t}{R_0} = \zeta^{(n+2)/2}, \qquad \zeta = R_s/R_0 \tag{2-82}$$

where n = 3, 2, 1, respectively, for spherical, cylindrical, and plane shocks; and τ^* is dimensionless time.

The characteristic radius

$$R_0 = \left[\left(\frac{n+2}{2}\right)^2 \frac{1}{B\gamma}\left(\frac{E_0}{p_0}\right)\right]^{1/n} \tag{2-83}$$

Here B is a geometric dependent parameter[20] (see Table 2-1).

The scaled overpressure is given by[6]

$$\bar{P}_s = \left(\frac{P_s}{p_0}\right) = \frac{2\gamma}{\gamma+1}(M_s^2 - 1) \tag{2-84}$$

For a strong shock, $M_s^2 >> 1$, and since $d\zeta/d\tau^* = M_s$, Eqs. 2-84 and 2-82 yield

$$P_s/p_0 = \frac{2\gamma}{\gamma+1}\left[\left(\frac{2}{n+2}\right)^2 \xi^{-n}\right] \tag{2-85}$$

For $P_s/p_0 < 10$, Sakurai's second approximation to Eq. 2-82 for the cylindrical ($n = 2$) is[21]

$$\left(\frac{a_0}{U_s}\right)^2\left(\frac{D_0}{R}\right)^2 = 4\left[1+\lambda_1\left(\frac{a_0}{U_s}\right)^2\right] \quad (2\text{-}86a)$$

neglecting terms of order $(a_0/U_s)^4$ and higher.

In Eq. 2-86a

$$D_0 = \left[\left(\frac{2}{\pi}\right)(E_0/\rho_0)\right]^{1/2} \quad (2\text{-}86b)$$

Integration* of Eq. 2-86a yields

$$\tau^* = \frac{1}{2\lambda_1}\left[1-(1-4\lambda_1\xi^2)^{1/2}\right] \quad (2\text{-}87)$$

where $\lambda_1 = -1.989$

Eq. 2-87 has the proper limiting value $\tau^* \rightarrow \xi^2$ as $\xi \rightarrow 0$ (strong shock). But $\tau^* \rightarrow (\xi/|\lambda_1|^{1/2})$ instead of the acoustic limit $\tau^* = \xi$ as $\xi \rightarrow \infty$. Vlases and Jones[22] found that Eq. 2-87 is a poor fit to intermediate shock trajectory data from an inverse pinch discharge. However, if one sets $\lambda_1 = -1$, Eq. 2-87 becomes

$$\tau^* = [(1+4\xi)^{1/2}-1]/2 \quad (2\text{-}88)$$

which yields the correct weak limit as $\xi \rightarrow \infty$. To match both limits for spherical, cylindrical, and plane blast, Jones assumed "the generalized correct limit trajectory equation",

$$\tau^* = a_J\left[\left(1+b_J\,\xi^{d_J}\right)^{e_J}-1\right] \quad (2\text{-}89)$$

To check the strong blast limit, Eq. 2-82, one has as $\xi \rightarrow 0$

$$a_J\,b_J\,e_J = 1 \text{ and } d_J = (n+2)/2 \quad (2\text{-}90)$$

To check the weak limit, Eq. 2-88, one has as $\xi \rightarrow \infty$

$$a_J\,b_J\,\xi^{e_J} = 1, \qquad e_J = 1/d_J = \frac{2}{n+2} \quad (2\text{-}91)$$

Solving Eqs. 2-90 and 2-91, one obtains in Eq. 2-89

$$b_J = \left(\frac{n+2}{2}\right)^{(n+2)n}, \qquad d_J = \left(\frac{2}{n+2}\right)^{2/n} \quad (2\text{-}92)$$

where a_J is 0.543, 0.500, and 0.444 and b_J is 4.61, 4.00, and 3.38 for spherical, cylindrical, and plane shocks (n = 3,2,1), respectively. Recalling that $d\xi/d\tau^* = M_s$, (the derivative of Eq. 2-89, being the derivative of a second-order approximation, is not as accurate as the Eq. 2-82 itself), substitution of the derivative from Eq. 2-89 into Eq. 2-84 predicts fast decay (for instance, in the case of cylindrical wave it leads to exactly Eq. 2-85), but in the weak limit P_s/p_0 is $[R_s\,(\ell n\,R_s)^{1/2}]$*, $R_s^{-3/4}$, and $R_s^{-1/2}$ for spherical, cylindrical, and plane shocks, respectively (Bethe[23]). So one has to return to the correct limit approach. Rewriting Eq. 2-85 in the form

$$Q_J = \frac{p_0}{P_s}\left(\frac{2\gamma}{\gamma+1}\right)\left(\frac{2}{n+2}\right)^2 = \xi^m\left(\frac{R_s}{R_0}\right)^m \quad (2\text{-}93)$$

in the strong limit, $m = n$.

In the weak limit, one may assume

$$\frac{P_s}{p_0} \text{ proportional to } \xi^{-q_J} \quad (2\text{-}94)$$

where

$$q_J = \frac{2n-1}{2n} = m \quad (2\text{-}95)$$

which yields the correct value $q_J = +\,3/4$ and $+\,1/2$ for cylindrical (n = 2) and plane (n = 1) shock, respectively. However, $\xi^{-5/6}$ was used to approximate $[\xi\,(\ell n\xi)^{1/2}]^{-1}$ for spherical

*$a_0/U_s = 1/M_s = d\tau^*/d\xi$ and Eq. 2-86a is therefore a differential equation which can be integrated.

*This limit for weak spherical shock can also be derived from Eqs. (41) and (34) of Whitham[24].

shocks, which decay faster than the approximate "limit equation" Eq. 2-93, with m given by Eq. 2-95. As before, to match the solution, assume

$$Q_J = C_J\left[\left(1+h_J\xi^{f_J}\right)^{q_J} - 1\right] \quad (2\text{-}96)$$

The strong shock limit ($\xi \to 0$) yields

$$q_J C_J h_J = 1 \text{ and } f_J = n \quad (2\text{-}97)$$

The weak shock limit ($\xi \to \infty$) yields

$$C_J h_J \xi^{q_J} = 1 \text{ and}$$
$$q_J = (2n-1)/(2n^2) \quad (2\text{-}98)$$

Eqs. 2-97 and 2-98 can then be solved for C_J

$$C_J = [2n^2/(2n-1)]^{-(2n-1)/(2n^2-2n+1)} \quad (2\text{-}99)$$

and

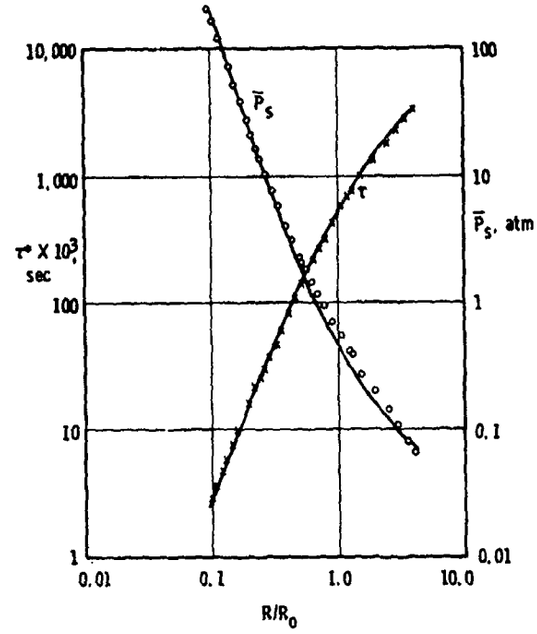
$$h_J = [2n^2/(2n-1)]^{2n^2/(2n^2-2n+1)} \quad (2\text{-}100)$$

The general equation for scaled peak overpressure is then

$$\frac{P_s}{p_0} = \frac{\frac{2\gamma}{\gamma+1}\left(\frac{2}{n+2}\right)^2}{C_J\left[\left(1+h_J\xi^n\right)^{(2n-1)/2n^2} - 1\right]} \quad (2\text{-}101)$$

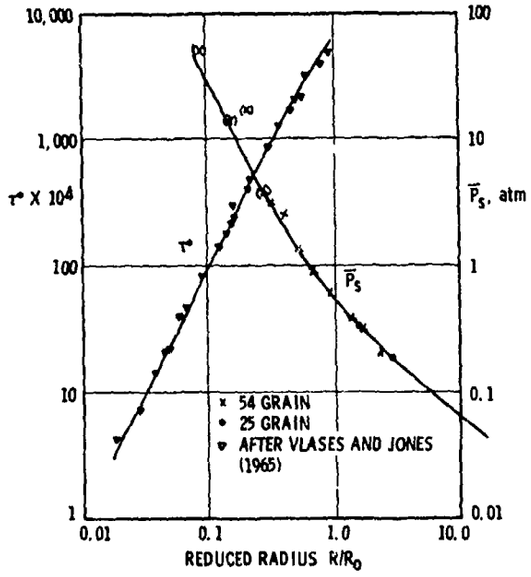
where C_J is 0.611, 0.555, and 0.500 and h_J is 5.89, 4.80, and 4.00 for spherical, cylindrical, and plane blast, respectively.

Results from Eqs. 2-89 and 2-101 have been compared with Brode's numerical solutions[8] for spherical shocks, Fig. 2-8. The trajectory is in excellent agreement while the overpressure did not agree too well near the weak limit, as may be expected; but, in the range shown, the worst error is less than 22%. Results from Eqs. 2-89 and 2-101 for cylin-



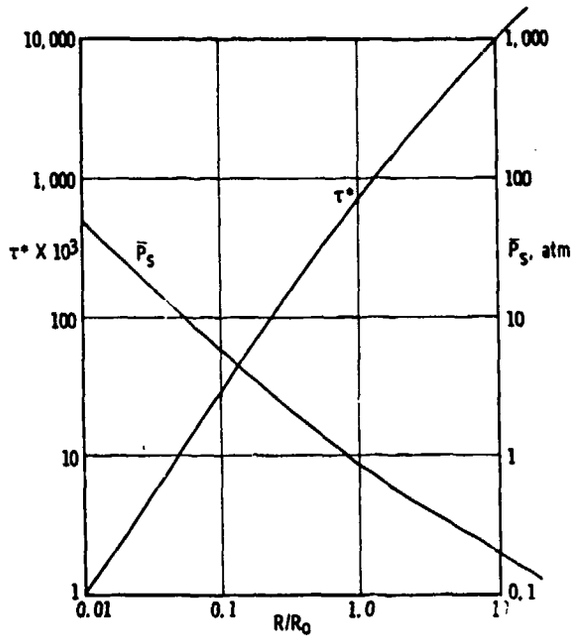
The solid curves are calculated from Eqs. 2-89 and 2-101 n = 3 for τ and $\bar{P}_s$, respectively. The data points are the calculated values of Brode.

Figure 2-8. Spherical Blast Wave[8]



The solid curves are calculated from Eqs. 2-89 and 2-101 n = 2 for τ and P_s, respectively. The data points on the τ curve are from the measurements of Vlases and Jones[22]. On the P_s curve the data points represent the work of Plooster.

Figure 2-9. Cylindrical Blast Wave



The solid curves are calculated from Eqs. 2-89 and 2-101 (n = 1) for τ and P_s, respectively.

Figure 2-10. Plane Blast Wave[8]

drical waves were in very good agreement with available experimental results, as seen in Fig. 2-9. Results for the plane shock wave are shown in Fig. 2-10.

It is noted that if the shock trajectory $R_s(t)$ is measured at one or more points, Eq. 2-89 will give R_0 and thus E_0 from Eq. 2-83 by successive approximations, although for cylindrical cases this is unnecessary as

$$E_0 = \frac{B\gamma p_0}{4}\left(\frac{R_s^2 - a_0^2 t^2}{a_0 t}\right)$$

then all points on the trajectory as well as overpressure may be calculated.

Similarly, if the overpressure is known, Eqs. 2-101 and 2-83 yield

$$E_0 = \left\{p_0\, B\gamma\,[2/(n+2)]^2\, R_s^n\, h_J\right\} \times \left\{\left[\frac{1}{C_J}\left(\frac{p_0}{P_s}\right)\left(\frac{2\gamma}{\gamma+1}\right)\left(\frac{2}{n+2}\right)^2 + 1\right]^{2n^2/(2n-1)} - 1\right\}^{-1} \quad (2\text{-}103)$$

then overpressure at all points as well as the trajectory may be calculated.

Jones[19] gave possible applications of these equations such as thermonuclear explosions, solar flares, lightning discharges and the like which may possess strength in the intermediate range. Nevertheless, the information obtained on shock trajectory and overpressure is insufficient in many applications, and additional (time-dependent) information behind the shock front needs to be calculated or supplemented by a numerical procedure.

2-3.5 THEILHEIMER'S SOLUTION FOR THE "TIME CONSTANT" OF AN AIR BLAST WAVE

A useful partial solution in blast wave theory has been generated by Theilheimer[30]. He defines a "time constant" from the empirical definition of time history of pressure*

$$p(t) = p_0 + P_s e^{-t/\theta} \quad (2\text{-}104)$$

where θ is the time constant. From this definition, one can see immediately that θ is given by the equation

$$\theta = -\frac{(p - p_0)}{\partial p/\partial t} \quad (2\text{-}105)$$

If this latter formula is assumed to define θ, then θ defines the initial pressure decay behind the shock front when evaluated at $t = 0^+$,

$$\theta = -\frac{P_s}{(\partial p/\partial t)\,|\,t = 0^+} \quad (2\text{-}106)$$

Theilheimer[30] derived formulas for θ from the basic equations for spherical shock waves, Eqs. 2-7 and 2-19 through 2-21. He used one additional definition for sound velocity behind the shock front,

$$a^2 = \left(\frac{\partial p}{\partial \rho}\right)_S \quad (2\text{-}107)$$

*This definition is identical to Eq. 1-4 in Chapter 1, with c replaced by $1/\theta$.

By taking total derivatives and by manipulating the basic equations, Theilheimer arrived at four equations

$$\left.\begin{aligned} &\rho\left(\frac{\partial u}{\partial t}+u\frac{\partial u}{\partial r}\right)+\frac{\partial p}{\partial r}=0 \\ &\frac{\partial p}{\partial t}+u\left(\frac{\partial p}{\partial r}\right)+a^2\rho\left(\frac{\partial u}{\partial r}\right)+\frac{2a^2\rho u}{r}=0 \\ &\frac{dp}{dR}=\frac{\partial p}{\partial r}+\frac{1}{U}\left(\frac{\partial p}{\partial t}\right) \\ &\frac{du}{dR}=\frac{\partial u}{\partial r}+\frac{1}{U}\left(\frac{\partial u}{\partial t}\right) \end{aligned}\right\} \quad (2\text{-}108)$$

These equations were combined to yield a single equation for $\frac{\partial p}{\partial t}$,

$$\frac{\partial p}{\partial t}=U\left\{\frac{2\rho u a^2}{R}(U-u)+\frac{dp}{dR}\left[a^2+u(U-u)\right]+\frac{du}{dR}a^2\rho U\right\} \times \left[a^2-(U-u)^2\right]^{-1} \quad (2\text{-}109)$$

If the various shock parameters and their spatial derivatives are known immediately behind the shock front, Eq. 2-109 permits calculation of the initial decay of the pressure-time history. By introducing the nondimensional overpressure

$$\bar{P}_s=P_s/p_0=(p-p_0)/p_0 \quad (2\text{-}110)$$

Eq. 2-109 can be rewritten as

$$\frac{1}{\theta}=-U\left[\frac{2\rho u a^2}{Rp_0}(U-u)+\frac{d\bar{P}_s}{dR}\times\left(a^2+u(U-u)\right)+\frac{du}{dR}\left(\frac{a^2\rho U}{p_0}\right)\right] \times\left\{\bar{P}_s\left[a^2-(U-u)^2\right]\right\} \quad (2\text{-}111)$$

Eq. 2-109 can be further reduced using the Rankine-Hugoniot Eq. 2-15, and an explicit equation of state for air. Theilheimer makes this reduction using the perfect gas law with ratio of specific heat $\gamma = 1.4$. When this is done, Eq. 2-111 becomes

$$\frac{1}{\theta}=-a_0\left(\frac{6\bar{P}_s+7}{7}\right)^{1/2}\left[\frac{7(\bar{P}_s+1)}{3\bar{P}_s R}+\frac{d\bar{P}_s}{dR}\left(\frac{7}{3\bar{P}_s^2}+\frac{7}{2\bar{P}_s}+\frac{2}{\bar{P}_s+7}\right)\right] \quad (2\text{-}112)$$

This equation is explicit in dimensionless overpressure $\bar{P}_s$, shock front radius R, and the first derivative of $\bar{P}_s$ with respect to shock front radius R. So, if the "shock line" of $\bar{P}_s$ versus R is known from theory or experiment, then Eq. 2-112 allows determination of the time constant. Theilheimer[30] computes θ from this equation using an empirical fit to the shock line for Pentolite spheres obtained by Stoner and Bleakney[31] (see also Chapter 5).

This particular partial solution is potentially useful for comparison with overpressure gage records, because it allows an independent check of the initial decay rate of these records.

2-4 SUMMARY OF PERTINENT EQUATIONS

In a chapter with over one hundred numbered equations, it is sometimes difficult for the reader to assess which equations are the important ones, and which are merely used in exposition or development of other equations. We will attempt to list here those equations most likely to be used by a blast analyst, under brief descriptive subheadings. The numbers used in earlier paragraphs in this chapter will be retained.

2-4.1 BASIC EQUATIONS OF MOTION

Momentum

$$\frac{\partial u_i}{\partial t} + \sum_{j=1}^{3} u_j \frac{\partial u_i}{\partial x_j} + \frac{1}{\rho} \frac{\partial p}{\partial x_i} = 0 \qquad (2\text{-}8)$$

Mass

$$\frac{\partial \rho}{\partial t} + \sum_{i=1}^{3} \frac{\partial (\rho u_i)}{\partial x_i} = 0 \qquad (2\text{-}9)$$

Energy

$$\frac{\partial S}{\partial t} + \sum_{i=1}^{3} u_i \left(\frac{\partial S}{\partial x_i}\right) = 0 \qquad (2\text{-}10)$$

State

$$p = f(\rho, S) \qquad (2\text{-}11)$$

2-4.2 RANKINE-HUGONIOT CONDITIONS

$$\rho_1 (u_1 - U) = \rho_2 (u_2 - U)$$

$$p_1 + \rho_1 (u_1 - U)^2 = p_2 + \rho_2 (u_2 - U)^2 \qquad (2\text{-}15)$$

$$\rho_1 (u_1^2/2 + e_1)(u_1 - U) + p_1 u_1 = \rho_2 (u_2^2/2 + e_2)(u_2 - U) + p_2 u_2$$

2-4.3 BASIC EQUATIONS FOR SPHERICALLY SYMMETRIC FLOW

Momentum

$$\frac{\partial u}{\partial t} + u \left(\frac{\partial u}{\partial r}\right) + \frac{1}{\rho} \left(\frac{\partial p}{\partial r}\right) = 0 \qquad (2\text{-}19)$$

Mass

$$\frac{\partial \rho}{\partial t} + u \left(\frac{\partial \rho}{\partial r}\right) + \rho \left(\frac{\partial u}{\partial r}\right) + \frac{2u\rho}{r} = 0 \qquad (2\text{-}20)$$

Energy

$$\frac{\partial S}{\partial t} + u \left(\frac{\partial S}{\partial r}\right) = 0 \qquad (2\text{-}21)$$

State

$$p = f(\rho, S) \qquad (2\text{-}11)$$

2-4.4 TAYLOR'S SIMILARITY SOLUTION

Energy

$$E = 5.36\, \rho_0 A^2 \qquad (2\text{-}50)$$

Maximum Pressure

$$p_{max} = p_1 = 0.155\, R^{-3} E$$

Shock Velocity

$$U = R^{-3/2} E^{1/2} (B\rho_0)^{-1/2} \qquad (2\text{-}51)$$

Arrival Time

$$t_a = 0.926\, R^{3/2} \rho_0^{1/2} E^{-1/2}$$

Shock Radius

$$R = \left[\frac{5}{2}\left(\frac{E_0^{1/2} \rho_0^{-1/2}}{\sqrt{5.36}}\right) t\right]^{2/5} \qquad (2\text{-}52)$$

2-4.5 THEILHEIMER'S SOLUTION FOR INITIAL DECAY OF A SHOCK

Initial Decay of Pressure

$$\frac{\partial p}{\partial t} = U \left\{ \frac{2\rho u a^2}{R} (U-u) + \frac{dp}{dR}\left[a^2 + u(U-u)\right] + \frac{du}{dR} a^2 \rho U \right\} [a^2 - (U-u)^2]^{-1} \qquad (2\text{-}109)$$

Inverse of Time Constant

$$\frac{1}{\theta} = -U\left[\frac{2\rho ua^2}{Rp_0}(U-u) + \frac{d\bar{P}_s}{dR}\left(a^2 + u(U-u)\right) + \frac{du}{dR}\left(\frac{a^2\rho U}{p_0}\right)\right] \times \left\{\bar{P}_s\left[a^2 - (U-u)^2\right]\right\}^{-1} \quad (2\text{-}111)$$

Inverse of Time Constant, $\gamma = 1.4$

$$\frac{1}{\theta} = -a_0\left(\frac{6\bar{P}_s + 7}{7}\right)^{1/2}\left[\frac{7(\bar{P}_s + 1)}{3\bar{P}_s R} + \frac{d\bar{P}_s}{dR} \times \left(\frac{7}{3\bar{P}_s} + \frac{7}{2\bar{P}_s} + \frac{2}{\bar{P}_s + 7}\right)\right] \quad (2\text{-}112)$$

REFERENCES

1. R. Courant and K. O. Friedrichs, *Supersonic Flow and Shock Waves*, Interscience Pub., Inc., New York, 1948.

2. W. Döering and G. Burkhardt, *Contributions to the Theory of Detonation*, TR No. F-TS-1227-1A, Wright-Patterson AFB, Ohio, May 1949.

3. H. Hugoniot, "Memoire sur la propagation du mouvement dans les corps et specialement dans les gaz parfaits", *J. del l'école Polytech. Paris*, 57 (1887), and 58 (1889).

4. G. I. Taylor, "The Formation of a Blast Wave by a Very Intense Explosion, *Proc. Roy. Soc.*, **A201**, 159 (1950).

5. S. K. Garg and J. Siekmann, "Approximate Solution of the Propagation of an Axisymmetric Blast Wave Generated by a Finite Spherical Charge", ZAMP, **17**, 1, 108-121 (1966).

6. H. W. Liepmann and A. E. Puckett, *Introduction to Aerodynamics of a Compressible Fluid*, John Wiley & Sons, New York, 1947.

7. Shao-Chi Lin, "Cylindrical Shock Waves Produced by an Instantaneous Energy Release", Jour. Appl. Phys., **25**, 1 (1954).

8. H. L. Brode, "Numerical Solutions of Spherical Blast Waves", Jour. Appl. Phys., **26**, 6, 766-775 (1955).

9. A. K. Oppenheim, *The No-man's Land of Gas Dynamics of Explosions*, AIAA Paper No. 66-517, *AIAA 6th Aerospace Sciences Meeting*, Los Angeles, California, June 1966.

10. La. B. Zeldovich and A. S. Kompaneets, *Theory of Detonation*, Academic Press, New York, 1960.

11. R. E. Shear and E. Q. Wright, *Calculated Peak Pressure-Distance Curves for Pentolite and TNT*, BRL Memorandum Report No. 1423, Aberdeen Proving Ground, Maryland, August 1962.

12. P. I. Richards, *Sharp Shock Lagrangian Hydrodynamic Code*, Rept. No. TO-B 66-74, Ballistic Research Labs., Aberdeen Proving Ground, Maryland, October 1966.

13. S. I. Pai, *Introduction to Theory of Compressible Flow*, D. Van Nostrand Co., Inc., New York, 1959.

14. G. B. Whitham, "A New Approach to Problems of Shock Dynamics, Part II, Three-Dimensional Problems", Jour. Fluid Mechanics, **5**, Part 3, 369-386 (1959).

15. A. E. Bryson and R. W. F. Gross, "Diffraction of Strong Shocks by Cones, Cylinders and Spheres", Jour. Fluid Mechanics, **10**, Part 1, 1-16, (1961).

16. G. Rudinger, *Wave Diagrams for Non-steady Flow in Ducts*, D. Van Nostrand Co., Inc., New York, 1955.

17. G. G. Bach and J. H. S. Lee, "An Analytic Solution for Blast Waves", AIAA Journal, **8**,2 (1970).

18. R. S. Srivastava and M. G. Chopra, "Diffraction of Blast Wave for the Oblique Case", Jour. Fluid Mechanics, **40**, Part 4, 821-831 (1970).

19. D. L. Jones, "Intermediate Strength Blast Wave", Phys. of Fluids, **11**, 8 (1968).

20. D. L. Jones, *Energy Parameter B for Strong Blast Waves*, National Bureau Standards Tech. Note 155, 1962.

21. A. Sakurai, "On the Propagation of Structures of the Blast Wave, Part I", Jour. of Phys. Soc. of Japan, **8**, 5, 662-669 (1953). Also, "Part II , Jour. of Phys. Soc. of Japan, **9**, 2, 256-266 (1954).

22. G. C. Vlases and D. L. Jones, "Blast Waves from an Inverse Pinch Machine", Phys. of Fluids, **9**, 3, 478-484 (1966).

23. H. A. Bethe, *Shock Hydrodynamics and Blast Waves*, Los Alamos Scientific Lab., Univ. of Calif. Report AECD-2860, 1944.

24. G. B. Whitham, "The Propagation of Weak Spherical Shocks in Stars", Comm. Pure and Appl. Math., **VI**, 397-414 (1953).

25. M. H. Rogers, "Similarity Flows Behind Strong Shock Waves", Quart, Jour. Mech. Appl. Math., **11**, 411 (1958).

26. C. A. Rouse, "Theoretical Analysis of the Hydrodynamic Flow in Exploding Wire Phenomena", *Exploding Wires*, p. 227, Plenum Press, New York, 1959.

27. L. I. Sedov, *Similarity and Dimensional Methods in Mechanics*, p. 210, Academic Press, New York 1959.

28. D. L. Jones, "Strong Blast Waves in Spherical, Cylindrical and Plane Shocks", Phys. Fluids, **4**, 1183 (1961). (Also see Erratum, Phys. Fluids, **5**, 637. May 1962).

29. N. Gerber and J. M. Bartos, *Tables of Cylindrical Blast Functions*, BRL Memorandum Report 1376, Aberdeen Proving Ground, Maryland, 1961.

30. F. Theilheimer, *The Determination of the Time Constant of a Blast Wave from the Pressure-Distance Relation*, NAVORD Report 1734, U. S. Naval Ordnance Lab., December 1950.

31. R. G. Stoner and W. Bleakney, "The Attenuation of Spherical Shock Waves in Air", Jour. of Appl. Phys., **19**, 670-678, (1948).

32. G. I. Taylor, "The Propagation and Decay of Blast Waves", Paper 20 in *The Scientific Papers of Sir Geoffrey Ingram Taylor*, Vol. III, Cambridge Univ. Press, 1963, pp. 221-235.

33. W. Chester, *Phil. Mag.*, 45, pp. 1293-1301, 1954.

34. G. B. Whitham, "A New Approach to Problems of Shock Dynamics, Part I, Two Dimensional Problems", *Jour. Fluid Mechanics*, pp. 145-171, (1957).

CHAPTER 3

BLAST SCALING

3-0 LIST OF SYMBOLS

a = radius of perfect gas sphere simulating a blast source initially

a_0 = sound velocity in ambient air

b = acceleration

B_i = angular moments

c_p = specific heat at constant pressure

c_v = specific heat at constant volume

C_i = plastic moduli

d = diameter or characteristic dimension of blast source

e = specific energy

E = total energy of explosive

E_{st} = modulus of elasticity or plasticity of structural material

f_i = functions

F = force dimension

H = enthalpy

I = impulse (integral of pressure-time history)

I_r = reflected impulse

k = a scale factor

K = a scale factor, a force

ℓ_i = length ratios

L = length dimension

M = molar mass of gas

m, M_E, M_A, M_T = masses of gas, explosive, etc.

p = absolute pressure

p_0 = ambient pressure

p_r = reflected pressure

p_s = side-on overpressure

$p(t)$ = functional form of overpressure

$\bar{p}$ = shock strength; pressure ratio

P = peak overpressure

P_s = peak side-on overpressure

$\bar{P}, \bar{R}$, etc. = nondimensional pressure, distance, etc.

q = dynamic pressure

r = radius of blast source

r_i = nondimensional length ratios

r_I = initial radius of spherical explosive charge

R = distance from center of blast source

s = specific entropy

S = scaling factor used by John Dewey

t = time

t_a = arrival time of blast wave

T = duration of positive phase of blast wave, also time dimension

u = flow or particle velocity

U = shock wave velocity

V = flight velocity

W = weight or mass of explosive

Z = $R/E^{1/3}$ = scaled distance

α = a power

α_i = angles

δ = maximum permanent deflection in beam

γ = ratio of specific heats

ϵ_i = strains

ζ = $I/E^{1/3}$ = scaled impulse

θ = absolute temperature

λ = a scale factor, also Sachs' scaled distance

μ = viscosity

ξ = scaled size of blast source

π_i = a dimensionless product or group

ρ = density

ρ_{st} = density of structural material

σ_i = stresses

τ = $t/E^{1/3}$ = scaled time

3-1 INTRODUCTION

Experimental studies of blast wave phenomenology are often quite difficult and expensive, particularly when conducted on a large scale, and, as we will see in Chapter 4, methods of cor ation of blast wave characteristics are of so involved that one cannot repeat these computations economically while varying in a systematic manner all of the physical parameters that may affect the blast wave. Thus, almost from the outset of scientific and engineering studies of air blast, various investigators have attempted to generate model of scaling laws which would widen the applicability of their experiments or analyses.

3-2 SCALING LAWS FOR BLAST PARAMETERS

3-2.1 HOPKINSON SCALING

3-2.1.1 DEFINITION

The most common form of scaling (familiar to anyone who has had even a rudimentary introduction to blast) is Hopkinson or "cube-root" scaling. This law, first formulated by B. Hopkinson[1], states that self-similar blast (shock) waves are produced at identical scaled distances when two explosive charges of similar geometry and the same explosive composition, but of different size, are detonated in the same atmosphere. It is customary to use as the scaled distance a dimensional parameter, but this dimensional parameter uniquely determines a corresponding non-dimensional parameter, as we will show later. The customary dimensional scaled distance Z is either

$$Z = \frac{R}{W^{1/3}} \qquad (3\text{-}1a)$$

or

$$Z = \frac{R}{E^{1/3}} \qquad (3\text{-}1b)$$

where

R = distance from the center of the explosive source

E = energy of the explosive

W = weight of the explosive.

The use of E instead of W is preferred, for the reasons that follow.

In much of the reported work on air blast technology, W is given in pounds weight or pounds mass of the explosive, or in "TNT equivalent" (kilotons or megatons), which is common in reporting of blast data from nuclear weapon tests. But, any study of the physics of generation of blast waves demonstrates that the important parameters of the explosive source are its total energy E and its energy density, i.e., energy per unit volume or mass. This is apparent from simply considering the differences in nuclear and chemical explosives, for example; and the process which one must use in calculating a TNT equivalence for a nuclear weapon. It is obvious that the total weight or mass of explosive in a large TNT-filled bomb can be much greater than the mass of nuclear explosive in a nuclear weapon. Yet, even the smallest yield nuclear weapon has much more potential energy per unit mass than the largest TNT bomb because the total energy capable of being released is much greater for the nuclear weapon. Calculation of TNT equivalence for the nuclear weapon is, therefore, always based on a comparison of *energies* available in the two types of blast sources instead of explosive weights. Usually, the heat of detonation of about 1000 cal/g or 1.4×10^6 ft-lb_f/lb_m is used as the specific energy for TNT in such computations*.

The heat of detonation can be measured easily for chemical explosives in the laboratory by burning or detonating small quantities of the explosive in a bomb calorimeter that has been purged and pressurized with an inert gas. Procedures for measuring heats of explosion have been thoroughly described[2], and numerical values for many explosives have been reported[3]. Examples of the use of heats of explosion to estimate "TNT equivalents" and values for these equivalents for a number of common explosives will be given in Chapter 6.

The implications of Hopkinson scaling can perhaps be best described by the example illustrated in Fig. 3-1. An observer located a distance R from the center of an explosive source of characteristic dimension d will be subjected to a blast wave with an amplitude (peak overpressure) P, a duration T, and a characteristic pressure-time history $p(t)$. The positive impulse I in the blast wave is defined by

$$I = \int_{t_a}^{t_a + T} p(t)dt \qquad (3\text{-}2)$$

where t_a is arrival time of the shock front and $p(t)$ is the functional form of the time-varying overpressure. The positive impulse also is used often to characterize the blast wave. The Hopkinson scaling law states that an observer stationed a distance KR from the center of a similar explosive source of characteristic dimension Kd detonated in the same atmosphere will feel a blast wave of a similar form, the same amplitude P, but a duration KT and impulse KI. All characteristic times, such as arrival time t_a, are scaled by the same factor as the length scale factor K. In Hopkinson scaling, scaled blast wave pressures and velocities are unchanged at homologous* times.

3-2.1.2 EXPERIMENTAL VERIFICATION

Hopkinson scaling has been shown by many investigators to apply over a very wide range of distances and for a wide range of explosive source energies. One of the earliest confirmations of this law is reported by Kennedy[4] for blast measurements about a variety of bombs and explosive charges, which only crudely satisfied the requirements of

*One pound mass of TNT (W = 1 lb_m) therefore has a total energy E of 1.4×10^6 ft-lb_f.

*"Homologous" means "similar, but not necessarily equal".

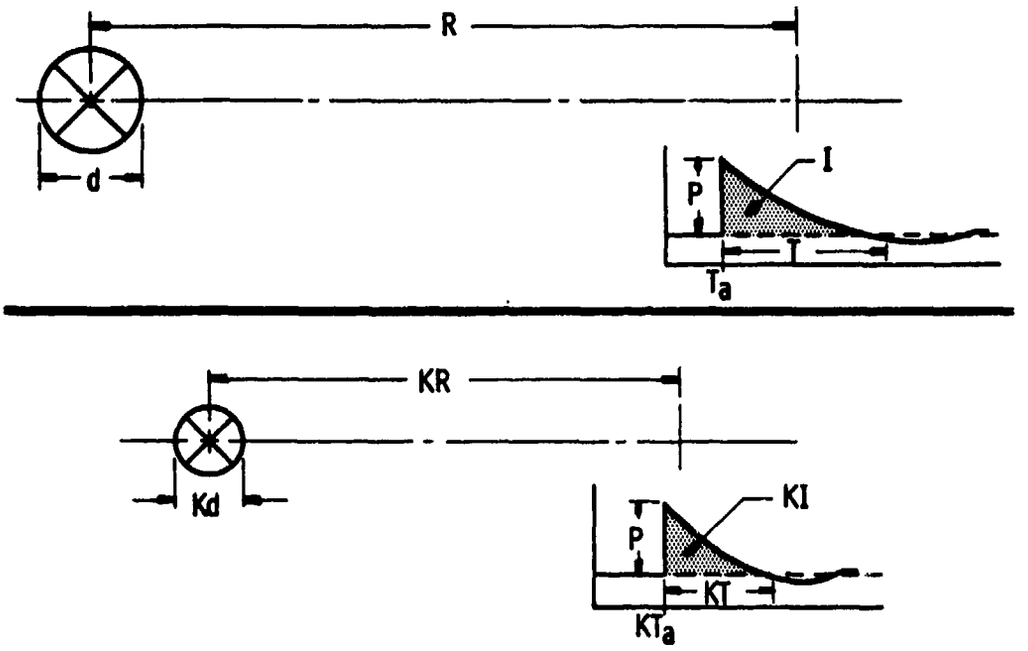


Figure 3-1. Hopkinson Blast Wave Scaling

geometrical similarity*. The charge masses used in these experiments ranged from a few pounds of explosive up to several thousand pounds. Comparisons of the peak overpressure and scaled positive impulse data from this World War II work are shown in Figs. 3-2 and 3-3. It can be seen in these figures that the "Hopkinson-scaled" curves for the data from various sources show the same general functional forms, but they differ in amplitude at some scaled distances by factors of as much as two.

Another example of early published work reporting Hopkinson-scaled blast wave data is that of Stoner and Bleakney[5], which demonstrated Hopkinson scaling for a limited range of distances and source energies. The validity of Hopkinson scaling of peak particle velocity has been well demonstrated for a much larger range of explosive charge weights by John Dewey[6], who measured such velocities in blast waves from TNT explosions. Fig. 3-4 shows the close agreement that Dewey found in his scaled data for various charge

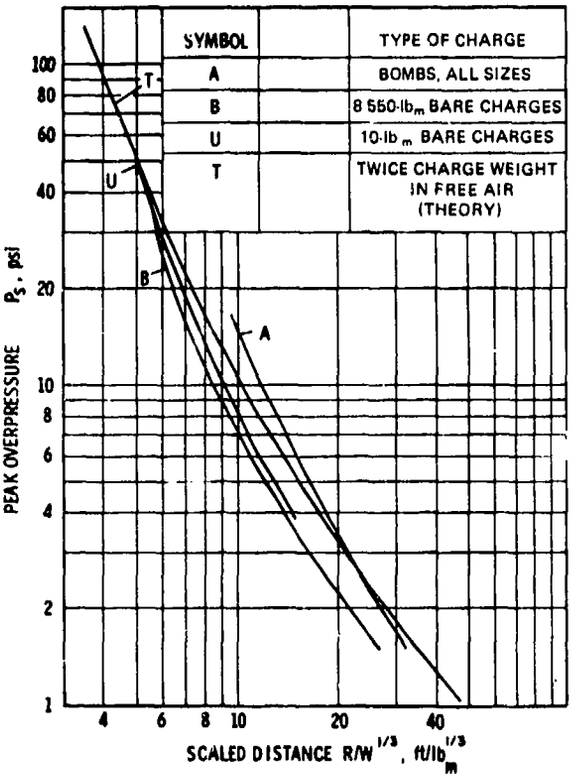


Figure 3-2. Pressure-distance Curve for Ground-burst Blast of Bare Charges[4]

*In reporting experimental data in this handbook, dimensions used in the original references usually will be retained.

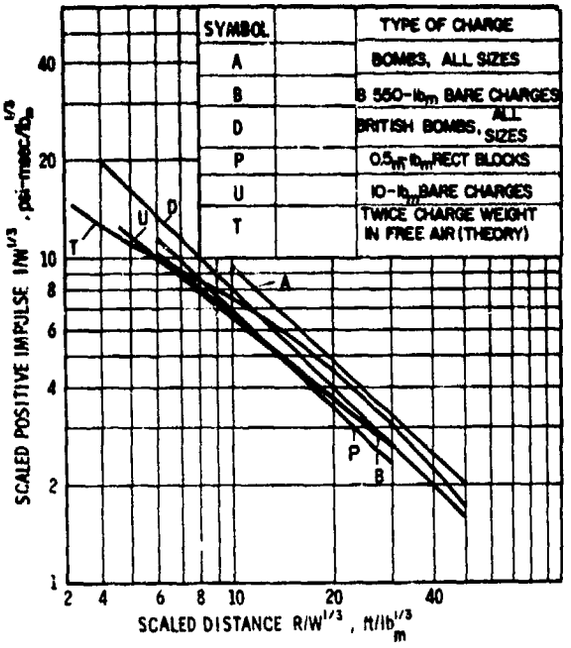


Figure 3-3. Experimental Positive Impulses vs Distance Curves (on ground) from Various Sources[4]

weights*. The list of other investigations corroborating this law is too long to include here, but in a recent report by Kingery[7] very good agreement was shown between blast data obtained during field tests with 5-, 20-, 100-, and 500-ton TNT detonations when scaled to a 1-lb TNT charge.

3-2.1.3 IMPLICATIONS

Hopkinson's scaling law, in fact, has become so universally used that blast data are almost always presented in terms of Hopkinson-scaled parameters

$$\left.\begin{aligned} Z &= R/E^{1/3} \quad \text{or } R/W^{1/3} \\ &\quad \text{(scaled distance)} \\ \tau &= t/E^{1/3} \quad \text{or } t/W^{1/3} \\ &\quad \text{(scaled time)} \\ \zeta &= I/E^{1/3} \quad \text{or } I/W^{1/3} \\ &\quad \text{(scaled impulse)} \end{aligned}\right\} \qquad (3\text{-}3)$$

*The quantity S used for scaling distance in Fig. 3-4 is given by $S = (W p_o)^{1/3}$, where W is in units of lb_m and p_o in sea level atmospheres.

This law implies that all quantities with dimension of pressure and velocity are unchanged in the scaling. Thus, side-on pressure p_s, dynamic pressure q, and reflected pressure p_r all remain identical at homologous times as well as both the shock velocity U and time histories of the particle velocity u. The law can be stated in another way

$$\left.\begin{aligned} p &= p(Z) \\ \tau &= \tau(Z) \\ U &= U(Z) \\ \zeta &= \zeta(Z) \end{aligned}\right\} \qquad (3\text{-}4)$$

i.e., each specific pressure, time, velocity, or scaled impulse is given by a unique function of scaled distance Z.

As an example of an application of Hopkinson's scaling, let us assume that a 1-lb_m hemispherical TNT charge (W = 1-lb_m) detonated on the ground surface produces a peak side-on overpressure P_s of 10 psi at a distance R of 9 ft. The positive duration T of this wave is 1.8 msec and the positive impulse I_s is 9 psi-msec. Hopkinson's law allows immediate prediction of the properties of the blast wave from any other hemispherical TNT charge at a certain specific distance defined by the law. The calculations are as follows:

W_1 = 1-lb_m, $(W_1)^{1/3} = (1\text{-}lb_m)^{1/3}$

R_1 = 9 ft

T_1 = 1.8 msec

I_{s_1} = 9 psi-msec

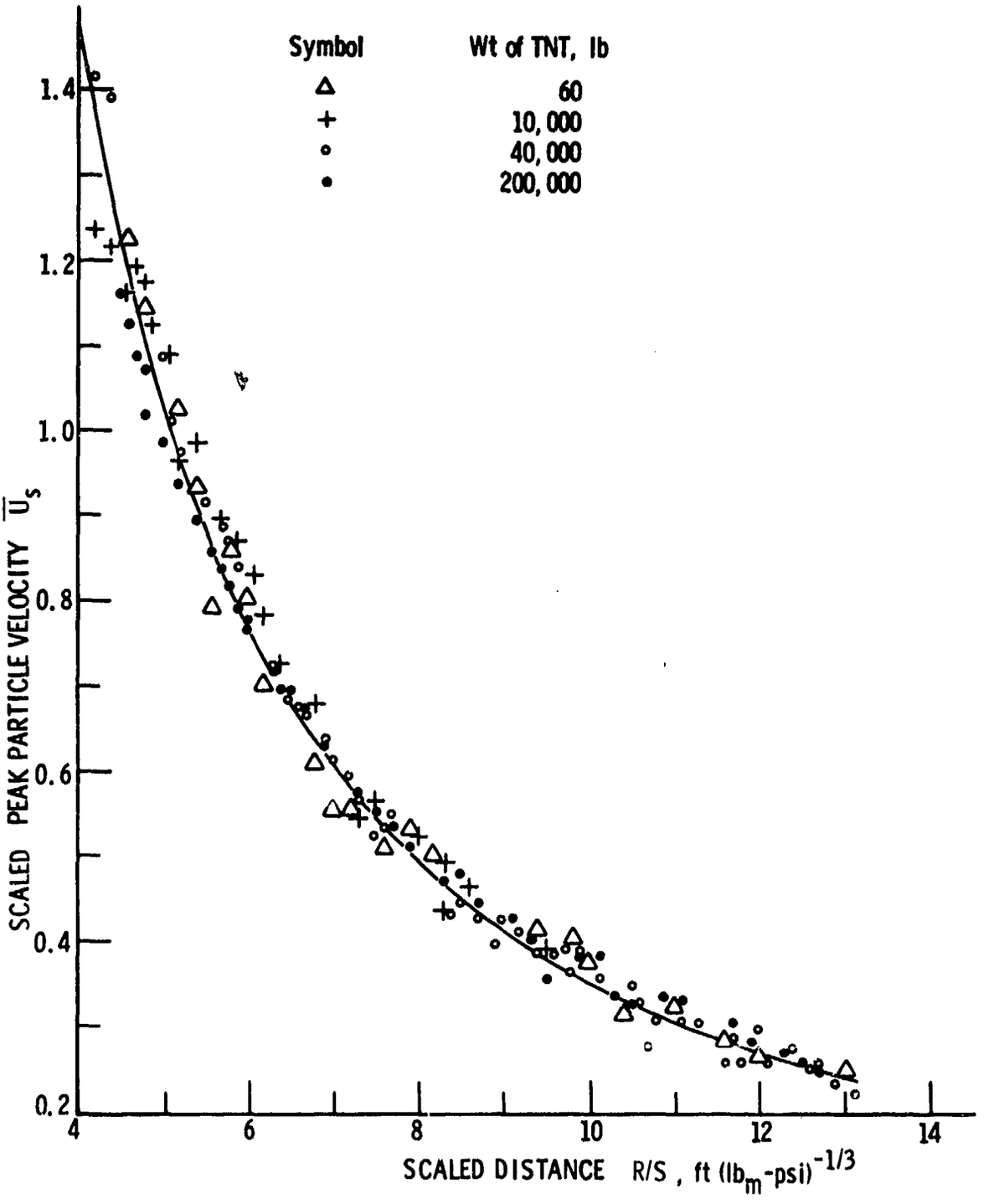
P_{s_1} = 10 psi

$Z_1 = R_1/(W_1^{1/3}) = 9$ ft/1-$lb_m)^{1/3}$

$= 9$ ft/$lb_m^{1/3}$

$\zeta_1 = I_{s_1}/(W_1^{1/3}) = 9$ psi-msec/$(1\text{-}lb_m)^{1/3}$

$= 9$ psi-msec/$lb_m^{1/3}$



The line shows the particle velocity calculated from the shock velocity.

Figure 3-4. Comparisons of Peak Particle Velocities for Surface Burst TNT Charges[6]

$$\tau_1 = T_1/(W_1^{1/3}) = 1.8 \text{ msec}/(1\text{-lb}_m)^{1/3}$$

$$= 1.8 \text{ msec/lb}_m^{1/3}$$

Now let $W_2 = 1000$ lb$_m$ of TNT. For $Z_1 = Z_2$, Hopkinson's law requires that $P_{s_1} = P_{s_2}$, $\zeta_1 = \zeta_2$, and $\tau_1 = \tau_2$, i.e., all scaled parameters are unchanged by the scaling. Because $Z_2 = R_2/W_2^{1/3}$, and $W_2^{1/3} = (1000 \text{ lb}_m)^{1/3} = 10 \text{ lb}_m^{1/3}$, $Z_1 = Z_2 = 9 \text{ ft/lb}_m^{1/3} = R_2/W_2^{1/3} = R_2 \text{ ft}/10 \text{ lb}_m^{1/3}$, and $R_2 = 9 \times 10 = 90$ ft.

Similarly, $I_{s_2} = 9 \times 10 = 90$ psi-msec and $T_2 = 1.8 \times 10 = 18$ msec. So, a 1000-lb$_m$ charge produces a blast wave with peak pressure $P_s = 10$ psi, having an impulse I_s of 90 psi-msec and lasting 18 msec at a distance R of 90 ft.

3-2.1.4 MODEL ANALYSIS

It is not immediately apparent that Hopkinson scaling is dimensionless modeling, because the parameters shown in Eq. 3-3 are not dimensionless. A model analysis will show, however, that the parameters indeed are defined uniquely by dimensionless groups. We will demonstrate this by listing a possible set of physical parameters that should govern blast waves in air under any given ambient conditions, together with their dimensions in a force-length-time (FLT) system, and then construct the dimensionless groups.

The source of blast energy is defined by its local energy E, a characteristic length r indicating the size of the source, and a group of nondimensional length ratios r_i that fix the entire geometry of the source and experiment. The latter term introduces the convention or shortand notation of a subscript i to denote a number of similar nondimensional parameters. Here we imply that there are enough such terms to completely describe the geometry of the entire experiment.

The distance R from the center of the blast source is an important parameter. We wish to observe or measure a number of physical properties of the blast wave at the location R. A primary one is the overpressure p as a function of time t. These two quantities should then be included in our list of parameters. Furthermore, we add to the list the shock front velocity U, the particle velocity (or flow velocity) u, and the density ρ in the air behind the shock front—all of which can be measured or predicted. We could also include temperature θ behind the shock front, but this can be determined from a separate physical relationship, an equation of state for air, if ρ and p are known.

Finally, we know from both theory and experiment in gas dynamics that the transmission of blast waves through a compressible fluid is affected by the ambient conditions in the fluid ahead of the shock front. Two such parameters will suffice to define these conditions, again under the presumption that an equation of state for the fluid is known*. Let us choose ambient pressure p_0 and sound velocity a_0. Although these parameters will not be varied between model and prototype in Hopkinson scaling, they are included because they are important in the physics of the problem—shock strengths and velocities are, indeed, functions of these two parameters.

The eleven physical parameters that have been described are listed in Table 3-1, together with their dimensions in a force-length-time (FLT) system**. Because we wish to emphasize the physical aspects of this problem rather than the mechanism of generation of a model law, we will simply present a possible set of Buckingham π terms which is consistent with the parameters of Table 3-1. We note that the eleven physical parameters, less three fundamental dimensions, dictate that there should be eight π terms. These eight terms are:

*Actually, three quantities are required to fully describe an equation of state for air, but one of these can be assumed to be the ratio of specific heats γ_i. It is omitted because it is already dimensionless and does not affect the model analysis.

**Any consistent set of units can be used. We would assume the English system and let the units for force F be pounds force, for length L be feet, and for time T be seconds. An equally valid set would result from use of the cgs system where the units of F are dynes, L are centimeters, and T are seconds.

TABLE 3-1

LIST OF PHYSICAL PARAMETERS FOR HOPKINSON BLAST SCALING

Symbol	Description	Units*
E	Total energy in blast source	FL
r	Size of source	L
r_i	Shape of source, geometry of experiment	—
R	Distance from source	L
p	Pressure in blast wave	F/L^2
U	Shock velocity	L/T
u	Particle velocity in blast wave	L/T
ρ	Density of gas in blast wave	FT^2/L^4
t	Time	T
p_0	Ambient pressure ahead of blast front	F/L^2
a_0	Sound velocity in ambient air	L/T

*F = force, L = length, and T = time.

$$\left.\begin{aligned} \pi_1 &= r_i & \pi_5 &= p/p_0 \\ \pi_2 &= R/r & \pi_6 &= pr^3/E \\ \pi_3 &= U/a_0 & \pi_7 &= \rho u^2/p \\ \pi_4 &= U/u & \pi_8 &= tu/r \end{aligned}\right\} \quad (3\text{-}5)$$

The set of Eqs. 3-5 constitute the model law. For strict adherence to the law, all eight dimensionless groups should remain invariant between model and prototype. This requires the following relationship between scale factors*:

$$\left.\begin{aligned} &\pi_1 \rightarrow \text{geometric similarity of blast sources} \\ &\pi_2 \rightarrow \lambda_R = \lambda_r \qquad \pi_6 \rightarrow \lambda_p \lambda_r^3 = \lambda_E \\ &\pi_3 \rightarrow \lambda_U = \lambda_{a_0} \qquad \pi_7 \rightarrow \lambda_\rho \lambda_u^2 = \lambda_p \\ &\pi_4 \rightarrow \lambda_U = \lambda_u \qquad \pi_8 \rightarrow \lambda_t \lambda_u = \lambda_r \\ &\pi_5 \rightarrow \lambda_p = \lambda_{p_0} \end{aligned}\right\} \quad (3\text{-}6)$$

*The symbol λ with a subscript defines the ratio of model to prototype for the particular physical quantity indicated by the subscript.

The model law, Eq. 3-5, is quite general until additional restrictions are imposed. First, recall that Hopkinson scaling is limited to model and prototype experiments conducted under identical atmospheric conditions. Scale factors for p_0 and a_0, relating the model and prototype, are, therefore, unity for this type of scaling, i.e.,

$$\lambda_{p_0} = \lambda_{a_0} = 1 \tag{3-7}$$

This restriction drastically reduces the generality of Eqs. 3-6, as follows:

$$\left.\begin{aligned}
&\pi_1 \rightarrow \text{geometric similarity of blast sources}\\
&\pi_2 \rightarrow \lambda_R = \lambda_r, \text{ geometric similarity of entire experiment}\\
&\pi_3 \rightarrow \lambda_U = 1, \text{ equivalence of shock velocity}\\
&\pi_3, \pi_4 \rightarrow \lambda_u = 1, \text{ equivalence of particle velocity}\\
&\pi_5 \rightarrow \lambda_p = 1, \text{ equivalence of blast pressure}\\
&\pi_5, \pi_6 \rightarrow \lambda_E = \lambda_r^3, \text{ scaling of blast energy}\\
&\pi_4, \pi_5, \pi_7 \rightarrow \lambda_\rho = 1, \text{ equivalence of density}\\
&\pi_4, \pi_8 \rightarrow \lambda_t = \lambda_r, \text{ equivalence of time and space scaling}
\end{aligned}\right\} \tag{3-8}$$

Eq. 3-8 is, indeed, Hopkinson's law. If one drops from Eq. 3-5 all terms which are identically satisfied by the assumptions*, Eq. 3-5 can then be rewritten as

$$\frac{pr^3}{E} = f(r_i, R/r, ta_0/r, \ldots) \tag{3-9}$$

which states that a scaled pressure parameter is a function of scaled geometry and time. Had this form been used in reporting scaled blast data, then the Hopkinson-scaled data would have been dimensionless. Introduction of dimensions in the usual sense of Eqs. 3-1 and 3-3 occurs if one applies to Eq. 3-9 the relations $\lambda_{a_0} = 1$, $\lambda_r^3 = \lambda_E$, and the cube root of this latter expression, $\lambda_r = \lambda_E^{1/3}$. Then Eq. 3-9 becomes

$$p = f(r_i, R/E^{1/3}, t/E^{1/3}, \ldots) \tag{3-10}$$

We have now seen how *dimensionless* products uniquely determine functional forms for certain *dimensional* groups, given specific restrictions on a model-prototype comparison.

3-2.2 SACHS' SCALING

In an attempt to account for the effects of altitude or other changes in ambient conditions on air blast waves, Sachs[8] proposed a more general blast scaling law than that of Hopkinson. Sachs' scaling law states that dimensionless groups can be formed which involve pressure, time, impulse, and certain parameters for the ambient air; and that these groups are unique functions of a dimensionless distance parameter. Specifically the groups

$$\left(\frac{p}{p_0}, \frac{Ia_0}{E^{1/3} p_0^{2/3}}, \frac{ta_0 p_0^{1/3}}{E^{1/3}}\right)$$

are stated to be unique functions of $(Rp_0^{1/3}/E^{1/3})$.

Sample Calculation

An experiment conducted under sea level atmospheric conditions yields a prediction of blast parameters under any other ambient conditions. A TNT sphere weighing 2 lb_m is detonated in free air at sea level ambient conditions given by p_0 = 14.7 psi and a_0 = 1100 ft/sec. At a distance R = 9 ft from the center of the charge, the measured overpressure is P_s = 10 psi, positive duration is T = 1.8 msec, and positive impulse is I_s = 9 psi-msec. We wish to know how this measurement scales according to Sachs' law at an altitude of 40,000 ft where p_0 = 2.73 psi and a_0 = 968 ft/sec, with the same explosive source.

*By "identically satisfied", we mean that *all* scale factors on both sides of one of the Eq. 3-8 are unity.

Sachs' scaled distance is $Rp_0^{1/3}/E^{1/3}$. The total energy E is obtained by multiplying the charge mass W by the specific energy for TNT of 1.4×10^6 ft-lb$_f$/lb$_m$.

$$E = 2 \times 1.4 \times 10^6$$

$$= 2.8 \times 10^6 \text{ ft-lb}_f$$

Then,

$$\bar{R} = \frac{R\,p_0^{1/3}}{E^{1/3}}$$

$$= \frac{9 \text{ ft} \times \left(14.7 \frac{\text{lb}_f}{\text{in.}^2} \times 144 \frac{\text{in.}^2}{\text{ft}^2}\right)^{1/3}}{(2.8 \times 10^6 \text{ ft-lb}_f)^{1/3}}$$

$$= \frac{9 \times 12.8}{140.9}$$

$$\bar{R} = 0.821$$

Note that this parameter is rendered *dimensionless* by suitable choice of units. Similarly, the three other groups in Sachs' law can be made dimensionless, as follows:

$$\bar{I}_s = P_s/p_0 = 10 \text{ psi}/14.7 \text{ psi} = 0.680$$

$$I_s = \frac{I_s\,a_0}{E^{1/3} p_0^{2/3}}$$

$$= \left(9 \frac{\text{lb}_f \text{ msec}}{\text{in.}^2}\right) \times \left(10^{-3} \frac{\text{sec}}{\text{msec}}\right) \times \left(1100 \frac{\text{ft}}{\text{sec}}\right) \times \left(12 \frac{\text{in.}}{\text{ft}}\right) \times \left[\left(2.8 \times 10^6 \text{ ft-lb}_f \times 12 \frac{\text{in.}}{\text{ft}}\right)^{1/3} \times \left(14.7 \frac{\text{lb}_f}{\text{in.}^2}\right)^{2/3}\right]^{-1}$$

$$\bar{I}_s = 0.0615$$

$$\bar{T} = \frac{T a_0 p_0^{1/3}}{E^{1/3}}$$

$$= (1.8 \text{ msec}) \times \left(10^{-3} \frac{\text{sec}}{\text{msec}}\right) \times \left(1100 \frac{\text{ft}}{\text{sec}}\right) \times \left(12 \frac{\text{in.}}{\text{ft}}\right) \times \left(14.7 \frac{\text{lb}_f}{\text{in.}^2}\right)^{1/3} \times \left[\left(2.8 \times 10^6 \text{ ft-lb}_f \times 12 \frac{\text{in.}}{\text{ft}}\right)^{1/3}\right]^{-1}$$

$$\bar{T} = 0.230$$

These values scale to the specified altitude conditions as follows:

$$0.821 = \frac{R(\text{ft}) \times \left(2.73 \frac{\text{lb}_f}{\text{in.}^2} \times 144 \frac{\text{in.}^2}{\text{ft}^2}\right)^{1/3}}{140.9 \ (\text{ft-lb}_f)^{1/3}}$$

$$R = \frac{140.9 \times 0.821}{7.31} = 15.8 \text{ ft}$$

$$0.680 = P_s \text{ (psi)}/ 2.73 \text{ psi}$$

$$P_s = 2.73 \times 0.680 = 1.79 \text{ psi}$$

$$0.0615 = I_s \text{ (psi-msec)} \times \left(10^{-3} \frac{\text{sec}}{\text{msec}}\right) \times \left(968 \frac{\text{ft}}{\text{sec}}\right) \times \left(12 \frac{\text{in.}}{\text{ft}}\right) \times \left[322 \text{ (in.-lb)}^{1/3} \times (2.73 \text{ psi})^{2/3}\right]^{-1}$$

$$I_s = \frac{0.0615 \times 322 \times 1.955}{10^{-3} \times 968 \times 12} = 3.34 \text{ psi-msec}$$

$$0.230 = T(\text{msec}) \times \left(10^{-3}\ \frac{\text{sec}}{\text{msec}}\right) \times \left(968\ \frac{\text{ft}}{\text{sec}}\right) \times \left(12\ \frac{\text{in.}}{\text{ft}}\right) \times (2.73\ \text{psi})^{1/3} \times \left[322\ (\text{in.-lb})^{1/3}\right]^{-1}$$

$$T = \frac{0.230 \times 322}{10^{-3} \times 968 \times 12 \times 1.397} = 4.57\ \text{msec}$$

3-2.2.1 ASSUMPTIONS

Sperrazza[9] has presented a careful derivation of Sachs' scaling law, using dimensional analysis techniques. Let us follow this derivation to show the manner in which such a law is determined and to indicate the simplifying assumptions that are inherent in the law.

Stating the principles of similitude in the usual way, that a relation expressed in all relevant dimensionless variables must be invariant to changes in dimensional variables, it is only possible to obtain a definite scaling law for shock propagation by making certain assumptions. It is assumed that the only relevant parameter of the explosive charge is its total energy of detonation. This assumption restricts the scaling law to distances large in comparison with some characteristic dimension of the explosive charge. Thus, the initial formation of the shock, which depends to some extent on charge density (or radius), is assumed not to affect the blast parameters at large distances from the charge. It also is assumed that peak overpressure P is a function of the parameters: ρ_0 the density of the undisturbed air, a_0 the velocity of sound in the undisturbed air, E the detonation energy, and R the distance from the blast source center,

$$P = P(R, \rho_0, a_0, E) \tag{3-11}$$

3-2.2.2 MODEL ANALYSIS

According to the π-theorem of dimensional analysis, the product

$$\pi = \left(P^{\alpha_P}\right)\left(R^{\alpha_R}\right)\left(\rho_0^{\alpha_\rho}\right)\left(a_0^{\alpha_a}\right)\left(E^{\alpha_E}\right) \tag{3-12}$$

must be dimensionless. Substituting the dimensions of each parameter from Table 3-2, into Eq. 3-12, results in the equation

$$\pi = (M)^{\alpha_P + \alpha_\rho + \alpha_E} \times (L)^{-\alpha_P + \alpha_R - 3\alpha_\rho + \alpha_a + 3\alpha_E} \times (T)^{-2\alpha_P - \alpha_a - 2\alpha_E} \tag{3-13}$$

TABLE 3-2

SACHS' SCALING PARAMETERS

Parameter	Dimension
P	$ML^{-1}\ T^{-1}$
R	L
ρ_0	ML^{-3}
a_0	LT^{-1}
E	$ML^2\ T^{-2}$

Since π is dimensionless, the exponents of M, L, and T must vanish. Hence

$$\left.\begin{aligned} \alpha_E &= -\alpha_\rho - \alpha_P \\ \alpha_a &= 2\alpha_\rho \\ \alpha_R &= 3\alpha_\rho + 3\alpha_P \end{aligned}\right\} \tag{3-14}$$

Substituting Eq. 3-14 into Eq. 3-12 results in

$$\pi = \left(\frac{PR^3}{E}\right)^{\alpha_P} \left(\frac{\rho_0 a_0^2 R^3}{E}\right)^{\alpha_\rho} \tag{3-15}$$

Each term in parentheses of Eq. 3-15 is dimensionless. Furthermore, each term is independent since each contains a parameter not existing in the other. The general solution relating the five parameters now can be written in the form

$$\psi\left(\frac{PR^3}{E}\ ,\ \frac{\rho_0 a_0^2 R^3}{E}\right) = 0. \qquad (3\text{-}16)$$

We now apply the theory of modeling to Eq. 3-16. The parameters at sea-level and at some altitude h above sea-level are specified by the subscript (0) and superscript (h), respectively. We substitute the scaling factors

$$\left.\begin{aligned} k_P &= \frac{P^{(h)}}{P^{(0)}}, \quad k_R = \frac{R^{(h)}}{R^{(0)}}, \\ k_\rho &= \frac{\rho_0^{(h)}}{\rho_0^{(0)}}, \quad k_a = \frac{a_0^{(h)}}{a_0^{(0)}}, \\ k_E &= \frac{E^{(h)}}{E^{(0)}} \end{aligned}\right\} \qquad (3\text{-}17)$$

into Eq. 3-16 to obtain

$$\psi\begin{bmatrix} \dfrac{k_E}{k_P k_R^3} & \dfrac{P^{(h)} R^{(h)3}}{E^{(h)}} \\ \dfrac{k_E}{k_\rho k_a^2 k_R^3} & \dfrac{\rho^{(h)} a_0^{(h)2} R^{(h)3}}{E^{(h)}} \end{bmatrix} = 0 \qquad (3\text{-}18)$$

In order that the general solution be invariant, i.e., the form of the solution be the same for both the unscaled model (at sea-level) and the scaled model (at altitude h) it is necessary that each dimensionless product in Eq. 3-18 remain invariant, therefore,

$$\frac{k_E}{k_P k_R^3} = 1, \quad \frac{k_E}{k_\rho k_a^2 k_R^3} = 1. \qquad (3\text{-}19)$$

These equations establish a relationship among the five scaling factors, three of which are arbitrary. Suppose k_ρ, k_a, and k_E are specified. Then from Eq. 3-19

$$k_R = \left(\frac{k_E}{k_\rho k_a^2}\right)^{1/3}, \quad k_P = k_\rho k_a^2 . \qquad (3\text{-}20)$$

If we are dealing with shock pressures less than several hundred psi, then air can be assumed to act as an ideal gas and therefore

$$\left.\begin{aligned} k_a^2 &= \left[\frac{a_0^{(h)}}{a_0^{(0)}}\right]^2 = \frac{\theta_0^{(h)}}{\theta_0^{(0)}}, \\ a_0^2 &= \gamma\left(\frac{p_0}{\rho_0}\right) \end{aligned}\right\} \qquad (3\text{-}21)$$

where θ_0 is the absolute temperature, p_0 is the ambient pressure, and γ is the ratio of specific heats of the ambient air. When we substitute Eqs. 3-17 and 3-21 into Eq. 3-20, the scaling factors for pressure and distance become

$$\left.\begin{aligned} k_P &= \frac{\rho_0^{(h)}}{\rho_0^{(0)}} \left\{\frac{\gamma\left[\dfrac{p_0^{(h)}}{\rho_0^{(h)}}\right]}{\gamma\left[\dfrac{p_0^{(0)}}{\rho_0^{(0)}}\right]}\right\} = \frac{p_0^{(h)}}{p_0^{(0)}}, \\ k_R &= \frac{\left[\dfrac{E^{(h)}}{E^{(0)}}\right]^{1/3}}{\left[\dfrac{p_0^{(h)}}{p_0^{(0)}}\right]} \end{aligned}\right\} \qquad (3\text{-}22)$$

By equating the pressure and distance scaling factors of Eq. 3-17 with those of Eq. 3-22 one obtains Sachs' general scaling law for peak overpressure

$$\frac{P^{(h)}}{p_0^{(h)}} = \frac{P^{(0)}}{p_0^{(0)}}$$

$$\left(\frac{p_0^{(h)}}{E^{(h)}}\right)^{1/3} \times R^{(h)} = \left(\frac{p_0^{(0)}}{E^{(0)}}\right)^{1/3} \times R^{(0)} \tag{3-23}$$

Making use of the fact that the time scaling factor is defined as

$$k_t = \frac{t^{(h)}}{t^{(0)}} = \frac{k_R}{k_a} \tag{3-24}$$

and that the definition of positive impulse is given by Eq. 3-2, we obtain the equation

$$I^{(0)} = \frac{k_a}{k_P k_R} I^{(h)} \tag{3-25}$$

By substitution of Eqs. 3-17, 3-20, and 3-21 into Eq. 3-25, one obtains Sachs' general scaling law for positive impulse

$$\left.\begin{aligned}\left[\frac{a_0^{(h)}}{E^{(h)^{1/3}}\, p_0^{(h)^{2/3}}}\right] I^{(h)} = \\ \left[\frac{a_0{}^{(0)}}{E^{(0)^{1/3}}\, p_0^{(0)^{2/3}}}\right] I^{(0)}\end{aligned}\right\} \tag{3-26}$$

3-2.2.3 EXPERIMENTAL VERIFICATION

Sachs' law has been confirmed by experiments of Jane Dewey and Sperrazza[10], Ericsson and Edin[11], and Olson, et al.[12] The most extensive series of model-prototype comparisons by far were the experiments of Dewey and Sperrazza. Dewey and Sperrazza conducted their tests with several sizes of bare Pentolite spheres in an altitude-simulating chamber in which both the ambient pressure and temperature could be varied. Arrays of side-on blast pressure transducers were mounted at various distances from the explosive spheres, and time histories of pressure were recorded. The two primary blast parameters reported were peak overpressure P and positive impulse I. A number of repeat tests were conducted for any given condition and distance. Fig. 3-5 shows their data for peak overpressure which has been scaled according to Sachs' law. Their data for impulse with Hopkinson scaling applied are shown in Fig. 3-6, and with Sachs' scaling applied, in Fig. 3-7. One can see that, within the limits of scaled distance covered by Dewey and Sperrazza[10], Sachs' law is indeed verified by their tests.*

Experiments performed at scaled distances close to explosive sources and under very low ambient pressure conditions (simulating high altitudes above sea-level) by Jack and Armendt[13] showed that the entire character of the blast wave changes at such distances and ambient conditions and that Sachs' scaling for pressures does not apply. The reason for this is that the assumption that air behaves like a perfect gas is untrue for tests close to the blast source, and Sachs' scaling is based on this assumption. An anomaly observed by both Olson, et al.[12] and Jack and Armendt[13] is that this law apparently *does* apply for the reflected impulse parameter, even very close to the explosive source. We note here that this agreement is strictly fortuitous, and an explanation is given later in par. 3-2.3.2.

3-2.2.4 APPLICATION

Sachs' law is used almost universally to predict effects of change in ambient temperature and pressure on blast parameters. Most authors correctly identify the law as due to Sachs, but some, such as Brode[14] and Glasstone[15], simply use it with no mention of its author.

Inherent in both Hopkinson's and Sachs'

*As in other experiments reported in this chapter for corroboration of scaling laws the units used by the original authors are retained. Dewey and Sperrazza use p_0 in sea level atmosphere, and charge weight W of Pentolite rather than energy E.

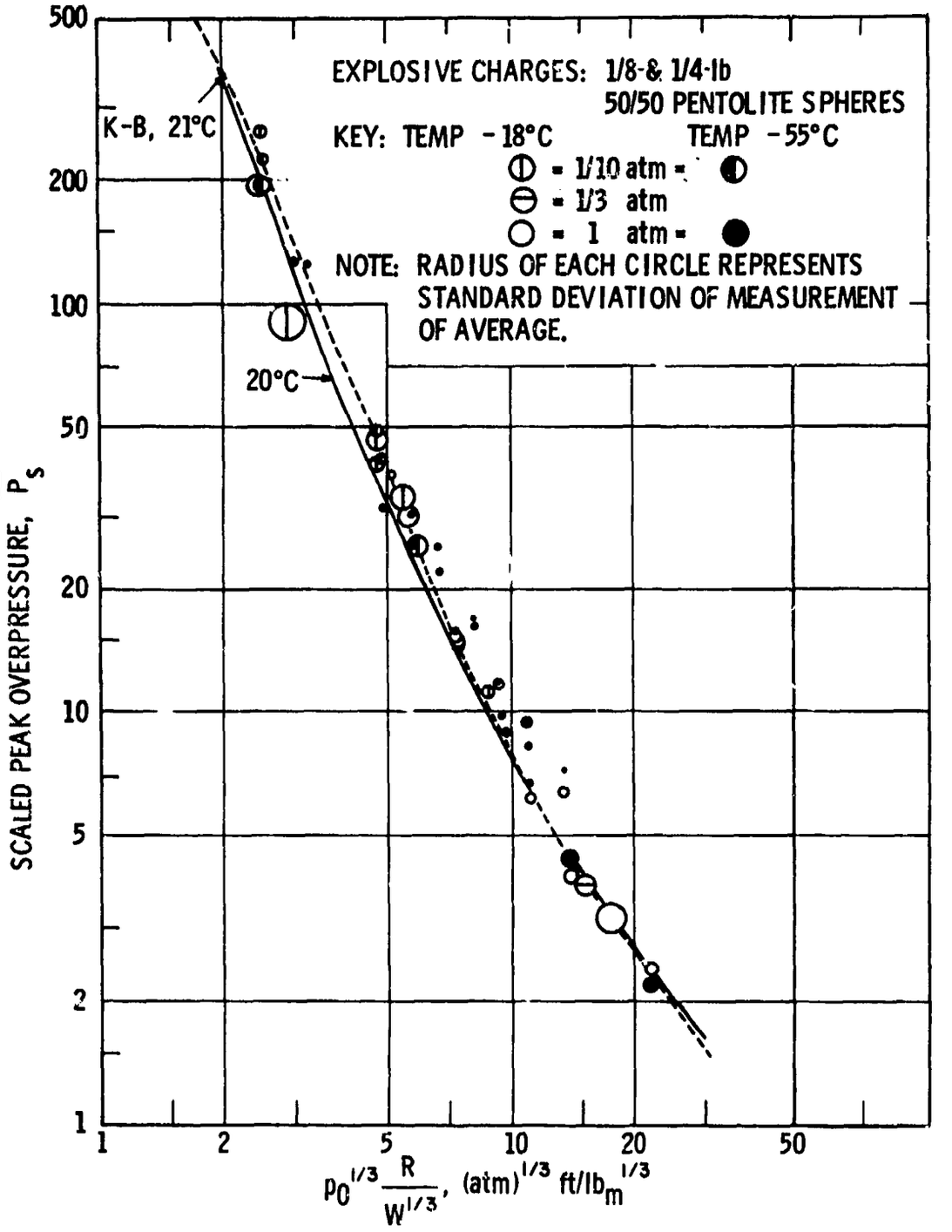


Figure 3-5. Peak Overpressure vs Sachs' Scaled Distance[10]

law, in addition to the assumption in Sachs' law that air behaves as a perfect gas, are the assumptions that gravity and viscosity effects are negligible. Sachs' law includes Hopkinson scaling as the special case when there are no changes in ambient pressure and temperature conditions between model and prototype experiments.

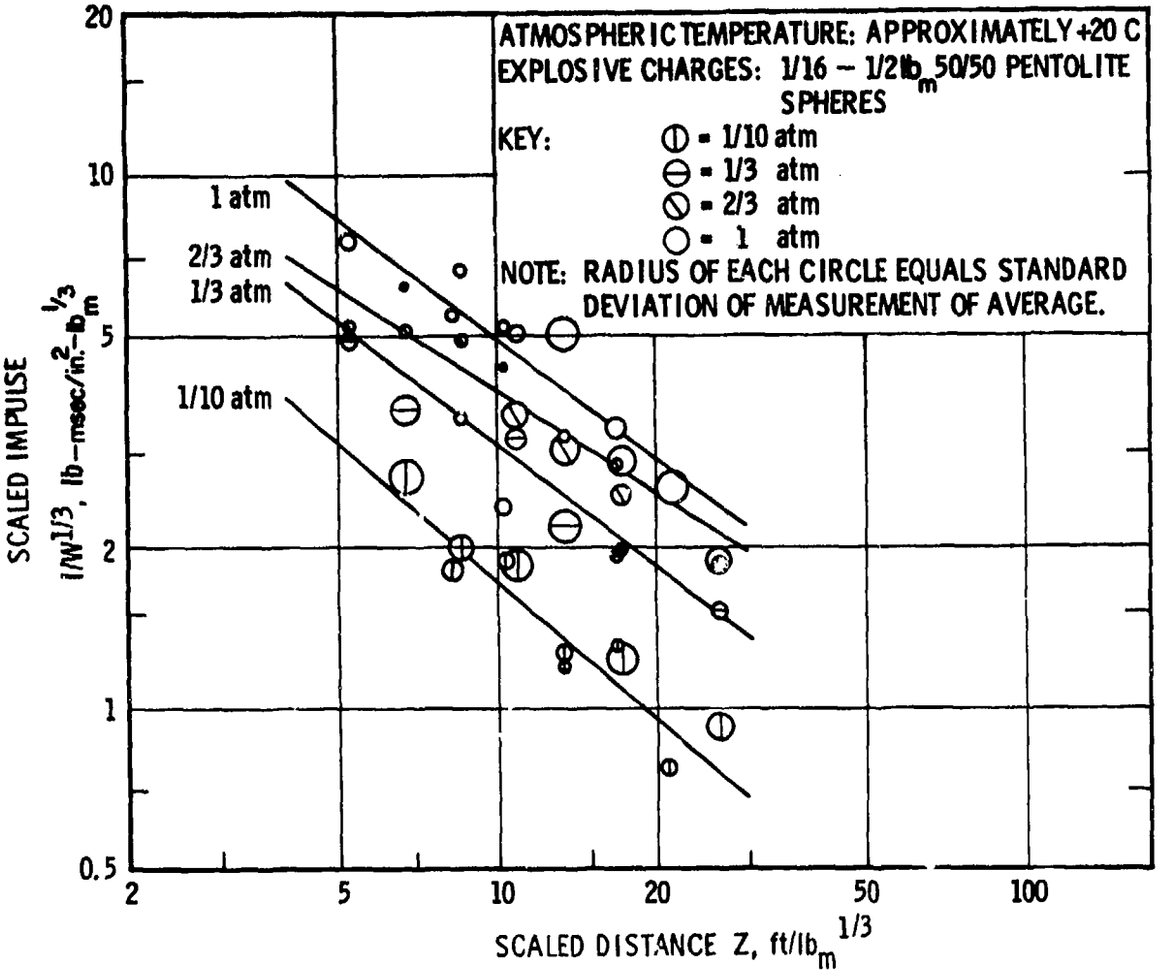


Figure 3-6. Hopkinson Scaled Impulse vs Scaled Distance[10]

3-2.3 OTHER SCALING LAWS FOR BLAST PARAMETERS

3-2.3.1 ADDITIONAL BLAST SOURCE PARAMETER

Hopkinson's and Sachs' laws are by far the most widely used in scaling of air blast parameters, but other investigators have proposed laws which differ somewhat from these two. Lutzky and Lehto[16] have proposed a modification of Sachs' law to allow inclusion of another parameter to describe the blast source in addition to its energy E. The source is assumed to consist initially of an ideal gas with the internal energy uniformly distributed throughout a sphere of radius a. These authors identify the governing physical parameters as a, E, p_0, ρ_0, R, t, γ; and form the fundamental dimensionless sets:

$$\left.\begin{aligned} \gamma &= \gamma \\ \lambda &= R\left(\frac{p_0}{E}\right)^{1/3} \\ \tau &= \frac{t\,p_0^{5/6}}{E^{1/3}\rho_0^{1/2}} \\ \xi &= a\left(\frac{p_0}{E}\right)^{1/3} \end{aligned}\right\} \qquad (3\text{-}27)$$

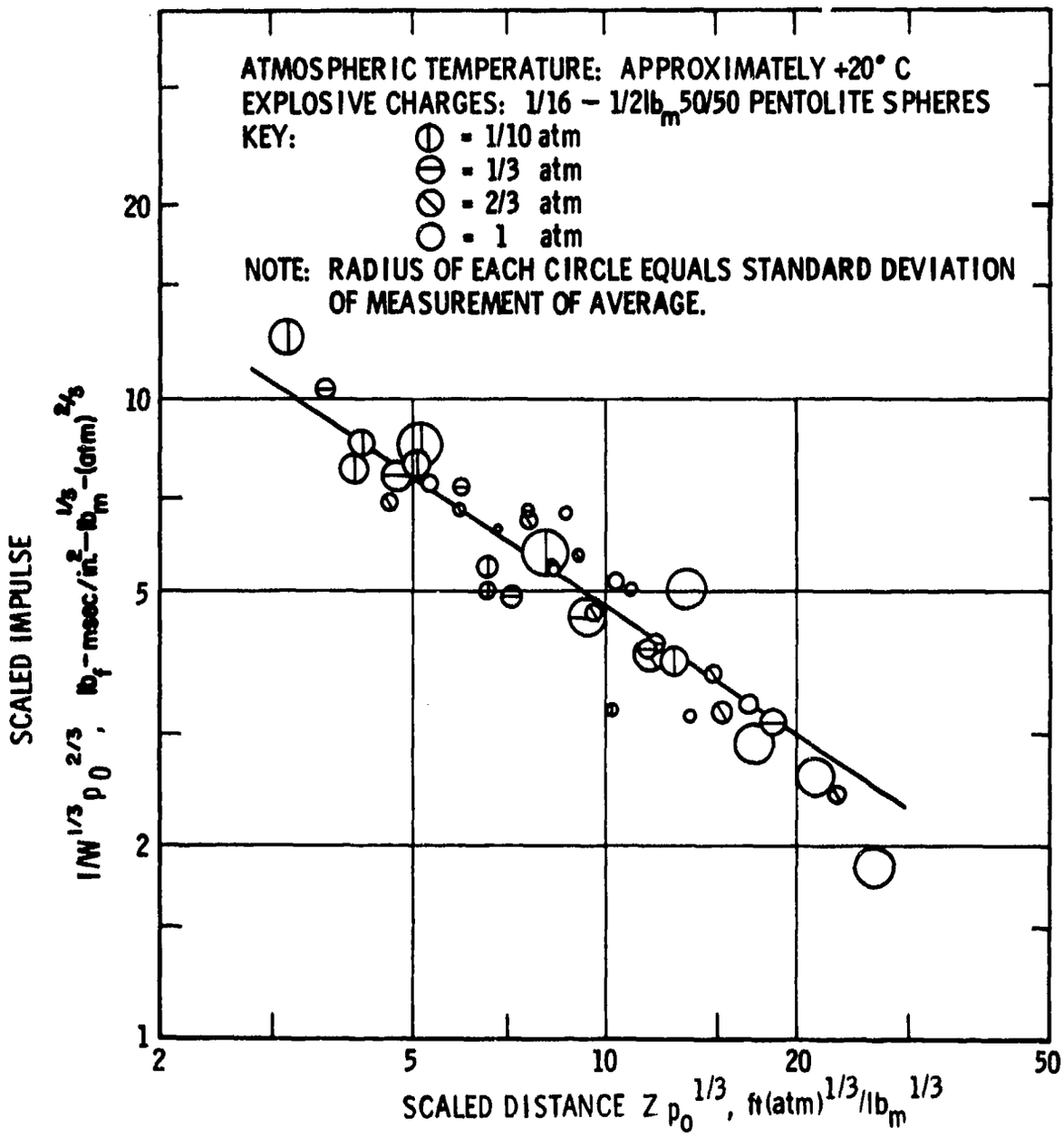


Figure 3-7. Sachs' Scaled Impulse vs Scaled Distance[10]

The shock strength p/p_0 can then be expressed as

$$\bar{p} = \frac{p}{p_0} = f_1(\lambda,\xi) \qquad (3\text{-}28)$$

where p is the absolute pressure, provided model and prototype experiments are conducted in atmospheres having the same γ. We can see that this scaling extends Sachs' scaling

by introducing the additional parameters ξ, the scaled size of the blast source. The scaled time parameter τ also can be written for an ideal gas and with no change in γ, as

$$\tau = ta_0 \left(\frac{p_0}{E}\right)^{1/3} = f_2(\lambda, \xi) \qquad (3\text{-}29)$$

The scaled time parameter is the same as for Sachs' scaling, but is also a function of two dimensionless parameters, rather than one.

Lutzky and Lehto[16] computed the shock strength from a one-dimensional hydrodynamic computer code, for various values of ξ over a wide range of λ. For large enough λ, the shock strength was shown to be independent of ξ, i.e., Sachs' scaling applies in its original form (see Fig. 3-8).

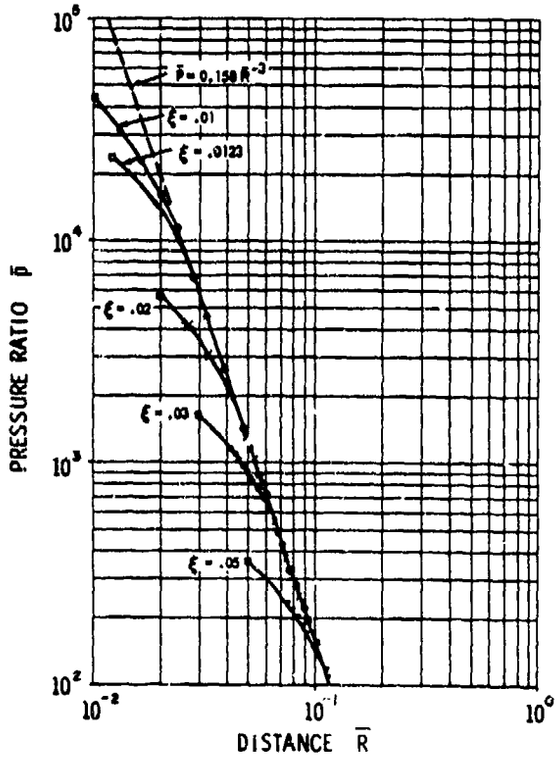


Figure 3-8. $\bar{p}$ vs $\bar{R}$ for Various Values of ξ, High $\bar{p}$ Range[16]

3-2.3.2 SMALL SCALED DISTANCES

Baker[17] has proposed a variation in the scaling law for reflected impulse under varying ambient conditions which apparently accounts for the anomaly of the successful applicability of Sachs' law in predicting values for this parameter, despite the violation of the perfect gas assumption for strong shocks—an anomaly which was mentioned earlier. This variation in Sachs' scaling is based on the rather accurate agreement at small scaled distances of the semi-analytic Eq. 3-30 for reflected impulse,

$$I_r = (2M_T E)^{1/2}/(4\pi R^2) \qquad (3\text{-}30)$$

(where M_T is the total mass of the explosive source plus the air engulfed by the shock front at radius R)

with the data of Olson, et al.[12] and Jack and Armendt[13], (shown in Figs. 3-9 and 3-10). Because this expression does agree well with experiment, one can generate from it a limited scaling law, applicable only for reflected impulse in strong shocks. If one assumes that the mass of the air M_A engulfed by the shock front is much less than the mass of the explosive M_E, i.e.,

$$M_A \ll M_E, \text{ where } M_T = M_E \qquad (3\text{-}31)$$

and one uses the fact that $M_E \propto E$, then one can manipulate Eq. 3-30 to form the scaling law

$$I_r/E^{1/3} = f_3(R/E^{1/3}). \qquad (3\text{-}32)$$

We see that this is identical to the Hopkinson's scaling for impulse given by Eq. 3-3 and, of course, that it is independent of ambient conditions. If we do not impose the restriction of Eq. 3-31, then the expression for impulse of Eq. 3-30 gives, for an ideal gas,

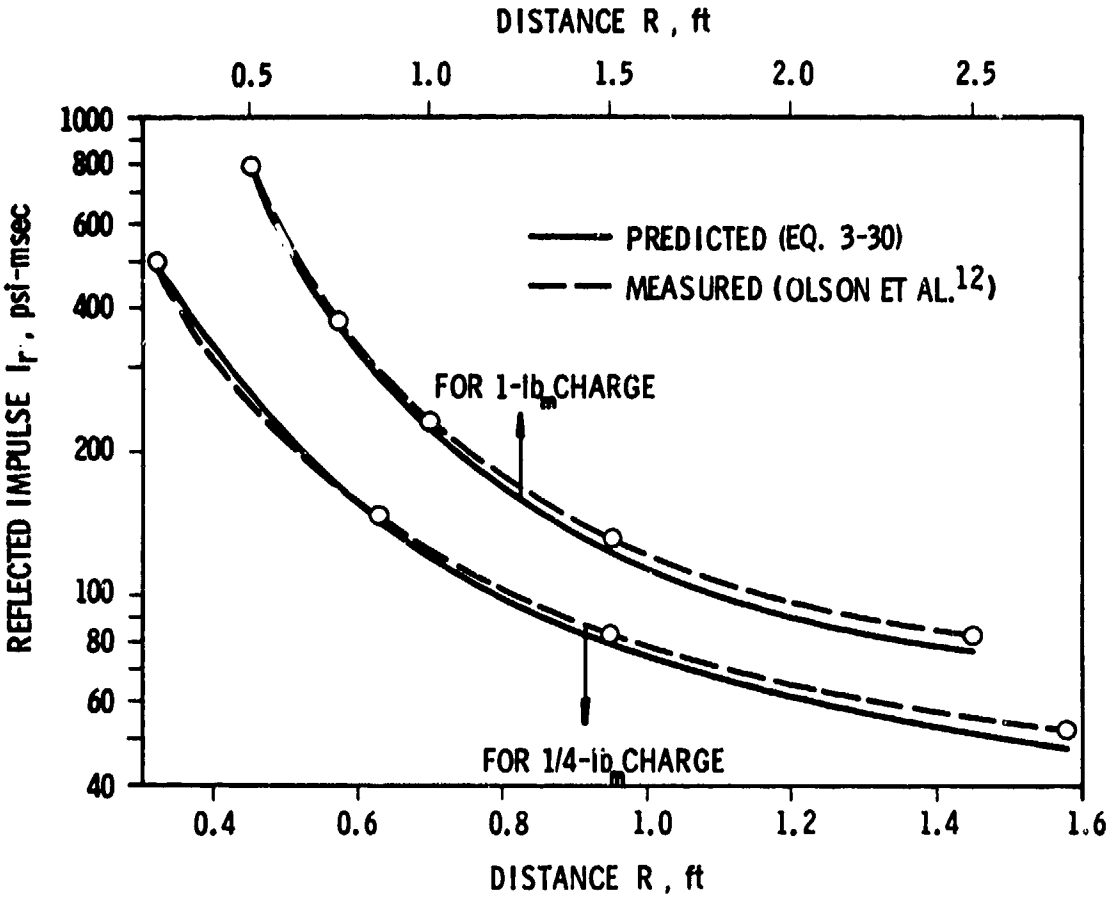


Figure 3-9. Comparison of Predicted and Measured Reflected Impulse I_r – Sea Level Conditions

$$M_A \propto R^3 p_0 / a_0^2 \qquad (3\text{-}33)$$

and

$$I_r \propto a(E/R^2) + \left[p_0^{1/2} E^{1/2} / \left(a_0 R^{1/2} \right) \right] \qquad (3\text{-}34)$$

If we make Eq. 3-34 nondimensional, then we obtain the scaling law

$$I_r a_0 / (E^{1/3} p_0^{2/3}) = f_4(a_0, p_0^{1/3} R / E^{1/3}) = f_4(a_0, \lambda) \qquad (3\text{-}35)$$

The scaled impulse parameter here is the same as for Sachs' scaling, but it is a function of ambient sound velocity as well as of scaled distance. To test this scaling law, one would have to conduct experiments with significant variation in a_0, at intermediate distances from the blast center, where shocks are still strong and the mass of air engulfed by the shock front is an appreciable fraction of the mass of explosive. Since this was not done in the work reported by Olson, et al.[12] and Jack and Armendt[13], one can see from Eq. 3-35 why Sachs' scaling appears to apply well to the data of those two references—the dependence on a_0 could not be determined because a_0 was not varied.

3-2.3.3 WECKEN'S LAWS

Several blast scaling laws have been proposed for spherically symmetric explosions by Wecken[18], who also discusses the history of blast scaling, and who attributes the Hopkinson law to Cranz[19] (even though he notes that Hopkinson apparently first derived it during World War I). Wecken[18] gives no derivations of his proposed laws, but he does indicate that they were obtained by use of the

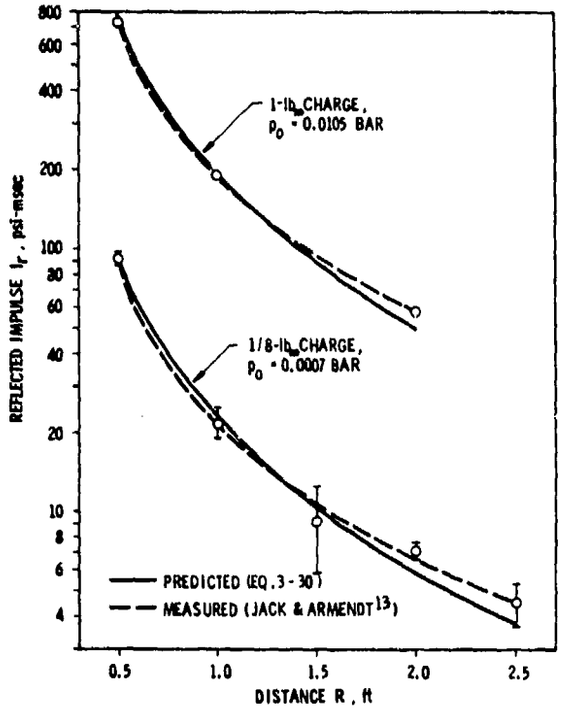


Figure 3-10. Comparison of Predicted and Measured Reflected Impulse I_r — Reduced Pressure Ambient Conditions

Buckingham π Theorem. He includes a number of parameters not considered in most other laws. In his presentation he first lists the significant physical parameters, and then he immediately drops all but one of any group which have identical dimensions (analogous to the technique of using nondimensional distance ratios, pressure ratios, etc.). He lists remaining parameters in a table with their dimensions in an M, L, T, θ system (θ being temperature), and enumerates four separate laws, simply by stating powers to which a basic scale factor must be raised to satisfy the particular law. The scale factor λ may or may not be the conventional geometric scale factor for any particular law. These laws are summarized in Table 3-3. In this table, parameters not included in other laws discussed in this chapter are mass of gas m, temperature θ, acceleration b, force K, specific energy e, specific heat at constant volume c_v, and molar mass of gas M. Other parameters included as ratios of those in Table 3-3, or already nondimensional, are given in Table 3-4.

TABLE 3-3

BLAST SCALING LAWS PROPOSED BY WECKEN[18]

Parameter	Dimensions	Law 1	Law 2	Law 3	Law 4
r	L	λ	1	1	1
t	T	λ	λ^{-1}	1	1
m	M	λ^3	1	λ	1
θ	θ	1	λ^2	1	λ
u	LT^{-1}	1	λ	1	1
ρ	ML^{-3}	1	1	λ	1
p	$ML^{-1}T^{-2}$	1	λ^2	λ	1
b	LT^{-2}	λ^{-1}	λ^2	1	1
K	MLT^{-2}	λ^2	λ^2	λ	1
W	ML^2T^{-2}	λ^3	λ^2	λ	1
e	L^2T^{-2}	1	λ^2	1	1
c_v	$L^2T^{-2}\theta^{-1}$	1	1	1	λ^{-1}
M	$L^{-3}T^3\theta$	1	1	1	λ

TABLE 3-4

ADDITIONAL PARAMETERS IN WECKEN'S ANALYSIS

Parameter		Dimensions
R	(distance from blast source center)	L
a_0	(ambient sound velocity)	LT^{-1}
U	(shock wave velocity)	LT^{-1}
H	(enthalpy)	ML^2T^{-2}
c_p	(specific heat at constant pressure)	$L^2T^{-2}\theta^{-1}$
s	(specific entropy)	$L^2T^{-2}\theta^{-1}$
γ	(ratio of specific heats)	—

Wecken speaks of the four laws in Table 3-3 as laws of similitude of length, velocity, density, and molar mass, respectively. That is, in each of these laws, one of the quantities r, u, ρ, M is varied (i.e., is assigned the scaling parameter λ), while the remainder are held constant (i.e., are assigned a scaling parameter of unity). The law of length (Law 1) is Hopkinson's law. The remaining three laws are special ones differing from any previous laws known by the authors. They all imply

model and prototype testing to the *same* geometrical scale, rather than a reduced scale for the model tests. The second law requires "model" testing at greatly reduced temperature ($\lambda_\theta = \lambda^2$) from the prototype to achieve the necessary reduced velocity scaling ($\lambda_u = \lambda$). The third law requires testing at reduced pressure and energy to achieve results at reduced density. The fourth law requires the use of a "model" gas with a different c_v (but with the same γ) at different temperatures from the prototype. Whether Laws 2 through 4 in Table 3-3 are useful scaling laws is doubtful. The paper by Wecken is an interesting one, however, and well worth reading for its other aspects, since it includes discussions of past theoretical work and of the history of blast scaling. For completeness, we include here in Table 3-5 a list of dimensionless parameters from which Wecken's analysis can be derived, even though he omitted this intermediate step in his paper.

3-3 SCALING LAWS FOR INTERACTION WITH STRUCTURES

Originally, we planned to limit the scope of this handbook to air blast phenomenology and specifically to exclude any detailed treatment of response of structures to air blast loading. We will now depart somewhat from this philosophy by discussing scaling laws for interaction of blast waves with structures, because we feel that (1) a modeling discussion would be incomplete without some indication of response scaling, and (2) the response model laws may prove quite useful to the reader.

TABLE 3-5

DIMENSIONLESS PRODUCTS CORRESPONDING TO WECKEN'S SCALING

π_1	$= ut/r$	π_9	$= c_v M$
π_2	$= \rho u^2/p$	π_{10}	$= U/u$
π_3	$= pr^3/W$	π_{11}	$= a_0/u$
π_4	$= bt/u$	π_{12}	$= H/W$
π_5	$= K/pr^2$	π_{13}	$= s/c_v$
π_6	$= mu^2/W$	π_{14}	$= R/r$
π_7	$= et^2/r^2$	π_{15}	$= \gamma = c_v/c_p$
π_8	$= c_v\theta/u^2$		

3-3.1 "REPLICA" SCALING

Model laws for elastic and plastic structural response to blast loading are of much more recent origin than the majority of the blast loading laws discussed previously in this chapter, and they usually receive scant attention in any blast scaling discussion. As far as we can determine, the first statement of a blast scaling law which included structural or solid material response is the law discussed by Döering and Burkhardt[20]. Their similarity theorem relates to the transmission of strong shocks into a solid from an explosive source located in a fluid of any type, and essentially is an extension of Hopkinson's size-scaling law to include shock properties in the solid. Their proof was based on the scaling of linear hydrodynamic equations, and on considerations of boundary conditions at the interface between fluid and solid media. They noted that viscosity, strain-rate, and gravity effects must be neglected, in both fluid and solid media, for their law to be applicable.

In a much more systematic treatment, H. N. Brown[21] considered the interaction of blast waves with elastic structures and inferred the same model law as that of Döering and Burkhardt from equations of motion. He limited his treatment to equations for small deformations and strains and assumed that pressures, stresses, and densities should be unchanged between model and prototype. Baker, et al.[22], later extended Brown's analysis to show that the same law could be used for prediction of large elastic and plastic deformations of structures, and conducted a series of experiments on the blast response of aluminum alloy cantilevers which verified the law. For want of a better name, this response scaling law is usually termed "replica scaling", since geometrical similarity must be maintained, and material and fluid media properties must be identical in model and proto-

type experiments. The law is shown conceptually in Fig. 3-11, and the experimental verification for appropriately scaled response parameters from the paper by Baker, et al.[22] given in Figs. 3-12 and 3-13. In Fig. 3-13, maximum permanent deflection δ divided by original beam length L is the nondimensional measure of beam response. As in Hopkinson's scaling, all quantities with dimensions of pressure and velocity are unchanged in replica response scaling. So, all stress components at scaled locations in the structure are unchanged. All response times (such as natural vibration periods and times for transmission of elastic or plastic waves) and displacements are scaled by the same factor as the length scale factor K. Strains, being dimensionless, are identical at homologous times in the model and prototype.

3-3.2 SCALING FOR IMPULSIVE LOADING

Although the replica response law can be quite useful, it also imposes severe restrictions on model testing. Other laws have been generated to allow greater flexibility in such testing. Nevill[23] proposed a limited model law for structural response which applies only for those structures whose characteristic response times are long enough for the blast loading to be considered impulsive. In his law, scale factors for length, time, and density are independent, so that these scales can be selected arbitrarily within limits imposed by available materials and fabrication techniques. Thus, he introduced the concept of "dissimilar material modeling", wherein structural response to impulsive loading can be modeled

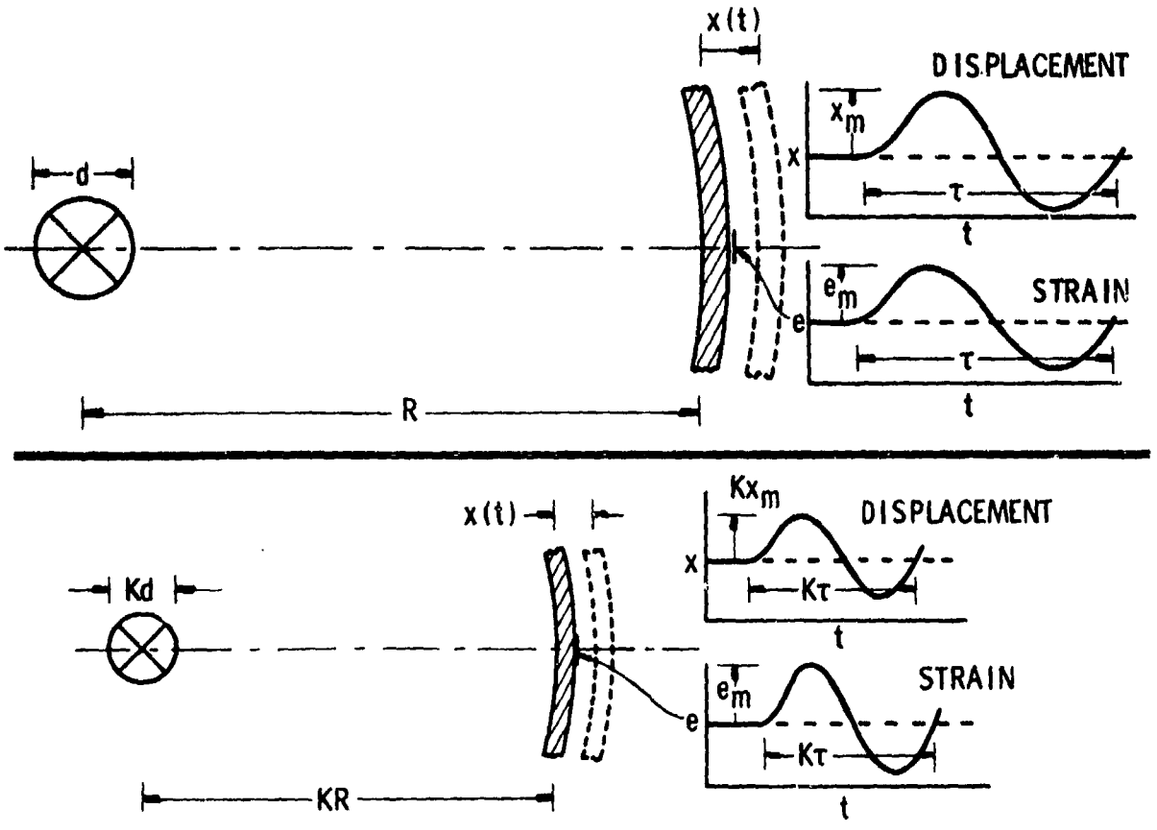


Figure 3-11. "Replica" Scaling of Response of Structures to Blast Loading

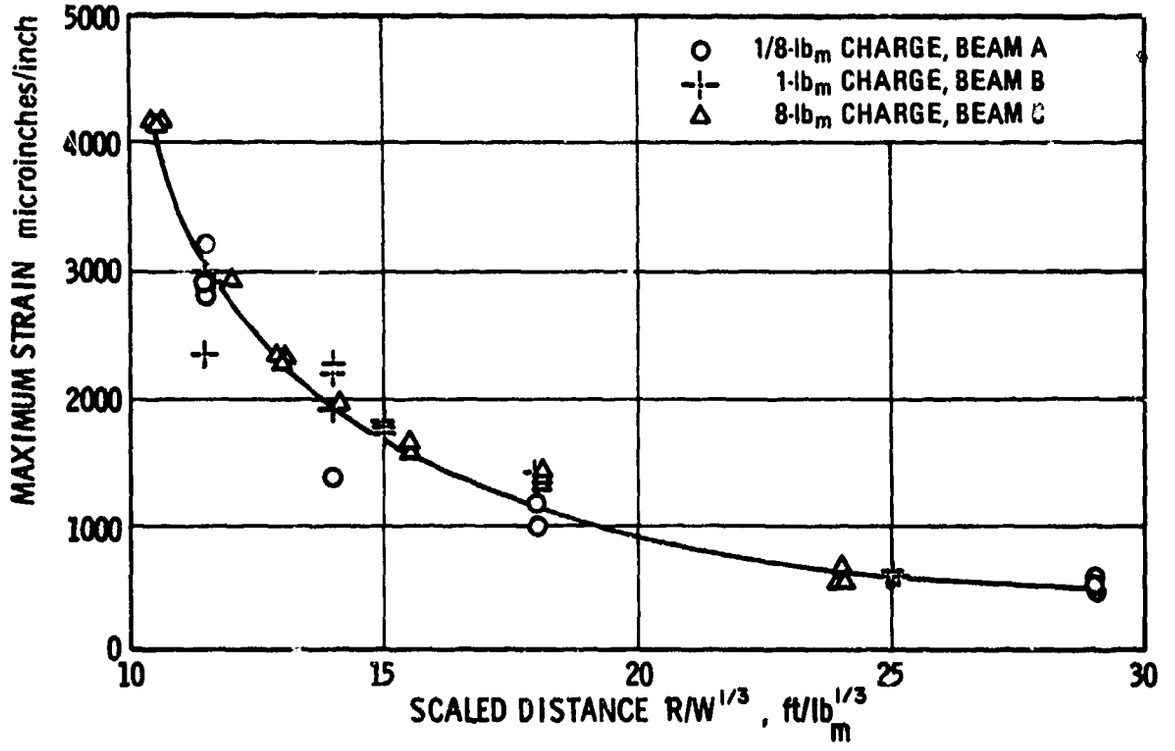


Figure 3-12. "Replica" Scaling of Elastic Response of Aluminum Cantilevers to Air Blast Waves

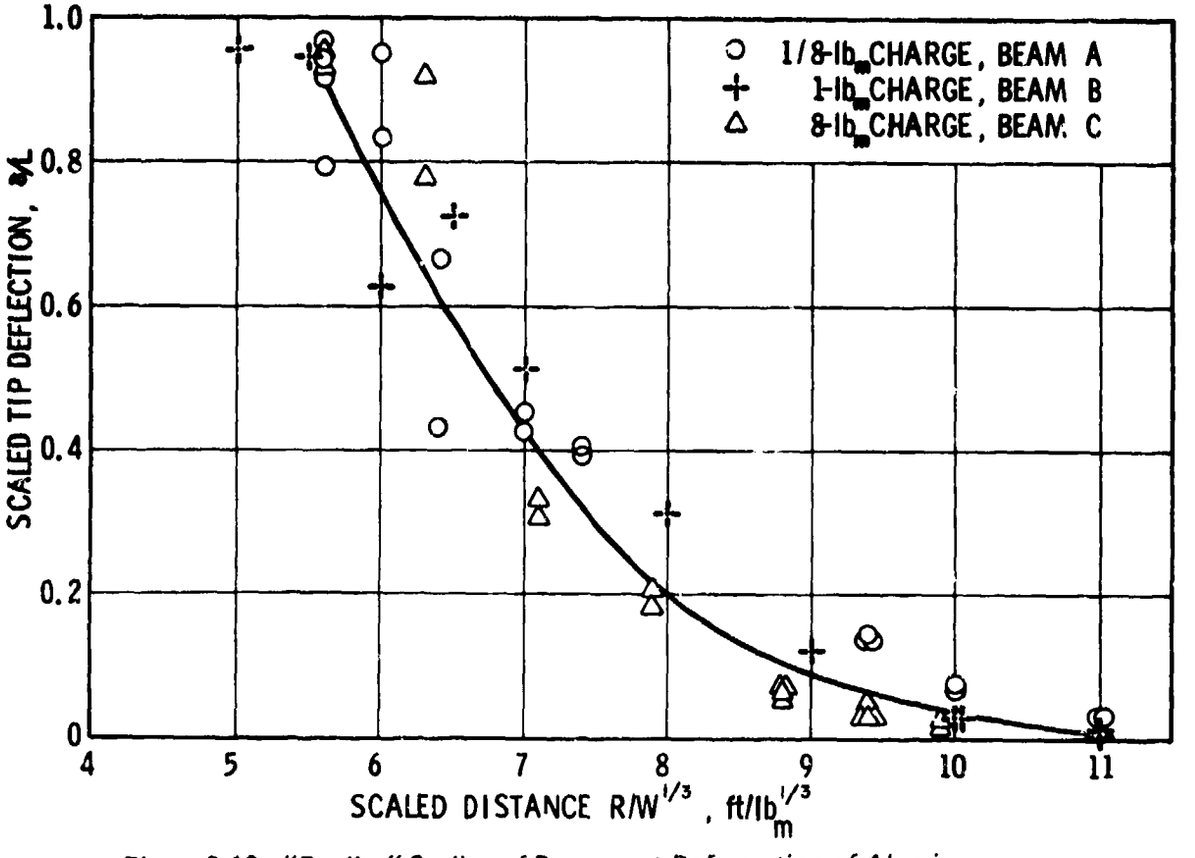


Figure 3-13. "Replica" Scaling of Permanent Deformation of Aluminum Cantilevers Under Air Blast Loading

accurately by the use of construction materials in the model structure which may be quite different from those in the prototype structure. He also reports experimental verification of this law in a limited series of tests of simple structures. In this law, geometric similarity is maintained, and strains in the model are unchanged from those in the prototype. The stress-strain curve for the model material must be similar to that of the prototype, but the elastic and plastic moduli can be quite different. The most important dimensionless parameter in this modeling law is

$$\pi_I = I/\left[L\,(\rho_{st}\,E_{st})^{1/2}\right] \tag{3-36}$$

where E_{st} is either the elastic or plastic modulus.

3-3.3 MISSILE RESPONSE TO AIR BLAST

In considering the complex problem of modeling of the structural response of a missile in flight to air blast loading, Baker, et al.[24], have generated a law which incorporates the concept of dissimilar materials. This law also allows for blast wave transmission through a different gaseous medium in the modeled situation than that of the prototype situation, and a difference in ambient conditions (p_0, ρ_0, and a_0) between the model and prototype situations. A total of eighteen physical parameters were identified as significant in the derivation of this law, and fifteen controlling primary dimensionless groups were formed in its derivation. These terms are listed in Table 3-6. If one does not attempt to maintain Reynolds number, term π_2, invariant (i.e., neglects viscosity effects), then a useful model law for a structure moving with a high velocity and deforming both elastically and plastically in response to air blast loading results. This general law includes the Hopkinson's and Sachs' scaling laws for blast loading, and *dictates* the use of structural materials for the model which differ in material characteristics from the prototype and for model experiments which are conducted under ambient conditions differing from those of the prototype. The neglect of gravity and strain-rate effects is also inherent in this law. The law implies geometrical similarity, and reduces to replica response modeling when ambient conditions are assumed identical to model and prototype.

3-4 LIMITATIONS OF SCALING LAWS

In discussing the various blast scaling laws in this chapter, we have attempted to note the assumptions made in derivation of the laws and, therefore, some of the limitations of

TABLE 3-6

PRIMARY BUCKINGHAM π TERMS. BLAST LOADING AND RESPONSE OF HIGH-SPEED STRUCTURE

Term		Description
π_1	$= V/a_0$	Vehicle Mach number
π_2	$= \rho_0 VL/\mu$	Reynolds number
π_3	$= p_i/(\rho_0 V^2)$	Pressure ratios
π_4	$= \gamma$	Ratio of specific heats
π_5	$= \rho_{st}/\rho_0$	Density ratio
π_6	$= R/L$	Hopkinson's scaling
π_7	$= E/(\rho_0 a_0^2 R^3)$	Sachs' scaling
π_8	$= E_i/\sigma_i$	Stress ratios
π_9	$= C_i/\sigma_i$	
π_{10}	$= \epsilon_i$	Strains
π_{11}	$= \ell_i/L$	Length ratios
π_{12}	$= \alpha_i$	Angles
π_{13}	$= B_i/(\rho_0 L^5)$	Angular momentum parameter
π_{14}	$= m_i/M$	Mass ratios
π_{15}	$= M/(\rho_0 L^3)$	Linear momentum parameter

these laws. A common feature of all of the laws is that rate-dependent effects (viscosity in fluids and strain-rate in solids) and gravity effects are assumed negligible. Thus, the laws may not accurately predict scaling of the details of loading and response where such effects are important. Examples of this limitation include the inability of these laws to predict the trajectories of missiles generated by blast loading, the rise of a fireball or heated air in the atmosphere, strains or stresses in heavily rate-dependent solid materials such as viscoelastics, etc.

Hopkinson's scaling, and the corresponding replica response scaling for structures, applies over a remarkably large range of length and energy scale factors. In the limit of small scale, one primarily is restricted by the practical considerations of one's ability to detonate tiny explosive charges and to fabricate accurate uniform structural models from very thin gages of material. Also, one is restricted by the lower limits of the size of transducers for measuring the loading and response of the structure. In the large scale limit, sheer size and expense of a single test usually provides the practical restriction. One is *not*, however, restricted in shock strength, amplitude of displacements, or strains, etc.

A limitation of the Sachs' law, the Lutzky and Lehto modification of this law, and the corresponding dissimilar materials response law is that shock strengths must be low enough for the gaseous medium transmitting the blast wave to behave as an ideal gas. For

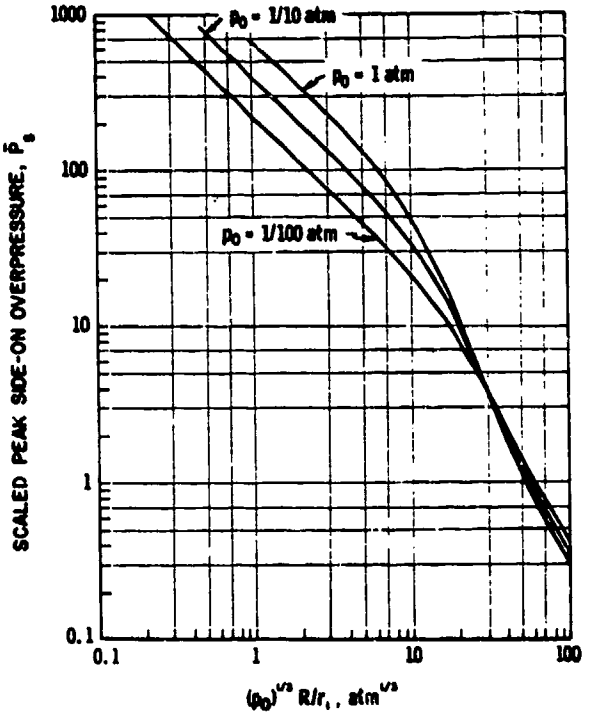


Figure 3-14. Peak Overpressure Ratio vs Scaled Distance[25]

sufficiently strong shocks, at distances close to the blast source, the ideal gas assumption is violated and these laws no longer apply. This has been demonstrated experimentally by Jack and Armendt[13] and analytically by Shear[25]. Fig. 3-14 shows some of the results of Shear's calculations where the deviations between the three curves indicate the degree of departure from Sachs' scaling due to violation of the ideal gas assumption for these conditions, $R \simeq r_1$ where r_1 is the charge radius.

REFERENCES

1. B. Hopkinson, *British Ordnance Board Minutes 13565*, 1915.

2. *Oxygen Bomb Calorimetry and Combustion Methods*, Technical Manual No. 130, Parr Instrument Co., Illinois, 1960.

3. AMCP 706-177, Engineering Design Handbook, *Properties of Explosives of Military Interest*, AD-814 964.

4. W. D. Kennedy, "Explosions and Explosives in Air", Chapter 2, Part II, Vol. 1, *Effects of Impact and Explosions*, Summary Tech. Report of Div. 2, NDRC, Washington D.C., 1946, AD-221 586.

5. R. G. Stoner and W. Bleakney, "The Attenuation of Spherical Shock Waves in Air", Journal of Appl. Physics, **19**, 7, 670-678 (1948).

6. John M. Dewey, "The Air Velocity in Blast Waves from TNT Explosions", *Proc. of the Royal Soc.*, A, 279, 1964, pp. 366-385.

7. C. N. Kingery, *Air Blast Parameters versus Distance for Hemispherical TNT Surface Bursts*, BRL Report 1344, Aberdeen Proving Ground, September 1966.

8. R. G. Sachs, *The Dependence of Blast on Ambient Pressure and Temperature*, BRL Report No. 466, Aberdeen Proving Ground, Md., 1944.

9. J. Sperrazza, "Modeling of Air Blast", *Use of Models and Scaling in Shock and Vibration* (W. E. Baker, Ed.), ASME, New York, November 1963, pp. 65-78.

10. Jane M. Dewey and J. Sperrazza, *The Effect of Atmospheric Pressure and Temperature on Air Shock*, BRL Report No. 721, Aberdeen Proving Ground, Md., 1950.

11. V. Ericsson and K. Edin, "On Complete Blast Scaling", Jour. of the Physics of Fluids, 3, 5, pp. 893-895 (September-October 1960).

12. W. C. Olson, Jr., J. D. Patterson, II, and J. S. Williams, *The Effect of Atmospheric Pressure on the Reflected Impulse From Blast Waves* BRL Memo Report No. 1421, Aberdeen Proving Ground, Md., January 1960.

13. W. H. Jack, Jr., and B. F. Armendt, Jr., *Measurements of Normally Reflected Shock Parameters From Explosive Charges Under Simulated High Altitude Conditions*, BRL Report No. 1280, Aberdeen Proving Ground, Md., April 1965.

14. H. L. Brode, "Numerical Solutions of Spherical Blast Waves", Jour. of Appl. Physics, 26, 6, pp. 766-775 (June 1955).

15. S. Glasstone, ' l., *The Effects of Nuclear Weapons*, U. Atomic Energy Commission, Rev. Ed., April 1962, pp. 128-129.

16. M. Lutzky and D. Lento, *On the Scaling of Pressures from Nuclear Explosions with Some Observations on the Validity of the Point-Source Solution*, NOLTR 65-74, U.S. Naval Ordnance Laboratory, White Oak, Md., September 1965.

17. W. E. Baker, "Production and Scaling of Reflected Impulse from Strong Blast Waves", Int. Jour. of Mech. Sci., 9, pp. 45-51 (1967).

18. F. Wecken, "Les Lois de Similitude dans les Explosions a Symetric Spherique", *Memorial de l'Artillerie Francaise*, Sciences et Technique de l' Armement, 35, 136, pp. 438-459 (1961).

19. C. Cranz, *Lehrbuch der Ballistik*, 2, Berlin, 1926, p. 181.

20. W. Döering and G. Burkhardt, "Beiträge zur Theorie der Detonation", Technische Akademie der Luftwaffe, Berlin-Gatow, April 1944, (translated from the German as *Contributions to the Theory of Detonation*. Tech. Report No. F-TS-1227-1A, by Brown Univ., May 1949).

21. H. N. Brown, *Effects of Scaling on the Interaction Between Shock Waves and Structures*, Appendix I to BRL Report No. 1011, Aberdeen Proving Ground, Md., March 1957.

22. W. E. Baker, W. O. Ewing, Jr., and J. W. Hanna, *Laws for Large Elastic Response and Permanent Deformation of Model Structures Subjected to Blast Loading*, BRL Report No. 1060, Aberdeen Proving Ground, Md., December 1958.

23. G. E. Nevill, Jr., *Similitude Studies of Re-Entry Vehicle Response to Impulsive Loading*, AFWL TDR 63-1, Vol. 1, Kirtland Air Force Base, New Mexico, 1963.

24. W. E. Baker, P. S. Westine, and S. Silverman, *Feasibility Study on Simulating the Structural Response of High Altitude Missiles to Blast Loading*. Final Tech. Rept., Contract No. DA-18-001-AMC-794(X), Southwest Research Institute, Texas, January 1966.

25. R. E. Shear, *Incident and Reflected Blast Pressures for Pentolite*, BRL Report No. 1262, Aberdeen Proving Ground, Md., September 1964.

CHAPTER 4

COMPUTATIONAL METHODS

4-0 LIST OF SYMBOLS

a_L = Lagrangian space coordinate

$A_{11}, A_{14}\ldots$ etc. = quantities in Kirkwood-Brinkley method

A_j^n, $V_{j-1/2}^n$ = areas of interfaces, volumes of zones in WUNDY code

c = sound speed

c_{VN} = dimensionless constant in fictitious viscosity coefficient

C_V, C_{V_1} = specific heats in WUNDY code

D = detonation velocity

e = internal energy

e_E = energy density in WUNDY code

E = energy

E_{int} = internal energy of explosive source

E_{tot} = total energy of explosive source

$f_{KB}, \mu_{KB}, \nu_{KB}$ = quantities in Kirkwood-Brinkley method

L, L_j = quantities in equations for stability criteria for plane shocks

M_B = number of grid zones in shock front

p = pressure

p_e = initial pressure in explosives or high pressure sphere

p_0 = ambient pressure

$\bar{P}_s$ = scaled peak overpressure

P, Q = Reimann variables in method of characteristics

Q = chemical energy released per unit mass of explosive

R = shock front distance, or search radius

R_j = charge radius

R_s = shock radius

s = subscript denoting shock front

S = entropy

t = Eulerian time coordinate

T = absolute temperature

u = particle or flow velocity

u, c, r, etc. = convergence of velocity, etc., between two points

u_j^n, x_j^{n+1}, etc. = finite-difference forms of velocity, radius, etc.

U = shock speed

v = specific volume

W_B = quantity in Brode's method

x, r = Eulerian space coordinates

x, τ etc. = dimensionless radius, time, etc., in Brode's method

y_i = specific partial derivatives

α, B = constant in WUNDY code

γ = ratio of specific heats; a polytropic index associated with intermolecular forces

Δt, Δx, etc. = an increment in time, space, etc.

ϵ, ϵ_B = characteristic length in Brode's method

η = constant ratio of specific heats

ρ = density

ρ_e = initial density in explosives or high pressure sphere

ρ_0 = density of ambient air

σ = fictitious viscosity coefficient, radial function in PAF method

τ = Langrangian time coordinate

μ_{KB} = constant

4-1 GENERAL

The governing equations for transmission of shock waves in air are given in Chapter 2, together with a few analytical solutions, which exist for limiting cases, and some special partial solutions. But, in general, the governing equations are too complex and too highly nonlinear to admit of analytical solutions. Only with the advent of large digital computers has prediction of air blast wave characteristics from the governing equations become possible. We differentiate in this handbook between such predictions and analytic solutions, because the former are not truly mathematical solutions. They are, instead, numerical computations that essentially satisfy a variety of conditions and restrictions, which are imposed by both the nature of the governing equations and the capabilities of the computing machines. In this chapter, we will discuss computational methods geared to digital computers.

As in most facets of air blast technology, little work in computation of blast wave properties was accomplished prior to World War II, and the initial impetus for such work was the result of research conducted during World War II. The best known of the early efforts are those of Kirkwood and Brinkley[1,2] and von Neumann and Richtmyer[3], the latter paper being a classic one on which many following computer programs have been based. More recent investigators who have contributed most heavily to advancements in computational methods have been Shear at BRL, Lutzky and co-workers at NOL, Brode at Rand Corp., and Chou and co-workers at Drexel University. Specific references to contributions of these and other individuals will be given with descriptions of their different methods of computation.

These computational methods can be divided into two basic classes: (1) methods with discontinuous shock fronts, and (2) methods which "smear" properties over shock fronts of finite thickness so that no discontinuities are permitted. In this chapter we will discuss a variety of methods falling within these two basic classes.

4-2 METHODS WITH DISCONTINUCUS SHOCK FRONTS

4-2.1 KIRKWOOD AND BRINKLEY METHOD

The method of Kirkwood and Brinkley[1,2,4,5] predicts the shock-front pressure-time history where the pressure p and energy E at the charge surface are given, or where the pressure p and slope of the pressure-distance curve dp/dR, at some fixed value of the shock front distance R, are given. The essentials of this method are reproduced here.

Let (a_L, τ) be the Lagrangian space and time coordinates, respectively, corresponding

to the Eulerian space and time, (r,t) in undisturbed air:*

$$a_L = a_L(r,t) \tag{4-1}$$

$$\tau = t$$

$$a_L(R_s,t_s) = R_s \text{ at } r = R_s, t = t_s \tag{4-2}$$

The conservation of mass in a spherical-shell element (a_L, da_L) and (r, dr) yields

$$4\pi\rho_0 a_L^2\, da_L = 4\pi\rho r^2\, dr \tag{4-3}$$

where ρ_0 is the Lagrangian density and ρ is the Eulerian density.

Thus

$$\left(\frac{\partial a_L}{\partial r}\right)_t = \frac{\rho r^2}{\rho_0 a_L^2} \quad \text{or} \quad \left(\frac{\partial r}{\partial a_L}\right)_\tau = \frac{\rho_0 a_L^2}{\rho r^2} \tag{4-4}$$

Eqs. 2-19 and 2-20 are, in Lagrangian coordinates,

$$\left(\frac{\partial u}{\partial \tau}\right)_{a_L} + \frac{1}{\rho}\left(\frac{\partial p}{\partial a_L}\right)_\tau \frac{\rho r^2}{\rho_0 a_L^2} = 0 \tag{4-5}$$

$$\left(\frac{\partial \rho}{\partial \tau}\right)_{a_L} + \rho\left(\frac{\partial u}{\partial a_L}\right)\frac{\rho r^2}{\rho_0 a_L^2} + \frac{2\rho u}{r} = 0 \tag{4-6}$$

where

$$\frac{dp}{d\rho} = c^2 \tag{4-7}$$

and c is the speed of sound. Just behind the shock front, (subscript 1) Eqs. 4-2, 4-5, 4-6, and 4-7 yield

$$\left(\frac{\partial u_1}{\partial \tau}\right)_{R_s} + \frac{1}{\rho_0}\left(\frac{\partial p_1}{\partial R_s}\right) = 0 \tag{4-8}**$$

$$\frac{\rho_1}{\rho_0}\left(\frac{\partial u_1}{\partial R_s}\right) + \frac{2u_1}{R_s} = -\frac{1}{\rho_1 c_1^2}\left(\frac{\partial p_1}{\partial \tau}\right)_{R_s} \tag{4-9}**$$

For a traveling shock, conservation of mass yields

$$p_1 - p_0 = \rho_0 U u_1 \tag{4-10}$$

where U is the shock speed.

The Stokes-type derivative of Eq. 4-10 (in the direction of the shock path) multiplied by du_1/dp_1, gives a third relation in addition to Eqs. 4-8 and 4-9

$$\rho_0 U\left(\frac{\partial u_1}{\partial \tau} + U\frac{\partial u_1}{\partial R_s}\right) + \left(\rho_0 u_1 \frac{dU}{dp_1} - 1\right)\left(\frac{\partial p_1}{\partial \tau} + U\frac{\partial p_1}{\partial R_s}\right) = 0 \tag{4-11}$$

Eq. 4-11 agrees with Eq. 4.28 of Ref. 5, while Eq. 3 of Shear and Wright[4] is an identity contrary to their statement derived as a third relation from Eq. 4-10.

A fourth relation, along with Eqs. 4-8, 4-9, and 4-11, is required to solve these equations for $\partial u_1/\partial\tau$, $\partial u_1/\partial R_s$, $\partial p_1/\partial\tau$, and $\partial p_1/\partial R_s$. This relation is supplied by equating the remaining energy E of the energy source at time t_s to the work that remains to be done on air by the blast wave as time goes to infinity.

$$E(R_s) = \int_{t_s}^{\infty} r^2(t_s)\,[p_1(t_s) - p_0]\,u_1(t_s)\,dt_s$$

$$= \int_{R_s}^{\infty} R_s^2\,(p_1 - p_0)\,u_1\,dR_s/U \tag{4-12}$$

$$= \int_{R_s}^{\infty} R_s^2 \rho_0 u_1^2\,dR_s$$

*We usually use the symbol a to represent sound speed in this handbook, but we have given this symbol another meaning here.

**Subscript R_s indicates that the quantity is evaluated for $r = R_s$

An empirical equation describing the energy time curves is

$$\frac{1}{\mu_{KB}} = -\left[\frac{\partial}{\partial \tau} \ln (r^2 pu)\right]_{\tau = t_s} \quad (4\text{-}13)$$

where μ_{KB} is a constant.

Let

$$t' = (t - t_s) / \mu_{KB},$$

then Eqs. 4-12 and 4-13 give

$$E(R_s) = R_s^2 p_1(t_s) u_1(t_s) \nu_{KB}(R_s) u_{KB} \quad (4\text{-}14)$$

where

$$\nu_{KB} = \int_0^\infty f_{KB}(R_s, t')\, dt' \quad (4\text{-}15)$$

$$f_{KB}(R_s, t') = \frac{r^2(t)\,[p_1(t) - p_0]\, u_1(t)}{R_s^2\,[p_1(t_s) - p_0]\, u_1(t_s)} \quad (4\text{-}16)$$

An approximate formula that depends on the shape of decay curve was derived by Kirkwood and Brinkley for blast in air as

$$\nu_{KB} \approx \left\{1 - (1/3)\, e^{-[(p_1 - p_0)/p_0]}\right\} \quad (4\text{-}17)$$

Eqs. 4-13 and 4-14 yield

$$-\frac{1}{\mu_{KB}} = \left[\frac{1}{u_1}\left(\frac{\partial u_1}{\partial \tau}\right) + \frac{1}{p_1}\left(\frac{\partial p_1}{\partial \tau}\right) + \left(\frac{2}{r}\right)u_1\right] = -\frac{R_s^2\, p_1\, u_1\, \nu_{KB}(R_s)}{E(R_s)} \quad (4\text{-}18)$$

where $\nu_{KB}(R_s)$ and $E(R_s)$ are given in Eqs. 4-17 and 4-12. Letting $y_i = \partial u_1/\partial \tau$, $\partial u_1/\partial R_s$, $\partial p_1/\partial \tau$, $\partial p_1/\partial R_s$ for $i = 1,2,3,4$, respectively, we see that Eqs. 4-8, 4-9, 4-11, and 4-18 are in the form

$$\sum_{j=1}^{4} A_{ij}\, y_j = b_i \text{ for } i = 1,2,3,4 \quad (4\text{-}19)$$

where the coefficients A_{ij} and b_i are given in Table 4-1.

From the Hugoniot equations, Cole[5] gives

$$U = \left[\frac{\rho_1}{\rho_0}\left(\frac{p_1 - p_0}{\rho_1 - \rho_0}\right)\right]^{1/2},$$

$$u_1 = \left(\frac{\rho_1 - \rho_0}{\rho_1}\right) U \quad (4\text{-}20)$$

as the solution of the conservation of mass and momentum equations for a shock wave moving into an undisturbed medium. This expresses U and u_1 as functions of pressure and density only. Eqs. 4-20 may be derived from Eqs. 2-15 where $\rho_2 = \rho_0$, $u_2 = u_0 = 0$. Eq. 2-63 on solution of Eqs. 4-20 yields

$$\frac{1}{\rho_1} = \frac{1}{\rho_0} + \frac{u_1^2}{p_1 - p_0} \quad (4\text{-}21)$$

From the equation of state,

$$c_1^2 = \left(\frac{\partial p}{\partial \rho}\right)_s \quad (4\text{-}22)$$

The coefficients in Eq. 4-19 (Table 4-1) are all functions of p_1, R_s, and E, since ρ_0 is a constant and u_1 and U can be found as in Eq. 4-20. Inversion of Eq. 4-19 yields

$$y_i = \sum_{j=1}^{4} A_{ij}^{-1} b_j, \quad i = 1,2,3,4 \quad (4\text{-}23)$$

where A_{ij}^{-1} is the ij-element of the inverse matrix of A.

From Eq. 4-23 and the coefficients A_{ij} one could find in particular

$$\frac{\partial p_1}{\partial R_s} = \frac{d_{f\,1}}{dR_s} = \bar{f}_1(u_1, U, p_1, R_s, E) = \bar{f}_1(p_1, E, R_s) \quad (4\text{-}24)$$

where $\bar{f}$ can be obtained by algebraic elimination of u_1 and U from f_1. The derivative of

TABLE 4-1

COEFFICIENTS OF PARTIAL DERIVATIVES IN KIRKWOOD-BRINKLEY METHOD

A_{ij}			b_i
$A_{11} = 1$	$A_{31} = \rho_0 U$		$b_i = 0$
$A_{12} = 0$	$A_{32} = \rho_0 U^2$		$b_2 = -2u_1/R_s$
$A_{13} = 0$	$A_{33} = [(\rho_0 u_1\, dU/dp_1) - 1]$		$b_3 = 0$
$A_{14} = 1/\rho_0$	$A_{34} = [(\rho_0 u_1\, dU/dp_1) - 1]\, U$		$b_4 = -[R_s^2\, p_1\, u_1\, \nu_{KB}(R_s)]/E(R_s)$
$A_{21} = 0$	$A_{41} = 1/u_1$		
$A_{22} = \rho_1/\rho_0$	$A_{42} = 0$		
$A_{23} = 1/(\rho_1 c_1^2)$	$A_{43} = 1/p_1$		
$A_{24} = 0$	$A_{44} = 0$		

Eq. 4-12 with respect to R_s gives

$$\frac{dE}{dR_s} = \rho_0\, u_1^2\, R_s^2 \qquad (4\text{-}25)$$

In principle, Eqs. 4-24 and 4-25 can be solved simultaneously – given E and p_1, or given p_1 and $\partial p_1/\partial R_s$ – at the charge surface R, or at a fixed value of R_s. Details may be best found in the original paper by Kirkwood and Brinkley[1]. Some misprints are suspected in the group of equations quoted by Shear and Wright[4].

With measured initial values of p_1 and E at the charge surface, Shear[6] obtained a pressure distance curve (see Fig. 4-1). Calculations based on measured p_1 and $\partial p_1/\partial R_s$ at 20 charge radii made by Shear and Wright[4] are compared with experimental data in Fig. 4-1. Agreement seems to be good, except at early stages where $R \approx R_I$. It appears in this case that the initial conditions near the charge radius, i.e., $R \approx R_I$, are suspect just as they also were in the results of Brode[7]. With good initial conditions, the Kirkwood-Brinkley theory appears to be valid as long as the approximation Eq. 4-17 holds. Discussions on initial conditions are given in Chapter 2.

4-2.2 GRÄNSTROM METHOD

One of the few blast wave computations made by other than U. S. investigators is that reported by Gränstrom[8]. He uses a semi-empirical approach. The pressure-time history at a fixed distance r is measured; or, instead, if the shock front and general shape of the blast wave are measured, the physical quan-

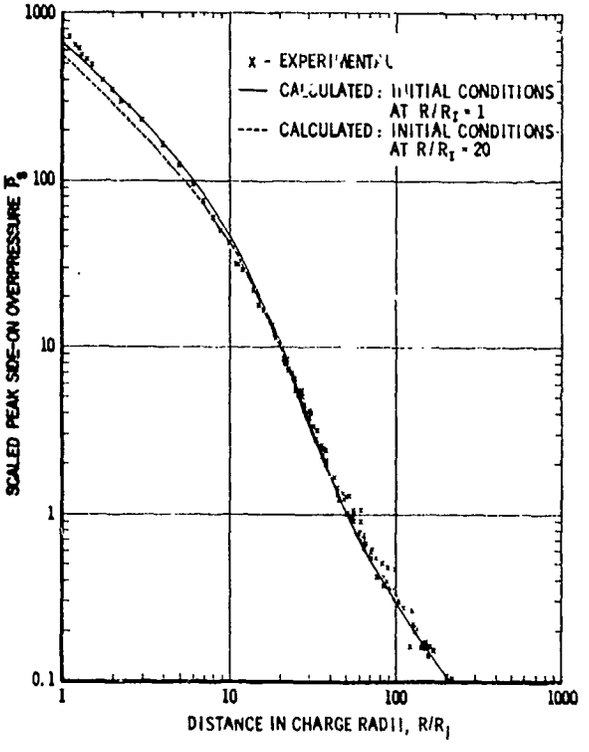


Figure 4-1. Peak Excess Pressure Ratio vs Distance in Charge Radii for Pentolite at a Loading Density of 1.65 g/cm³

tities just after passing of the shock are known from the Rankine-Hugoniot relations and are then varied adiabatically with known equations of state of the hot gas. A curve $E/(RT_0)$ versus ρ_0/ρ is obtained. Its slope is equal to $-p/p_0$. No additional relations were shown by Gränstrom[8] to yield time histories at a fixed point, although the peak pressure-distance history would have been known. Gränstrom further calculated the momentum in space between the front and tail of the shock at specific times. No sophisticated theory was given. This paper is briefed mainly because it is the only Swedish paper available. It does, however, contain an excellent discussion of blast wave phenomenology in general.

4-2.3 METHOD OF CHARACTERISTICS

Chou[9,10,11] and his associates extended Hartree's method of characteristics[12,13], for a given time interval, to a spherical explosion with a shock front, while constant entropy is assumed as in the previous investigations by Unwin[14] and Fox and Ralston[15].

In Rudinger's[16] terminology for one-dimensional unsteady flow, there are Riemann's P waves and Q waves, and entropy S waves for which

$$\frac{dx}{dt} = u + c, \quad u - c, \quad u, \text{ respectively.} \tag{4-26}$$

In Lagrangian coordinates the respective properties of the P, Q, and S waves are (Rudinger, Ref. 16, p. 37)

$$\left.\begin{aligned} \Delta_+ P &= -\frac{n}{r}(cu\Delta_+ \tau) \\ \Delta_- Q &= -\frac{n}{r}(cu\Delta_- \tau) \\ S &= \text{constant or } p/p_0 = (\rho/\rho_0)^\gamma \end{aligned}\right\} \tag{4-27}$$

where $n = 0,1,2$ for one-dimensional plane, cylindrical, and spherical waves, respectively.

The well-known Riemann variables are defined as

$$\left.\begin{aligned} P &= \left(\frac{2}{\gamma-1}\right)c + u \\ Q &= \left(\frac{2}{\gamma-1}\right)c - u \end{aligned}\right\} \tag{4-28}$$

The notation I, II, III is used by Chou, et al.[11], for P, Q, and S waves, respectively. Along with the notation I, II, III, one has, for the P, Q, and S waves in Eulerian coordinates respectively,

$$\Delta_\pm x/\Delta_\pm t = \tilde{u}_\pm \tilde{c}, \quad \Delta x/\Delta t = \tilde{u} \tag{4-29}$$

$$\Delta\pm u = \mp (c/p)(\Delta\pm p/\gamma) \mp 2(\tilde{u}\,\tilde{c}/\tilde{r})\,\Delta\pm t,$$

$$p/p_0 = (c/c_0)^{2\gamma/(\gamma-1)} \tag{4-30}$$

where the tilde means convergence between two points.

Eqs. 4-29 are obtained from Eqs. 4-27 with the perfect gas law assumption. The waves as singularities, starting from the origin $t_1 = 0$, $r = r_0$, are shown in Fig. 4-2. In Fig. 4-2, r_0 is the initial radius of the sphere of high pressure gas.

Rudinger[16] uses a table for the conditions behind the shock, which is not suitable for computer calculation. For the right-traveling shock (Fig. 4-2), at $t = \Delta t$, Chou, et al.[11], derived from the Rankine-Hugoniot equations and the constant surface conditions $p_3 = p_4$, $u_3 = u_4$ that

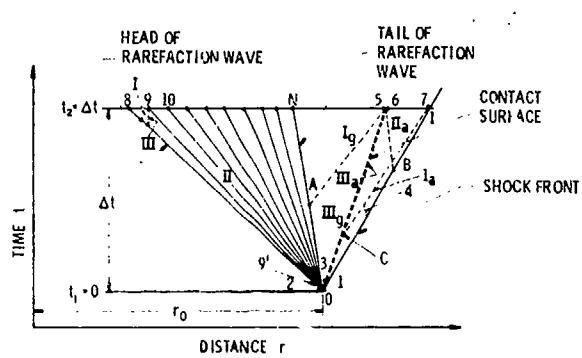


Figure 4-2. Initial Singularity in Method of Characteristics

$$\frac{p_1}{p_2} = \frac{p_1}{p_4}\left\{1 - \left(\frac{\gamma_2 - 1}{2\gamma_1}\right)\frac{c_1}{c_2}\right.$$

$$\left.\frac{(p_4/p_1) - 1}{\left[1 + \left(\frac{\gamma_1 + 1}{2\gamma_1}\right)\left(\frac{p_4}{p_1} - 1\right)\right]^{1/2}}\right\}^{\frac{2\gamma_2}{\gamma_2 - 1}} \qquad (4\text{-}31)$$

where subscripts are related to points shown in Fig. 4-2. It is noted that Point 1 is the undisturbed ambient state and Point 2 is the unexpended explosive. Point 3 is ahead of the "tail" of the rarefaction waves behind the contact surface, while Point 4 is just behind the shock (ahead of the contact surface).

Since 1 and 2 are known states, the only unknown in Eq. 4-31 is p_4. The Newton-Raphson iterative process was used to solve p_4 from this equation without encountering any difficulty. U_0, u_4, and c_4, are then given from the same set of equations (Eqs. 4-27 through 4-31) by

$$U_4 = U_0 = c_1\left\{[(\gamma_1 + 1)/(2\gamma_1)] \times [(p_4/p_1) - 1] + 1\right\}^{1/2} \qquad (4\text{-}32)$$

$$u_4 = [2c_1/(\gamma_1 + 1)] \times [(U_0/c_1) - (c_1/U_0)] \qquad (4\text{-}33)$$

$$c_4 = c_1\left\{1 + [2(\gamma_1 - 1)/(\gamma_1 + 1)^2] \times [\gamma(U_0/c_1) - (c_1/U_0) - (\gamma_1 - 1)]\right\}^{1/2} \qquad (4\text{-}34)$$

The computation is not straightforward. Different cases must be tested and branched properly. The details of the iteration procedures are given by Huang and Chou[10]. For example, the solutions, for p, r, u, c at points 5,6,7 in Fig. 4-2, consisting of 12 unknowns, are related to points A,B,C through physical and state characteristic equations and shock relations. The solutions p, u, c at points A,B,C, depending on their location (r, t), require nine interpolation formulas. There are five waves, I_a, I_g, II, III_a, III_g; there are 12 physical and state characteristic equations, 3 shock relations, and 3 contact surface conditions ($u_5 = u_6$, $p_5 = p_6$, $r_5 = r_6$).

Wave I_a introduces U_7 which can be eliminated by the shock slope condition

$$\tilde{U} = \frac{U_7 + U_4}{2} = \frac{r_7 - r_0}{\Delta t} \qquad (4\text{-}35)$$

In addition, (r, t) at A,B,C are related to x_N, x_7, x_6, Δt by three slope conditions:

$$\frac{r_N - r_0}{\Delta t} = \frac{r_A - r_0}{t_A}, \quad \frac{r_7 - r_0}{\Delta t} = \frac{r_B - r_0}{t_B},$$

$$\frac{r_6 - r_0}{\Delta t} = \frac{r_C - r_0}{t_C} \qquad (4\text{-}36)$$

Hence there are a total of 9 + 12 + 3 + 3 + 1 = 28 equations for the 28 unknowns p_5, r_5, u_5, c_5, p_6, r_6, u_6, c_6, p_7, r_7, u_7, c_7, p_A, u_A, c_A, P_B, u_B, c_B, p_C, u_C, c_C, U_7, t_a, t_b, t_C, r_A, r_B, r_C. If one eliminates three variables by the three simple contact surface conditions, there are 25 equations governing 25 unknowns to be solved simultaneously[10]. The near-initial-stage numerical solution of Chou and Huang agreed within 0.25% of McFadden's[17] short time power series solution at a time when the head of the rarefaction wave traveled a distance of 5% of the initial radius of the sphere.

The schematic of the region of numerical solution is shown in Fig. 4-3. AD was chosen so that its slope is smaller than that of the local P-characteristics; thus the second shock does not affect the regions to the right of it.

The second shock, main shock, and the contact surface in the physical plane are shown in Fig. 4-4. In this figure, dimensionless time τ and dimensionless distance λ are used as ordinate and abscissa, respectively. The quantity ϵ is a length expressing energy and pressure scaling, $\epsilon^3 = E_0/p_1$. This is similar to Brode's quantity ϵ_B.

In addition, the likelihood of late-stage equivalence with equal initial energy released E_0, but different pressure and density ratios (p_e/p_0, ρ_e/ρ_0), is demonstrated by the four examples shown in Fig. 4-5. Here, the quantities p_e, ρ_e are the initial values of pressure and density in the explosives or high pressure sphere; p_0, ρ_0 are those ahead of the main shock (Point 1), while the total energy E_0 is given by

$$E_0 = \frac{4\pi}{3} \frac{(p_e - p_0)}{(\gamma - 1)} r_0^3 \qquad (4\text{-}37)$$

4-3 METHODS WITH FICTITIOUS VISCOSITY

As noted before, the idea of introducing fictitious viscosity into the governing equation and the corresponding finite difference equation was originated by von Neumann and Richtmyer[3] for plane shock waves. Instead of approximating the thin but continuous shock layer by a mathematical discontinuity, it is approximated by a layer of the order of the thickness of one mesh size. von Neumann and Richtmyer's work[3] is very well known, and only the fictitious viscosity term and stability criterion will be summarized.

Fictitious viscosity coefficient,

$$\sigma = \frac{2 (c_{VN} \Delta a_L)^2}{v\rho_0} \left| \frac{\partial u}{\partial a_L} \right| ,$$

where c_{VN} is a dimensionless constant nearly unity, which satisfies the requirements that (1) the governing equations must possess solutions without discontinuities, (2) the thickness of the shock layers must be everywhere of the same order as the interval length Δa_L used in the numerical computation,

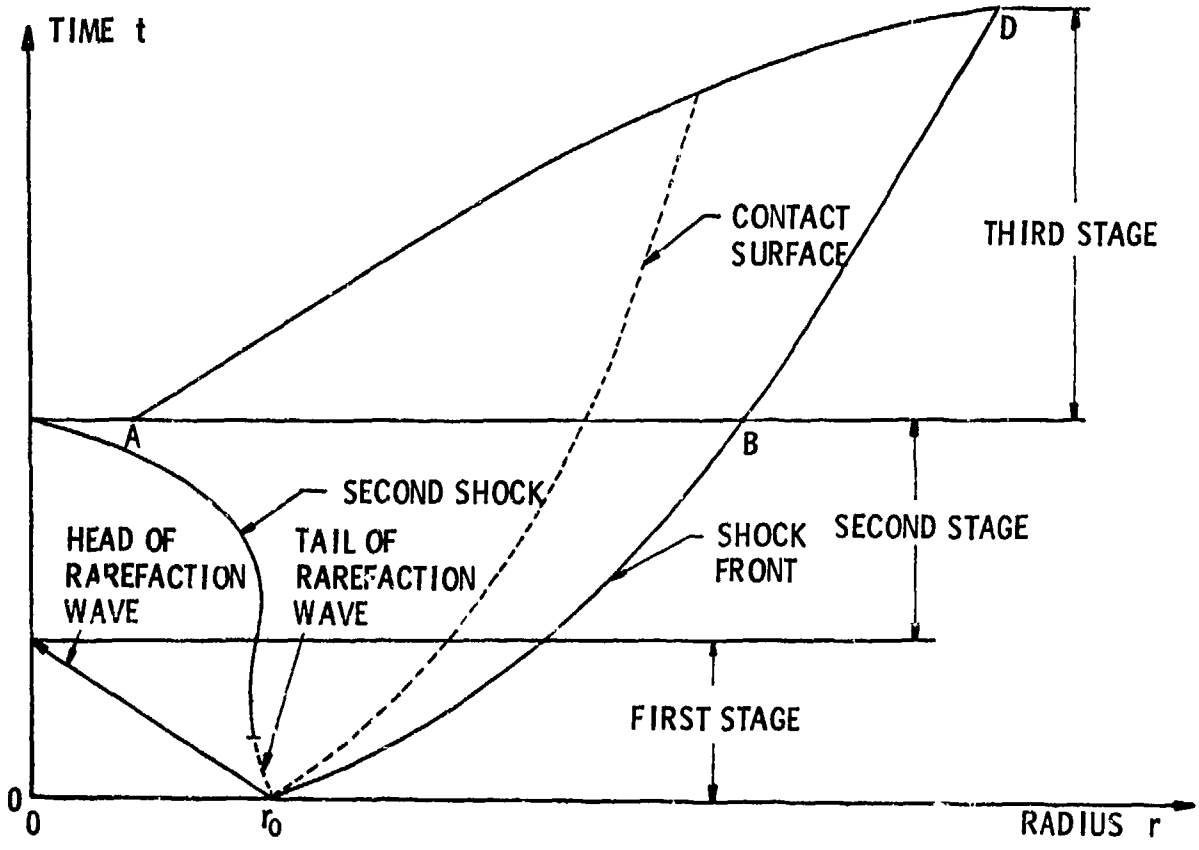


Figure 4-3. Schematic of Region of Numerical Solution for Method of Characteristics

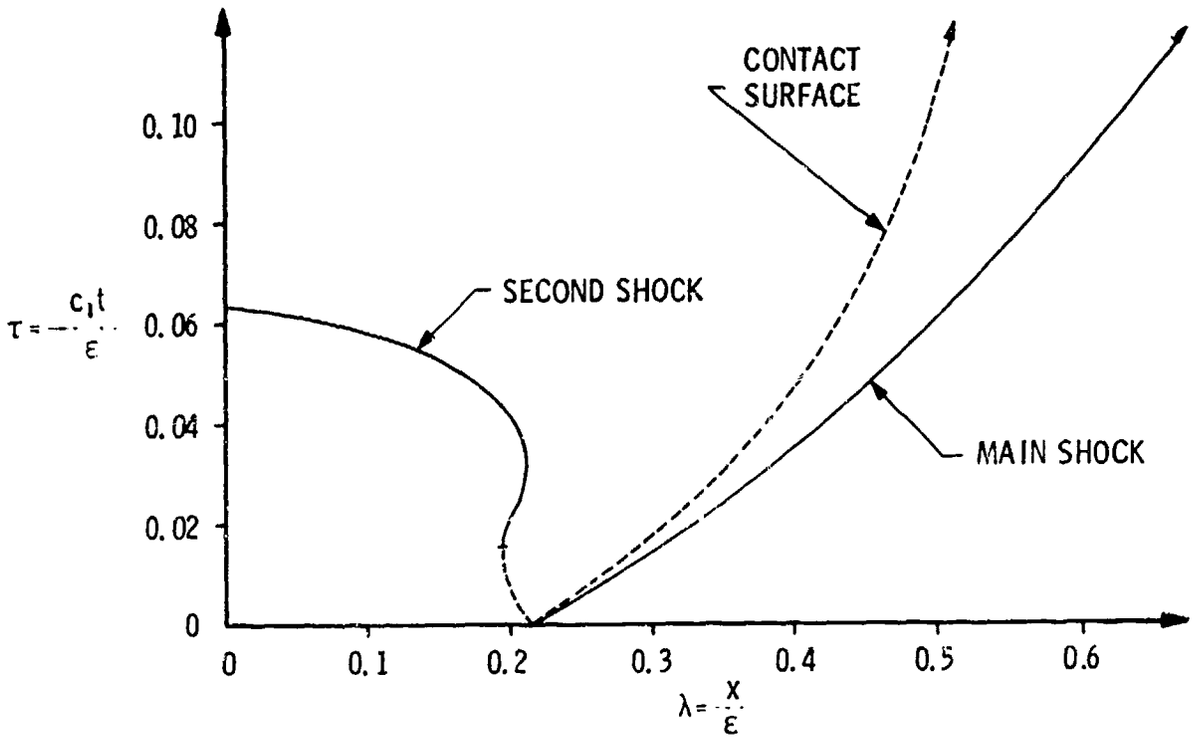


Figure 4-4. Physical Plane Showing the Main Shock, Contact Surface, and Second Shock

independent of the strength of the shock and the condition of the material into which it is running, (3), the effect of the fictitious viscous term must be negligible outside of the shock layers, and (4) the Hugoniot equations must hold when all other dimensions characterizing the flow are large compared to the shock thickness.

Stability criteria for plane shock are:

$$L = \frac{S_0 \Delta t}{\Delta a_L} \leqslant 1 \quad \text{outside the shock,}$$

$$L_f = \frac{S_{of} \Delta t}{\Delta x} \leqslant \gamma^{1/2} / (2 c_{VN}) \quad \text{in the shock region,}$$

where

$$S_0 = [\gamma p/(v \rho_0^2)]^{1/2}$$

$$S_{of} = S_0 = [\gamma p_f/(v_f \rho_0)]^{1/2} \text{ behind the shock.}$$

The choice of $c_{VN} = 1$ has been found to yield good results in practice for the representation of shocks.

4-3.1 BRODE'S METHOD

Brode[18] was apparently the first to apply von Neumann and Richtmyer's fictitious viscosity technique to spherical blast waves. The integration process consists of the stepwise solution of difference equations which approximate the differential equations of motion of the gas. The practical conditions to be satisfied as stated by Brode are that: (1) the differencing scheme must be stable, (2) it must offer reasonable desired results, (3) it must conserve numerical significance, and (4) when put in the form of coded instructions for a high-speed computer, must be fast enough to reach desired solutions with a reasonable expenditure of machine time.

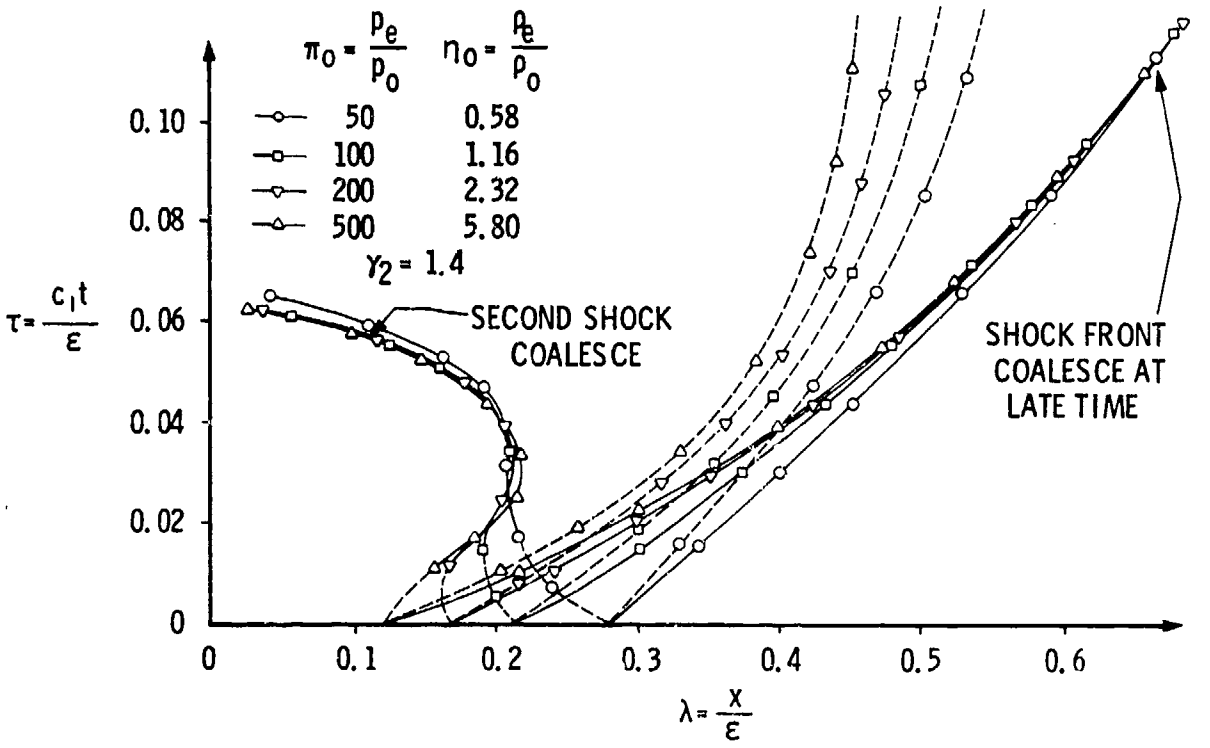


Figure 4-5. Physical Plane (λ-τ) Showing Shock Front, Contact Surface, and Second Shock for Cases With Equal Initial Energy and Equal Initial Mass

The Lagrangian form of equations of motion is used. Let

$$\epsilon_B^3 = E_{tot}/p_0 = \frac{4\pi}{p_0}\int_0^{R_s} \rho\left(E_{int} + \frac{u^2}{2}\right) r^2\, dr - \frac{4\pi R_L^3}{3(\gamma-1)} \quad (4\text{-}38)$$

where

ϵ_B = scaling length

E_{tot} = total blast energy

E_{int} = specific internal energy

R_s = shock radius

and the subtracted term represents the part of the total energy ambient pressure ratio due to pre-shock internal energy of the compressed sphere.

Let

$$\bar{x} = \frac{1}{3}\left(\frac{r_0}{\epsilon_B}\right)^3 = \frac{1}{3}\left(\frac{a_L}{\epsilon_B}\right)^3,$$

$$\bar{\tau} = a_0\, \tau/\epsilon_B$$

be the nondimensionalized Lagrangian type coordinates, and let the Eulerian nondimensional coordinates be

$$\bar{r} = r/\epsilon_B,\ \bar{t} = a_0 \bar{t}/\epsilon_B = \bar{\tau},\ \bar{p} = p/p_0,$$

$$\bar{\rho} = \rho/\rho_0,\ \bar{u} = u a_0.$$

The governing equations are then

$$\frac{\partial \bar{r}}{\partial x} = \frac{1}{\bar{\rho}\bar{r}^2} \text{ or}$$

$$\frac{\partial \bar{\rho}}{\partial \bar{\tau}} = -\bar{\rho}\left(\frac{2\bar{u}}{\bar{r}} + \frac{\partial \bar{u}/\partial \bar{x}}{\partial \bar{r}/\partial \bar{x}}\right) \text{ (mass)} \quad (4\text{-}39)$$

$$\frac{\partial \bar{u}}{\partial \bar{\tau}} = -\frac{\bar{r}^2}{\gamma}\frac{\partial}{\partial x}(\bar{p} + \bar{q}) \quad \text{(momentum)} \quad (4\text{-}40)$$

$$\frac{\partial \bar{p}}{\partial \bar{\tau}} = \frac{1}{\bar{\rho}} \frac{\partial \bar{\rho}}{\partial \bar{\tau}} [\gamma \bar{p} + (\gamma - 1)\bar{q}],$$

(energy) (4-41)

$$\bar{u} = \frac{\partial \bar{r}}{\partial \bar{t}} \qquad \text{(velocity)} \qquad (4\text{-}42)$$

where an ideal gas has been assumed for which the internal energy is

$$E_{int} = \frac{\bar{p}}{\bar{\rho}(\gamma - 1)} \left(\frac{\rho_0}{p_0}\right) \qquad (4\text{-}43)$$

and the entropy is given by Eq 2-30. Here q is nondimensional fictitious viscous pressures.

An appropriate viscosity for the case of an outward moving spherical shock wave is, according to Brode[18],

$$\bar{q} = \frac{9\gamma(\gamma+1)}{4} \left(\frac{M_B}{3\pi}\right)^2 \bar{\rho}(\Delta\bar{x})^2 \times \left(\frac{\partial \bar{u}}{\partial \bar{x}} - \left|\frac{\partial \bar{u}}{\partial \bar{x}}\right|\right) \frac{\partial \bar{u}}{\partial \bar{x}} \qquad (4\text{-}44)$$

where $\Delta\bar{x}$ is the grid size and M_B is number of grid zones in the shock front. In this form q vanishes in the regions of expansion where $\partial\bar{u}/\partial\bar{x} > 0$ and is nonzero only in the compression phase of shock, where $\partial\bar{u}/\partial\bar{x}$ is large and negative.

The difference equations are approximated by

$$\bar{u}_{\ell}^{n+\frac{1}{2}} = \bar{u}_{\ell}^{n-\frac{1}{2}} - \frac{\Delta\bar{\tau}(\bar{r}_{\ell}^{n})^2}{(\Delta\bar{x})_{\ell}\gamma} \left[\bar{p}_{\ell+\frac{1}{2}}^{n} - \bar{p}_{\ell-\frac{1}{2}}^{n} + \bar{q}_{\ell+\frac{1}{2}}^{n-\frac{1}{2}} - \bar{q}_{\ell+\frac{1}{2}}^{n-\frac{1}{2}}\right] \qquad (4\text{-}45)$$

$$\bar{r}_{\ell}^{n+1} = \bar{r}_{\ell}^{n} + \bar{u}_{\ell}^{n+\frac{1}{2}} \Delta\bar{\tau} \qquad (4\text{-}46)$$

$$\bar{\rho}_{\ell-\frac{1}{2}}^{n+1} = \bar{\rho}_{\ell-\frac{1}{2}}^{n} \left(\frac{1 - W_B}{1 + W_B}\right) \qquad (4\text{-}47)$$

where ℓ indicates the ℓth node, etc.

$$W_B = \Delta\bar{\tau} \left[\frac{2\left(\bar{u}_{\ell}^{n+\frac{1}{2}} + \bar{u}_{\ell-1}^{n+\frac{1}{2}}\right)}{\bar{r}_{\ell}^{n+1} + \bar{r}_{\ell}^{n} + \bar{r}_{\ell-1}^{n+1} + \bar{r}_{\ell-1}^{n}} + \frac{\bar{u}_{\ell}^{n+\frac{1}{2}} - \bar{u}_{\ell-1}^{n+\frac{1}{2}}}{\bar{r}_{\ell}^{n+1} + \bar{r}_{\ell}^{n} - \bar{r}_{\ell-1}^{n+1} - \bar{r}_{\ell-1}^{n}}\right] \qquad (4\text{-}48)$$

$$\bar{q}_{\ell-\frac{1}{2}}^{n+\frac{1}{2}} = \frac{9\gamma(\gamma+1)}{2} \left(\frac{M_B}{3\pi}\right)^3 \bar{\rho}_{\ell-\frac{1}{2}}^{n+1} \times \left[\bar{u}_{\ell-1}^{n+\frac{1}{2}} - \bar{u}_{\ell}^{n+\frac{1}{2}}\right]^2$$

$$\text{for } \bar{u}_{\ell-1}^{n+\frac{1}{2}} > \bar{u}_{\ell}^{n+\frac{1}{2}} \qquad (4\text{-}49)$$

$$\bar{q}_{\ell-\frac{1}{2}}^{n+\frac{1}{2}} = 0 \quad \text{for } \bar{u}_{\ell-1}^{n+\frac{1}{2}} \leq \bar{u}_{\ell}^{n+\frac{1}{2}} \qquad (4\text{-}50)$$

$$\bar{p}_{\ell-\frac{1}{2}}^{n+1} = \left[\left(\frac{\gamma+1}{\gamma-1}\bar{\rho}_{\ell-\frac{1}{2}}^{n+\frac{1}{2}} - \bar{\rho}_{\ell-\frac{1}{2}}^{n}\right)\bar{p}_{\ell-\frac{1}{2}}^{n} + 2\left(\bar{\rho}_{\ell-\frac{1}{2}}^{n+1} - \bar{\rho}_{\ell-\frac{1}{2}}^{n}\right)\bar{q}_{\ell-\frac{1}{2}}^{n+\frac{1}{2}}\right] \times \left(\frac{\gamma+1}{\gamma-1}\bar{\rho}_{\ell-\frac{1}{2}}^{n} - \bar{\rho}_{\ell-\frac{1}{2}}^{n+1}\right)^{-1} \qquad (4\text{-}51)$$

The stability conditions are

$$\Delta\bar{\tau} \leq \Delta\bar{x} \Big/ \left[\bar{r}^2 (\bar{p}\bar{\rho})\right]_{max}^{\frac{1}{2}} \qquad (4\text{-}52)$$

$$\Delta\bar{t} \leq \frac{\gamma}{4}(\Delta\bar{x})^2\left(\frac{1}{\bar{r}^2\bar{q}}\left|\frac{\partial\bar{u}}{\partial\bar{x}}\right|\right)_{\min} \qquad (4\text{-}53)$$

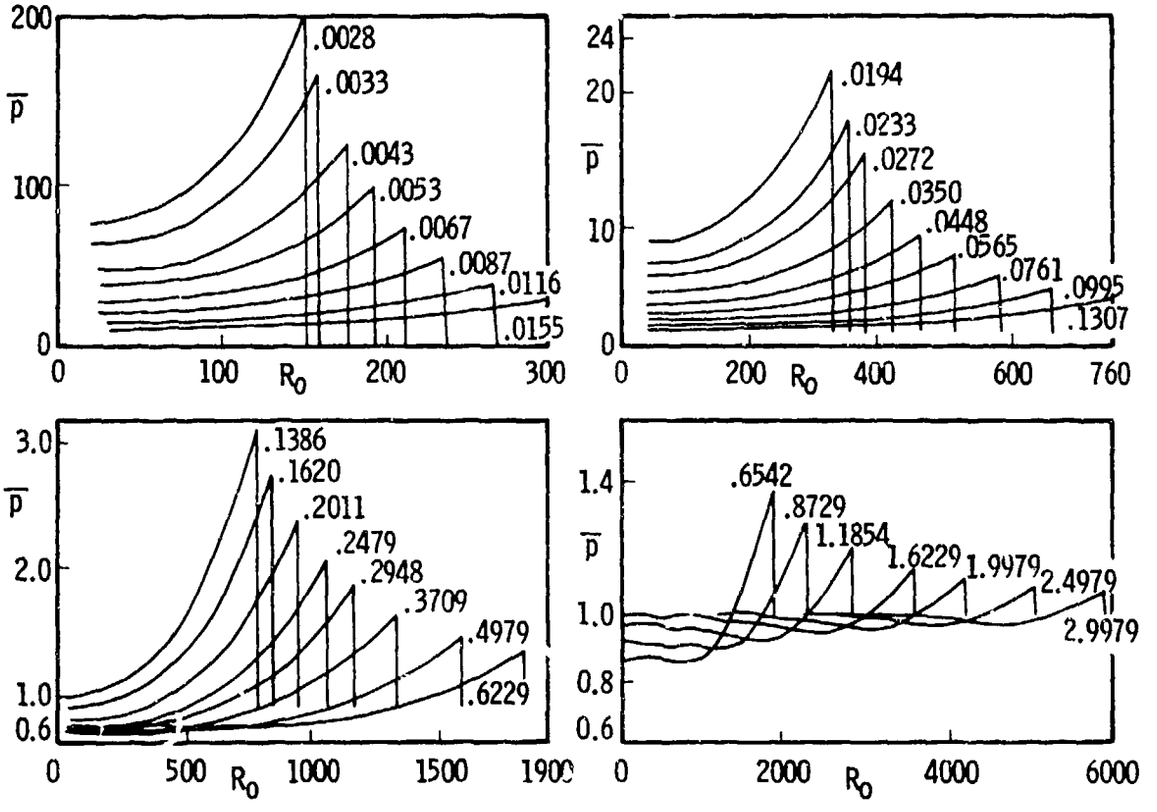
The size of the time step would automatically double if these conditions permit it to.

Unequal zone sizes are frequently convenient and may be time saving. For instance, the use of small zones through the shock front provides a sharp shock at very little cost in computing time. The use of such unequal zones was validated empirically in this problem by repeating calculations with quite different zone choices.

Two types of initial conditions were used--(1) a point source, and (2) an isothermal sphere. Discussions of initial conditions are given in Chapter 2.

Some attempts of Brode in reducing the required computing time of the stable differencing scheme of DuFort and Frankel for diffusion type equations were employed in place of explicitly carrying a viscosity quantity q. Some practical disadvantages of such a scheme exist. It requires carrying through a machine calculation sets of data for all space points for two different times. Furthermore, computing, changing time increments, and combining space points all become more tedious. Besides these disadvantages, additional terms must be introduced by the differencing scheme. On the other hand, the very general nature of the viscosity method, the ease of its applicability, and the precision with which it produces the Hugoniot condition across a shock would seem to offset the more stringent time requirements. Use of this method for nonideal gases is, however, not considered by Brode[18].

Some numerical results are given by Brode[18], e.g., Fig. 4-6. More examples are given in later papers by Brode[7,19,20].



Position is in (Brode) units of $(E/p_0)^{1/3}/1627.2$, and the time is in units of $(E/p_0)^{1/3}/c_0$

Figure 4-6. Pressure as a Function of Lagrange Position R_0 for the Point-source Solution at Times Indicated[18]

4-3.2 WUNDY CODE (NOL) AND LSZK EQUATION OF STATE

The von Neumann-Richtmyer method has been further developed by Lutzky and co-workers. Their computer code for one-dimensional blast waves are identified by the acronym WUNDY.

The first FORTRAN version of WUNDY written by Walker, et al.[21], was based on the KO-Code of the University of California Radiation Lab, Wilkins, et al.[22]. Several versions of the WUNDY Code now exist at NOL. The one to be described has been used in the calculation of some of the hydrodynamic aspects of nuclear explosions in air[23,24]. This is a one-dimensional code and is basically simple but with many options such as the inclusion of plane, axisymmetric, and spherical symmetries all in the same code. Complex equations of state can be included. The input and output routine usually requires considerable machine time.

The finite-difference equations for this program are

$$\left.\begin{aligned} u_j^{n+\frac{1}{2}} &= u_j^n + \Delta t_j^n \\ &\times \frac{\left(P_{j-\frac{1}{2}}^n - P_{j+\frac{1}{2}}^n\right)}{\left(m_{j-\frac{1}{2}} + m_{j+\frac{1}{2}}\right)/2} A_j^n - q \\ &\text{(momentum)} \end{aligned}\right\} \quad (4\text{-}54)$$

where m is the mass of a zone.

$$\left.\begin{aligned} x_j^{n+1} &= x_j^n + \Delta t_j^{n+\frac{1}{2}} \\ &\times u_j^{n+\frac{1}{2}} \\ &\text{(velocity)} \end{aligned}\right\} \quad (4\text{-}55)$$

$$\left.\begin{aligned} v_{j-\frac{1}{2}}^{n+1} &= V_{j-\frac{1}{2}}^{n+1} \Big/ m_{j-\frac{1}{2}} \\ &\text{(specific volume of a zone)} \end{aligned}\right\} \quad (4\text{-}56)$$

$$\left.\begin{aligned} p_{j-\frac{1}{2}}^{n+1} = &\left[2e_{j-\frac{1}{2}}^n - \left(p_{j-\frac{1}{2}}^n + 2q_{j-\frac{1}{2}}\right)\right. \\ &\left.\times\left(v_{j-\frac{1}{2}}^{n+1} - v_{j-\frac{1}{2}}^n\right)\right] \\ &\times\left[\left(\frac{\gamma+1}{\gamma-1}\right)v_{j-\frac{1}{2}}^{n+1} - v_{j-\frac{1}{2}}^n\right]^{-1} \end{aligned}\right\} \quad (4\text{-}57)$$

$$e_{j-\frac{1}{2}}^{n+\frac{1}{2}} = \frac{p_{j-\frac{1}{2}}^{n+1}\, v_{j-\frac{1}{2}}^{n+1}}{\gamma-1} \quad (4\text{-}58)$$

The derivation of Eq. 4-57 is less obvious but it can be derived from

$$\left.\begin{aligned} &\frac{\partial e}{\partial \tau} + (p+q)\frac{\partial v}{\partial t} = 0 \\ &\text{and } e = \frac{pv}{\gamma-1} \end{aligned}\right\} \quad (4\text{-}59)$$

Using a second-order finite difference approximation to the differential Eq. 4-59 with e^{n+1} as obtained from Eq. 4-59, one finds

$$\frac{p^{n+1}v^{n+1}}{\gamma-1} - e^n + \left[\left(p^{n+1}+p^n\right)/2 + q\right] \times \left(v^{n+1} - v^n\right) \approx 0 \quad (4\text{-}60)$$

provided that $q^{n+\frac{1}{2}}$ or $(q^{n+1}+q^n)/2$ is used. However, as q is artificial, q^n is usually used. Simple algebraic manipulation of Eq. 4-60 yields

$$\left(\frac{\gamma+1}{\gamma-1}\right)p^{n+1}v^{n+1} - p^{n+1}v^n = 2e^n - \left(p^n + 2q\right)\left(v^{n+1} - v^n\right) \quad (4\text{-}61)$$

from which Eq. 4-57 follows at the point $j - \frac{1}{2}$.

In Eqs. 4-54 through 4-61

x = distance from origin

u = velocity of interface

v = specific volume of zone

p = pressure in zone

q = artificial viscosity in zone*

P = $p + q$

g = acceleration of gravity component

A_j^n = area of interface j at time n; = $4\pi \times (x_j^n)^2$ for sphere

$V_{j-\frac{1}{2}}^n$ = volume of zone $j-\frac{1}{2}$, = $\frac{4}{3}\pi\ [(x_j^n)^3 - (x_{j-\frac{1}{2}}^n)^3]$ for sphere

Δt_j^n = time step = $\left(\Delta t_j^{n+\frac{1}{2}} + \Delta t_j^{n-\frac{1}{2}}\right)/2$

m = mass of zone

Appropriate modifications have to be made for other equations of state. Other details such as initialization, rezoning, summary routines, equation for γ, will not be given here.

Although calculations of the air shock motion produced by a spherical TNT explosion with the reaction considered gaseous have given satisfactory agreement with experimental results, the experimental motion of the explosive interface and of the second shock have not agreed with theoretical calculations. Initial attempts to improve the theory were made by Lutzky[24] using the Landau-Stanyukovich equation of state that was derived by drawing an analogy between the state of the detonation products of a condensed explosive and the crystal lattice of the solid. It is well known that the energy of a solid body has a two-fold origin; it is made up of an elastic energy arising from the binding forces between the atoms and molecules, and a thermal energy associated with oscillation of the atoms or molecules about their positions of stable equilibrium. Landau and Stanyukovich[25] have attempted to describe the behavior of the detonation products by considering them as a solid with the property that the elastic energy and the elastic part of the pressure are predominant. Their theory has been described and expanded by Zeldovich and Kompaneets[26] so that it is referred to as the LSZK equation of state, which is

$$p = \frac{B}{v^\gamma} + \frac{C_{V_1}\left(\frac{\gamma}{2} - \frac{1}{6}\right)T}{v} \qquad (4\text{-}62)$$

$$e_E = \frac{B}{(\gamma-1)\,v^{(\gamma-1)}} + C_V T \qquad (4\text{-}63)$$

e_E = energy density (per unit mass)

v = specific volume

T = temperature

and B, C_{V_1}, C_V, and γ are constants defined as follows: γ is a dimensionless constant serving as a polytropic index connected with the intermolecular forces, C_v is the specific heat at constant volume, C_{V_1} is a specific heat associated with the appropriate lattice vibrations, and B is a dimensional constant. The elastic part of the pressure is B/v^γ and $B/[(\gamma-1)\,v^{(\gamma-1)}]$ is the elastic part of the energy. Eliminating T from Eqs. 4-62 and 4-63 one has

$$p = \frac{e_E}{\alpha v} + \frac{B}{v^\gamma}\left[1 - \frac{1}{\alpha(\gamma-1)}\right] \qquad (4\text{-}64)$$

where

$$\alpha = \frac{C_V}{C_{V_1}\left(\frac{1}{\frac{\gamma}{2} - \frac{1}{6}}\right)}$$

Or, one may use

$$p = \frac{B}{v^\gamma} + \frac{C_V T}{\alpha v} = \frac{B}{v^\gamma}(1+y)$$

$$e_E = \frac{B}{(\gamma-1)\,v^{(\gamma-1)}} + C_V T$$

$$= \frac{B\alpha}{v^{(\gamma-1)}}\left[y + \frac{1}{\alpha(\gamma-1)}\right] \qquad (4\text{-}65)$$

where

*Lehto and Lutzky gave no expressions for q; however, in the KO-code there were two expressions, one linear and one quadratic. They are $q = \frac{1}{4} c_{KO}^2 \frac{\rho_0}{v}\left(\frac{\partial u}{\partial x}\right)(\Delta x)$ and $q = c_{KO}^2 \frac{\rho_0}{v}\left(\frac{\partial u}{\partial x}\right)^2 (\Delta x)^2$ with $c_{KO} = 2$. Presumably some expression similar to Eq. 4-44 was used.

$$y = \frac{C_V T}{\alpha B} \rho^{(\gamma-1)}$$

For an isentropic process, it can be shown that

$$p = K\rho^{-\frac{1+\alpha}{\alpha}} + B\rho^{\gamma} \qquad (4\text{-}66)$$

where

K = constant of integration
$= \left(p_0 - B\rho_0^{\gamma}\right)\rho_0^{-\frac{1+\alpha}{\alpha}}$, for example. (4-67)

From Eqs. 4-64 and 4-66

$$e_E = \alpha K \rho^{1/\alpha} + \frac{1}{(\gamma-1)} B\rho^{(\gamma-1)} \qquad (4\text{-}68)$$

from Eqs. 4-65 and 4-68,

$$T = \frac{\alpha K \rho^{1/\alpha}}{C_V} \qquad (4\text{-}69)$$

and From Eq. 4-66,

$$c^2 = \frac{dp}{d\rho} = K\left(\frac{1+\alpha}{\alpha}\right)\rho^{1/\alpha} + B\gamma\rho^{(\gamma-1)} \qquad (4\text{-}70)$$

The corresponding Chapman-Jouguet conditions* are summarized as follows:

$$v_0 = \left(\frac{B}{Q}\right)^{\frac{1}{(\gamma-1)}} \left\{\alpha y + \frac{1}{\gamma-1} - \frac{(y+1)^2}{2\left[\gamma + \left(\frac{1+\alpha}{\alpha}\right)y\right]}\right\}^{\frac{1}{(\gamma-1)}} \left[1 + \frac{1+y}{\gamma + \left(\frac{1+\alpha}{\alpha}\right)y}\right]$$

$$e_1 = \frac{B\alpha}{v_1^{(\gamma-1)}}\left[y + \frac{1}{\alpha(\gamma-1)}\right]$$

$$v_1 = \left(\frac{B}{Q}\left\{\alpha y + \frac{1}{\gamma-1} - \frac{(1+y)^2}{2\left[\gamma + \left(\frac{1+\alpha}{\alpha}\right)y\right]}\right\}\right)^{\frac{1}{(\gamma-1)}}$$

$$p_1 = \frac{2(e_1 - Q)}{v_0 - v_1}, \quad \text{if } p_0, e_0 \approx 0$$

$$c_1^2 = v_0 p_1 \Bigg/ \left\{\left[1 + \frac{1+y}{\gamma + \left(\frac{1+\alpha}{\alpha}\right)y}\right] \times \left[\frac{1+y}{\gamma + \left(\frac{1+\alpha}{\alpha}\right)y}\right]\right\}$$

$$U = D = c_1\left\{1 + \left[\frac{1+y}{\gamma + \left(\frac{1+\alpha}{\alpha}\right)y}\right]\right\}$$

$$u_1 = c_1\left[\frac{(1+y)}{\gamma + \left(\frac{1+\alpha}{\alpha}\right)y}\right]$$

$$\rho_1 = \left\{c_1^2 \Big/ \left[B\left(\gamma + \left(\frac{1+\alpha}{\alpha}\right)y\right)\right]\right\}^{\frac{1}{(\gamma-1)}}$$

(the last eight equations are (4-71))

where all quantities behind the detonation wave are related implicitly to the specific volume v_0 of the undetonated explosives ahead of the shock, and Q is the chemical energy released per unit mass of explosives.

The three undetermined parameters γ, α, and B/Q which appear in the LSZK equation of state can be evaluated by using experimental data. It is noted that if $1 + \alpha/\alpha < \gamma$ in the isentropic pressure Eq. 4-66, then $p \to K \times \rho^{(1+\alpha)/\alpha}$ as $\rho \to 0$; and if it is assumed that in the limit of low pressure the detonation

*These are the Rankine-Hugoniot relations for a reacting medium with heat release, e.g., Williams[27] using the LSZK equation of state.

products behave as ideal gases with a constant ratio of specific heats η then one must set $\alpha = 1/(\eta - 1)$. The remaining constants may be evaluated by referring to experimental results for the dependence of the detonation velocity on the density. After a particular value is assigned to γ (where $\gamma > \eta$) a series of values of B/Q may be obtained by carrying out a point by point comparison of the theoretical plot, obtained from Eqs. 4-71, of $\ell n\ D$ vs $\ell n \{\rho_0 + [1/(\gamma - 1)]\ \ell n\ (B/Q)\}$ with the experimental plot of $\ell n\ D$ vs $\ell n\ \rho_0$. Since B/Q must be a constant, the accuracy of the fit is determined by the amount of variation in the values of B/Q obtained, and γ may be adjusted to make this variation a minimum.

For TNT, the experiments of Explosive Research Laboratory at Bruceton, yielded $D = 0.1785 + 0.3225\ \rho_0$, where D is in cm/μsec and ρ_0 is in g/cc. Using $\eta = 1.34$, with $Q = 1{,}018$ cal/g, $\gamma = 2.78$, $B/Q = 0.53562$, and $\alpha = 2.9412$, results based on Eqs. 4-71 were in good agreement with experimental data (see Table 4-2).

TABLE 4-2

COMPARISON OF DETONATION VELOCITIES D CALCULATED FOR LSZK SUBSTANCE WITH DETONATION VELOCITIES DETERMINED AT BRUCETON

ρ_0, g/cc	D, cm/μsec; LSZK	D, cm/μsec; (Bruceton)
1.7935	0.7572	0.7569
1.6620	0.7146	0.7145
1.5535	0.6795	0.6795
1.4412	0.6433	0.6433
1.3655	0.6189	0.6189
1.2995	0.5977	0.5976
1.2412	0.5791	0.5788
1.1773	0.5588	0.5582
1.1320	0.5444	0.5436
1.1009	0.5345	0.5335
1.0034	0.5039	0.5021
0.9590	0.4900	0.4878
0.9256	0.4797	0.4770
0.9010	0.4720	0.4691
0.8565	0.4584	0.4547
0.8082	0.4437	0.4391
0.7703	0.4322	0.4269
0.7331	0.4211	0.4149

4-4 PARTICLE AND FORCE (PAF) METHOD[28]

This method is based on the concept of "particle" dynamic theory which is modified to take into account the dissipative effects in a fluid[28]. The particles are not molecules whose internal energy is carried by velocity fluctuations, but instead they are (fictitious) effective mean particles whose velocity represents the mean velocity of small finite masses of fluid. The macroscopic kinetic energy of the fluid is required to be exactly the sum of the kinetic energy of all the particles, so the internal energy must be represented by an additional variable. If this variable is expressed as a function of the particle position alone, only adiabatic motion can be represented. Compression and subsequent expansion would then return the set to their initial configurations with no dissipation; therefore, a special description is needed to describe the variations of particle internal energy.

Symbols

e_E = specific internal energy

E_j = internal energy of the jth particle

$\underset{\rightarrow}{f}_{ij}$ = force associated in form with equation of state

$\underset{\rightarrow}{F}_{ij}$ = force exerted by ith particle on jth particle

$\underset{\rightarrow}{g}_{ij}$ = fictitious dissipative force, corresponding effectively to the fictitious viscosity

H = total energy

i, j = indexes describing particle number

K_j = kinetic energy of jth particle, $m_j\ \underset{\rightarrow}{u}_j \cdot \underset{\rightarrow}{u}_j / 2$

m = particle mass (assumed constant)

m_j = mass of jth particle

$\underset{\rightarrow}{M}_j$ = $m_j \underset{\rightarrow}{u}_j$, momentum of jth particle

n = number density of particle (particles per unit area)

p_D = pressure ("force per unit distance", if two physical dimensions, i.e., force per unit distance per unit thickness)

$\underset{\rightarrow}{r}_j$ = space coordinate of jth particle

r_{ij} = $\left|\underset{\rightarrow}{r}_{ij}\right|$

$\underset{\rightarrow}{r}_{ij}$ = $\underset{\rightarrow}{r}_j - \underset{\rightarrow}{r}_i$

$\hat{\underset{\rightarrow}{r}}_{ij}$ = $\underset{\rightarrow}{r}_{ij} / r_{ij}$, a unit vector pointing from ith particle to jth particle

$\underset{\rightarrow}{u}_j$ = velocity of jth particle

x_D = r_{ij}

Σ_i^j = summation over i over certain neighbors of j (not including $i = j$)

4-4.1 GOVERNING EQUATIONS

One has

$$m_j \frac{d\underset{\rightarrow}{u}_j}{dt} = \Sigma_i^j \underset{\rightarrow}{F}_{ij} \tag{4-72}$$

$$\frac{d\underset{\rightarrow}{r}_j}{dt} = \underset{\rightarrow}{u}_j \tag{4-73}$$

$$\underset{\rightarrow}{F}_{ij} = \underset{\rightarrow}{f}_{ij} + \underset{\rightarrow}{g}_{ij} = f_{ij}\,\hat{\underset{\rightarrow}{r}}_{ij} + \underset{\rightarrow}{g}_{ij}$$

where

$$f_{ij} = f(r_{ij}, E_i, E_j) \tag{4-75}$$

In order to correspond to fluid mechanics, the following considerations must be made:

1. Conservation of mass holds.

2. Conservation of momentum holds where $\underset{\rightarrow}{F}_{ij} = -\underset{\rightarrow}{F}_{ji}$ is the same as in classical particle dynamics, so that momentum change of any subset of particles arises only through external forces; the contributions of any particular pair of particles in the subset to the momentum of the subset is $\underset{\rightarrow}{F}_{ij} + \underset{\rightarrow}{F}_{ji}$ (i, j in the subset) which must vanish. Thus, the restrictions imposed are

$$\left.\begin{aligned} &\underset{\rightarrow}{F}_{ij} = -\underset{\rightarrow}{F}_{ji} \\ &f_{ij} = f_{ji}\,, \quad (\hat{\underset{\rightarrow}{r}}_{ij} = -\hat{\underset{\rightarrow}{r}}_{ji}) \\ &\underset{\rightarrow}{g}_{ij} = -\underset{\rightarrow}{g}_{ji} \end{aligned}\right\} \tag{4-76}$$

3. Conservation of energy holds where the rate of change of energy of a particle should be given by the rate at which the other particles do work on it. However, a departure from particle dynamics is made by using $(\underset{\rightarrow}{u}_i + \underset{\rightarrow}{u}_j)/2$ instead of $\underset{\rightarrow}{u}_j$ for the proper systematic property. Thus we have the equation

$$\frac{d}{dt}(K_j + E_j) = \Sigma_i^j \underset{\rightarrow}{F}_{ij} \cdot \frac{1}{2}(\underset{\rightarrow}{u}_i + \underset{\rightarrow}{u}_j) \tag{4-77}$$

Since the total energy of an isolated system is conserved, summing Eq. 4-77 over all the j particles in such a system, yields

$$\frac{dH}{dt} = \frac{d}{dt}\Sigma_j (K_j + E_j) = \tfrac{1}{2}\Sigma_j \Sigma_i^j \underset{\rightarrow}{F}_{ij} \cdot (\underset{\rightarrow}{u}_i + \underset{\rightarrow}{u}_j) = 0 \tag{4-78}$$

in which the contribution for each pair of particles vanishes since $\underset{\rightarrow}{F}_{ij} = -\underset{\rightarrow}{F}_{ji}$. By definition $K_j = m_j \underset{\rightarrow}{u}_j \cdot \underset{\rightarrow}{u}_j / 2$ therefore, from Eq. 4-72

$$\frac{dK_j}{dt} = m_j \underset{\rightarrow}{u}_j \cdot \frac{d\underset{\rightarrow}{u}_j}{dt} = \underset{\rightarrow}{u} \cdot \Sigma_i^j \underset{\rightarrow}{F}_{ij} \quad (4\text{-}79)$$

Subtraction of Eq. 4-79 from Eq. 4-77 yields

$$\frac{dE_j}{dt} = (\tfrac{1}{2}) \Sigma_i^j \underset{\rightarrow}{F}_{ij} \cdot (\underset{\rightarrow}{u}_i - \underset{\rightarrow}{u}_j)$$

Therefore, using Eq. 4-74

$$\frac{dE_j}{dt} = -(\tfrac{1}{2}) \Sigma_i^j f_{ij} \underset{\rightarrow}{\hat{r}}_{ij} \cdot \frac{d\underset{\rightarrow}{r}_{ij}}{dt} + (\tfrac{1}{2}) \Sigma_i^j \underset{\rightarrow}{g}_{ij} \cdot (\underset{\rightarrow}{u}_i - \underset{\rightarrow}{u}_j),$$

where $\underset{\rightarrow}{r}_{ij} = r_{ij} \underset{\rightarrow}{\hat{r}}_{ij}$ gives

$$\frac{dE_j}{dt} = -(\tfrac{1}{2}) \Sigma_i^j f_{ij} \underset{\rightarrow}{\hat{r}}_{ij} \cdot \left[\underset{\rightarrow}{\hat{r}}_{ij} \frac{dr_{ij}}{dt} + r_{ij} \frac{d\underset{\rightarrow}{\hat{r}}_{ij}}{dt} \right] + (\tfrac{1}{2}) \Sigma_i^j \underset{\rightarrow}{g}_{ij} \cdot (\underset{\rightarrow}{u}_i - \underset{\rightarrow}{u}_j)$$

$$= -(\tfrac{1}{2}) \Sigma_i^j f_{ij} \left(\frac{dr_{ij}}{dt} + \underset{\rightarrow}{r}_{ij} \cdot \frac{d\underset{\rightarrow}{\hat{r}}_{ij}}{dt} \right) + (\tfrac{1}{2}) \Sigma_i^j \underset{\rightarrow}{g}_{ij} \cdot (\underset{\rightarrow}{u}_i - \underset{\rightarrow}{u}_j) \quad (4\text{-}80)$$

It is questionable in general that $d\underset{\rightarrow}{\hat{r}}_{ij}/dt$ is zero since the direction of $\underset{\rightarrow}{\hat{r}}_{ij}$ may be changing with time. This term was not present and has not been discussed by Daly, et al.[28]. However, for "one-dimensional flow", this term may vanish.

4-4.2 THE FINITE DIFFERENCE FORMS

The finite difference forms used by Daly, et al.[28] are:

$$m_j \frac{\left(\underset{\rightarrow}{u}_j^{n+1} - \underset{\rightarrow}{u}_j^{n} \right)}{\Delta t} = \Sigma_i^j \underset{\rightarrow}{F}_{ij}^{n}$$

(forward formula) (4-81)

$$\frac{\underset{\rightarrow}{r}_j^{n+1} - \underset{\rightarrow}{r}_j^{n}}{\Delta t} = \underset{\rightarrow}{u}_j^{n+1}$$

(backward formula)* (4-82)

$$\left. \begin{aligned} \frac{E_j^{n+1} - E_j^n}{\Delta t} &= (\tfrac{1}{2}) \Sigma_i^j \underset{\rightarrow}{F}_{ij}^{n} \\ &\cdot \left(\underset{\rightarrow}{u}_i^{n+\frac{1}{2}} - \underset{\rightarrow}{u}_j^{n+\frac{1}{2}} \right) \end{aligned} \right\} \quad (4\text{-}83)$$

where

$$\underset{\rightarrow}{u}^{n+\frac{1}{2}} = \left(\underset{\rightarrow}{u}^{n} + \underset{\rightarrow}{u}^{n+1} \right) \Big/ 2 \quad (4\text{-}84)$$

$$\frac{K_j^{n+1} - K_j^n}{\Delta t} = \Sigma_i^j F_{ij}^{n} u_j^{n+\frac{1}{2}} \quad (4\text{-}85)$$

$$\left. \begin{aligned} H_j^{n+1} - H_j^n &= \frac{\Delta t}{2} \Sigma_i^j \underset{\rightarrow}{F}_{ij}^{n} \\ &\cdot \left(\underset{\rightarrow}{u}_i^{n+\frac{1}{2}} + \underset{\rightarrow}{u}_j^{n+\frac{1}{2}} \right) \end{aligned} \right\} \quad (4\text{-}86)$$

Since $\underset{\rightarrow}{F}_{ij} = -\underset{\rightarrow}{F}_{ji}$, this would imply energy transfer from i to j is equal in magnitude to but opposite in sign from that transferred from j to i, thus one property of energy conservation is implied.

The choice of form Eq. 4-83 is based on monotonic dissipation. The use of this equation with the proper choice of $\underset{\rightarrow}{g}_{ij}$ from Eq. 4-74 will not result in decreased entropy, while most of the other alternatives examined can produce such decrease under certain circumstances.

4-4.2.1 NEIGHBORS

The neighbors are not clearly defined as neighboring fluid elements. A search radius R

* This is used in preference to a forward formula based on the argument of a stability requirement, Harlow and Meisner[29].

and a maximum number of neighbors N^* are predetermined for each problem, as described later. Among all of the particles in the system which lie within the search radius of the jth particle, the N^* closest particles are tentatively chosen to be neighbors; any of these which do not similarly find j as one of their N^* closest neighbors are then subtracted from the list. Good results have been attained by choosing N^* to be twice the number of the physical dimensions of the problem. An alternative method of achieving neighbor reciprocity is to add rather than subtract neighbors, but the subtractive method has the distinct programming advantage that a lower upper limit can be put on the storage requirements for inter-particle relations. Tests indicate that the two methods produce equally good results. However, physically, due to the selection of N^*, adding may be more realistic than subtracting.

The success of the PAF method depends to such a large extent upon the proper statistical averaging of inter-particle fluctuations that it seems necessary to search for neighbors every time cycle. It would be preferable to avoid this because it is by far the most time-consuming phase of the calculation, requiring 50% or more of the calculation time. Experiments "are" being performed to see under what circumstances the neighbor search can be conducted less often. In addition, an attempt has been made by Daly, et al., to speed up this part of the calculation as described in the paragraphs which follow.

The first step is to overlay the computational systems with a guide of square cells, each cell having a side of length R, the search radius. The particles are then classified according to the cells in which they fall and the actual search for neighbors begins. For any given particle j, the distances to all other particles within its own or a neighboring cell are computed and compared with R. If any such distance r_{ij} is less than R, then i is listed as a neighbor of j and j is listed as a neighbor of i, unless either i or j already has a full quota of neighbors. Then r_{ij} would be compared to distances of the other neighbors and the most distant particle would be dropped as a neighbor.

In order to achieve the greatest possible speed with this method, it is imperative to choose R as small as accuracy will permit. The customary choice is about one and a half times the anticipated particle separation in the least compressed region.

If one starts at the lower left corner of the cell mesh and works from left to right and upward through the cells, it is possible to restrict somewhat the number of cells which must be searched for any given particle. For instance, if the jth particle lies in cell (k, ℓ) then it is necessary only to search through cells (k, ℓ), $(k, \ell + 1)$, $(k + 1, \ell - 1)$, $(k + 1, \ell)$, and $(k + 1, \ell + 1)$ for neighbors of j. If j had additional neighbors in other cells bordering (k, ℓ) this fact would have already been determined in searching for neighbc of those particles.

After these tentative neighbor determinations have been made, a second pass is made through the particles dropping neighbors as necessary for reciprocity.

4-4.2.2 FORCES

The formulation is not yet complete until the forces are defined.

4-4.2.2.1 NONDISSIPATIVE

The nondissipative part of the force function f_{ij} should be associated with the equation of state of the fluid through an integral equation which in dimensional Cartesian space has the form[30]

$$\left.\begin{aligned} P_D\ (mn, e_E) &= \frac{\pi n^2}{2} \int_0^\infty x_D^2\, \sigma \\ &\times \left(n x_D^2\right) f\left(x_D,\ e_E\right) dx_D \end{aligned}\right\} \quad (4\text{-}87)$$

where σ is a radial function describing the

density of neighbors as defined in par. 4-4.2.1 and is restricted in form by the equation

$$\pi \int_0^\infty \sigma(\xi) d\xi = N^* \tag{4-88}$$

where the change in variable $\xi = n x_D^2$.

Harlow[30] solves Eq. 4-87 by approximating σ by a step function. This formulation has proven satisfactory when applied to a polytropic equation of state, but for more complicated equations of state it may lead to a force function that does not vanish at normal density and zero internal energy. The difficulty can be avoided if σ is chosen to satisfy these requirements. Daly, et al.[28], thus assume the equation of state can be expanded in powers of compression minus unity

$$\left.\begin{aligned} P_D(mn, e_E) &= \Sigma_k A_k(e_E) \\ &\times \left(\frac{mn}{\rho_0} - 1\right)^k \end{aligned}\right\} \tag{4-89}$$

where ρ_0 is ambient density.

The nondissipative part of the force function takes a similar form

$$\left.\begin{aligned} f(x_D, e_E) &= (x_D)^{\alpha_D} \Sigma_k B_k(e_E) \\ &\times \left(\frac{m}{\rho_0 x_D^2} - 1\right)^k \end{aligned}\right\} \tag{4-90}$$

The right hand side of Eq. 4-87 will consist of a series of integrals Ψ_k, summed over k. If we let $\rho = mn = \rho_0$ and since

$$P_D(\rho_0, e_E) = A_0(e_E) \tag{4-91}$$

from Eq. 4-89, then σ must take a form so that the rest of the integrals vanish at $\rho = \rho_0$.

From Eqs. 4-87 and 4-90 it can be seen that a term Ψ_k in the series of integrals is given by

$$\left.\begin{aligned} \Psi_k &= \frac{\pi n^2}{2} B_k(e_E) \int_0^\infty x_D^{(\alpha_D + 2)} \\ &\times \left(\frac{m}{\rho_0 x_D^2} - 1\right)^k \sigma(n x_D^2) dx_D \\ &= \frac{\pi}{4} n^{(1+\alpha_D)/2} B_K(e_E) \\ &\times \int_0^\infty \xi^{(1-\alpha_D)/2} \\ &\times \left[\frac{\rho}{\rho_0}\left(1 - \frac{\rho_0}{\rho}\xi\right)\right]^k \sigma(\xi) d\xi \end{aligned}\right\} \tag{4-92}$$

The form of the integral suggests that

$$\sigma = \hat{\sigma}\delta(\xi - 1) \tag{4-93}$$

Eqs. 4-88 and 4-93 yield

$$\hat{\sigma} = \frac{N^*}{\pi} \tag{4-94}$$

Substituting Eqs. 4-93 and 4-94 into Eq. 4-87 yields

$$\left.\begin{aligned} P_D(\rho, e_E) &= \frac{N^* n^2}{2} \int_0^\infty x_D^2 f(x_D, e_E) \\ &\times \delta(n x_D^2 - 1) dx_D \\ &= \frac{N^* n^{1/2}}{4} \int_0^\infty \xi^{1/2} \\ &\times f\left(\sqrt{\frac{\xi}{n}}, e_E\right) \\ &\times \delta(\xi - 1) d\xi \\ &= \frac{N^* n^{1/2}}{4} f(\sqrt{1/n}, e_E) \end{aligned}\right\} \tag{4-95}$$

In plane coordinates, at $\xi = 1$,

$$n = \frac{1}{r_{ij}^2} = \frac{1}{x_D^2} \tag{4-96}$$

Thus, from Eqs. 4-95 and 4-96

$$\left.\begin{aligned} f(r_{ij}, e_E) &= \left(\frac{4n_j}{N^*}\right) P_D\left(\frac{m}{r_{ij}^2}, e_E\right) \\ &= \left(\frac{4r_{ij}}{N^*}\right) p_D(\rho, e_E) \end{aligned}\right\} \tag{4-97}$$

For a polytropic equation of state,

$$\left.\begin{aligned} p_D &= (\gamma - 1)\,\rho\, e_E \\ &= (\gamma - 1)\left(\frac{m}{r_{ij}^2}\right) e_E \end{aligned}\right\} \tag{4-98}$$

Eqs. 4-96 and 4-98 yield

$$f(r_{ij}, e_E) = \frac{4(\gamma - 1)\, m\, e_E}{N^*\, r_{ij}} \tag{4-99}$$

Eqs. 4-97 and 4-99 according to Daly, et al.[28] can be shown to hold for any σ satisfying Eq. 4-88. For a "stiffened" gas equation of state

$$p_D = (\gamma - 1)\rho e_E + a_D(\rho - \rho_0) \tag{4-100}$$

The corresponding result from Eqs. 4-96, 4-97, and 4-100 is, analogously,

$$\left.\begin{aligned} f(r_{ij}, e_E) = {} & \frac{4(\gamma - 1)\, m\, e_E}{N^*\, r_{ij}} \\ & + \frac{4\, m\, a_D}{N^*\, r_{ij}} \\ & \times \left[1 - \frac{\rho_0\, r_{ij}^2}{m}\right] \end{aligned}\right\} \tag{4-101}$$

and the second term vanishes at $\rho = mn = m/r_{ij}^2 = \rho_0$, the normal density. If a step function is assumed for σ, the bracketed term in Eq. 4-101 would be $[1 - \pi\rho_0 r_{ij}^2/(3m)]$ which does not vanish at the normal density.

4-4.2.2.2 DISSIPATIVE

For practical application, the "main" requirement of a dissipative mechanism in the PAF is to prevent the growth of instability for finite difference methods which are not inherently stable. In all the numerical experiments carried out, the minimum amount of the "artificial viscosity" required for stability has been employed.

Dissipation is only required in those portions of the fluid which are undergoing compression; thus $\underset{\rightarrow}{g}_{ij} = 0$ for $(\hat{\underset{\rightarrow}{r}}_j - \hat{\underset{\rightarrow}{r}}_i) \cdot (\underset{\rightarrow}{u}_i - \underset{\rightarrow}{u}_j) = \hat{\underset{\rightarrow}{r}}_{ij} \cdot (\underset{\rightarrow}{u}_i - \underset{\rightarrow}{u}_j) < 0$, otherwise,

$$\underset{\rightarrow}{g}_{ij} = m\,\omega\,\hat{\underset{\rightarrow}{r}}_{ij}\left[\hat{\underset{\rightarrow}{r}}_{ij} \cdot (\underset{\rightarrow}{u}_i - \underset{\rightarrow}{u}_j)\right] \tag{4-102}$$

where ω is a constant with dimensions T^{-1}.

The form of $\underset{\rightarrow}{g}_{ij} = m\,\omega\,(\underset{\rightarrow}{u}_i - \underset{\rightarrow}{u}_j)$ used by Harlow and Meixner[29] was inferior to Eq. 4-102 because it did not rigorously conserve angular momentum. Further, the new alternative form gives a measure of the compression between particles i and j; thus, it is consistent with the one-dimensional stability analysis which assumes that all compression is head-on. Eq. 4-102 is also less likely to lead to inter-penetration for a large value of ω. Both forms, however, have the drawback of being independent of the inter-particle spacing. Therefore, further modifications used employ either

$$\left.\begin{aligned} \underset{\rightarrow}{g}_{ij} = {} & m\,\omega\left(\frac{|e_i + e_j|}{2m}\right)^{1/2} \\ & \times \left[\hat{\underset{\rightarrow}{r}}_{ij} \cdot (\underset{\rightarrow}{u}_i - \underset{\rightarrow}{u}_j)\right] \hat{\underset{\rightarrow}{r}}_{ij} \end{aligned}\right\} \tag{4-103}$$

or

$$\underset{\rightarrow}{g}_{ij} = \frac{m\,\omega'\,u_0\left[\underset{\rightarrow}{\hat{r}}_{ij}\cdot(\underset{\rightarrow}{u}_i - \underset{\rightarrow}{u}_j)\right]}{r_{ij}}\ \underset{\rightarrow}{\hat{r}}_{ij} \qquad (4\text{-}104)$$

where ω' is now a dimensionless constant, and u_0 is chosen to be a typical sound speed for the problem. The first of these two forms has been in the most common usage; the second one is reserved mainly for problems whose initial conditions require the material to be cold. The form of Eq. 4-103 was patterned after a form suggested by Landshoff; the square root factor is simply proportional to local sound speed in a polytropic gas and closely related to it for many other materials.

The discussions on boundary conditions and the use of images for rigid wall reflection will not be detailed here.

4-4.3 TEST CASES

Let subscripts 1 and 0 be used for input data related to shocked air and ambient air, respectively.

4-4.3.1 FLOW PAST A WEDGE

One of the test cases for the PAF method[28] was the rate of growth of a detached bow wave produced by the passage of a shock over a two-dimensional wedge of 90 deg "apex" angle suspended in air. The input data are given in Table 4-3. The locations of the detached bow wave at times of 18 and 46 μsec after impact are compared in Fig. 4-7 with shock tube experimental results given by Griffith[31]. The PAF results are the dashed lines while the experiments are solid lines. The shapes at the first observation time (18 μsec) are somewhat different but essentially the same at the second time, (46 μsec) except for the reflection on the PAF curve which was caused by interaction with the top reflected boundary.

TABLE 4-3

INPUT DATA FOR FLOW PAST A WEDGE – PAF METHOD

Variable	Value	Units
u_1	0.0755	cm/μsec
u_0	0	cm/μsec
v_1*	0	cm/μsec
v_0*	0	cm/μsec
e_1	1.0403×10^{-2}	joule
e_0	0.3932×10^{-2}	joule
Δx_1	0.0635	cm
Δy_1	0.0635	cm
Δx_0	0.1243	cm
Δy_0	0.1243	cm (particle spacings)
m	1.861×10^{-5}	g (particle mass)
Δt	0.1	μsec
ω'	0.07	– (using Eq. 4-102)

*here v is y- component of velocity.

Griffith's value of $M_s = 1.35$, however, may be subject to an experimental error as much as 5%; thus, the qualitative agreement between the two curves is as much as could be expected and demonstrates that PAF calculates early bow wave development correctly (at least qualitatively).

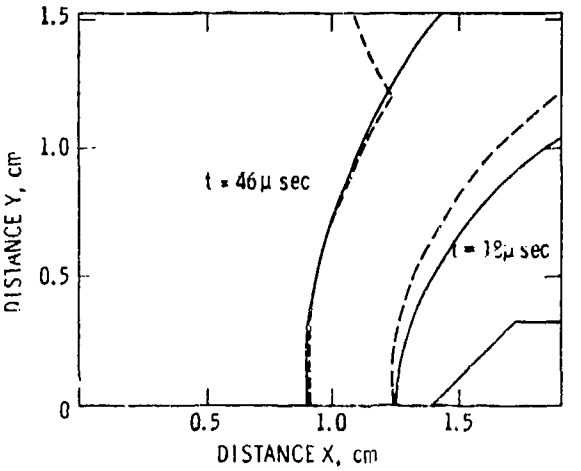


Figure 4-7. A Comparison of the PAF Detached Bow Wave Positions (Dashed Lines) After Impact With Those Observed in a Shock Tube Experiment Involving a Mach 1.35 Flow Past a Wedge[28]

4-4.3.2 FLOW PAST A BLUNT CYLINDER

The detached shock front observed experimentally in a Mach number 1.58 flow past a blunt, axially symmetric cylinder is plotted on a late time PAF particle configuration from the calculation of the same problem in Fig. 4-8. In the figure, the dots show particle locations which originally constituted an equally spaced grid in nondimensional radial and axial positions.

4-4.3.3 FLOW PAST A CONE

For a shock of $M = 1.41$ passing a 75 deg cone, the steady-state pressure along the obstacle face and the final bow wave shape were compared with those observed experimentally by Marschner[3 2] in Figs. 4-9 and 4-10. The nondimensional free stream conditions are: $u_0 = 1.41$, $v_0 = 0$; $c_0 = 1.0$; $\Delta z_0 = 0.1$, $\Delta r_0 = 0.1$; $\Delta t = 0.01$; $\omega = 1.0$ (using Eq. 4-103).* In Fig. 4-9, X is measured as the distance along the cone force from the nose, and S is the short length of the cone face to the shoulder. For PAF prediction, p_s is the theoretical stagnation pressure which develops

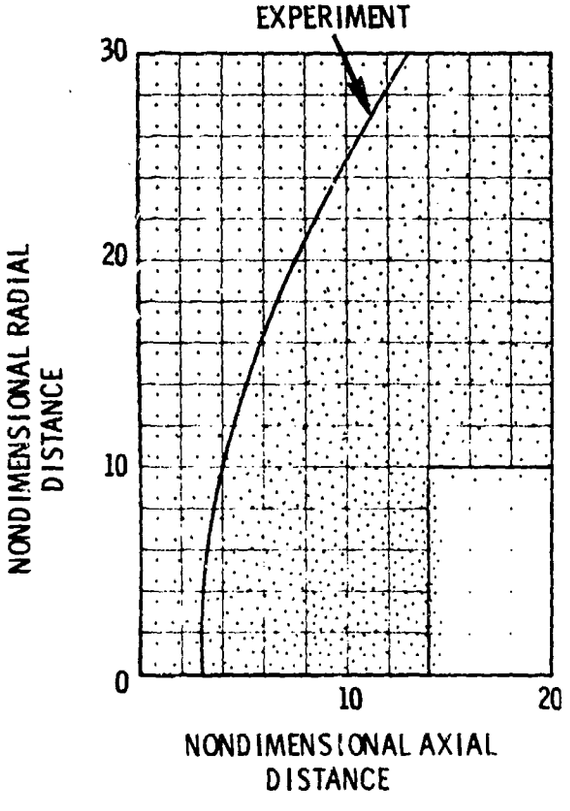


Figure 4-8. The Steady-state Detached Shock Front Position in a Mach 1.58 Flow Past a Blunt Cylinder

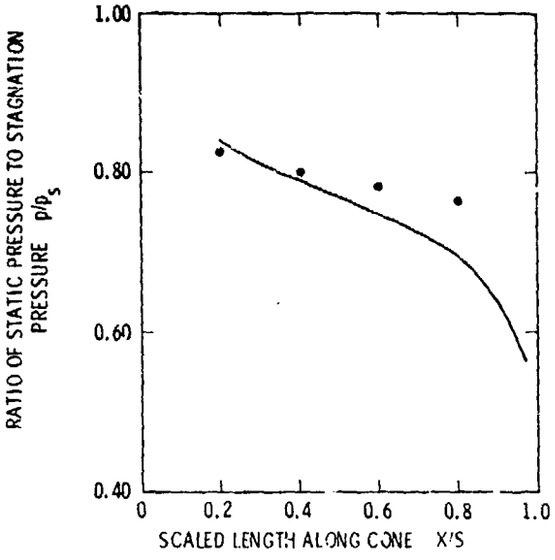


Figure 4-9. A Comparison of Steady-state PAF Pressures (the Dots) Along the Cone Face With Experimental Values Observed in a Mach 1.41 Flow Past a 75-deg Cone

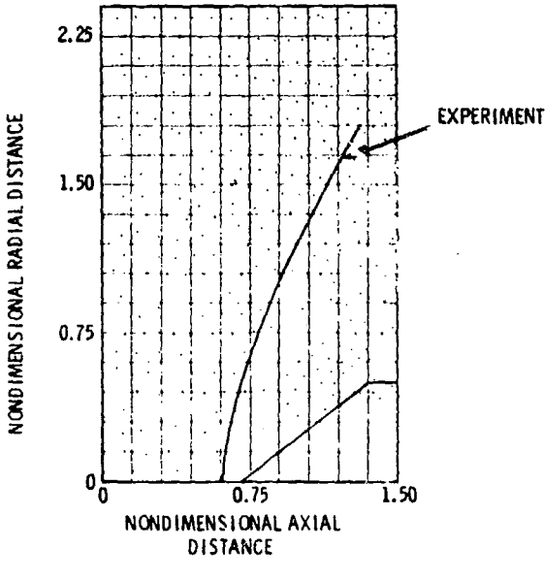


Figure 4-10. A Late-time PAF Particle Plot (the Dots) Compared to an Experimental Steady-state Bow Wave

*z is axial distance.

on the blunt cone subject to the given free stream conditions, while Marschner's p_s is a measured value.

The agreement of the calculated p/p_s with experiment was considered to be good, although there is less variation in PAF pressure across the cone face than was observed. This was attributed to the PAF strategy of destroying light particles as they move up the cone face a. d distributing their mass, momentum, and energy among their heavier neighbors as described in the discussion of boundary conditions[28]. However, the good agreement near the nose conforms with the results in the other two test cases.

4-5 PARTICLE-IN-CELL (PIC) METHOD

This technique[35,36] is a finite-difference method of expressing the equations of motion of a compressible fluid. The computational framework is achieved by dividing the system into an Eulerian mesh of cells and superimposing a mesh of particles whose distribution and mass are such as to describe the initial configuration of the fluid. The differential equations of motion with transport terms neglected are written in finite difference form relative to the system of cells. The transport effect is obtained by allowing particles to communicate between neighboring cells according to their velocities. This transport mechanism produces a "nonlinear dissipative force" which is effective in reducing the fluctuations that arise as a result of the differencing technique. This dissipative term is of the form of a "true" viscosity in the sense that it is proportional to the velocity gradient. However, artificial viscosity (of linear form) must be introduced for stability in the low speed region. Artificial viscosity might be eliminated, according to Daly[31], by proper choice of the parameters of the system to obtain a tolerable maximum error, which is bounded due to the transport mechanism. Details in the paragraphs which follow are mainly based on those of Harlow[38]. The variables relating to the ijth cell, C_{ij}, are defined:

u_{ij}, v_{ij} = x-, y- component of velocity, respectively

$M_{ij}^{(\ell)}$ = mass of ℓth material in C_{ij}; ℓ 1,2, . . .

M_{ij} = $\sum_{\ell} M_{ij}^{(\ell)}$, total mass in C_{ij}

$e_{ij}^{(\ell)}$ = specific internal energy of ℓth material in C_{ij}

p_{ij} = pressure in C_{ij}

q_{ij} = fictitious viscosity pressure in C_{ij}

ΔQ_{ij} = Phase-I change in total internal energy

$E_{ij}^{(\ell)}$ = total energy of ℓth material in C_{ij}

X_{ij}, Y_{ij} = total x, y momentum in C_{ij}

Superscript ℓ for quantities related to ℓth material, $\ell = 1, 2, \ldots$

4-5.1 STATE EQUATIONS

Some remarks on pressure p_{ij} must be made. Let the equation of state for the ℓth material be $p^{(\ell)} = f^{(\ell)}(\rho^{(\ell)}, e_E^{(\ell)})$. If $e = 1,2$, and if the fraction of a cell occupied by the first material is $\sigma_{ij}^{(1)}$, then the condition of pressure continuity across an interface yields

$$\left.\begin{aligned} p_{ij}^{(1)} &= f^{(1)}\left(\rho_{ij}^{(1)}, \; e_{ij}^{(1)}\right) = p_{ij}^{(2)} \\ &= f^{(2)}\left(\rho_{ij}^{(2)}, e_{ij}^{(2)}\right) \end{aligned}\right\} \quad (4\text{-}105)$$

where

$$\left.\begin{aligned} \rho_{ij}^{(\ell)} &= f^{(\ell)}\left(\frac{M_{ij}^{(\ell)}}{\sigma_{ij}^{(\ell)} \Delta x \Delta y}\right) e_{ij}^{(\ell)} \\ \ell &= 1,2 \end{aligned}\right\} \quad (4\text{-}106)$$

$$\sigma_{ij}^{(2)} = 1 - \sigma_{ij}^{(1)} \tag{4-107}$$

Eqs. 4-105 and 4-106 determine $\sigma_{ij}^{(1)}$, thus also $\sigma_{ij}^{(2)}$. If there is no interface but rather a cell consisting of mixtures, then the total pressure is related to the partial pressure by

$$\left.\begin{aligned} p_{ij} = \sum_{\ell}^{2} \rho_{ij}^{(\ell)} &= f^{(1)}\left(\rho_{ij}^{(1)}, e_{ij}^{(1)}\right) \\ &+ f^{(2)}\left(\rho_{ij}^{(2)}, e_{ij}^{(2)}\right) \end{aligned}\right\} \tag{4-108}$$

Eq. 4-108 may be sufficiently accurate even if the equations of state are complicated, but it is "strictly valid if pressure is proportional to the density for both materials".[38] Thus, in some cases, Eq. 4-108 may yield results far from reasonable and the following approximation to Eq. 4-106 was found useful on several occasions:

$$\left.\begin{aligned} p_{ij} = \frac{1}{2}\Big\{ & f^{(1)}\left[\rho_{ij}^{(1)}, e_{ij}^{(1)}\right] \\ & + f^{(2)}\left[\rho_{ij}^{(2)}, e_{ij}^{(2)}\right]\Big\} \end{aligned}\right\} \tag{4-109}$$

The assumption here is that the volume fraction of material 1 in cell ij is

$$\left.\begin{aligned} \sigma_{ij}^{(1)} \approx \sigma_{0ij} &= \frac{M_{ij}^{(1)}}{M_{ij}^{(1)} + R_M M_{ij}^{(2)}} \\ &= 1 - \sigma_{ij}^{(2)} \end{aligned}\right\} \tag{4-110}$$

(where subscript 0 means ambient condition and R_M is the ratio of the initial densities,* $\rho_0^{(2)} / \rho_0^{(1)}$) and that the compression of each of the two materials is in the same ratio as their initial compressions. It is easily seen from Eq. 4-110 that if $\rho_0^{(2)} = 0$, then $\sigma_{ij}^{(1)} \to 1$, and if $\rho_0^{(1)} = 0$, $\sigma_{ij}^{(1)} \to 0$.

*In Harlow's paper,[38] the dot material is material 1 and the x material is material 2; however, his R is wrong in the limiting case of $\rho_0^{(2)} \to 0$ and $\rho_0^{(1)} \to 0$.

4-5.2 TWO-DIMENSIONAL DEMONSTRATION PROBLEM

The computations in the PIC method are divided into three phases which are demonstrated by the following two-dimensional problem, the dynamics of ℓ materials confined to a two-dimensional rectangular box with rigid walls that allow perfect slippage.

4-5.2.1 PHASE 1 OF CALCULATION

In the first step of calculation, the particles are assumed to be "not moved" and the transport terms are neglected leading to the finite-difference equations

$$\left.\begin{aligned} \rho_{ij}\left(\frac{\partial u}{\partial t}\right)_{ij} \approx & -\frac{1}{\Delta x}\Big[P_{i+\frac{1}{2},j} \\ & - P_{i-\frac{1}{2},j}\Big] \end{aligned}\right\} \tag{4-111}$$

$$\left.\begin{aligned} \rho_{ij}\left(\frac{\partial v}{\partial t}\right)_{ij} \approx & -\frac{1}{\Delta y}\Big[P_{i,j+\frac{1}{2}} \\ & - P_{i,j-\frac{1}{2}}\Big] \end{aligned}\right\} \tag{4-112}$$

where $P_{ij} = p_{ij} + q_{ij}$. Based on experience, the effects of p_{ij} and q_{ij} are best treated separately. Cell boundary velocities are averaged from adjacent cells. The reason that p_{ij} and q_{ij} are treated in different fashion is that p_{ij} is basically a cell-centered quantity, while the fictitious viscous pressure q_{ij} depends on velocity differences, and is basically a cell-boundary quantity (in the PIC method). The transport terms are again neglected in the finite-difference energy equation

$$\rho_{ij}\left(\frac{\partial e_{ij}}{\partial t}\right) = \Big\{ - P_{ij}\left(\frac{u_{i+\frac{1}{2},j} - u_{i-\frac{1}{2},j}}{\Delta x} + \frac{v_{i,j+\frac{1}{2}} - v_{i,j-\frac{1}{2}}}{\Delta y}\right)$$

equation continued on page 4-26

$$- \frac{[(qu)_{i+\frac{1}{2},j} - (qu)_{i-\frac{1}{2},j}]}{\Delta x}$$

$$- \frac{[(qv)_{i,j+\frac{1}{2}} - (qv)_{i,j-\frac{1}{2}}]}{\Delta y}$$

$$+ u_{ij}\left(\frac{q_{i+\frac{1}{2},j} - q_{i-\frac{1}{2},j}}{\Delta x}\right)$$

$$+ v_{ij}\left(\frac{q_{i,j+\frac{1}{2}} - q_{i,j-\frac{1}{2}}}{\Delta y}\right)\Bigg\} \quad (4\text{-}113)$$

The tentative new velocities—the tilde indicates tentative new values—computed from those at the beginning of the calculation cycle are

$$\left.\begin{aligned} \tilde{u}_{ij} &\approx u_{ij} + (\Delta t)\left(\frac{\partial u}{\partial t}\right)_{ij} \\ &\approx u_{ij} - \frac{(\Delta y)(\Delta t)}{M_{ij}} \\ &\quad \times (P_{i+\frac{1}{2},j} - P_{i-\frac{1}{2}j}) \\ \tilde{v}_{ij} &\approx v_{ij} + (\Delta t)\left(\frac{\partial v}{\partial t}\right)_{ij} \\ &\approx v_{ij} - \frac{(\Delta x)(\Delta t)}{M_{ij}} \\ &\quad \times (P_{i,j+\frac{1}{2}} - P_{i,j-\frac{1}{2}}) \end{aligned}\right\} \quad (4\text{-}114)$$

To define the specific internal energy for a mixed cell, set

$$\rho_{ij}\left(\frac{\partial e_{ij}}{\partial t}\right) \rightarrow \frac{1}{(\Delta x)(\Delta y)}\left(\frac{\partial E_{ij}}{\partial t}\right) \quad (4\text{-}115)$$

where E_{ij} is the total internal energy of the cell.

For rigorous energy conservation, one may not use the similar approximation

$$\tilde{E}_{ij} = E_{ij} + \Delta t\left(\frac{\partial E_{ij}}{\partial t}\right) \quad (4\text{-}116)$$

(where the tilde means tentative new values) but, instead, with

$$\bar{u} = (u + \tilde{u})/2, \bar{v} = (v + \tilde{v})/2 \quad (4\text{-}117)$$

the proper form to use is

$$\begin{aligned} \frac{\Delta E_{ij}}{\Delta t} = &- p_{ij}[\Delta y(\bar{u}_{i+\frac{1}{2},j} - \bar{u}_{i-\frac{1}{2},j}) \\ &+ \Delta x(\bar{v}_{i,j+\frac{1}{2}} - \bar{v}_{i,j-\frac{1}{2}})]. \\ &- \Delta y[(q\bar{u})_{i+\frac{1}{2},j} - (q\bar{u})_{i-\frac{1}{2},j} \\ &- \bar{u}_{ij}(q_{i+\frac{1}{2},j} - q_{i-\frac{1}{2},j})] \\ &- \Delta x[(q\bar{v})_{i,j+\frac{1}{2}} - (q\bar{v})_{i,j-\frac{1}{2}} \\ &- v_{i,j}(q_{i,j+\frac{1}{2}} - q_{i,j-\frac{1}{2}})] \end{aligned} \quad (4\text{-}118)$$

The total energy of the cell is given by

$$H_{ij} = E_{ij} + M_{ij}\left(u_{ij}^2 + v_{ij}^2\right)/2 \quad (4\text{-}119)$$

For an unmixed cell of ℓth material only,

$$\tilde{e}_{ij}^{(\ell)} \approx e_{ij}^{(\ell)} + \frac{\Delta E_{ij}^{(\ell)}}{M_{ij}} \quad (4\text{-}120)$$

If the cell is mixed, then at least three possible procedures for distributing energy changes to the general materials may be used.

(1) The materials could be treated as though each had been compressed or expanded adiabatically through the same pressure change.

(2) Each could be given the same change in total internal energy.

(3) Each could be given the same change in specific internal energy.

The first and second were proven to be satisfactory in several trials, while the third inhibited the flow of energy across an interface in a test problem.

4-5.2.2 PHASE 2 OF CALCULATION (THE TRANSPORT OF MATERIAL)

First, there is a calculation of cell-wise energies and momenta from quantities obtained in Phase 1 through the equations

$$\widetilde{H}^{(\ell)} = M^{(\ell)} \left\{ \widetilde{E}^{(\ell)} + \tfrac{1}{2} \left[(\tilde{u}^{(\ell)})^2 + (\tilde{v}^{(\ell)})^2 \right] \right\}, \quad \ell = 1,2 \tag{4-121}$$

$$\widetilde{X} = \sum_{\ell} M^{(\ell)} \tilde{u} \tag{4-122}$$

$$\widetilde{Y} = \sum_{\ell} M^{(\ell)} \tilde{v} \tag{4-123}$$

Next, the particles are moved, the coordinates of each mass point become

$$\left.\begin{aligned} x' &= x + u_{eff}\,\Delta t \\ y' &= y + v_{eff}\,\Delta t \end{aligned}\right\} \tag{4-124}$$

In this step, for better accuracy, the u_{eff}, v_{eff} are calculated by a process called "velocity weighting" which is much more time-consuming than just using the cell value of $\tilde{u}$ and $\tilde{v}$, but this increase in accuracy could not be achieved by increasing the mesh fineness, which would consume equal machine time.

Finally, the final velocities for the cycle are computed from the equations

$$u' = \frac{x'}{\sum_{\ell} M^{(\ell)}}, \quad v' = \frac{y'}{\sum_{\ell} M^{(\ell)}} \tag{4-125}$$

and from these the final specific energies for the cycle are computed from the equation

$$\left.\begin{aligned} e'_E &= \frac{H'^{(\ell)}}{M'^{(\ell)}} - \frac{1}{2}\left[(u')^2 + (v')^2\right], \\ \ell &= 1,2, \end{aligned}\right\} \tag{4-126}$$

4-5.2.3 PHASE 3 OF CALCULATION (FUNCTIONALS OF MOTION)

To allow immediate entry into Phase 1 of the next cycle, various functionals for each material – such as the total kinetic energy and internal energy, the components of total momentum, positions of centers of mass, entropy, and numerous other quantities – are computed. In some cases, total boundary fluxes may be used as a check on the changes of these quantities. For rigid walls the total energy should be rigorously conserved within bounds of round-off-error. Likewise, some of the boundary forces can be used to check changes in momentum components. Such checks were found valuable to indicate machine or coding error.

4-5.3 OTHER BOUNDARY CONDITIONS

For other boundary conditions, besides those of the example of par. 4-5.2, the momentum of the system can easily be shown to be conserved. Some slight manipulation is required to show that the energy equation is also conservative. The flux of physical quantities across a boundary of a rectangular cell is illustrated for the specific case of the energy flux

$$(\text{energy flow})_{i+\frac{1}{2},j} = \frac{1}{2}\left(p_{i+1,j}\,\bar{u}_{ij} + p_{ij}\,\bar{u}_{1+i,j}\right) + (q\bar{u})_{i+\frac{1}{2},j} \tag{4-127}$$

If the boundary is adjacent to an empty cell say, $i + 1$, then the properties of cell $i + 1$ used in computation of the properties of cell i are determined by vanishing of energy flux, which is attained by setting

$$\left.\begin{aligned} p_{ij+1} &= -p_{i,j} \\ \bar{u}_{i+1,j} &= -\bar{u}_{i,j} \\ \bar{q}_{i+\frac{1}{2},j} &= 0 \end{aligned}\right\} \qquad (4\text{-}128)$$

If the boundary had been a perfectly rigid wall, then the fictitious cell, $i + 1$, beyond the wall, must be assigned the following properties in the computations for cell i:

$$\left.\begin{aligned} p_{i,j+1} &= p_{i,j} \\ \bar{u}_{i+1,j} &= -u_{i,j} \\ \bar{u}_{i+\frac{1}{2},j} &= 0 \end{aligned}\right\} \qquad (4\text{-}129)$$

These properties are assigned such that the interpolated velocity at the wall between i and $i + 1$ is zero. Calculation of the boundary value of $q_{i+\frac{1}{2},j}$ uses appropriate reflected quantities.

In the velocity weighting procedure, a rectangle of cell size is imagined to be located about each particle, the particle being at the center. Such a rectangle then overlaps four adjacent cells and the effective velocity for moving the particle is taken as the weighted average of the four cell-wise tilde velocities, the weighting being proportional to the overlap areas. If the surrounding rectangle lies partly in an empty cell, then that cell may be assumed to have the same velocity as does the cell with the particle. If it lies partly outside the walls of the computation region, assumed rigid, then the fictitious outside cells may be given either reflected velocity or the same velocity as in the adjacent interior cells. In the former case, (partly in an open cell) no particle will be lost but may lead to "boundary catastrophe" discussed by Harlow, et al.[35]. In the latter case (partly outside), it is necessary to reflect the particle back in; the particle then carries a change in momentum as though entering from a cell with reflected velocity, and the boundary catastrophe is avoided.

If the particle remains in the same cell from which it started, there is no modification to the cell-wise quantities. Some of the particles may end up in new cells; then the mass, momentum, and energy of the particles should be subtracted from the original cell and added into those of the new cells where they are now located.

For curved obstacles oblique to the cells, partial cells must be employed as in the FLIC method; similar difficulties may be encountered and treated with locally smaller time steps and more cycles, etc.

Several examples are given even though they do not directly relate to air blast. The result of a shock in nitrogen passing around a 90-deg corner was given by Harlow, et al.*[35] and is reproduced in Fig. 4-11 for t = 12.593**, M_s = 1.008; and in Fig. 4-12 for t = 6.329, M_s = 1.588. The rarefaction front in both cases is not in too good agreement with experiment, thus suggesting that refinements may be required for accurate prediction of flow behind the shock. Some discrepancy in the shock front is also seen, which would possibly worsen as time increases. As will be commented in the FLIC method, Phase 1 of the PIC method may also need improvement.

Harlow states that the strong advantage of the PIC method is its applicability to flow with large distortions or in which voids may open or close. Its disadvantages are:

1. Lack of rotational and translational invariance; (not a serious disadvantage in most cases)

2. Lack of resolution of the fine detail of a large system

3. A relatively great consumption of computer storage space (both the Lagrangian and the Eulerian meshes require storage) which also leads to somewhat greater computation time. Computation must be made for both

*Harlow, et al.[35] use first and second ordinary viscosity coefficient while Harlow[38], uses

$$q_{ij} = \left(\tfrac{1}{4}\rho\,|u_j|\,\Delta x_j\right)\frac{\partial u_i}{\partial x_j}$$

**The unit was not given, nor is t nondimensionalized; perhaps it is in seconds.

Solid and long-dashed lines represent, respectively, the computed and observed positions of shock and rarefaction fronts. Short-dashed line is a theoretical Prandtl-Meyer streamline.

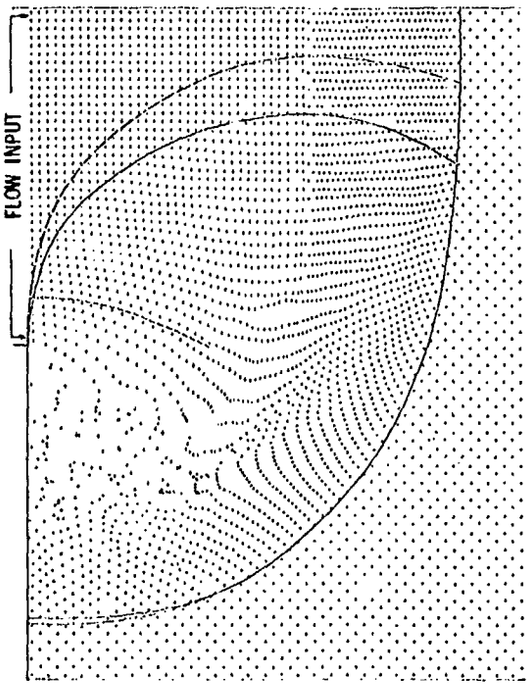


Figure 4-11. Configuration of Mass Points at Time t = 12.593 for the Calculation for Nitrogen With M_s = 1.008

meshes, and therefore the computing is nearly double that required for a Lagrangian or Eulerian mesh alone.

4. Inappropriateness for subsonic flow (this disadvantage, shared with other methods of solution for compressible flow problems, arises from the necessity of having sound velocity travel less than a cell width in one time cycle).

4-6 FLUID-IN-CELL (FLIC) METHOD

The FLIC method[33] is an improvement on the particle-in-cell (PIC) method described in par. 4-5 which was a combined Eulerian-Lagrangian scheme *for a single fluid.* The PIC method utilized both an Eulerian and a Lagrangian scheme, since the Lagrangian scheme by itself would have lost accuracy when fluid distortion was large. The PIC method used fluid particles to transport mass, momentum, and energy through a Eulerian mesh of cells. While the use of these particles facilitated the calculation of multi-fluid problems, it also resulted in nonphysical fluctuations of the fluid quantities. The PIC method placed great demands on computer memory capacity and calculation time due to the use of the dual coordinate system. The FLIC method uses concepts similar to those of the PIC method but eliminates the computation of the motion of particles, and it is a "Eulerian differencing method". The scheme to be described is suitable for problems with symmetry about an axis or a plane.

4-6.1 COMPUTING MESH

Gentry, et al.[33] use a mesh composed of uniform rectangles to demonstrate the FLIC method. To be more precise, for the plane case and the axisymmetric case, these ele-

Solid and long-dashed lines represent, respectively, the computed and observed positions of shock and rarefaction fronts. Short-dashed line is a theoretical Prandtl-Meyer streamline.

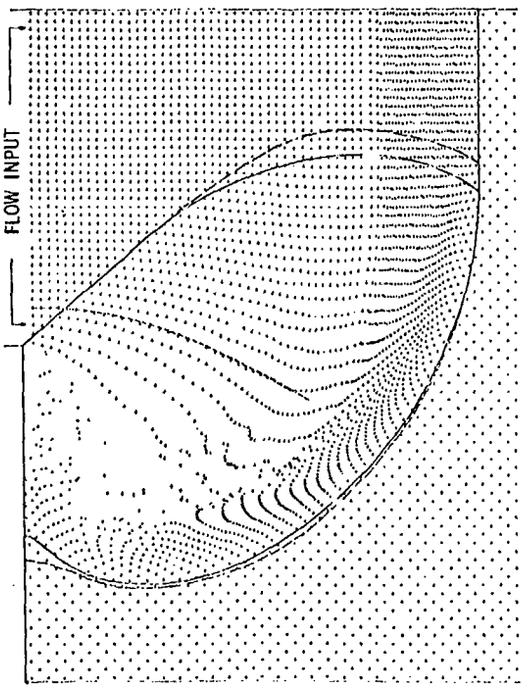


Figure 4-12. Configuration of Mass Points at Time t = 6.329 for the Calculation for Nitrogen With M_s = 1.588

ments are rectangles and toruses, respectively. The latter is to be discussed.

If cylindrical coordinates r, θ, z are used, the cell, ik – which has the center $(i + \frac{1}{2}, k + \frac{1}{2})$, r varying from $k\,(\Delta z)$ to $(k + 1)\,(\Delta z)$, and z varying from $i\,(\Delta r)$ to $(i + 1)\,(\Delta r)$–has the properties that

$V_i \approx 2\pi\,(i + \frac{1}{2})\,(\Delta r)^2\,(\Delta z)$, volume of the ikth cell

$S_i^z \approx 2\pi\,(i + \frac{1}{2})\,(\Delta r)^2$, area of contact of cell ik and cell i, $k + 1$, k in z-direction

$S_{i+\frac{1}{2}}^r \approx 2\pi\,(i + 1)\,(\Delta r)\,(\Delta z)$, area of contact of cell ik and cell $i + 1$, k in r-direction

The basic state variables are density ρ; velocities u and w along r, z, respectively; and specific internal energy e_E (or $e_{i,k}$). Pressure and sound speed c are determined through the equation of state which is, for a polytropic gas,

$$p = (\gamma - 1)\,\rho\,e_E \qquad (4\text{-}130)$$

where γ, the ratio of specific heats, can be a function of ρ and e_E. Many other forms of equation of state can be used with equal ease.

4-6.2 THE DIFFERENCE EQUATIONS

The initial values of ρ, u, w, and e_E are assigned to each cell at the beginning of the problem. The value of each cell quantity is advanced by using a two-step scheme per cycle. First, intermediate values of u, w, e_E are calculated with the effect of pressure gradient. Second, transport effects are calculated.

By using the intermediate values of physical quantities calculated in the donor cells, the transport of mass, momentum, and energy from a donor cell can be calculated.

One can compute either the specific internal energy e_E or the total energy h_T. Although the latter is generally chosen for a Eulerian scheme, because it lends itself more readily to the energy conservation requirements, the FLIC method calculates the internal energy directly, using the equation

$$\frac{\partial e_E}{\partial t} + \underset{\rightarrow}{u} \cdot \nabla e_E = - p \nabla \cdot \underset{\rightarrow}{u} \qquad (4\text{-}131)$$

Energy conservation is achieved by the two step per cycle scheme and with proper choice of time entering the difference Eq. 4-131.

4-6.2.1 STEP 1

Let subscript i,k be used for quantities in cell i, k. Then $p_{i,k}^n$ is first calculated for each cell using the equation of state Eq. 130 and $p_{i,k}^n, e_{i,k}^n$. With

$$\left.\begin{aligned} p_{i,k+\frac{1}{2}}^n &= \frac{1}{2}\left(p_{i,k}^n + p_{i,k+1}^n\right) \\ \bar{u}_{i,k} &= \frac{1}{2}\left(u_{i,k} + \tilde{u}_{i,k}\right) \end{aligned}\right\} \qquad (4\text{-}132)$$

one then calculates

$$\tilde{w}_{i,k} = w_{i,k}^n - \frac{(\Delta t)\,\epsilon_{i,k}^z}{\rho_{i,k}^n\,(\Delta z)} \times \left\{(p+q)_{i,k+\frac{1}{2}}^n - (p+q)_{i,k-\frac{1}{2}}^n\right\}$$

$$\tilde{u}_{i,k} = \left[u_{i,k}^n - \frac{(\Delta t)\,\epsilon_{i,k}^r}{\rho_{i,k}^n}\right.$$

(Continued on page 4-31)

$$\times \left\{ \frac{1}{2V_i} \left[S^r_{i+\frac{1}{2}} \left(p^n_{i+1,k} - p^n_{i,k} \right) + S^r_{i-\frac{1}{2}} \left(p^n_{i,k} - p^n_{i-1,k} \right) \right] + \frac{1}{\Delta r} \left(q^n_{i+\frac{1}{2},k} - q^n_{i-\frac{1}{2},k} \right) \right\} \quad (4\text{-}133)$$

$$\tilde{e}_{i,k} = e^n_{i,k} - \frac{(\Delta t)}{\rho^n_{i,k} V_i} \left(\epsilon^r_{i,k} \left[p^n_{i,k} \left(S^r_{i+\frac{1}{2}} \times \bar{u}^n_{i,k} - S^r_{i-\frac{1}{2}} \bar{u}^n_{i,k} \right) + \frac{1}{2} q^n_{i+\frac{1}{2},k} \left(S^r_{i+1} \bar{u}^n_{i+1,k} + S^r_i \bar{u}^n_{i,k} \right) - \frac{1}{2} q^n_{i-\frac{1}{2},k} \left(S^r_i \bar{u}^n_{i,k} + S^r_{i-1} \bar{u}_{i-1,k} \right) - \bar{u}^n_{i,k} S^r_i \left(q^n_{i+\frac{1}{2},k} - q^n_{i-\frac{1}{2},k} \right) \right] + \epsilon^z_{i,k} \left\{ S^z_i \left[\bar{w}^n_{i,k+\frac{1}{2}} \left(p^n_{i,k} + q^n_{i,k+\frac{1}{2}} \right) - \bar{w}^n_{i,k-\frac{1}{2}} \left(p^n_{i,k} + q^n_{i,k-\frac{1}{2}} \right) \right] - \bar{w}_{i,k} S^z_i \left(q^n_{i,k+\frac{1}{2}} - q^n_{i,k-\frac{1}{2}} \right) \right\} \right)$$

where $\epsilon^r_{i,k}$ and $\epsilon^z_{i,k}$ are unity for a full cell. For partial cells, these quantities will be defined later in this paragraph.

This step is a first approximation, neglecting convective terms in the Eulerian equations, to get first estimates of u, w, e_E. In the next step the effect of convective terms is calculated by taking mass, momentum, and energy transport into the cell into consideration. A fictitious viscosity term is introduced in Eqs. 4-132 "to enhance the stability properties of the difference equations in regions where the fluid velocity is small compared to the local sound speed",[33] and this term is given by

$$q^n_{i,k+\frac{1}{2}} = \epsilon_B B_G c^n_{i,k+\frac{1}{2}} \rho^n_{i,k+\frac{1}{2}} \times \left(w^n_{i,k} - w^n_{i,k+1} \right) \quad (4\text{-}134)$$

if

$$K_G (u^2 + w^2)^n_{i,k+\frac{1}{2}} < (c^2)^n_{i,k+\frac{1}{2}}$$

$$w^n_{i,k} > w^n_{i,k+1}, \text{ and}$$

$$q^n_{i,k+\frac{1}{2}} = 0$$

Otherwise

$$q^n_{i+\frac{1}{2},k} = \epsilon_B B_G c^n_{i+\frac{1}{2},k} \rho^n_{i+\frac{1}{2},k} \times \left(u^n_{i,k} - u^n_{i+1,k} \right) \quad (4\text{-}135)$$

if

$$K_G (u^2 + w^2)_{i+\frac{1}{2},k} < (c^2)^n_{i+\frac{1}{2},k}$$

$$u^n_{i,k} > u^n_{i+1,k}, \text{ and}$$

$$q_{i+\frac{1}{2},k} = 0,$$

where ϵ_B is fraction of cell filled, and is unity for a full cell, and c is the local speed of sound. K_G is a constant determining the maximum value of the Mach number at a cell interface for which the fictitious viscosity will be applied. B_G is also a constant which determines the magnitude of the viscous pressure term, which should be large enough to insure stability but small enough to avoid obscuring important details of the solution. Generally, B_G need not exceed a value of 0.5.

4-6.2.2 STEP 2

The transport effects are calculated in this step. The mass flows from cell to cell are

taken as being directly proportional to the density of the donor cell, which precludes the possibility of developing negative density in a cell, and which results in good stability properties for the far subsonic regions of the mesh. This is known as "donor cell, mass flow differencing" method.

Let $\Delta M^n_{i,k+\frac{1}{2}}$ be the mass flowing across the area S^z_i during time Δt, and $\Delta M^n_{i+\frac{1}{2},k}$ be that across the area $S^r_{i+\frac{1}{2}}$, respectively, then the mass flow from the "right" side* of the cell i,k is given by

$$\Delta M^n_{i,k+\frac{1}{2}} = \alpha^z_{i,k+\frac{1}{2}} S^z_i \rho^n_{i,k} \bar{w}^n_{i,k+\frac{1}{2}} \Delta t,$$

$$\text{if } \bar{w}^n_{i,k+\frac{1}{2}} > 0 \text{ (flow out)}$$

$$= \alpha^z_{i,k+\frac{1}{2}} S^z_i \rho^n_{i,k+1} \bar{w}_{i,k+\frac{1}{2}} \Delta t,$$

$$\text{if } \bar{w}_{i,k+\frac{1}{2}} < 0 \text{ (flow in)} \qquad (4\text{-}136)$$

and similarly, the mass flow for the upper side of cell i,k is given by

$$\Delta M^n_{i+\frac{1}{2},k} = \alpha^r_{i+\frac{1}{2},k} S^r_{i+\frac{1}{2}} \rho^n_{i,k} \tilde{u}_{i+\frac{1}{2},k} \Delta t,$$

$$\text{if } \tilde{u}_{i+\frac{1}{2},k} > 0 \text{ (flow out)}$$

$$= \alpha^r_{i+\frac{1}{2},k} S^r_{i+\frac{1}{2}} \rho^n_{i+1,k} \tilde{u}_{i+\frac{1}{2},k} \Delta t,$$

$$\text{if } \tilde{u}_{i+\frac{1}{2},k} < 0 \text{ (flow in)} \qquad (4\text{-}137)$$

where $\alpha^z_{k+\frac{1}{2}}$ and $\alpha^r_{i+\frac{1}{2}}$ are unity for a full cell. The new value of $\rho_{i,k}$ can be obtained by consideration of the conservation of mass

$$\rho^{n+1}_{i,k} = \rho^n_{i,k} + \frac{1}{\tau_{i,k} V_i} (\Delta M^n_{i-\frac{1}{2},k} + \Delta M^n_{i,k-\frac{1}{2}} - \Delta M^n_{i+\frac{1}{2},k} - \Delta M^n_{i,k+\frac{1}{2}}) \qquad (4\text{-}138)$$

*z-axis is in the "horizontal" direction pointing "to the right".

where $\tau_{i,k}$ is unity for a full cell.

To determine the momentum and energy transport, if j = 1,2,3,4 be the left, lower, right, and upper boundaries of the ikth cell, respectively, with an axis z pointing to the right and axis r pointing upward, and if a $T_{i,k}(j)$ is defined such that

$$\left.\begin{aligned} T_{i,k}(j) &= 1, \text{ if fluid flow into cell } i,k \text{ across side } j \\ &= 0, \text{ if fluid flows out of cell } i,k \text{ across side } j \end{aligned}\right\} \qquad (4\text{-}139)$$

then the transport equations are given by

$$F^{n+1}_{i,k} \frac{1}{\rho^{n+1}_{i,k} \tau_{i,k} V_i} \Big(T_{i,k(1)} \bar{F}^n_{i,k-1} \Delta M^n_{i,k-\frac{1}{2}}$$

$$+ T_{i,k(2)} \bar{F}^n_{i-1,k} \Delta M^n_{i-\frac{1}{2},k}$$

$$- T_{i,k(3)} \bar{F}^n_{i,k+1} \Delta M_{i,k+\frac{1}{2}}$$

$$- T_{i,k(4)} \tilde{F}^n_{i+1,k} \Delta M_{i+\frac{1}{2},k}$$

$$+ \tilde{F}^n_{i,k} \Big\{ \rho^n_{i,k} \tau_{i,k} V_i$$

$$+ [1 - T_{i,k(1)}] \Delta M^n_{i,k-\frac{1}{2}}$$

$$+ [1 - T_{i,k(2)}] \Delta M^n_{i-\frac{1}{2},k}$$

$$- [1 - T_{i,k(3)}] \Delta M^n_{i,k+\frac{1}{2}}$$

$$- [1 - T_{i,k(4)}] \Delta M^n_{i+\frac{1}{2},i} \qquad (4\text{-}140)^*$$

where $F_{i,k}$ is $w_{i,k}$, $u_{i,k}$, $h_{i,k}$, respectively, and

$$\left.\begin{aligned} e^{n+1}_{i,k} &= h^{n+1}_{i,k} \\ &\quad - \tfrac{1}{2}\left(w^2_{i,k} + u^2_{i,k}\right) \end{aligned}\right\} \qquad (4\text{-}141)$$

*The introduction of T_{ij} is to conform with the "donor cell mass flow differencing" idea.

These two steps complete a cycle.

Since the first step neglects the convective term, it is not necessarily a better approximation; thus, it appears that improvement of the formula may be needed to yield a more reliable first approximation.

4-6.2.3 BOUNDARY CONDITIONS AND STABILITY

When a flow is past a solid obstacle, the normal velocity, flux of momentum, and flux of energy are obviously not through it. A general curved boundary representing such a solid obstacle is approximated as a sequence of straight cutting across the boundaries of cells adjacent to the obstacle which generates partial cells. Each partial cell is characterized by five geometric quantities - $\tau_{i,k}$, $\alpha^r_{i,k-\frac{1}{2}}$, $\alpha^r_{k+\frac{1}{2}}$, $\alpha^z_{i-\frac{1}{2},k}$, $\alpha^z_{i+\frac{1}{2},k}$ - which represent the fraction of volume V_j (in the case of $\tau_{i,k}$) and the fraction of area between cells (i,k) and $(i,k-1)$, between cells (i,k) and $(i-1,k)$, and between cells (i,k) and $(i+1,k)$ inside the fluid domain. Fictitious image cells are created to obtain the reflective boundary condition. In the difference Eqs. 4-132, $\epsilon^r_{i,k} = \max(\alpha_{i+\frac{1}{2},k}, \alpha_{i-\frac{1}{2},k})/\tau_{i,k}$, $\epsilon^z_{i,k} = \max(\alpha_{i,k+\frac{1}{2}}, \alpha_{i,k-\frac{1}{2}})/\tau_{i,k}$, and $\epsilon_B = 2$. However, the use of partial cells can cause difficulty in cases where they are much smaller than the full-sized cells, because the maximum value of Δt is limited by minimum cell dimension for stability and accuracy. Consequently, the use of these cells should be avoided whenever possible; but, if they should prove to be essential, then the time limitation may be overcome by using more computing cycles per unit time for the partial cells than for the rest of the mesh.

A one dimensional stability criterion for the difference scheme is[33]

$$\frac{c\,\Delta t}{\Delta x} < \lambda_{min} \qquad (4\text{-}142)$$

where

$$\lambda_{min} = \min\left[B_G > 1, -\gamma B_G + [\gamma^2 B_G + 4\gamma]^{\frac{1}{2}}, \gamma B_G/(\gamma+1)\right]$$

This difference scheme is therefore unstable without fictitious viscosity, i.e., ($B_G = 0$); however, in certain types of two-dimensional problems a stable solution can be obtained without artificial viscosity.

Several examples of the FLIC method are given by Gentry, et al.[33]. One is the shock-on-shock problem. The measured and calculated shock positions at the time of first reflection for $M_1 = M_s = 3.15$ are shown in Fig. 4-13. M_1 is the initial Mach number of the incoming, head-on blast wave. The dark lines are taken from photographic data obtained by Merritt and Aronson[34], and the grey lines are "isopycnic" lines plotted from the corresponding numerical solution. Other examples include the diffraction of a shock by a z-shaped tunnel and the diffraction of a plane shock by a cone.

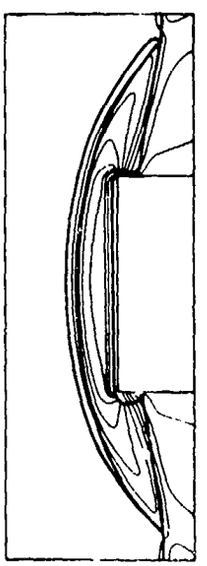


Figure 4-13. Measured and Calculated Shock Positions at the Time of First Shock Reflection $M_1 = M_S = 3.15$

4-7 COMPARISONS OF VARIOUS METHODS

A comparison of methods for calculating time-dependent fluid dynamics with artificial viscosity is given in Table 4-4 (Daly[28]). The FLIC method was not listed in this table. It has the advantages of the PIC method but with much less storage requirement; however, it is devised for a single fluid and may also require some modification when the shock or fluid moves into a void. As discussed in related paragraphs, the FLIC, PIC, and PAF methods are not all yet perfected to yield reliable results over the whole field.

The method of characteristics is most general in the methods with sharp discontinuities; however, it appears more cumbersome than the numerical methods for extended application to problems with more than one

TABLE 4-4

A COMPARISON OF METHODS FOR CALCULATING TIME DEPENDENT FLUID DYNAMICS

Methods	Some Advantages	Some Disadvantages
Pure Lagrangian (L)	1. Follows material interfaces. 2. Allows fine resolution areas to move with fluid. 3. Is translationally, rotationally invariant. 4. Requires mesh of cells only where needed.	1. Tends to break down with large distortions. 2. Does not allow internal slip except along *a priori* known lines. 3. Does not allow for formation or closure of arbitrary internal cavities.
Pure Eulerian (E)	1. Calculates large distortions well. 2. Allows spontaneous generation of internal slip lines.	1. Produces diffusion of material interfaces. 2. Requires mesh of cells at all points where fluid will be, whether or not needed at some instant. 3. Does not allow for localized resolution. 4. Is not translationally or rotationally invariant.
PIC	L-1,[a] E-1, E-2-plus handle cavitation easily.	E-2, E-3, E-4-plus require exceptionally large amount of storage.
PAF	L-1, L-2, L-3, L-4, E-2-plus handle cavitation easily.	None of above, but may need bigger and faster machine, since calculations are somewhat time consuming and require a large amount of storage.

[a] L and E, respectively, refer to the Lagrangian and Eulerian topics described in the table.

space dimension. For complex situations such as strong Mach reflection, the usefulness and accuracy of all these methods remain to be shown. However, if one shares the optimism of von Neumann and Richtmyer[3] that the method of artificial viscosity would be able to treat "all shocks correctly and automatically whenever and wherever they may arise", this approach seems to be more powerful than the method of characteristics. The statement of von Neumann and Richtmyer could be true if appropriate mesh and artificial viscosity constants were used and if needed refinements and/or modifications are introduced. Nevertheless, the method of artificial viscosity would be unable to obtain more refined information such as the effect of true viscosity and energy dissipation.

REFERENCES

1. J. G. Kirkwood and S. R. Brinkley, Jr., *Theory of the Propagation of Shock Waves from Explosive Sources in Air and Water*, OSRD Report 4814, 1945.

2. S. R. Brinkley, Jr., and J. G. Kirkwood, "Theory of the Propagation of Shock Waves", *Phys. Rev.*, 71, p. 606 (1947).

3. J. von Neumann and R. D. Richtmyer, "A Method for the Numerical Calculation of Hydrodynamic Shocks", *J. Appl. Phys.*, 21, pp. 223-237 (1950).

4. R. E. Shear and E. Q. Wright, *Calculated Peak Pressure Distance Curves for Pentolite and TNT*, BRL MR-1423, Ballistic Research Lab., Aberdeen Proving Ground, Md., August 1962.

5. R. H. Cole, *Underwater Explosions*, Dover Publications, Inc., New York, 1965.

6. R. E. Shear, *Detonation Properties of Pentolite*, BRL Rept. No. 1159, 1961.

7. H. L. Brode, *A Calculation of the Blast Wave from a Spherical Charge of TNT*, The Rand Corp., RM-1965, August 1957, AD 144 302.

8. S. A. Gränstrom, "Loading Characteristics of Air Blasts from Detonating Charges", *Acta Polytechnica*, 196 (1956). Also, Trans. of the Royal Institute of Technology, Stockholm, Sweden, No. 100, 1956.

9. P. C. Chou and R. R. Karpp, *Solution of the Blast Wave by the Method of Characteristics*, DIT Rept. No. 125-7, Contract No. DA-36-034-ORD-3672RD, Drexel Inst. of Tech., September 1965.

10. S. L. Huang and P. C. Chou, *Solution of Blast Waves by a Constant Time Scheme in the Method of Characteristics*, Rept. No. 125-9, Contract No. DA-18001-AMC876(X), Drexel Inst. of Tech., August 1966.

11. P. C. Chou, R. R. Karpp, and S. L. Huang, "Numerical Calculation of Blast Waves by the Method of Characteristics", AIAA Journal, 5, 4, pp. 618-623 (April 1967).

12. A. Ralson and H. S. Wilf, *Mathematical Methods for Digital Computers*, John Wiley & Sons, Inc., New York, 1960.

13. D. R. Hartree, *Some Practical Methods of Using Method of Characteristics in the Calculation of Non-Steady Compressible Flows*, Los Alamos Report LA-HU-1, 1952.

14. J. J. Unwin, *The Production of Wave by the Sudden Release of a Spherical Distribution of Compressed Air in the Atmosphere, Proc. Roy. Soc.*, A 178, 1941.

15. P. Fox and A. Ralston, "On the Solution of Equations for Spherical Waves of Finite Amplitude", J. Math. and Phys., 36, 4 (Jan. 1958).

16. G. Rudinger, *Wave Diagrams for Non-Steady Flow in Ducts*, D. Van Nostrand Co., Inc., 1955.

17. J. A. McFadden, "Initial Behavior of a Spherical Blast", *J. Appl. Phys.* (1952).

18. H. L. Brode, "Numerical Solution of Spherical Blast Waves", J. Appl. Phys., **26**, 6 (June 1955).

19. H. L. Brode, *Point Source Explosion in Air*, The Rand Corp., RM-1824-AEC, December 3, 1956.

20. H. L. Brode, *Theoretical Solutions of Spherical Shock Tube Blast*, RM-1974, The Rand Corp., September 1957, AD-206 491.

21. W. A. Walker, D. Piacesi, and H. M. Sternberg, *A Fortran Program for the Numerical Solution of Explosion and Shock Hydro-Dynamic Problems in One-Space Dimensions*, U.S. Naval Ordnance Lab., NOLTR 64-114.

22. M. Wilkins et al., *A Computer Program for Calculating One-Dimensional Hydrodynamic Flow - KO Code*, Univ. of Calif. Radiation Lab., UCRL 6919, July 1962.

23. D. Lehto and M. Lutzky, *One-Dimensional Hydrodynamic Code for Nuclear Explosion Calculations*, NOLTR 62-168, DASA-1518, U.S. Naval Ordnance Lab., White Oak, Silver Spring, Md., March 1965.

24. M. Lutzky, *The Flow Field Behind a Spherical Detonation in TNT Using Landau-Stanyukovich Equation of State for Detonation Products*, NOLTR-64-40, U. S. Naval Ordnance Lab., White Oak, Md., December 1964.

25. L. D. Landau and K. P. Stanyukovich, "On the Study of Detonation in Condensed Explosive", *Doklady Akad., Nauk SSSR*, 46, 399 (1945).

26. Ia. B. Zeldovich and A. S. Kompaneets, *Theory of Detonation*, Academic Press, Chapter 14, 1960.

27. F. A. Williams, *Combustion Theory*, Addison-Wesley Publishing Co., Inc., 1965.

28. B. J. Daly, F. H. Harlow, J. E. Welch, et al., *Numerical Fluid Dynamics Using the Particle-and-Force Method*, Los Alamos Sci. Lab., LA 3144, September 1964.

29. F. H. Harlow and B. D. Meixner, *The Particle-and-Force Computing Method in Fluid Dynamics*, Los Alamos Scientific Lab., Report LAMS-2567, June 1961.

30. F. H. Harlow, *Theory of Correspondence Between Fluid Dynamics and Particle and Force Models*, Los Alamos Scientific Lab., Report LA 2806, November 1962.

31. W. Griffith, "Shock Tube Studies of Transonic Flow Over Wedge Profiles", J. Aero. Sci., **19**, 249 (1949).

32. B. W. Marschner, "An Investigation of Detached Shock Waves", M. S. Thesis, California Inst. of Tech., 1948.

33. R. A. Gentry, R. E. Martin, and B. J. Daly, "An Eulerian Differencing Method for Unsteady Compressible Flow Problems", *J. of Computational Physics*, 1, pp. 87-118 (1966).

34. D. L. Merritt and P. M. Aronson, "Study of Blast-Bow Wave Intersections in a Wind Tunnel", AIAA Paper No. 65-5 presented at the AIAA Second Aerospace Science Meeting, New York, January 1965. (Also, private communication with Gentry, et al.),

35. F. H. Harlow, et al., *Two-Dimensional Hydrodynamic Calculations*, LA-2301, Los Alamos Scientific Lab., Los Alamos, New Mexico, September 1959.

36. F. H. Harlow, "Hydrodynamic Problems

Involving Large Fluid Distortion", J. Assn. Comp. Machinery 4,2 (April 1957).

37. B. J. Daly, *The Bounding of Instabilities of the PIC Difference Equations*, Rept. No. LA 2414, Appendix I, Los Alamos Scientific Lab., 1962.

38. F. H. Harlow, "The Particle-in-Cell Method for Numerical Solution of Problems in Fluid Dynamics", *Symposia in Appl. Math., Proc.*, Vol. XV, 1963.

CHAPTER 5

AIR BLAST EXPERIMENTATION

5-0 LIST OF SYMBOLS

d = horizontal distance from "ground zero" for charge burst above a surface

E = total energy in explosive charge

h = height of charge

H = height of gage

H_y = height of triple point

I_r = positive phase impulse of normally reflected blast wave

I_s = positive phase impulse of side-on blast wave

kT = yield of nuclear weapon, kilotons of TNT

p_0 = ambient pressure

P_r = normally reflected (face-on) peak overpressure

P_s = side-on peak overpressure

$\bar{P}_s$ = scaled peak side-on overpressure

Q = peak dynamic pressure

R = distance from center of blast source

S = parameter (Dewey) proportional to $(W/p_0)^{1/3}$

t = time

t_a = arrival time

T = positive phase duration

u = particle velocity

U = shock front velocity

W = mass of explosive

X = distance in charge radii

Y = scaled height of Mach stem

Z = scaled distance

ρ = specific gravity of explosive source (Stoner and Bleakney)

τ = volume of explosive source (Stoner and Bleakney)

5-1 GENERAL

Before one can perform air blast experiments, he must have an intimate knowledge of one or more techniques and/or systems for measuring various properties of the blast waves. As in all systems for measuring physical quantities, one cannot make good measurements with inferior equipment or equipment whose capabilities and limitations he does not understand. But, because some readers may be interested in results of blast experiments and not in the nuances of acquiring valid data, we will defer until later chapters our discussion of blast measurement hardware and give here the results of experiments by competent investigators. The reader is warned, however, that the figures in this chapter are not intended for use in calculating or predicting blast parameters, and grids are often deliberately omitted. Predictions should

instead be made from tables and graphs in Chapter 6.

5-2 UNITS AND DIMENSIONS FOR BLAST DATA

Blast data are reported by various investigators in a variety of different units and combinations of units, and dimensions are given in the English or metric system, and combinations of units, and dimensions are given in the English or metric system, and sometimes in a combination of these systems. We will not attempt in this chapter to convert reported data to a single system of measurement, but will instead present data in the most commonly used system in the U.S. and U.K. is the English system, and the most commonly used units are an unfortunate mixture of English units. For explosions of chemical sources, these units are:

Pressures, P_s, P_r, p_0, etc.: pounds force per square inch (psi or $lb_f/in.^2$)

Times, t_a, T, etc.: milliseconds (msec)

Impulses, I_s, I_r: pounds force times milliseconds per square inch (psi-msec or lb_f $msec/in.^2$)

Distances, R: feet

Velocities, U, u: feet per second

Blast energy, W: pounds mass of TNT or other explosive.

For nuclear explosives, similar units are usually used, with the exception that blast energy is usually given in units of "kilotons of TNT (kT)", and times are sometimes quoted in seconds. By "kilotons of TNT" one does *not* mean that the nuclear explosive source has a *mass* equal to the specified mass of TNT. Instead, he implies an *energy* released by the nuclear explosive which produces a blast wave which matches in intensities and durations, over some range of distances, the blast wave from the specified mass of TNT The use of these mixed units can sometimes lead to confusion, particularly if pounds *mass* of an explosive are assumed incorrectly to be pounds *force*. Such confusion can be eliminated by use of true energy units of force times length, rather than mass of an explosive which simply happens to be proportional to energy.

Most blast experimentalists are familiar with Hopkinson's scaling law of Chapter 3 (even though they may not know it by that name) and report their data in Hopkinson-scaled units. These scaled units will, therefore, appear often in this chapter. Some investigators simply state that their data are scaled to one pound (mass) of TNT, or one kiloton of nuclear yield, and do not enter the units associated with the Hopkinson scaling. We do not condone this practice—we merely report it.

5-3 "FREE-AIR" MEASUREMENTS

Many small-charge blast experiments have been conducted with the explosive charges and the blast transducers far enough from the nearest reflecting surface (usually the ground) that the entire time history of the blast wave can be recorded prior to arrival of any reflected waves. Such measurements are usually termed "free-air" measurements, and form much of the empirical data base for prediction of air blast parameters and for comparison with theory.

The original free air blast measurements were made by various groups in the U.S. and the U.K. during World War II. In the earliest work, the investigators failed to recognize that shape of the explosive charge could have a significant effect on the blast wave and that the geometry of the blast transducers could affect pressure by altering flow behind the shock front[1]. In spite of these failings, results of a number of experiments were averaged and are reported in Ref. 1 as smooth curves. These curves for peak overpressure and positive impulse from TNT are reproduced here as Figs. 5-1 and 5-2. No detailed data are given in Ref. 1, so the curves in Figs. 5-1 and 5-2 should be used only as indications of the

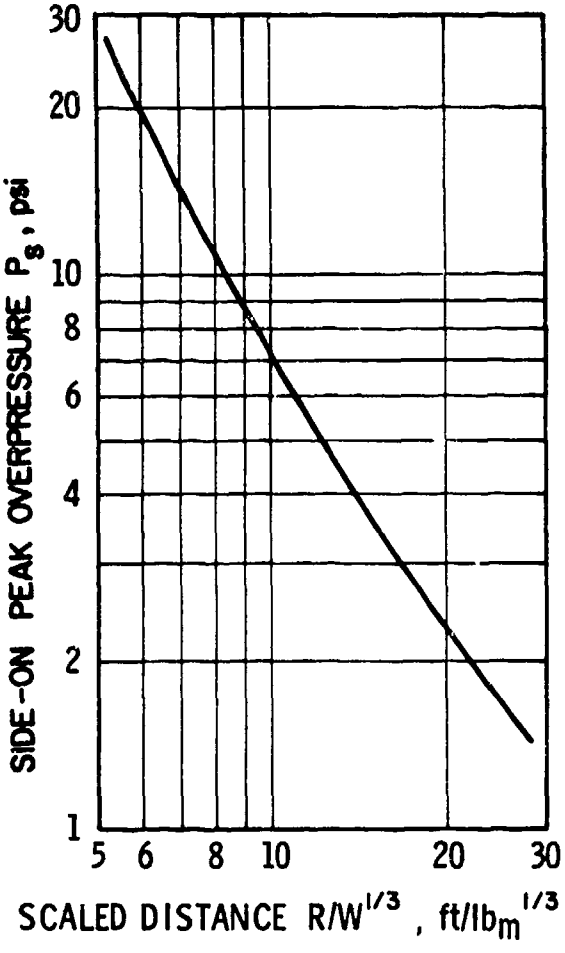


Figure 5-1. Logarithmic Plot of Free-Air Pressure vs Scaled Distance for Cast TNT[1]

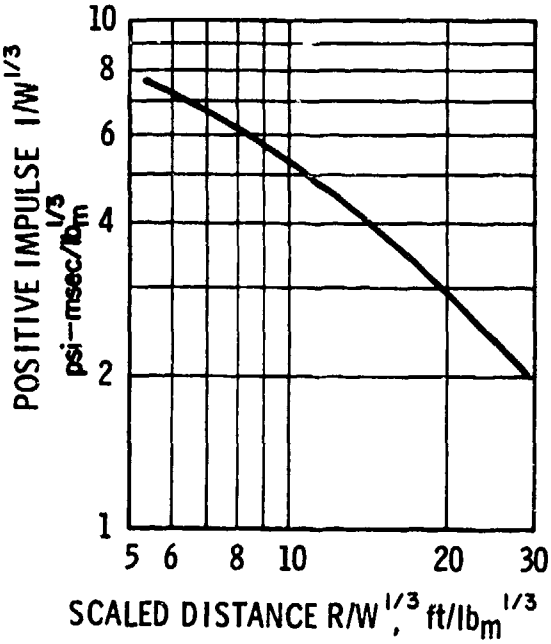


Figure 5-2. Logarithmic Plot of Positive Impulse vs Scaled Distance in Free Air for Cast TNT[1]

ranges of parameters over which measurements were taken, and the specific parameters which were reported.

Stoner and Bleakney[2] were early investigators who reported the results of free-air experiments conducted with small TNT and Pentolite charges of various shapes. Because of uncertainties of flow effects about the side-on blast pressure transducers available at that time, these investigators chose to report only peak overpressures which were inferred from measurements of shock velocities through the Rankine-Hugoniot relations. Their data are shown graphically in Fig. 5-3. They also obtained empirical fits to their data, as quoted from Ref. 2:

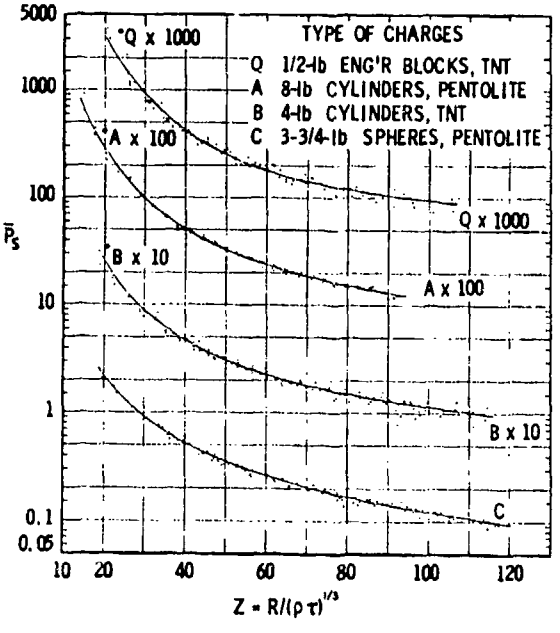


Figure 5-3. Experimental Pressure vs Scaled Distance for Four Types of Charges[2]

"The pressure-distance relations for the four principal charge types are given by the following fitted equations, in which P_s represents excess peak pressure in atmospheres, and the distance, scaled according to charge weight, is given by the nondimensional variable $Z = R/(\rho\tau)^{1/3}$ where R is the distance from a charge of volume τ and specific gravity ρ:

½-lb rectangular blocks, TNT,
$\overline{P}_{sQ} = 13.50/Z - 769.9/Z^2 + 36280/Z^3$;

8-lb cylinders, Pentolite,
$\overline{P}_{sA} = 10.49/Z - 135.5/Z^2 + 21070/Z^3$;

4-lb cylinders, TNT,
$\overline{P}_{sB} = 11.34/Z - 185.9/Z^2 + 19210/Z^3$;

3.75-lb spheres, Pentolite,
$\overline{P}_{sC} = 8.63/Z + 295.1/Z^2 + 7823/Z^3$.

These equations are valid for values of Z between approximately 18 and 110. The indicated probable error of the fitted curves is of the order of one percent for intermediate distances, increasing to from two to seven percent at the extremes of the distance range covered."

After World War II, the majority of the free-field blast measurements in the U.S. were made by various investigators at the U. S. Army Ballistic Research Laboratories and at the U. S. Naval Ordnance Laboratory. Pentolite was established as a standard in most of these experiments because it gave reproducible data when detonated in small quantities. On the other hand, the more familiar explosive TNT proved difficult to detonate reproducibly in quantities of one pound mass and less[3]. To avoid effects of charge shape, cast spheres were used exclusively. Rather than list the numerous reported and unreported efforts of these two laboratories, we will instead cite two reports which condense and compile free-field blast data*. The first, by Goodman at BRL[4], has become more or less a "bible" for air blast technologists. It compiles measurements of peak overpressure, positive impulse and positive durations from bare, spherical Pentolite which were taken from 1945 to 1960. Spreads in each set of reported data are given, both graphically and numerically. Empirical fits are made to the data for side-on peak overpressure and positive impulse. Goodman also compiled data for normally-reflected blast waves in Ref. 4. Figs. 5-4 through 5-6 are graphs reproduced from this reference. The second report, by Lutzky at NOL[5], is primarily a comparison of theory with experiment, but also reports free-air blast parameters which are seldom reported, such as first and second shock arrival times and the time history of motion of the contact surface (the boundary between the hot explosion products and the surrounding air). Such data are shown in Fig. 5-7, taken from Ref. 5.

We know that the British have also conducted free-air blast experiments, but we

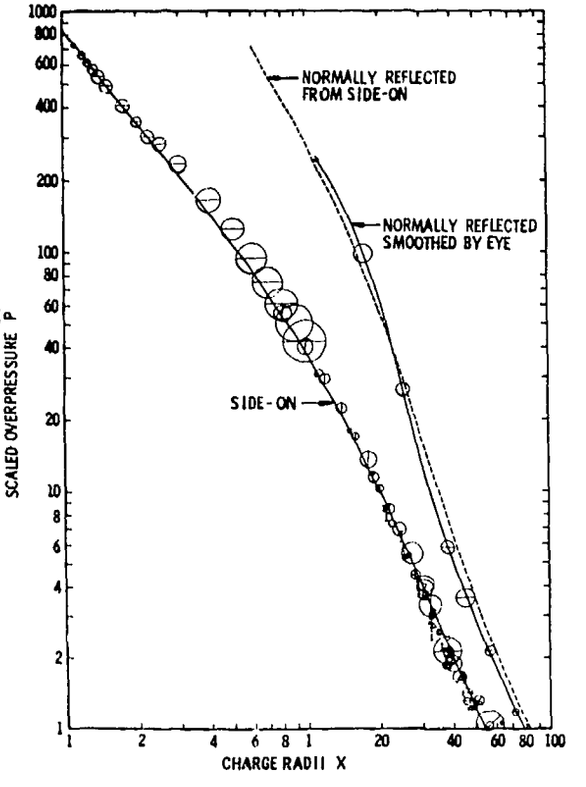


Figure 5-4(A). Side-on and Normally Reflected Pressure vs Scaled Distance[4]

*The many BRL and NOL reports summarized here are listed in the Bibliography.

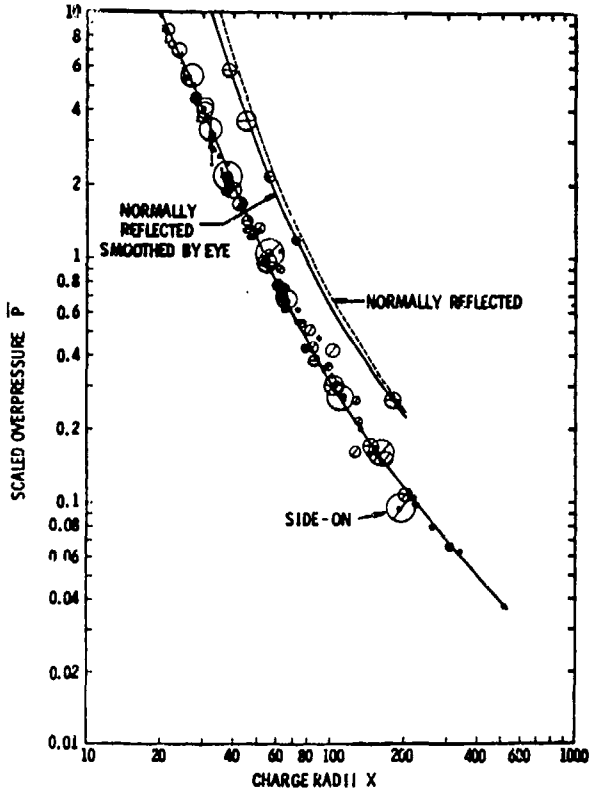


Figure 5-4(B). Side-on and Normally Reflected Pressure vs Scaled Distance[4]

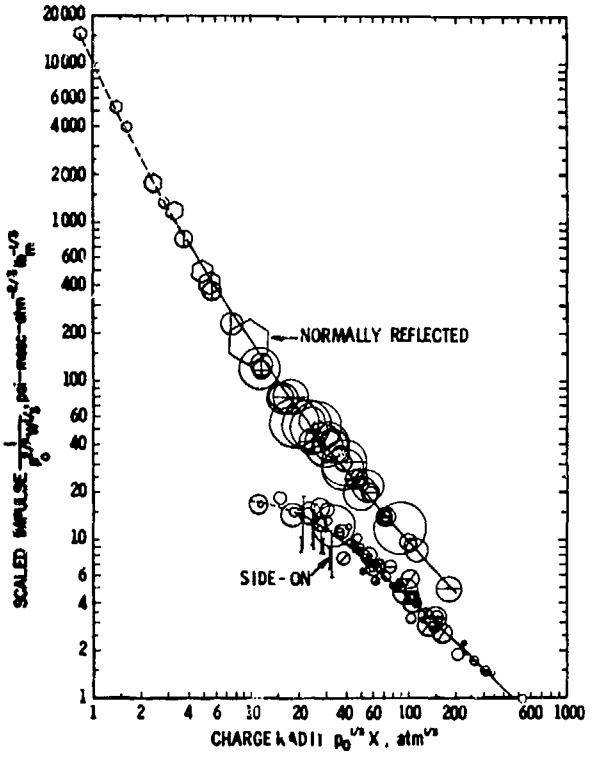


Figure 5-5. Side-on and Normally Reflected Impulse vs Scaled Distance[4]

cannot report their data in this volume because, unlike their American counterparts, the British consider much of their blast data to be classified.

Finally, let us note those free-air blast parameters which have apparently *not* been measured. There are no reported data for dynamic pressure; essentially none for negative phase pressure durations, impulses, and amplitudes; and essentially no measurements of density or temperature in either positive or negative phase. Usually, no data exist because there are no suitable transducers or measurement techniques for obtaining the data. But, for negative phase data, we suspect that no data are available primarily because this phase of the blast wave was considered unimportant relative to the positive phase which has much greater amplitude and impulse.

5-4 MEASUREMENTS FOR BLAST SOURCES ON THE GROUND

If a blast source is placed on or near a reflecting surface such as the ground, then the initial shock is very quickly reflected, and the

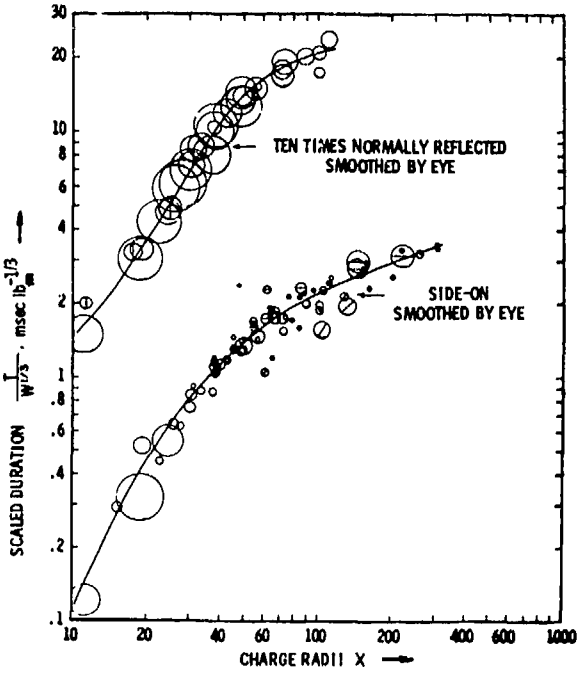


Figure 5-6. Side-on and Normally Reflected Duration vs Scaled Distance[4]

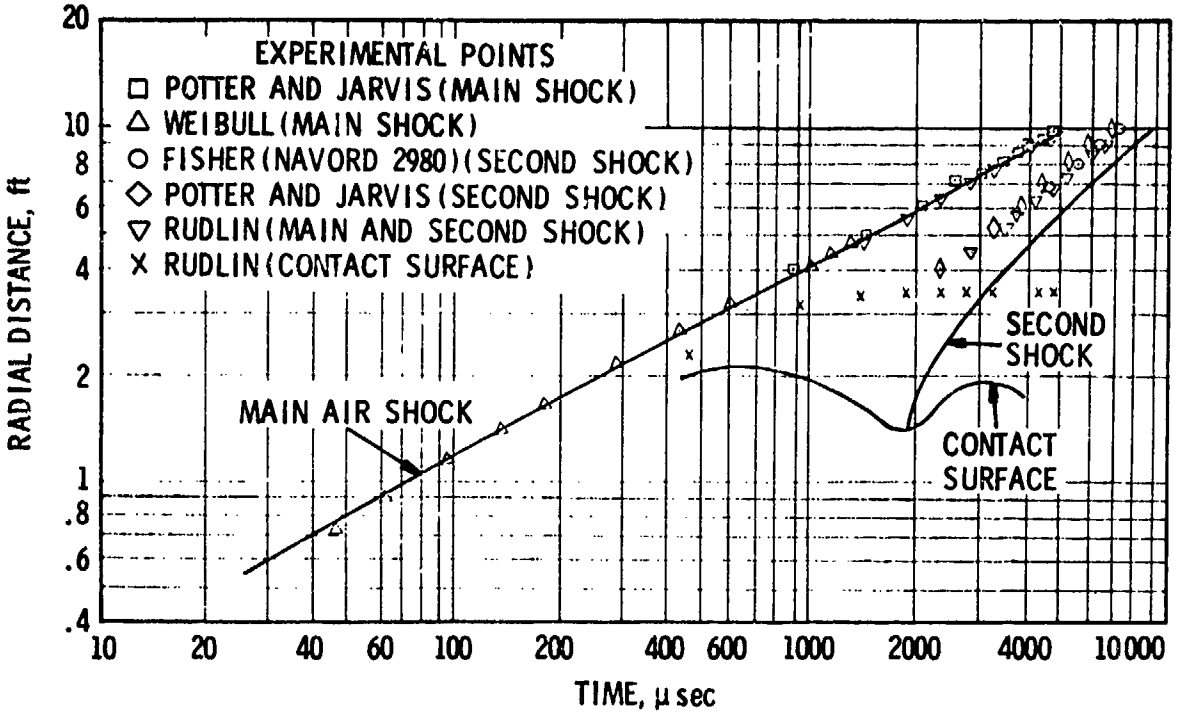


Figure 5-7. Radius-time Curves for 1-lb$_m$ Sphere of TNT at Sea Level Conditions[5]

reflected wave merges with the incident wave so rapidly that a single, strengthened blast wave is formed. The characteristics of this single wave are often almost identical with the characteristics of blast waves in free-air experiments, with the exception that the blast source appears to have greater energy than for free-air tests. The proportion of energy reflected from the ground is a function of how perfect a reflector it is, i.e., how little energy is imparted to the ground in cratering, ground shock, etc. If the ground were a perfectly rigid surface, then the equivalent "free-air" energy driving the air blast wave would be $E' = 2E$. The other extreme case is that of a perfect absorber, for which $E' = E$. All actual tests will have equivalent free-air energies lying between these limits.

There have been very few large scale free-air experiments because of practical limits on height above ground at which the experiments must be conducted to avoid ground reflection effects. For ground burst experiments, this limit is removed, and the scale of the blast test is limited only by available real estate or, for nuclear weapons, treaties which prohibit testing. So, there is a considerable body of experimental data for large-scale ground bursts of conventional and nuclear weapons, as well as data for small-scale experiments. An advantage of the large-scale experiments is that it is often possible to use transducers, recording equipment and measurement techniques with relatively low frequency response or time resolution, and therefore obtain measurements which cannot be made during very small scale tests. An offsetting disadvantage of the large-scale tests is the great cost in money, time, and manpower.

Measurements of air blast from ground-burst explosive sources date from the same initial efforts in World War II as do free-air blast data. In the early test results reported in Ref. 1, it is noted that there is more scatter in the data than for free-air measurements. Data reported are peak overpressures and positive impulses, and blast sources range from 8 lb of bare explosives such as Composition B and TNT to bombs with steel casings containing

up to several thousand pounds of explosives. Typical curves from Ref. 1 are reproduced here as Figs. 5-8 and 5-9. In these plots, Kennedy has attempted to eliminate differences due to use of different explosives and of bomb casings by use of suitable conversion factors. This early work is more of interest for its historical value rather than for its accuracy, because it has been largely superseded by later experiments done with better equipment and at a more leisurely pace.

It is apparent that a number of measurements of blast wave properties have been made during nuclear tests, but until recently, these data were classified. Some are now available in Refs. 6, 7, and 8. Measurements reported are times of shock arrival, peak overpressures, positive impulses, and positive durations. Kingery[7,9] reports data from ground bursts of hemispherical TNT charges ranging in weight from 5 tons to 500 tons and of nuclear devices ranging in yield from 20

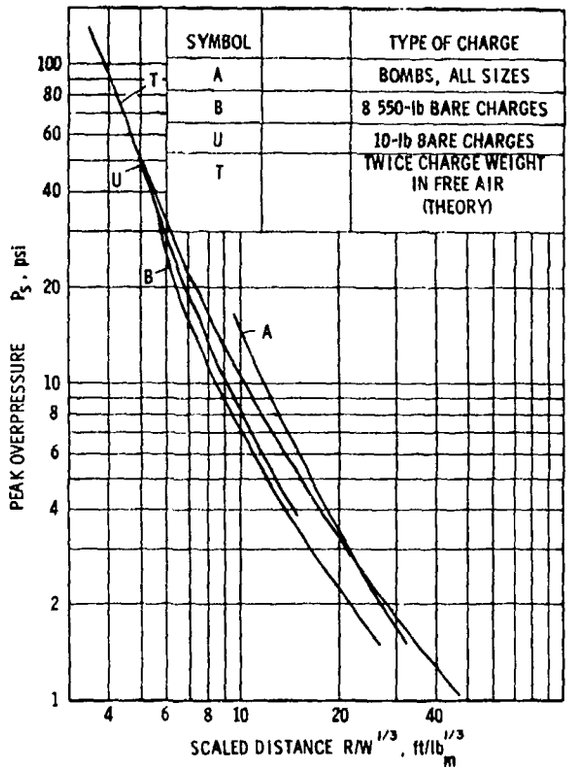


Figure 5-8. Pressure-distance Curves (Experimental and Theoretical) for Ground Burst Blast of Bare Charges[2]

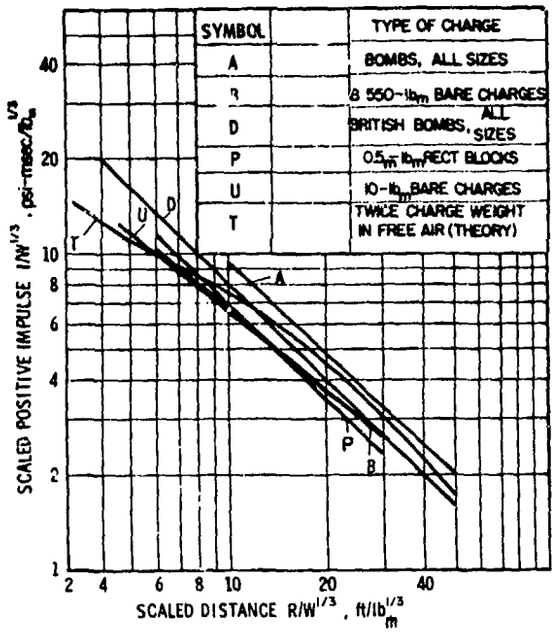


Figure 5-9. Experimental Positive Impulses vs Distance Curves (on ground) from Various Sources[1]

tons to 1.8 kT, while Haskel, et al.[8] report blast data for nuclear devices detonated at several heights of burst. Smooth curves fitted to the TNT data and data points for nuclear test data are shown for various blast parameters in Figs. 5-10 through 5-13. Note that the blast yield of the nuclear devices is assumed to be only half the blast yield of TNT in these comparisons. Kingery also notes[7] that multi-kiloton nuclear tests also produce essentially the same scaled data at scaled distances greater than $200\,ft/(kT)^{1/3}$.

The majority of the experimental data from large explosive sources detonated on the ground have been accumulated during recent years for TNT hemispheres ranging up to 500 tons in weight at the Suffield Experiment Station in Canada. There are a number of reports for results from individual tests, such as Ref. 10. The smooth curves in Figs. 5-10 through 5-13 are fits to Hopkinson-scaled data from a number of these tests. In addition to the usual blast parameters, other parameters which have been seldom measured in other tests were carefully measured during

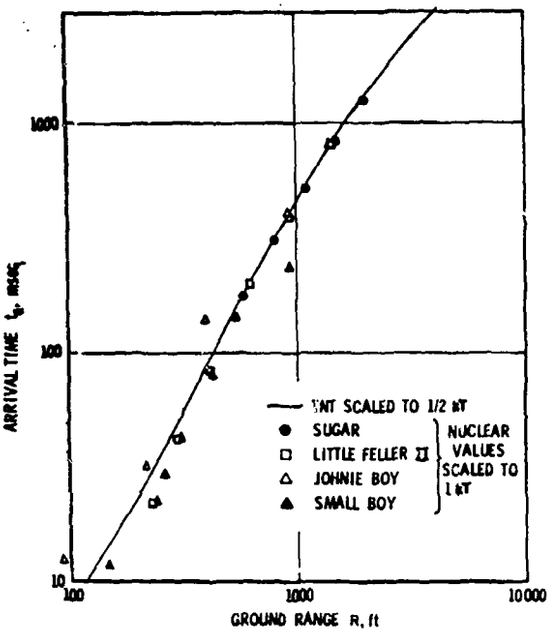


Figure 5-10. Scaled Arrival Time vs Ground Range[7]

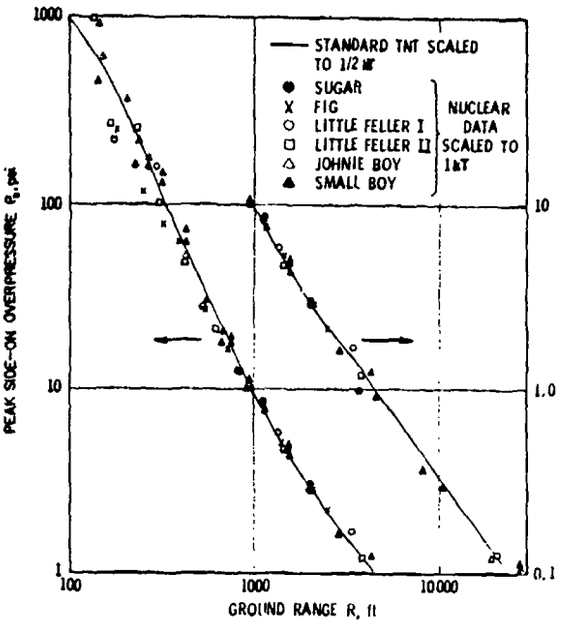


Figure 5-11. Scaled Peak Overpressure vs Ground Range[7]

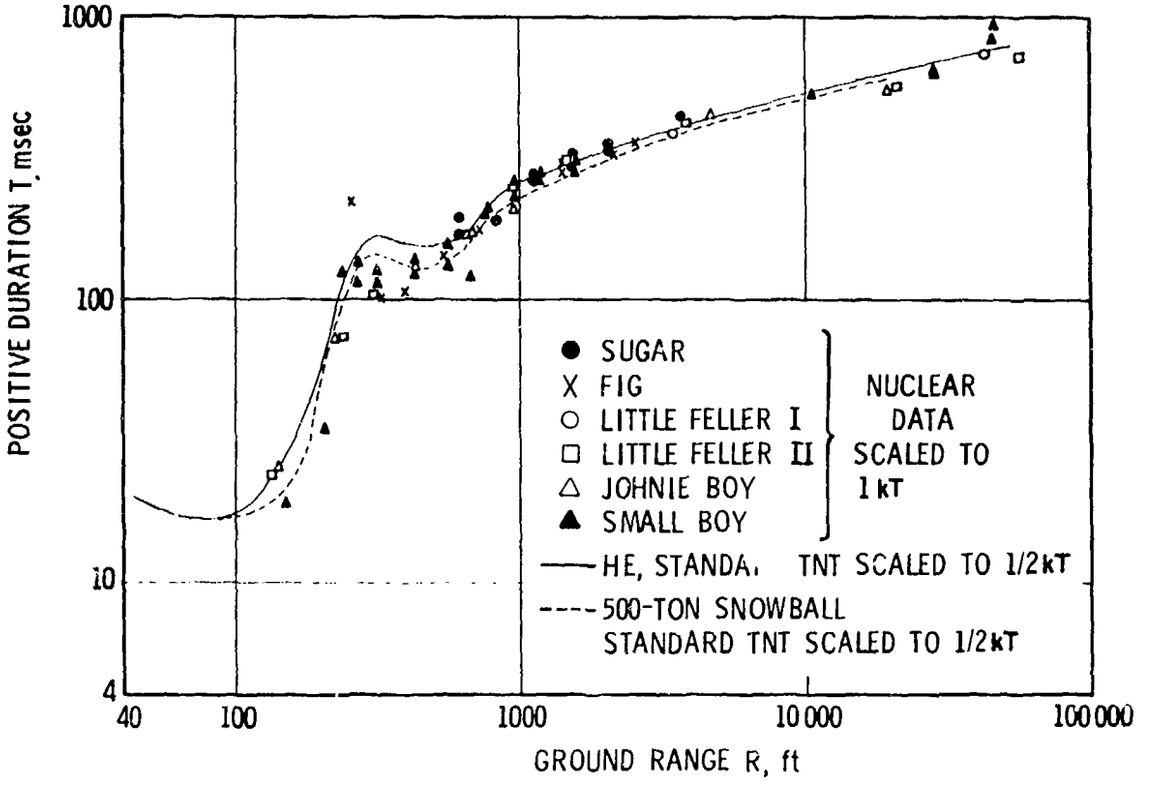


Figure 5-12. Scaled Positive Duration vs Ground Range[7]

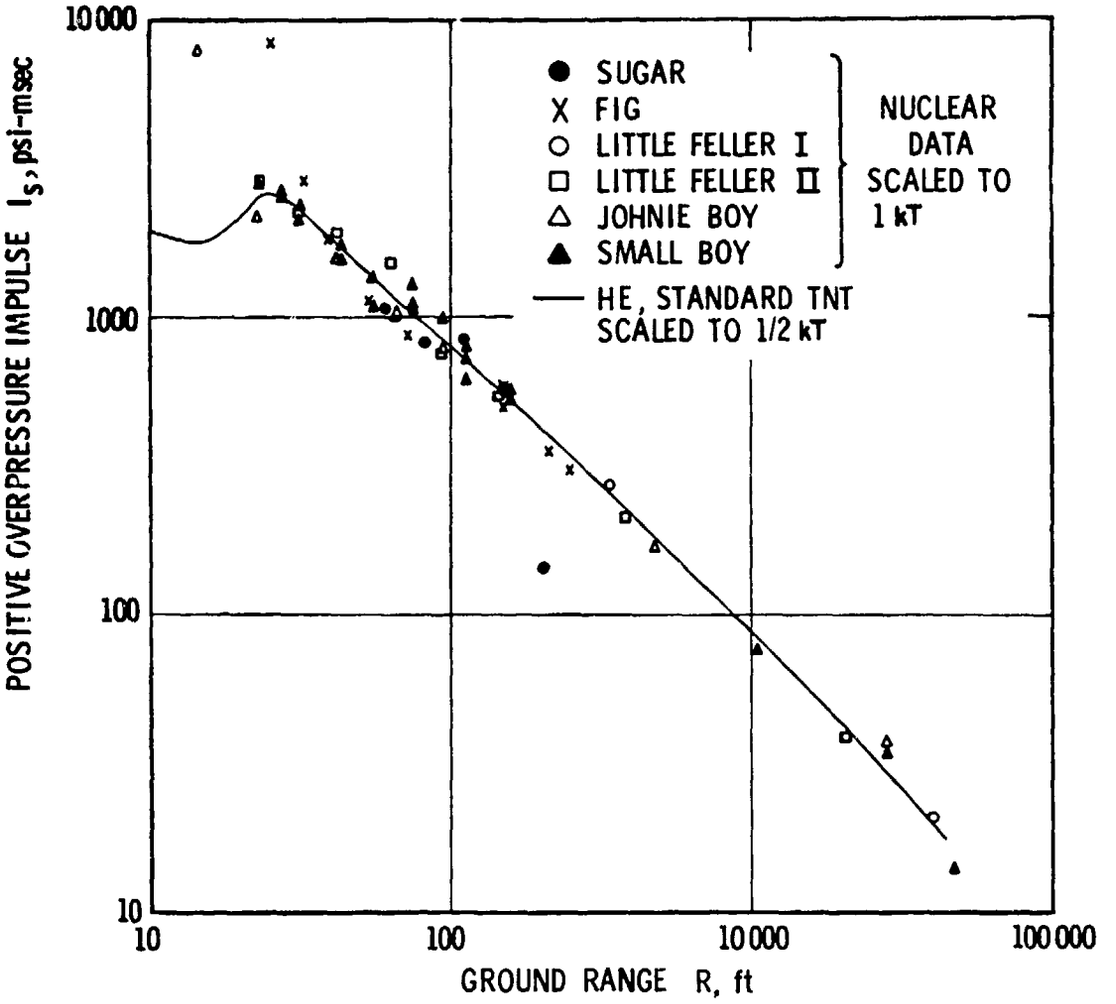


Figure 5-13. Scaled Positive Overpressure Impulse vs Ground Range[7]

many of the Canadian experiments. (These tests were also the first to demonstrate the "wavy" shape of the curves of scaled impulse and scaled duration at relatively small scaled distances.) These include time histories of particle velocity and density. John M. Dewey[11] reports data for particle velocity for a range of TNT charges from 30 to 200,000 lb. Typical data from Ref. 11 taken from high speed motion picture photography of smoke trails displaced by flow behind the shock front, are shown in Figs. 5-14 through 5-16. Dewey has also made an empirical fit (see Eq. 1-10, Ref. 11) to an equation for time history of decay of velocity in a blast wave. (Dewey's parameter S is proportional to $(W/\rho_0)^{1/3}$.) Anson and Dewey[12] also report some measurements of time history of density, but they are insufficient in number to establish the variation of this parameter with scaled distance. The final set of large-scale ground-burst tests which we will note here were conducted at Nevada Proving Ground with 20-ton spherical TNT charges half-buried in the ground[13]. The purpose of these tests (Code name Flat Top I, II and III) was to obtain airblast data in the high overpressure region of 10 to 10,000 psi, and to compare with previous data from the Canadian tests. Three tests were conducted and data collected on arrival times, side-on overpressures and impulses, and dynamic pressures. Overpressures were slightly lower than predicted for $P_s > 10$ psi, presumably because the charge was half-buried. In the same range, durations were longer than predicted. Typical plots of data

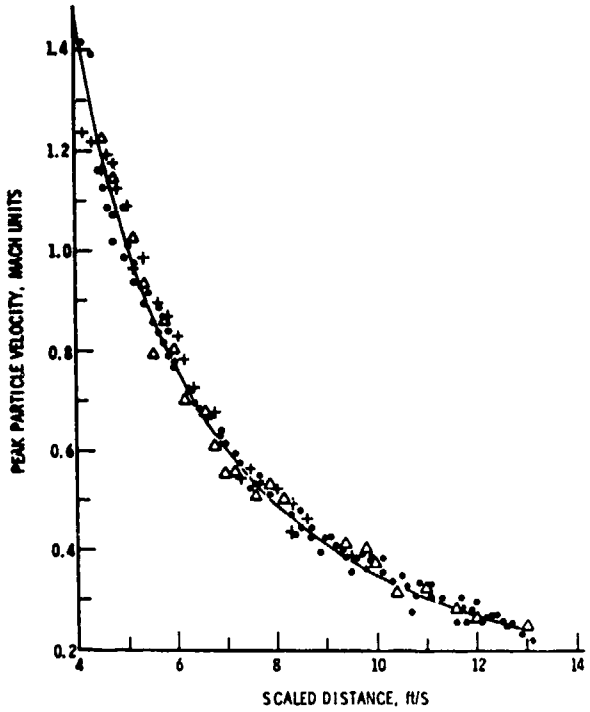


Figure 5-14. Comparisons of Peak Particle Velocities for Surface Burst TNT Charges of Various Weights from 60 lb_m to 20,000 lb_m[11]

are shown in Figs. 5-17 through 5-21. In this report, the authors note that a reflection factor of 1.7 gave reasonably good correlation with free-air data, but that pressures were higher over a rock surface than over alluvium.

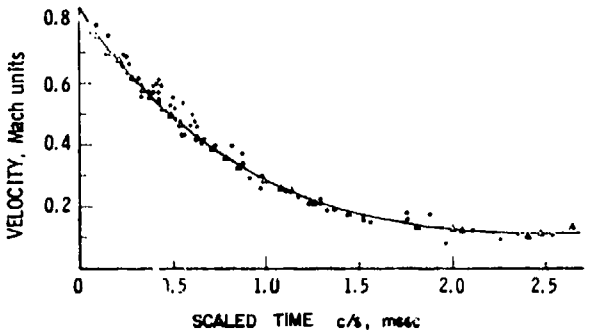


Figure 5-15. Comparison of the Time Varition of Velocity at a Specific Scaled Distance from Surface Burst TNT Charges from 60 lb_m to 200,000 lb_m[11]

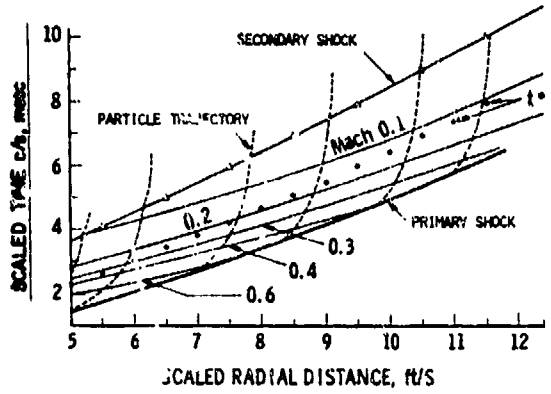


Figure 5-16. x-t Diagram from Particle Velocity and Shock Front Data[11]

5-5 MEASUREMENTS OF MACH WAVES AND OTHER OBLIQUELY REFLECTED WAVES

The formation of Mach waves for explosive sources located in finite distance above a reflecting surface is discussed in Chapter 1. The initial impetus for experimental studies of these waves and waves in the region of regular reflection came from suggestions early in World War II that blast damage from bombs and warheads could be increased by

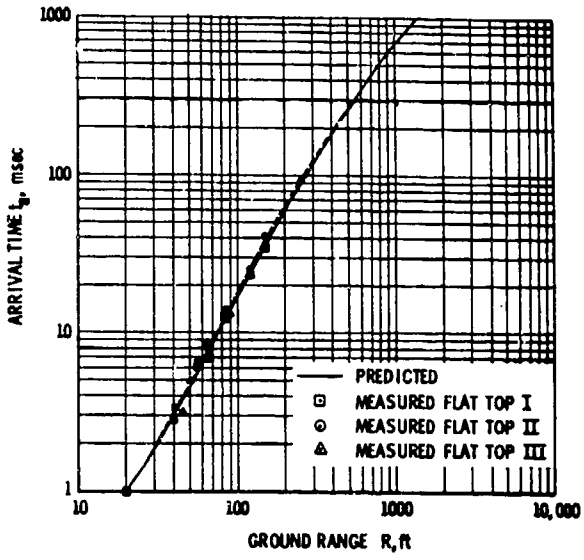


Figure 5-17. Measured Arrival Times for Flat Top I, II, and III Compared With Prediction[13]

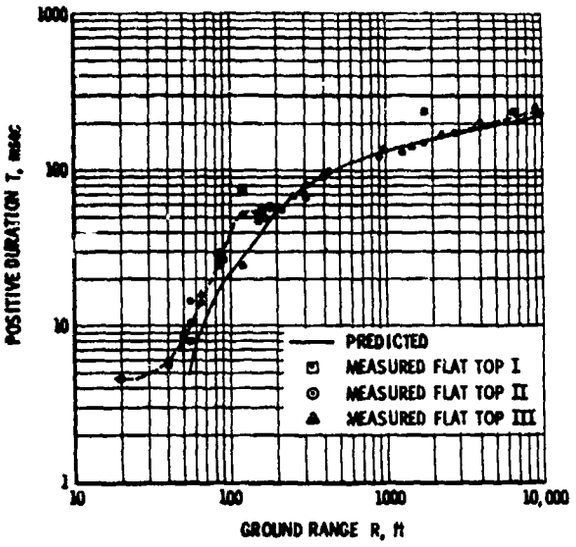


Figure 5-18. Measured Positive Duration for Flat Top I, II, and III Compared With Prediction[13]

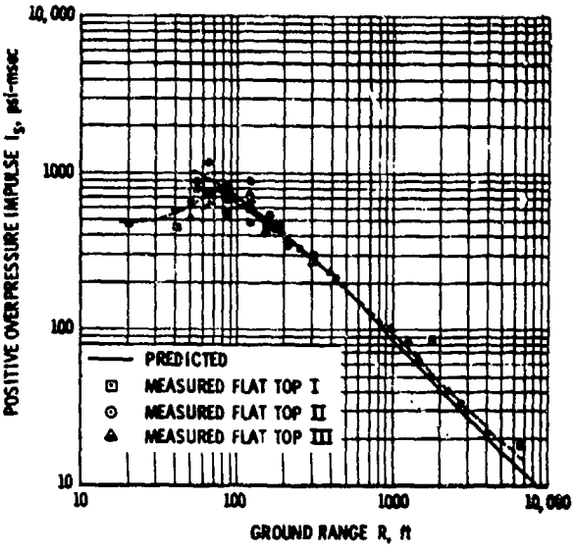


Figure 5-20. Measured Positive Overpressure Impulse for Flat Top I, II, and III Compared With Prediction[13]

bursting in air rather than on the ground[1]. It was first thought that such an increase in damage would be due to a reduction in the screening of one building by another. However, early experiments reported in Ref. 1 showed that screening had little effect; instead, peak pressures and impulses both increased over large areas as charges were elevated off the ground, up to some optimum height of burst. Later tests conducted to follow up these findings were aimed primarily at determining these optimum heights for use by weapon designers. Loci of the triple point were determined experimentally, as shown in Fig. 5-22.

Few additional experiments have been performed since the early work summarized in Ref. 1. The author has been able to locate

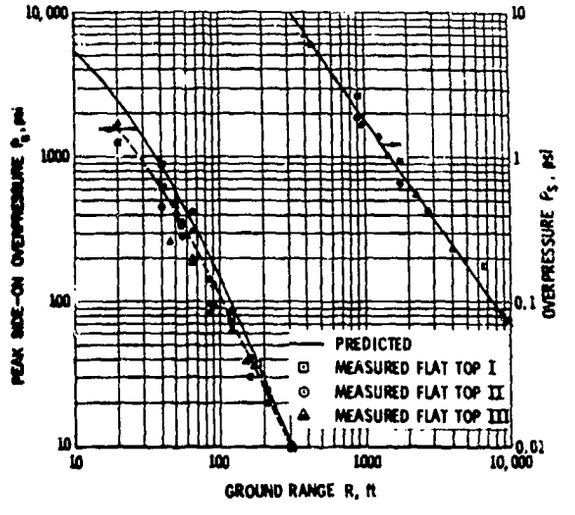


Figure 5-19. Measured Overpressure for Flat Top I, II, and III Compared With Prediction[13]

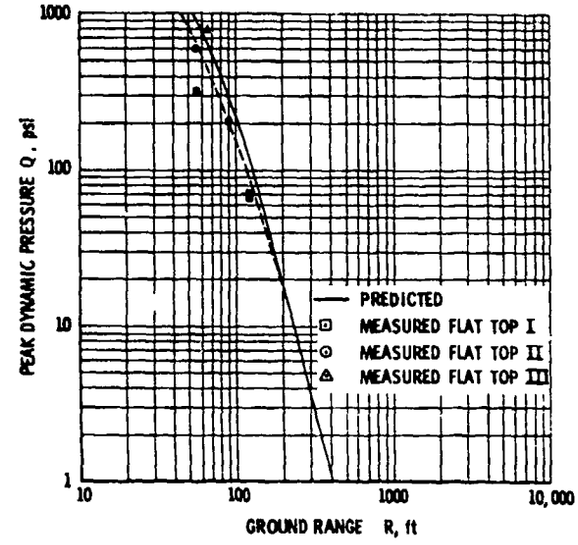


Figure 5-21. Measured Dynamic Pressure for Flat Top I, II, and III Compared With Prediction[13]

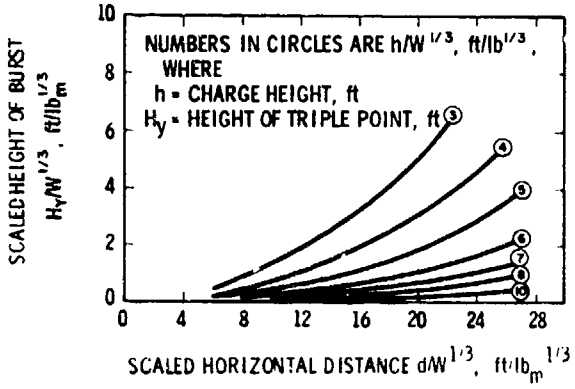


Figure 5-22. Paths of Triple Point[1]

only two references reporting such experiments. The first of these is an investigation by Bryant, et al.[14] of tripie-point loci for Pentolite spheres detonated over hard packed dirt and dry sand surfaces. Typical gage records recorded during this program are shown in Fig. 5-23. These authors reported that the incident and reflected shocks coalesced more rapidly than indicated in Fig. 5-22. Plots of triple-point loci from Ref. 14 are reproduced here as Fig. 5-24. The second reference consists of more recent experiments by Schleuter, et al.[15], wherein the primary purpose of the tests was to determine the detailed time histories of the blast waves in the region of regular reflection at various scaled heights over an essentially rigid (concrete) surface. These authors also used Pentolite spheres. Typical time histories of data obtained by these investigators are shown in

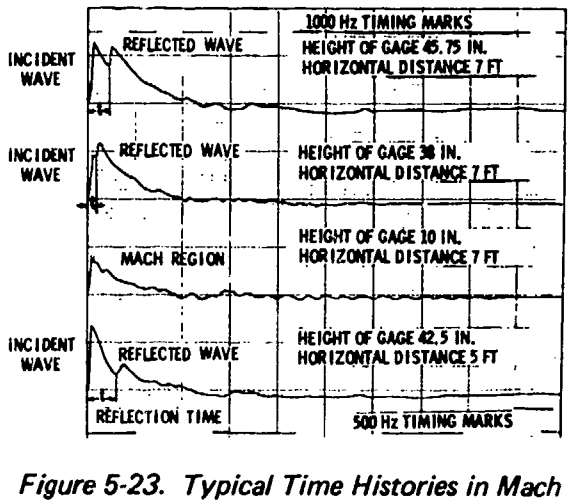


Figure 5-23. Typical Time Histories in Mach Reflection Region[14]

Fig. 5-25. Note that secondary shocks in the incident wave are quite apparent, and that they occur at various times relative to arrival of the obliquely reflected wave. In both Refs. 14 and 15, detailed data are reported accurately, and the reader should obtain them if he is interested in detailed measurements of obliquely reflected shocks.

5-6 MEASUREMENTS OF NORMALLY REFLECTED WAVES

When an air blast wave is reflected normally from a large, rigid surface, then the pressures and impulses are considerably enhanced. The physics of normal reflection is discussed in Chapter 1. Because the normally reflected parameters represent upper bounds to blast loading of structures, a number of investigators have measured them. Most of these experiments have been conducted using small Pentolite spheres.

The first comprehensive set of measurements was accomplished by Hoffman and Mills[16], with piezoelectric gages of their own design (see Chapter 7) which were flush-mounted in a reinforced concrete wall. Reflected peak pressures and impulses were reported in Ref. 16, over the range in which the authors felt that gage response was reliable (up to about 1500 psi overpressure). The curves in Figs. 5-4(A) and 5-4(B) for normally reflected pressure are based on this reference. Next, Johnson, et al.[17] devised a simple mechanical means for measurement of impulse in normally reflected blast waves (see Chapter 7) which allowed measurement of this specific blast parameter with excellent accuracy to very small scaled distances. These measurements, conducted for a range of charge weights, agreed with Hopkinson's scaling law and considerably extended the range of the previous measurements. In 1961, Olson and Wenig[18] employed a different experimental technique to extend the range of measurements of reflected pressure-time histories. Their technique consisted of simultaneously detonating two equal charges placed equidistant from a suitable oriented side-on blast transducer, and measuring the time

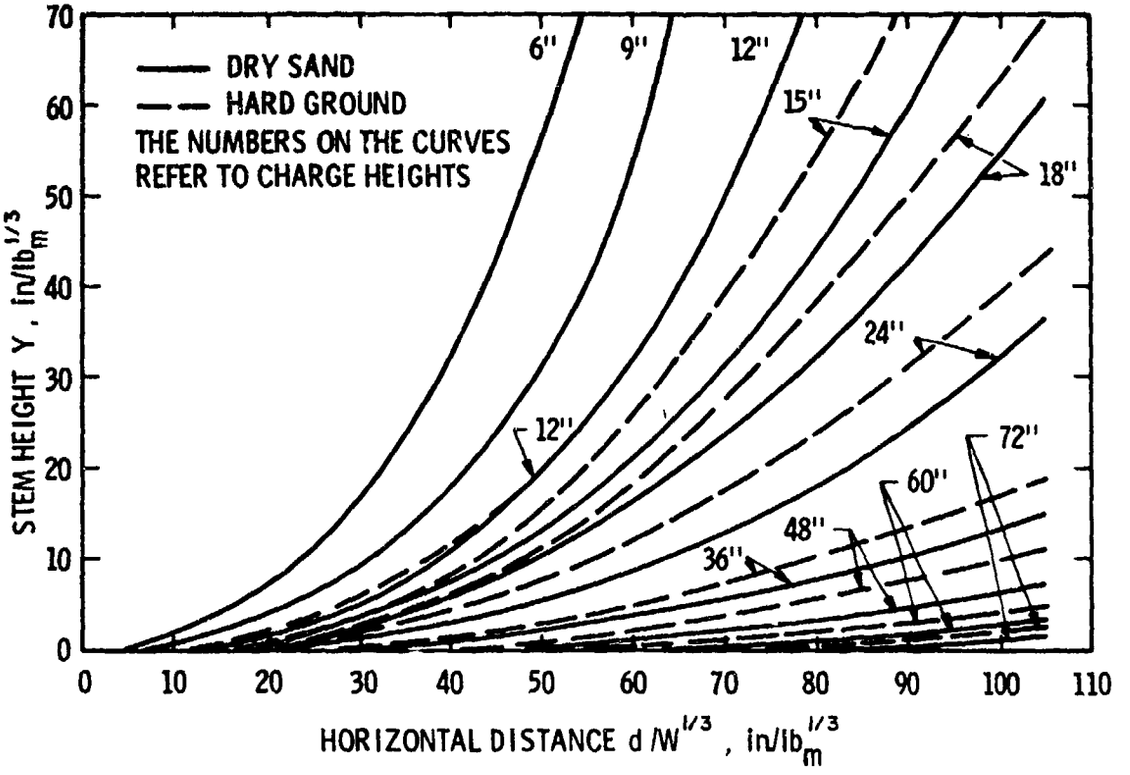


Figure 5-24. Triple Point Loci Over Reflecting Surfaces of Hard-packed Dirt and Dry Sand[14]

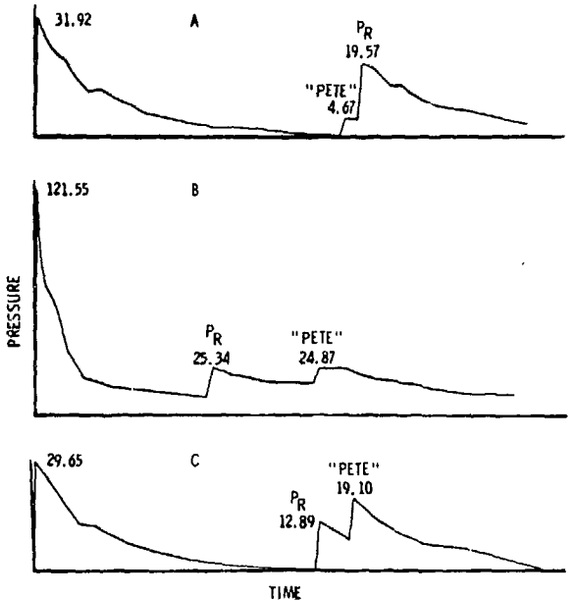


Figure 5-25. Typical Complex Shock Waves Observed in Reflection Studies[15]

histories of the colliding waves. With good experimental control, this technique produces the same reflected blast wave characteriestics as reflection from a rigid wall. Measurements were made to overpressures as great as 3600 psi. The development of improved gages for recording short-duration pressures up to much higher pressures allowed Jack[19] in 1963 to further extend the range of measurement of time histories of reflected pressure. The technique used in these experiments was essentially identical to that employed earlier by Hoffman and Mills[16], but quite small Pentolite spheres (1/8 lb) were used. Data were obtained for peak reflected overpressures up to nearly 30,000 psi. Comparisons of data from Refs. 16 through 19 are shown in Figs. 5-26 and 5-27, taken from Ref. 19.

5-7 MEASUREMENTS UNDER REAL AND SIMULATED ALTITUDE CONDITIONS

When a blast source releases energy at high altitude, the characteristics of the resulting blast wave are affected significantly by the

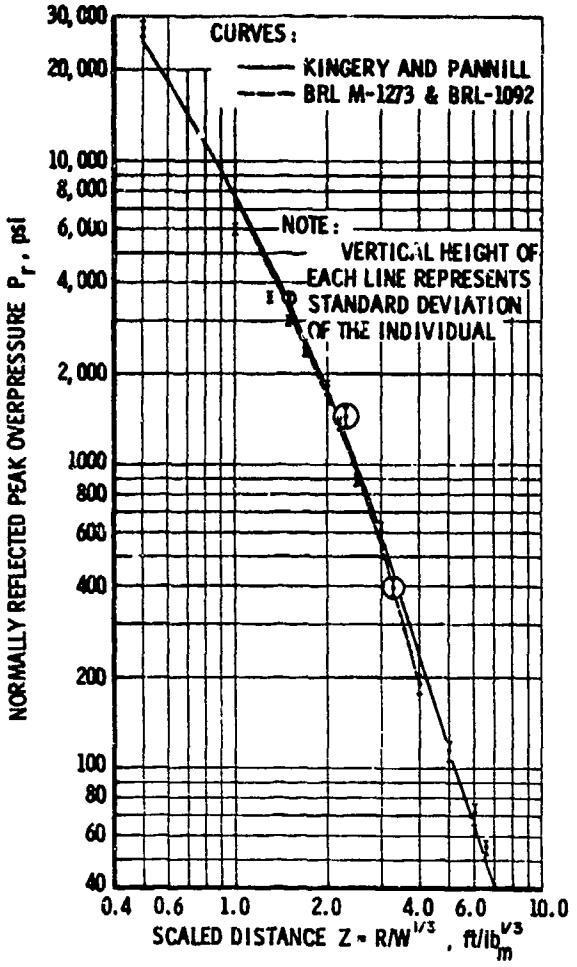


Figure 5-26. Normally Reflected Peak Overpressure vs Scaled Distance[19]

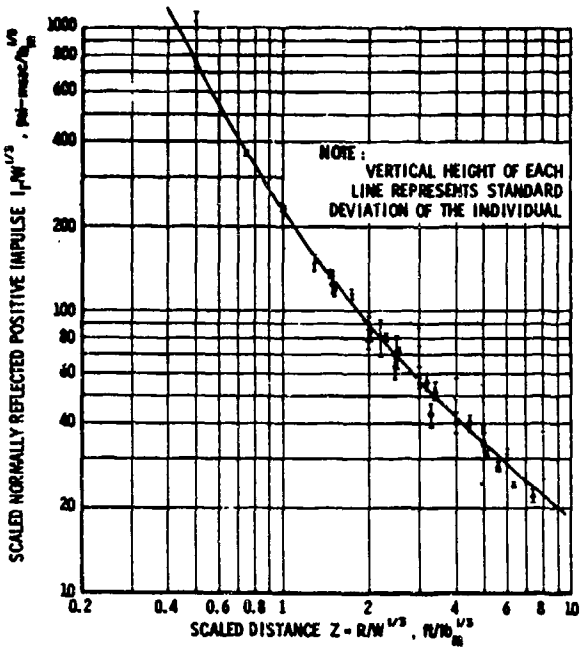


Figure 5-27. Scaled Normally Reflected Positive Impulse vs Scaled Distance[19]

change in ambient pressure and temperature from sea level conditions. Probable magnitudes for these effects were predicted by Sachs[20] when he generated his scaling law for effect of ambient conditions on air blast (see Chapter 3 for a more complete discussion and derivation of Sachs' Law). These predictions predated any measurements under altitude conditions. Kennedy[1] reports that limited series of tests were conducted late in World War II with side-on peak pressures and impulses being measured at altitudes of 650, 6600, and 14,000 ft above sea level. These results did not disagree with predictions based on scaling sea-level data using Sachs' law. There are apparently no other reported measurements of blast parameters measured at high altitudes. Instead, most measurements have been made in altitude simulating chambers under conditions of reduced pressure and temperature or both. Because such chambers are necessarily limited in size, most of these measurements have been made using relatively small explosive charges. The first series of tests under simulated altitude conditions is reported by Dewey and Sperrazza[21]. In these experiments, side-on pressures and impulses were measured for a limited range of spherical Pentolite charge weights and a limited range of scaled distances under conditions simulating several altitudes up to 55,000 ft. These measurements confirmed the adequacy of Sachs' scaling law over the range of altitudes and scaled distances possible in the test chamber.

After the work of Dewey and Sperrazza[21], most of the tests under simulated altitude conditions involved measurement of normally reflected blast parameters. Olson, et al.[22], measured reflected impulse for bare, spherical Pentolite in an altitude-simulating chamber in which ambient pressure could be varied (but not temperature), using the "flying-plug" technique described in Chapter 7. Ambient pressures as low as 8 mm Hg, simulating an

altitude of 100,000 ft, were utilized. Tests were conducted at quite small scaled distances, for a limited range of small explosive charge weights. Results for these tests are shown graphically in Fig. 5-28. These investigators noted that the data appeared to be consistent with Sachs' scaling law, even though a basic assumption in Sachs' law is violated for such strong shock waves. Dewey, et al.[23], followed this work with additional experiments using the same technique, to investigate further the apparent agreement of reflected impulse data with Sachs' law. Their results are shown graphically in Fig. 5-29. They discovered that ambient pressure had no effect on impulse at "small enough" scaled distances. They noted that agreement with Sachs' law was strictly fortuitous, and dependent on the functional relationship of reflected impulse with distance close to the explosive source. They also noted that Hopkinson's Law is more appropriate for this particular blast parameter close to explosive sources. The most recent set of measurements is that of Jack and Armendt[24], wherein parameters of reflected blast waves were measured with pressure transducers flush-mounted in the wall of a test chamber. These authors report peak reflected overpressures, reflected impulses, arrival times, and positive durations at ambient pressures down to 0.1 mm Hg (approximately equivalent to 210,000-ft altitude). Pentolite spheres of nominal 1/8-lb weight were used, with a range

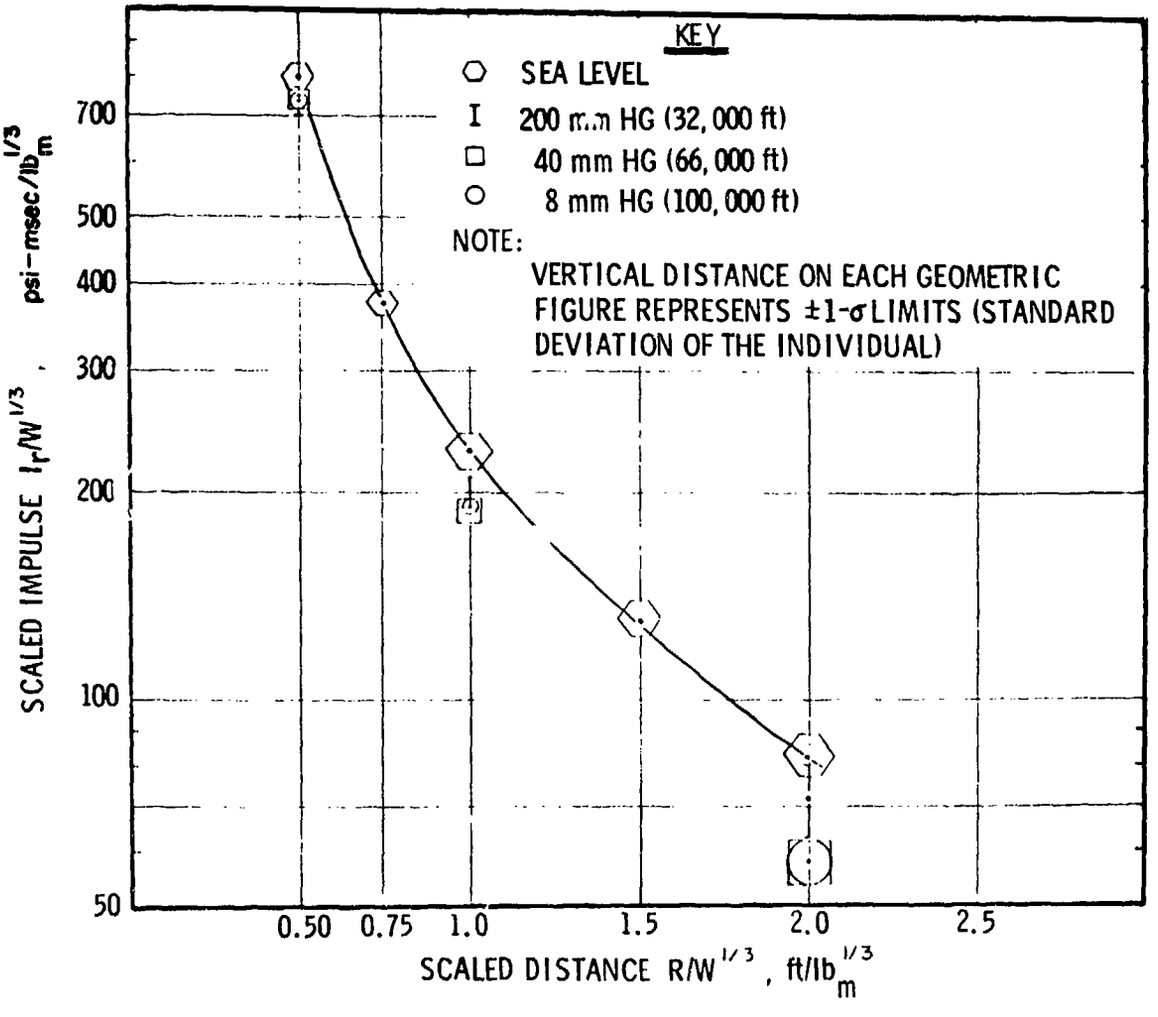


Figure 5-28. Geometrically Scaled Reflected Impulse vs Scaled Distance at Different Atmospheric Pressures[22]

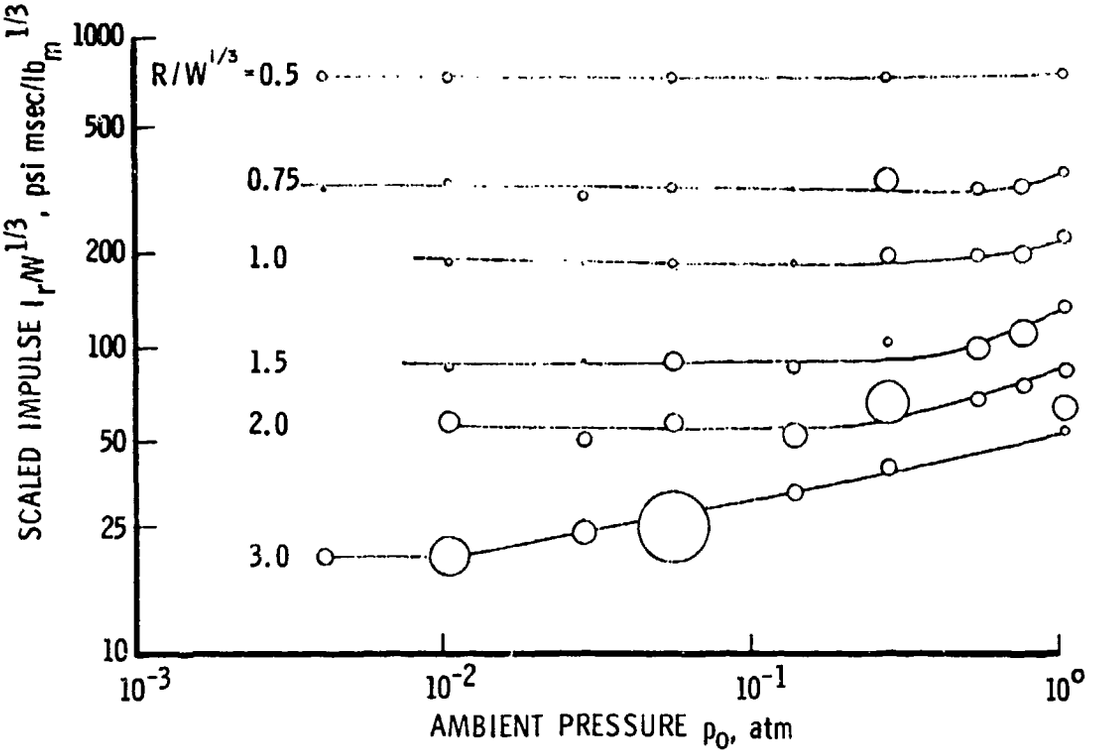


Figure 5-29. Normally Reflected Positive Impulse as a Function of Scaled Distance ($R/W^{1/3}$) and Ambient Pressure p_0 [23]

of scaled distances similar to that reported in Refs. 22 and 23. These investigators noted that the entire time history of the reflected blast wave changed character below about 8 mm Hg ambient pressure, with the usual sharp shock front being almost indistinguishable below about 0.5 mm Hg. A typical time history at 0.1 mm Hg is shown in Fig. 5-30. Impulses obtained by integrating the pressure traces agreed well with data from Refs. 22 and 23, although the experimental scatter was greater than for the moving plug method. Reflected pressures in excess of 4500 psi are reported in this reference. These authors also noted that Sachs' scaling law cannot be used for scaling all blast parameters close to explosive sources.

Indicative of the small amount of data obtained under actual high altitude conditions, and of the difficulties of obtaining such data, are Refs. 8 and 25. These references add little to the data obtained in altitude-simulating chambers, with the exception of a few data points for very large scaled distances.

5-8 MEASUREMENTS FOR SEQUENTIAL EXPLOSIONS

When high explosives are stored in large quantities, an important consideration in determining safe distances from these storage areas is the physics of interaction of the blast waves from closely-spaced, sequentially initiated piles of explosive. Accidental detonation of one storage pile often will cause detonation of an adjacent pile with a significant time lag between the two detonations. Such questions as, "Do the two blast waves coalesce?" "Where and at what time do they coalesce?" are important in determining possible blast loading of structures.

To obtain answers to these questions, some blast measurements have been made on both small and large scale. All have involved deton-

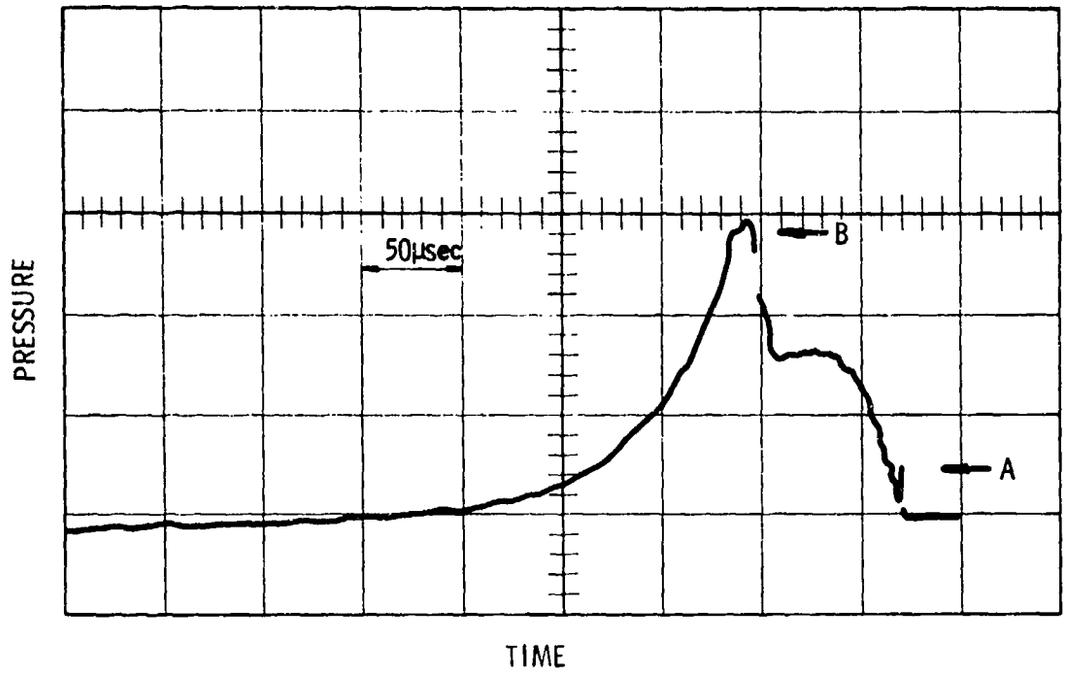


Figure 5-30. Normally Reflected Pressure-Time History, Scaled Distance = 0.10 ft/lb$_m^{1/3}$ 0.1 mm Hg (approx. 210,000-ft altitude)[24]

ation of bare explosive charges on the ground, and measurements of the side-on blast parameters with gages flush-mounted in the ground or located a few feet above the ground. Some initial exploratory measurements were made by Wilton and Kaplan[26], using pairs of 0.25-lb hemispherical charges located close to each other on a steel plate with a steel separating wall, and various programmed delays between times of detonation. Measurements of blast pressures orthogonal to the line of centers of the two charges indicated that blast waves from the two charges would coalesce, even for appreciable delays in detonation time. A series of pressure records showing this phenomenon is reproduced in Fig. 5-31. A limited series of larger scale tests was conducted at the Naval Weapons Center following this initial study[27]. Following the few experiments reported in Refs. 26 and 27, a much more comprehensive study was undertaken by Zaker[28]. This work included both analysis and experiments, with the experiments consisting of detonation of a number of pairs of small hemispherical C-4

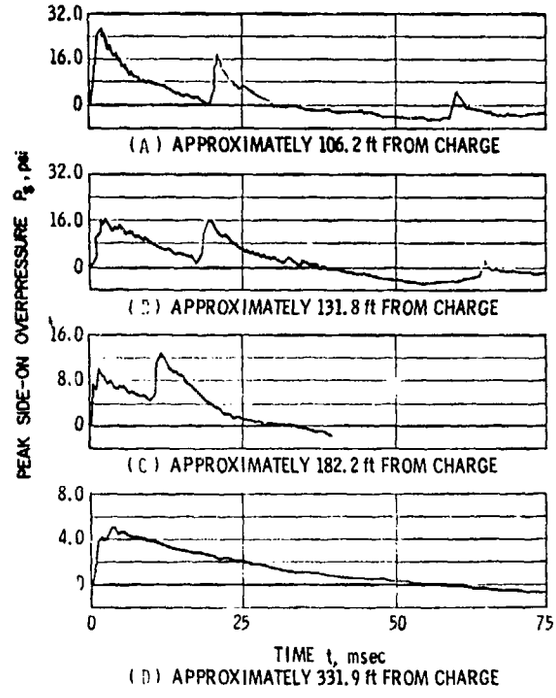


Figure 5-31. Phenomenon of Blast Wave Coalescence for Two Charges Detonated With Time Delay[28]

explosive charges of varying weight ratios and delay times. Time histories of the blast waves were measured along two orthogonal gage lines. Delays were varied over a large enough range to determine the limits for scaled time for which the waves did not coalesce. Shock coalescence was found to be a strong function of orientation as well as delay time, as can be seen from Fig. 5-32. In this figure, "axial" refers to the gage line orthogonal to the line of centers of the two charges, and "lateral" refers to the gage line containing the line of centers. This excellent report[28] should be considered the basic reference in any study of sequential explosions.

5-9 ACCURACY OF MEASUREMENT OF BLAST PARAMETERS

We will close this chapter with a brief discussion of the accuracy with which one can expect to measure various air blast wave parameters, using present experimental equipment and techniques. Accuracy of measurement of course, is, affected by many factors such as repeatability and linearity of transducers, amplifiers, and recorders; changes in gage sensitivity with changing ambient conditions; spurious response of transducers to thermal pulses, electromagnetic pulses, etc.; cable noise due to triboelectric effect; sufficient high and/or low frequency response of recording system; gage size and shape effects; reading errors in data reduction. If factors such as those cited have not been considered by an experimental investigator, then it is quite possible that totally meaningless data can be collected and reported, and a discussion of possible accuracy in measuring blast parameters is as meaningless as the data. We must also differentiate between *accuracy* and *precision*, with the former term indicating correspondence between measurements and physical reality, and the latter term indicating the number of significant figures (or "least count") of any given measurement. Good precision is not necessarily a sign of good accuracy. In discussing accuracy, we then *presume* that one will employ as nearly an optimum system as he can for conducting his blast experiments. In presenting estimates of accuracy, we employ the common statistical measure of $\pm 1\ \sigma$, or ± one standard deviation of the mean, expressed as a percent of the mean.

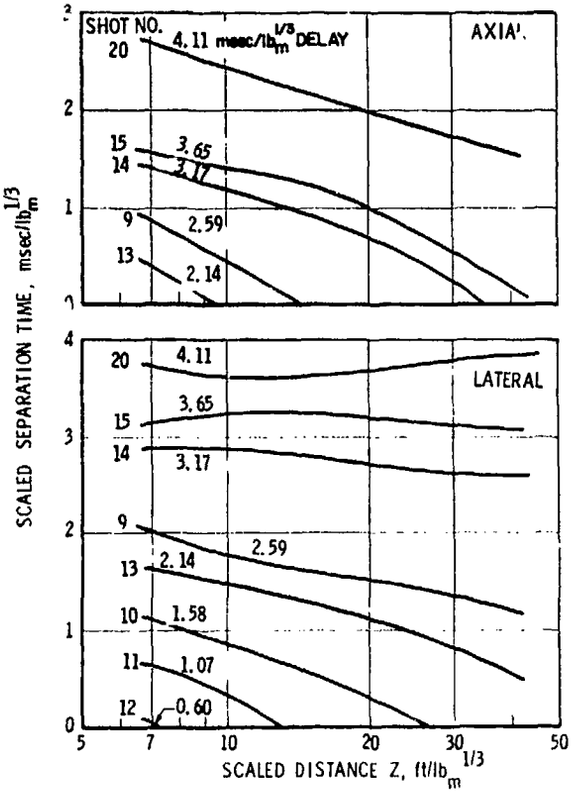


Figure 5-32. Scaled Delays Between Shock Fronts from Sequential Explosions[28]

Many of the measurements reported in figures in this chapter show their accuracy graphically by scatter in individual data points, or by symbols or bars indicating standard deviations of individual sets of measurements. By surveying these and other data reports, by personal experience, and by discussion with active investigators in blast experimentation we have ascribed approximate error bounds for various blast parameters.

Of all of the air blast wave parameters, the ones which can be measured most accurately are those based on measurements of time of travel over known distances in a fixed physical frame of reference. This is so because times can be measured to sub-microsecond precision (and accuracy) with counter chrono-

graphs or from precise timing marks impressed on high-speed film, and detector locations relative to a fixed blast source and to each other can also be surveyed quite accurately. Such parameters as time of shock arrival and time of travel of a shock front over a known short baseline (and consequently shock velocity) then can be measured in the field over a large range of blast wave strengths to about ± 2%. Somewhat better accuracy may be possible in controlled "laboratory" experiments in blast chambers.

The accuracy of various parameters extracted from recordings of pressure-time histories of either face-on or side-on blast pressure transducers varies. Face-on peak overpressures P_r can be measured, up to levels of several thousand psi, with an accuracy of about ± 5%. This same accuracy can be quoted for side-on peak overpressures P_s below shock strengths at which flow effects around the transducer head are important. No specific upper bound for overpressures can be cited here because the aerodynamic shape of the transducer is all-important. For gages mounted flush in a level surface, however, the ± 5% accuracy is possible up to several thousand psi. For impulses integrated from both reflected and side-on pressure-time histories, I_r and I_s, accuracy is poorer, say about ± 10%, than for peak overpressures. Lastly, one can expect even poorer accuracy in duration of positive overpressure T, say ± 20%. This last parameter is inaccurate because the approximately exponential decay of pressure approaches ambient pressure nearly asymptotically, and the exact time at which pressure returns to ambient therefore cannot be measured with good accuracy. For blast parameters such as dynamic pressure which cannot be measured by a single transducer but must be synthesized by subtracting signals either electrically or by data reduction from separate transducers, the accuracy is somewhat reduced. Peak dynamic overpressures are probably not accurate to better than ± 10%; dynamic pressure impulses, to better than ± 20%. So few reliable measurements have been made of duration of dynamic overpressure that no accuracy can be quoted. Similarly, not enough direct measurements have been made of time histories of density to quote a probable accuracy.

Finally, one of the simplest of measurement techniques for a blast parameter yield data with excellent accuracy and repeatability. The "flying plug" technique[15] for measurement of reflected impulse I_r has been shown to be capable of an accuracy of about ± 2%.

The numerical accuracies stated in preceding paragraphs should by no means be considered as "gospel truth". They represent the author's opinion of what one can expect to achieve in blast experiments, with four to five replications of any measurement. Much larger spreads in test results probably indicate that something is amiss, and that one should carefully review his entire procedure. Significantly smaller spreads are probably a sign of either quite careful work or of enough replication of tests to insure small statistical scatter because of large sample size.

REFERENCES

1. W. D. Kennedy, "Explosions and Explosives in Air", Chapter 2, Part II, Vol. I, *Effects of Impact and Explosions*, Summary Tech. Report of Div. 2, NDRC, Washington, D.C., 1946.

2. R. G. Stoner and W. Bleakney, "The Attenuation of Spherical Shock Waves in Air", *Journal of Applied Physics*, 19, pp. 670-678 (July 1948).

3. E. M. Fisher and J. F. Pittman, *Air Blast Resulting from the Detonation of Small TNT Charges*, NAVORD Report 2890, U.S. Naval Ordnance Laboratory, White Oak, Maryland, July 1953. AD-208 580.

4. H. J. Goodman, *Compiled Free-Air Blast Data on Bare Spherical Pentolite*, BRL Report No. 1092, Feb. 1960, AD-235 278.

5. M. Lutzky, *Theoretical Versus Experimental Results for Air Blast from One-Pound Spherical TNT and Pentolite Charges at Sea Level Conditions*, NOLR 65-57, July 1965. AD-619 438.

6. E. J. Bryant, N. H. Ethridge, and J. H. Keefer, *Measurements of Air-Blast Phenomena with Self-Recording Gages*, WT-1155, Feb.-May 1955, AD-617 170.

7. C. N. Kingery, *Parametric Analysis of Sub-Kiloton Nuclear and High Explosive Air Blast*, BRL Report No. 1393, Feb. 1968, AD-833 698.

8. N. A. Haskell, J. A. Fava, and R. M. Brubaker, *Measurement of Free Air Atomic Blast Pressures*, WT-1101, Operation TEAPOT-Project 1.1, Headquarters Field Command, Armed Forces Special Weapons Project, Sandia Base, Albuquerque, New Mexico, Feb. 1958, AD-460 280.

9. C. N. Kingery, *Air Blast Parameters Versus Distance for Hemispherical TNT Surface Bursts*, BRL Report No. 1344, Sept. 1966.

10. R. E. Reisler, J. H. Keefer, and L. Giglio-Tos, *Basic Air Blast Measurements from a 500-ton TNT Detonation Project 1.1 Operation Snowball*, BRL Memorandum Report No. 1818, Dec. 1966.

11. J. M. Dewey, "The Air Velocity in Blast Waves from TNT Explosions", *Proc. of the Royal Soc.*, A, 279, pp. 366-385 (1964).

12. W. A. Anson and J. M. Dewey, *Density Measurements in the Blast Wave from a Surface Burst 500-ton TNT Hemispherical Charge*, Suffield Technical Paper No. 305, S.E.S., Ralston, Alberta, Canada, Aug. 1965.

13. R. E. Reisler, L. Giglio-Tos, and R. C. Kellner, *Ferris Wheel Series, Flat Top Event, Project Officers Report - Project 1.1, Airblast Phenomena*, POR-3001, Oct. 1966, AD-801 665.

14. E. J. Bryant, R. A. Eberhard, and C. N. Kingery, *Mach Reflection Over Hard Packed Dirt and Dry Sand*, BRL Report No. 809, July 1952.

15. S. D. Schleuter, R. G. Hippensteel, and B. F. Armendt, *Measurements of Air Blast Parameters Above a Reflecting Surface*, BRL Memorandum Report No. 1645, April 1965.

16. A. J. Hoffman and S. N. Mills, Jr., *Air Blast Measurements About Explosive Charges at Side-On and Normal Incidence*, BRL Report No. 988, July 1956.

17. O. T. Johnson, J. D. Patterson, II, and W. C. Olson, *A Simple Mechanical Method for Measuring the Reflected Impulse of Air Blast Waves*, BRL Memorandum Report No. 1088, July 1957, (also, *Proc. of 3rd U. S. Nat. Cong. of Appl. Mech.*, ASME, New York, pp. 203-207, June 1958).

18. W. Olson and J. Wenig, *A Double-Charge Technique to Measure Face-On Blast*, BRL Memorandum Report No. 1347, May 1966.

19. W. H. Jack, Jr., *Measurements of Normally Reflected Shock Waves from Explosive Charges*, BRL Memorandum Report No. 1499, July 1963, AD-422 866.

20. R. G. Sachs, *The Dependence of Blast on Ambient Pressure and Temperature*, BRL Report No. 466, May 1944.

21. J. Dewey and J. Sperrazza, *The Effect of Atmospheric Pressure and Temperature on Air Shock*, BRL Report No. 721, May 1950.

22. W. C. Olson, J. D. Patterson II, and J. S. Williams, *The Effect of Atmospheric Pressure on the Reflected Impulse from Air Blast Waves*, BRL Memorandum Report No. 1241, Jan. 1960.

23. J. M. Dewey, O. T. Johnson, and J. D. Patterson II, *Mechanical Impulse Measurements Close to Explosive Charges,* BRL Report No. 1182, November 1962.

24. W. H. Jack, Jr., and B. F. Armendt, Jr., *Measurements of Normally Reflected Shock Parameters from Explosive Charges Under Simulated High Altitude Conditions*, BRL Report No. 1280, April 1965.

25. J. G. Schmidt, *Interim Report, Phase I and II, Project BANSHEE*, BRL Memorandum Report No. 1413, DASA Report No. 1293, Aberdeen Proving Ground, Md., June 1962,. AD-287 140.

26. C. Wilton and K. Kaplan, *Preliminary Investigation of Pulse Shapes from a Near-Simultaneous Detonation of Two High-Explosive Charges in a Barricaded Enclosure,* Final Report URS 649A-1, URS, Burlingame, Cal., April 1966.

27. URS Research Company, *Evaluation of Explosives Simultaneity Tests,* NWC TP 4720, Naval Weapons Center, China Lake, Cal., May 1969.

28. T. A. Zaker, *Blast Pressures from Sequential Explosions,* Final Report J6166, IITRI, October 1969.

CHAPTER 6

COMPILED AIR BLAST PARAMETERS

6-0 LIST OF SYMBOLS

a_0 = sound velocity in ambient air

b = constant related to initial decay of side-on overpressure

B = a constant in an asymptotic relation for $\bar{P}_s$

d = horizontal distance for oblique shocks

e = specific internal energy in air

e_0 = specific internal energy in ambient air

E = explosive charge energy

g_0 = acceleration of gravity at sea level

H = height of burst

I_r = reflected specific positive impulse

I_s = side-on specific positive impulse

p_0 = ambient atmospheric pressure

p_r = reflected overpressure

p_s = side-on overpressure

P_r = peak reflected overpressure

P_s = peak side-on overpressure

q = dynamic pressure

Q = peak dynamic pressure

R = distance

$\bar{R}, \bar{t}, \bar{P}_s, \bar{P}_r$, etc. = dimensionless quantities associated with corresponding dimensional quantities (see Table 6-2)

t = time

t_a = arrival time

T_r = duration of positive phase of reflected overpressure

T_s = duration of positive phase of side-on overpressure

u = particle velocity

u_0 = particle velocity ahead of shock front

u_s = peak particle velocity

U = shock velocity

V = volume

W = explosive charge weight (mass)

Z = Hopkinson-scaled distance

α_2 = angle of reflection of oblique shock

α_{ex} = extreme angle for regular reflection

α_I = angle of incidence of oblique shock

γ = ratio of specific heats

η = scaled time

θ = temperature

θ_0 = temperature in ambient air

θ_r = peak temperature in reflected wave

θ_s = peak temperature in side-on blast wave

ρ = density

ρ_E = density of explosive

ρ_0 = density of ambient atmosphere

ρ_r = peak density in reflected wave

ρ_s = peak density in side-on blast wave

τ = modified scaled time

6-1 GENERAL

In previous chapters, we have discussed both air blast theory and experimentation, with descriptions of results obtained by a number of investigators. The actual values of parameters which characterize air blast waves, of course, differ from one set of computations or experimental results to another, so that one can obtain considerably different predictions of peak overpressures, impulses, durations, etc. from different sources of original work. We feel that a more or less "standard" set of parameters – defined over as wide a range as possible of source energies, distances, and times – would prove very helpful to scientists and engineers engaged in air blast studies. These parameters should be presented in both tabular and graphical form, in much the same manner as the properties of steam are presented in steam tables and Mollier diagrams. This chapter will be devoted to a discussion of the limitations of current references which present compiled blast parameters, the manner in which we have generated such "standard" parameters, and tables and both small-scale and large-scale graphs presenting the data. Particular emphasis has been given to making the data as internally consistent as possible, and to coverage of a very wide range of input parameters.

6-2 SOURCES OF COMPILED DATA ON AIR BLAST

The most widely used sources for air blast properties are probably Goodman's compiled data for Pentolite[1], Brode's theoretical predictions for point and distributed sources[2,3], and *The Effects of Nuclear Weapons*[4]. Goodman reports primarily experimental data on bare spherical Pentolite charges, giving properties for both free air and normally reflected blast waves. He does supplement the experimental results with values for shock velocity and arrival time, derived from application of the Rankine-Hugoniot conditions to the experimental curve for peak side-on overpressure versus distance. He reports his data in both tabular and graphical form. For many of the parameters presented by Goodman[1], the range of distances or energies is somewhat limited, in accord with the limits of the original experiments which he has compiled. Brode,[2,3] gives his results in purely graphical form, on plots which are reproduced on such a small scale that accurate reading is quite difficult. His curves do cover a rather large range of scaled distances, and he presents some parameters which Goodman does not, because they are more easily computed than measured. All of Brode's data represent the blast waves from free-air sources. The blast data in *Effects of Nuclear Weapons*[4] also are given in purely graphical form, on small plots which obviate accurate reading. Because original work is not properly referenced in that publication, it is impossible to ascertain whether the curves are based on theory, or experiment, or a combination of both. The data in Ref. 4 are given for ground burst of nuclear blast sources.

In an attempt to generate air blast data in a form which would allow relatively rapid

estimation of various blast wave parameters for a moving target, Baker and Schuman[5] generated graphical plots of both blast front parameters and time histories of overpressure, density, and particle velocity, based partly on Goodman's compiled experimental data[1], and partly on Brode's theoretical calculations[3]. These authors noted that their data were *not* internally consistent, because the properties at the front were based on experimental data alone and the time histories were based primarily on adjusted theoretical calculations. They also noted that there were internal inconsistencies in Brode's work. Mills, et al.[6] generated similar graphical plots of blast parameters for TNT, by "marrying" experimental data from a variety of sources with a set of theoretical calculations performed by Lehto and Lutzky[7]. Their curves cover a considerably wider range of scaled distances than does Ref. 5, and the data are internally consistent from plot to plot and agree with the Rankine-Hugoniot conditions at the shock front. Finally, Ruetenik and Lewis[8] have proposed an interesting method of graphical presentation of blast data which is a modification of the more usual presentations of the scaled distance-time plots of Refs. 5 and 6, by introducing a modified scaled time τ defined by

$$\tau = \eta - Z \tag{6-1}$$

where

$\eta = t/W^{1/3}$

$Z = R/W^{1/3}$

t = time

W = explosive charge weight

R = distance

These authors claim better reading accuracy from plots made on a (Z, τ) coordinate system than from conventional plots on a (Z, η) system.

6-3 GENERATION OF TABLES AND GRAPHS OF AIR BLAST WAVE PROPERTIES

The air blast parameters which we will present in tables in this chapter and in the large graphs in the envelope in the back cover have been generated in much the same manner as in Ref. 6, i.e., by combination of experiment with theory, and iterative adjustment of the two. They differ from the data of Ref. 6 primarily in the inclusion of additional parameters, in coverage of a wider range of scaled distances, and in omission of time-distance plots. First, we will present the parameters associated with the shock front, including shock velocity and peak values of side-on and reflected overpressure, dynamic pressure, density, and temperature. Next, we will give data for durations of both side-on and reflected overpressure, and the integrated quantities side-on and reflected impulse. Initial decay of side-on overpressure also is presented as a parameter.

Because we wish to present the blast parameters in dimensionless form, we will use the Sachs-scaled parameters for many plots even though this scaling law does not apply for strong shocks (see Chapter 3). It is possible to present Hopkinson-scaled parameters in dimensionless form (see also Chapter 3), but this form would be unfamiliar to the majority of air blast investigators. The basic blast sources for all data are bare Pentolite spheres detonated under standard sea level ambient conditions. Standard conditions taken from Ref. 9, are:

Density $\rho_0 = 1.146277 \times 10^{-7}$ $lb_f sec^2/in.^4$

Gravitational acceleration $g_0 = 386.08859$ in./sec^2

Pressure $p_0 = 14.695951$ $lb_f/in.^2$

Sound speed $a_0 = 13397.324$ in./sec

Temperature $\theta_0 = 518.688°R = 59.0°F$

Some data in the literature are presented in terms of charge radii, and many more in terms of charge weight W. We will use energy E exclusively. For conversion to charge radius or weight, one needs to know explosive density and specific energy release per unit weight, mass, or volume. Densities, energies of detonation per unit weight and volume, and radii of spheres weighing one pound are given in Table 6-1 for a few common explosives. Similar values for many other condensed chemical explosives can be calculated easily from data in Ref. 10.

In the graphs and tables in this chapter, quantities with a bar – i.e., $\bar{p}, \bar{u}$, etc. – designate the Sachs-scaled dimensionless values, for which no dimensions need be given. Quantities without bars are dimensional, and dimensions will usually be given in the English system of lb_f, in., and sec. (If the subscript is omitted in units for pounds, pound *force* is implied.) The nondimensional parameters that will be presented in this chapter are listed and defined in Table 6-2.

6-3.1 SHOCK-FRONT PARAMETERS

The first blast parameters which will be documented are the shock-front parameters for incident and normally reflected blast waves. The tables and curves for these parameters will be presented over as wide a range of scaled distances as possible, using sources of compiled data and theory, as necessary. The basic blast source will be assumed to be bare, spherical Pentolite and all parameters will be presented for free-air bursts under standard ambient conditions.

Once one of the front parameters for incident waves has been determined as a function of scaled distance, all other parameters can be computed using the Rankine-Hugoniot conditions and a simple integration scheme. For completeness, the basic equations are given as Eq. 6-2 under the assumption of zero particle velocity ahead of the shock front ($u_0 = 0$), followed by forms derived from Eq. 6-2, for air behaving as a perfect gas with ratio of specific heats equal to γ (see Ref. 11):

6-3.1.1 RANKINE-HUGONIOT EQUATIONS.

These equations hold for a unit mass of material.

$$\left.\begin{aligned} &\text{Mass:} \\ &\rho_s (U - u_s) = \rho_0 U \\ &\text{Momentum:} \\ &\rho_s (U - u_s)^2 + p_s = \rho_0 U^2 + p_0 \\ &\text{Energy:} \\ &(U - u_s)^2/2 + e + p_s/\rho_s = U^2/2 \\ &\qquad + e_0 + p_0/\rho_0 \end{aligned}\right\} \quad (6\text{-}2)$$

TABLE 6-1

EXPLOSIVE PROPERTIES

Explosive	Specific Gravity	Density ρ_E, $lb_f sec^2/in.^4$	Weight Specific Energy, E/W, $in.\text{-}lb_f/lb_m$	Volume Specific Energy, E/V, $in.\text{-}lb_f/in.^3$	Radius r of 1-lb Sphere, in.
Pentolite (50/50)	1.66	1.551×10^{-4}	20.50×10^6	1.230×10^6	1.584
TNT	1.60	1.496×10^{-4}	18.13×10^6	1.048×10^6	1.604
RDX	1.65	1.542×10^{-4}	21.5×10^6	1.283×10^6	1.588
Comp B (60/40)	1.69	1.580×10^{-4}	20.8×10^6	1.271×10^6	1.575
HBX-1	1.69	1.580×10^{-4}	15.42×10^6	0.944×10^6	1.575

6-3.1.2 EXPRESSIONS FOR PERFECT GAS IN TERMS OF OVERPRESSURE ($\bar{P}_s \leq 3.5$)

$$\bar{u}_s^2 = \frac{2\bar{P}_s^2}{\gamma[(\gamma+1)\bar{P}_s + 2\gamma]} \tag{6-3}$$

$$\bar{U}^2 = 1 + \frac{\gamma+1}{2\gamma}\bar{P}_s \tag{6-4}$$

$$e - e_0 = \frac{a_0^2\,\bar{P}_s(\bar{P}_s+2)}{\gamma[(\gamma+1)\bar{P}_s + 2\gamma]} \tag{6-5}$$

$$\bar{\rho}_s = \frac{(\gamma+1)\bar{P}_s + 2\gamma}{(\gamma-1)\bar{P}_s + 2\gamma} \tag{6-6}$$

$$\bar{\theta}_s - 1 = \frac{(\gamma-1)(\bar{P}_s+2)}{(\gamma+1)\bar{P}_s + 2\gamma} \tag{6-7}$$

6-3.1.3 EXPRESSIONS FOR PERFECT GAS IN TERMS OF SHOCK VELOCITY ($U < 2.0$)

$$\bar{P}_s = \frac{2\gamma}{\gamma+1}(\bar{U}^2 - 1) \tag{6-8}$$

TABLE 6-2

SACHS' SCALED NONDIMENSIONAL BLAST PARAMETERS

Parameter	Symbol	Equation
Peak side-on overpressure	$\bar{P}_s$	P_s/p_0
Peak normally reflected overpressure	$\bar{P}_r$	P_r/p_0
Peak dynamic pressure	$\bar{Q}$	Q/p_0
Side-on overpressure	$\bar{p}_s$	p_s/p_0
Normally reflected overpressure	$\bar{p}_r$	p_r/p_0
Dynamic pressure	$\bar{q}$	q/p_0
Density	$\bar{\rho}$	ρ/ρ_0
Temperature	$\bar{\theta}$	θ/θ_0
Shock velocity	$\bar{U}$	U/a_0
Peak particle velocity	$\bar{u}_s$	u_s/a_0
Particle velocity	$\bar{u}$	u/a_0
Time of arrival	$\bar{t}_a$	$t_a a_0 p_0^{1/3}/E^{1/3}$
Duration of side-on overpressure	$\bar{T}_s$	$T_s a_0 p_0^{1/3}/E^{1/3}$
Duration of reflected overpressure	$\bar{T}_r$	$T_r a_0 p_0^{1/3}/E^{1/3}$
Scaled time	$\bar{t}$	$t a_0 p_0^{1/3}/E^{1/3}$
Side-on positive impulse*	$\bar{I}_s$	$I_s a_0/(p_0^{2/3}E^{1/3})$
Normally reflected positive impulse*	$\bar{I}_r$	$I_r a_0/(p_0^{2/3}E^{1/3})$
Scaled distance	$\bar{R}$	$R p_0^{1/3}/E^{1/3\ 1/3}$
Initial decay of pressure	$\bar{b}$	[See Eq. 6-30]
Scaled height of burst	$\bar{H}$	$H p_0^{1/3}/E^{1/3}$

*I_s and I_r are *specific* impulses, having dimensions of FT/L^2, rather than true impulses with dimensions of FT.

$$\bar{u}_s = \frac{2}{\gamma+1}\left[\bar{U} - (1/\bar{U})\right] \qquad (6\text{-}9)$$

$$\bar{P}_s = \frac{(\gamma+1)\,\bar{U}^2}{(\gamma-1)\,\bar{U}^2 + 2} \qquad (6\text{-}10)$$

$$\bar{\theta}_s - 1 = \frac{2(\bar{U}^2-1)(\gamma-1)}{(\gamma+1)^2\,\bar{U}^2}\,(\gamma\,\bar{U}^2+1) \qquad (6\text{-}11)$$

Shear and Day in Ref. 11 present tables of shock-front Hugoniots for air, for both strong and weak shocks. "Real" air properties, including effects of dissociation and ionization at high pressures and temperatures, were considered in use of Eqs. 6-2 to obtain these properties for values of $\bar{P}_s > 3.5$. We will use data of Ref. 11 to obtain all properties except $\bar{P}_s$, and extend the data in that reference by Eqs. 6-3 through 6-11. For weak shocks, acoustic approximations developed from these latter equations will be used. Somewhat arbitrarily, we will assume that the acoustic approximations hold for $\bar{P}_s \leqslant 10^{-3}$. These asymptotes are:

$$\bar{P}_s = \frac{0.1153}{\bar{R}} \qquad (6\text{-}12)^*$$

$$\bar{u}_s = \frac{\bar{P}_s}{\gamma} = \frac{0.0824}{\bar{R}} \qquad (6\text{-}13)$$

$$\bar{\rho}_s = 1 + \frac{\bar{P}_s}{\gamma} = 1 + \frac{0.0824}{\bar{R}} \qquad (6\text{-}14)$$

$$\left.\begin{aligned}\bar{U} &= 1 + \left(\frac{\gamma+1}{4\gamma}\right)\bar{P}_s \\ &= 1 + \frac{0.0494}{\bar{R}}\end{aligned}\right\} \qquad (6\text{-}15)$$

$$\left.\begin{aligned}\bar{\theta}_s &= 1 + \left(\frac{\gamma-1}{\gamma}\right)\bar{P}_s \\ &= 1 + \frac{0.0330}{\bar{R}}\end{aligned}\right\} \qquad (6\text{-}16)$$

*Note: The constant is determined empirically.

The basic front parameter will be assumed to be scaled peak side-on overpressure $\bar{P}_s$, because most experimental data and theoretical predictions center on this parameter. There are many measurements of $\bar{P}_s$ for bare, spherical Pentolite detonated in free air from the surface of the explosive out to values $\bar{R}$ of about 4. The majority of these are reported, and a curve fitted to them, by Goodman in Ref. 1. This could be used to describe completely the functional dependence of $\bar{P}_s$ with $\bar{R}$. But unfortunately, Goodman adjusts his curve to fit an asymptotic relationship at large $\bar{R}$ of a form

$$\bar{P}_s = A/\left\{\bar{R}[\ln(\bar{R}/B)]^{1/2}\right\} \qquad (6\text{-}17)$$

The author feels that this form is physically incorrect because it does not agree with the acoustic approximation of Eq. 6-12.

An alternative curve for $\bar{P}_s$ versus $\bar{R}$, extending over a very large range of the dependent variable, is generated by Lehto and Larson[12] for TNT spheres detonated in air. This curve is based entirely on numerical computations using the von Neumann-Richtmyer artificial viscosity method, which is discussed in Chapter 4. When curves from Refs. 1 and 12 are compared, the pressures are seen to be greater for Goodman's curve for small $\bar{R}$, to agree almost exactly over an intermediate range, and then to be significantly greater again for Goodman's curve for $\bar{R} > 0.6$. The curve from Ref. 12 approaches the asymptote of Eq. 6-12. The very limited data for $\bar{R} > 3$ agree much better with the Lehto and Larson curve.

The relationship which we use to define the variation of $\bar{P}_s$ with $\bar{R}$ is a combination of those given in Refs. 1 and 12, designed to fit available experimental data as well as possible over the entire range, and to approach acoustic asymptotes for very large $\bar{R}$. The range of definition is from $\bar{R} = 0.01423$ (surface of explosive) to $\bar{R} = 1004$, with Ref. 1 controlling over the inner range. For $\bar{R} > 1004$, Eqs.

6-12 through 6-16 define the acoustic wave.

As noted previously, all other front parameters for the incident wave can be determined once $\bar{P}_s$ is defined. For values of $\bar{R}$ from 0.01423 to 1.2, the parameters $\bar{u}_s$, $\bar{U}$, $\bar{\rho}_s$ and $\bar{\theta}_s$ are determined from the Hugoniot tables in Ref. 11. For larger $\bar{R}$, Eqs. 6-3 through 6-7 are used, with $\gamma = 1.4$. Peak dynamic pressure $\bar{Q}$ is obtained from $\bar{u}_s$ and $\bar{\rho}_s$ using the definition

$$\bar{Q} = \frac{\gamma}{2} \bar{\rho}_s \bar{u}_s^2 \qquad (6\text{-}18)$$

Scaled arrival time for the shock front, based on a zero of shock arrival at the explosive surface, can be obtained directly from Ref. 1 out to $\bar{R} = 0.244$. For larger scaled distances, this parameter is obtained by integrating the incremental relationship

$$\Delta \bar{t}_a = \frac{\Delta \bar{R}}{\bar{U}_{av}} \qquad (6\text{-}19)$$

and adding the increments in arrival time to the value at $\bar{R} = 0.244$. All front parameters are given numerically in Table 6-3 and graphically in Fig. 6-1. This figure is reproduced in small scale in the text, and also in large-scale graphs which can be read to three significant figures, in a pocket inside the back cover of this Handbook.

Parameters immediately behind the shock fronts which are normally reflected from a rigid wall can be determined from knowledge of the incident front parameters and from the boundary condition that $u = 0$ during reflection. Measurements have been made of peak reflected overpressure P_r up to 27,000 psi by Jack[13]; and Shear and McCane[14] have used the tables of Ref. 11 plus thermodynamic properties of real air to calculate pressures, densities, and temperatures behind reflected shocks. In Ref. 14, $\bar{P}_r$ is limited to values of less than 1000 because no real air data exist above this pressure at temperatures existing in reflected shocks. For values of $\bar{P}_r < 3.5$, equations for normally reflected shock front parameters in a perfect gas will hold. These are[15]:

$$\bar{P}_r = 2\bar{P}_s + \frac{(\gamma+1)\bar{P}_s^2}{(\gamma-1)\bar{P}_s + 2\gamma} \qquad (6\text{-}20)$$

$$\bar{\rho}_r = \frac{\gamma(\bar{P}_s+1)\ [(\gamma+1)\bar{P}_s + 2\gamma]}{[(\gamma-1)\bar{P}_s + \gamma]\ [\gamma-1)\bar{P}_s + 2\gamma]} \qquad (6\text{-}21)$$

$$\bar{\theta}_r = \frac{[(\gamma-1)\bar{P}_s + \gamma]\ [(3\gamma-1)\bar{P}_s + 2\gamma}{\gamma\,[(\gamma+1)\bar{P}_s + 2\gamma]} \qquad (6\text{-}22)$$

The acoustic asymptotes for these parameters are:

$$\bar{P}_r = 2\bar{P}_s = \frac{0.2306}{\bar{R}} \qquad (6\text{-}23)$$

$$\left.\begin{aligned} \bar{\rho}_r &= 1 + 2\bar{P}_s/\gamma \\ &= 1 + \frac{0.1648}{\bar{R}} \end{aligned}\right\} \qquad (6\text{-}24)$$

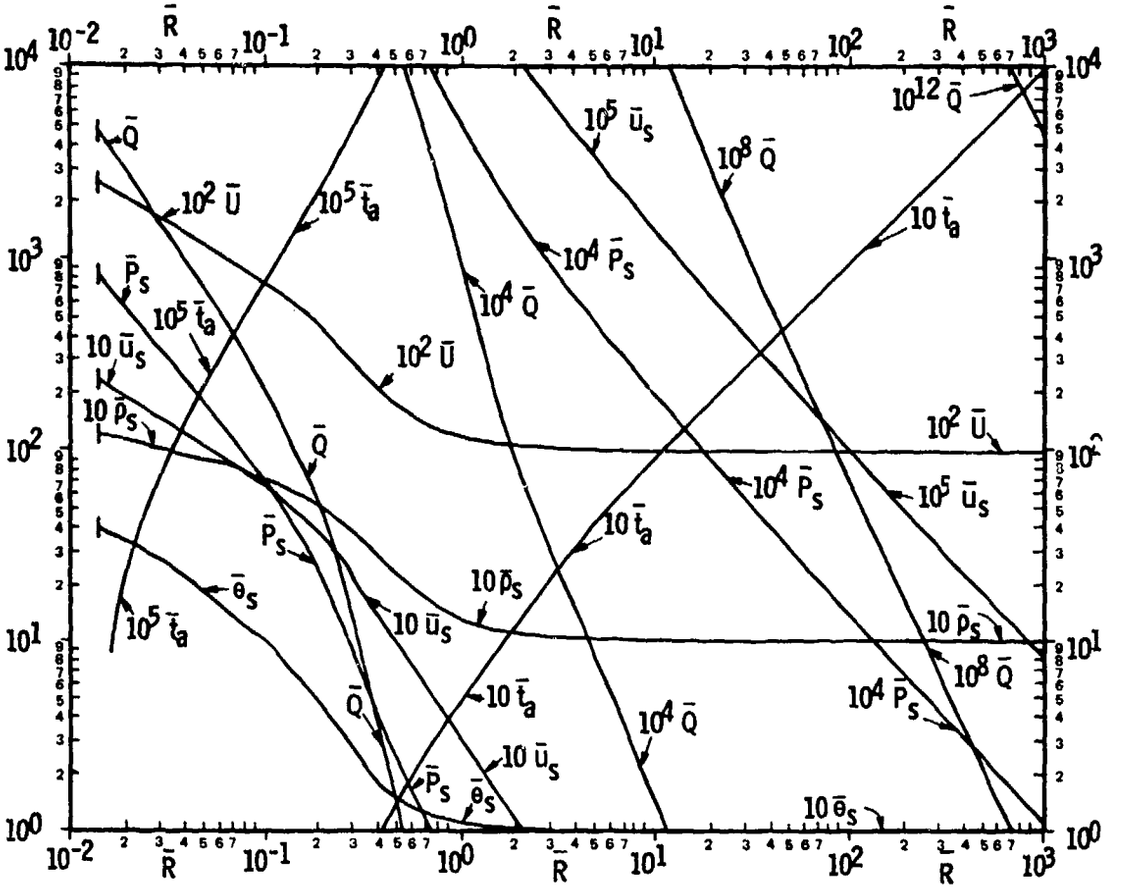
$$\left.\begin{aligned} \bar{\theta}_r &= 1 + 2(\gamma-1)\bar{P}_s/\gamma \\ &= 1 + \frac{0.0660}{\bar{R}} \end{aligned}\right\} \qquad (6\text{-}25)$$

Front parameters for normally reflected waves are given in functions of $\bar{R}$ in Table 6-4, and graphically in Fig. 6-2, based on Jack's data[13] for $\bar{P}_r$ for high pressures, Shear and McCane's calculations[14] for intermediate pressures, and Eqs. 6-20 through 6-25 at low pressures.

TABLE 6-3 SCALED SHOCK-FRONT PARAMETERS FOR INCIDENT BLAST WAVES

$\bar{R}$	$\bar{P}_s$	$\bar{u}_s$	$\bar{U}$	$\bar{t}_a$	$\bar{\rho}_s$	$\bar{Q}$	$\bar{\theta}_s$
0.01423	819	23.2	25.2	0	12.18	4570	39.9
0.016	703	31.5	23.6	7.16-5*	11.9	3850	36.7
0.018	605	19.8	21.9	1.66-4	11.6	3240	34.7
0.020	531	18.6	20.6	2.58-4	11.3	2760	33.1
0.030	324	14.4	16.1	8.05-4	10.1	1450	26.0
0.040	225	12.0	13.5	1.48-3	9.28	935	21.1
0.050	170	10.4	11.7	2.27-3	8.88	670	17.7
0.100	67.9	6.47	7.50	7.62-3	7.02	205	9.85
0.150	37.2	4.61	5.55	1.54-2	5.91	87.2	6.20
0.200	20.4	3.50	4.27	2.55-2	4.92	44.1	4.31
0.250	11.9	2.69	3.33	3.82-2	4.20	20.8	3.21
0.300	7.28	1.95	2.66	5.41-2	3.59	9.45	2.48
0.400	3.46	1.25	2.00	9.90-2	2.66	2.79	1.68
0.500	2.05	0.888	1.67	0.157	2.09	1.08	1.43
0.600	1.38	0.672	1.48	0.218	1.81	0.570	1.30
0.800	0.772	0.427	1.28	0.340	1.49	0.212	1.18
1.00	0.506	0.302	1.19	0.466	1.33	9.40-2*	1.12
1.50	0.254	0.165	1.11	0.830	1.17	1.96-2	1.07
2.00	0.161	0.107	1.0733	1.26	1.11	7.58-3	1.0436
2.50	0.115	0.0797	1.0481	1.71	1.0809	4.23-3	1.0306
3.00	0.0889	0.0631	1.0374	2.20	1.0628	2.70-3	1.0247
4.00	0.0616	0.0441	1.0257	3.21	1.0436	1.37-3	1.0172
5.00	0.0468	0.0336	1.0198	4.21	1.0332	8.20-4	1.0134
6.00	0.0374	0.0268	1.0159	5.19	1.0266	5.15-4	1.0107
8.00	0.0261	0.0190	1.0111	7.15	1.0186	2.50-4	1.00745
10.0	0.0198	0.0144	1.00850	9.10	1.0141	1.43-4	1.00565
20.0	8.70-3*	6.21-3*	1.00372	18.9	1.00620	2.76-5	1.00248
30.0	5.43-3	3.90-3	1.00232	28.8	1.00387	1.07-5	1.00155
40.0	3.91-3	2.79-3	1.00167	38.9	1.00279	5.52-6	1.00112
50.0	3.04-3	2.17-3	1.00130	48.9	1.00217	3.31-6	1.000870
60.0	2.48-3	1.77-3	1.00106	58.8	1.00177	2.19-6	1.000709
80.0	1.81-3	1.28-3	1.000618	78.5	1.00103	1.15-6	1.000413
100	1.41-3	1.00-3	1.000494	98.5	1.000824	6.95-7	1.000330
500	2.42-4	1.73-4	1.0000988	499	1.000173	2.03-8	1.0000660
1000	1.153-4	8.20-5	1.0000494	1000	1.0000824	4.71-9	1.0000330

Digits preceded by minus sign indicate negative powers of 10.



This chart is reproduced to a larger scale located in the rear of the handbook.

Figure 6-1. Compiled Shock-front Parameters for Incident Air Blast Waves

6-3.2 IMPULSES AND DURATIONS

The second class of blast parameters to be presented includes some of the quantities that can be abstracted from experimental data and theoretical predictions behind incident and normally reflected shock fronts. Theoretically, one could present data for durations of positive phases of overpressure, density in excess of ambient, particle velocity, temperature in excess of ambient, etc., in addition to integrated quantities over these durations. Also, it is theoretically possible to report negative phase amplitudes and durations of various quantities. We will, however, limit our presentation to those quantities for which sufficient experimental data exist to assure reasonably good correlation with theory. Theoretical estimates will only be used to extend data to acoustic asymptotes at large $\bar{R}$.

The parameters reported are scaled impulses and durations for positive phases of side-on and normally reflected blast waves. They are given numerically in Table 6-5 and graphically in Fig. 6-3 for a large range of $\bar{R}$. Two sources of data are used for side-on duration and impulse, $\bar{T}_s$ and $\bar{I}_s$; these are Goodman[1] and Kingery[16]. The former includes scaled data for Pentolite spheres detonated in free air, and the latter gives data from large, hemispherical charges of TNT detonated on the ground. To convert to "equivalent" free-air Pentolite data, the data of Ref. 16 are converted by multiplying blast energies by appropriate ratios of weight specific energy from Table 6-1 and by a ground reflectivity factor of 1.8.

Data for $\bar{I}_s$ from Refs. 1 and 16 agree quite closely, with the data from Ref. 16 extending

to much greater $\bar{R}$. These data are extended to merge smoothly with a straight line of slope minus one on a logarithmic plot of $\bar{I}_s$ versus $\bar{R}$ beyond $\bar{R} = 500$. This corresponds to an acoustic asymptote at large $\bar{R}$, given by

$$\bar{I}_s = \frac{2.88 \times 10^{-2}}{\bar{R}} \qquad (6\text{-}26)$$

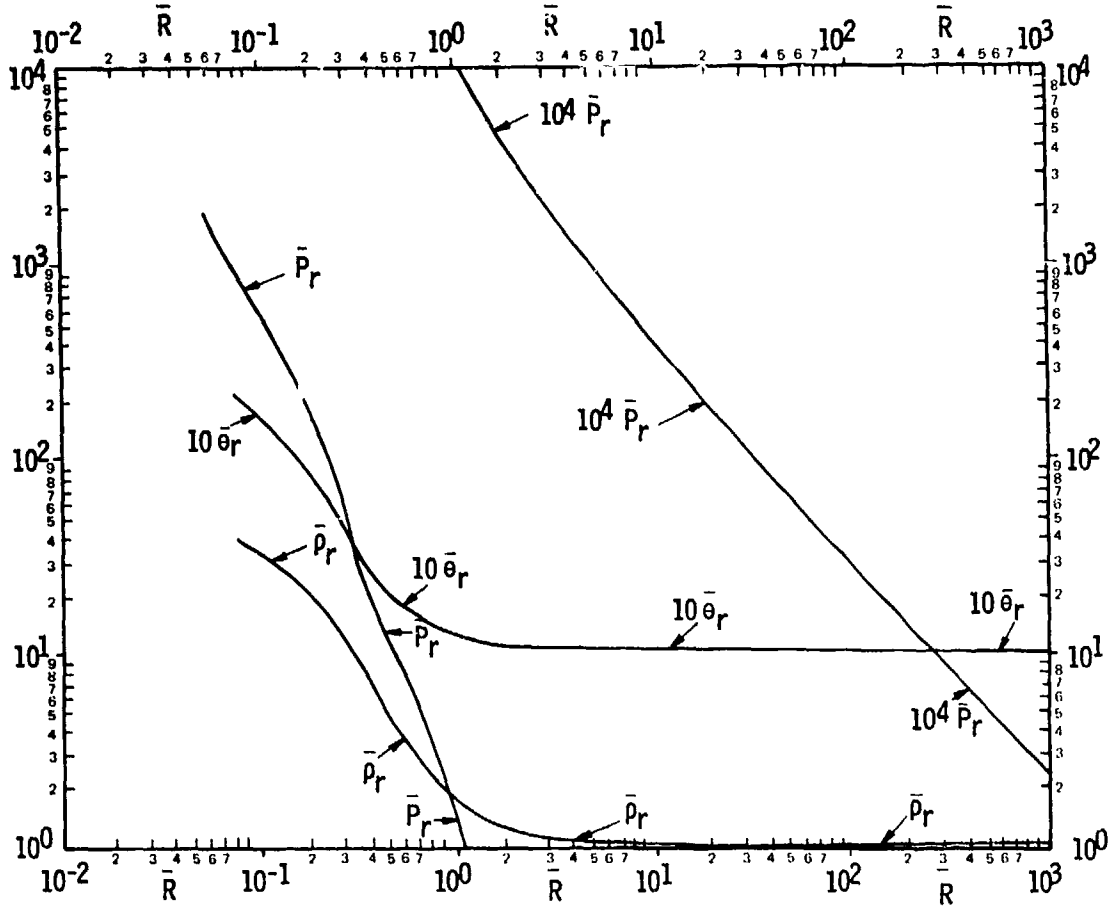
Although side-on impulse data from the two references agree quite well, side-on duration data do not. These are large differences for values of $\bar{R} < 0.8$, with Goodman's data lying well below that of Kingery. The reasons for these discrepancies are not clear, but a possible explanation is a difference in accounting for the effect of second shocks in lengthening the positive phase when they arrive before pressure has decreased to ambient. Perhaps these were ignored in Ref. 1 and accounted for in Ref. 16. The data that we will present here are essentially those of Kingery[16], because they represent later measurements and because they cover a much wider range of $\bar{R}$. At large $\bar{R}$, the experimental curve for $\bar{T}_s$ has been extended by a smooth curve fitted by eye to a horizontal asymptote at $\bar{R} = 1000$.

Reflected impulses and durations have been measured by a number of investigators at

TABLE 6-4. SCALED SHOCK-FRONT PARAMETERS FOR REFLECTED BLAST WAVES

$\bar{R}$	$\bar{P}_r$	$\bar{\rho r}$	$\bar{\theta}_r$
0.0538	1840	–	. .
0.070	1110	–	–
0.080	860	37.8	20.7
0.100	585	33.2	16.8
0.150	277	24.4	12.1
0.200	146	18.1	7.46
0.250	80.3	13.5	5.15
0.300	37.7	10.0	3.71
0.400	15.3	6.10	2.42
0.500	9.40	4.16	1.90
0.600	6.05	3.14	1.65
0.800	2.63	2.12	1.39
1.00	1.31	1.66	1.26
1.50	0.580	1.32	1.13
2.00	0.358	1.22	1.088
2.50	0.250	1.16	1.0612
3.00	0.188	1.12	1.0594
4.00	0.126	1.087	1.0344
5.00	9.48-2*	1.0664	1.0268
6.00	7.65-2	1.0532	1.0214
8.00	5.36-2	1.0392	1.0149
10.0	4.01-2	1.0282	1.0113
20.0	1.76-2	1.0124	1.00496
30.0	1.10-2	1.00774	1.00310
40.0	7.88-3	1.00558	1.00224
50.0	6.12-3	1.00434	1.00174
60.0	4.96-3	1.00354	1.00142
80.0	3.58-3	1.00206	1.000825
100	2.80-3	1.00165	1.000660
500	4.86-4	1.000330	1.000132
1000	2.31-4	1.000165	1.0000660

*Digits preceded by minus sign indicate negative powers of 10.



This chart is reproduced to a larger scale located in the rear of the handbook.

Figure 6-2. Compiled Shock — front Parameters for Normally Reflected Air Blast Waves

BRL (see Chapter 5). These data are gathered in Ref. 13, and this reference has been used to generate the curves and numerical values of $\bar{I}_r$ and $\bar{T}_r$. No extension has been made for the latter parameter, but $\bar{I}_r$ has been extended to large $\bar{R}$ by using the approximate relation

$$\bar{I}_r = \bar{I}_s \frac{\bar{P}_r}{\bar{P}_s} \qquad (6\text{-}27)$$

over the range of $0.6 \leqslant \bar{R} \leqslant 100$. Beyond this range, the acoustic approximation

$$\bar{I}_r = 2\,\bar{I}_s \qquad (6\text{-}28)$$

is sufficiently accurate and has been used. Although no data exist for $\bar{T}_r$ beyond $\bar{R} = 0.7$, Hoffman and Mills'[17] experiments indicate that durations are not greatly different from durations of side-on waves. One can, therefore, use the curves and tabular data for $\bar{T}_s$ to estimate $\bar{T}_r$ for $\bar{R} > 0.7$.

6-3.3 TIME CONSTANT AND INITIAL DECAY RATE

Refs. 5 and 6 present compiled blast parameters in graphical plots, in the scaled distance $\bar{R}$ versus scaled time $\bar{t}$ domain, of scaled physical quantities such as side-on overpressure $\bar{p}_s$, particle velocity $\bar{u}$, dynamic pressure $\bar{q}$, temperature $\bar{\theta}$, and density $\bar{\rho}$. The curves in Ref. 6 are consistent with the shock front parameters in that reference, but not necessarily with the parameters presented in Figs. 6-1 through 6-3. Rather than present scaled $\bar{R} - \bar{t}$ plots here, we instead calculate an additional parameter which will allow the reader to generate his own time histories for the positive phase of side-on overpressure.

The empirical Friedlander equation of Chapter 1,

$$\left.\begin{aligned}\bar{p}_s &= \bar{P}_s\left(1-\frac{\bar{t}-\bar{t}_a}{\bar{T}_s}\right)\\ &\times \exp\left[-b\,(\bar{t}-\bar{t}_a)/\bar{T}_s\right]\end{aligned}\right\} \quad (6\text{-}29)$$

is integrated over the positive phase, $0 \leq (\bar{t}-\bar{t}_a) \leq \bar{T}_s$, to obtain impulse $\bar{I}_s$ and, the decay constant b is determined from the resulting transcendental equation

$$\bar{I}_s = \frac{\bar{P}_s\,\bar{T}_s}{b}\left[1-\frac{(1-e^{-b})}{b}\right] \quad (6\text{-}30)$$

The initial (dimensionless) slope of the pressure-time curve can also be determined by differentiating Eq. 6-29, and is given by

$$\left.\frac{d\bar{p}}{d\bar{t}}\right|_{(\bar{t}-\bar{t}_a)=0} = \frac{-\bar{P}_s\,(b+1)}{\bar{T}_s} \quad (6\text{-}31)$$

Values of b and initial decay rate are given in Table 6-6, together with intermediate quantities used in the calculation. The parameter b is also plotted graphically in Fig. 6-3.

If the reader desires time-distance curves for blast parameters, it is suggested that he obtain Ref. 6.

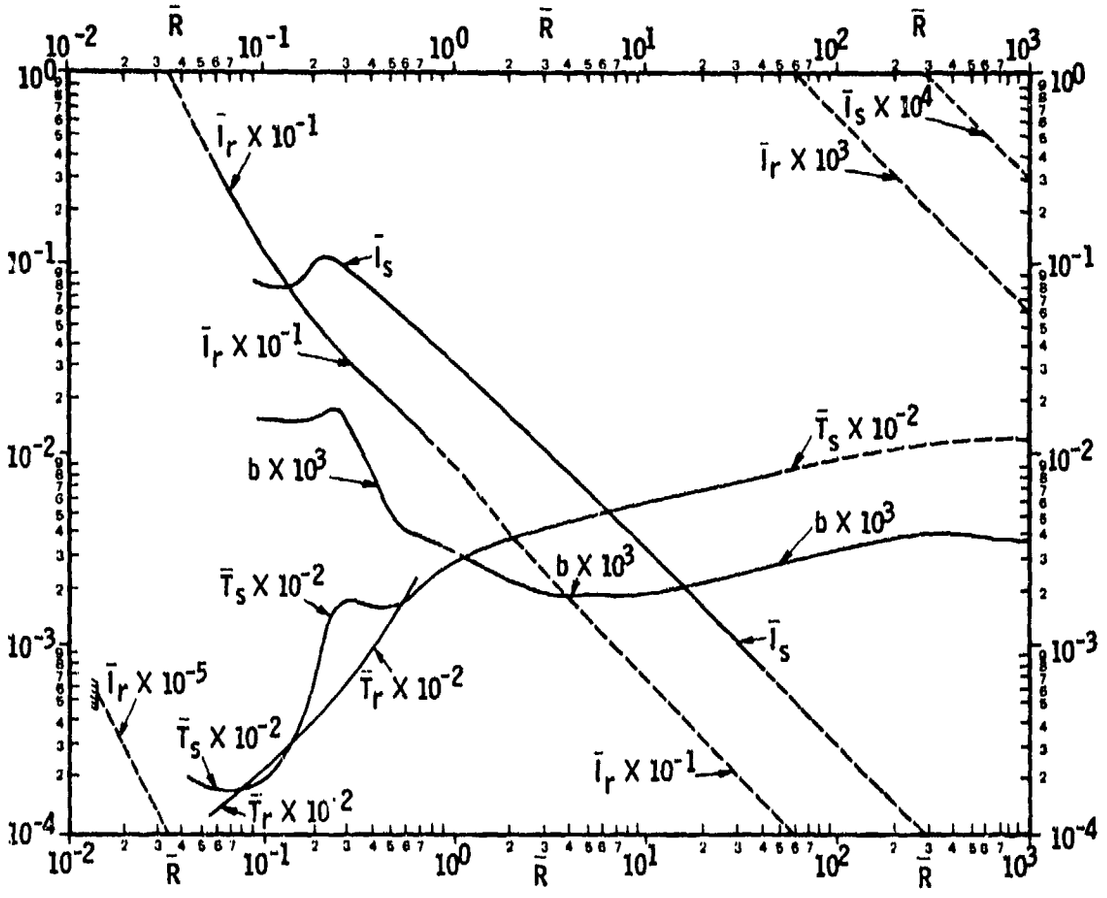
6-3.4 OBLIQUE REFLECTION DATA

All of the scaled blast parameters presented numerically and graphically in previous paragraphs of this chapter represent the two limiting cases of waves freely transmitted

TABLE 6-5. SCALED IMPULSES AND DURATIONS OF OVERPRESSURE

$\bar{R}$	$\bar{I}_s$	$\bar{I}_r$	$\bar{T}_s$	$\bar{T}_r$
0.0400	–	–	2.06-2*	–
0.0500	–	–	1.84-2	–
0.0600	–	3.08	1.75-2	1.40-2*
0.0800	–	1.86	1.75-2	1.80-2
0.100	7.85-2*	1.27	1.91-2	2.19-2
0.150	7.88-2	0.677	3.41-2	3.15-2
0.200	1.06-1	0.456	8.85-2	4.25-2
0.250	1.03-1	0.355	0.157	5.42-2
0.300	8.85-2	0.294	0.171	6.84-2
0.400	6.95-2	0.222	0.158	0.103
0.500	5.70-2	0.178	0.162	0.147
0.600	4.82-2	0.150	0.181	0.195
0.800	3.71-2	0.112	0.232	–
1.00	3.02-2	8.85-2*	0.268	–
2.00	1.58-2	3.77-2	0.362	–
4.00	8.12-3	1.73-2	0.445	–
6.00	5.46-3	1.12-2	0.495	–
8.00	4.10-3	8.40-3	0.532	–
10.0	3.25-3	6.58-3	0.564	–
20.0	1.58-3	3.20-3	0.666	–
40.0	7.64-4	1.54-3	0.781	–
60.0	4.98-4	9.96-4	0.856	–
100	2.93-4	5.86-4	0.960	–
500	5.75-5	1.15-4	1.24	–
1000	2.88-5	5.76-5	1.25	–

*Digits preceded by minus sign indicate negative powers of 10.



This chart is reproduced to a larger scale located in the rear of the handbook.

Figure 6-3. Compiled Impulses and Durations

through the air and waves normally reflected from an infinite rigid wall. The intermediate case of oblique reflection of waves from spherical blast sources located at various heights of burst above a rigid, plane surface is also of considerable interest (see Chapter 1). It is much more difficult to present compiled blast parameters in concise form for this case because an additional geometric parameter, height of burst *H* or angle of incidence α_I, is required to define the geometry of the shock reflection. Fig. 6-4 shows this geometry in the region of regular reflection, i.e., for α_I small enough that the Mach stem has not been formed (see Chapter 1). Because the reflecting surface of most interest is the ground, data for oblique reflections seldom are presented in Sachs-scaled parameters, but instead are given for either Hopkinson-scaled or unscaled quantities for standard sea level ambient conditions[4,18]. These data can, however, be easily converted to the Sachs-scaled parameters of Table 6-2.

Data for overpressure ratios for relatively weak shocks at all angles of incidence up to grazing (α_I = 90 deg) are reproduced graphically here in Fig. 6-5 from a set of curves in Ref. 4. Although the measurements on which these curves are based are not described in Ref. 4, it is likely that they date from World War II or shortly thereafter, and consist of tests using small TNT or Pentolite charges. Recent work at BRL indicates that these old curves may still be reasonably accurate over the indicated range of shock strengths.

Kingery and Panill[18] have generated a comprehensive set of tables and graphs for prediction of a number of shock-front param-

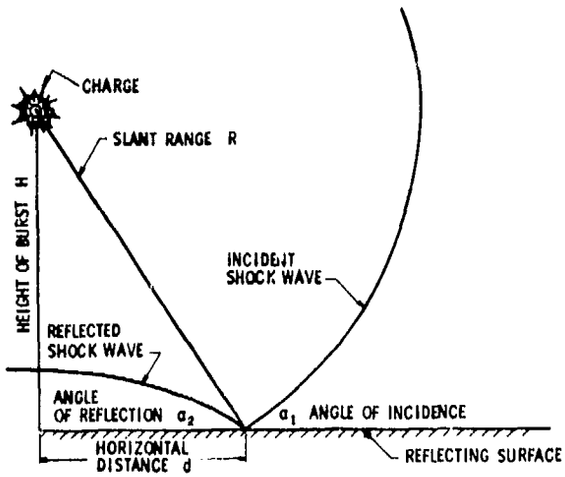


Figure 6-4. Geometry for Regular Reflection

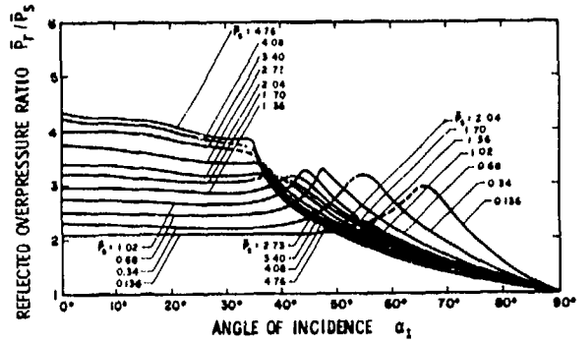


Figure 6-5. Reflected Overpressure Ratio as Function of Angle of Incidence for Various Side-on Overpressures[4]

eters for obliquely reflected strong air blasts in the region of regular reflection. Their data are based on Goodman's[1] curve for side-on overpressure, and use variable ratios of specific heat γ for strong shocks to compute peak reflected overpressure P_r, peak dynamic pressure Q, and angle of reflected shock α_2 for various heights of burst H and horizontal distances d. The value of α_2 at which regular reflection ceases and the Mach stem starts to

TABLE 6-6

TIME CONSTANT AND INITIAL DECAY RATE OF $\bar{p}_s$

$\bar{R}$	$\bar{P}_s$	$\bar{I}_s$	$\bar{T}_s$	$\frac{\bar{I}_s}{\bar{P}_s \bar{T}_s}$	b	$\left.\frac{d\bar{p}}{d\bar{t}}\right\|_0$
0.100	67.9	7.85-2*	1.91-2*	6.07-2*	15.5	-5.86+4*
0.150	37.2	7.88-2	3.41-2	6.21-2	15.0	-1.64+4
0.200	20.4	1.06-1	[illegible]-2	5.88-2	16.0	-3.91+3
0.250	11.9	1.03-1	[illegible]67	5.52-2	17.0	-1.37+3
0.300	7.28	8.85-2	0.171	7.11-2	12.9	-5.91+2
0.400	3.46	6.95-2	0.158	0.127	6.76	-1.70+2
0.500	2.05	5.70-2	0.162	0.172	4.56	-7.02+1
0.600	1.38	4.82-2	0.181	0.193	3.87	-3.72+1
0.800	0.772	3.71-2	0.232	0.207	3.48	-1.49+1
1.00	0.506	3.02-2	0.268	0.223	3.08	-7.70
2.00	0.161	1.58-2	0.362	0.271	2.19	-1.42
4.00	6.16-2*	8.12-3	0.445	0.297	1.81	-3.89-1
6.00	3.74-2	5.46-3	0.495	0.295	1.84	-2.15-1
8.00	2.61-2	4.10-3	0.532	0.296	1.83	-1.39-1
10.0	1.98-2	3.25-3	0.564	0.292	1.87	-1.01-1
20.0	8.70-3	1.58-3	0.666	0.273	2.17	-4.14-2
40.0	3.91-3	7.64-4	0.781	0.250	2.55	-1.78-2
60.0	2.48-3	4.98-4	0.856	0.234	2.87	-1.12-2
100	1.41-3	2.93-4	0.960	0.217	3.25	-6.24-3
500	2.42-4	5.75-5	1.24	0.192	3.90	-9.55-4
1000	1.153-4	2.88-5	1.25	0.200	3.67	-4.31-4

*Digits preceded by minus (plus) sign indicate negative (positive) powers of 10.

form is also given as a function of shock strength. The data in Ref. 18 are all given in dimensional units for one pound of spherical Pentolite at standard sea level ambient conditions. They are much too voluminous to reproduce here, but some typical data are shown in Tables 6-7 and 6-8, and Figs. 6-6 and 6-7. It is suggested that the reader obtain Ref. 18 if he wishes to predict front parameters for obliquely reflected strong shocks.

6-3.5 CONVERSION FACTORS

The nondimensional presentation of blast parameters used here has the great advantage of being independent of systems of units. It

TABLE 6-7

COMPILED DATA FOR STRONG, OBLIQUELY REFLECTED SHOCKS[18]*

Height of Burst H = 2.5 ft

Horizontal Distance d, ft	Peak Overpressure		Peak Dynamic Pressure Q, psi	Incident Angle α_1, deg	Reflected Angle α_2, deg
	Incident P_s, psi	Reflected P_r, psi			
0.000	169.47	982.55	0.00	0.00	0.00
0.158	168.73	974.81	6.09	3.62	1.41
0.388	165.11	937.61	34.92	8.83	3.51
0.527	161.60	902.32	61.19	11.91	4.84
0.637	158.18	868.83	85.12	14.31	5.95
0.732	154.86	837.05	106.92	16.32	6.94
0.817	151.62	806.86	126.78	18.09	7.87
0.894	148.48	778.20	144.88	19.67	8.76
0.966	145.42	750.99	161.38	21.12	9.62
1.033	142.44	725.15	176.42	22.45	10.46
1.097	139.55	700.59	190.16	23.69	11.30
1.158	136.73	677.26	202.71	24.85	12.13
1.216	133.98	655.10	214.20	25.94	12.97
1.272	131.30	634.05	224.76	26.97	13.81
1.326	128.70	614.07	234.48	27.95	14.66
1.379	126.16	595.10	243.47	28.88	15.53
1.430	123.68	577.11	251.84	29.77	16.41
1.480	121.27	560.06	259.69	30.62	17.32
1.528	118.92	543.94	267.13	31.43	18.24
1.575	116.63	528.72	274.26	32.22	19.20
1.622	114.40	514.38	281.21	32.97	20.19
1.667	112.22	500.92	288.11	33.70	21.22
1.712	110.09	488.33	295.09	34.40	22.30
1.756	108.02	476.65	302.37	35.08	23.44
1.799	106.00	465.93	310.17	35.74	24.65
1.841	104.03	456.26	318.86	36.38	25.95
1.883	102.10	447.81	328.95	36.99	27.38
1.925	100.22	440.89	341.36	37.59	28.98
1.965	98.39	436.18	357.90	38.17	30.85
2.005	96.61	435.57	383.48	38.74	33.25
2.045	94.87			39.29	

*All data for 1-lb Pentolite spheres detonated at sea level.

TABLE 6-8

LIMIT OF REGULAR REFLECTION $\alpha_{extreme}$ VS SHOCK STRENGTH [18]**

ξ***	$\alpha_{extreme}$ α_{ex}, deg	Peak Side-on Overpressure P_s, psi	Slant Range R, ft	Height of Burst H, ft	Horizontal Distance d, ft
0.002	0.4657 + 2*	0.7335 + 4*	0.1969	0.1353	0.1430
.003	.4552 + 2	.4885 + 4	.2734	.1915	.1951
.004	.4502 + 2	.3660 + 4	.3452	.2440	.2442
.005	.4480 + 2	.2925 + 4	.4134	.2933	.2913
.006	.4450 + 2	.2435 + 4	.4779	.3408	.3350
.007	.4416 + 2	.2085 + 4	.5397	.3871	.3760
.008	.4379 + 2	.1822 + 4	.5989	.4323	.4145
.009	.4345 + 2	.1618 + 4	.6556	.4759	.4509
.01	.4315 + 2	.1455 + 4	.7099	.5179	.4855
.02	.4151 + 2	.7203 + 3	.1154 + 1*	.8642	.7650
.03	.4072 + 2	.4753 + 3	.1482 + 1	.1123 + 1*	.9674
.04	.4032 + 2	.3528 + 3	.1745 + 1	.1330 + 1	.1129 + 1*
.05	.4004 + 2	.2793 + 3	.1968 + 1	.1507 + 1	.1266 + 1
.06	.3983 + 2	.2303 + 3	.2165 + 1	.1662 + 1	.1386 + 1
.07	.3967 + 2	.1953 + 3	.2340 + 1	.1801 + 1	.1494 + 1
.08	.3956 + 2	.1690 + 3	.2502 + 1	.1929 + 1	.1594 + 1
.09	.3948 + 2	.1486 + 3	.2653 + 1	.2048 + 1	.1687 + 1
.10	.3942 + 2	.1323 + 3	.2795 + 1	.2159 + 1	.1775 + 1
.15	.3926 + 2	.8330 + 2	.3414 + 1	.2643 + 1	.2160 + 1
.20	.3932 + 2	.5880 + 2	.3955 + 1	.3059 + 1	.2506 + 1
.25	.3953 + 2	.4410 + 2	.4462 + 1	.3441 + 1	.2840 + 1
.30	.3988 + 2	.3430 + 2	.4960 + 1	.3806 + 1	.3180 + 1
.35	.4034 + 2	.2730 + 2	.5467 + 1	.4167 + 1	.3539 + 1
.40	.4093 + 2	.2205 + 2	.5997 + 1	.4530 + 1	.3929 + 1
.45	.4165 + 2	.1796 + 2	.6567 + 1	.4906 + 1	.4365 + 1
.50	.4252 + 2	.1470 + 2	.7158 + 1	.5275 + 1	.4838 + 1
.55	.4355 + 2	.1202 + 2	.7914 + 1	.5735 + 1	.5453 + 1
.60	.4477 + 2	.9800 + 1	.8731 + 1	.6198 + 1	.6150 + 1
.65	.4622 + 2	.7915 + 1	.9734 + 1	.6734 + 1	.7029 + 1
.70	.4797 + 2	.6300 + 1	.1099 + 2	.7363 + 1	.8169 + 1
.75	.5009 + 2	.4900 + 1	.1269 + 2	.8146 + 1	.9740 + 1
.80	.5273 + 2	.3675 + 1	.1516 + 2	.9179 + 1	.1206 + 2
.85	.5615 + 2	.2594 + 1	.1916 + 2	.1067 + 2	.1592 + 2
.90	.6082 + 2	.1633 + 1	.2713 + 2	.1322 + 2	.2369 + 2
.95	.6802 + 2	.7736	.5088 + 2	.1903 + 2	.4718 + 2

*Digits preceded by plus sign indicate positive powers of 10.

**All data for 1-lb Pentolite spheres detonated at sea level

***The parameter $\xi = p_0/(P_s + p_0)$

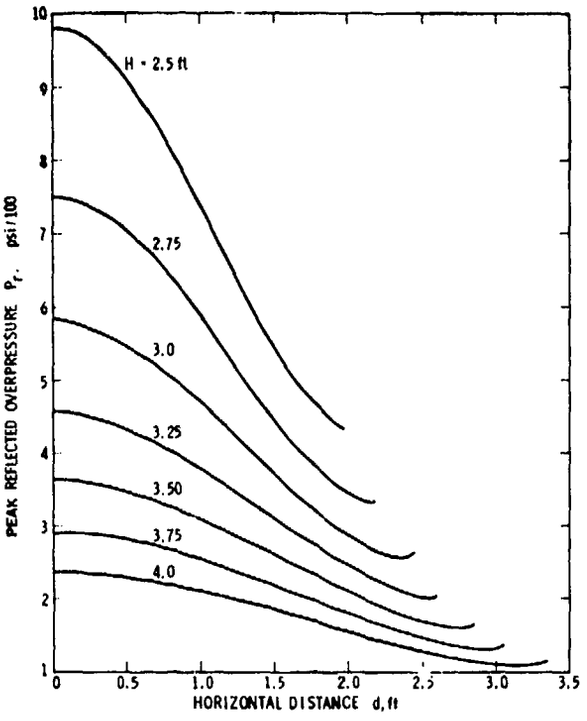


Figure 6-6. Typical Reflected Overpressure vs Horizontal Distance for Selected Heights of Burst, 1 lb_m Pentolite at Sea Level[18]

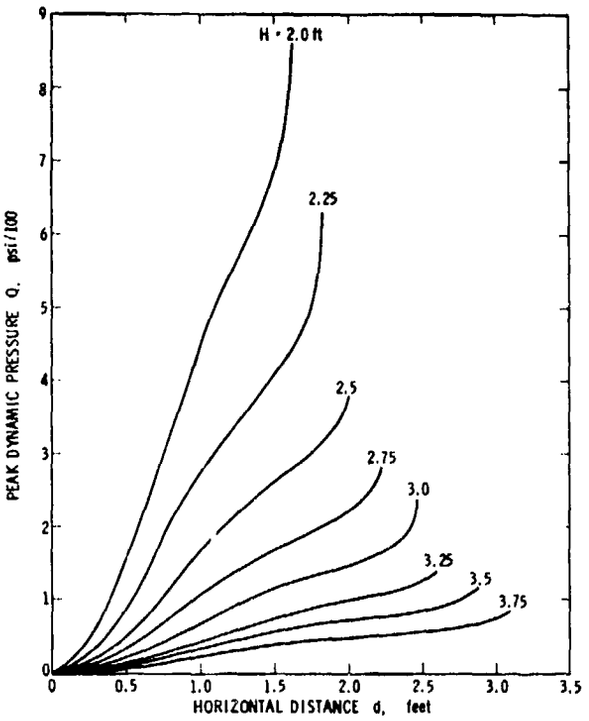


Figure 6-7. Typical Dynamic Pressure vs Distance for Selected Heights of Burst 1 lb_m Pentolite at Sea Level[18]

does, however, have the disadvantage of differing from the presentation in most other sources of blast properties, with the exception of Brode[2,3]. Some conversion factors are listed in Table 6-9 for those who wish to convert the nondimensional parameters of Table 6-2 to dimensional ones, or vice versa. The standard atmospheric conditions given previously are assumed in calculating these conversion factors.

6-4 EXAMPLE CALCULATIONS

To demonstrate the use of figures and tables in this chapter, we will present here some example calculations.

Example 1. We wish to predict blast parameters in free air at 10 ft from the center of a 1-lb_m Pentolite sphere detonated under sea level ambient conditions, R = 120 in., W = 1 lb_m.

From Table 6-1, weight specific energy for Pentolite is

$$E/W = 20.50 \times 10^6 \text{ in.-lb}_f/\text{lb}_m$$

So,

$$E = W \times 20.50 \times 10^6$$

$$= 1 \times 20.50 \times 10^6$$

$$= 20.50 \times 10^6 \text{ in.-lb}_f$$

Standard sea level ambient conditions are:

$$p_0 = 14.70 \text{ lb}_f/\text{in.}^2$$

$$\rho_0 = 1.146 \times 10^{-7} \text{ lb}_f\text{-sec}^2/\text{in.}^4$$

$$a_0 = 13{,}400 \text{ in./sec}$$

$$\theta_0 = 519^\circ\text{R}$$

TABLE 6-9

CONVERSION FACTORS FOR SCALED BLAST WAVE PROPERTIES

Multiply	in units of	from	by	to obtain
$R\left(\frac{p_0}{W}\right)^{1/3}$	ft $\left(\frac{\text{atm}}{\text{lb}_m}\right)^{1/3}$	Goodman[1], Mills, et al.[6], Baker & Schuman[5]	0.1075	$\bar{R}$
$\frac{P_s}{p_0}$, $\frac{P_r}{p_0}$	atm	Goodman[1], Mills, et al[6]	1	$\bar{P}_s$, $\bar{P}_r$
X	charge radii	Goodman[1]	0.01428	$\bar{R}$
$\left(\frac{T}{W^{1/3}}\right)$, $\left(\frac{t_a}{W^{1/3}}\right)$	$\frac{\text{msec}}{\text{lb}_m^{1/3}}$	Goodman[1], Mills, et al.[6], Baker & Schuman[5]	0.120	$\bar{T}$, $\bar{t}_a$
$I_s/(p_0^{2/3}W^{1/3})$, $I_r/(p_0^{2/3}W^{1/3})$	$\frac{\text{psi-msec}}{\text{atm}^{2/3}\ \text{lb}_m^{1/3}}$	Goodman[1], Mills, et al.[6]	4.92×10^{-3}	$\bar{I}_s$, $\bar{I}_r$
P_s, P_r	psi	Lehto & Larson[12], Goodman, etc.	0.0681	$\bar{P}_s$, $\bar{P}_r$
R	meters	Lehto & Larson[12]	0.353	$\bar{R}$
$\bar{R}$	–	Brode[2,3]	1.13	$\bar{R}$
$\bar{T}$, $\bar{t}_a$	–	Brode[2,3]	1.18	$\bar{T}$, $\bar{t}_a$

Scaled distance $\bar{R} = Rp_0^{1/3}/E^{1/3}$ (Table 6-2)

$$\bar{R} = \frac{120 \times 14.70^{1/3}}{20.50^{1/3} \times 10^2} \text{ in.} \left(\frac{\text{lb}_f^{1/3}}{\text{in.}^{2/3}}\right) \times \left(\frac{1}{\text{in.}^{1/3}\ \text{lb}_f^{1/3}}\right) = \frac{1.20 \times 2.45}{2.74 \times 10^2} = 1.072^*$$

We enter Tables 6-3 and 6-5, or Figs. 6-1 and 6-3, for the calculated value of $\bar{R}$ and write down all of the side-on scaled parameters we can find. These are:

$\bar{P}_s$	= 0.450	$\bar{Q}$	$= 7.20 \times 10^{-2}$
$\bar{u}_s$	= 0.276	$\bar{\theta}_s$	= 1.12
$\bar{U}$	= 1.17	$\bar{I}_s$	$= 2.85 \times 10^{-2}$
$\bar{t}_a$	= 0.520	$\bar{T}_s$	= 0.280
$\bar{\rho}_s$	= 1.30		

*Note that all dimensions cancel, as they should in calculating the dimensionless parameter $\bar{R}$.

We next convert these dimensionless quantities to dimensional ones, using Table 6-2, as follows:

$$P_s = \bar{P}_s \times p_0 = 0.450 \times 14.70 \text{ psi} = 6.61 \text{ psi}$$

$$u_s = \bar{u}_s \times a_0 = 0.276 \times 13{,}400 \text{ in./sec}$$

$$= 3700 \text{ in./sec}$$

$$U = \bar{U} \times a_0 = 1.17 \times 13{,}400 \text{ in./sec}$$

$$= 15{,}700 \text{ in./sec}$$

$$\bar{t}_a = \frac{\bar{t}_a \times E^{1/3}}{a_0 \times p_0^{1/3}} = \frac{0.520 \times 2.74 \times 10^2}{1.34 \times 10^4 \times 2.45}$$

$$= 4.33 \times 10^{-3} \text{ sec} = 4.33 \text{ msec}$$

$$\rho_s = \bar{\rho}_s \times \rho_0 = 1.30 \times 1.146 \times 10^{-7}$$

$$= 1.490 \times 10^{-7} \text{ lb-sec}^2/\text{in.}^4$$

$$Q = \bar{Q} \times p_0 = 7.20 \times 10^{-2} \times 14.70 \text{ psi}$$

$$= 1.06 \text{ psi}$$

$$\theta_s = \bar{\theta}_s \times \theta_0 = 1.12 \times 519°\text{R} = 581°\text{R}$$

$$I_s = \frac{\bar{I}_s \times p_0^{2/3} \times E^{1/3}}{a_0}$$

$$= \frac{2.85 \times 10^{-2} \times (14.70)^{2/3} \times 2.74 \times 10^2}{1.34 \times 10^4}$$

$$\times \frac{(\text{lb}_f/\text{in.}^2)^{2/3} \times (\text{in.-lb}_f)^{1/3}}{(\text{in./sec})}$$

$$= 3.49 \times 10^{-3} \text{ lb-sec/in.}^2$$

$$= 3.49 \text{ psi-msec}$$

$$T_s = \frac{\bar{T}_s \times E^{1/3}}{a_0 \times p_0^{1/3}} = \frac{0.280 \times 2.74 \times 10^2}{1.34 \times 10^4 \times 2.45}$$

$$= 2.33 \times 10^{-3} \text{ sec}$$

$$= 2.33 \text{ msec}$$

Note that the choice of units was arbitrary. We could have used metric units, or English units with feet as the length unit rather than inches. The basic tables and graphs are *independent* of choice of system of units.

Example 2. We wish to predict properties of a blast wave normally reflected from a rigid wall located $R = 15$ ft from the center of a $W = 10$ lb_m RDX sphere, in an altitude chamber which is at sea level temperature, but at reduced pressure and density which are 1/10 of sea level values.

From Table 6-1, weight specific energy for RDX is

$$E/W = 21.5 \times 10^6 \text{ in.-lb}_f/\text{lb}_m$$

So,

$$E = W \times 21.5 \times 10^6$$

$$= 10 \times 21.5 \times 10^6$$

$$= 2.15 \times 10^8 \text{ in.-lb}_f$$

Ambient conditions are:

$$p_0 = 0.1 \times 14.70 = 1.470 \text{ lb}_f/\text{in.}^2$$

$$\rho_0 = 0.1 \times 1.146 \times 10^{-7} = 1.146 \times 10^{-8} \text{ lb}_f\text{-sec}^2/\text{in.}^4$$

$$a_0 = 13{,}400 \text{ in./sec}^*$$

$$\theta_0 = 519°\text{R}$$

*Sound velocity a_0 is a function only of ambient temperature θ_0. It is therefore the same as for Example 1, since temperature is the same.

Scaled distance $\bar{R} = Rp_0^{1/3}/E^{1/3}$

$$= \frac{15 \times 12 \times (1.47)^{1/3}}{(0.215 \times 10^9)^{1/3}}$$

$$= \frac{15 \times 12 \times 1.137}{600} = 0.341$$

We now enter Tables 6-4 and 6-5, or Figs. 6-2 and 6-3, for the calculated value of $\bar{R}$ and write down all of the reflected scaled parameters we can find. These are:

$\bar{P}_r = 23.5$

$\bar{\rho}_r = 8.05$

$\bar{\theta}_r = 3.03$

$\bar{I}_r = 0.258$

$\bar{T}_r = 8.20 \times 10^{-2}$

We next convert these dimensionless quantities to dimensional ones, as follows:

$P_r = \bar{P}_r \times p_0 = 23.5 \times 1.470$ psi

$= 34.6$ psi

$\rho_r = \bar{\rho}_r \times \rho_0 = 8.05 \times 1.146 \times 10^{-8}$

$= 9.20 \times 10^{-8}$ lb$_f$-sec^2/in^4

$\theta_r = \bar{\theta}_r \times \theta_0 = 3.03 \times 519°\text{R} = 1570°\text{R}$

$$I_r = \frac{\bar{I}_r \times p_0^{2/3} \times E^{1/3}}{a_0}$$

$$= \frac{0.258 \times (1.47)^{2/3} \times 600}{1.34 \times 10^4}$$

$= 15.00 \times 10^{-3}$ lb$_f$-sec/in^2

$= 15.00$ psi-msec

$$T_r = \frac{\bar{T}_r \times E^{1/3}}{a_0 \times p_0^{1/3}} = \frac{8.20 \times 10^{-2} \times 600}{1.34 \times 10^4 \times 1.137}$$

$= 3.23 \times 10^{-3}$ sec

$= 3.23$ msec

Example 3. We wish to estimate the overpressure which the charge of Example 1 would apply to a plane surface at a slant range R equal to the standoff distance of Example 1, but at an angle of incidence $\alpha_I = 50$ deg.

From Example 1, $\bar{P}_s = 0.450$. Entering Fig. 6-5 at $\alpha_I = 50$ deg, and interpolating for $\bar{P}_s = 0.45$, we get $\bar{P}_r/\bar{P}_s = 2.8$. Then,

$\bar{P}_r = 2.8 \times \bar{P}_s$

$= 2.8 \times 0.45 = 1.26$

$P_r = \bar{P}_r \times p_0$

$= 1.26 \times 14.7$ psi $= 18.5$ psi

Example 4. For the situation described in Example 3, is the oblique reflection within the region of regular reflection or not? The incident overpressure is (see Example 1) $P_s = 6.61$ psi. Comparing with the third column in Table 6-8, we find that this lies between 7.915 psi and 6.300 psi. By interpolating in the second column, we get:

$$\alpha_{ex} = 47.97 - \left[\frac{(47.97 - 46.22)(6.61 - 6.30)}{(7.915 - 6.300)}\right]$$

$= 47.97 - 0.34$

$= 47.63$ deg

The angle of incidence $\alpha_I = 50$ deg and $\alpha_{ex} < \alpha_I$. Therefore, the reflection is out of the region of regular reflection, and the Mach stem has begun to form.

REFERENCES

1. H. J. Goodman, *Compiled Free-Air Blast Data on Bare Spherical Pentolite*, Ballistic Research Laboratories Report No. 1092, February 1960.

2. H. L. Brode, "Numerical Solutions of Spherical Blast Waves", *Jour. of Appl. Physics*, 26, 6, pp. 766-775 (June 1955).

3. H. L. Brode, *A Calculation of the Blast Wave from a Spherical Charge of TNT*, Rand Corp., Report RM-1965, August 1957.

4. S. Glasstone, Ed., *The Effects of Nuclear Weapons*, U. S. Atomic Energy Commission, Rev. Ed., April 1962.

5. W. E. Baker and W. J. Schuman, Jr., *Air Blast Data for Correlation with Moving Airfoil Tests*, Ballistic Research Laboratories Technical Note No. 1421, August 1961.

6. R. R. Mills, Jr., F. J. Fisch, B. W. Jezek, and W. E. Baker, *Self-Consistent Blast Wave Parameters*, DASA-1559, October 1965.

7. D. Lehto and M. Lutzky, *One Dimensional Hydrodynamic Code for Nuclear-Explosion Calculations*, NOL TR 62-168, U. S. Naval Ordnance Laboratory, Maryland.

8. J. R. Ruetenik and S. D. Lewis, *Computation of Blast Properties for Spherical TNT or Pentolite from Measured Pressure Histories*, AFFDL-TR-66-47, October 1966, AD-807 756.

9. R. A. Minzner, K. S. W. Champion and H. L. Pond, *The ARDC Model Atmosphere, 1959*, AFCRC-TR-59-267, August 1969, AD-229 482.

10. AMCP 706-177, Engineering Design Handbook, *Explosives Series, Properties of Explosives of Military Interest.*

11. R. E. Shear and B. D. Day, *Tables of Thermodynamic and Shock Front Parameters for Air*, BRL Memo Report No. 1206, May 1959.

12. D. L. Lehto and R. A. Larson, *Long Range Propagation of Spherical Shockwaves from Explosions in Air*, NOLTR 69-88, U.S. Naval Ord. Lab., White Oak, Md., July 1969.

13. W. H. Jack, Jr., *Measurements of Normally Reflected Shock Waves from Explosive Charges*, BRL Memo Report No. 1499, July 1963.

14. R. E. Shear and P. McCane, *Normally Reflected Shock Front Parameters*, BRL Memo Report No. 1273, May 1960.

15. W. Doering and G. Burkhardt, *Contributions to the Theory of Detonation*, TR No. F-TS-1227-1A, Wright-Patterson AFB, Ohio, May 1949, Table 6.

16. C. N. Kingery, *Air Blast Parameters Versus Distance for Hemispherical TNT Surface Bursts*, BRL Report No. 1344, Sept. 1966.

17. A. J. Hoffman and S. N. Mills, Jr., *Air Blast Measurements About Explosive Charges at Side-On and Normal Incidence*, BRL Report No. 988, Aberdeen Proving Ground, Maryland, July 1956.

18. C. N. Kingery and B. F. Panill, *Parametric Analysis of the Regular Reflection of Air Blast*, BRL Report No. 1249, Aberdeen Proving Ground, Maryland, June 1964.

CHAPTER 7

AIR BLAST TRANSDUCERS

7-0 LIST OF SYMBOLS

C_D = drag coefficient

D = drag force

p_h = "total head" or stagnation pressure

P_s = peak side-on overpressure

P_D = peak drag pressure

q = dynamic pressure

S = projected area

u = particle speed

u_s = peak side-on particle speed

$\bar{P}_s$ = scaled side-on peak overpressure

ρ = density in blast wave

7-1 GENERAL

In this chapter, we will discuss the various types of transducers that have been used to sense the physical properties of air blast waves, and to convert these properties into signals that can be recorded by some type of instrumentation system. Strictly speaking, transducers are only elements of blast instrumentation systems, but they are so critical in the proper functioning of these systems that we feel they deserve special treatment. In many experimental air blast programs, the investigator is indeed restricted to measuring those blast parameters that can be properly sensed, or for which proper sensors can be easily built, rather than the parameters that he would like to measure but cannot because no suitable sensor exists or can be made. In his dreams, the blast experimentalist can imagine perfect transducers—for sensing the rapidly varying pressure, density, temperature, particle velocity, and shock velocity—which have (1) infinite frequency response to faithfully follow all variations in these parameters, (2) infinitesimal size to offer no disturbance to the transient flow field associated with the blast wave, (3) sensitivity to *only* the desired physical property, (4) great output signal for small changes in input, (5) linear response for either very small or very large input signals, and (6) excellent stability so that they need be calibrated only once. In reality, he must accept many compromises between these desired characteristics. He will find many types of more or less suitable pressure transducers, one type of density transducer, some devices which sense impulse, essentially no suitable temperature transducers, and limited techniques for measuring shock or particle velocity at discrete locations. We will discuss in this chapter many of the past and present air blast transducers, both commercial and those developed in Government laboratories.

7-2 PRESSURE TRANSDUCERS

7-2.1 SIDE-ON GAGES

If one wishes to record the free-field history of the pressure in the blast wave at various distances from the blast source, then it is essential that he employ transducers that do not seriously interfere with the flow behind the shock front. The geometry of the transducer housing and mounting is then very important. A number of different types of such "side-on" blast gages have been developed, primarily by U. S. and British government laboratories. They all have the common characteristic that the sensing elements are mounted in the side of some type of rather

slender, streamlined housing. They are all directional, in the sense that they will read properly the free field blast properties only when properly oriented with respect to the direction of shock travel. *No* suitable omnidirectional blast transducer of this type has as yet been developed.

Many of the different types of side-on blast gage employ either natural or synthetic piezoelectric materials as sensing elements. The natural crystals are usually either tourmaline or quartz, while the synthetic materials may be barium titanate, lead zirconate, lead metaniobate, or other materials of compositions which are considered as proprietary by their manufacturers. Natural crystals only can be used in the form of flat plates or discs cut along certain crystal planes, while the synthetic materials can be made and polarized in a wide variety of different geometries. The synthetic materials are usually much more sensitive than the natural, but are apt to exhibit appreciable changes in sensitivity with change in ambient temperature, while the natural materials do not. Advantages to use of piezoelectric pressure sensing elements are (1) the elements are self-generating and very linear over extremely wide ranges in applied pressure, (2) very high frequency response is possible, and (3) most of the piezoelectric materials are quite strong mechanically and therefore can survive high pressures and much rough handling. Disadvantages are (1) they do not respond to static pressure and so are difficult to calibrate, (2) they are brittle, (3) they are without exception also pyroelectric so that one must guard against direct heating of the elements during passage of a blast wave, (4) they are sensitive to acceleration, and (5) they only can be employed properly with recording equipment of very high input impedance to minimize leakage of the electrical charge generated under application of pressure.

7-2.1.1 BRL SIDE-ON GAGES

Much of the development of side-on blast pressure gages in the U. S. has been done at the Ballistic Research Laboratories (BRL) or under their supervision. Some of the early difficulties in attempting to use gages that were not streamlined are mentioned by Stoner and Bleakney[1]. The design which has evolved at BRL is shown schematically in Fig. 7-1. Gages of this general design often are called colloquially "pancake" or "lollipop" gages because of the flat disc shape of the housing. The sensing elements consist of stacks of even numbers of piezoelectric discs placed in a cavity in the housing as shown, and interleaved with metal foil discs and tabs. The individual piezoelectric discs are alternated in polarity in the stack, with all tabs of one polarity being connected to an insulated electrical lead in the stem, and the others being grounded to the metal housing. Electrical connection is made to a coaxial connector at the end of the stem.

The elements must be made of a material that is sensitive to hydrostatic pressure for this gage to function properly—usually either tourmaline or a synthetic pizeoelectric ceramic*. The head of this gage is made in a variety of sizes, depending on desired sensitivity and scale of experiment, but the ratio of diameter to thickness always is kept greater than 10:1 to minimize flow effects. In use it normally is mounted at the end of a long tube with the stem parallel to the direction of travel of the blast front. It can be employed, however, for measurement of any blast wave whose direction of propagation lies in the plane of the gage head, and has been used to measure the characteristics of two blast waves striking head-on[2]. As far as we know, there is no presently available commercial counterpart to this type of gage.

7-2.1.2 SOUTHWEST RESEARCH INSTITUTE SIDE-ON GAGES

A gage similar in basic design to the BRL gage has been developed at Southwest Research Institute (SwRI). The basic components of this gage are shown in Fig. 7-2(A), and completed gages in Fig. 7-2(B). The sensing element is a two-crystal piezoelectric

*Quartz is insensitive to hydrostatic pressure.

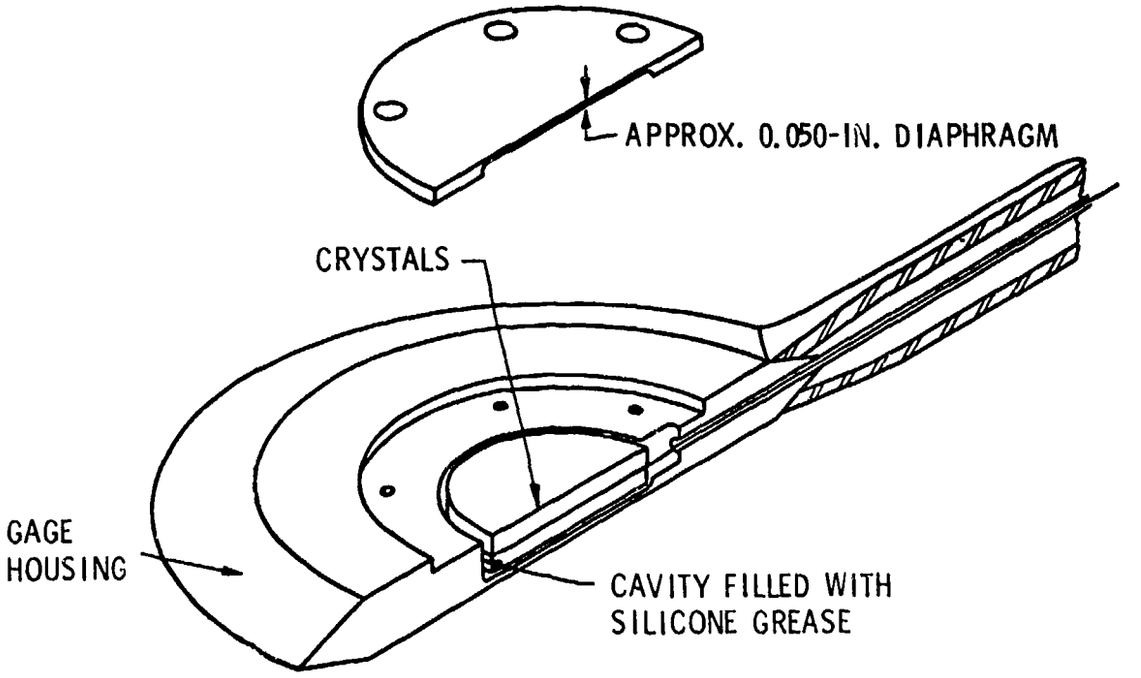
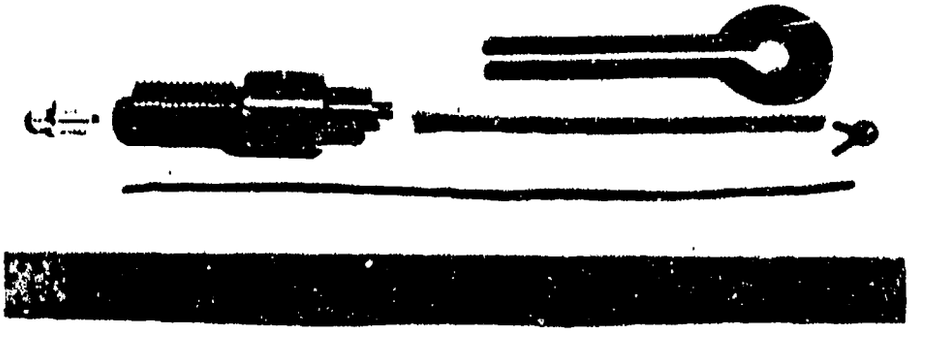
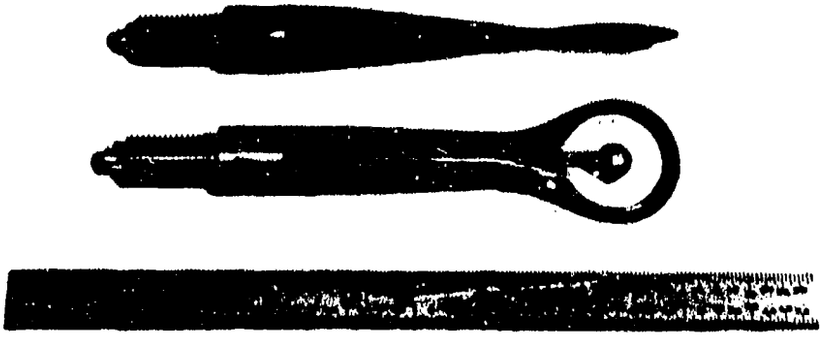


Figure 7-1. Schematic of BRL Piezoelectric Side-on Blast Gage



(A) GAGE COMPONENTS



(B) ASSEMBLED GAGE

(Courtesy of Southwest Research Institute)

Figure 7-2. SwRI Side-on Gage

stack of lead zirconate, 0.060-in. thick, and 0.125-in. in diameter. The gage components are assembled in a mold, and the housing cast from an epoxy resin. The sensing element is isolated mechanically from the housing by a thin layer of silicone rubber painted on before casting. It is considerably smaller than the smallest BRL gage, being intended for use in quite miniature-scale experiments. Possible advantages over the BRL gage in addition to the small size are a superior aerodynamic shape with very high diameter-to-thickness ratio of the "pancake" head and smooth transition of head into stem, fast rise-time because of small sensor diameter, and relative ease of manufacture. These particular gages are designed for mounting in the end of a 0.5-in. diameter tube. In spite of their small size, they have good sensitivity and can be used to measure low overpressures with long lines in the field.

7-2.1.3 ATLANTIC RESEARCH CORPORATION SIDE-ON GAGES

Cylindrical side-on blast gages ("pencil" gages) employing synthetic piezoelectric elements are made commercially by Atlantic Research Corp. These gages originally were developed under contract to BRL. One is shown in Fig. 7-3. The sensing element is a small hollow cylinder of barium titanate or lead zirconate which has been polarized radially. This element is shock isolated from the housing by mounting on corprene rings, and is covered by an outer neoprene sheath that provides electrical and heat insulation. Electrical connections are made to an integral coaxial connector at the rear of the housing. In use, this type of transducer is mounted in much the same manner as the BRL "pancake" gage, with the exception that its axis always must be closely aligned with the direction of blast wave travel if it is to record side-on pressures.

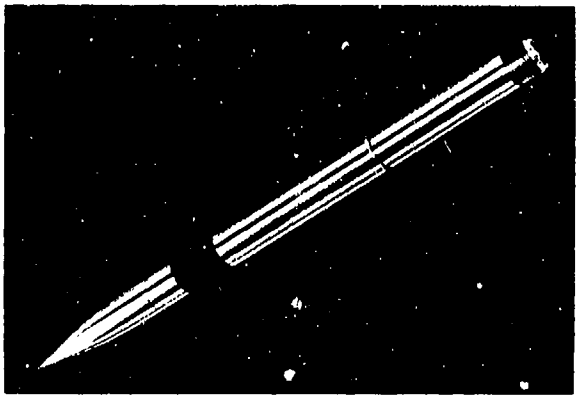


Figure 7-3. Atlantic Research Corp. Pencil Blast Gage, Type LC-13 (Courtesy of Atlantic Research Corp.)

7-2.1.4 BRITISH SIDE-ON GAGES

At several British laboratories, side-on piezoelectric gages have been developed and used for air blast measurements. Several versions of a more or less standard basic design have been evolved at Royal Armanent Research and Development Establishment (RARDE). The basic design is the standard H3 gage illustrated in Fig. 7-4. The sensitive element consists of twelve X-cut quartz crystals sandwiched between a pair of one-inch diameter pistons that serve to communicate the pressure to the crystal pile. The whole pile is suspended between neoprene rubber diaphragms that are clamped around their periphery to the gage body and provide a radially compliant mounting. This feature helps to reduce the response of the crystal pile to axial acceleration forces when the gage is struck by a blast wave. The gage housing is made of stainless steel, with a molded plastic rear section. The gage has a nominal sensitivity of approximately 100 *pC/psi, but the actual sensitivity of individual gages is determined, in the laboratory, by a quasi-static calibration system. These calibrations are repeated at regular intervals and in practice the sensitivity constant of a well-made gage, used normally, changes very little even over a period of years. The undamped natural frequency of the crystal pile has been calculated to be about 200 kHz. Field experiments have shown that only if the gage is subjected to high shock strengths do marked oscillations appear in the decay curve and that these die out very rapidly. The measured frequency of

*pC = picocoulomb



Figure 7-4. British H3 Side-on Gage

(British Crown copyright reserved. Reproduced with the permission of the Controller, Her Brittanic Majesty's Stationery Office.)

the damped oscillations is approximately 130 kHz, and it is concluded that the crystal pile is very nearly critically damped.

In use at high overpressures ($P_s > 3$), the rear portion of the H3 gage was found to be too weak. A stronger design was evolved, using the same hatchet-shaped front position, but a streamlined brass rear section that was threaded to mate with a 1.25-in. O.D. tube. This gage, designated H3B, is shown in Fig. 7-5. The British report use of this gage in free-field and Mach stem measurements of pressures up to and exceeding P_s = 20. The H3B gage has been calibrated under the conditions of use, i.e., using explosively generated blast waves of widely differing intensities and hence flow velocities. The peak overpressures indicated by the H3B gages were compared with those given by a completely independent system, and excellent agreement was obtained.

A third version of the basic H3 gage is designated H3C, and is illustrated in Fig. 7-6. The sensing element is identical to that in the other two designs, but the housing is similar to the BRL pancake design. The disc-shaped head of the gage is made of aluminum alloy, and has an aspect ratio of greater than 12/1. The head is attached to a streamlined brass rear section that is threaded to mate with 1.25-in. O. D. tubing, as is the H3B gage. The British report that the use of this gage is similar to use of the H3B, but with omnidirectional properties in one plane.

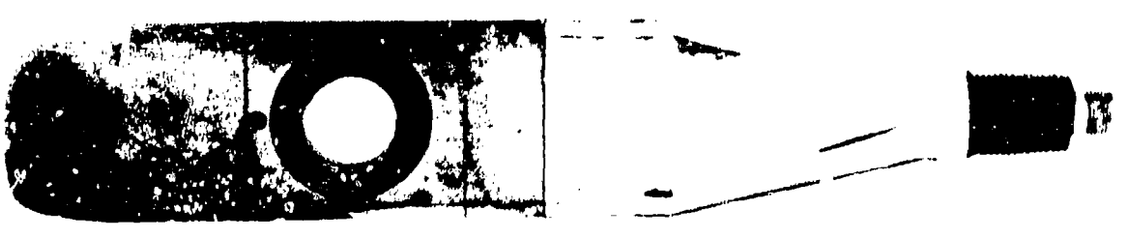


Figure 7-5. The British H3B Blast Gage

(British Crown copyright reserved. Reproduced with the permission of the Controller, Her Brittanic Majesty's Stationery Office.)

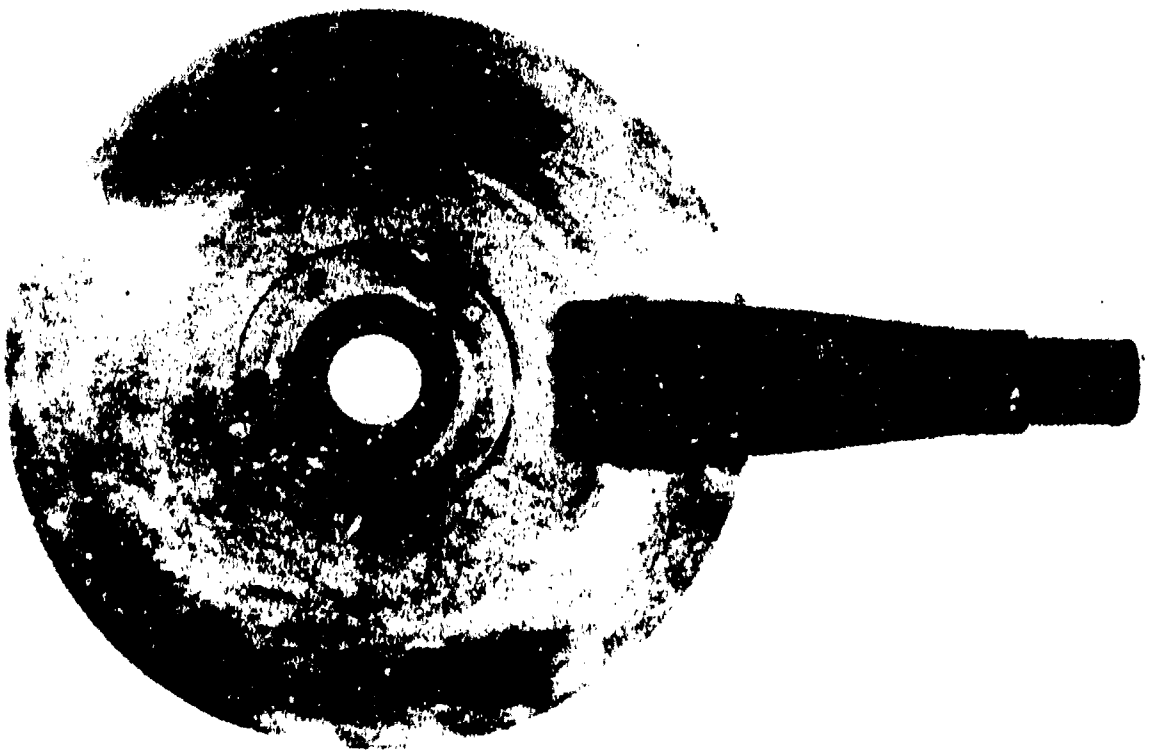


Figure 7-6. The British H3C Blast Gage

(British Crown copyright reserved. Reproduced with the permission of the Controller, Her Brittanic Majesty's Stationery Office.)

7-2.1.5 OTHER SIDE-ON GAGES

Many types of miniature pressure transducers can also be employed as side-on gages, provided they are small enough to be mounted in one or both sides of a pancake head or other suitable streamlined housing. Ruetenik and Lewis[5] report of the use of small, commercial transducers in this manner. The design, shown schematically in Fig. 7-7, is nearly identical in geometry to the BRL side-on gages. Pierce and Manning[6] also have used very small flush-diaphragm gages of NASA design in a similar manner. Whiteside[7] discussed the use of a number of different types of piezoelectric elements made in the British Atomic Weapons Research Establishment (AWRE), Foulness, in side-on transducers. We will defer until later in this chapter the discussion of the characteristics of these and other miniature transducers which could be used in suitable housings as side-on gages, because their use as blast transducers is not limited to this application. We merely note here that some types may be preferable to piezoelectric gages for long duration blast waves, because they have DC response and are less sensitive to temperature or acceleration.

7-2.2 REFLECTED PRESSURE GAGES

In the measurement of blast pressures

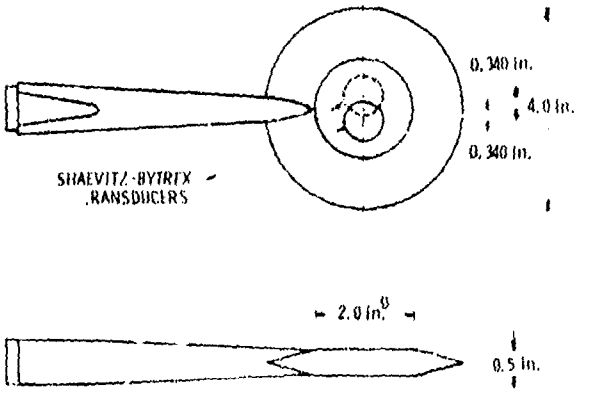


Figure 7-7. Side-on Blast Gage Using Small Flush-diaphragm Transducers

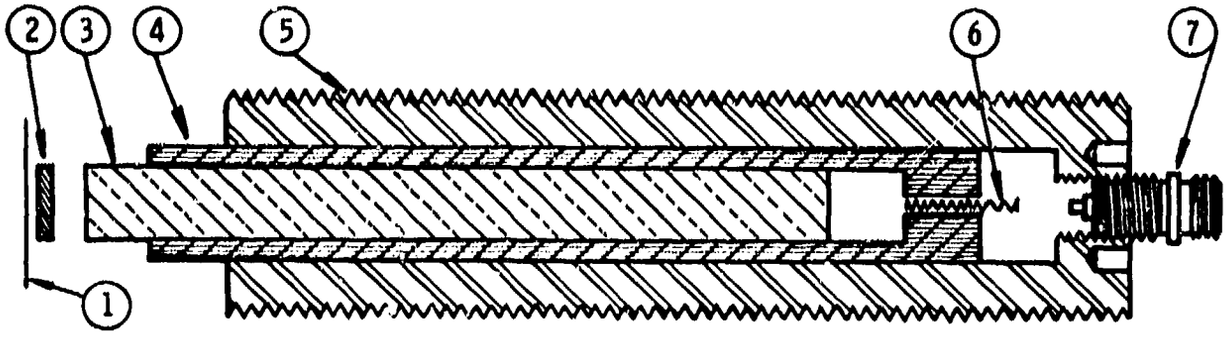
reflected at normal or oblique incidence from a rigid plane surface, flow and diffraction effects are no longer important, provided that the pressure transducer is capable of being mounted with its sensing element or diaphragm flush with the reflecting surface. Many more types of transducers thus can be satisfactorily used for measurement of reflected pressures than can be used for side-on pressures. We will confine our discussion here to those gages that either have been designed specifically for reflected pressure measurements, or are too large to be classified as miniature transducers.

The majority of the data reported to date on reflected blast waves from small explosive charges were obtained using a reflected pressure gage designed by Hoffman and Mills at BRL[5]. This gage used tourmaline or synthetic piezoelectric sensing elements mounted in a cavity in the face of a massive metal housing. The length of the gage housing effectively determined the lower limit on response time, i.e., several times greater than the transit time of an elastic dilatational wave along the length of the housing. This gage produced acceptable time histories for reflected pressures up to about 1500 psi. Granath and Coulter[6] later improved somewhat on this design, developing the gage shown in Fig. 7-8. This gage has been used successfully for reflected pressure measurements up to 4500 psi. It is also sold commercially.

Finally, the British at RARDE have developed a gage for reflected pressure measurements using the basic quartz sensing element of their H3 side-on gages. No data are available regarding the upper limit of pressure at which it is considered usable.

7-2.3 MINIATURE PRESSURE GAGES

Many types of miniature pressure transducers have been found to be suitable as air blast gages, either for mounting in small models or structures to measure details of diffracted pressure loading, for mounting in a large flat surface to measure reflected pressures, or for mounting in streamlined housings to record side-on blast wave pressures. Aside from their small size, the transducers that perform well under blast loading all appear to



1 METAL GROUNDING WIRE
2 PIEZOELECTRIC ELEMENT
3 BRASS ACOUSTIC WAVE GUIDE
4 NYLON OR TEFLON INSERT
5 STAINLESS STEEL GAGE CASE
6 CONTACT SPRING
7 COAXIAL CONNECTOR

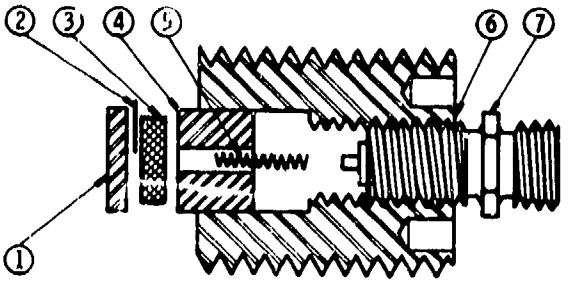
Figure 7-8. Reflected Pressure Gage of Granath and Coulter[6]

have several characteristics in common. They all have a sensing surface that can be mounted flush with the surface of some housing or structure. This surface may be a diaphragm whose displacement under applied pressure is sensed, a diaphragm or piston transmitting pressure to an interior piezoelectric sensor, or a surface containing one or more ports leading to a very small interior chamber containing an interior sensor. They all employ quite simple and rugged construction. Most have been developed specifically for measurement of blast pressures, and are designed to minimize spurious signals from acceleration and heat. Some also are designed to minimize effects of nuclear radiation on output or sensitivity. Those transducers which are of complex internal construction, particularly those employing unbonded wire strain gages, have generally proven to be quite unsuitable for air blast measurements.

In paragraphs that follow we will limit our discussion to those transducers that have been tested thoroughly and have been proven adequate as air blast transducers.

7-2.3.1. BRL MINIATURE TRANSDUCERS

Let us first discuss the miniature transducers that have been developed at Government laboratories. Several types of gage employing piezoelectric elements have been developed at BRL. Two types, designed and made by Granath and Coulter[6] for mounting in small models, are shown in sectional view in Fig. 7-9. The smaller of these gages is 0.31 in. in diameter and 0.31 in. long. Somewhat similar gages were designed by Baker and Ewing[9] for flush-mounting in the surfaces of airfoils subjected to blast loading. These latter gages, about 0.5 in. in diameter and 0.5 in. long, were designed to minimize acceleration and transient temperature sensitivity. One type is shown in sectional view in Fig. 7-10. From sinusoidal vibration tests, the signals generated under accelerations of one "g" normal to the gage face were determined to be less than that which would be generated by 0.004 psi blast pressure, over a wide range of excitation frequencies. The frequency response of these gages is dependent on the diameter of the piezoelectric discs that constitute the sensing element and the velocity of the shock front passing over the gage, rather than on the inherent frequency response of the sensing element. For weak shock fronts moving at near sonic velocity, rise times are in the order of 10-12 microsec. The lower limit on frequency is dependent on the input impedance of the associated amplifiers, as is true for any capacitive device.



1 NYLON CAP
2 METAL FOIL GROUNDING TAB
3 CERAMIC PIEZOELECTRIC ELEMENT
4 NYLON INSERT
5 CONTACT SPRING
6 STAINLESS STEEL GAGE CASE
7 COAXIAL CONNECTOR

Figure 7-9. Exploded View of Half-inch Gage of Granath and Coulter[6]

Ewing at BRL also has designed and built several other types of miniature gages employing natural and synthetic piezoelectric elements as sensors which are about the same size and external configuration as gages of Granath and Coulter. These are similar to the previous transducers of Ewing and Baker in internal construction, except that a different matrix material is employed in the cavity containing the sensing elements.

7-2.3.2 LANGLEY RESEARCH CENTER MINIATURE TRANSDUCERS

At the Langley Research Center of NASA, several types of small transducers have been developed for measurement of blast waves interacting with model airfoils and for measurement of free air blast wave pressures. All

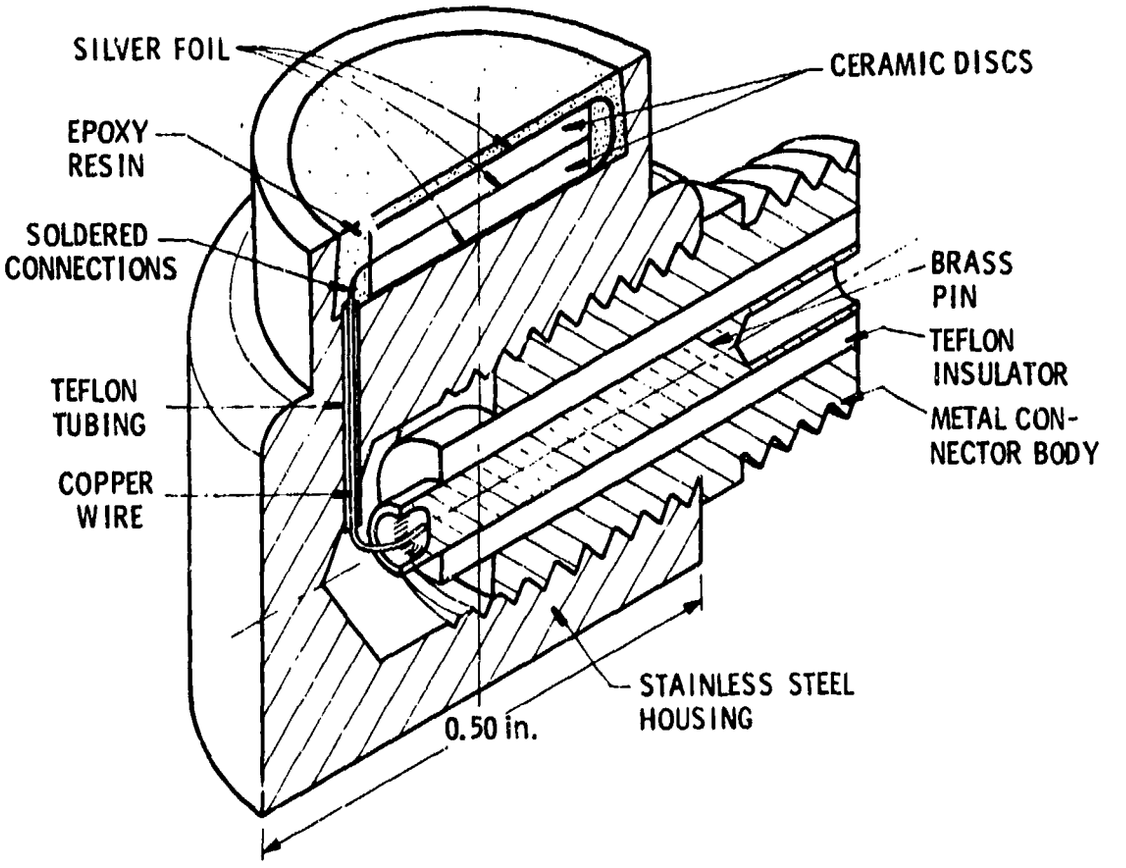


Figure 7-10. Sectional View of Gage of Baker and Ewing[9]

employ the principle of sensing of deflection of a ferromagnetic diaphragm under pressure by measurement of change in inductance of small electrical coils placed adjacent to the diaphragm. The first NASA design was evolved by Patterson[10]. The basic size of the transducer was 7/16-in. in diameter by 1/4-in. thick. A rather novel characteristic of this transducer is that it can be used for differential pressure measurement between two sides of an airfoil or other model, as well as absolute pressure measurement at one surface. When used with a suitable carrier amplifier system, this gage has frequency response from DC to an upper frequency which is dependent on the acoustic resonance of the cavities within the gage housing and on the fundamental vibration frequency of the diaphragm. Usually the acoustical resonance controls, yielding a flat response up to about 1000 Hz. Various pressure ranges are achieved by employing diaphragms of different thickness. Possible nonlinear response of thin diaphragms is minimized by pre-tensioning. Two very attractive features of this gage are its very low sensitivity to temperature and acceleration effects. Patterson reports, over a temperature range of -50° to 200°F, zero drift of less than 0.02 percent of full scale per degree and change in sensitivity of less than 0.02 percent of full scale per degree. For a gage whose full-scale pressure range was 8 psi, vibration tests conducted normal to the diaphragm showed an acceleration response of 0.001 psi/g. Accelerations in the plane of the diaphragm produce negligible gage response. The first design was later modified and decreased in size, as reported by Morton and Patterson[11], resulting in one of the smallest of miniature blast transducers. This tiny gage, shown schematically in Fig. 7-11, employs a single coil to sense displacement of a flush diaphragm. Its basic dimensions are 3/16-in. in diameter by 1/10-in. thick. Frequency response is flat from DC to 20 kHz for gages of full-scale range of 30 psi or greater, and is

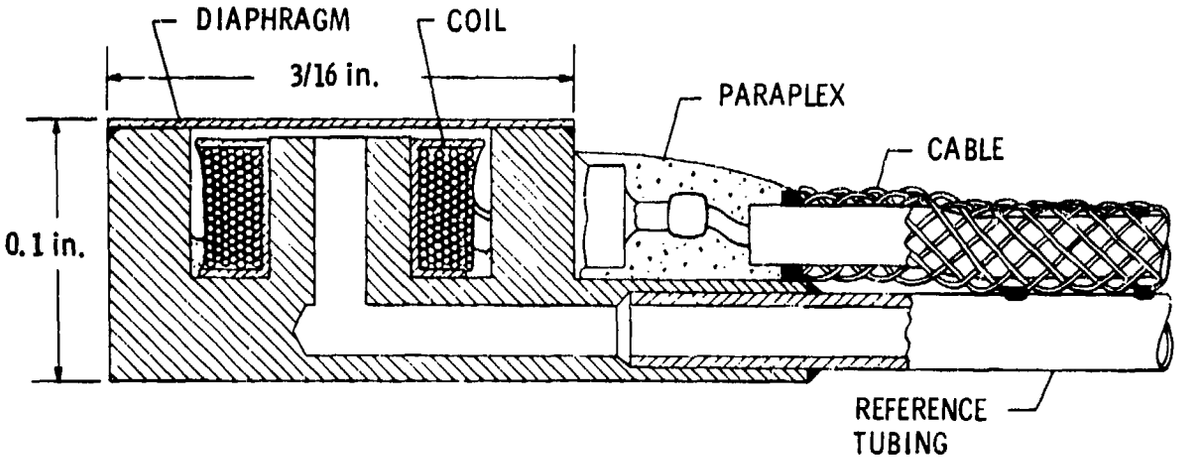


Figure 7-11. Sectional View of NASA Miniature Transducer of Morton and Patterson[11]

slightly less for more sensitive gages. As for the earlier design, this gage exhibits quite low sensitivity to temperature and acceleration.

7-2.3.3 OTHER MINIATURE TRANSDUCERS

Several commercial firms manufacture miniature pressure transducers that employ piezoelectric materials as sensors. Atlantic Research Corp. produces several types. Photographs of several of these gages are reproduced in Fig. 7-12. The smallest (Type LD-80) is 0.14 in. in diameter and 0.5 in. long. All employ synthetic piezoelectric materials as sensors. The manufacturer does not report sensitivity to temperature or accelerations. The Type LD-80 transducer is claimed to be usable for shock pressures as high as 10,000 psi and to have face-on rise times of less than one microsecond.

The Kistler Instrument Corp. makes several types of pressure transducers employing quartz as the piezoelectric sensing element. One type in particular, Model 603A, has been employed as a miniature blast pressure transducer. This gage, shown in Fig. 7-13, is 0.22 in. in diameter by 0.45 in. long. A novel feature is the inclusion of additional quartz discs to compensate for acceleration, as shown schematically in Fig. 7-14. Acceleration sensitivity of 0.001 psi/g and temperature sensitivity of 0.01 percent of full scale per one degree Fahrenheit are claimed by the manufacturer, rendering this transducer much less sensitive to these effects than are most other piezoelectric transducers. Response time to reflected shock waves has been demonstrated to be about one microsecond.

The Kaman Nuclear Division of Kaman Aircraft Corp. manufactures a line of variable reluctance blast pressure transducers which act on an eddy-current loss principle. Magnetic flux lines, emanating from a coil, pass into a diaphragm and produce eddy currents in the conductive diaphragm circuit. As the diaphragm is brought closer to the coil, more flux lines are intercepted and the losses become greater; and, as the diaphragm is moved away from the coil, the losses become less. When the coil is connected as an arm of a conventional AC bridge circuit, the coil impedance will change with applied pressure; and this in turn will result in a change of the AC output signal from the bridge circuit. The electrical output of the bridge can be made linear with respect to the applied pressure by proper selection of the diaphragm thickness, active diaphragm area, diaphragm material, and diaphragm-to-coil spacing. The basic element is shown in Fig. 7-15. The smallest gage is somewhat larger than the other miniature gages discussed previously, but all of the Kaman Nuclear gages are shielded from nu-

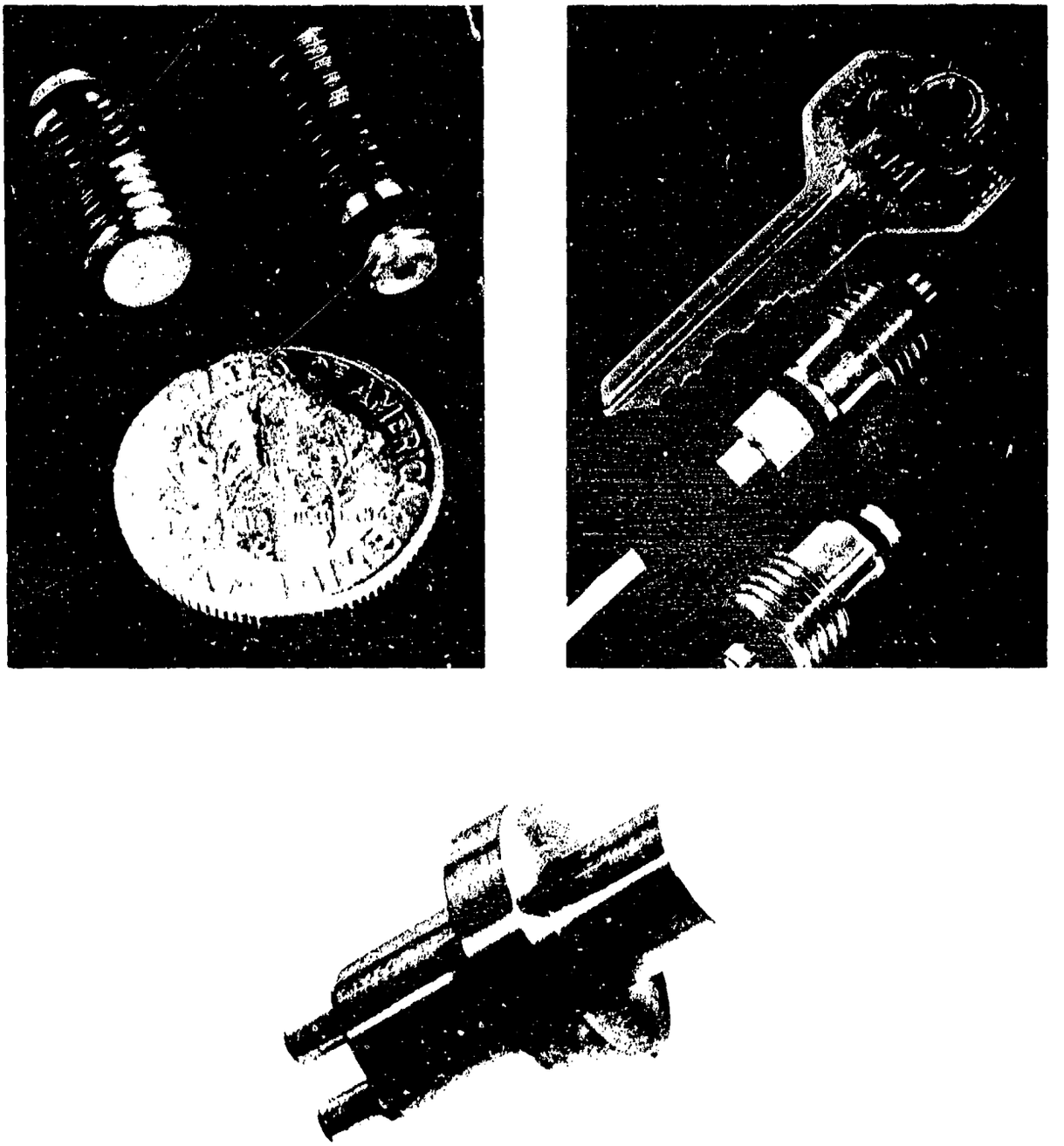


Figure 7-12. Atlantic Research Corp. Miniature Pressure Transducers (Courtesy of Atlantic Research Corp.)

clear radiation effects, as well as being designed to minimize temperature and acceleration sensitivity. Acceleration sensitivity of the Model K-1200 gage is stated as 0.01 percent of full scale per "g", depending on pressure range and output sensitivity. The Kaman Nuclear gages all have response, when used with suitable carrier systems.

One of the few types of miniature strain gage pressure transducer that has proven useful for blast wave measurements has been

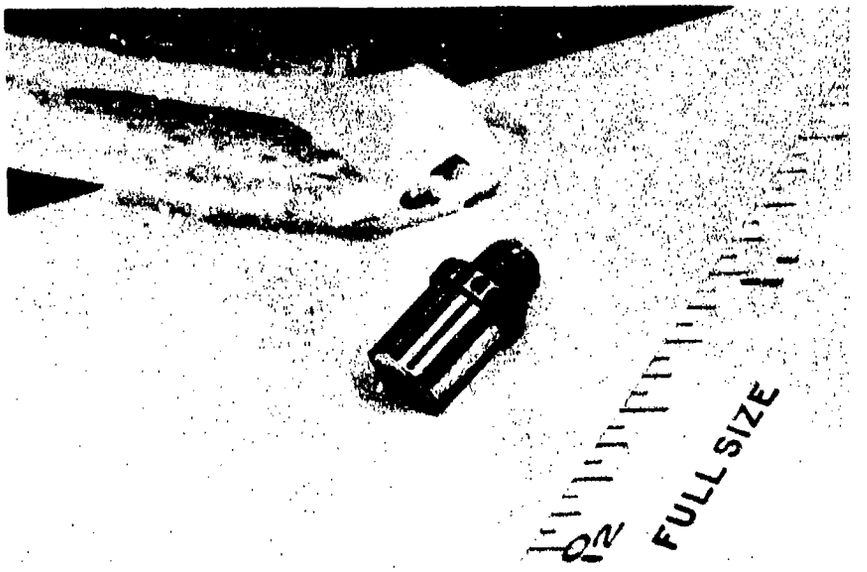


Figure 7-13. Kistler Model 603A Quartz Miniature Pressure Transducer (Courtesy of Kistler Inst. Corp.)

developed by Shaevitz-Bytrex, Inc. These gages employ semiconductor strain gages on minute columns supporting flush-mounted diaphragms as pressure sensors. Several models are shown in Fig. 7-16. The smallest of these is 1/8 in. in diameter by 5/8 in. long. Certain models have been proven by test to have quite low temperature and acceleration sensitivity. One model has a thermal drift of less than 0.01 percent of full scale per degree Fahrenheit, and thermal effect on sensitivity of less than 0.01 percent of reading per degree Fahrenheit. Acceleration sensitivity for motion normal to the diaphragm (the most sensitive direction) is 0.006 psi/g for a 0-15 psi range gage, and 0.001 psi/g for a 0-1000 psi range gage. Frequency response is flat from zero to at least 20 kHz for all gages in this series.

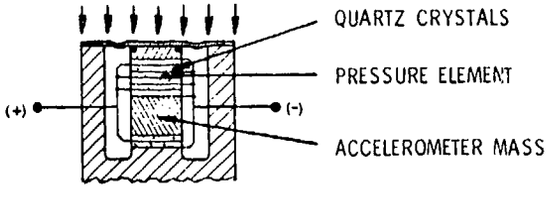
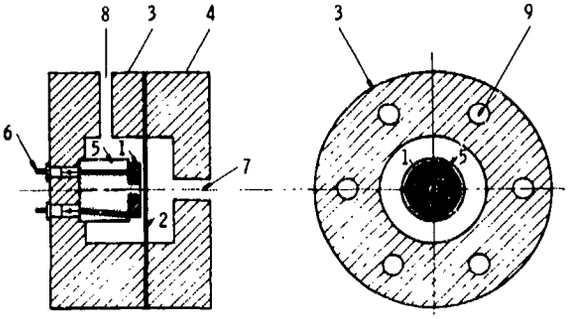


Figure 7-14. Internal Schematic of Kistler Model 603A Pressure Transducer Showing Scheme for Acceleration Compensation

Miniature piezoelectric transducers with acceleration compensating elements, similar to the Kistler Model 603A gages but somewhat smaller, have been developed by Levine at the Naval Ordnance Laboratory[1,2]. The internal construction and principle of operation seem similar to Kistler gages. The primary difference is the use of quartz as the piezoelectric element in the Kistler trans-



1 - FLAT COIL
2 - DIAPHRAGM
3 - CASE HOUSING
4 - CASE COVER
5 - COIL FORM
6 - ELECTRICAL TERMINAL
7 - MAIN PRESSURE INLET PORT
8 - REFERENCE PRESSURE PORT
9 GAGE ASSEMBLY SCREW HOLE

Figure 7-15. Basic Single Coil Variable Impedance Pressure Transducer, Kaman Nuclear
(Courtesy of Kaman Nuclear Corp.)

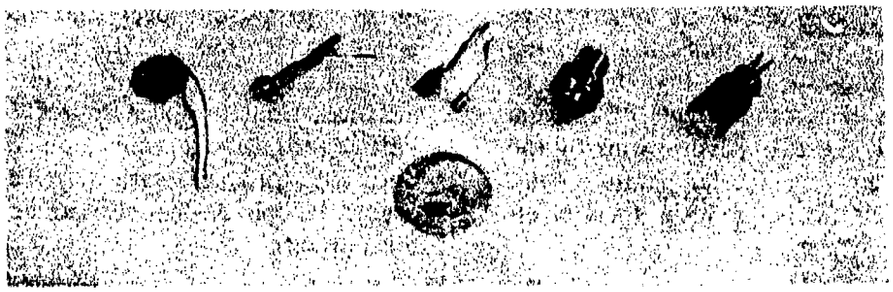


Figure 7-16. Shaevitz-Bytrex Miniature Pressure Transducers
(Courtesy of Shaevitz-Bytrex, Inc.)

ducer, and a ceramic element such as barium titanate or lead zirconate in the NOL transducer. Levine[12] notes that one must be quite careful in the design and construction of such a transducer to isolate completely the accelerometer-element from direct pressure and from the effects of pressure on the element housing.

Two types of commercial miniature transducers of very similar internal design have been employed on nuclear or long-duration conventional air blast tests[8]. Both sense the deformation of a diaphragm by strain gages bonded to a cylindrical tube that supports the diaphragm. A schematic of one of these, the Dynisco PT 76, is shown in Fig. 7-17. Strain elements are bonded to a thin cylinder that has one end secured to the case and the other attached to the diaphragm. The small mass and minute deflection resolution result in very-high-frequency response characteristics, but the bonded strain-wire gages have low sensitivity output about 2 to 4 mV/V full scale. Although the design and assembly of the gages reportedly make them insensitive to

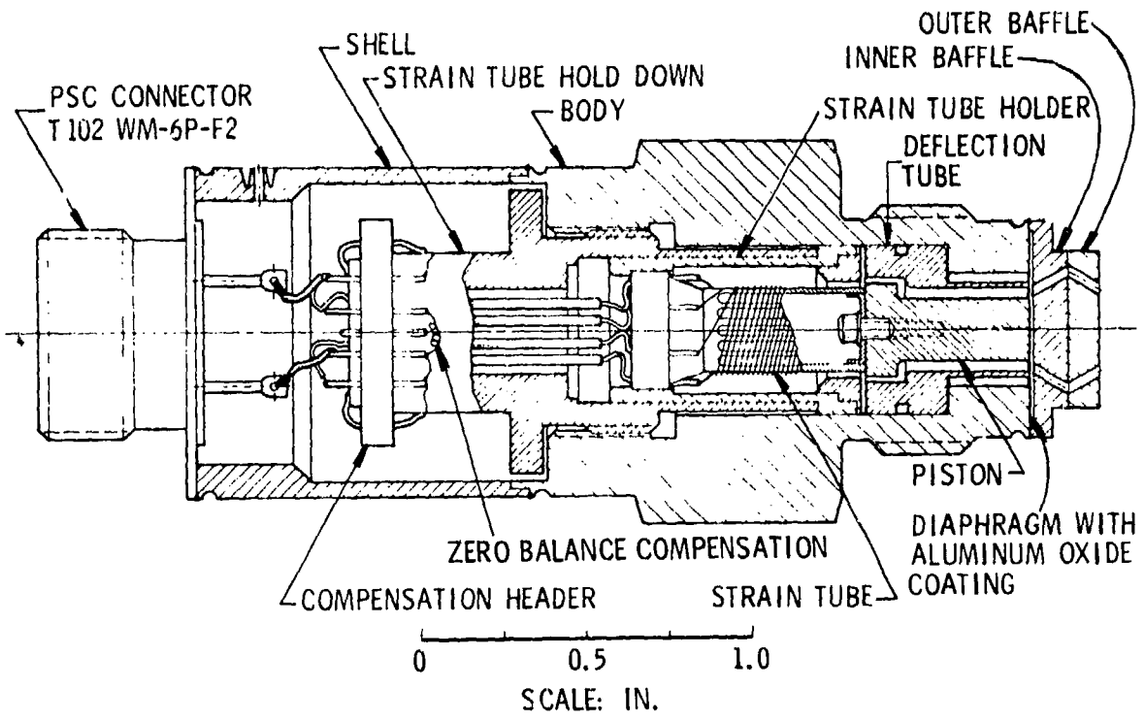


Figure 7-17. Dynisco Pressure Transducer[8]

vibration and accelerations no quantitative values are given by Rowland[8]. Bonding the strain gages to the tube rather than directly to the diaphragm delays the effects of thermal transients, and the two passive arms of the bridge circuit are used for temperature compensation which further reduces thermal effects.

In an attempt to reduce the temperature response, BRL has tested Dynisco transducers fitted with special diaphragms. The normal stainless steel diaphragm was replaced with others of various materials intended either to reflect, insulate, or evenly distribute the heat. Nickel, copper laminated with stainless steel, stainless steel covered with Teflon, and stainless steel coated with flame-sprayed aluminum oxide were tested. For very high pressure studies near the detonation point of underground nuclear blasts, BRL protects the diaphragm with a baffle consisting of a heat-shield with eight double-angle inlet ports and a small cavity between the inlet holes and the diaphragm, as well as the aluminum oxide (Fig. 7-17).

A number of types of gages designed and made at the Atomic Weapons Research Establishment (AWRE) in Great Britain deserve mention here, even though most of them are too large to be truly classed as "miniature" transducers. All employ quartz as the sensing element, and all are intended for use in a variety of applications, as indicated in Table 7-1. The internal construction of one of these gages is shown very clearly in Fig. 7-18. Gage characteristics also are summarized in Table 7-1. As one can see from the diameters, only the MQ 20 type gage truly can be classed as a miniature gage.

7-3 ARRIVAL-TIME GAGES AND ZERO-TIME MARKERS

Because it is possible to infer all other shock front properties from measurement of shock velocity and ambient conditions through the Rankine-Hugoniot equations (Chapter 2), relatively simple transducers often are used for detecting the time of travel of the blast front over known, accurately measured base lines, or the time of arrival of the front at a number of stations at various distances from the blast source. To measure time-of-arrival, one must detect a "zero time", or time of start of release of blast energy. Simple devices also are employed for this purpose.

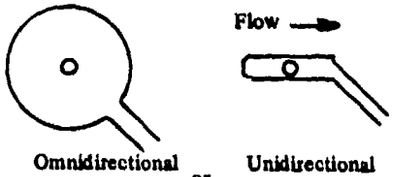
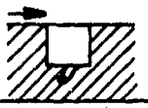
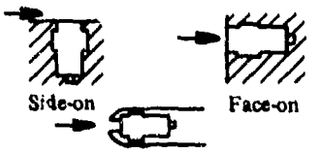
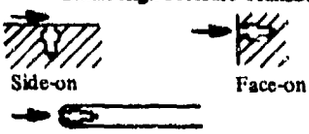
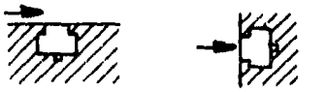
One of the first types of arrival-time transducer used in air blast measurements consisted of a blast-actuated switch, shown schematically in Fig. 7-19. On shock arrival, a light aluminum foil diaphragm that had been stretched over the face of a metal tube housing was displaced until it contacted the tip of a metal screw and closed an electrical circuit. This transducer was very simple and inexpensive, but often gave erroneous indications of arrival time because it had a relatively slow response time, and this time was a function of the initial gap between the foil and the tip of the screw. Also, if the transducer was used to measure blast waves from cased explosive charges, it often was triggered prematurely by ballistic shocks generated by case fragments.

Side-on blast gages, described previously in this chapter, can be used to determine times of arrival. Unless their sensing elements are quite small, they are not optimum for this use. This is because their rise-times are limited by time of travel of the shock front over the element, and the exact times of arrival are then difficult to determine from recorded time histories.

A compromise between the very simple mechanical blast switch and the much more sophisticated side-on blast pressure transducer has proven to be superior to either as a transducer for indicating time of arrival. The compromise consists of using a pressure transducing sensitive element, but mounting the element in a simple and inexpensive housing. The transducer is also designed so that the element is struck normally by the blast front, and the rise-time is therefore quite short. No particular care need be taken in construction of the transducer to minimize oscillations or

TABLE 7-1

SUMMARY OF PROPERTIES OF AWRE FOULNESS PATTERN STANDARD PIEZOELECTRIC TRANSDUCERS

Transducer Diameter, inches	Transducer Type	Maximum Pressure, psi	Sensitivity pC/psi	Sensitivity mV/psi with Cable Supplied	Applications
6-1/2	FQ 11c Pressure Insert	300	100	-	Free-Air Measurements: Mounted In  Omnidirectional Baffle B12 or Unidirectional Baffle B2
1-7/8	MQ 10	500	100	-	Sensitive Flush Mounted Transducer  Mainly Used for "Side-On" Measurements
1-1/4	MQ 18	300	24	300	Acceleration Compensated Flush Mounted Transducer  Total Head Pressure Measurements Using Baffle BS 2
7/16	MQ 20	30 000	0-5	2-5	Small High-Pressure Transducer  Total Head Pressure Measurements Using Baffle BS 5
-	MQ 23	20 000	2-0	8	Fast-Response High-Pressure Transducer 

reflections after shock arrival, since one is interested only in generating a large signal on arrival of the front. Watson and Wilson[13] describe a transducer of this type which is in current use at BRL. It is shown in cross section in Fig. 7-20. The gage uses a commercially available feed-through coaxial connector, and a dust cap for this connector, as basic parts. The sensing element is a single piezoelectric disc, mounted on a brass pedestal and "potted" in epoxy resin.

There are also several time-of-arrival gages available commercially. Atlantic Research

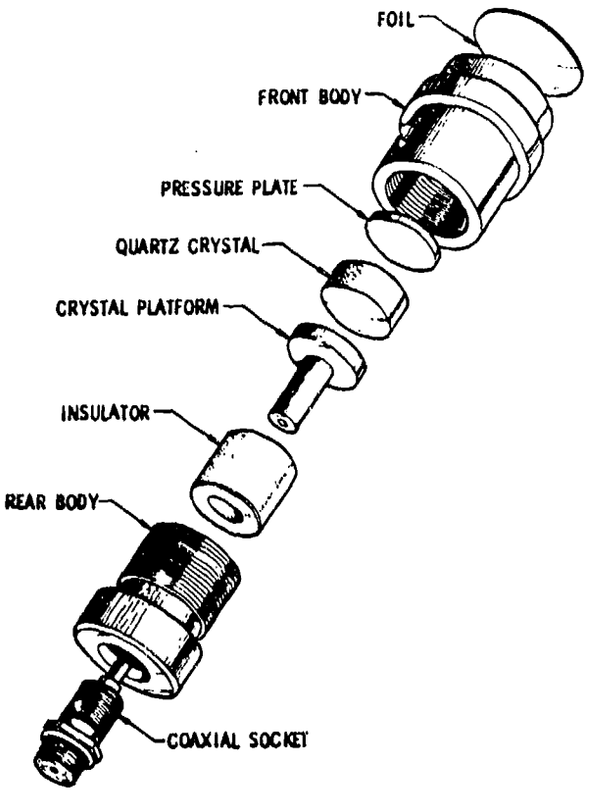


Figure 7-18. British AWRE MQ20 Pressure Transducer

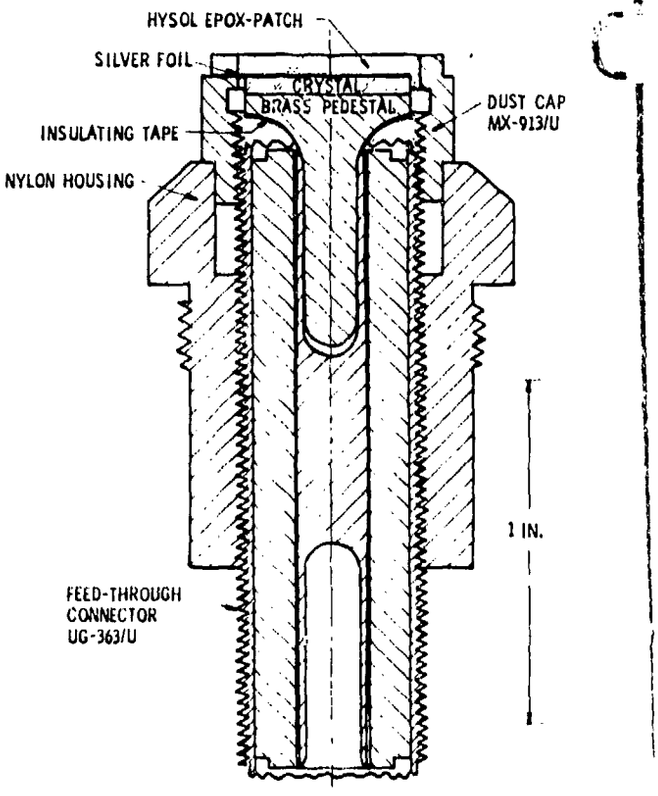


Figure 7-20. BRL Arrival-time Gage of Watson and Wilson[13]

Corporation manufactures several types, on the same principle as the BRL gage, and also using commercial coaxial connectors as the gage housings. Kaman Nuclear Division of Kaman Aircraft Corp., also makes a blast arrival time system, using a pressure transducer, similar to that described elsewhere in this chapter.

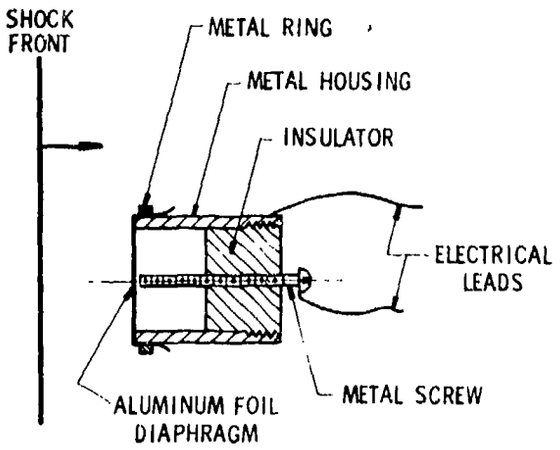


Figure 7-19. Early Type of Blast Switch

Zero-time transducers can be almost revoltingly simple, and *must* be inexpensive, because they are invariably destroyed by the explosion. Any device will suffice, provided it generates a sharp signal or rapidly opens or closes an electrical circuit. A small piezoelectric crystal mounted on the blast source will generate a large charge on detonation; a twisted pair of insulated bell wire leads will provide a "normally open" circuit that is closed by the highly ionized gases generated by many blast sources; and a closed loop of the same bell wire will provide a "normally closed" circuit that is opened when the loop is ruptured by the explosion. These three devices have been used quite often, but by no means include all of the possible schemes which one could use. Our advice here is to simply use your imagination *something* simple and inexpensive will work.

7-4 TOTAL HEAD GAGES AND DRAG GAGES

An important parameter of blast waves, particularly for determining loading on targets for waves of long duration, is the dynamic pressure q

$$q = \rho u^2/2 \qquad (7\text{-}1)$$

where

ρ = density in blast wave

u = particle speed

A number of different types of gages have been developed by BRL and other agencies for measurement of the time histories of this parameter, or of the "total head" or stagnation pressure p_h

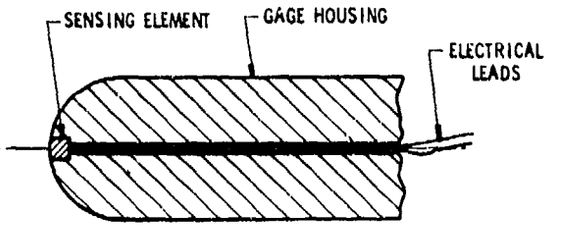
$$p_h = P_s + \rho u^2/2 = P_s + q \qquad (7\text{-}2)$$

where

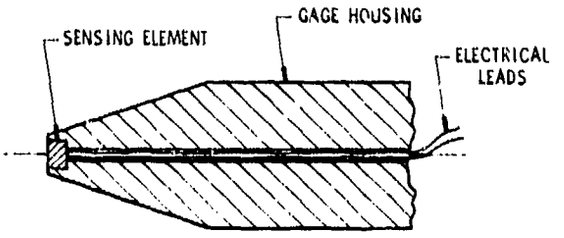
P_s = peak side-on pressure

7-4.1 TOTAL HEAD GAGES

The total head gages resemble pitot tubes that are used to measure this same parameter in steady or slowly-varying flow fields. They consist of axisymmetric housings with blunt noses, and sensing elements located at stagnation points for flow around the housings (see Fig. 7-21). For gages intended to be used for relatively weak blast waves where peak particle speed u_s is considerably less than sound speed, the nose is hemispherical (Fig. 7-21(A)). For stronger shocks where u_s approaches or exceeds sound speed, a truncated conical nose shown in Fig. 7-21(B) is used. These gages have been made only in rather large sizes for use in field tests of large chemical or nuclear blast sources.



(A) LOW MACH NUMBER FLOW



(B) HIGH MACH NUMBER FLOW

Figure 7-21. Cross Sections of Typical BRL Total Head Gages

7-4.2 DRAG GAGES

Drag or dynamic pressure gages are designed to measure only the dynamic pressure q. They consist of bodies of some regular shape for which steady-state wind-tunnel drag data exist, mounted on or incorporated in a sensing system that measures total drag force on the body, or one or more components of this force. Drag pressures are then inferred from the outputs of the sensors, using the conventional aerodynamic drag formula

$$D = C_D S \rho u^2/2 \qquad (7\text{-}3)$$

where

D = drag force

C_D = a drag coefficient which is presumed to be known for the particular shape of body

S = projected area of the body normal to the flow direction

For these gages to function properly, the drag body must be small compared to the length of the blast wave, and the lowest vibration period of the body-sensor system must be much shorter than the blast wave duration.

7-4.2.1 DRAG GAGE OF JOHNSON AND EWING

An example of a drag gage is discussed by Johnson and Ewing[14]. Their gage consists of a cantilever beam of circular tubular cross section which protrudes above a base plate. Bending strains are sensed in the tube near its base, in two orthogonal planes. The averages of each strain-time history recorded as a blast wave sweeps past the gage are measures of two orthogonal components of drag pressure. The gage was intended for use in blast fields from surface-burst or low-height-of-burst sources where the exact direction of travel of the shock front is not known precisely. Tubes with fundamental frequencies of 500 Hz and 1000 Hz were tested, for use with blast waves of 10 msec or greater duration. A typical trace recorded in a shock tube is shown in Fig. 7-22.

Various other types of drag gages have been made for nuclear field tests or tests with large conventional explosive charges (Rowland 1967). Some of these are described in the paragraphs that follow.

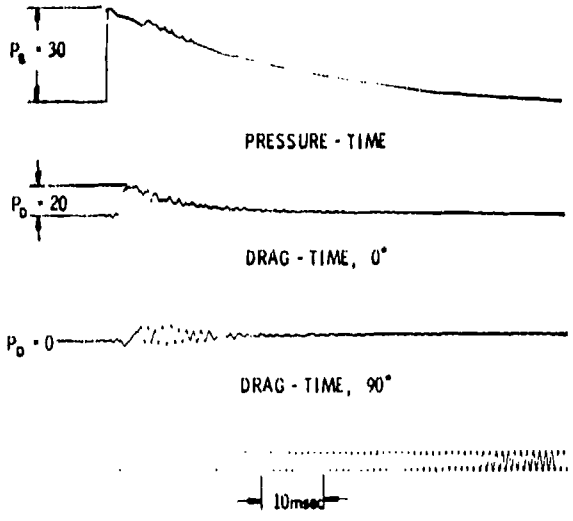


Figure 7-22. Comparison of Pressure-Time and Drag-Time Traces for 0 deg and 90 deg to Flow Direction, Gage of Johnson and Ewing[14]

7-4.2.2 NOL DRAG FORCE GAGES

NOL developed and used three-component force gages in a number of nuclear tests. These gages measured the blast-wave-induced forces on a small target in three mutually perpendicular axes. The targets were spheres, cubes, cylinders, and parallelepipeds. Variable-inductance sensing elements contained within the target responded to the excitation produced by the blast wave. The targets were spring-mounted on sets of springs located in three orthogonal directions. Each axis of the force gage had its own natural frequency. The frequencies were limited by the mass of the moving parts of the gage and the spring constants required to allow this mass to move only as far as necessary to generate the required electric signal. These frequencies ranged from 85 Hz to 550 Hz. This relatively low frequency response prohibits the use of these gages for measuring short-duration diffraction forces; hence, their usefulness was limited to the long-duration drag phase of the shock wave interaction.

7-4.2.3 SRI DRAG PROBES

Stanford Research Institute (SRI) has made a drag probe whose drag-sensitive target is a hollow short section of a much longer mounting cylinder (Fig. 7-23). The mounting cylinder is positioned rigidly with its long axis parallel with the ground and at right angles to the direction of air flow. The target element is at the center of the mounting tube in order to minimize the effects of flow around the end of the element. The sensing elements are strain gages attached to an octagonal proving ring within the hollow target cylinder. Blast-induced drag forces produce a small displacement of the target cylinder, which is measured by the strain gages on the proving ring. This probe senses only one component of drag pressure. The initial design was for four different maximum overpressure ranges vary-

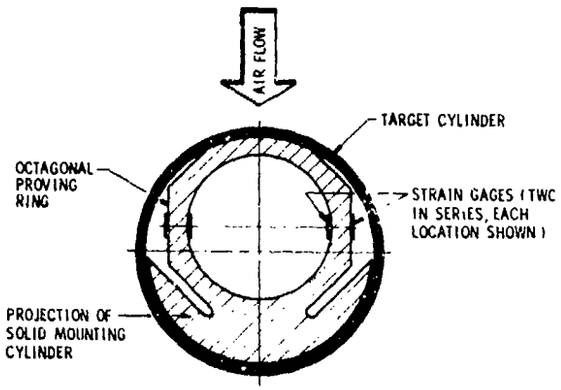


Figure 7-23. SRI Total Drag Probe Assembly Schematic Cross Section[8]

ing from 50 to 500 psi. The natural frequency of these gages varied from 4 kHz to 5.5 kHz.

7-4.2.4 BRL BIAXIAL DRAG GAGE

BRL has constructed a biaxial drag gage for measuring the magnitude and direction of dynamic blast pressure. The sensing element is a load cell that senses forces in two cross axes in a target area that behaves approximately like a section of a cylinder of infinite length. Fig. 7-24 is an assembly drawing of the completed probe. The entire surface of the gage from the nose cone to the cylindrical center section is given a rough knurled finish. This is to promote turbulent flow about the body and minimize variations in drag coefficient in the transition region of flow. Gage natural frequency ranged from 2.5 kHz to 5.0 kHz.

7-5 DENSITY GAGE

A blast wave density gage has been developed by Dewey and Anson[15] for use in large-scale field experiments. The general configuration is shown in Fig. 7-25. It consists essentially of two 4-ft X 2-ft X 3.5-in. aluminum sections, each rigidly bolted to a 0.5-in. steel base plate. The leading and top edges of the sections are bevelled to knife edges and the inner surfaces are plane so that, when the gage is aligned with the charge center, the blast wave receives little distortion as it passes between the sections. One section contains a β-source and the other a detector unit consisting of a phosphor scintillator, a photomultiplier, and an amplifier. The spacing between the two sections may be varied. When a blast wave passes between the two sections, the increase of air density causes a greater absorption of β-particles producing a

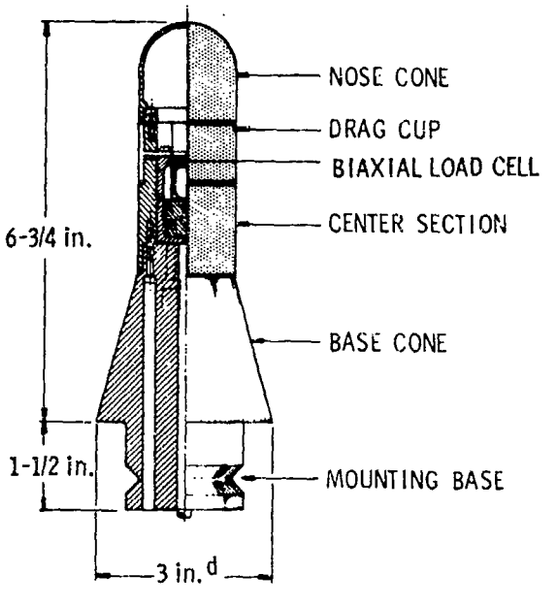
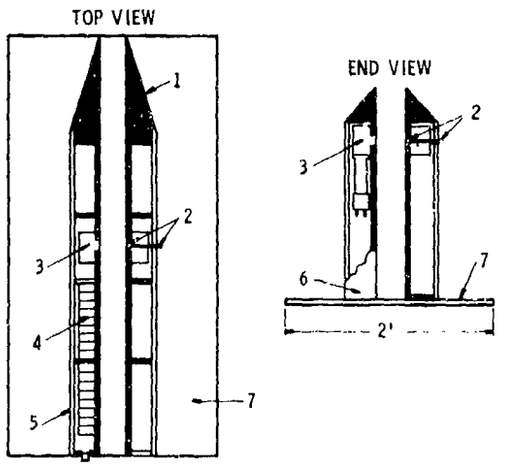


Figure 7-24. Assembly Drawing of BRL Biaxial Drag Gage[8]



1-SOLID CAST ALUMINUM SECTIONS; 2-β-SOURCE AND LOCKING ASSEMBLY; 3-DETECTOR; 4-BATTERIES; 5-SIDE COVER PLATES; 6-POWER SUPPLY SWITCHES AND OUTPUT CONNECTORS; 7-STEEL BASE PLATE.

Figure 7-25. Diagram of Density Gage of Dewey and Anson[15]

change of the detector output. This signal is amplified and transmitted via several thousand feet of coaxial cable to an instrumentation bunker where it is recorded as a frequency-modulated signal on magnetic tape.

Calibration of the gage can be achieved easily by inserting foils of aluminum or Mylar of known mass per unit area between the source and the detector, and recording the output of the detector. In practice, a disc with inserts of materials of different areal density is rotated through the beam path to provide multistep calibration.

A typical trace of density in a blast wave from a large chemical energy source is shown in Fig. 7-26. The "noisiness" is inherent in this type of gage, because the output of the scintillator detector consists of a series of discrete bursts rather than a continuous signal.

This ingenious gage is, as far as the authors are aware, the only successful one for continuous analog recording of time histories of density in blast waves. Some optical methods exist, as discussed in Chapter 9, but they are more useful in shock tube studies than in field experiments.

7-6 IMPULSE TRANSDUCERS

7-6.1 FREE PLUG TRANSDUCER

In measuring the time histories of pressure in reflected air blast waves with piezoelectric transducers, investigators at BRL found that the limits for satisfactory function of these gages were in the range of several thousand psi. To determine at least some blast parameter accurately at high overpressure levels, they then developed a free plug transducer for measurement of reflected impulse[16]. This device consists simply of a cylindrical plug that is lightly held in a hole in a large, rigid plate and is accelerated by a normally-reflected blast wave. Measurement of the plug velocity after blast wave passage, and knowledge of its area presented to the blast front and its mass allows determination of the reflected impulse from the impulse-momentum theorem. In use, the plug velocity is measured either by photographing its flight against a scale background with an accurately timed motion picture camera, or by some

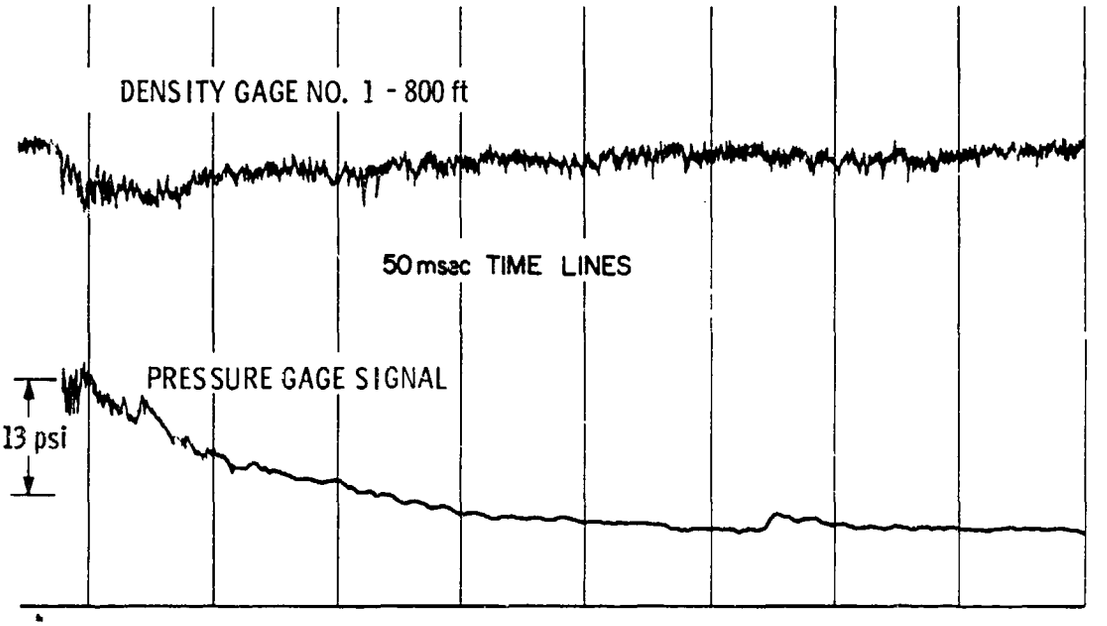


Figure 7-26. Record from Density Gage of Dewey and Anson[15]

otner means of accurately measuring time of travel over a known base line. The "flying plug" has been used under simulated altitude conditions[17] as well as sea level conditions. This simple method is quite accurate and precise, provided one adjusts the plug mass so that little motion occurs during the total duration of the blast wave. Measurements are made routinely at very small scaled distances (down to 6 in. from the center of 1-lb explosive charges of Pentolite), where piezoelectric transducers have been either erratic or useless.

7-6.2 SLIDING PISTON GAGE

In theory, a modification of the technique described in par. 7-6.1 for measuring reflected impulse should prove adaptable for measurement of side-on impulse. One such device is described by Kennedy[18] as being used at Underwater Explosions Research Laboratory during World War II. The gage was described as having a freely-sliding piston, and being provided with a rotating drum carrying recording paper on which a stylus attached to the piston writes. The resulting record is a plot of the integral of impulse versus time. Thus, the impulse at any time is proportional to the slope of the curve at that time, and the positive impulse is proportional to the maximum (positive) slope of the curve. The gage records the negative impulse as well. In practice, this device apparently was much less accurate than integration of time histories from side-on pressure transducers, since no appreciable amount of data appears to have been generated with it. Other attempts at BRL for measurement of side-on impulse using relatively simple transducers that would mechanically integrate the pressure-time history also has proven abortive.

7-6.3 SPRING PISTON GAGE

For measurement of blast intensities from charges of moderate size for which the positive durations encountered are not extremely long, Kennedy[18] claims that a spring piston gage is capable of precise measurement of positive impulse. For this purpose, the piston mass and spring strength are adjusted so that the natural period of the mass is about four times the positive duration of the blast. Under these conditions, the maximum compression of the spring is a measure of the positive impulse. Again, no data are given, so the usefulness of such an impulse transducer is questionable.

7-7 VARIOUS MECHANICAL GAGES

Throughout the history of air blast testing, there have been sporadic efforts to replace the complex instrumentation usually required to measure blast parameters with simple mechanical gages requiring either no or very unsophisticated recording equipment. One must sacrifice exact knowledge of the complete time history of pressure, etc., with such simple devices, and be content with estimates of peak overpressure alone, or peak drag pressure, or drag impulse, or perhaps only an effective equivalent explosive charge energy. Balancing this disadvantage is the extreme simplicity and relative cheapness of mechanical devices—one can easily emplace dozens or hundreds of properly calibrated mechanical gages during a field test.

7-7.1 DEFORMATION GAGES

The simplest possible gages are those permanently deformed by the blast wave. Many such devices have been used by both U. S. and British investigators. Ref. 18 includes descriptions of a number of such devices used prior to and during World War II. Examples of this group are two types of gage used by the Research Department, Woolwich, England, up to the beginning of World War II, both of which gave an empirical estimate of blast. They were the "foil gage" and the "cylinder gage". In both the deformation of copper discs under the action of the blast wave was measured.

The foil gage consisted of thin annealed copper discs rigidly clamped round their periphery over holes in a steel plate. The gages were calibrated by clamping simple discs over the open end of a cylinder connected to an air

supply and measuring the deflection as the air pressure was increased progressively. In the field the discs were exposed face-on to the blast, and from their deformation the so-called "equivalent static pressure" in the blast was measured by reference to the calibration curve.

The larger and much thicker discs of the cylinder gage were clamped on to form the opposite airtight ends of a steel cylinder some 6 in. in diameter and 10 in. long. These gages were placed with the axes of the cylinders at right angles to the direction of the blast wave; the discs were therefore exposed approximately side-on to the blast. Their deformation was used as a comparative measure of the blast from different charges.

Another simple blast meter of the deformation type used in England consists of a number of aluminum strips, of different thicknesses, clamped at their centers to a steel post to form a series of double cantilever beams. These blast "flags" have been used to determine the high-explosive equivalent of propellant explosions. They are calibrated by exposing sample strips to the blast from known weights of explosive and determining the relation, for each thickness, among the charge weight, the distance from the charge to the cantilever in question, and the angle of deflection of the cantilever. The deflection of a given strip decreases rapidly with distance from a charge and the device is also reported to be subject to a scale effect; as the charge weight was increased a disproportionate increase in deflection was observed. Wind velocity can also affect the deflection of the strip. The calibration requires care, and the use of blast "flags" must be restricted to the range of charge weights for which they are calibrated. Their main virtue, as with many simple mechanical gages, is that their comparative cheapness permits them to be used in sufficiently large numbers for the results to be treated statistically and so to yield significant answers. A U. S. variant of this same type of blast gage[19] employs single aluminum cantilever beams clamped in simple vises that are mounted on relatively massive base plates. Calibration was achieved in the same manner as for the British "flags". Typical calibration curves from Ref. 20 are shown in Fig. 7-27.

Exposing a series of stiff vertical wires, mounted as cantilevers, has also been tried by the British. Under blast loading a given wire will be bent through an angle which at any particular distance is a function of the drag force experienced and therefore of the weight or energy of explosive detonated. This function can be determined by experiment. The circular cross section of the wires makes gages of this type omnidirectional, thus they can be used to indicate asymmetry of the blast wave. They also have been used in atomic weapon tests to measure the dynamic pressure in the blast wave.

Another use of very simple gages occurred during an early atomic weapon test at Bikini. Sir William Penney, who was present as an observer, deployed around the test site a large number of empty gasoline tins; these tins deformed to various degrees by the blast wave. He was able to estimate the peak pressure to which the tins had been subjected by measuring the change in internal volume which each had sustained. In this way considerable amount of data was gained at a trial in which some of the more sophisticated methods of measurement failed. One-gallon empty varnish cans were later used in the same manner by other investigators[21] to compare the relative blast effectiveness of conventional explosives. The advent of atomic weapons in fact renewed interest in mechanical gages. There were two main reasons for this. Firstly, the duration of an atomic blast wave was so long that the use of mechanical systems for accurate measurements became feasible, despite their inherent low frequency response. Secondly, the electromagnetic radiation emitted by nuclear devices interfered with the use of piezoelectric systems.

7-7.2 PEAK PRESSURE GAGES

Peak-pressure gages have been devised to operate on the principle that a thin diaphragm, stretched over a hole in a rigid plate,

will rupture at a certain pressure when the diaphragm is subjected to a blast wave. If several such diaphragms are provided, covering holes of various sizes, the pressure required to rupture a diaphragm over a given hole will depend on the hole size. Hence, given a calibration of the device, the peak pressure of a blast wave is established as less than that required to break the diaphragm of the largest hole unbroken, and greater than, or equal to, the pressure required to break the diaphragm over the smallest hole broken. In theory, the pressure in thus bracketed quite closely, simply by having a sufficient number of holes of graduated sizes.

The first device of this type was apparently a "paper blast meter". It consisted of two boards clamped together with a sheet of paper held tightly between them. Holes of about ten

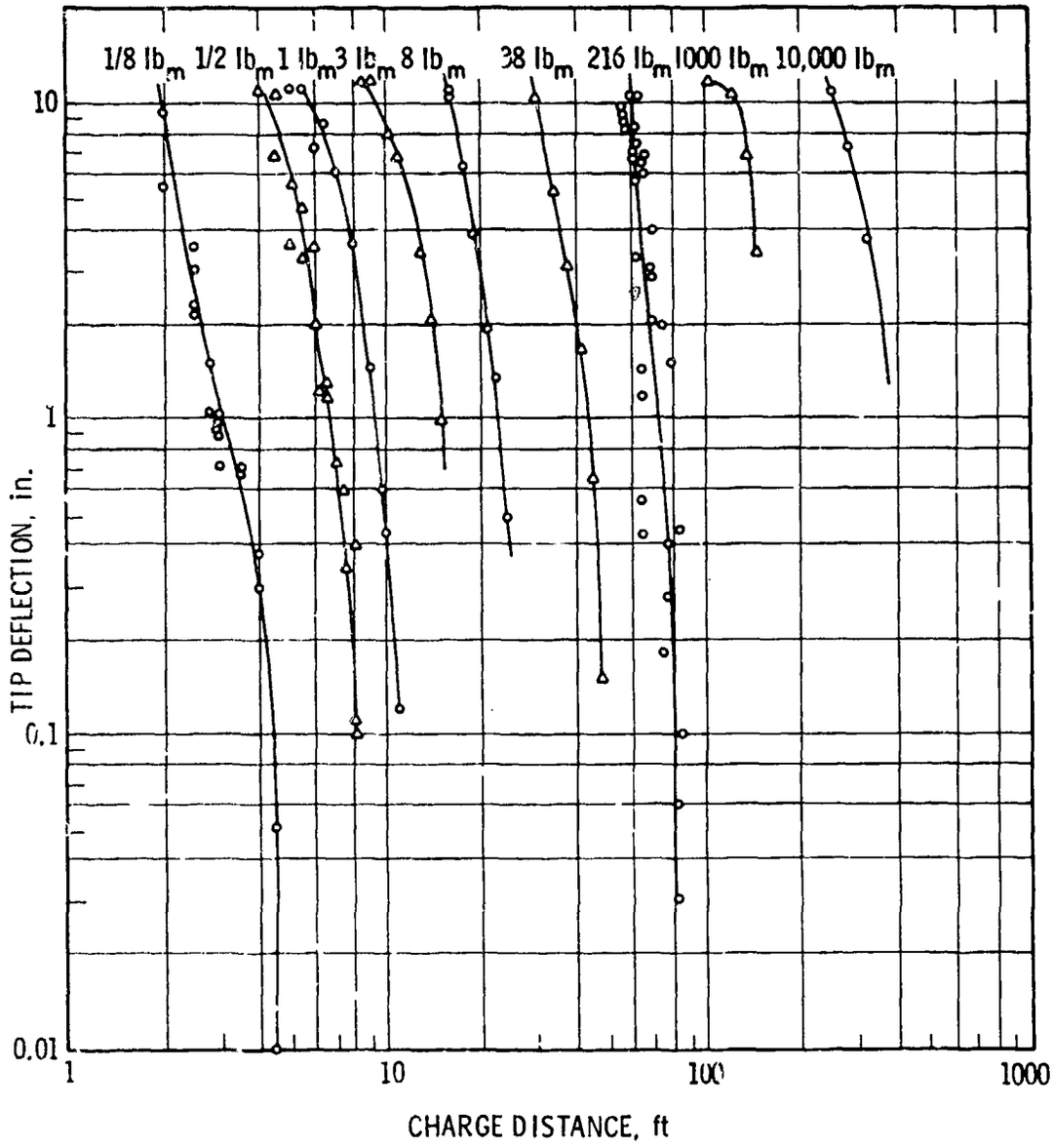
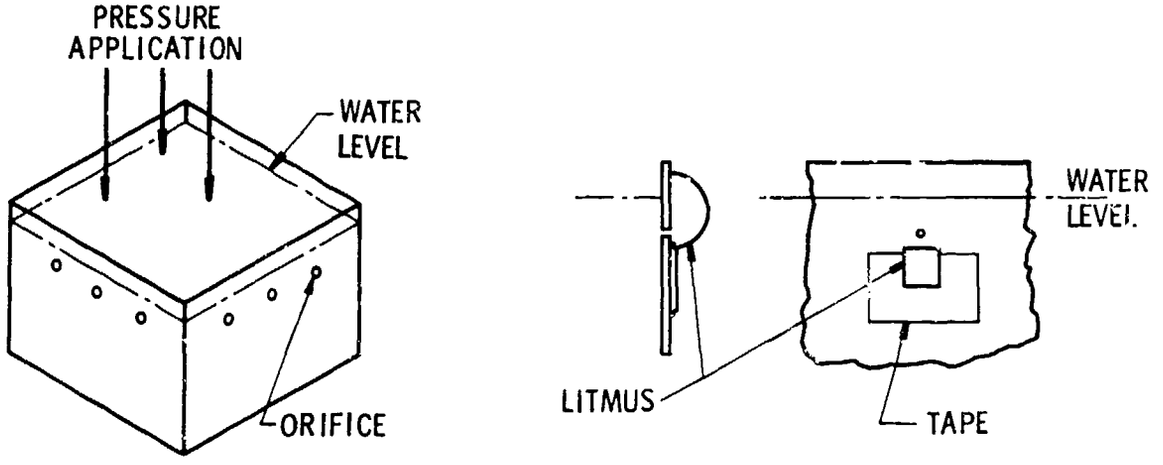


Figure 7-27. Permanent Tip Deflection of 0.051-in. 6061 Aluminum Alloy Beam vs Distance for Spherical Pentolite or TNT

different sizes were bored through both boards, in register. The gage was mounted with the plane of the diaphragm face-on to the wave.

A later modification of this gage was the foilmeter, or "Bikini gage", which consisted of a wooden or metal box with one open end over which was clamped an assembly similar to the paper blast meter but with aluminum foil instead of paper. Foil was used because it is much less sensitive than paper to changes in atmospheric conditions such as temperature and humidity. The box gage could be oriented either face-on or side-on to the direction of propagation of the blast, since the box prevented blast from acting on the reverse side of the diaphragm. The great advantage of this type of peak-pressure gage was its simplicity. The operation and the interpretation of results were simple, and no elaborate machine work was involved. Its great limitation was that the precision of results was not high, and the limits within which the pressure could be bracketed with a reasonable number of holes were rather wide. Such gages have been used on both conventional and nuclear explosion tests.

Two types of simple peak pressure gages that employ liquids have been developed at Suffield Experiment Station, Canada. One is termed a "surface tension gage", and employs the principle that the pressure required to break a surface film of a liquid over an orifice is directly proportional to the surface tension of the liquid and inversely proportional to the diameter of the orifice. As reported in Ref. 23 and shown in Fig. 7-29, the gage developed on this principle consisted of a can filled with a very dilute acid to a level above that of a series of orifices of different diameters. On application of pressure to the surface of the liquid, surface films over some orifices would break, ejecting the liquid. Detection was recorded by litmus paper located beneath each orifice. Thus, the peak pressure could be bracketed in the same manner as for paper blast meters or Bikini gages. The authors claim a response time of 3 msec and accuracy to within ± 0.01 psi in the range of 0.015 to 0.15 psi, using orifices ranging from 8 to 60 mils diameter. They also state that a modified version using mercury as a liquid and catching trays beneath each orifice could be used to measure peak pressures in the range 0.1 to 1.2 psi, with a response time of 10 msec. The second type of gage was termed a "squirt gage". It is shown schematically in Fig. 7-29, and described in Ref. 24. This gage functions on the principles that the velocity of stream line flow in a tube is directly proportional to



(A) Schematic of Surface Tension Pressure Gage

(B) Use of Litmus Paper to Record Ejection of Acidified Liquid

Figure 7-28. Surface Tension Blast Pressure Gage of Muirhead and McMurtry[23]

the pressure causing the flow, and that the distance which a horizontally-ejected jet travels before falling to earth is a unique function of its velocity. In practice, the device consisted of an ink reservoir, a nozzle arranged for horizontal ejection of ink, and a "catching" material located on a horizontal plane below the nozzle. Everything but the upper surface of the ink reservoir was protected from the overpressure in a blast wave. A typical calibration curve is shown in Fig. 7-29. The authors claim a response time of less than 4 msec. They also note that the device is temperature-dependent, because of change in viscosity of the ink. Both of the devices described are limited in use to measurement of peak pressures for relatively long-duration blast waves, i.e., those whose positive phases are several times as long as the quoted gage response times.

The ranges of some of the mechanical devices can be extended by use of relatively simple instrumentation of low frequency response. Peak bending strains of slender cantilever beams have been recorded in this manner, on direct writing oscillograph systems with frequency response limited to about 100 Hz, and correlated with blast source energy[19, 20] Because the beams only are deformed elastically, they can be reused for many tests, rather than being replaced as must all devices that are permanently deformed. For this simple device, it is possible to predict analytically the dynamic response under blast loading[20] so that the specific blast parameters that affect the gage response can be identified.

One or more of the types of mechanical gages described here can prove to be quite useful, particularly in large-scale field tests, but should be used always with caution and the knowledge that they yield only partial and sometimes misleading information about the blast wave characteristics.

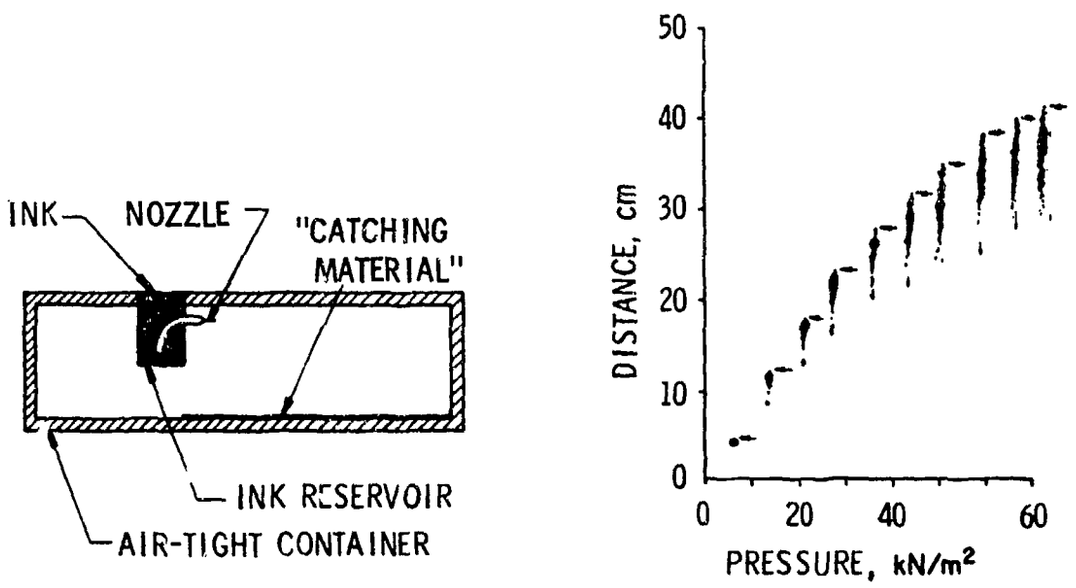


Figure 7-29. Squirt Blast Pressure Gage of Palmer and Muirhead[24]

7-8 SUMMARY

Most of the air blast transducers discussed in this chapter, and all of those illustrated, have been proven in use and carefully calibrated. Some are large and have inherent low frequency response so that they can only be used for sensing properties of long duration waves from large chemical or nuclear blast sources. Others are designed primarily for the short durations of small charge experiments. These limitations have been noted in the discussions of specific transducers in this chapter.

Two tables have been prepared to summarize the characteristics of some of the transducers discussed in this chapter, plus some additional commercial transducers. Table 7-2 lists data for side-on transducers, and Table 7-3 similar data for flush-mounted transducers. Model numbers or types are given together with manufacturer's names, sensing principle, and physical dimensions which we felt were important. Useful ranges of pressure are given, and upper and lower cut-off frequencies. Electrical characteristics are listed. Lastly, responses to other stimuli than pressure (temperature and acceleration) are given if they are known. These tables are by no means exhaustive, but do represent a sample of the transducers available to the blast experimenter.

The subject of air blast transducers is given special treatment in this handbook because

TABLE 7-2

CHARACTERISTICS OF SIDE-ON PRESSURE TRANSDUCERS

Transducer	Sensing Principle	Type of Element	Shape	Aspect Ratio of Housing	Overall Length, in.	Sensing Element Length, in.	Sensitivity pC/psi	Pressure Range, psi	High Freq* Cutoff, kHz	Accel. Sensitivity	Temp. Sensitivity, %/°F	Gage Resistance, ohm	Gage Capacitance, pF
Susquehanna Instr. Model ST-7	piezoelectric	lead metaniobate	pencil	0.055	16.0	0.188	20.0	0.1-500	250	Unknown	0.1	10^{10}	150
Celesco (Atlantic Res. Corp.) LC-13	piezoelectric	lead zirconate titanate	pencil	0.072	5.20	0.125	610	0.1-500	>120	Unknown	Unknown	10^{8}	1750
Celesco (Atlantic Res. Corp.) LC-33	piezoelectric	lead zirconate titanate	pencil	0.063	10.0	0.25	3150	0.01-500	>67	Unknown	0.25	2.5×10^{9}	4500
BRL Pancake	piezoelectric	tourmaline, lead zirconate, etc.	pancake	0.10 0.20	18	0.25 1.00	Varies	5-500	12-70	Unknown	Varies with type of element	10^{8}	Varies
SwRI Pancake	piezoelectric	lead zirconate	pancake	0.063	4.2	0.125	20	0.01-50	120	Unknown	Unknown	10^{8}	350
British H-3	piezoelectric	quartz	hatchet	0.082	12	1.00	100	0.1-300	60	Unknown	Unknown	10^{10}	Unknown

*The low frequency cut off for all gages in this table is a function of the input characteristics of the first amplifier seen by the gage, because all gages are capactive devices.

TABLE 7-3

CHARACTERISTICS OF FLUSH-MOUNTED PRESSURE TRANSDUCERS

Transducer	Sensing Principle	Sensing Element	Dia. of Sensing Surface, in.	Sensitivity	Pressure Range, psi	Low Freq. Cut-off, Hz	High Freq. Cut-off, kHz	Accel. Sensitivity	Gage Capacitance, pF	Gage Resistance, ohm	Temp. Sensitivity	Operating Temp. Range, °F
Susquehanna Instr. Model ST-2	piezoelectric	lead metaniobate	0.210	20.0 pC/psi	0.1-500	*	250		150	10^{10}	1%/10°C	Unknown
Susquehanna Instr. Model ST-3	piezoelectric	lead zirconate	0.375	100.0 pC/psi	0.1-100	*	100	Unknown	Unknown	10^{10}	Unknown	Unknown
Susquehanna Instr. Model ST-4, 2000	piezoelectric	tourmaline	0.210	0.05	10-2000	*	1500	Unknown	10	10^{10}	Unknown	Unknown
Model ST-4 10000	piezoelectric	tourmaline	0.210	0.01 pC/psi	10-10,000	**	1500	Unknown	10	10^{10}	Unknown	Unknown

*Function of amplifiers

TABLE 7-3 (Cont.)

Transducer	Sensing Principle	Sensing Element	Dia. of Sensing Surface, in.	Sensitivity	Pressure Range, psi	Low Freq. Cut-off, Hz	High Freq. Cut-off, kHz	Accel. Sensitivity	Gage Capacitance, pF	Gage Resistance, ohm	Temp. Sensitivity	Operating Temp. Range, °F
Celesco (Atlantic Res. Corp.) Model LD-25	piezoelectric	lead zirconate titanate	0.375	35 pC/psi	† – 3000	*	350	Unknown	240	5×10^8	Unknown	– 40 to 225
Celesco (Atlantic Res. Corp.) Model LC-60 & LC-65	piezoelectric	lead zirconate titanate	0.375	1200 pC/psi	– 200	*	50	0.012-0.019 psi/g	4700	2.5×10^9	0.26%/°F	– 40 to 225
Celesco (Atlantic Res. Corp.) Model LC-70 & LC-71	piezoelectric	lead zirconate titanate	0.208	120 pC/psi	– 300	*	150	0.013-0.013 psi/g	800	2.5×10^9	0.14%/°F	– 40 to 225

*Function of amplifiers

† Lower value unknown; not given by manufacturer

TABLE 7-3 (Cont.)

Transducer	Sensing Principle	Sensing Element	Dia. of Sensing Surface, in.	Sensitivity	Pressure Range, psi	Low Freq. Cut-off, Hz	High Freq. Cut-off, kHz	Accel. Sensitivity	Gage Capacitance, pF	Gage Resistance, ohm	Temp. Sensitivity	Operating Temp. Range, °F
Kistler Instr. Corp. Model 601A	piezo-electric	crystal-line quartz	0.25	1.0 pC/psi	10-3000	*	130	0.01 psi/g	5	10^{14}	0.01%/ ° F	−450 to 500
Kistler Instr. Corp. Model 701A	piezo-electric	crystal-line quartz	0.37	5	0.01-30 pC/psi	*	60	0.02 psi/g	10	10^{14}	0.01%/ ° F	−450 to 500
Kistler Instr. Corp. Model 603A	piezo-electric	crystal-line quartz	0.22	0.35 pC/psi	−3,000	*	400	0.001 psi/g	20	10^{13}	0.01%/ ° F	−450 to 500
Kistler Instr. Corp. Model 607A	piezo-electric	crystal-line quartz	Un-known	0.15 pC/psi	−75,000	*	240	0.02 psi/g	5	10^{13}	0.01%/ ° F	−450 to 500

*Function of amplifiers

TABLE 7-3 (Cont.)

Transducer	Sensing Principle	Sensing Element	Dia. of Sensing Surface, in.	Sensitivity	Pressure Range, psi	Low Freq. Cut-off, Hz	High Freq. Cut-off, kHz	Accel. Sensitivity	Gage Capacitance, pF	Temp. Resistance ohm	Temp. Sensitivity	Operating Temp. Range, °F
Validyne Eng. Corp. Model P66	variable reluctance	diaphragm & coil	0.94	4% of excitation voltage for max pressure	0-1 to 0-3000	0	–	Unknown	–	–	0.01%/°F	-65 to 250
CEC Model Type 4-311	strain gage	diaphragm & strain gage	0.500	0.33 to 0.0133 mV/psi	0-100 to 0-5000	0	8	Poor	–	350	0.01%/°F	-65 to 165
CEC Model Type 4-313	strain gage	diaphragm & strain gage	0.625	2.56 to 0.0133 mV/psi	0-26 to 0-5000	0	6-15	Poor	–	350	0.01%/°F	-65 to 250
Pace (Whittaker Corp.) (Model P24)	variable reluctance	–	0.936	5% of excit. voltage for max pressure	0-15 to 0-5000	0	–	Unknown	–	–	0.01%/°F	-423 to 250

TABLE 7-3 (Cont.)

Transducer	Sensing Principle	Sensing Element	Dia. of Sensing Surface, in.	Sensitivity	Pressure Range psi	Low Freq. Cut-off, Hz	High Freq. Cut-off, kHz	Accel. Sensitivity	Gage Capacitance pF	Gage Resistance, ohm	Temp. Sensitivity	Operating Temp. Range, °F
Pace (Whittaker Corp) Model SP45	strain gage	semiconductor strain gage	0.182	3% of excit. voltage for max pressure	0-300 to 0-3000	0	–	Unknown	–	400	Unknown	-100 to 350
Wiancko (Whittaker Corp.) (Model P2700)	variable reluctance	–	N/A	8% of excit. voltage for max pressure	0-5 to 0-10,000	0	5	Unknown	–	–	0.02%/°F	-65 to 250
Dynisco Model PT311	strain gage	(See Fig. 7-17)	0.65	3% of excit. voltage for max pressure	0-50 to 0-5000	0	11	Unknowr.	–	350	0.02%/°F	0 to 250
Schaevitz-Bytrex Mod. HFD	strain gage	diaphragm and strain gage	0.075	5 mV/psi	0-2 to 0-25	0	60	0.075 to 0.006% g	–	900	0.03%/°F	+30 to 180

TABLE 7-3 (Cont.)

Transducer	Sensing Principle	Sensing Element	Dia. of Sensing Surface, in.	Sensitivity	Pressure Range, psi	Low Freq. Cut-off, Hz	High Freq. Cut-off, kHz	Accel. Sensitivity	Gage Capacitance, pF	Gage Resistance, ohm	Temp. Sensitivity	Operating Temp. Range, °F
Schaevitz-Bytrex Model HFK	strain gage	diaphragm and strain gage	0.125	10 mV/psi	0-2 to 0-25	0	20	0.0525 to 0.0042%/g	–	900	0.03%/°F	+ 30 to 180
Schaevitz-Bytrex Model HFM	strain gage	diaphragm and strain gage	0.250	200 mV for max. pressure	0-2000 to to 0-20,000	0	100	0.0003 to 0.0001%/g	–	450	0.01%/°F	-65 to 300

suitable transducers are critical to success in blast instrumentation. An investigator who is new to this field should view with caution manufacturers' claims of transducer performance. Their use in sensing blast wave properties is a special application that requires special attention to method of mounting, effects of simultaneous pressure, temperature and acceleration transients, etc. The designs presented in this chapter have without exception required considerable development, calibration, and test before they were accepted as suitable blast transducers.

REFERENCES

1. R. G. Stoner and W. Bleakney, "The Attenuation of Spherical Shock Waves in Air", *Jour. Appl. Physics,* 19, pp. 670-678 (July 1948).

2. W. Olson and J. Wenig, *A Double-Charge Technique to Measure Face-On Blast,* BRL Memorandum Report No. 1347, Aberdeen Proving Ground, Md., May 1961.

3. J. R. Ruetenik and S. D. Lewis, *Pressure Probe and System for Measuring Large Blast Waves,* Tech. Rept. AFFDL-TDR-65-35, A. F. Flight Dynamics Lab., Wright-Patterson AFB, Ohio, June 1965.

4. H. B. Pierce and J. C. Manning, *Experimental Investigation of Blast Loading on an Airfoil in Mach Number 0.7 Airflow With Initial Angle-of-Attack Change of 20°,* NASA TN D-1603, February 1963.

5. A. J. Hoffman and S. N. Mills, Jr., *Air Blast Measurements About Explosive Charges at Side-On and Normal Incidence*, BRL Report No. 988, Aberdeen Proving Ground, Maryland, July 1956.

6. B. A. Granath and G. A. Coulter, *BRL Shock Tube Piezo-Electric Blast Gages,* BRL Technical Note No. 1478, Aberdeen Proving Ground, Maryland, August 1962.

7. T. Whiteside, *Instrument Development Section Notes,* U.K.A.E.A., Atomic Weapons Research Establishment, A.W.R.E., Foulness, Jan. 1967.

8. R. H. Rowland, *Blast and Shock Measurement, State-of-the-Art Review,* DASA 1986, Nov. 1967 (AD-824 160).

9. W. E. Baker and W. O. Ewing, Jr., *Miniature Piezoelectric Gages for Measuring Transient Pressures on Airfoils,* BRL Memorandum Report No. 1329, Aberdeen Proving Ground, Maryland, March 1961.

10. J. L. Patterson, *A Miniature Electrical Pressure Gage Utilizing a Stretched Flat Diaphragm,* NACA TN 2659, April 1962.

11. R. W. Morton and J. L. Patterson, *A Transient Pressure Measurement System for Blast Effect Research,* Paper 148-LA-61-1, Los Angeles, California, September 1961.

12. David Levine, *Acceleration-Compensating Pressure Transducers for Surface-Pressure Measurements,* NAVORD Report 6834, 18 January 1961.

13. G. T. Watson and R. D. Wilson, *BRL Time-of-Arrival Blast Gage,* BRL Technical Note No. 1476, August 1962.

14. O. T. Johnson and W. O. Ewing, Jr., *An Omnidirectional Gage for Measuring the Dynamic Pressure Behind a Shock Front,* BRL Memorandum Report No. 1324, March 1962.

15. J. M. Dewey and W. A. Anson, "A Blast Wave Density Gage Using Beta-Radiation", *J. Sci. Instrum.*, Vol. 40.

16. O. T. Johnson, W. C. Olsen, and J. D. Patterson, II, *A Simple Mechanical Method for Measuring the Reflected Impulse of Air Blast Waves, Proc. of 3rd U.S. National Congress of Appl. Mech.*, ASME, New York, 1958, pp. 203-207.

17. W. C. Olson, J. D. Patterson, II, and J. S. Williams, *The Effect of Atmospheric Pressure on the Reflected Impulse from Blast Waves*, BRL Memo. Report No. 1241, Aberdeen Proving Ground, Md., January 1960.

18. W. D. Kennedy, "Explosions and Explosives in Air", Chapter 2, Vol. I *Effects of Impact and Explosion*, Summary Tech. Rept. of Division 2, NDRC, Washington, D. C., 1946 (AD-221 586).

19. W. C. Ewing, Jr. and J. W. Hanna, *A Cantilever for Measuring Air Blast*, BRL Tech. Note No. 1139, August 1957.

20. W. E. Baker, W. O. Ewing, Jr., J. W. Hanna, and G. W. Bunnewith, *The Elastic and Plastic Response of Cantilevers to Air Blast Loading, Proc. of the Fourth U. S. Natl. Congress of Appl. Mech.*, ASME, New York, 1962, pp. 853-866.

21. W. E. Baker and O. T. Johnson, *Some Crude Comparative Tests of Damage with Explosive Charges of Pentolite and Metalized Tetranitromethane*, BRL Tech. Note No. 287, September 1950.

22. R. G. Sachs, *The Calibration of Paper Blast Meters*, BRL Report No. 472, Aberdeen Proving Ground, Md., June 1944.

23. J. C. Muirhead and W. M. McMurtry, "Surface Tension Gauges for the Measurement of Low Transient Pressures", *Review of Sci. Inst.*, 33, 12, pp. 1473-1474 (December 1962).

24. W. O. Palmer and J. C. Muirhead, "A Squirt Gauge for Peak Blast Pressure Indication", *Review of Sci. Inst.*, 40, 12, pp. 1637-1638 (December 1969).

CHAPTER 8

INSTRUMENTATION SYSTEMS

8-1 GENERAL

Although the various types of transducers discussed in Chapter 7 are critical to the measurement of air blast wave parameters, they are only one element in the entire instrumentation system that is required to record the data. The signal from the transducer must be transmitted over cables or by telemetry to a recording instrument. The signal usually is amplified or conditioned in some manner before being recorded, often with several stages of amplification. Other types of ancillary equipment often are included in recording systems to calibrate electrically each channel, to provide accurate timing marks, etc. Blast instrumentation systems can differ radically in the type and size of equipment, depending on whether they are intended for use in fixed or semi-fixed installations, or in portable installations such as airborne or missile-borne systems. The elements of a system are also quite dependent on the type of recorder used. First we will discuss ground-based systems in this chapter, followed by a discussion of airborne or other portable systems.

8-2 GROUND-BASED INSTRUMENTATION SYSTEMS

8-2.1 CATHODE-RAY-TUBE SYSTEMS

The earliest type of ground-based blast recording system, and still one of the most popular and versatile, is a system based on cathode-ray-tube (CRT) oscilloscopes. A simplified block diagram of such a system is shown in Fig. 8-1. Multichannel CRT oscilloscope systems were built specifically for

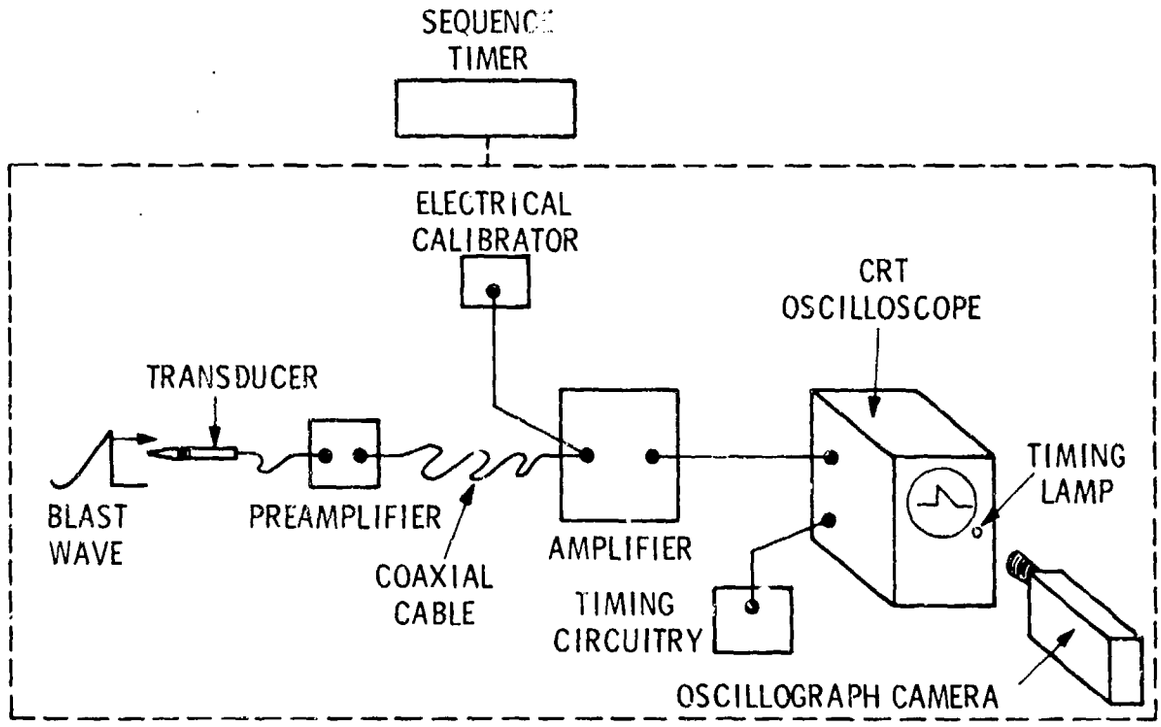


Figure 8-1. Block Diagram of CRT Oscilloscope Recording System

recording the outputs of piezoelectric blast gages in World War II research[1] because no adequate commercially available systems or components were available at that time. These early systems employed tourmaline or quartz crystal transducers; did not use a preamplifier; employed relatively wide-band (0 to 100 kHz) vacuum-tube amplifiers; and used moving-film oscillograph cameras to provide the time axis for the recording. Several cathode-ray tubes were in the field of view of each camera so that several channels of information could be recorded on each film strip. Ancillary equipment included an electrical calibrator to display one or more calibration steps on each trace, timing circuitry and one or more timing lamps in the field of view of each camera to calibrate the time axis, and a sequence timer to sequence all events in a test. Current CRT systems in use for multichannel blast recording are remarkably similar to the early systems used in the 1940's. They may employ commercial components for many of the subsystems and may have superior frequency response, linearity, etc., and be much more compact, but the system is essentially the same.

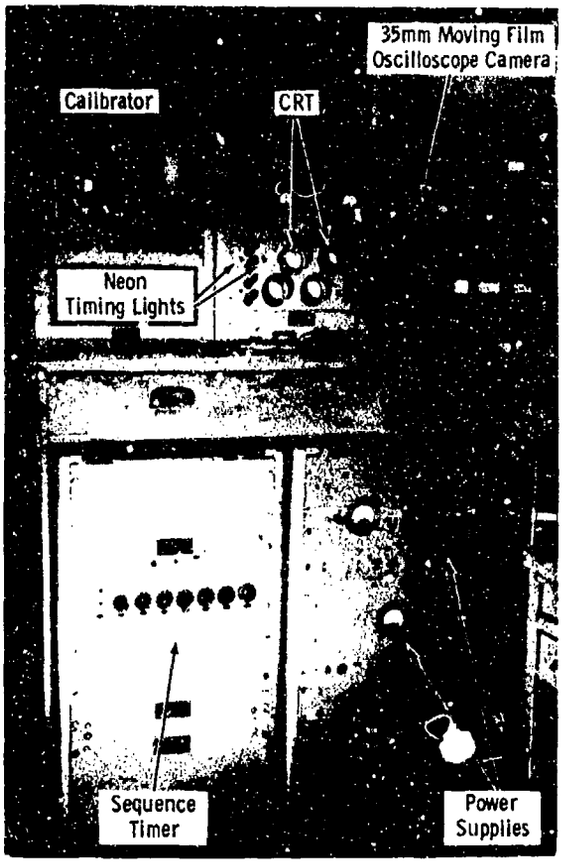


Figure 8-2. BRL Four-channel Recording Equipment

8-2.1.1 THE BRL CRT SYSTEMS

A CRT recording system that has been in use for a number of years at the Ballistic Research Laboratories (BRL) consists of four-channel units incorporating all of the elements shown in Fig 8-2. Frequency response of the system is somewhat dependent on amplifier gain, but is at least flat from 0 - 100 kHz. Film speed of the 35-mm camera is adjustable up to a maximum of 100 ft/sec, providing a resolution of up to 1.2 in./msec. All circuits are switched on and off in proper sequence, including imposition of four-step calibrations prior to charge detonation, by the sequence timer. The system is designed for use with piezoelectric transducers and cannot be used with other types. The only commercially available component in the system is the oscillograph camera.

Although a number of the units of the type described are still in use, they are being replaced by another CRT system that is assembled in eight-channel units. This system was designed by B. Soroka and G. T. Watson[2]. It is built around commercially available oscilloscopes and drum cameras and is shown in Figs. 8-3 and 8-4, and in block diagram in Fig. 8-5. Frequency response for the system is 0.03 Hz to 250 kHz. The drum camera can be operated at film speeds ranging from 0.024 to 2.5 in./msec, recording all eight channels on a 12-cm wide film strip. The system also can be used as an eight-channel, single-sweep recording system using Polaroid cameras. It is much more versatile than the earlier BRL system because it can accept signals from a variety of types of transducers—including piezoelectric, potentiometer, thermocouples, and strain gages. As in the older system, an integral part is a sequence timer that automatically sequences all events once the timer is started. It is much more compact per channel, occupy-

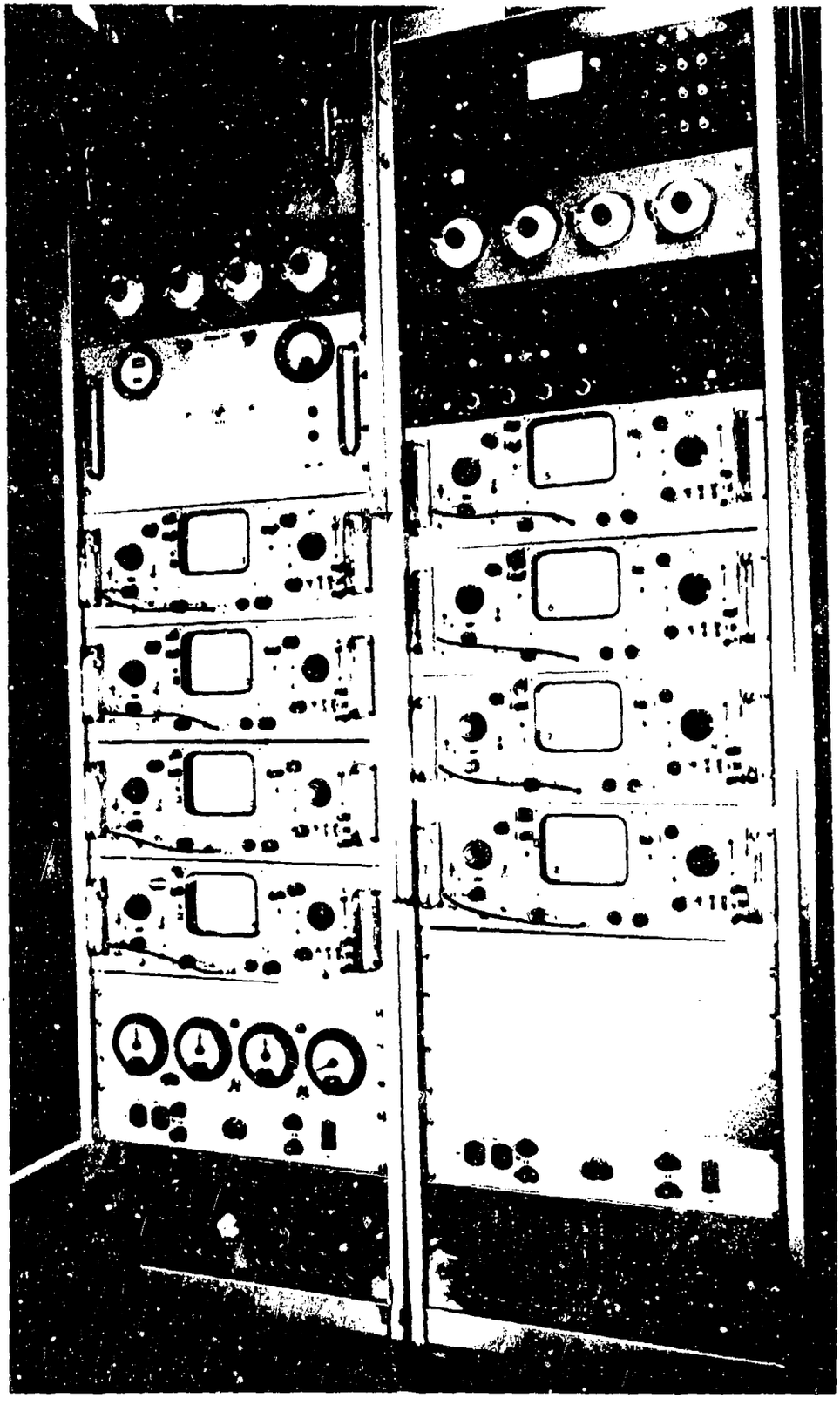


Figure 8-3. Eight-channel BRL Recorder[2]



Figure 8-4. Drum Camera for Eight-channel BRL Recorder[2]

ing less space than the basic four-channel unit of the older system.

8-2.1.2 THE CEC TYPE 5-140 CRT SYSTEM

Another multichannel system that still is used widely in blast recording is the Consolidated Electrodynamics Corporation (CEC) Type 5-140. Unfortunately, this versatile and relatively compact system is no longer manufactured. It is shown in Fig. 8-6. The heart of the system consists of eight dual-beam oscilloscopes that are arranged below an optical system and camera magazine, as shown in the left of the figure (the oscilloscopes are opened for adjustment in operation, their faces are out of sight below the optical system). The optical system refocusses the images on the oscilloscope faces in register across 12-in. wide photographic film or paper in the magazine. Each channel has a separate plug-in amplifier, and separate bridge-balance units are available for energizing and recording outputs of strain-gage type transducers. Film can be run through the magazine at a wide variety of speeds, up to a maximum of 400 in./sec. A sequence timer also is included in the system.

8-2.1.3 BRITISH CRT SYSTEMS

Commercial CRT recording systems made in Great Britain are used by British laboratories involved in air blast testing. These are made by Southern Instruments in four-channel units. They have a bandwidth of 120 kHz. A rotating-drum camera is used to photograph the deflections of the four recording tubes and two time-marker tubes on recording paper or film of 5-in. width. The time-marker tubes can be pulsed at frequencies between 10 Hz and 1000 Hz, and the camera drum speed is continuously variable up to fifty rps. The circumference of the drum around which the sensitive film is wrapped is 50 in., thus a maximum peripheral recording speed of 2500 in./sec can be obtained. This camera apparently is identical to the one used in the new BRL recorder.

The British system includes all of the other peripheral equipment for internal calibration, sequencing, preamplifying, etc., described in the BRL system.

8-2.1.4 THE DENVER RESEARCH INSTITUTE CRT SYSTEM

Denver Research Institute operates a multichannel CRT system for air blast recording, which was built entirely by personnel at that Institute. The equipment and its design and operation are described in Ref. 3. It is built into a semi-trailer which houses the twelve-channel system, a dark room, and work area. Frequency response is 0 to 80 kHz, and recording is on drum cameras with film speeds from 1 to 5 m/sec. Sequence timers, calibration units, amplifiers, etc., are included in the

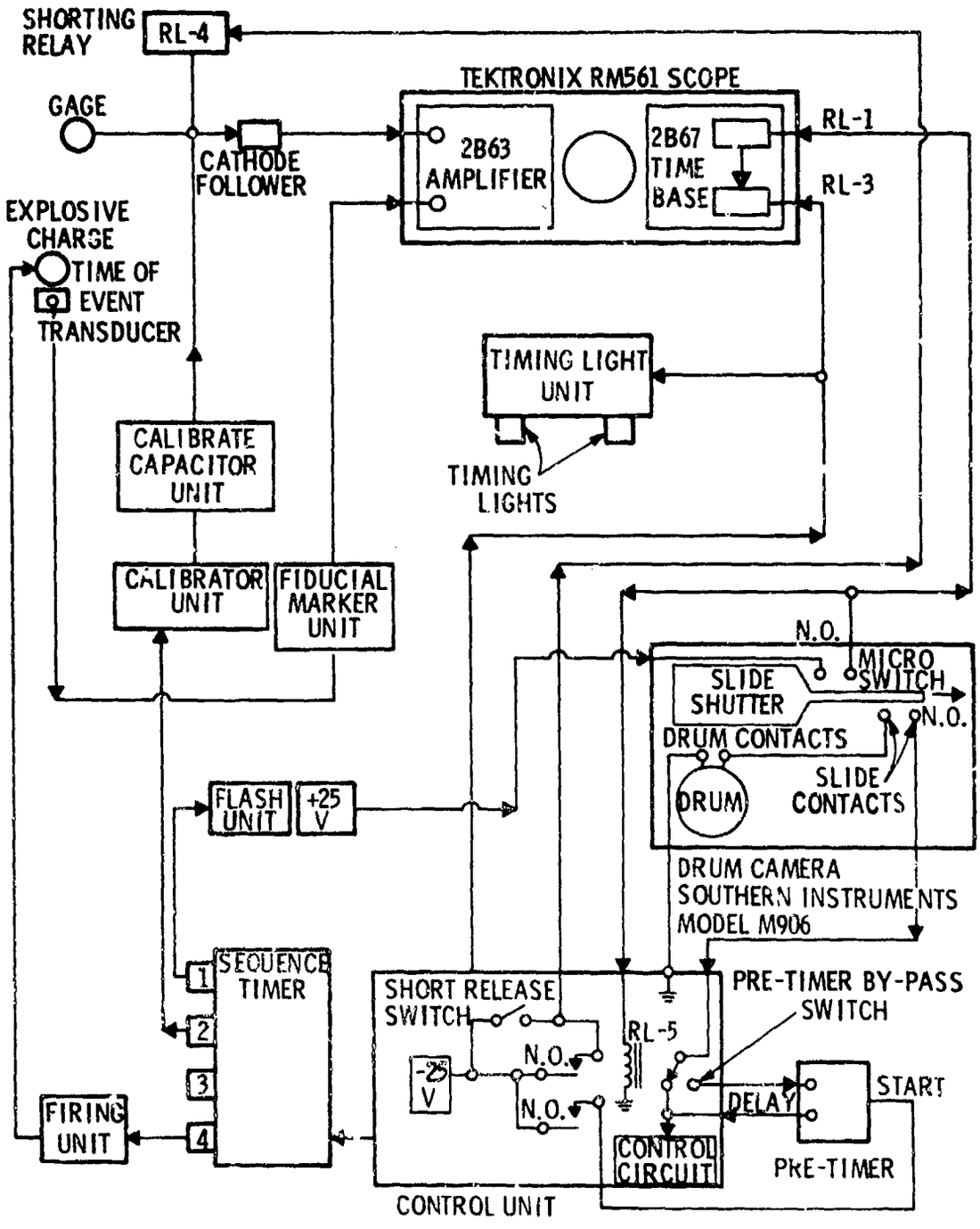


Figure 8-5. Block Diagram of Eight-channel BRL Recorder[2]

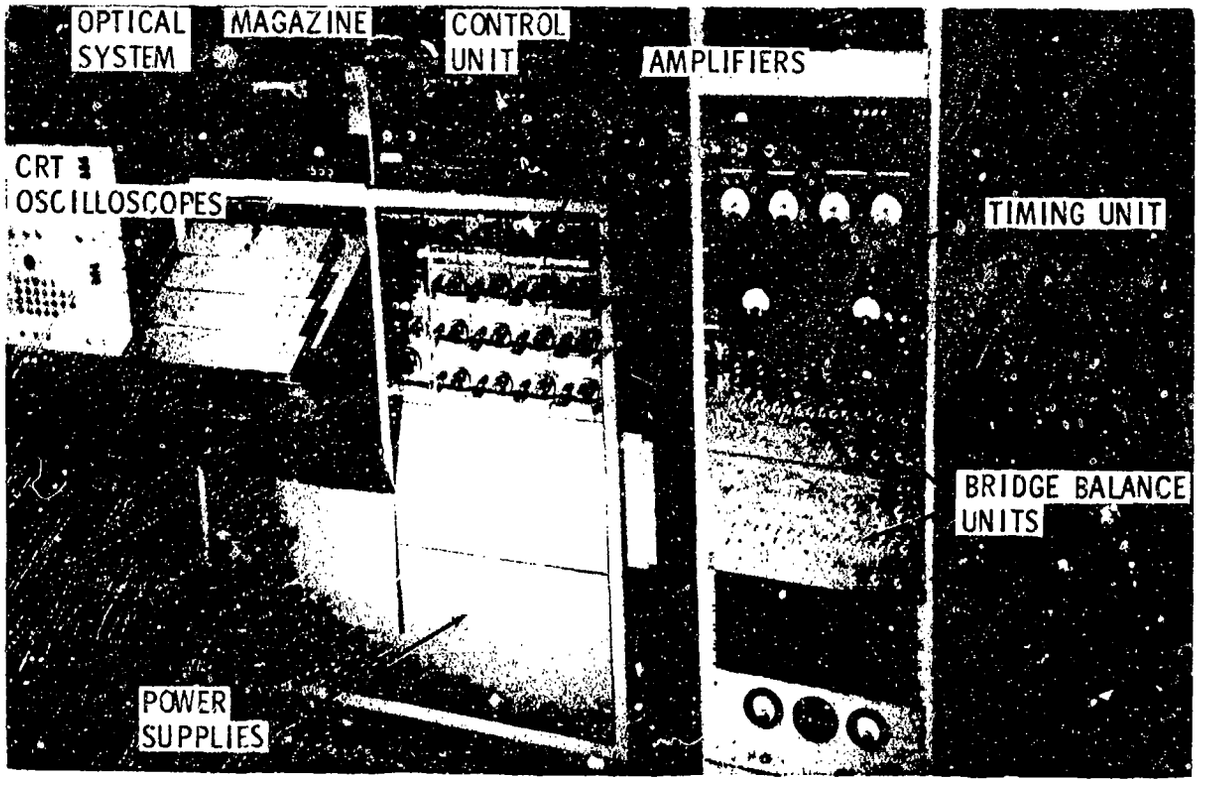


Figure 8-6. CEC Sixteen-channel Oscillograph Recorder

system in much the same manner as in the BRL and British systems. The system is intended for use exclusively with piezoelectric transducers.

8-2.1.5 THE LANGLEY RESEARCH CENTER CRT SYSTEM

Morton and Patterson[4] at Langley Research Center of NASA designed and built a fourteen-channel CRT air blast recording system that was installed in an instrumentation shelter at Wallops Island, Virginia. This system uses seven commercial dual-channel oscilloscopes, but in all other respects was designed and built by NASA personnel. It is shown in Fig. 8-7. The system was designed specifically for use with the NASA miniature gages described in Chapter 7. A carrier amplifier system with 120 kHz carrier provides system response flat from 0 to 20 kHz, with recording over long cable lengths. Traces are recorded on seven homemade drum cameras. As in other systems described here, timing circuitry, calibration, etc., are built in as part of the system.

8-2.1.6 OTHER CRT SYSTEMS

Other agencies, such as the U.S. Naval Ordnance Laboratory and the Naval Ship Research and Development Center, are known to have and use multichannel CRT systems for blast recording, but the author could find no explicit descriptions of their systems.

8-2.2 MAGNETIC TAPE SYSTEMS

Blast recording systems built around magnetic tape recorders are now as popular or more popular than CRT systems. The heart of such systems are multichannel, instrument-grade tape recorders made by several different manufacturers. The recorders are usually either 7-channel or 14-channel units, and commonly employ FM signal electronics. Such systems with a frequency response of

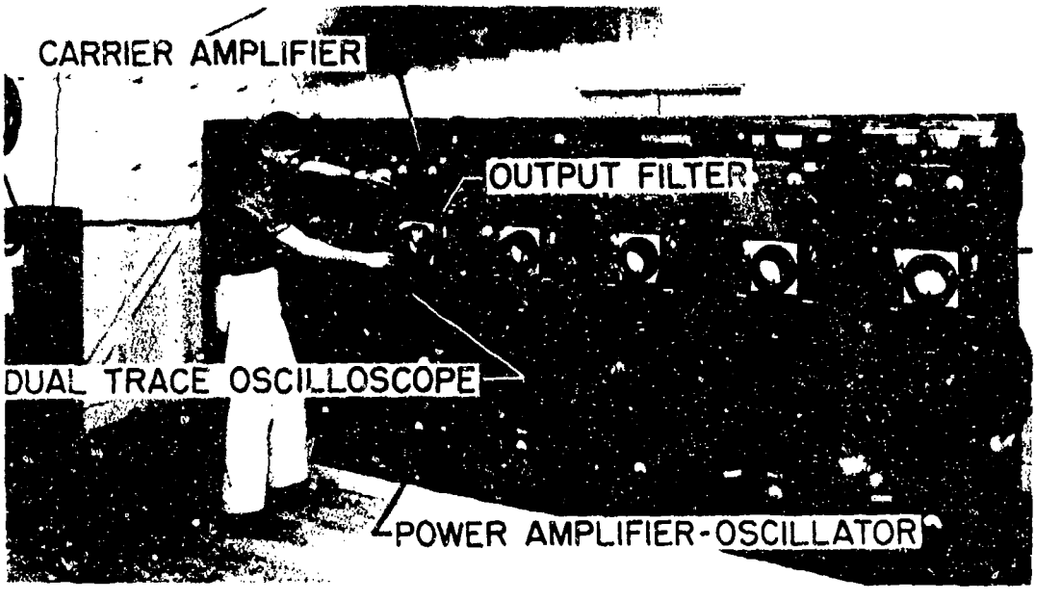


Figure 8-7. NASA Langley Fourteen-channel CRT Recording System (Courtesy of NASA)

0-10 kHz probably were first employed for blast recording during nuclear tests shortly after World War II. Similar recorders using FM electronics with twice this frequency range have been available for some years, and currently three manufacturers can supply such recorders with response of about 0-400 kHz.

The basic elements of such systems are included in block diagrams for two magnetic tape recorder systems discussed in Refs. 6 and 7, reproduced here as Figs. 8-8 and 8-9, respectively. The system of Fig. 8-8 installed in an instrument trailer is shown in Fig. 8-10. The basic elements of these systems are:

(1) Transducer and cable

(2) Zero time circuit

(3) Input amplifier or amplifiers

(4) Tape recorder with FM electronics

(5) Output amplifiers

(6) Galvanometer oscillograph.

The two systems differ in minor ways, with the primary difference being that the SwRI system (Fig. 8-8) employs a single input amplifier while the IITRI system (Fig. 8-9) uses two stages of such amplification. Both systems are basically fourteen channel and have an ancillary capability for several channels of CRT recording. Eventual readout is on photographic paper in the galvanometer oscillograph, played back at much lower tape recorder speed to avoid limitation of frequency response due to the lower response of the galvanometer oscillograph and to expand the time scale.

The primary advantage of systems of this type for recording blast data are (1) the data are stored on the tape and therefore can be retrieved at any time, (2) good time correlation between channels is always possible, (3) the system employs commercially available components almost entirely, and (4) it can be used for recording other types of transient data simultaneously or with some minor changes. "Bad" data can often be recovered by playback through suitable band-pass filters. Disadvantages are somewhat poorer frequency response than CRT systems and dif-

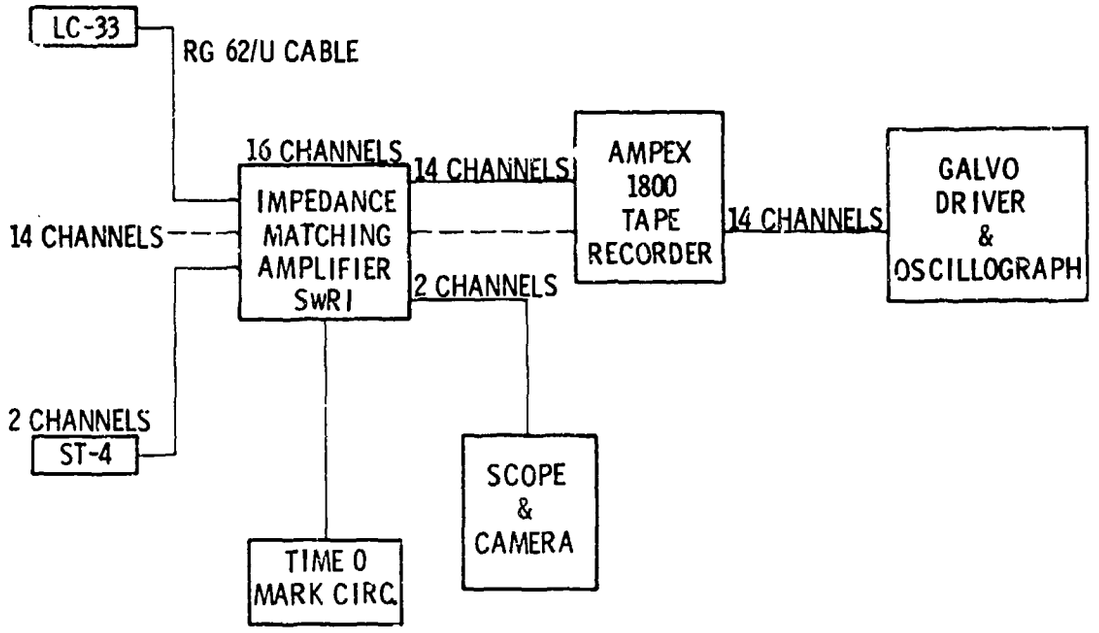


Figure 8-8. Block Diagram of SwRI Magnetic Tape Recorder System[6]

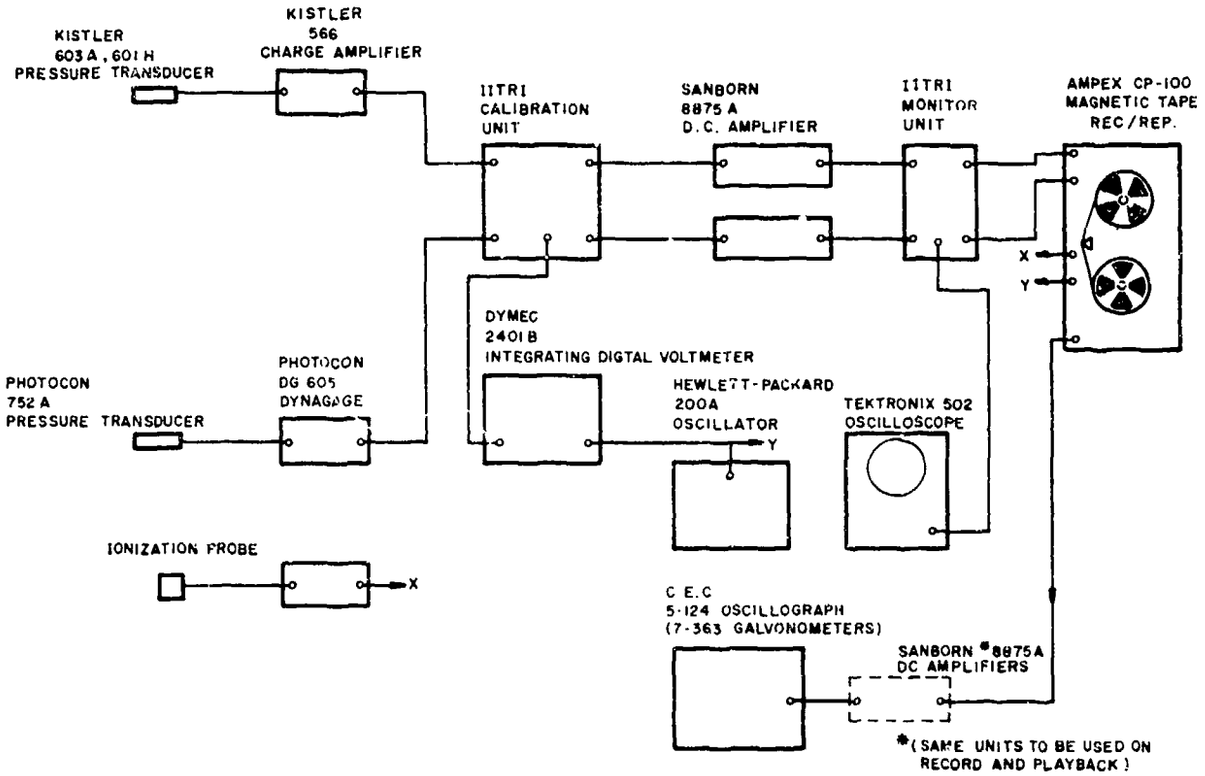


Figure 8-9. Block Diagram of IITRI Record-reproduce Instrumentation[7]

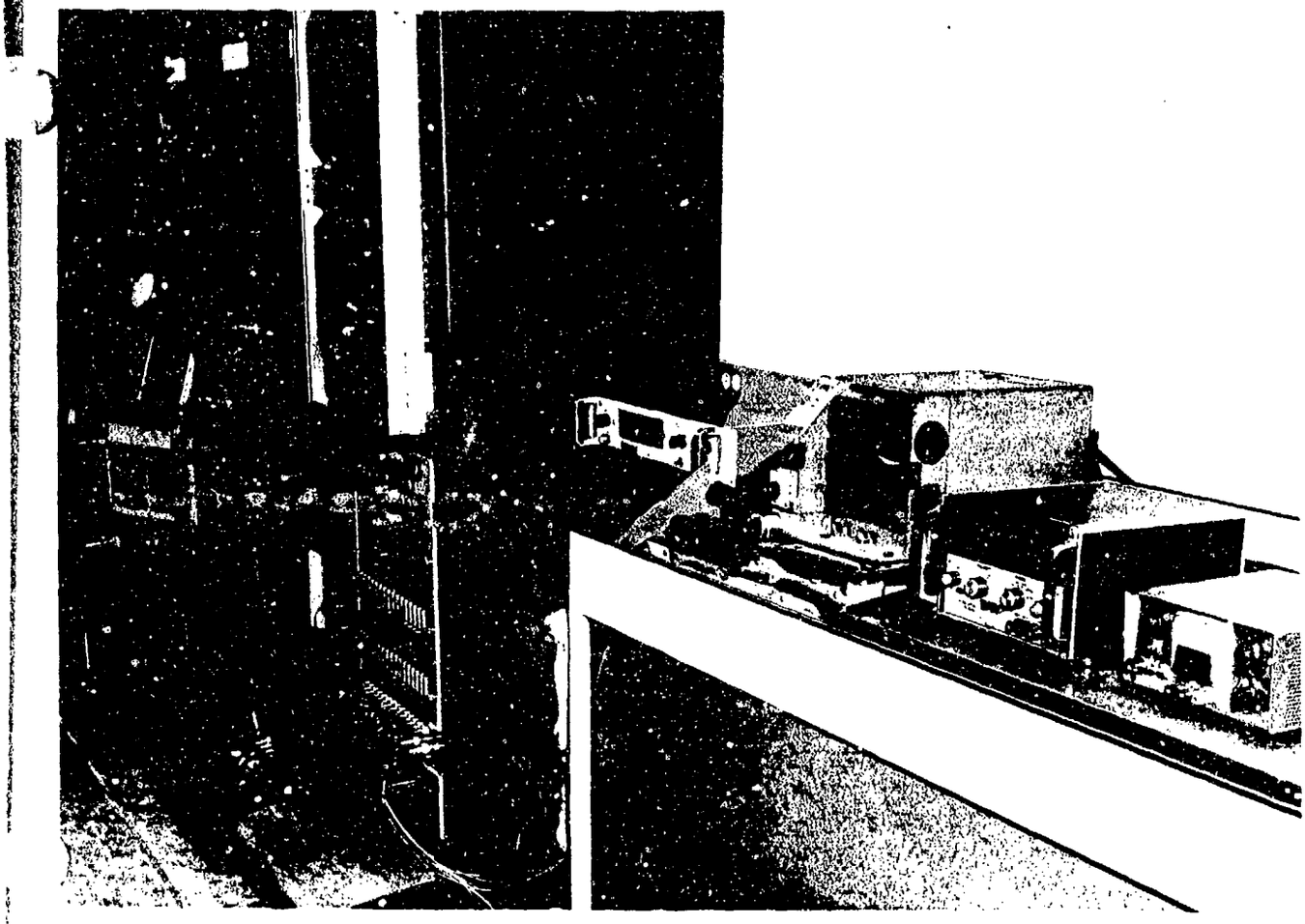


Figure 8-10. Magnetic Tape Recorder System for Air Blast Recording
(Courtesy of Southwest Research Institute)

ficulty of incorporation of automatic electrical calibration in a firing sequence without construction of special circuitry.

The two examples of ground-based magnetic oscillograph systems described here are indicative of how such systems are usually arranged.

Other agencies use similar systems, as is apparent from Refs. 6 and 8. We will make no mention of specific manufacturers, model numbers, or specifications for the basic magnetic tape recorders both because comparable units are made by several companies and because, in this highly competitive field, new units can appear quite frequently.

8-2.3 GALVANOMETER OSCILLOGRAPH SYSTEMS

As noted previously, galvanometer oscillographs are used for analog recording of magnetic tape systems, using low playback speeds to overcome their relatively low frequency response. For recording of blast data from nuclear or very large chemical explosions, the frequency response can be adequate, and systems based on direct recording on galvanometer oscillographs are used.

A typical blast recording system of this type consists of resistance- or reluctance-bridge pressure transducers, carrier amplifiers, and a galvanometer oscillograph. Typical transducers would be the Norwood, Dynisco, or Shaevitz-Bytrex strain-gage types described in Chapter 7.

Two types of carrier amplifiers, both made by Consolidated Electrodynamics Corp. (CEC), have been used quite widely. One is designated by CEC as System D. The System

D will record static and dynamic outputs between 0 and 600 Hz. It uses an amplitude-modulated, suppressed-carrier signal, with the amplified gage signal transmitted to an oscillographic recorder. The system may be used with any type of two- or four-arm bridge transducers operating on the resistance change or variable reluctance principle. A signal of ± 1 mV will cause a full-scale deflection. Attenuators enable the system to operate with input signals in the range of +1 V to −1 V. The system includes an oscillator power supply for sensor excitation with an output of 10 V at 3 kHz, an attenuator to vary the input signal levels, an amplifier to boost low-signal levels, and a phase-sensitive demodulator to provide correct polarity to the signal output. Under the condition of zero stress on the sensor, the output signal amplitude is zero. The signal is amplified, transmitted, and admitted to the demodulator, where the carrier is decoded and the proper sign and magnitude given to the signal. The basic "building blocks" of this system are groups of four carrier amplifiers and an oscillator-power supply capable of energizing up to twelve amplifiers. A compact twelve-channel unit can be mounted on a single shock-mount base.

The second CEC carrier amplifier system is their Type 1-127, sometimes called "System E". The CEC System E, like the System D, operates on the AM-suppressed carrier principle and functions in essentially the same way as the System D; however, the System E uses a carrier frequency of 20,000 Hz, with a bandpass of 0 to 3000 Hz, which permits recording of a much higher frequency from the gage. The basic building block for this system contains four channels of carrier amplifiers, and the necessary power supply and oscillator in a single compact unit.

8-2.4 TRANSIENT RECORDERS

For some blast experimentation, such as "cook-off" tests of ordnance items, the time at which the explosion occurs may vary by minutes from test to test. Many of the blast-recording systems discussed earlier in this chapter have short total recording times and can be used only if the time of explosion is known and controlled within milliseconds. Even magnetic tape recorders and oscillograph recorders, which have relatively long recording times, cannot be used efficiently if they must run for many minutes to record an event lasting milliseconds.

A recent (1970) addition to instrumentation systems designed to solve this problem is a line of transient recorders manufactured by Biomation. These devices accept signals from transducers when initiated by external triggers, or when triggered by the transient signal itself, with no loss of the initial portion of a record. They store the signal digitally in an internal memory bank. The signal can be played back later in analog form on a CRT oscilloscope, tape recorder, or oscillograph recorder; or in digital form to a digital recorder or directly to a computer for processing. Amplitudes and time scales can be adjusted at will during playback. Recording times can be adjusted over wide ranges, 20 sec to 5 hr, depending on the expected event and the particular recorder model. These recorders have proven to be quite versatile and useful in blast recording, and undoubtedly will be used more widely in the future.

8-2.5 INSTRUMENTATION PROBLEMS ASSOCIATED WITH NUCLEAR BLAST TESTS

Ground-based systems have been used to record air blast data during many nuclear weapon tests, and these systems are basically the same as those discussed previously in this chapter. There are some special problems associated with such testing which are caused by nuclear radiation and electromagnetic pulse effects associated with the nuclear detonation, and by the necessity of using long recording cables, remote-operated recorders, etc. Many of these problems are reviewed in Ref. 9, and much of the discussion that follows is taken from that reference.

When attempting any measurement in an intense nuclear radiation environment, an investigator is faced with severe restrictions with respect to the choice and deployment of his instrumentation. Two radiation manifestations are noted: first, an effect on electronics due to transient radiation (TREE) caused by the direct interaction of the ionizing radiation with the measuring system, and second, electromagnetic pulse (EMP) effects whereby the measuring system acts as an antenna to receive a transient EM signal produced by the burst*.

For many systems, the problem of the effects of nuclear detonations cannot be segregated clearly into EMP problems, TREE problems, thermal problems, blast problems, etc. Rather, these effects can interact in a way such that the combined effect is much more serious than is any particular effect taken alone. A related design problem is that while it is often comparatively simple to protect a system from one particular effect, the protection can actually soften the system to some other effect. Thus, the system designer must always keep in mind the necessity of obtaining a realistic balanced system hardness.

8-2.5.1 TREE

The TREE effects on electronic measuring systems can be both transient and permanent in nature. The permanent effects usually are due to displacement of atoms located in crystalline lattices and are produced by close collisions between incident nuclear particles and the crystal atoms. These permanent effects are normally of little concern in blast and shock measurements, for they degrade only such semiconductors (and quartz crystals) which depend upon a very high degree of crystal regularity for proper function.

Most transient effects result from the generation of ion pairs in the system by the incident radiation. These ion pairs ultimately cause either photocurrents in transistors or diodes, or leakage currents in dielectrics.

*This EM signal is not unique to a nuclear detonation, but can also be observed in large chemical explosions.

8-2.5.2 EMP

The EMP signal is characterized by high power but low energy, a consequence of its highly transient nature. Low-frequency components of the pulse may propogate both electric and magnetic fields to considerable distances from the burst and to considerable depths below the surface of the earth. The signal peaks at about 10^{-8} sec and lasts about 5 to 10 μsec, but the effective fields are reduced to 1/10 peak magnitude within one msec.

8-2.5.2.1 EMP GENERATION

The chief agent for the production of electromagnetic fields from nuclear explosions is the gamma radiation. The gamma rays produce a current of Compton recoil electrons that acts as a source of fields and, by ionization processes, makes the air a conducting medium. However, most of the detonation energy is ordinarily emitted in the form of X rays. By Compton scattering and photoelectric absorption in the air, these also produce electric currents and lead to effects similar to the gamma-ray-induced effects, especially at high altitudes. The fields produced by these effects are generally smaller than those produced by gamma rays.

The electron current that initiates the nuclear electromagnetic pulse (EMP) and the conductivity that shapes the EMP pulse are products of Compton collisions of prompt gamma rays. The Compton current and the ionization rate are complicated functions of time at any point. These functions reflect the arrival times, angles, and energies of gamma rays.

8-2.5.2.2 NEAR SURFACE BURST

The gamma rays that enter the ground (or ocean) from a detonation slightly above the surface are absorbed in a very short distance, a few meters at the most. Thus, over most of the distances where there are sizable Compton currents in the air, there are none in the ground. We thus have a hemispherical distri-

bution of Compton currents in the air. However, the ground is usually a better conductor than the air (except very near the burst), so that the current of conduction electrons, instead of flowing radially inwards, will flow partly to and in the ground (Fig. 8-11). Thus current loops are formed, with Compton electrons flowing outward in the air, and conduction electrons returning in the air and ground. These current loops give rise to a magnetic field, which is largest at the surface of the ground, and which runs clockwise azimuthally around the burst point. The electric field is tilted near the ground so as to be roughly perpendicular to the ground, and is directed upwards so as to drive conduction electrons into the ground.

8-2.5.2.3 FREE AIR BURST

The previous paragraph discussed the fields produced by the gamma-ray-induced Compton recoil electrons, neglecting the effect of the magnetic field of the earth. In all cases the asymmetries (ground, air, and bomb) were in the gamma-ray flux, production of Compton electrons, and ionization. The net electron motion was radial, and thus the source for the EM fields was a pulse, a *radial* current expanding with light speed from the burst point.

In the presence of the geomagnetic field, the Compton recoil electrons are deflected from their initially radial directions. The current pulse then contains transverse as well as radial components. Thus, even with complete symmetry of gamma-ray flux and electron production, there are sources for magnetic and nonradial electric fields. In fact, this

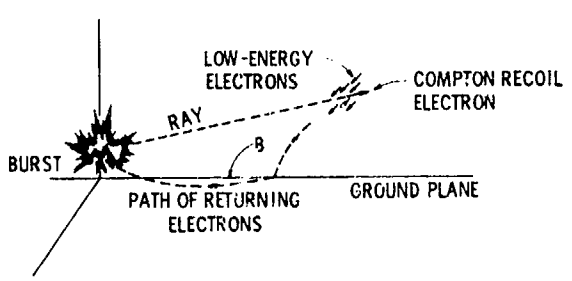


Figure 8-11. Influence of Ground on Return Conduction Current[9]

mechanism generates very intense high-frequency EM fields and becomes increasingly important as the burst altitude is increased.

8-2.5.2.4 EMP INTERACTION WITH SYSTEMS

The EMP interaction with systems is singular among nuclear weapons effects in that the interaction is often with the configuration of the entire system and not necessarily with any subsystem by itself. The complete system forms an antenna that responds as a whole to the EMP. Damage may occur at the gage, in the cable, or at the recording site.

8-2.5.2.4.1 GAGES

The major problem results from transducer inductance coils being short circuited. Damage has not been significant with balanced-reluctance gages. The most serious trouble has been permanent grounding of one circuit by flashover, causing disturbances on other traces.

8-2.5.2.4.2 INDUCTION OF CURRENTS INTO CABLES

The influence of the electric and magnetic fields near the surface of the ground on electrical conductors depends on the configuration of the conductor. The manner in which the conductor is coupled to the electric field is affected by the presence or absence of insulation, the type of insulation, and the quality of contact between the conductor and the soil. The effectiveness of shielded cables depends on these factors and the manner in which the shield is terminated. In addition, the implications of a signal induced on a conductor are determined largely by the sensitivity of the system served by the conductor. Thus, for example, a given pulse may cause serious malfunction if it is induced in a circuit designed for low-level signals, whereas the same pulse induced in a power circuit would be of no consequence. A more complete discussion of effects in insulated, bare, and shielded conductors is given in Ref. 9.

8-2.5.2.4.3. RECORDING SYSTEMS

Whereas in the case of long cable systems the EMP coupling was principally through the electric field, the EMP coupling into compact recording systems is principally a magnetic field interaction. Time-varying magnetic fields induce circulating currents in conducting loops found in compact systems. Associated with these circulating currents are voltages determined by a characteristic impedance of the loops. These voltage differences appear to systems as signals and may cause severe disruption in system operation.

Magnetic cores, tapes, and tape heads have been found relatively insensitive to pulsed magnetic fields. In experiments, typical selections of these components have withstood pulsed fields of over 10 gauss with no detrimental effect to either the component or the system. Thin-film memory devices, however, are expected to be more sensitive to transient magnetic fields.

The importance of the EMP interaction with a recording system is determined by the magnitude of the induced signal, the normal signal levels in the system, and the filtering and noise rejection properties of the system. Methods for minimizing the EMP interaction with recording systems are discussed in Ref. 9.

Some specific problems which one should consider in instrumenting nuclear blast tests include:

(1) High susceptibility to radiation damage of transducers employing semi-conductor strain gage sensors

(2) Fogging of film or paper photographic records by gamma radiation

(3) Burnout of galvanometers in galvo oscillographs due to EMP.

8-3 PORTABLE SYSTEMS

In the early days of blast experimentation, no compact blast-recording systems existed which were capable of being carried in aircraft, missiles, or rocket sleds, or of functioning in a severe blast, ground shock, or radiation environment. With the development of solid-state electronic components to replace electron tubes and with the development of compact recorders specifically designed to function in severe environments, complete blast recording systems that were essentially portable and self-contained could be and were developed. These systems often contain the same elements as the ground-based systems discussed earlier in this chapter, with the addition of a bank of batteries for power. They have been carried in aircraft, missiles, rocket sleds, balloon-borne canisters, etc., and have been used for field measurements to circumvent problems of recording over long cable lengths. Typical systems will now be described.

8-3.1 GALVANOMETER OSCILLOGRAPH SYSTEMS

The first "portable" systems were probably identical to those described under this same heading for ground-based systems, with the possible exception of substitution of a battery power supply for external power. The CEC Systems D and E are designed to function under moderate shock and vibration environments, and easily can be adapted for remote operation. An example of their use for blast recording is given in Ref. 10, with the equipment being housed in a light shelter that is subjected to blast at standoffs of about 500 ft from 640-lb HBX explosive charges. NASA 49 TP pressure transducers (see Chapter 7) were used successfully on this program. The same system functioned inadequately when mounted on a rocket sled for recording of blast pressures on moving airfoils[10] because of malfunction caused by the severe acceleration and vibration environment in the instrumentation compartment on the sled. Another limitation of this system is the maximum frequency response of 0-3 kHz, which is inadequate for recording blast waves from small blast sources. The galvanometer oscillograph systems have been supplanted largely

by systems based on small, rugged tape recorders, which will be discussed next.

8-3.2 MAGNETIC TAPE RECORDER SYSTEMS

Prior to discussion of complete systems, let us first discuss the compact, multichannel tape recorders that make these systems possible. Two units have been used extensively in blast recording, the Leach MTR-1200 and the Genisco Data 10-110.

8-3.2.1 THE LEACH MTR-1200 RECORDER

The Leach MTR-1200 recorder is a compact, rugged piece of equipment specifically designed for use under extreme environmental conditions such as those encountered in rocket sled testing. It is a self-contained unit capable of recording fourteen channels of wide band FM and/or direct analog information. The data signals are recorded on 1-in. magnetic instrumentation tape. Any of the fourteen data channels may be used to record self-generated 100-kHz time reference signals that in turn may be used for wow and flutter compensation. Two seven-track record heads and one erase head are provided on tape transport. The recording heads also have provision for playback. A summary of the recorder characteristics listed by the manufacturer is given in Table 8-1. Response time (±5%) has been measured in the laboratory using a square wave input and found to be 100 μsec, using a standard filter; with a gaussian filter the response was about 70 μsec, but the output was noisy.

In general, all data are recorded on wide band FM channels, which provide better signal resolution than analog recording and also respond to DC signals. To reduce the number of recorder channels required, data can be multiplexed and recorded on analog channels but with some sacrifice in frequency response. However, the high power limit on frequency response for the analog channels usually precludes blast recording for all but very short duration waves.

8-3.2.2 THE GENISCO DATA 10-110 RECORDER

The Genisco Data 10-110 was designed for use in adverse environmental conditions. The 10-110 is small (7 X 10 X 12.5 in.), lightweight (28 lb), and portable. The system uses a unique Cobelt tape drive and transport

TABLE 8-1. CHARACTERISTICS OF LEACH MTR-1200 TAPE RECORDER

Power Consumption	Warmup. 1 A, 24-32 VDC Record. 3 A, 24-32 VDC
Recording Time	120 sec with 600 ft of 1.0-mil Mylar tape
Input Signal Required	FM channels. ± 2.5 V pk. - pk. Analog channels. 0.050 to 1.5 V RMS
Frequency Response	FM channels. ± 0.5 dB from 0 to 10 kHz Analog channels. ± 3 dB from 100 Hz to 100 kHz
Flutter	0.5% RMS
Total Harmonic Distortion	Less than 3% during analog recording
Reference Oscillator Frequency	100 Hz ± 50 Hz
Overall System Accuracy	± 3% from input during FM recording

which is claimed by the manufacturer to eliminate many problems inherent in tape transports using reels and pinch rollers.

The Cobelt drive scheme was first applied to the Genisco recorder designed for use on a rocket sled. This recorder has several features designed to permit it to operate satisfactorily under heavy vibration and accelerations up to several hundred g. In the recorder, no conventional reels are used. Instead the recorder is constructed very rigidly on both sides of precision spaces only 0.0001-in. thicker than the tape width. The tape, instead of being supported between reel sides, is handled by the blocks of metal which form the body of the recorder. When the recorder is assembled, the entire tape guide function is carried out by these side plates. For withstanding shock, this construction is claimed to be much superior to one using a reel of any kind since a reel side necessarily must be relatively flimsy.

The data channels are wide-band FM (±40% deviation) with 54-kHz center frequency, thus giving a frequency response of 0 to 10 kHz. The minimum input to the voltage-controlled oscillator (VCO) for full-scale deviation is ± 250 mV. Thus, a high output transducer may be used directly into the VCO and give full-scale deviation without the use of a preamplifier. These characteristics are similar to the Leach recorder, and other specifications are probably also similar to those in Table 8-1.

An advantage of this recorder is its ability to operate with the center frequency shifted, thus giving a much higher signal-to-noise ratio when using the extended frequency band. With commercial DC amplifiers, a signal of 2 mV will drive the system to full-scale deviation.

8-3.2.3 TYPICAL PORTABLE MAGNETIC TAPE RECORDER SYSTEMS

In Ref. 11, successful use is reported of a portable system using the Leach MTR-1200 recorders for recording many channels of blast data on a moving airfoil subjected to blast loading. The system employed up to seven 14-channel recorders, as many as 100 absolute or differential pressure transducers, amplifiers for each transducer, battery power supplies, and ancillary equipment for remote stop and start. A schematic of the system is shown in Fig. 8-12. Note that the system is capable of recording either absolute pressure from a single flush-mounted transducer or differential pressure between a pair of matched transducers. Transducers employed in this system were Shaevitz-Bytrex Model HF (see Chapter 7), and the amplifiers were small, solid-state units made by the same manufacturer. As indicated in Fig. 8-12, electrical calibration signals can be applied to each channel.

A similar, but smaller, system was employed for blast line instrumentation on the same program. The elements of the system were identical to those used on the rocket sled, but it consisted of a single Leach MTR recorder and associated electronics installed in a steel box near the rocket track. The adaptation of the Bytrex gages for free-field measurement on this program has been described in Chapter 7.

Another complete system using a magnetic tape recorder has been developed for recording of nuclear blast data. This system bears the acronym "DAQ-PAC". It is described in Ref. 9, from which the discussion that follows was taken.

The DAQ-PAC system, developed by the MRD Division of General American Transportation Corporation for AFWL, is a self-contained portable package to obtain measurement under severe shock, pressure, radiation, and EMP environments. Table 8-2 lists the operating environmental specifications.

The DAQ-PAC consists basically of two parts: (1) a signal conditioning section that provides excitation voltages for transducers, automatic calibration, bridge balance, and bridge completion and a balanced differential preamplifier to provide adequate signal levels

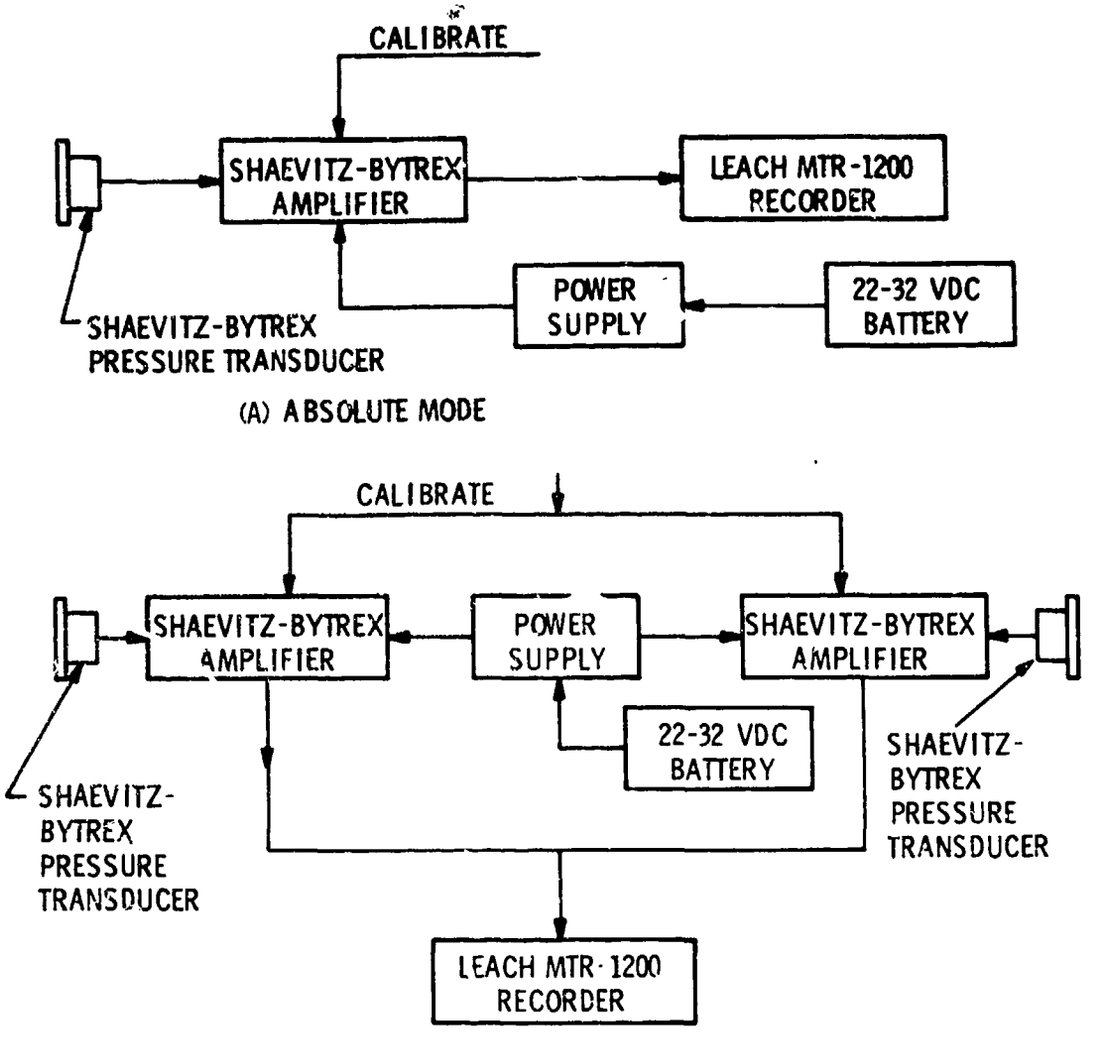


Figure 8-12. Typical Pressure Instrumentation System Employing Magnetic Tape Recorder[11]

for recording; and (2) an analog magnetic tape recording system for recording in both direct and FM format per IRIG specification 106-60.

All components of the system are plug-in modules, so that a wide variety of transducers can be used to obtain magnetic tape recording without additional circuitry. After recording, the tape is recovered and played back on any standard IRIG magnetic tape playback system. A total of twelve data channels plus two channels for flutter compensation and time reference data are provided.

The DAQ-PAC also contains a programmer, electromagnetic pulse (EMP) input circuit protection, and internal power supply. Upon activation by external control signals the programmer automatically directs the DAQ-PAC through a series of operations including pre-test warm-up and calibration, shorting input lines for EMP protection, data measurements recording, and post-test calibration. Thus, the DAQ-PAC is a complete instrumentation system and requires no external support other than the initial activation. The high shock and nuclear radiation resistance has been obtained by an all solid-state design and the careful selection of components.

TABLE 8-2. OPERATING ENVIRONMENTAL SPECIFICATIONS FOR DAQ-PAC

Shock	100 g, 1/2 sine wave, 11 msec duration
Neutron Radiation	10^{13} NVT (preamps and record electronics—10^{14} NVT)
Gamma Radiation	10^{8} rad/sec (C) intermittent, recover 0.1 msec; 10^{6} rad/sec (C) continuous
EMP	16,000-ampere turns/meter magnetic field; 5,000 V/m electric field 5 kHz to 25 kHz
Temperature	−20° to + 55° C
Overpressure	500 psi minimum
Moisture	Waterproof—150 psi hydrostatic pressure

The DAQ-PAC uses a modular construction to achieve a broad flexibility for measurement purposes. A combination of modules or cards is provided which allows measurement of low frequency phenomena (DC-600 Hz) using a 3-kHz carrier for transducer excitation, or wide band linear (200-200,000 Hz) processing for applications requiring high frequency response. Wide band recording over the range of DC to 20,000 Hz is also available as an optional feature for those applications where both relatively high frequency response and DC levels must be recorded (see Table 8-3). Tape speeds of 3.75 to 60 in. per sec can be provided, depending on the frequency response requirements. The corresponding recording times range from 60 to 4 min, respectively.

8-3.3 SELF-RECORDING GAGES

The last type of portable blast recording system that will be discussed differs markedly from the two previous systems. These latter systems, termed "self-recording gages", were developed originally by BRL in the 1950's for recording time histories of blast pressure from nuclear explosions in air. They have since been refined and further developed, and have been used for field blast measurements for conventional explosive tests as well as nuclear tests.

The design of these gages is described well in Appendix A, Ref. 12, which will be paraphrased here. The basic component of the system is a pressure-sensing capsule consisting of two concentrically convoluted diaphragms, nested together to reduce volume, and silver soldered together around their periphery. In brief, these capsules operate by an increase in outside air pressure entering through a small inlet hole, causing expansion of the diaphragms. A light spring stylus soldered to the center of the free diaphragm transmits this motion and produces a scratch on a coated-glass recording blank. The amplitude of this scratch is proportional to the movement of the diaphragm, which in turn is proportional to the applied pressure. A sapphire-tipped phonograph needle, with a 0.5-mil radius tip soldered to the stylus arm, is used to insure a very fine scratch. Ten ranges of capsules, from 0 to 1 psi to 0 to 400 psi, are in general use in BRL self-recording gages. The basic specifications are:

TABLE 8-3. DAQ-PAC SPECIFICATIONS

GENERAL CHARACTERISTICS

Accuracy	± 2% of full scale FM mode; ± 5% of full scale FM mode under specified environment
Tape speed	Standard 3.75 through 60 in./sec
Tape width	1 in.
Recording time	4 min of 60 in./sec
Track numbering and spacing	Per IRIG Specification 106-60 (analog)
Recommended tape	3M Tape 951-1
Start-stop time	1.0 sec maximum
Tape speed accuracy	0.5% from nominal at 60 in./sec
Flutter	< 1.0% peak to peak DC to 300 Hz at 60 in./sec
Calibration	Automatic 0 and single shunt
Frequency response and input impedance	See plug-in modules
Transducer connection	Standard 4-wire system under environment. 6-wire remote calibration for long lines in absence of EMP

Diaphragm material	Ni-Span C (0 - 1 psi phosphor bronze)
Deflection (at rated pressure)	0.020 in. min; 0.060 in. max
Linearity	± 0.5%
Hysteresis	± 0.5%
Natural Frequency (undamped)	1400 - 2000 Hz
Rise time	3 msec or less
Operating range	0 - 150% of nominal full-scale
Diameter	0.75 to 2.00 in. (depending on range).

A very-low-pressure gage has been designed using a single phosphor bronze, convoluted diaphragm, 5.75 in. in diameter. This diaphragm forms one side of the gage case. Any pressure differential existing between the inside and outside of the gage causes the diaphragm to deflect. This deflection is transmitted to and scratched on a coated-glass recording blank by a stylus soldered to the center of the diaphragm. The stylus point is the same as used on the pressure capsules.

In these early systems, the glass-coated recording blank was driven at a constant rotational speed by a small, governed electric motor driven by batteries. The cylindrical housing for the system has been mounted with the face containing the pressure orifices flush with the ground surface for measuring side-on pressure-time histories and in stream-

lined housings to record dynamic pressure or total pressure. The gage also incorporates a simple system for remote actuation. Data recorded with these gages are shown in Ref. 12.

The design of the original BRL self-recording gages formed the basis for an improved design by Bendix Corp., under contract to BRL. The development of the improved design is described by Wells[13]. This reference also contains a good history of improvements in the original BRL design for the 1953-1963 period that is presented here.

8-3.3.1 BLAST PRESSURE SENSORS

The basic element in blast pressure sensors has been the metal diaphragm. The diaphragm has been defined as a pressure responsive element that is movable in a direction substantially perpendicular to its flexible surface. The sensor of an early blast pressure gage consisted of a capsule formed by two nested corrugated diaphragm discs joined by a brazed circumferential seam. A mounting block, brazed to the center of one of the diaphragms, provided support for the sensor and, by means of a through hole, connected the small sensing volume of the capsule with the atmosphere. A stylus was mounted on a flat spring brazed to the center of the opposite diaphragm. Thus, the stylus motion was controlled directly by the motion of the diaphragm in response to changes in sensed pressure. While this sensor performed fairly well, the principal faults were the relatively slow rate of response and the tendency for the unguided stylus to wander from a straight line motion. During 1960 and 1961, shock tube tests at BRL indicated that single-diaphragm sensors would provide higher rates of response to pressure changes. The motion of the original single diaphragms (1-5/8 in. diameter) was about one-half that of the capsule design; but, in general, the response time was less than 1 msec. In 1962, a new design blast sensor based on the single diaphragm was introduced. This design used a similar 1.25-in. O.D. Ni-Span C diaphragm, spot welded to a formed Ni-Span C support. The stylus motion was restricted to a single axis by a Teflon bushing in the support member. Refinements followed rapidly. For example, a stainless steel flange was added to the assembly to facilitate sealing the sensor to the gage housing with an O-ring. Later, alignment pins were placed in the flange to orient the stylus in proper relation to the recorder when installed in the gage housing. Still later, the separate support and flange were replaced with a single stainless steel support disc incorporating an O-ring groove, alignment pins, and a jewel bearing to guide the stylus.

Some typical performance specifications for a series of 1963 model blast pressure sensors were:

Pressure range: 0-1000 psi (in steps such as 0-1; 0-2; 0-5; . . . .0-100; etc.)

Motion for each range: 0.015 to 0.031 in. with a mean value of about 0.022 in.

Response time: 1 msec or less except in the lowest pressure range

Linearity: 0.5 to 5%

Hysteresis: up to 1.1%

Another aspect of sensor development concerns the techniques used to provide damping. The damper used in the early gages consisted of an outer screen over a tabular cavity leading to the sensing volume of the capsule. Later, interchangeable aperture plates made it possible to provide multiple holes of various diameters for optimum damping in specific environments.

8-3.3.2 TIME BASE

A reliable time base is an essential requirement for analyzing the recorded data obtained from the self-recording instruments. At least two methods have been used to measure time intervals on the recordings. One method, used on the earlier gages, employed a constant speed electric motor to drive a disc on which the test data were recorded. The time base

was governed chronometrically to about 5%. Power for the motor was supplied by self-contained batteries. A second method, a time marker, was developed for metal tape recording systems where there is an inherent variation in the linear speed of the tape due to the change in radius as the tape unwinds from a constant speed spool. The early time markers consisted of a solenoid-operated oscillator. The stylus scribed an oscillating timing trace on the moving recording tape simultaneously with the test data traces. The nominal frequency of the timer trace was 50 Hz. The principal faults in this time marker were its low frequency and its sensitivity to shock.

8-3.3.3 INITIATION METHODS

Since the self-recording instruments have a limited operating period (about 20 sec), initiation of the recorder must precede arrival of the event to be measured by as short a time interval as possible, consistent with accelerating the recording medium (tape or disc) to normal speed. A number of methods have been used by BRL to accomplish initiation, such as:

(1) The visible light output from the monitored detonation operated a self-recording instrument photocell that closed a relay and started the recorder motor.

(2) The thermal radiation from a large-scale detonation melted low temperature solder in a thermal link on the self-recording instrument. The link supported a spring-loaded plunger that, when released by the melting solder, closed a switch that started the recorder motor.

(3) Closure of an electrical switch in an external circuit attached by wire to the self-recording instrument closed a relay that started the recorder motor.

8-3.3.4 ACCELERATION METHODS

Closely associated with initiation methods are means for rapidly accelerating the recording medium to normal speed following the initiation signal. The negator-spring powered recorders accelerate more rapidly then electric motor driven turntable models. Nevertheless, the following special techniques have been developed to further reduce the spring-drawn recorder acceleration time to very short intervals:

(1) Closure of the relay (by any of the initiating methods previously given) completes a circuit to a solenoid that releases a kick spring and accelerates the recorder to operating speed in an average of 18.4 msec.

(2) When the solenoid in (1) was replaced by an explosive piston actuator and fired electrically by the relay closure, acceleration time was reduced to an estimated 10 to 15 msec.

(3) The acceleration time of the recorder was reduced to 5 msec or less by means of a rack and pinion starter, driven by an explosive piston actuator, fired directly from the initiation line.

Based on the BRL developments up to 1963, requirements for an improved system were developed and used as guidelines by Bendix Corp. in their contract. These requirements are listed in Table 8-4. Bendix developed a number of prototype units based on these requirements. These units were subjected to a number of laboratory tests, as well as field testing with a 500-ton TNT blast source[14]. Based on their work, an improved self-recording system emerged with capabilities as listed in Table 8-5. Whether the improved system has been produced in sufficient quantity for wide field use is not known.

8-4 CALIBRATION TECHNIQUES

In air blast experimentation, some type of calibration of transducers and/or recording systems usually is employed. Most blast testing involves measurement of times and pressures. Calibration of time bases for oscilloscope sweeps, timing marks for moving film records, etc., is accomplished in a variety of

TABLE 8-4. GENERAL REQUIREMENTS FOR BLAST PRESSURE GAGE

Stylus pressure: sufficient to provide a readable trace at 40x magnification

Damping 0.5 to 0.7 critical ratio
Initiation: external line closure with internal latching

Power: rechargeable dry cells not subject to radiation damage
Physical size: (as small and as light as possible)

4 in. diameter

6 in. length

6 lb weight max

Error band: ± 5%
Hysteresis: ± 1%
Time base: 200 to 250 Hz accurate to 1% or less

Recording speed: 3 in./sec
Recording time: 10 to 30 sec
Start-up time: 5 msec desired, up to 150 msec allowable, if electric motor drive is used

Deflection at full scale: 0.015 in.
Temperature range: −65° to + 165°F operational
Radiation: 10^{15} neutrons/cm^2
10^{11} rad/sec

Pressure sensor: interchangeable in gage housing, flange mounted, designed to cover the specified pressure range in incremental steps

Pressure range: 2 to 1000 psi
Natural frequency: 1 to 10 kHz

Vibration: 10 to 80 Hz at 0.06 in. double amplitude
80 to 2000 Hz at 20g

Acceleration: 100g steady-state minimum

Thermal pulse: 300 cal/cm^2 total dose seen at entrance to present port
Shock: 500g for 11 msec min, 1000g desired

ways. Usually, timing is compared with signals from secondary standards such as crystal-controlled oscillators or timing mark generators, counter chronographs, etc. Periodically, these secondary standards can be checked against standard time signals broadcast by the National Bureau of Standards over Station WWV. With care, time bases for blast recording equipment can be calibrated with submicrosecond accuracy. No more specific methods will be discussed here, because the methods are very dependent on the type of recording system in use.

Calibration of blast pressure transducers is accomplished in a number of ways, which are

TABLE 8-5. CAPABILITIES OF IMPROVED SELF-RECORDING BLAST PRESSURE SYSTEM

Sensor:	Interchangeable assembly with O-ring seal, alignment dowel pins and integral reference stylus
	Range: Up to 0-600 psi tested. Higher ranges feasible.
	Deflection: 0.015 in. min, full scale each range
	Linearity: 5% max
	Hysteresis: 1% max
	Natural Frequency: Greater than 1 kHz except in ranges below 0-2 psi
Recorder:	Negator-spring powered with separate metal recording tape. Nominal tape speed of 3 in./sec and 20 sec min running time. Start-up time with explosive piston actuator; 0.5 msec
	Recording Tape: magnetic stainless steel, 3/8 in. width x 0.001 thick x 60 in. maximum length
Time Base:	Fluidic type time marker, nominal frequency 475 Hz ± 1% at constant temperature and nominal 20 psi gas supply pressure
Initiation:	External line (electrical) or gamma radiation of 1.5×10^4 rad/sec or more
Power:	Rechargeable dry cell, 12 V nominal
Physical Size:	Gage: 4.75 in. diameter (flange) x 4.5 in. length. Fluid supply and Regulator: 4-11/16 x 2-11/16 x 1-3/4 in.
Mounting:	Flange
Weight:	4.6 lb
Environmental:	
Temperature:	(Timer only) -65° to $+165^\circ$F
Vibration:	10 to 80 Hz, 0.06-in. double amplitude and 80 to 2000 Hz at 20g
Acceleration:	75 g tested
Shock:	100g, 10 msec. At shock levels of 300 to 500g, the pressure trace is subject to an error of ± 3 to ±7%.

dependent on the type and geometry of transducer, its pressure range, the amplifying and recording system, etc. In general, the types of calibration employed, probably in increasing order of desirability, are:

(1) Electrical calibration

(2) Static pressure calibration

(3) Quasi-static pressure calibration

(4) Dynamic calibration.

In calibrating a pressure transducer and recording system electrically, one generates a step change in electrical signal by switching an appropriate circuit element into the transducer output circuit. For resistance-type

transducers, a fixed resistor usually is paralleled with the resistive gage element to generate a voltage change. For piezoelectric transducers, a step in electrical charge is generated by switching into the gage circuit a known capacitance applied to a standard voltage. Often, electrical calibration will be accomplished in an automatic sequence in blast recording equipment prior to charge detonation. Calibration steps of several different amplitudes usually are impressed on records in this manner. The accuracy of purely electrical calibrations of this type is totally dependent on separate static or dynamic calibration of the transducers, so that the step changes in voltage can be correlated with equivalent pressure changes. For the electrical calibration method to be useful, the pressure transducers must be stable and preferably linear in their outputs.

Static pressure calibration can be accomplished with any means of applying static pressure to a transducer and a number of methods of recording output. The applied pressure is measured by manometer, precision bourdon gage, or any of a number of other means. Transducer output can be measured by digital or analog voltmeter, galvanometer oscillograph, etc. With suitable equipment for accurate measurement of pressure and transducer output, those types of blast pressure transducers that have DC response often can be calibrated accurately by static methods. In a static pressure calibration, one, of course, obtains no information on shock response of a transducer. This method is useless for calibration of piezoelectric transducers because they have no DC response.

By quasi-static pressure calibration we imply calibration by application of a pressure increase or decrease to a transducer in a relatively long time (i.e., a number of milliseconds) but a time short enough for adequate response of a transducer and associated recording system having a finite electrical time constant. Calibration systems of this type, commonly used for piezoelectric transducers, are pneumatic and usually employ solenoid valves to rapidly fill (from a much larger reservoir) a small chamber containing the transducer, or rapidly dump pressure from the small chamber. A schematic of one such system used for laboratory calibration[25] is shown in Fig. 8-13. This particular system includes a means of superimposing an electrical calibration step on the pressure calibration record. Recording is accomplished by a CRT oscilloscope. By multiple exposure of film in an oscillograph record camera and adjustment of initial oscilloscope sweep position, multiple calibrations can be obtained easily on one piece of film, as shown in an inset in Fig. 8-13. A similar system for field calibration is shown in Fig. 8-14. Here, an Atlantic Model LC-33 transducer is shown in the calibration chamber. This particular system is light and portable, and can be taken into the field to calibrate an entire blast pressure recording system. Quasi-static pneumatic systems can be used for calibration up to several hundred psi.

Dynamic calibration of pressure transducers has been accomplished in several ways. Rathke[26] reports a clever adaptation of a simple drop test device for applying a known half-sine pulse at very high pressure amplitudes (up to 20,000 psi). The pressure chamber and contained liquid deform elastically under impact of the drop weight, acting amazingly like a linear spring. By varying drop height and mass of the impacting weight, the amplitude and duration of the pressure pulse easily can be varied over wide ranges. A schematic of Rathke's apparatus and typical pressure traces are shown in Fig. 8-15. This system is suitable for calibration of all types of flush-mounted blast pressure transducers. Rathke used a common calibration technique here of comparison with a reference or standard transducer, which presumably had been calibrated separately by some other means.

The best method of dynamic calibration of air blast transducers is essentially a "bootstrap" method. One subjects the transducer to a blast or shock wave itself and, by independently measuring shock velocity or equiva-

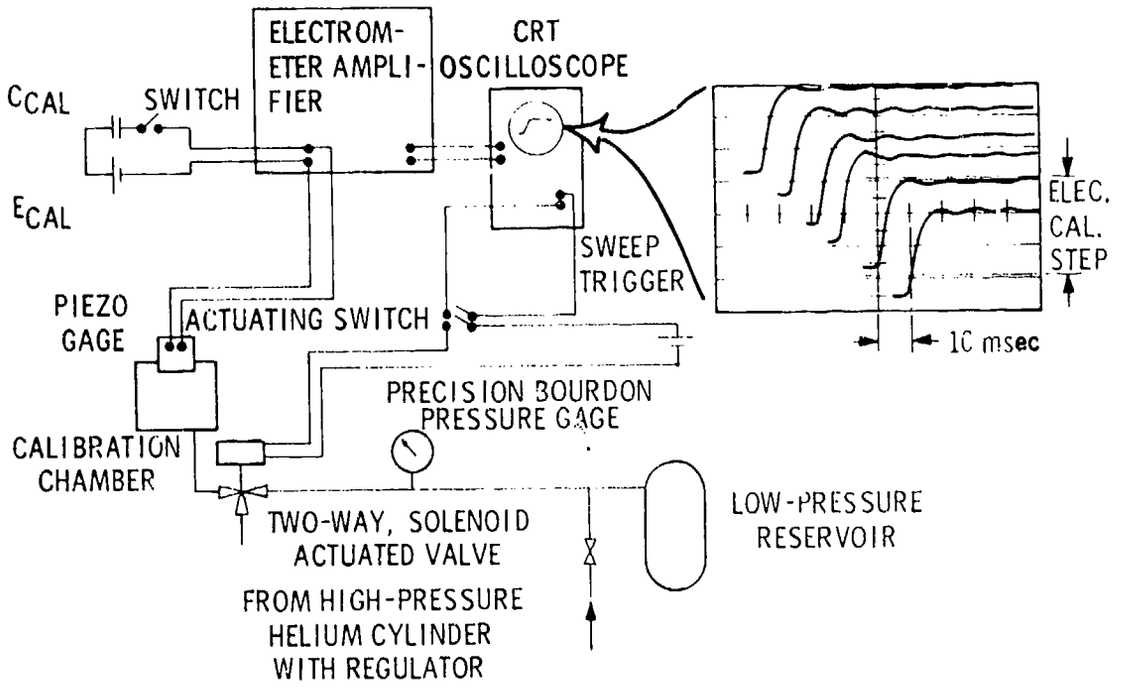


Figure 8-13. Schematic Diagram of Quasi-static Gage Calibration Apparatus

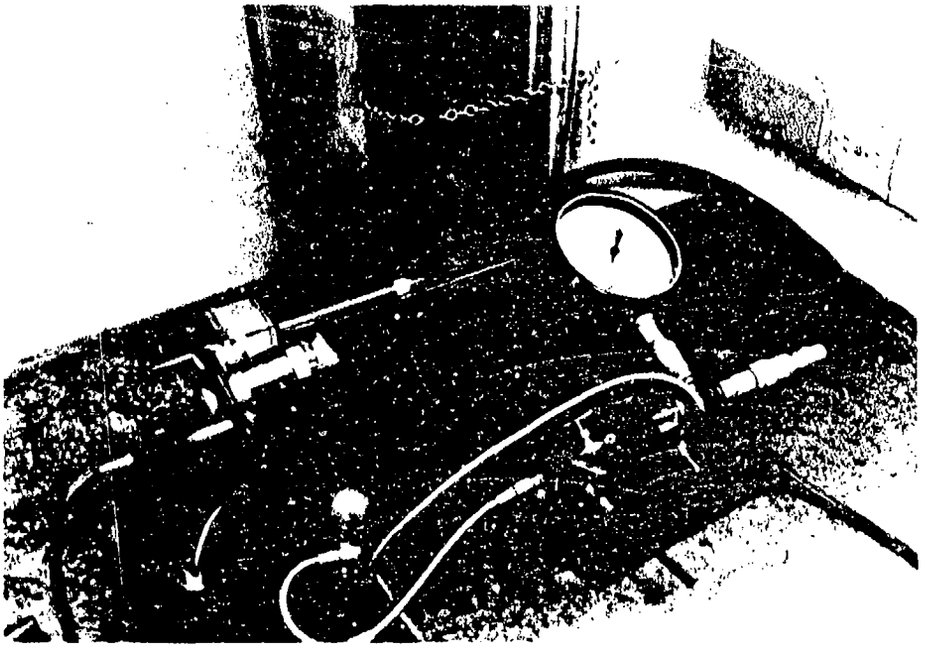


Figure 8-14. Quasi-static Pressure Calibrator for Field Use (Courtesy of Southwest Research Institute)

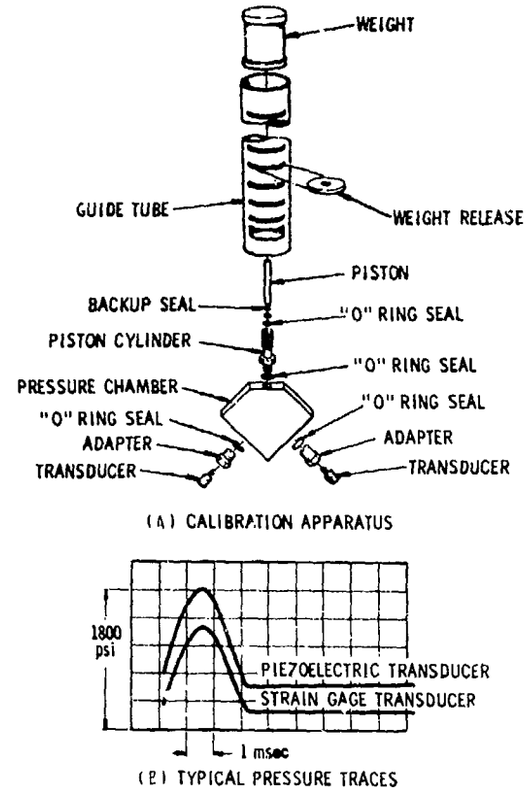


Figure 8-15. Dynamic Pressure Calibrator of Rathke[16]

lently shock arrival times at stations surrounding or near the transducer, infers the overpressure through use of the Rankine-Hugoniot relations (see Chapter 2). Flush-mounted transducers can be calibrated in this manner by mounting in the wall or end plate of a shock tube, or flush with the ground surface for field detonation of explosive charges. Side-on transducers can be supported in shock tubes on streamlined stings, or mounted in the field on their regular mounts. The accuracy of this method is dependent on good accuracy in measurement of spacing of time-of-arrival gages and of time. For low overpressures (about 2 psi or less) one must use long, accurately measured baselines and quite accurate time measurement to calibrate by this method, as well as corrections for wind and accurate estimate of sound speed. We call this the "best" calibration method because the entire transducer and recording system is calibrated under conditions best simulating actual use. Gage "ringing" and other spurious response will be evident here, when they will not be apparent under static or quasi-static calibration.

REFERENCES

1. W. D. Kennedy, *Explosions and Explosives in Air*, Chapter 2, *Effects of Impact and Explosion*, Summary Tech. Rept. of Division 2, NDRC, Washington, D. C., 1964, pp. 70-71.

2. B. Soroka and G. T. Watson, *An Eight-Channel High-Performance Oscillograph Recording System*, BRL Memorandum Report No. 1965, May 1966.

3. J. N. Brooks, *DRI Blast Recording Equipment*, Phase Report No. 5, Contract NOrd 16009, Denver Research Institute, Denver, Colorado, 27 March 1957.

4. R. W. Morton and John L. Patterson, *A Transient Pressure Measurement System for Blast Effect Research*, Paper 148-LA-61-1.

5. E. A. Zeitlin, *The Blast Environment: Methodology and Instrumentation Techniques with Applications to New Facilities*, NAVWEPS Report 8782, U. S. Naval Ordnance Test Station, China Lake, Cal., Aug. 1965, (AD-622 980).

6. A. B. Wenzel and R. L. Bessey, *Barricaded and Unbarricaded Blast Measurements*, Contract No. DAHC04-69-C-0028, Subcontract 1-OU-431. Southwest Research Institute, Oct. 1969.

7. T. A. Zaker, *Blast Pressure from Sequential Explosions*, Final Report J6166, IITRI, Oct. 1969.

8. E. G. Johnson, *Propellant Hazards Research Facility*, Technical Report S-152,

Rohm & Haas Co., Huntsville, Ala., Oct. 1967, (AD-822 133).

9. R. H. Rowland, *Blast and Shock Measurements, State-of-the-Art Review*, DASA 1986, DAS/AC Special Report 45, Aug. 1967, (AD-824 160).

10. R. L. Jarvis, et al., *A Program to Induce High Blast-Induced Airloads and Structural Response of Lifting Surfaces*, ASD-TDR-63-764, Vol. II, July 1964, (AD-605 407).

11. I. O. Wolf, et al., *An Experimental Investigation of Blast-Induced Airloads and Response of Lifting Surfaces*, AFFDL-TR-64-176, March 1965, (AD-465 721).

12. E. J. Bryant, N. H. Ethridge and J. H. Keefer, *Measurements of Air-Blast Phenomena with Self-Recording Gages*, WT-1155 Operation TEAPOT – Project 1.14b, Feb.-May 1955, (AD-617 170).

13. H. S. Wells, *Development and Test of Prototype Miniature, Rugged Self-Recording Air-Blast Instrumentation*, Report No. E.I.R. 700, The Bendix Corp., Baltimore, Md., Nov. 1966.

14. D. P. LeFevre, *Evaluation of New Self-Recording Air Blast Instrumentation: Project 1:36 Operation SNOWBALL*, BRL Memorandum Report No. 1815, Jan. 1967.

15. W. E. Baker and W. O. Ewing, Jr., *Miniature Piezoelectric Gages for Measuring Transient Pressures on Airfoils*, BRL Memorandum Report No. 1329, March 1966.

16. T. S. Rathke, *A System for Dynamic Calibration of Pressure Transducers*, Inst. Soc. of Am. Preprint No. P19-2-PHYMMID-67, 22nd ISA Conference and Exhibit, Chicago, III., Sept. 1967.

CHAPTER 9

PHOTOGRAPHY OF BLAST WAVES

9-1 GENERAL

A variety of different optical methods can be and has been used to observe both strong and weak air blast waves. Aside from the purely documentary and graphical value of good still or motion pictures of blast waves, these and other film records have proven to be very valuable sources of experimental data for such parameters as shock front velocity, time of shock arrival, and particle velocity. The prime requirement for blast wave photography is that the particular camera or device being used have a short enough exposure time per frame, or a fast enough writing rate, essentially to "stop" the motion of the shock front. The scale of the test and field of view of the camera or device affect the actual values of exposure times that will render shock fronts visible; hence a wide variety of types of photographic equipment may prove useful for different types of tests. In this chapter, specific equipment and applications will be discussed in some detail. However, we will not attempt a complete review of high-speed photographic techniques and equipment in general. The reader instead is referred to good general texts on this topic, such as Refs. 1-3.

9-2 MOTION PICTURE EQUIPMENT

9-2.1 LOW-SPEED FRAMING CAMERAS

Many types of motion picture camera have proven suitable for blast wave photography, depending on the scale of the experiment. Let us define a low-speed framing camera as one that employs an intermittent film drive (see Chapter 1 of Ref. 2, and Fig. 9-1), wherein the film is advanced between frames with a shutter closed, and the shutter opened with the film momentarily stationary. All conventional movie cameras employ such mechanisms. Some can be driven at framing rates up to 400 fps, using 16-mm film, and have been used for distant photography of blast waves from large blast sources. Acceptable types and makes of such cameras are too numerous to mention.

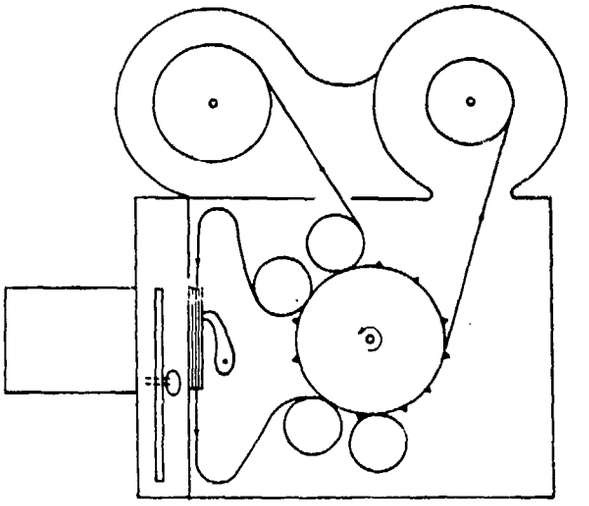


Figure 9-1. Schematic Diagram of an Intermittent-type Camera[2]

(Reprinted by permission of W. G. Hyzer, Engineering and Scientific High-Speed Photography, *The Macmillan Co., N. Y., 1962.)*

Attempts to extend this principle to operation at higher speeds reach their limits at 400 fps because the accelerations required for film movement between frames are greater than those which can be tolerated by the film, and so tearing results.

9-2.2 HIGH-SPEED FRAMING CAMERAS

9-2.2.1 ROTATING PRISM CAMERAS

It, therefore, follows that if intermittent movement is not possible at framing rates above 400 fps, continuous film motion must be adopted and the problem then consists of preventing a blurred image from being record-

ed by a fixed lens on to a moving film. Most cameras available at the moment use optical compensation by means of a rotating glass block or prism interposed between lens and film. The principle of operations of such cameras is shown in Figs. 9-2 and 9-3. Many models of camera have been made on this principle. One of the first was the Eastman High Speed Camera, using 16-mm film and capable of framing rates up to 3500 fps. For many years, various models of the Fastax camera—accepting 8-mm, 16-mm, and 35-mm film and capable of rates up to about 10,000 fps—were considered to be the best available cameras of this type. The mechanisms for these cameras are often considerably simpler than for intermittent cameras, as can be seen from Fig. 9-4. These early rotating-prism cameras did not operate at a controlled framing rate, but instead the film would continuously accelerate during operation. Some auxiliary method of impressing accurate timing marks on the edge of the film was, therefore, mandatory for accurate determination of framing rate and was incorporated in each camera. For use in large-scale field tests where good time correlation between different cameras is required, coded real-time signals often are impressed on the films. Newer designs of rotating-prism cameras are exemplified by the Red Lake Laboratories Hycam cameras, capable of rates up to 44,000 fps with 16-mm film. These cameras employ a controlled drive mechanism that fixes the framing rate at a preselected value after a short acceleration period. The control allows their use as low-speed framing cameras, if desired. The optical system employed in the Hycam cameras is shown in Fig. 9-5. Most of the rotating-prism cameras employ built-in or auxiliary timing mechanisms to allow remote actuation and/or synchronization with rapid processes.

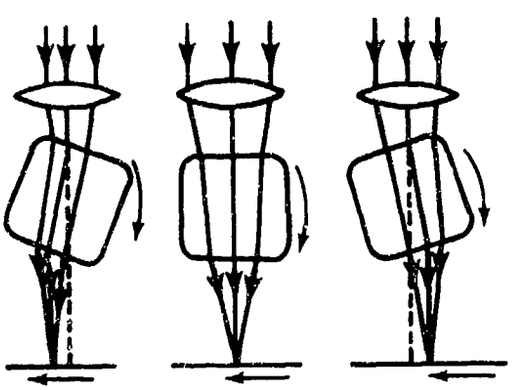
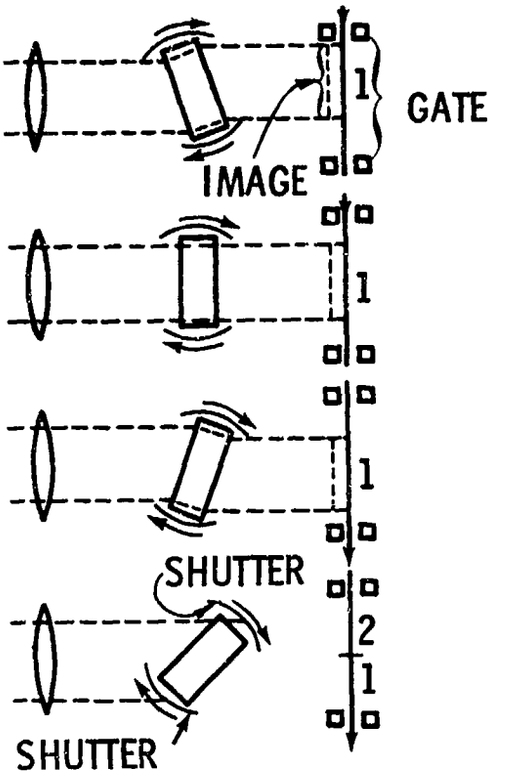


Figure 9-2. Principle of Operation of Rotating Prism Camera[3]

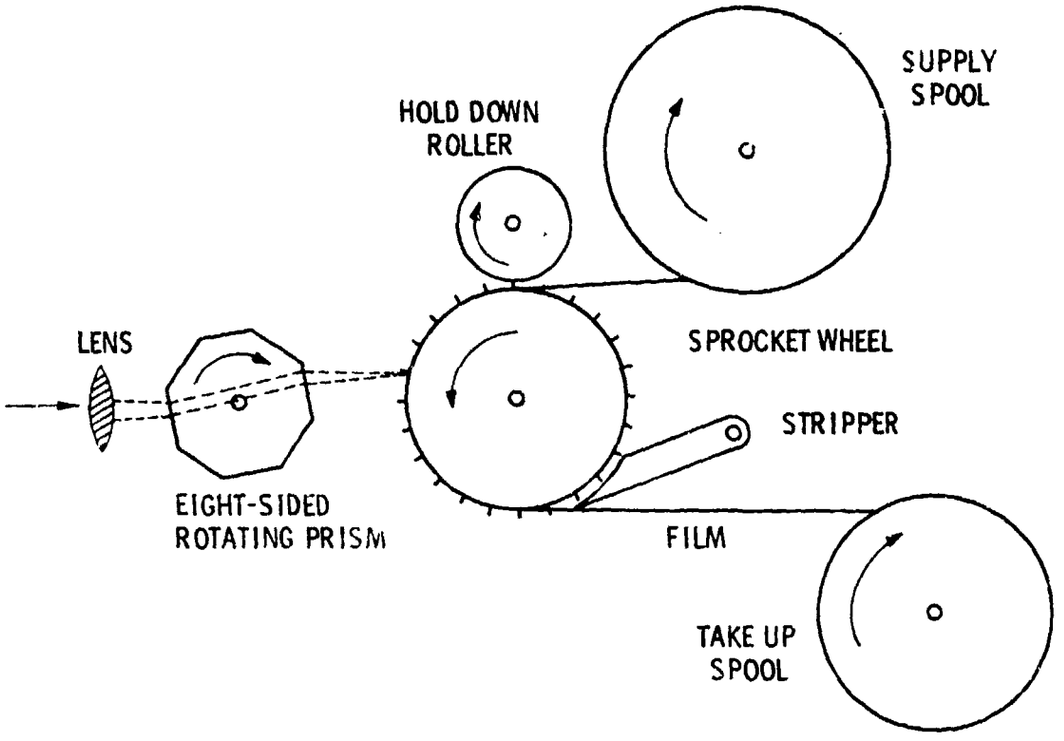


The diagram shows four stages in the revolution of the glass block, the dotted lines indicating the refraction of the beam of light from the lens.

Figure 9-3. Rotating Plane Prism Used in the Eastman High Speed Camera[1]

9-2.2.2 ROTATING DRUM CAMERAS

A high-speed motion picture camera with approximately the same framing rate capability as the rotating-prism cameras has been built and sold under the trade name Dynafax by the Beckman and Whitley Co. This camera employs a rotating mirror and concentric rotating drum that supports a film strip. Maximum framing rate is 25,600 fps, but



(Reprinted by permission of W. G. Hyzer, Engineering and Scientific High-Speed Photography, *The Macmillan Co., N.Y. 1962.)*

Figure 9-4. Schematic Diagram of Fastax 8-mm Rotary Prism High-Speed Camera[2]

coverage is limited to 224 total frames. Advantages claimed are that the camera can be brought up to speed and maintained ready to photograph a rapid, unsynchronized event. The principle of operation is described in Ref. 2, and will not be repeated here.

9-2.2.3 ROTATING MIRROR CAMERAS

To achieve framing rates significantly higher than available with rotating-prism and drum cameras, camera designers have had to employ entirely different designs. All of these designs are based on reducing the moving elements to a single, small, rotating mirror that can be made of very strong material and spun at very high rotation rates. All of these ultra-high-speed cameras sacrifice total number of frames, resolution, or both in achieving their very high framing rates. Because the total "time-window" for these cameras is very small, elaborate timing and synchronization equipment is a necessity. Most of these cameras operate on the principle indicated in Fig. 9-6. The plane of the image of the event to be photographed is arranged to pass through the axis of rotation of a rotating mirror, and the light, after reflection at the rotating axis mirror, passes in turn through each one of a series of secondary lenses, arranged to produce a focused image of the event on the film that is positioned along an arc of a circle the center of which coincides with the axis of rotation of the mirror. Each secondary lens will produce an image on the film only while the light reflected from the mirror is passing through it, and therefore the images recorded on the film will be separated in time by an amount directly proportional to the rotational speed of the mirror.

In order that the beam of light reflected by the mirror shall not be so broad that several secondary lenses are passing light at the same time, the system is usually arranged as shown

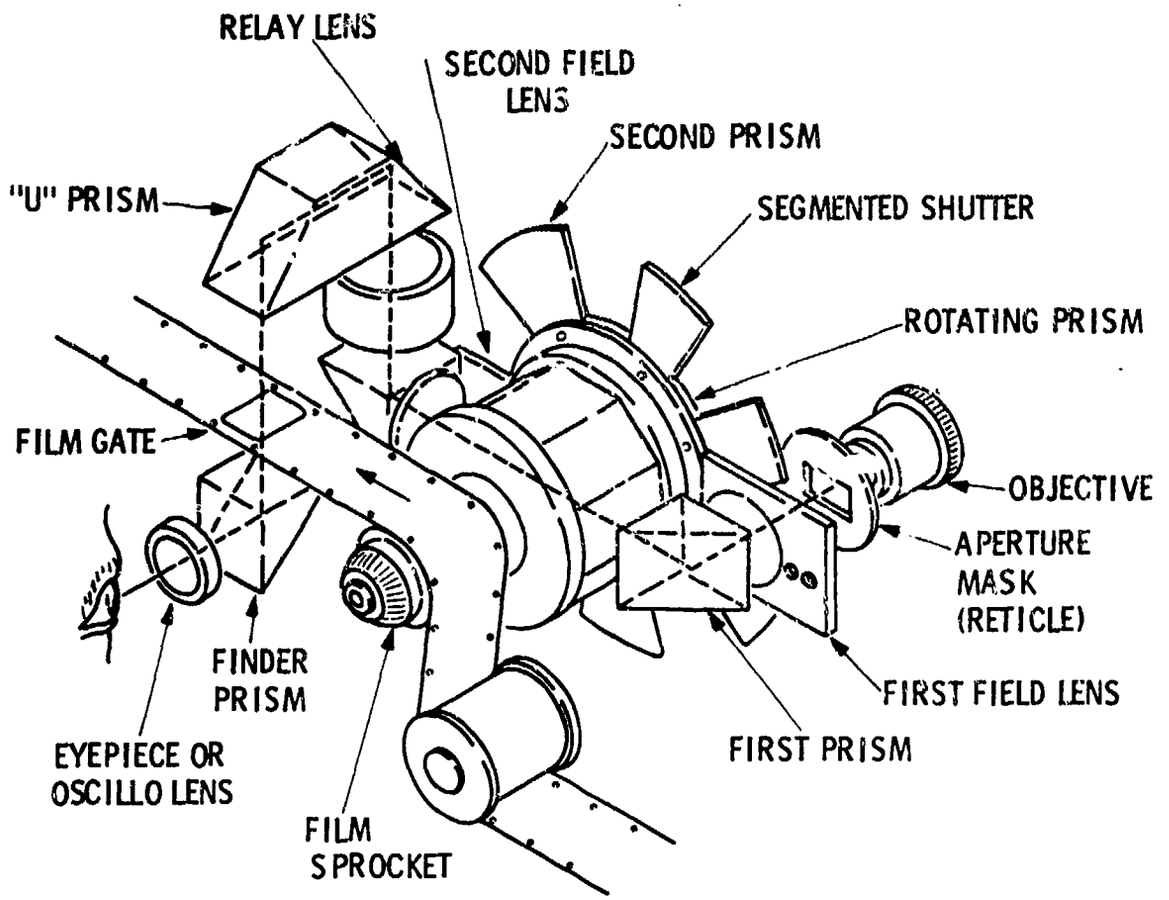


Figure 9-5. Mechanism for Hycam Rotating Prism Cameras
(Courtesy of Red Lake Labs., Inc.)

in Fig. 9-7. Here an objective lens and a diaphragm are placed in front of the main lens as shown. The objective lens forms an image of the object, and this image is then focused by the main lens on the rotating mirror. The diaphragm is placed in the plane of the image formed by the objective lens and serves to limit the angle of the marginal rays of light in the system thereafter, so as to prevent more than two of the secondary lenses from being illuminated at any instant.

The first commercially available cameras of the type discussed were made by the Beckman and Whitley Co., and were very large and heavy instruments suitable only for laboratory use. This company and later the Cordin Co. have since made lighter and more portable models. Typical Cordin cameras are shown in Fig. 9-10. These cameras record at framing rates as high as 5×10^6 fps, but are limited to about 25 total frames. To project their films as motion pictures, they must be rephotographed frame-by-frame and run repetitively.

9-2.2.4 IMAGE DISSECTOR CAMERAS

The final type of motion picture camera which can be used for blast wave photography is termed an image dissector camera. The system works fundamentally by means of a grid that splits the picture up into a large number of parallel strips. If the grid has relatively narrow transparent spaces and opaque bands, any single picture taken through it, stationary, will consist of a number of narrow bands of image with unexposed material between. Obviously, by moving the grid sideways through the width of one of the spaces in it, another picture can be taken on this unexposed portion, and so on until the whole of the surface of the plate has been

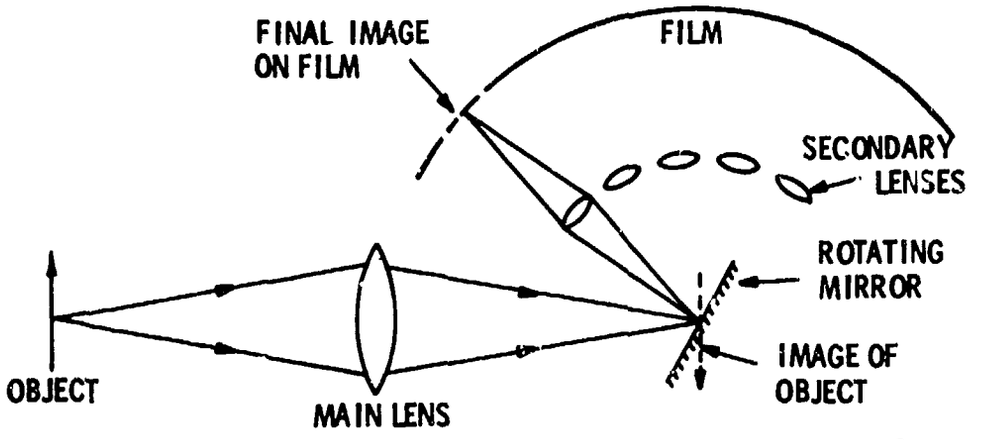


Figure 9-6. Essential Features of a Rotating-mirror Framing Camera[3]

(Reprinted from High-speed Photography by R. F. Saxe, copyrighted 1966 by the Focal Press, London and New York. Used by permission of the publisher.)

used. After processing, the result will appear to the eye to be a mere jumble until the grid is placed over the picture, when once again any of the pictures recorded can be selected.

The number of pictures which can be taken depends upon the width of the transparent spaces in the grid and naturally there is a limit to the amount of unused space, relative to the amount of picture space, at which the picture becomes too "diluted" to be observed properly. In practice, it is possible to use a series of clear slits 0.0005 in. wide cut at intervals of 0.015 in. in an opaque plate. Thus each line will occupy only one-thirtieth of the total area on to which it can be photographed, and it is possible to obtain thirty pictures in succession by means of a movement of the grid of 0.015 in. At first sight it might be supposed that this would lead to a very unsatisfactory picture from the point of view of continuity and definition. However, each picture, when the grid is in position, seems very nearly continuous, in spite of the fact that twenty-nine thirtieths of it is missing. In the simplest form of this device, the grid is placed in the focal plane of the lens, almost in contact with the stationary film. When the operation is to be photographed, the grid is moved through 0.015 in. as quickly as possible and during that period of time a streak containing the elements of thirty pictures is

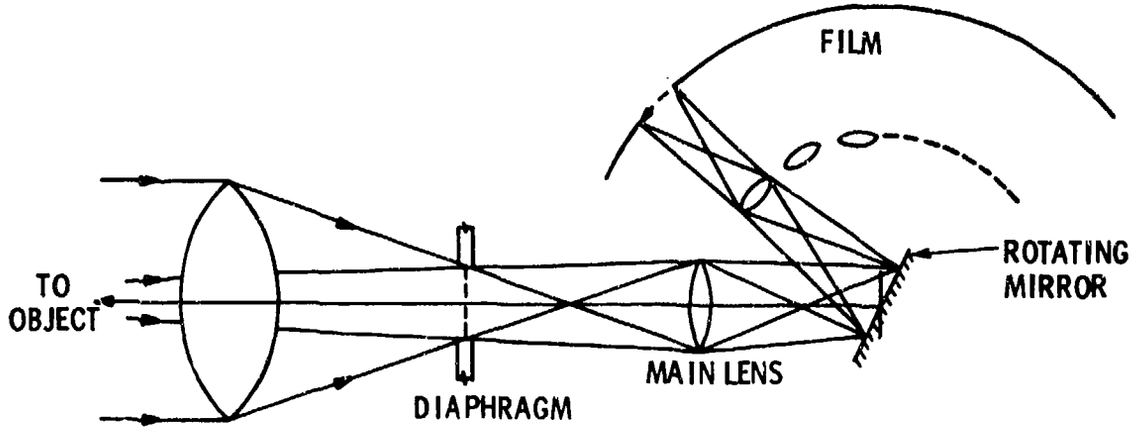


Figure 9-7. Rotating-mirror Framing Camera With Diaphragm[3]

(Reprinted from High-Speed Photography by R. F. Saxe, copyrighted 1966 by the Focal Press, London and New York. Used by permission of the publisher.)

made. The resulting picture either can be analyzed subsequently into thirty separate exposures, or the grid can be moved at uniform slow speed, thus producing a flickerless motion picture. It should be emphasized that, under these circumstances, the image produced on the film is not actually a series of separate pictures but is a smear which is analyzed subsequently by the grid; the resolving power of the system is determined, therefore, by the characteristics of the grid. One camera which has been built on this principle has been described by Sultanoff[4]; this camera uses a focal plane shutter with slits 0.0001 in. wide moving at 10,000 in. per sec and thus producing 100,000,000 pictures per sec. It is difficult to move an actual grid across the film at such a speed. An image of it, therefore, is moved by reflection from a rotating mirror, the grid itself being placed in the optical system in such a place that the objective forms an image on to it. The image is then reprojected, by means of a second lens, through a rotating mirror on to the film plane (Fig. 9-8).

9-3 STREAK PHOTOGRAPHY EQUIPMENT

In laboratory and small-scale photographic studies of air shocks, streak cameras can provide useful data on shock front motions. They yield continuous plots of these motions versus time, rather than the discrete pictures at successive frozen instants of time which framing cameras record. They are, of course, simpler in design and construction than the framing cameras.

The streak camera is used to obtain a continuous monitoring of the rate and direction of the propagation of light along a line defined by a slit in the camera. No information is recorded about the behavior at points other than those on the line selected. It follows, therefore, that this method mainly is used where circular symmetry is expected and the line then is selected as a diameter.

The essential features of a streak camera are shown in Fig. 9-10. An image of the object to be studied is formed by the first lens in the plane of the slit, which is adjusted to let through only that part of the image which is to be studied. The light that passes through the slit is focused by the second lens, via the mirror, on to the film. The mirror is mounted on a shaft perpendicular to the plane of the diagram and the film is constrained to form an arc of a circle with the mirror shaft as its center.

Streak cameras are available commercially from a number of manufacturers, including Beckman and Whitley Co. and Cordin Co. A Cordin streak camera is shown in Fig. 9-10. Writing speeds of up to 20 mm/μsec are possible with such cameras. The Dynafax and Fastax framing cameras mentioned earlier also are convertible to streak camera configuration, but at slower writing speeds.

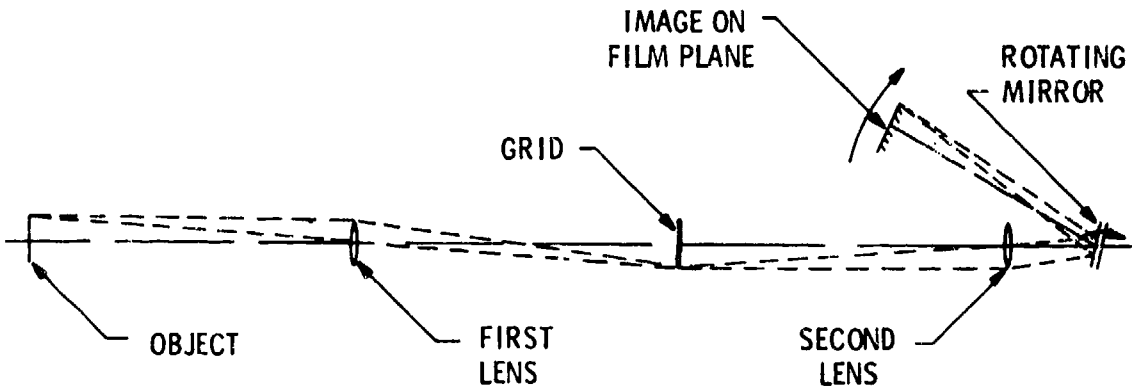


Figure 9-8. Optical System of Sultanoff's High-speed Camera[4]

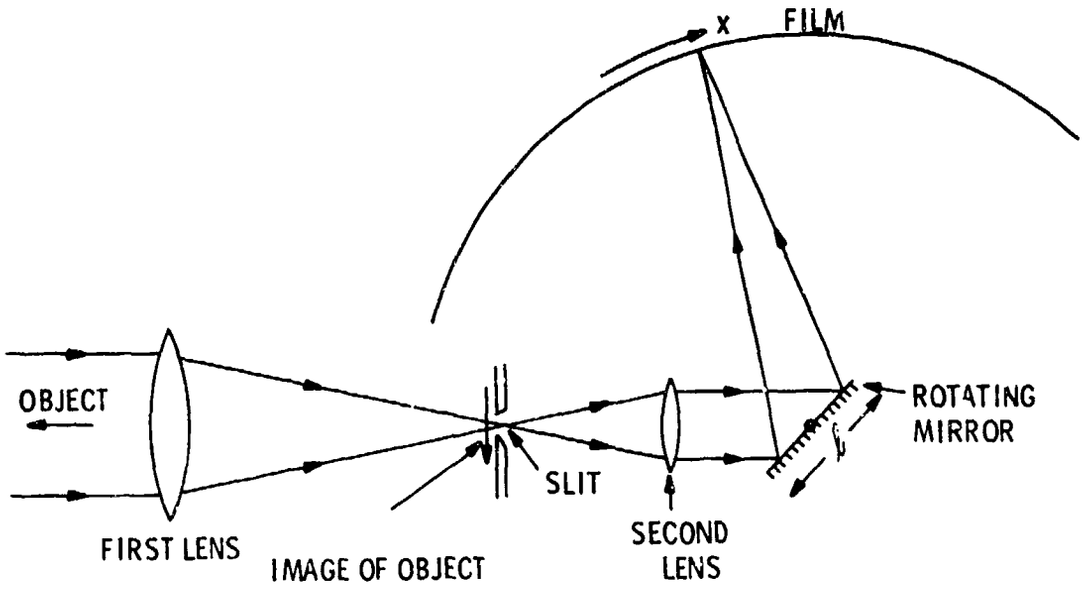


Figure 9-9. Essential Features of a Streak Camera

(Reprinted from High-speed Photography by R. F. Saxe, copyrighted 1966 by the Focal Press, London and New York. Used by permission of the publisher.)

A test arrangement used at BRL for simultaneous streak and still photography of blast waves from small spherical Pentolite charges is shown in Fig. 9-11. The tests are conducted in a blast chamber, with the optical instrumentation observing the experiment through a viewing port. The shock wave is backlit with an exploding wire light source and a Fresnel lens collimator. An objective lens focuses the light on the slit in a streak camera, and simultaneously on the focal plane in a Kerr cell still camera (see par. 9-4 for a description of such cameras) through an angled half-silvered mirror. Examples of streak camera records obtained with this test arrangement are shown in Fig. 9-12. The traces of the shock front and the front surface of the explosive products are clearly visible in these records.

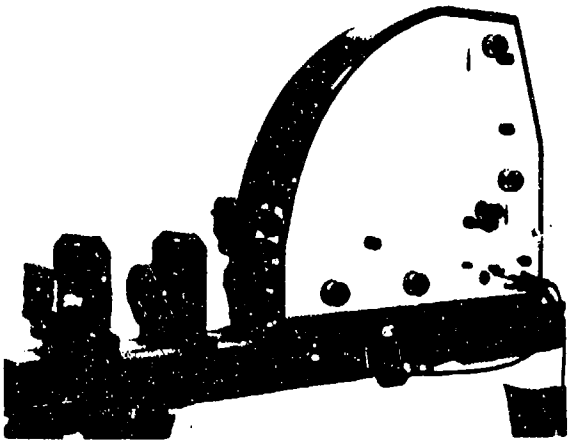
9-4 STILL PHOTOGRAPHY EQUIPMENT

9-4.1 CONVENTIONAL CAMERAS

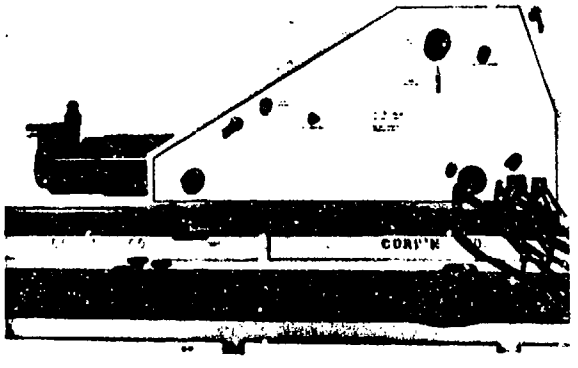
Many types of still cameras have been used for photography of air blast waves. For photographs of large chemical and nuclear explosions taken at some distance, any type of conventional still camera with a reasonably fast shutter speed (e.g., $\leqslant 1/200$ sec) can be used. Fig. 9-13 is an example of a photograph taken with such a camera in which the shock front is clearly visible. There is no point in listing or suggesting suitable cameras of this type, because there are very many on the market.

9-4.2 FAST SHUTTER CAMERAS

We are more concerned here with description of the special scientific devices which have much shorter exposure times than that given for conventional cameras. Most of these are true cameras with very fast special shutters, but some are not. One type of fast shutter, developed by Edgerton, employs the Faraday magneto-optic effect. A cylindrical slug of polarized glass is surrounded by an electrical coil. On discharge of a heavy current pulse through the coil, the strong transient magnetic field depolarizes the glass slug, and "opens" the shutter. By proper choice of electrical circuit parameters, the depolarization can be made to last less than a microsecond. A second type of fast shutter is the Kerr cell, which relies for its action on the birefrin-



(A) FRAMING CAMERA



(B) STREAK CAMERA

Figure 9-10. Typical Rotating-mirror Cameras (Courtesy of Cordin Co.)

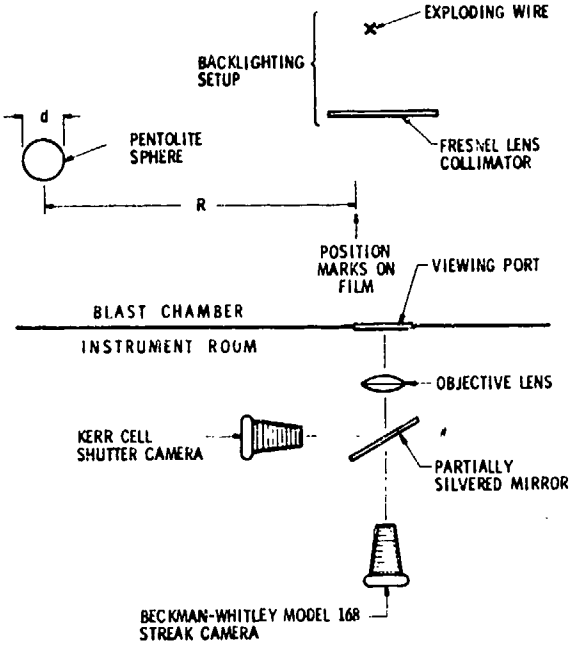


Figure 9-11. Test Arrangement Used at BRL for Simultaneous Streak and Kerr Cell Photography of Blast Waves

gence induced in certain liquids by the application of an electric stress. The cell consists of a transparent container for holding the liquid and the electrodes between which the electric stress is set up in a direction perpendicular to the optical axis. This cell is placed between two polarizers whose directions of polarization are mutually perpendicular, and are inclined at angles of 45 deg to the direction of the electric stress. In these circumstances, in the absence of an applied electric stress, no light will pass through the system owing to the crossed polarizers. If an electric stress is applied to the liquid, birefringence is caused, and some of the light will be able to pass through the second polarizer. The onset of birefringence, when an electric field is established, occurs at the speed of light, so that a fast-acting shutter may be obtained if the electric stress can be applied and removed rapidly.

Kerr cell photographs of shock waves from small Pentolite spheres, taken at BRL using the test arrangement of Fig. 9-11, are shown in Fig. 9-14. These backlit photographs show smooth shock fronts in most cases, but also an occasional protuberance. They also show pronounced irregularities in the contact surface between the expanding gases that had been the explosive charge, and the surrounding air.

No cameras based on the magneto-optic principle are available commercially at present, but some firms do market Kerr cell cameras. Cordin Co. in particular offers a line of such cameras. A disadvantage of both types is that there is considerable loss of light intensity in the "open" position.

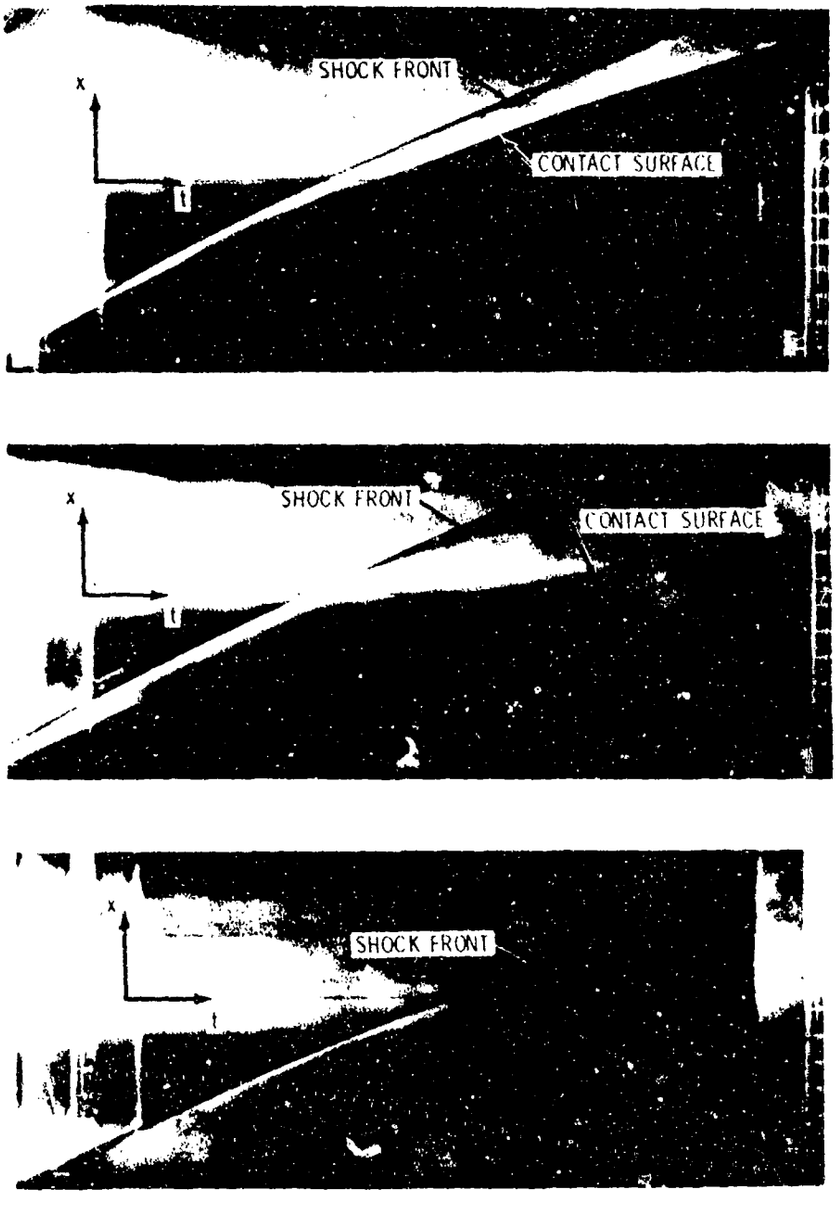


Figure 9-12. Streak Camera Photographs of Blast from 1-lb Pentolite Spheres

9-4.3 IMAGE CONVERTER CAMERAS

The final type of still "camera" used in shock wave photography is not in a strict sense a camera at all, but is instead an adaptation of a cathode ray tube. Devices using such tubes are termed image tubes or image converter tubes. A schematic of an image tube is shown in Fig. 9-15. It consists of a photo-cathode, an electron lens, and a fluorescent screen placed within an evacuated glass envelope. The photo-cathode and fluorescent screen are on opposite end faces as shown. If an optical image is formed on the photo-cathode by means of an optical system (on the left hand side in Fig. 9-15) electrons

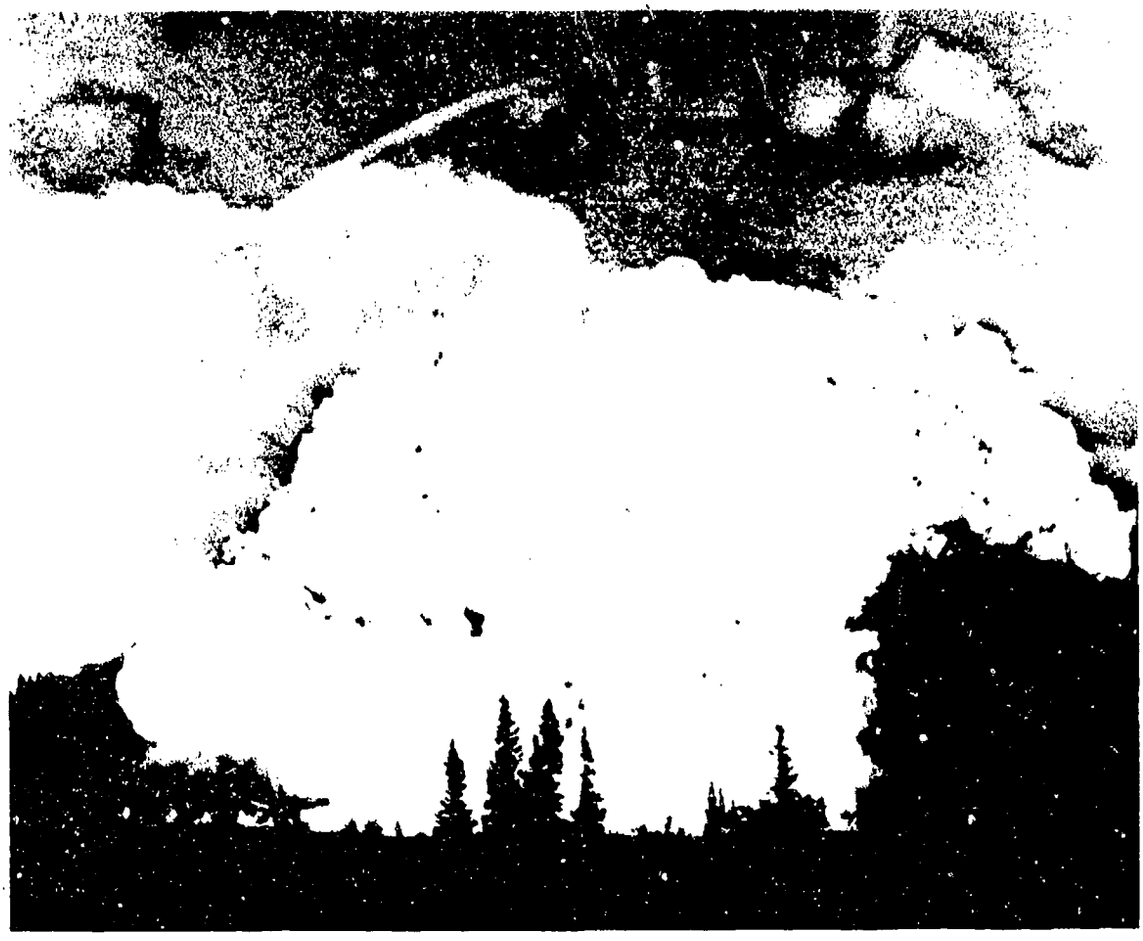


Figure 9-13. Still Photography of Large Chemical Explosion

will be emitted from the photo-cathode from the illuminated regions of the image. Unless some limitation occurs, at any instant the current density of the photo-electrons emitted from a point on the photo-cathode will be directly proportional to the light intensity of the image on that point of the photo-cathode at the same instant of time. If a potential difference is established between the fluorescent screen and the photo-cathode, these photo-electrons will be accelerated away from the photo-cathode and towards the fluorescent screen, being focused by the electron lens to form an electron image resembling the optical image on the photo-cathode at the fluorescent screen. The bombardment of the fluorescent screen by energetic electrons causes the screen to emit light, thereby reproducing the original optical image formed on the photo-cathode. The optical quality of the final image obtained will depend to some extent on the design of the image tube and to some extent on its method of operation.

A schematic of a complete camera employing an image tube, manufactured by STL, is shown in Fig. 9-16. The STL Image-converter Camera consists of an objective lens, image converter tube, rear lens, film holder, and plug-in unit and power supply control console packaged into a single instrument. The objective lens focuses the light radiated from the event under study on the photo-cathode of a curved cathode image-converter tube. The photo-cathode transforms the photon image into an electron image thereby permitting

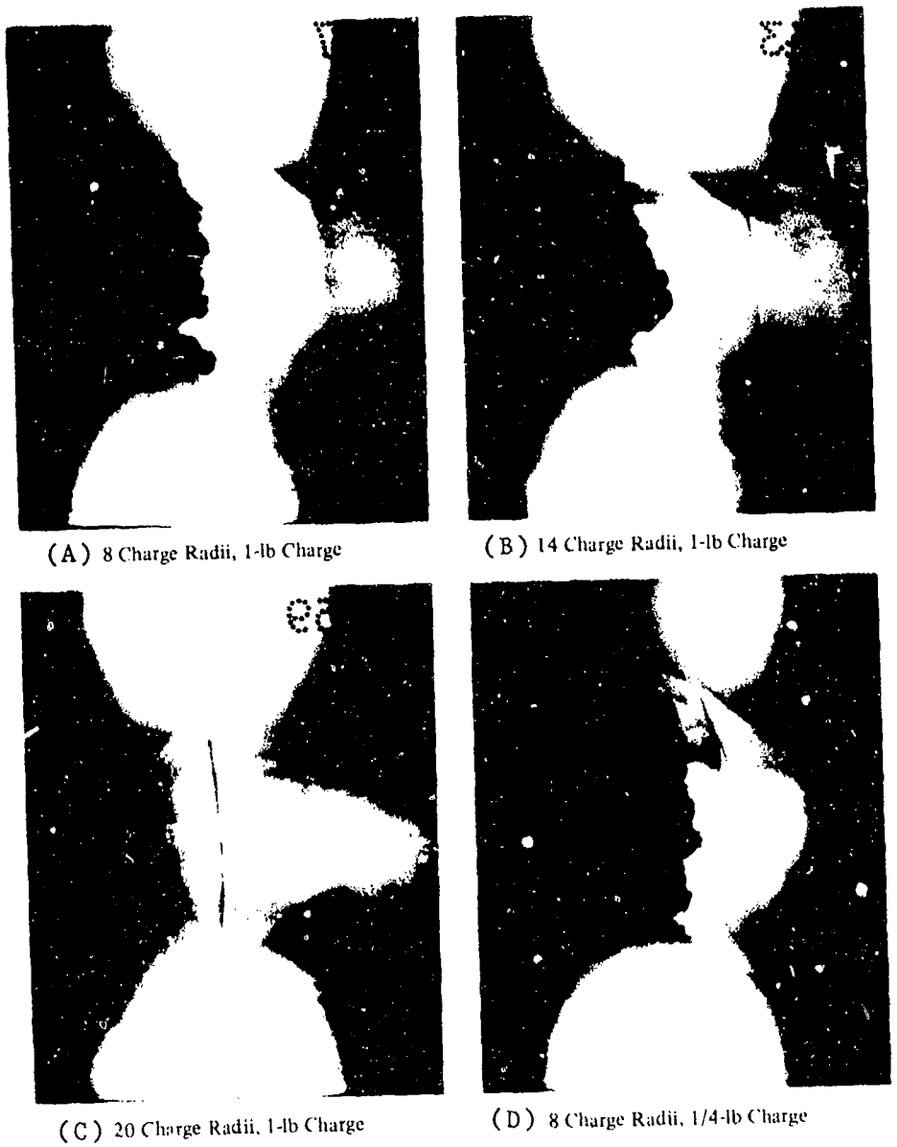


Figure 9-14. Backlit Kerr Cell Photographs of Blast Waves from Small Pentolite Spheres

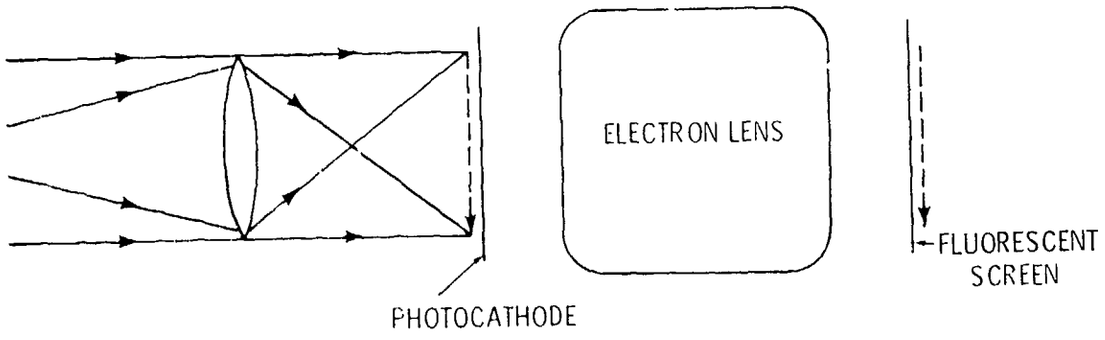


Figure 9-15. Image Tube Diagrammatic[3]

(Reprinted from High-Speed Photography by R. F. Saxe, copyrighted 1966 by the Focal Press, London and New York. Used by permission of the publisher.)

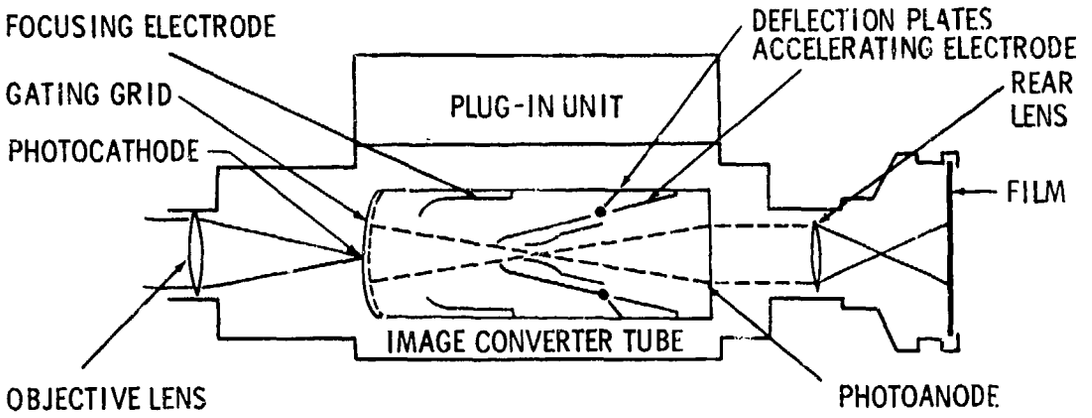


Figure 9-16. Schematic of Image-converter Camera (Courtesy of STL)

shuttering and amplification to be accomplished electronically. The electron image is focused to cross over between the deflection plates for distortion-free image deflection and is imaged on the photo-anode where it is converted into a higher intensity photon image. The photon image is relayed to the film by a double-coated lens system. The gating grid in the image-converter tube serves as the ultra-high-speed electronic shutter permitting electrons to flow only when it is pulsed. The shutter-opened to shutter-closed light transmission is better than 10^6. The response time from the introduction of a trigger signal to the start of recording is 12 nsec with exposure times as short as 5 nsec.

Cordin Co. manufactures a number of types of image-converter cameras. A schematic of one is shown in Fig. 9-17. This

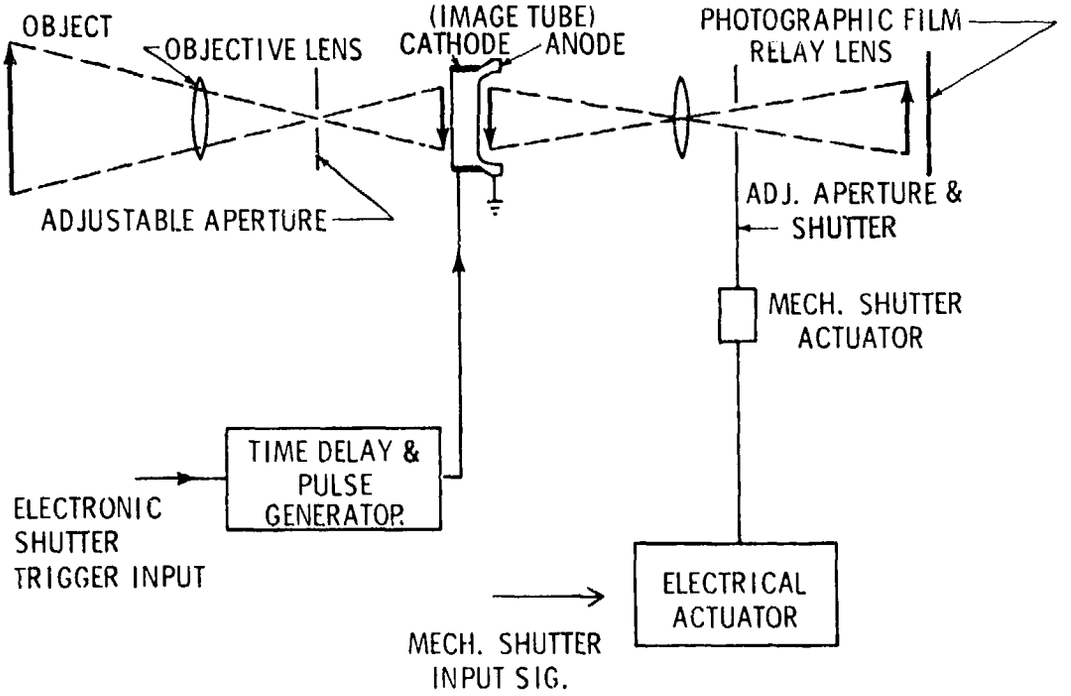


Figure 9-17. Diagram of Cordin Biplaner Image-converter Camera (Courtesy of Cordin Co.)

particular camera records two frames with the same minimum exposure time as the STL camera. A series of backlit photographs of weak shock waves taken with a Cordin Image-converter Camera is shown in Fig. 9-18.

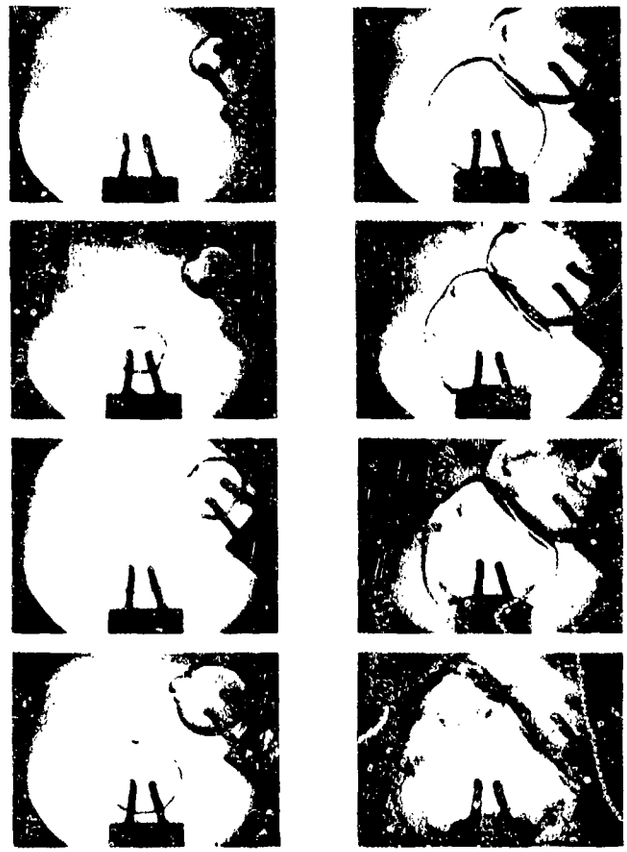
Advantages of image converters over both Kerr cell and magneto-optic effect cameras are shorter exposure times and much greater sensitivity (images are intensified significantly, rather than attenuated).

9-5 SHADOWGRAPH AND SCHLIEREN EQUIPMENT

Some very simple equipment can be used to obtain single pictures of air blast waves. This equipment also is used widely in wind tunnel and shock tube photography.

9-5.1 SHADOWGRAPH EQUIPMENT

The simplest equipment of all is shadowgraph equipment, shown schematically in Fig. 9-19. A light source L is placed so that the



SUBJECT: 8 FRAME SEQUENCE OF 2 AIR GAP DISCHARGES IN AIR; VOLTAGE SIMULTANEOUSLY APPLIED.
EXPOSURE: 5 ns
INTERFRAME TIME: 1/2 µs BETWEEN FRAMES 1 & 2, 2 & 3 AND 3 & 4; 1.0 µs BETWEEN FRAMES 4 & 5, 5 & 6 AND 6 & 7; 2.0 µs BETWEEN FRAMES 7 & 8
FILM: POLAROID ASA 3000
FRAME SIZE: 3-1/2 IN. DIAMETER
CAMERA: MODEL 500E BIPLANAR IMAGE CONVERTER CAMERA

Figure 9-18. Sequence of Backlit Image-converter Photographs of Weak Air Shocks (Courtesy of Cordin Co.)

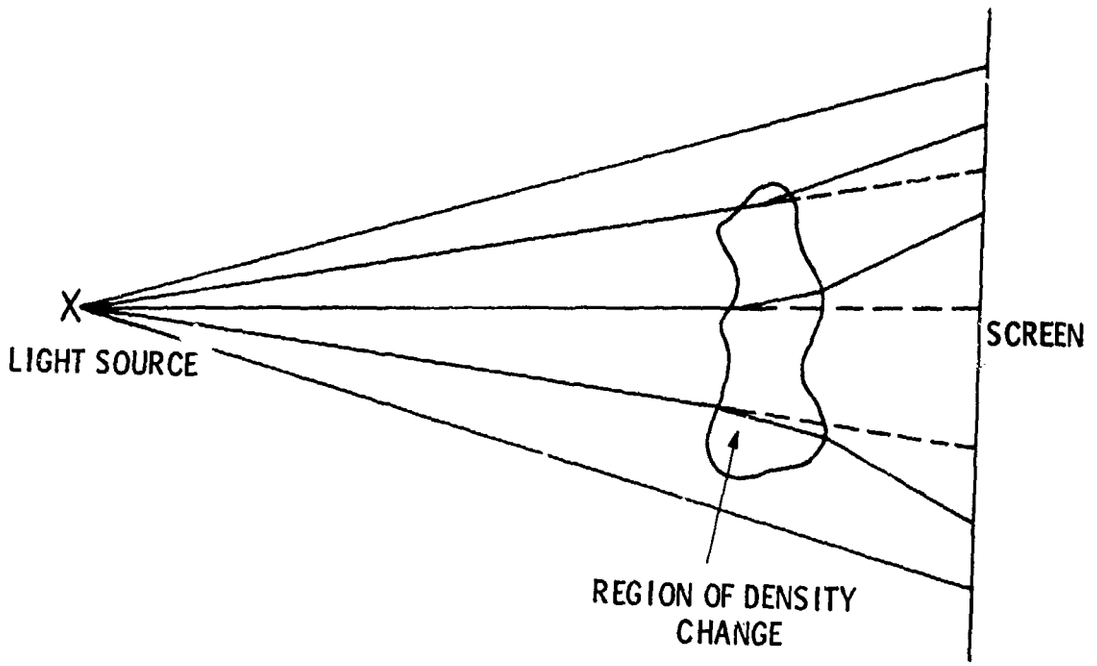


Figure 9-19. Shadowgraph Diagrammatic

(Reprinted from High-Speed Photography by R. F. Saxe, copyrighted 1966 by the Focal Press, London and New York. Used by permission of the publisher.)

region of density change is between it and a screen S. In the absence of the region of density change, and with an isotropically emitting source L, the illumination on the screen would be sensibly uniform, varying only as $\cos\theta$, where θ is the angle subtended at the point source by the line joining the point of observation on the screen and the foot of the normal from the source to the screen.

However, if the region of density change is interposed, the evenness of illumination on the screen is upset as shown in Fig. 9-19, and a shadowgraph of the region of varying density is obtained on the screen.

If a permanent record is required, a photographic emulsion can be substituted for the screen and a record made either by transiently opening a shutter in front of the emulsion, or by transiently illuminating the system by flashing the point source under otherwise dark conditions.

The disadvantages of the direct shadowgraph method are that the observed effects are due to the second spatial derivative of the density, and also that the resolution is to a large extent dependent on the distance ratio of source-to-object to source-to-screen.

9-5.2 SCHLIEREN EQUIPMENT

If a density variation exists such that there is a refractive index gradient in a direction normal to that of the light rays, the light rays will be deflected. This deflection may be observed by means of a Schlieren system. A Schlieren apparatus is shown in Fig. 9-20. The light source L is placed at the focus of a concave mirror, and the reflected rays form a parallel beam of light that illuminates the "working section". This parallel beam of light is then refocused by another concave mirror to a point focus at P. A lens ℓ, placed behind the focus point P, images in a plane p in the working section on the screen S. If in the plane p, a small section exhibits a refractive index gradient different from the rest of the plane, the light rays will be deflected and focused at P. However, the lens ℓ still will form an image of the region ab on the same

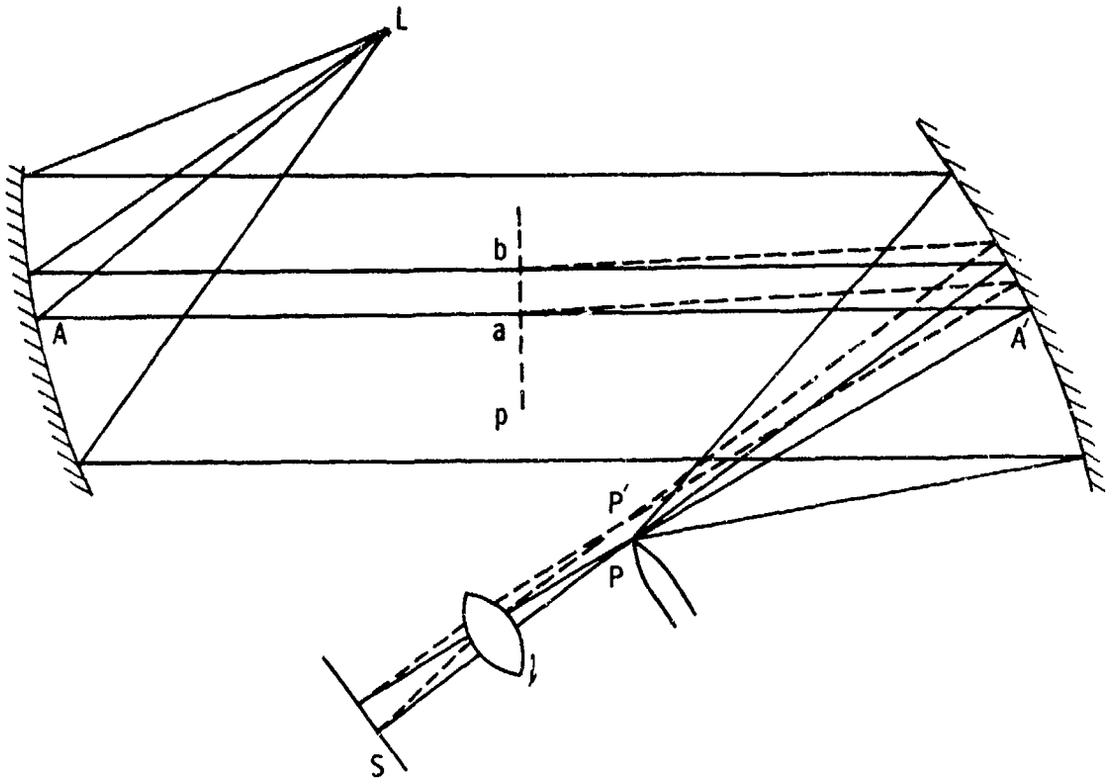


Figure 9-20. Schlieren System Diagrammatic

(Reprinted from High-speed Photography by R. F. Saxe, copyrighted 1966 by the Focal Press, London and New York. Used by permission of the publisher.)

part of screen S as when the rays were undeflected.

One method for rendering detectable the movement of the focus point from P to P′ is to use a knife edge. A knife edge is introduced at the focal plane P so as partially to cut off the light passing through the focus P. If now the light from the region ab is deflected to P′, the corresponding region on screen S will be more brightly illuminated than was the case when the rays were undeflected. Conversely, if the region ab is such that the deflection is in the opposite sense, the corresponding region on screen S will be less brightly illuminated. A Schlieren picture of an exploding, pressurized glass sphere obtained at the University of Toronto is shown in Fig. 9-21.

One of the disadvantages of the Schlieren method is the difficulty of obtaining quantitative data regarding the values and positions of the gradients that give rise to the observed picture. Normally, the Schlieren method measures the total angular deflection suffered by a ray of light in crossing between the mirrors, and the system thus integrates the effects experienced along this path length. The method gives no indication of the behavior of the rays of light from a particular region in the length between the mirrors. It is quite possible that the light rays may suffer the same total deflection and yet have been subjected to quite different conditions.

The Schlieren method can be combined with a streak camera to obtain density gradient information in one direction as a function of time.

9-6 TECHNIQUES IN PHOTOGRAPHY OF AIR BLAST WAVES

The techniques applied by various investigators in acquiring air blast data by photographic means have been as varied as the equipment available to them. The primary data obtainable from either motion picture or still photographs are the shape and position of

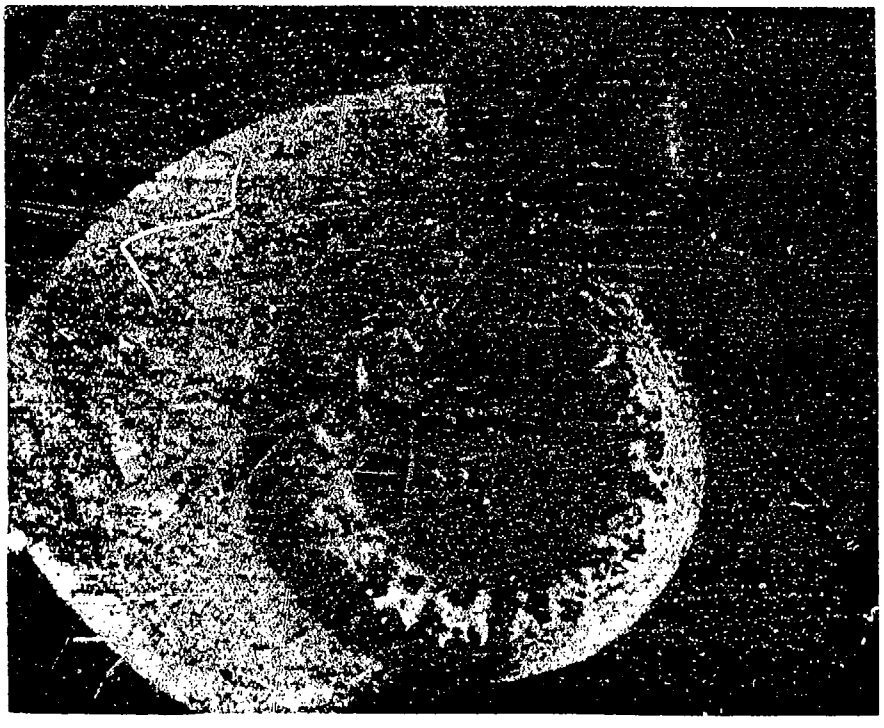


Figure 9-21. Schlieren Picture of Blast from a Pressurized Glass Sphere (Courtesy of Dr. I.I. Glass, Univ. of Toronto)

the blast front at either a single known time or a series of accurately known successive times. Positions of particles behind the shock front have been traced by observing displacements of smoke trails from rockets. Obviously, motion pictures provide more data than do stills, and allow estimation of velocities by frame-by-frame data reduction methods. A good description of motion picture photography techniques employing cameras such as the Fastax and Hycam rotating prism types is given in Ref. 5, and advantages and disadvantages are compared for other instrumentation techniques. This reference is paraphrased in the ensuing discussion.

The advantages of an optical system in measuring the position of a shock front are well known. The most important is that an optical system does not disturb the blast wave that is to be measured. Second, an optical system detects the contour of a shock, whereas pressure transducers or other devices that indicate the position-time relation of the shock—unless used in prohibitively large numbers—only "sample" the position of the shock in specific directions. Third, a very great amount of data may be obtained photographically with relatively little effort. An optical system cannot completely replace pressure transducers, however, because the latter provide additional information on the pressure-time history at specific points. A photooptical system can be used to show the contour of a shock at small time intervals and, from velocities estimated from these contours, other shock front properties obtained via the Rankine-Hugoniot equations (see Chapter 2).

At the shock front—where a very rapid and almost discontinuous rise in pressure, density, and temperature occurs—a similar change also occurs in the refractive index of the gas. Accordingly, a ray of light passing through the region immediately behind the shock front generated by an explosion is deflected towards the high-pressure region. This principle is used widely in shadowgraph and Schlieren techniques and is used also to

measure the peak overpressure from nuclear explosions. In this last case, rocket trails are established in a region behind the explosion and photographed through the expanding shock with cine cameras. Those rays of light from elements of rocket trails to the camera which pass through the region immediately behind the shock front are refracted, and the photographs of the rocket trails show apparent breaks corresponding to the position of the shock front. The technique described here is an extension of this idea to chemical explosions and consists merely of photographing the moving shock against a screen or backdrop painted with alternate black and white stripes. Here the position of the shock profile is clearly detectable by the distortion of the regular pattern of stripes introduced by the presence of the blast front. The major differences between the application to nuclear explosions and to chemical explosions are in the illumination available and the speed of the cameras required. In the nuclear case, the illumination provided by the fireball reaches a value of several hundred suns, the field of view is measured in thousands of feet, and the time of travel of the shock to low-pressure levels is measured in seconds. In the chemical case, the illumination provided by the fireball is negligible compared with that of the sun, except for a brief interval after the detonation; the field of view may be as small as a few feet; and the time of travel of the shock to the pressure level of lowest interest may be only a few milliseconds. Accordingly, cameras having a much higher framing rate and lower exposure interval are required, and either supplementary illumination or very sensitive film must be used. For nuclear tests, intermittent movie cameras with framing rates as low as 100 fps have proven satisfactory; for tests with small blast sources such as 8-lb TNT spheres, rotating-prism cameras with framing rates of at least 3000 fps are required.

Although interrupted backgrounds for detection of shock fronts had been used during large chemical blast tests as early as 1948, Groves is apparently the first to report their systematic use[5]. His method is described in the paragraphs that follow.

The equipment to obtain the position-time relation of the shock profile from chemical explosions consists of a striped screen or backdrop (at times supplemented by smoke trails), one or more high-speed cameras, a source of illumination, and a timing system.

The striped backdrop consists of a pattern of alternate black and white stripes, of a width suitable for the field of view concerned; and painted on wood, canvas, or metal. Usually the lines are sloped at 45 deg or 60 deg towards the vertical plane through the camera and ground zero. The backdrop generally is placed at an expected overpressure level of 4 psi; at this level the blast brings the backdrop down, but causes no appreciable damage to it. Markers are placed in the backdrop plane or in a plane in front of it perpendicular to the camera-ground-zero line in order to obtain distance measurements from the films, independent of viewing or projection lens conditions. Films are analyzed by projection at a magnification of about 20 onto a horizontal plotting table in order to obtain frame-by-frame observations of the progress of the shocks.

This system of measurement has been applied to tracing triple-point loci, and to deriving overpressures in the Mach wave and the incident wave from over a hundred TNT charges consisting of air-burst spheres of 8 lb_m to 1000 lb_m and ground burst spheres and hemispheres of from 8 lb_m to 5 tons in weight. Observations show that the striped backdrop permits delineation of the blast contour quite readily down to 1 psi, which is the lowest pressure to which it has been applied. The second shock from TNT also is frequently discernible. An example of the shock wave in the Mach reflection region from Ref. 5 is shown in Fig. 9-22.

John Dewey[6] has utilized motion picture photography of smoke trails from rockets to determine time histories of particle velocity behind the blast front. Displacement of these smoke trails can be seen clearly in Fig. 9-23. Here, the smoke trails lie initially in a plane through the blast source, rather than in a

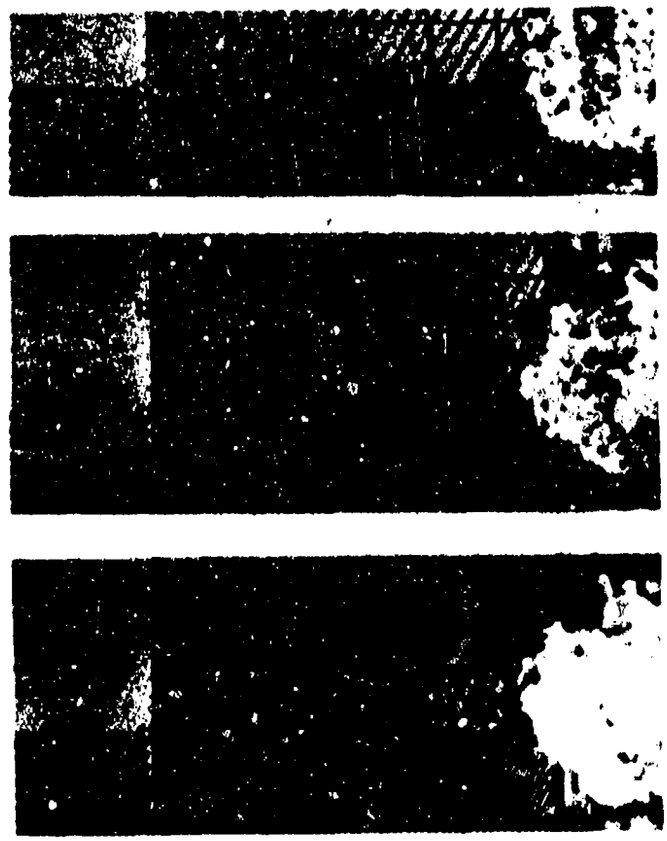


Figure 9-22. Views of Shock Wave from 8-lb_m TNT Spheres Detonated 8-ft Above Concrete[5]

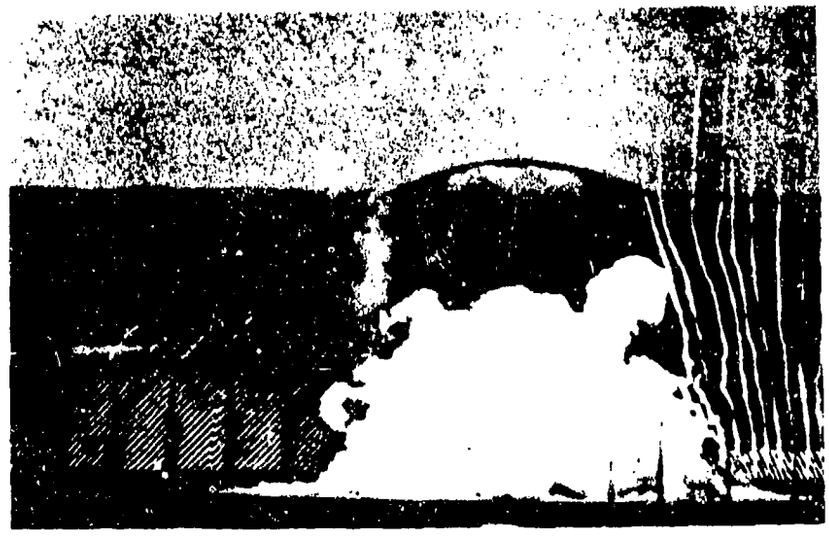


Figure 9-23. View of Shock Wave from 5-ton TNT Ground-burst Hemisphere[5]

plane behind the source as described by Groves[5].

Streak camera photography of air blast waves can provide time-distance plots of shock front motion along a chosen line. It has been used only for small scale tests in blast chambers or in the field. For very strong shocks close enough to explosive sources that the shock front is self-luminous, direct streak photography will record the time history of shock front motion. Sultanoff and McVey[7] used this technique in obtaining shock velocity measurements close to Pentolite spheres detonated in air. The use of the streak camera can be extended to much weaker shock waves by backlighting techniques, with spark discharges, exploding wires, gas-filled flash tubes, or argon bombs being used as the intense light sources for backlighting. Glass[8] also has applied backlighting to a Schlieren streak system to obtain time histories along a line of shock-front motion, plus density gradients. One of Glass's streak records is reproduced here as Fig. 9-24.

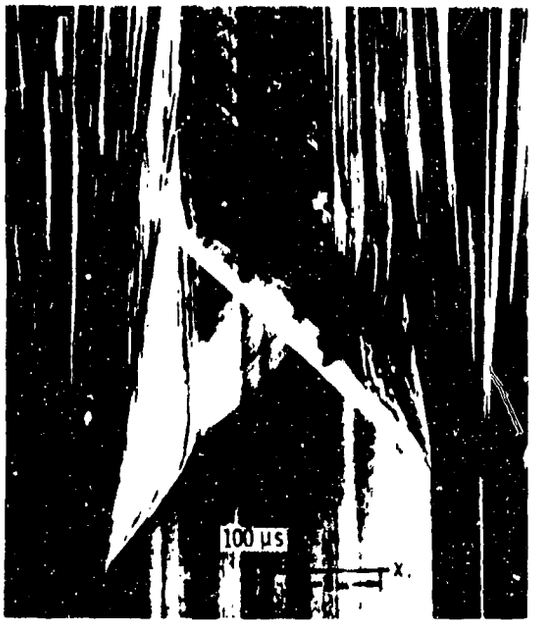


Figure 9-24. Schlieren Streak Record of the Collision of Two Unequal Spherical Shock Waves.[8] (Courtesy of Dr. I.I. Glass, Univ. of Toronto)

Still photography of air blast waves as a source of blast data suffers in comparison with either motion picture photography or streak photography because only a single picture is obtained. But, because of the wide variety of types of equipment available and the ease and low cost of use of much of this equipment, it is used widely for photography of air blast waves from all possible energy sources.

The simplest equipment for still shock wave photography, the shadowgraph, often has been used on a laboratory scale to photograph shock fronts. The equipment usually requires that the test be conducted in a darkroom. For a blast source such as a chemical explosive that emits considerable light, the film must be shielded from this light by a mask. An excellent example of shadowgraph photography is given in Fig. 9-25, due to Glass[8]. The shadowgraph technique has been adapted by Edgerton to blast wave photography in daylight (see Ref. 2, pp. 427-428). Two of the principal disadvantages of the conventional shadow method of shock wave photography are the requirements for (1) complete darkness during the test, and (2) a large film size approximating that of the area to be studied. The technique used by Dr. Edgerton utilizes a large sheet of Scotchlite sheeting, either No. 244, Signal Silver, for use in the dark; or No. 234, Black "C", for daylight operation. Scotchlite sheeting manufactured by the Minnesota Mining and Manufacturing Corporation, has a high degree of reflective brilliance by returning light directly back to its source with an efficiency twenty to over two hundred times that of a white painted surface. In the Edgerton technique, the Scotchlite sheeting is used as a backdrop behind the explosive phenomenon to be photographed. A single light source close to the camera lens provides the necessary illumination. Light from the source that strikes the screen normal to its surface is reflected back directly into the camera lens. The size of the area covered by this method is limited only by the size of the backdrop material and by the level of light available to make the exposure. Dr. Edgerton has made excellent



Figure 9-25. Spark Shadowgram of the Explosion Generated from a Pressurized Glass Sphere[8] (Courtesy of Dr. I.I. Glass, Univ. of Toronto)

photographs at a 20-ft distance from Signal Silver Scotchlite sheeting.

Kerr cell and magneto-optic shutter cameras both require intense light sources for sufficient film exposure. They can be used in both indoor blast chambers and for field photography within the range of strong shocks where they can detect shock fronts. Self-luminous shocks can be photographed directly, and somewhat less intense shocks by backlighting techniques. An example of an intense, self-luminous shock taken with a magneto-optic shutter is shown in Fig. 9-26. As is common in such photography, this figure is a double exposure, with the background being pre-exposed before the charge detonation. A typical system for backlit photography employing a Kerr cell shutter is shown in Fig. 9-27[9].

No special techniques are needed for use of conventional cameras in still photography other than snapping the shutter at the right time and employing a short enough exposure time to "stop" the shock front. If interrupted backgrounds have been set up, such as in Fig. 9-22, a conventional still camera will "see" the shock fronts as well as a movie camera. Fig. 9-13 is indicative of good quality still photography of air blast waves.

The coverage in this chapter of photography of air blast waves as a source of blast data is by no means exhaustive. The author instead has attempted to cover, with a few examples, the kinds of equipment and techniques for use of this equipment which have been employed by successful experimentalists. Data obtained by such investigators are included in much of the work reported in Chapter 5, and are scattered throughout the air blast literature. Shock photography does offer by far the most spectacular and graphic coverage of air blast phenomenology.



Figure 9-26. Double Exposure Photograph of Moving Explosive Charge Detonation (Courtesy U.S. Army BRL)

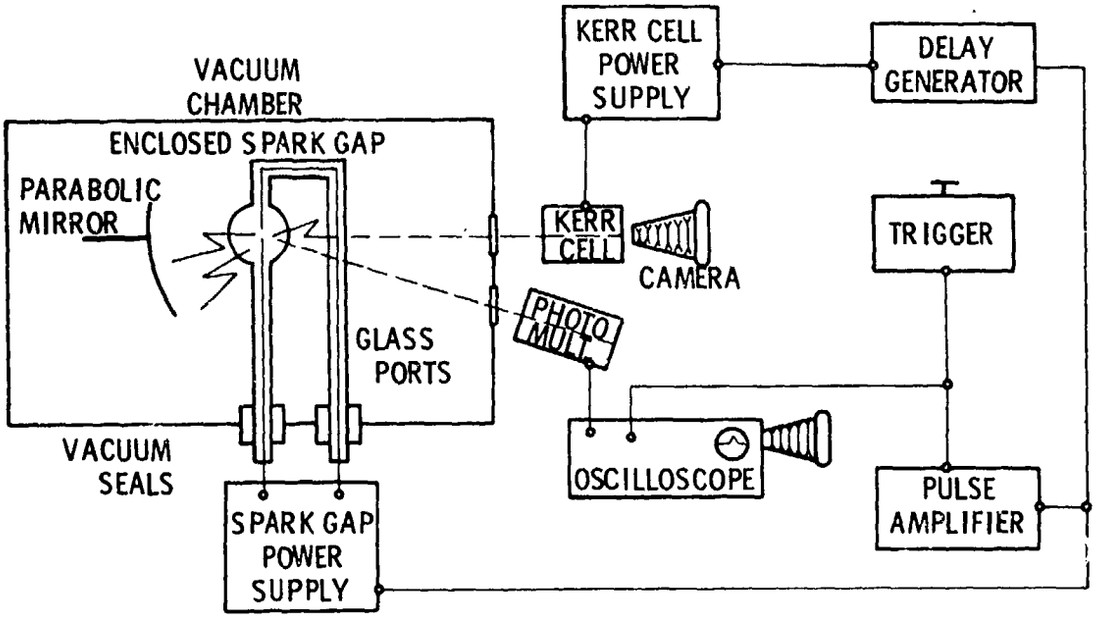


Figure 9-27. Block Diagram of Instrumentation for Backlit Photography of Air Shocks[9]

REFERENCES

1. G. A. Jones, *High Speed Photography*, John Wiley and Sons, Inc., N. Y., 1952.

2. W. G. Hyzer, *Engineering and Scientific High-Speed Photography*, The Macmillan Co., N. Y., 1962.

3. R. F. Saxe, *High-Speed Photography*, The Focal Press, London and N. Y., 1966.

4. M. Sultanoff, "A 100,000,000-frame-per-second Camera", *Rev. Sci. Instr.*, 21, pp. 653-6 (July 1950).

5. T. K. Groves, "A Photo-Optical System of Recording Shock Profiles from Chemical Explosions", *Shock, Vibration and Associated Environments*, Bulletin No. 28, Part III, pp. 59-68 (September 1960).

6. J. M. Dewey, "The Air Velocity in Blast Waves from TNT Explosions", *Proc. of the Royal Soc.*, A, 279, pp. 366-85 (1964).

7. M. Sultanoff and G. McVey, *Shock-Pressure at and Close to the Surface of Spherical Pentolite Charges Inferred from Optical Measurements*, BRL Report No. 917, Aberdeen Proving Ground, Md., August 1954.

8. I. I. Glass, *Aerodynamics of Blasts*, UTIA Review No. 17, Inst. of Aerophysics, Univ. of Toronto, September 1960.

9. J. S. Williams, *A High Intensity, Short Duration Photographic Light Source for Use at Low Ambient Pressure*, BRL Technical Note No. 1618, Aberdeen Proving Ground, Md., June 1966.

CHAPTER 10

DATA REDUCTION METHODS

10-0 LIST OF SYMBOLS

a,b,c,d = distances associated with geometry of camera, charge, and background (see Fig. 10-11)

M = Mach number

M_s = ratio of shock velocity in still air to sound velocity in air ahead of shock (Mach number of the shock wave)

p_0 = ambient atmospheric pressure

P_p = total head pressure $M > 1$

P_s = free stream side-on overpressure; peak side-on overpressure

P_t = free stream total pressure $M < 1$

q = dynamic pressure

r = shock radius

r' = shock radius at velocity $\bar{V}$

R = grid size

t = time

$\bar{V}$ = average shock front velocity

γ = ratio of specific heats

θ = angle

10-1 GENERAL

An essential step in any experimental air blast program is the reduction of the raw data, either for simple reporting of the test results or for comparison with theory. These data may exist in many forms. The most common are multiple photographic traces recorded on moving film or paper or on fixed film in oscillograph record cameras, and multichannel magnetic tapes. Some self-recording gages generate either polar or rectilinear traces on metal discs or tapes, or on glass discs. All of the preceding types of raw data represent continuous time histories of some blast wave property, recorded at a specific location. Other types of data may include motion and still pictures of shock fronts passing some regular background, recorded times from electronic counters for shock fronts to pass stations known distances apart, or "blips" recorded on moving photographic film or paper by time-of-arrival gages. Data from simple mechanical gages may consist of measurements of permanent deformation or peak strain of simple structures such as cantilever beams, or change in volume of cans, or determination of smallest size of a series of diaphragms which are ruptured by the blast wave. In this chapter, we will discuss methods of reduction of these various types of raw data, and problems encountered and corrections that can or must be made during such reduction.

10-2 REDUCTION OF FILM AND PAPER TRACES

10-2.1 TYPES OF RECORDS

In reduction of photographic film or paper traces, one may be faced with a wide variety of sizes and types of record. The simplest type is that recorded by an oscillograph record camera that has photographed an oscilloscope face through a graticule. Usually, a single trace is represented on one record, with a separate calibration signal (perhaps doubly exposed on the same record) to establish the scale for the blast parameter, and the time scale is given by the calibrated sweep rate for the oscilloscope. Two examples of blast pressure records of this type, from Refs. 1 and 2, are shown in Fig. 10-1. Fig. 10-1(A)

is a record from a side-on gage, and Fig. 10-1(B) from a face-on gage. Because dual- and four-beam scopes are now in common usage, records of this type may include as many as four traces, recorded simultaneously.

More common in blast measurement are multichannel traces recorded on moving film or paper. In Fig. 10-2(A) we see traces from a four-channel system impressed on 35-mm film[3], while in Fig. 10-2(B) are traces from a similar system[1] on 5-in. wide paper. Fig. 10-3 shows a typical record from an eight-channel recorder[4]. As many as sixteen data traces may be recorded on a single record up to 12 in. wide by certain types of blast recorders.

In addition to being of various widths and being either transparent or opaque, the blast records may contain either much or little additional data. Any time history worth reducing must of course have an accurate time

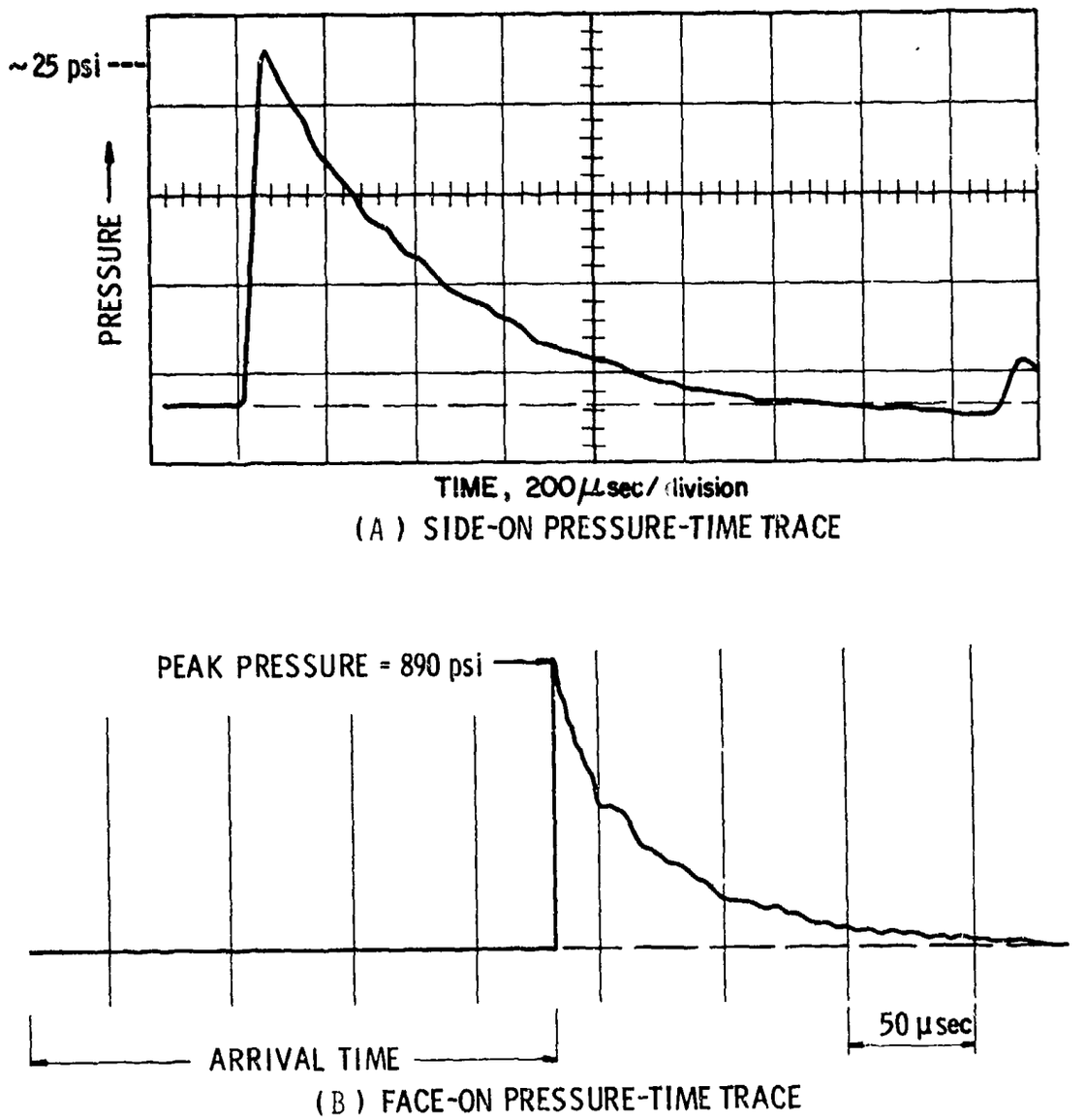
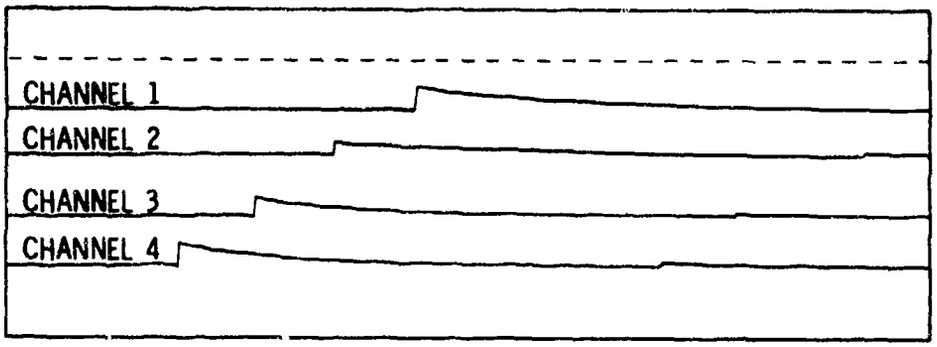
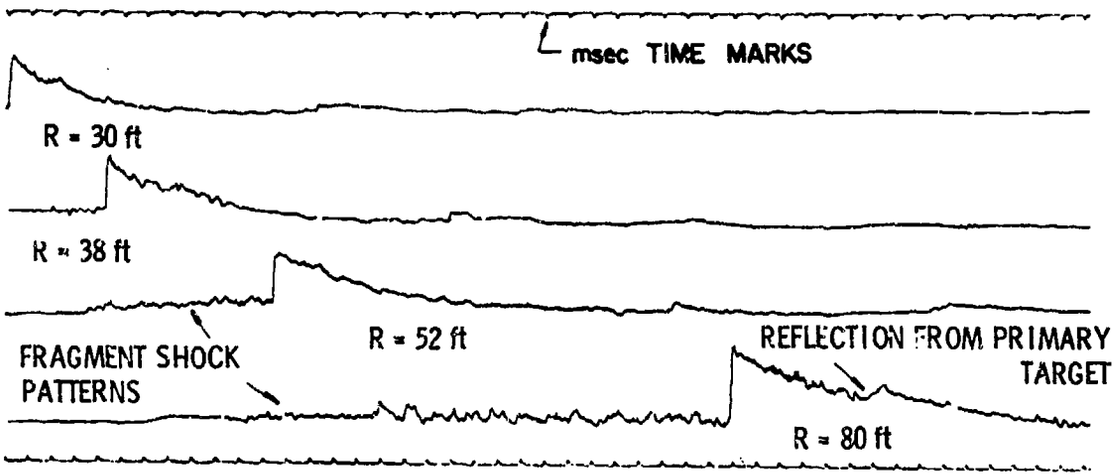


Figure 10-1. Typical Traces from Oscillograph Record Cameras



(A) MOVING FILM PRESSURE-TIME TRACES



(B) MOVING PAPER PRESSURE-TIME TRACES

Figure 10-2. Typical Traces from Four-channel Blast Recorders

base superimposed. In fixed-film records such as those in Fig. 10-1 this time base is provided by the graticule lines and accurate internal sweep circuits in the oscilloscope. In moving-film records such as Figs. 10-2 and 10-3 the time base is provided by periodic voltage deflection of continuous traces, or by flashing of neon lights on and off at controlled rates. These systems can be adapted to provide a real-time base for accurate time correlation with other events in a complex test by applying binary-coded signals received from some central timing source. Usually, electrical calibration signals in one or more steps precede the blast record on each trace. Because the traces from multichannel recorders are not necessarily "in register" across the record, some common zero time mark (or fiducial mark) usually is superimposed on all traces.

10-2.2 READING OF RECORDS

The data that one usually wishes to obtain from film or paper records include amplitudes (peak pressures), characteristic times (shock arrival at various transducer locations, duration of positive overpressure, duration of negative pressure), positive or negative impulses, and other details of the time-histories such as initial decay rates, etc.

Regardless of the equipment used to reduce the film or paper records, certain operations must be performed. The records must first be "read", i.e., various distances and areas must be measured and tabulated. These include heights of calibration steps, amplitudes of vertical deflections of traces (perhaps at a number of closely-spaced intervals), distances between timing marks, distances representing

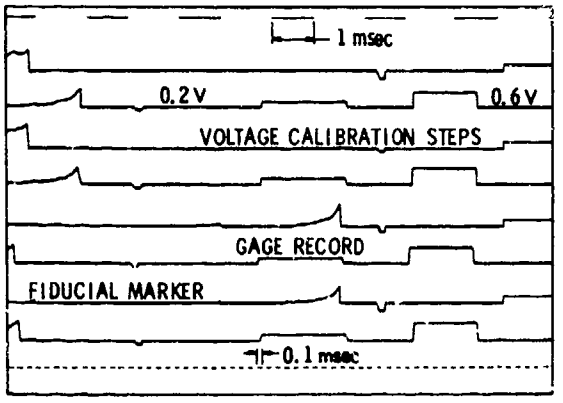


Figure 10-3. Typical Trace from Eight-channel BRL Blast Recorder

characteristic times on traces, etc. The equipment used to read records can be as simple as a transparent scale with a fine grid and a magnifying glass, or as complex as a semi-automatic data reduction system with projection screen, digital readout and card punch, and associated digital computer. The choice of the system to be used is very much dependent on the equipment available, the number of records to be reduced, and one's budget for the test program. When each record is read, certain operations must be performed to convert the distances measured on the record to the desired blast parameters. If the designers of the instrumentation systems and the transducers have done their jobs well, the ordinates on the records will be simply proportional to some physical parameter, and the abscissas will be simply proportional to time. The operations performed after record reading will then be quite simple, consisting merely of multiplying trace ordinates and abscissas by appropriate constants to obtain pressures, etc., and times. Only the more complex operations involve the determination of areas (positive and negative impulses) and slopes (decay rates, rise times). These can be done graphically from enlargements of the traces themselves, or numerically by relatively simple mathematical operations on the readings from the traces. If either the transducer or some part of the instrumentation system has nonlinear response so that the ordinates are not proportional to a physical parameter, or the time base is not linear because film or sweep speed is varying, then the record is distorted and reduction of data is considerably complicated. One must then obtain a careful calibration curve for the transducer and recorder so that each measured ordinate can be converted individually into the appropriate physical parameter, and individual times must be read accurately from the nonlinear time base. Final data reduction from distorted records usually is accomplished most expeditiously using digital data reduction systems and simple computer programs which contain the nonlinear calibrations.

10-2.3 RECORD CORRECTION FOR GAGE SIZE AND FLOW EFFECTS

Certain corrections sometimes must be applied to blast gage records to account for failure of a transducer or recording system to faithfully transduce or respond to the rapid variations in pressure, etc., during blast traversal. Finite high frequency response of any part of the transducing and recording system usually will limit the recorded rise-time of a measured blast parameter, and low-frequency cutoff will affect the long duration portions of a record. These problems have been prevalent in blast measurement for many years, and much effort has been devoted in design of blast recorders to minimize such errors. One, therefore, usually can assume that no corrections need be made for inadequate frequency response. But, for side-on blast pressure gages, one may have to correct for two types of transducer error in data reduction. The first of these is termed "gage-size error" or "transit-time error". It is introduced because the sensitive element of the gage is of finite size relative to the thickness of the shock front, so that the front requires a finite time to traverse the element. Again, this error long has been recognized, as evidenced from Fig. 10-4[5]. If the gage-size error is not too great, corrections can be made, as indicated in Fig. 10-5. The technique illustrated in Fig. 10-5 is used both in England[1] and in the United States[6]. The second type of transducer error is that due to

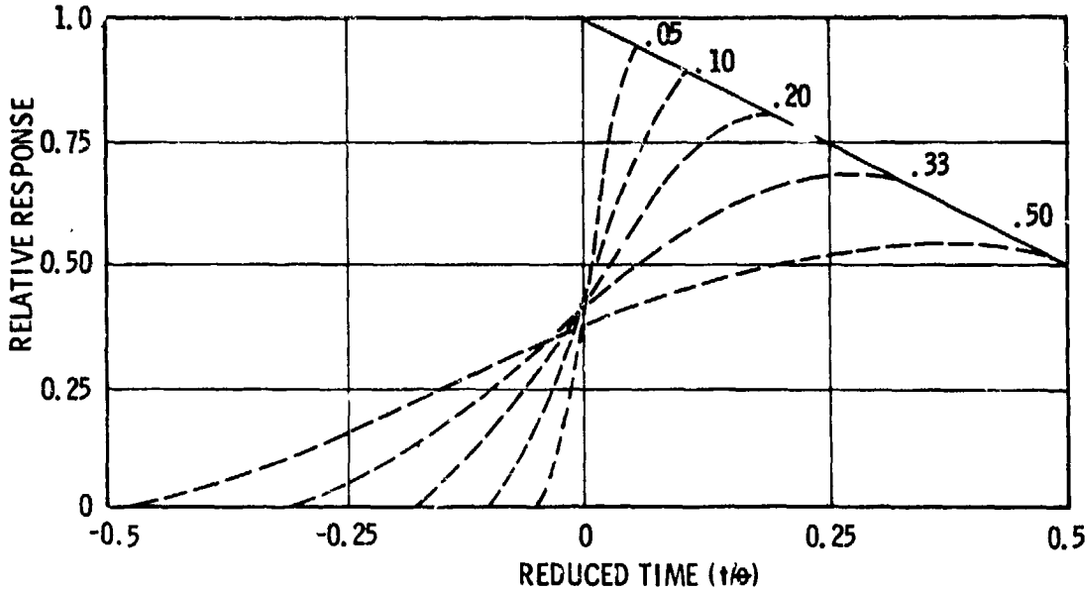


Figure 10-4. Calculated Response of a Gage of Finite Diameter to Linearly Decaying Pressure[5]

flow effects. Accurate corrections for errors in pressure due to flow effects can be determined only for a particular gage geometry by carefully conducted shock tube or wind tunnel tests. Ruetenik and Lewis[7] report calibrations and a correction method for a pancake side-on gage, and Goodman[8] reports the results of an extensive wind tunnel investigation on flow effects around side-on gages of several different geometries. Correction for flow effects about even well-streamlined gages are indicated by these authors to be as great as 10-20 percent for shocks which are strong enough for flows to be of sonic or greater Mach number. For relatively weak shocks (flow of small Mach number), flow effect corrections are negligible provided the gage housing is well streamlined.

10-2.4 REDUCTION OF DYNAMIC PRESSURE DATA

A special case in data reduction occurs in determination of an important blast wave parameter, i.e., the dynamic pressure, from measured pressures. This parameter is usually not measured directly, but must instead be inferred from separate measurements of "total head" and side-on pressure, with several intermediate calculations. In these calculations pressure as a function of time is obtained from the individual total head and side-on record The difference between the measured and the true free stream total head pressure in the absence of the probe has been

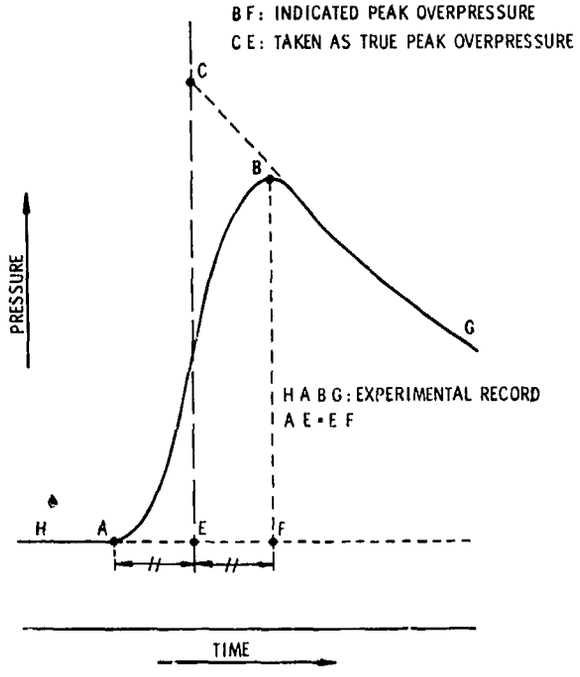


Figure 10-5. Method of Extrapolation of Experimental Records

determined by wind tunnel tests. These correction factors, which are a function of the Mach number M of the particle flow behind the shock wave, must be applied to the uncorrected data. The Mach number of the flow is found by the use of the following two equations:

$$\frac{P_t}{P_s} = \left[1 + \left(\frac{\gamma - 1}{2}\right)M^2\right]^{\frac{\gamma}{\gamma - 1}} \quad \text{for } M < 1 \qquad (10\text{-}1)$$

$$\frac{P_p}{P_s} = \left\{\frac{\left[\left(\frac{\gamma + 1}{2}\right) M^2\right]^{\gamma}}{\left(\frac{2}{\gamma+1}\right)M^2 - \frac{\gamma - 1}{\gamma + 1}}\right\}^{\frac{1}{\gamma - 1}} \quad \text{for } M > 1 \qquad (10\text{-}2)$$

where

P_t = free stream total pressure $M < 1$

P_p = total head pressure $M > 1$

P_s = free stream side-on overpressure

γ = ratio of specific heats = 1.4 for air

The dynamic pressure q is related to the side-on pressure and the flow Mach number by the following relationship:

$$q = \frac{\gamma P_s M^2}{2} \qquad (10\text{-}3)$$

Using the total head and side-on pressure-time histories, one employs the following steps to obtain corrected dynamic pressure:

Step 1. The ratio of the total head pressure to the side-on pressure is used in Eq. 10-1 or Eq. 10-2, depending on velocity of the particle flow, to calculate a free stream Mach number.

Step 2. The gage corrections then are applied to the total head pressure data. This correction is applied to the data by use of a Mach number versus percent of error curve obtained from wind tunnel calibration data for the probe used.

Step 3. The first step then is repeated using the corrected total head pressure to calculate a new Mach number. This process is repeated until sufficient accuracy of the Mach number is obtained.

Step 4. The adjusted Mach number obtained by this iteration process and the free-stream side-on pressure finally is used in Eq. 10-3 to calculate the dynamic pressure as a function of time.

Typical dynamic pressure-time histories obtained from the calculations are plotted in Fig. 10-6, along with total head and side-on pressure records.

EXAMPLE CALCULATION

At a given time after shock arrival, P_t = 25 psi and P_s = 17 psi. From Eq. 10-1,

$$\frac{25}{17} = \left[1 + \left(\frac{1.4 - 1}{}\right)M^2\right]^{\frac{1.4}{1.4-1}}$$

$$1.470 = (1 + 0.2\,M^2)^{7/2}$$

$$M^2 = (1.470^{2/7} - 1)/0.2$$

$$M = \left[\frac{(1.1165 - 1)}{0.2}\right]^{1/2} = 0.758$$

This is less than one, so we have used the correct choice of equations for calculating Mach number. From Eq. 10-3,

$$q = \frac{1.4 \times 17 \times (0.758)^2}{2}$$

$$q = 6.83 \text{ psi}$$

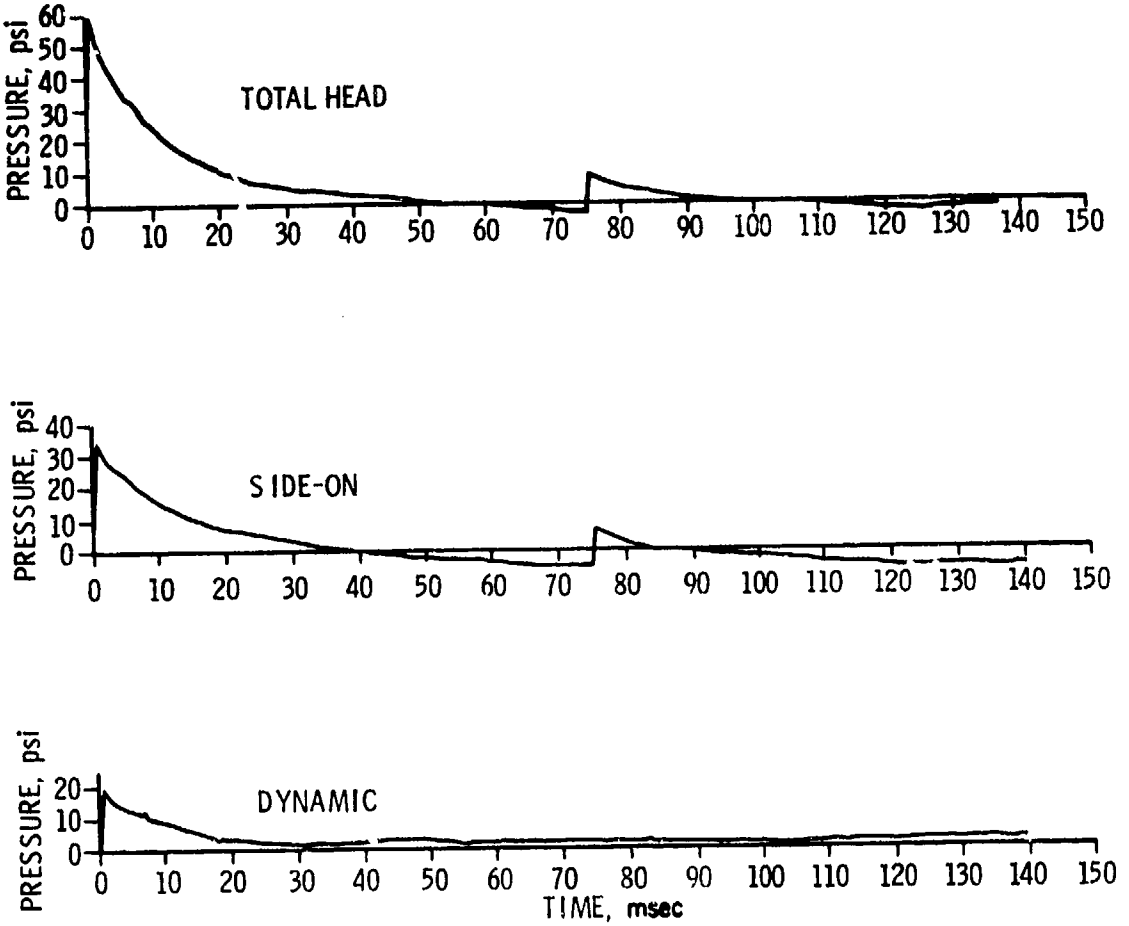


Figure 10-6. Recorded Side-on and Total Head Pressure-Time Histories and Calculated Dynamic Pressure-Time History

Had M been greater than one, recalculation using Eq. 10-2 would have been required before substitution in Eq. 10-3.

10-2.5 DETERMINATION OF POSITIVE PHASE DURATION

In addition to correction of peak pressure for gage size error, a recurring problem in blast data reduction is that of accurate determination of the duration of the positive phase of a pressure-time history. Relatively large variations in this blast parameter are almost unavoidable because of the more or less exponential character of the pressure decay and consequent nearly horizontal slopes of blast pressure records on return to ambient pressure. Ethridge[9] has proposed graphical methods for reading and smoothing pressure-time data which allow correction for gage size and frequency response errors in peak pressure, and better estimation of positive phase duration than by direct reading of records. His procedure consists of replotting the standard linear records such as shown in Figs. 10-1 through 10-3 on semi-logarithmic plots, and fitting straight lines to these plots to obtain estimates of peak pressure and duration. A linear plot such as Fig. 10-7 is transformed into a semi-logarithmic plot (pressure on the logarithmic scale) as in Fig. 10-8 to obtain an estimate of the true peak pressure and initial decay rate. Because the initial decay rate is nearly exponential, a straight line can be accurately fitted to the initial portion of the record. For estimating

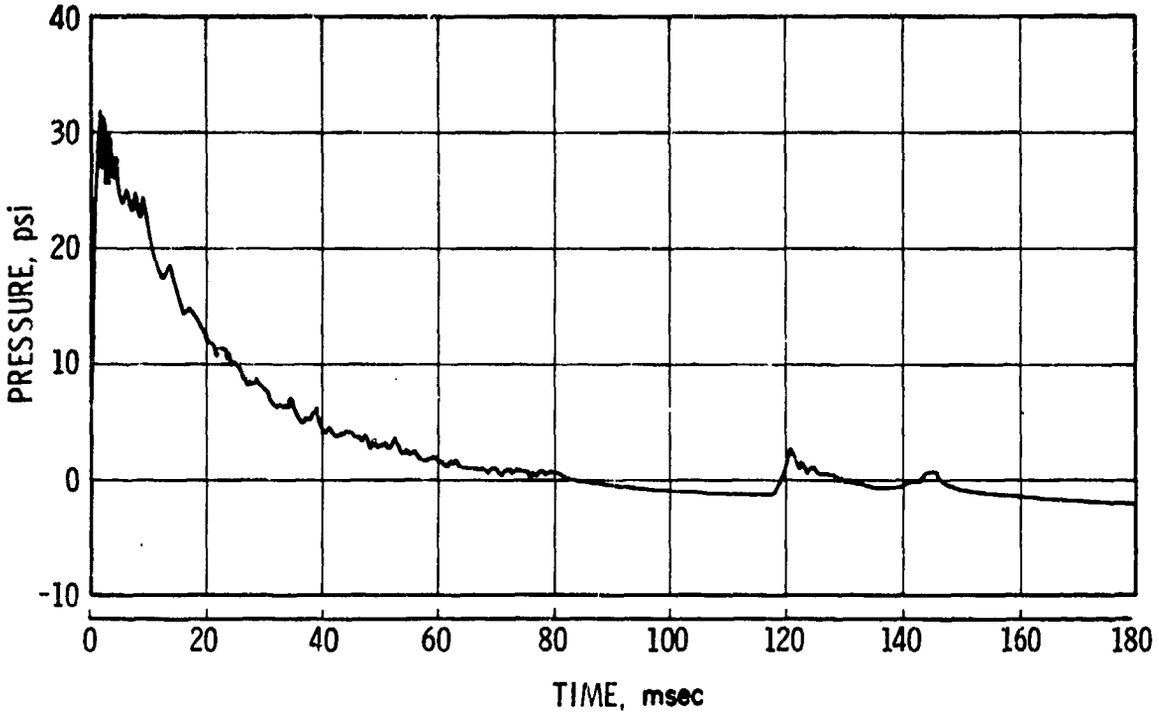


Figure 10-7. Linear Plot of BRL Self-Recording Gage Record Obtained at a Ground Range of 334 ft from the 1961 Canadian 100-ton HE Test[9]

positive phase duration, time is plotted logarithmically as in Fig. 10-9, and a curve fitted to the new plot.

Although no limiting exponential is approached at the end of the positive phase, Fig. 10-9 does allow more accurate determination of the end of the positive phase and the final slope of the positive phase, as is apparent in the figure. Ethridge also claims that the semi-logarithmic plots are useful for manually developing a smoothed waveform.

We have discussed so far the reduction of data under the assumption that the traces are "clean" and easily read. But, unfortunately, in blast research, one often must attempt to recover data from records of poor quality. The particular test may be an expensive "one-shot" affair that cannot be repeated; a transducer may be knowingly or unknowingly subjected to blast waves that are too strong for it and generate erratic or ringing response;

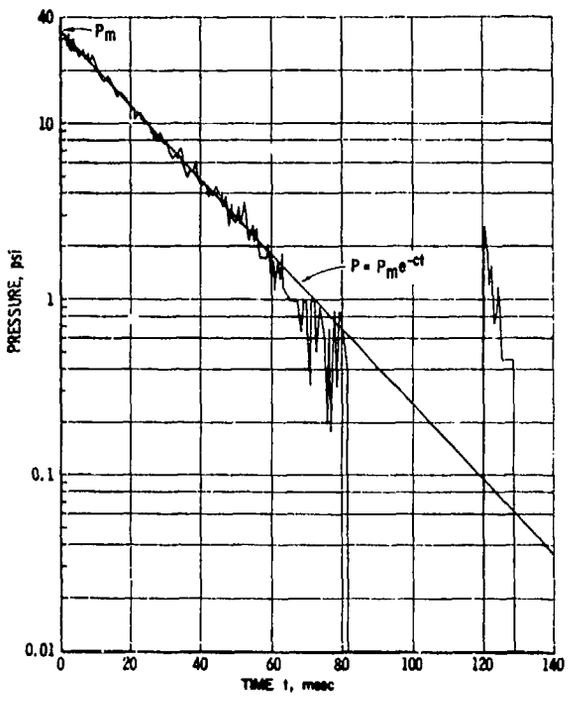


Figure 10-8. Semi-logarithmic Plot of GageRecord With Pressure Plotted Against the Logarithmic Scale[9]

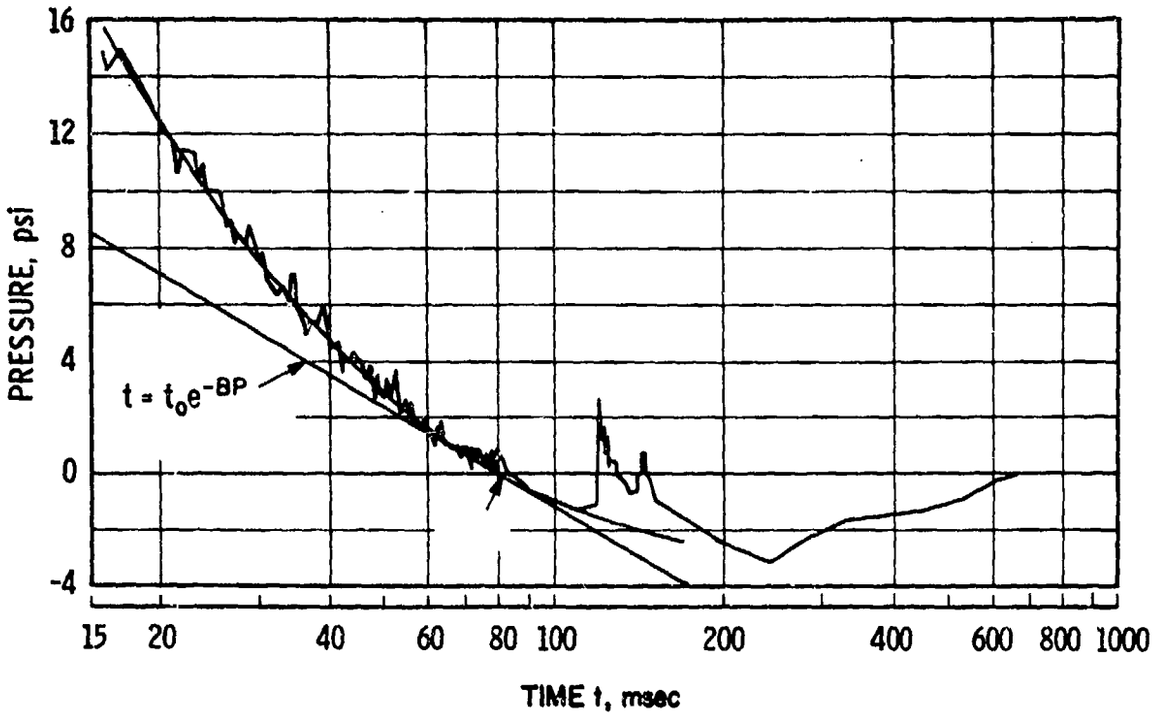


Figure 10-9. Semi-logarithmic Plot of Gage Record With Time Plotted Against the Logarithmic Scale[9]

etc. How does one reduce data from such poor quality records, or decide that these data should be discarded? Unfortunately, we cannot answer this question for you. We can only warn you that you will, at some time, need to find the answer for yourself if you are involved in blast testing.

10-3 REDUCTION OF MAGNETIC TAPE DATA

Magnetic tape systems used in recording blast or other dynamic data usually employ either seven- or fourteen-channel recorders, with one channel being reserved for a timing signal. So, either six or thirteen data channels are recorded simultaneously. The raw data consist of the magnetic tapes themselves. Conceivably, completely automated systems could be employed directly to reduce the magnetic tape data—reading the voltages generated by the tapes as they are played back at discrete time intervals, comparing these with voltage calibration steps, entering calibration data, printing out numerical results, and re-plotting the records on known pressure and time scales. This process requires quite elaborate and sophisticated equipment and a somewhat complex digital computer program, and usually is *not* employed in reduction of blast data, or is employed only after careful scrutiny of oscillograph traces recorded on playback of the tapes. No one conversant with blast measurement technology apparently is willing to entrust his data to machines for reduction without first examining the time histories. The usual procedure is simply to playback the magnetic tape and record on magnetic oscillographs, with calibration steps on the same records. The data are then in the form of paper photographic traces, very similar to those obtained from multichannel oscilloscope blast recording systems. Data reduction then can be accomplished by the methods described earlier in the chapter.

Magnetic tape records offer one important advantage over direct recording on film or paper. One can, by playing back through suitable filters, recover data from "ringing" transducers or recording systems which otherwise would be lost or seriously reduced in usefulness. Also, rather low frequency response oscillographs can be used to reproduce tape data by playing back at tape drive speeds somewhat less than those used to record the data originally.

10-4 REDUCTION OF DATA FROM SELF-RECORDING GAGES

The data from self-recording gages consist of lines that have been scribed by styli on the surface of rotating polished metal or silvered glass discs, or of translating polished metal tapes. Deflections of the styli (and corresponding trace amplitudes) are of the order of 0.020 to 0.060 in. The records may or may not have a superimposed fiducial mark indicating some common zero time, or timing marks on a separate trace to give the time base. Amplitude calibration is almost never included on the record, but instead is determined by a separate laboratory test. Although it would be desirable to show typical records here, this cannot be done because they do not reproduce well.

Because the traces from these gages are of small amplitude, they must be magnified considerably to be read. At BRL[10] records from self-recording gages are read with the aid of a toolmaker's microscope modified to use magnetic reading heads. Output signals from the heads are fed into suitable conditioning equipment that punches the x- and y-coordinates of each point read into an IBM card. These cards, representing readings taken at short intervals throughout the span of the record, together with cards representing calibration steps and time interval information, are used as input to a digital computer. The pressure values are calculated from a straight-line interpolation between the various calibration steps. A time calibration is applied to the readings, and at the same time the impulse is summed as the cards are processed. The outputs are time (msec), pressure (psi), and impulse (psi-msec), which are punched on IBM cards. These cards are used for plotting and tabulating the results.

10-5 REDUCTION OF DATA FROM MOTION OR STILL PHOTOGRAPHS

Motion or short duration still photographs often are taken of blast experiments for documentary or publicity purposes. (One can tell at a glance that an engineer or scientist has participated in nuclear or large-scale conventional explosive tests by the beautiful color photographs of fireballs or mushroom clouds which adorn his office walls.) Such distant overall views are even useful at times in detecting anomalies in large-scale explosions. To be useful for obtaining data on blast wave parameters, cameras and background must be carefully arranged, as described in Chapter 9. Usually, only the shock front can be observed (see Fig. 10-10), so one can only obtain those properties that can be inferred from successive positions of this front at known time intervals.

A method for obtaining peak air blast pressures employing photographic techniques requires observing the passage of the shock wave on an interrupted background. This technique is dependent upon the principle of light refraction. Light waves passing obliquely from one medium to another, in this case from undisturbed air to the compressed region immediately behind the shock wave, undergo an abrupt change in direction. The "bending" of light rays by the shock wave causes an apparent displacement of the background against which the shock is viewed. The data consist of a series of photographs or frames, similar to those in Fig. 10-10.

Peak overpressures can be inferred from shock velocities computed from such data by use of the Rankine-Hugoniot equation which expresses pressure as a function of shock velocity.

$$P_s = \frac{2\gamma}{\gamma + 1}\left(M_s^2 - 1\right) p_0 \qquad (10\text{-}4)$$

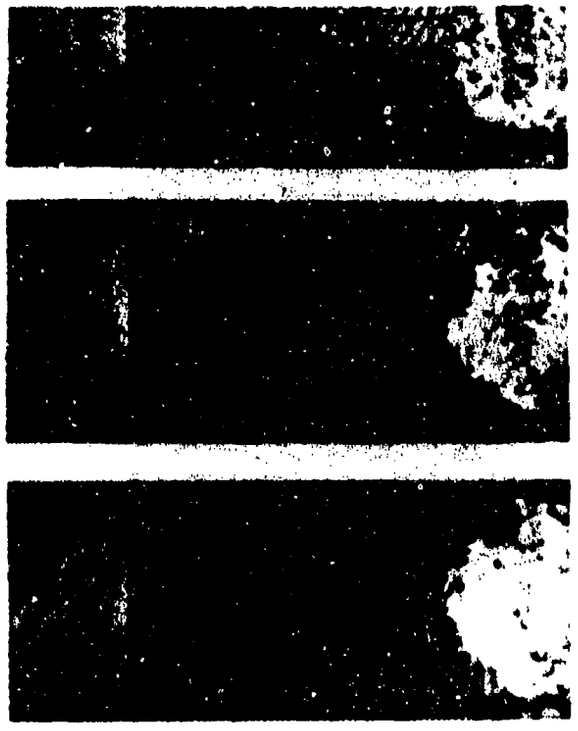


Figure 10-10. Photo-optical Records of Shock Front Profile[11]

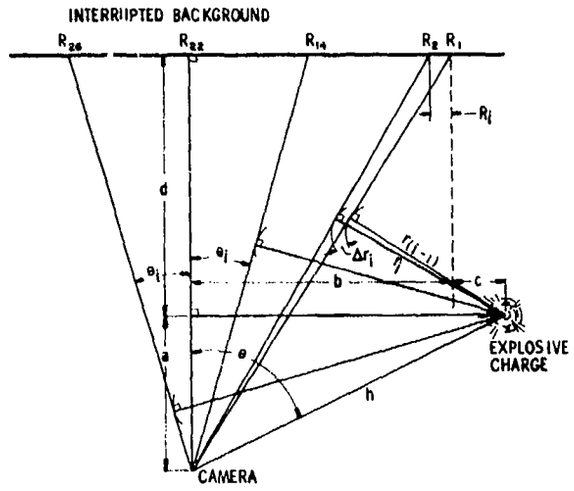


Figure 10-11. Velocity Field Setup

where

P_s = peak side-on overpressure

γ = ratio of specific heats ($\gamma = 1.4$ for air)

M_s = ratio of shock velocity in still air to sound velocity in air ahead of shock (Mach number of the shock wave)

p_0 = ambient atmospheric pressure

Fig. 10-11 illustrates the geometry of camera, charge, and background. In this figure, R_i is the grid size for the interrupted background, r_i is the radius of the shock wave at t_i, and t_i is the arrival time of the shock wave at r_i. From geometry

$$\theta = \mathrm{Tan}^{-1}\left(\frac{b+c}{a}\right);$$

$$\left.\begin{aligned}\theta_i &= \mathrm{Tan}^{-1}\left(\frac{b-R_i}{a+d}\right) \text{ for } i \leqslant 22\\ \theta_i &= \mathrm{Tan}^{-1}\left(\frac{R_i-b}{a+d}\right) \text{ for } i \geqslant 23\end{aligned}\right\} \quad (10\text{-}5)^*$$

$$\left.\begin{aligned}r_i &= h \sin(\theta - \theta_i),\ i \leqslant 22\\ r_i &= h \sin(\theta + \theta_i),\ i \geqslant 23\end{aligned}\right\} \quad (10\text{-}6)$$

$$\left.\begin{aligned}\bar{V}_i &= \frac{\Delta r_i}{\Delta t_i} = \frac{r_i - r_{(i-1)}}{t_i - t_{(i-1)}},\\ \bar{V}_i &= \text{average shock front velocity}\end{aligned}\right\} \quad (10\text{-}7)$$

$$\left.\begin{aligned}r_i' &= \frac{r_i\, r_{(i-1)}}{2},\\ r_i' &= \text{radius of shock at } \bar{V}_i\end{aligned}\right\} \quad (10\text{-}8)$$

*The subscript number i is an index indicating the particular interval of the grid background, starting at one edge of the field of view of the camera. In this particular example, R_{22} is located on the normal between the camera location and the plane of the interrupted background.

The velocity component of the prevailing winds parallel to the interrupted background at the time of the test should be stripped from all velocity measurements before application of these data to the Rankine-Hugoniot equation. This is necessary as the wind effectively increases or decreases the velocity of the shock front, depending upon the direction of the wind vector in relation to shock wave propagation. A wind vector tangent to the shock front will have no effect on shock velocity measurements.

10-6 OTHER DATA REDUCTION

Data obtained from air blast transducers such as the mechanical transducers described in Chapter 7 usually can be reduced quite simply, once the devices are "calibrated". Only limited information, such as effective energy yield of the explosive usually is obtained, rather than estimates or measures of specific blast wave parameters. The relatively simple measures of damage (such as permanent tip deflection of a metal cantilever beam) can be used to estimate effective energy yield from calibration curves such as shown in Chapter 7, provided only that the distance from explosive energy source to the mechanical gage is known.

Data from the simple "plug" gage for measurement of reflected impulse which has been so widely used by BRL (see also Chapter 7) consist of either motion picture films of the plug in flight, or of times recorded on an electronic counter for the plug to travel a known distance. The apparatus is usually oriented so that the plug is accelerated by gravity as well as by the blast wave.

If the time origin is known, as for computing the impulse from counter data, impulse is calculated directly from Eq. 10-9 by measuring the time taken for the plug to travel a known distance.

$$I = \frac{m}{A}\left(\frac{X}{t} - gt/2\right) \qquad (10\text{-}9)$$

where

I = impulse, psi-msec

m = mass of plug, lb-msec^2/in.

A = area of plug, in.^{2}

X = distance plug travels between top and bottom plate, in.

g = acceleration due to gravity, in./msec^2

t = time of travel, msec

For the optical measurements, where the time origin is not known but the time interval over a predetermined distance is known, velocity at distance X_i is given in terms of a known time interval by

$$\dot{X}_1 = \frac{X_2 - X_1}{t_2 - t_1} - g(t_2 - t_1)/2 \qquad (10\text{-}10)$$

where

$X_2 - X_1$ = predetermined distance for optical methods

$t_2 - t_1$ = time interval to travel $(X_2 - X_1)$ interval, msec

$\dot{X}_1$ = velocity of plug at X_1

The initial velocity $\dot{X}_0$ velocity of plug at X_0 (top plate) – or impulse I is then computed from

$$\dot{X}_0 = \frac{A}{m} I = \sqrt{\dot{X}_1^2 - 2gX_1} \qquad (10\text{-}11)$$

REFERENCES

1. K. J. Jarvis, *The Measurement of Air Blast*, Armament Research and Development Establishment, Ft. Halstead, Kent, England.

2. W. H. Jack, Jr., *Measurements of Normally Reflected Shock Waves from Explosive Charges*, BRL Memorandum Report No. 1499, Aberdeen Proving Ground, Maryland, July 1963.

3. W. C. Olson and H. Goldstein, *Air Blast Measurements Around Water-Filled Simulated Nuclear Research Core Vessels*, BRL Memorandum Report No. 1219, Aberdeen Proving Ground, Maryland, July 1959.

4. B. Soroka and G. T. Watson, *An Eight-Channel High-Performance Oscillograph Recording System*, BRL Memorandum Report No. 1765, Aberdeen Proving Ground, Maryland, May 1966.

5. R. H. Cole, *Underwater Explosions*, Dover Pub., Inc., New York, 1965, pp. 200-204.

6. B. F. Armendt, R. Smith and R. C. Wise, *The Initial Decay of Pressure Behind Shock Front: Comparison of Experimental and Calculated Results*, BRL Memorandum Report No. 997, Aberdeen Proving Ground, Maryland, April 1956.

7. J. R. Ruetenik and S. D. Lewis, *Pressure Probe and System for Measuring Blast Waves*, AFFDL-TDR-65-35, Air Force Flight Dynamics Lab., Wright-Patterson Air Force Base, Ohio, June 1965.

8. H. J. Goodman, *Aerodynamic and Frequency Dependent Errors in an Air Blast Gage*, BRL Report No. 1345, October 1966.

9. N. H. Ethridge, *A Procedure for Reading and Smoothing Pressure-Time Data from H. E. and Nuclear Explosions*, BRL Memorandum Report No. 1691, September 1965.

10. R. E. Reisler, J. H. Keefer, and L. Giglio-Tos, *Basic Air Blast Measurements from a 500-ton TNT Detonation Project 1.1 Operation Snowball*, BRL Memorandum Report No. 1818, December 1966.

BIBLIOGRAPHY

V. V. Adushkin and A. I. Korotkov, "Parameters of a Shock Wave Near an Explosive Charge in an Explosion in Air", *Zhurnal Prikladnoi Mekhaniki i Tekh Nicheskoi Fiziki* (Journal of Applied Mechanics and Technical Physics), 5, 119-23, 1961.

A. A. Amsden, *The Particle-In-Cell Method for the Calculation of the Dynamics of Compressible Fluids*, LA-3466, June 1966.

W. A. Anson, *A Portable Shock Tube for Calibration of Piezoelectric Pressure Transducers in Situ*, Suffield Tech. Note No. 191, Dec. 1967.

W. A. Anson and J. M. Dewey, *Density Measurements in the Blast Wave from a Surface Burst 500-Ton TNT Hemispherical Charge*, Suffield Technical Paper No. 305, SES, Ralston, Alberta, Canada, August 1966.

B. F. Armendt, R. Smith and R. C. Wise, *The Initial Decay of Pressure Behind a Shock Front: Comparison of Experimental and Calculated Results*, BRL Memo Report No. 997, April 1956.

G. G. Bach and J. H. S. Lee, "An Analytic Solution for Blast Waves", *AIAA Journal*, 8, 2 (Feb 1970)

W. E. Baker, "Prediction and Scaling of Reflected Impulse from Strong Blast Waves", *Int. Jour. of Mech. Sci.*, 9, 45-51 (1967).

W. E. Baker and W. O. Ewing, Jr., *Miniature Piezoelectric Gauges for Measuring Transient Pressures on Airfoils*, BRL Memo Report No. 1329, Aberdeen Proving Ground, Md., March 1961.

W. E. Baker, W. O. Ewing, Jr., and J. W. Hanna, *Laws for Large Elastic Response and Permanent Deformation of Model Structures Subjected to Blast Loading*, BRL Report No. 1080, Aberdeen Proving Ground, Md., December 1958.

W. E. Baker, W. O. Ewing, Jr., J. W. Hanna and G. W. Bunnewith, "The Elastic and Plastic Response of Cantilevers to Air Blast Loading", *Proc. of the Fourth U. S. Natl. Congress of Appl. Mech.*, ASME, N.Y. 853-866 (1962).

W. E. Baker, and O. T. Johnson, *Some Crude Comparative Tests of Damage with Explosive Charges of Pentolite and Metalized Tetranitromethane*, BRL Tech. Note No. 287, September 1950.

W. E. Baker, S. Silverman, and T. D. Dunham, *Study of Explosions in the NASA-MSC Vibration and Acoustic Test Facility (VATF)*, Final Report on Contract NAS9-7749, March 1968.

W. E. Baker, P. S. Westine and S. Silverman, *Feasibility Study on Simulating the Structural Response of High Altitude Missiles to Blast Loading*, Final Tech. Report, Contract No. DA-18-001-AMC-749(X). Southwest Research Institute, Texas, January 1966.

F. A. Baum, K. P. Stanyukovich, and B. I. Shekter, *Physics of Explosion* (Russ. Book FIZMATGIZ, Moscow, 1959, Translated by Research Information Service. 122 E. 55th St., N. Y.).

W. W. Berning, *Investigation of the Propagation of Blast Waves Over Relatively Large Distances and the Damaging Possibilities of Such Propagation*, BRL Report No. 675, Aberdeen Proving Ground, Md., November 1948.

H. A. Bethe, *Shock Hydrodynamics and Blast Waves*, Report AECD-2860, Los Alamos Scientific Lab., Univ. of Calif., 1944.

H. A. Bethe, K. Fuchs, J. von Neumann, R. Peierls, and W. G. Penney, *Shock Hydrodynamics and Blast Waves*, Report AECD-2860, Los Alamos Scientific Laboratory, 1944.

V. J. Bishop, R. D. Rowe, *The Interaction of a Long Duration Friedlander Shaped Blast Wave with an Infinitely Long Right Circular Cylinder. Incident Blast Wave 20.7 psi; Positive Duration 50 ms and a 16 cm Diameter Cylinder.* AWRE Report No. 0-38/67, Atomic Weapons Research Establishment, Aldermaston, Berkshire, England, April 1967.

W. Bleakney, *The Diffraction of Shock Waves Around Obstacles and the Transient Loading of Structures,* Tech. Report II-3, Princeton University, Dept. of Physics, March 16, 1950.

W. Bleakney, *Rectangular Block, Diffraction of a Shock Wave Around an Obstacle,* Princeton Univ., Dept. of Physics, December 17, 1949.

W. Bleakney, *Shock Loading of Rectangular Structures,* Tech. Report 11-1[illegible], Princeton Univ., Dept. of Physics, January 10, 1952.

W. Bleakney and A. H. Taub, "Interaction of Shock Waves", *Rev. Mod. Physics,* 21, 584 (1949).

W. Bleakney, D. R. White and W. C. Griffith, "Measurements of Diffraction of Shock Waves and Resulting Loading of Structures", *Journal of Appl. Mech.*, 17, 1. 439-445 (March 1950).

D. W. Boyer, *Spherical Implosions and Explosions,* UTIA Report No. 58, 1959.

D. W. Boyer, H. L. Brode, I. I. Glass, and J. G. Hall, *Blast from a Pressurized Sphere,* UTIA Report No. 48, 1958.

V. M. Boyle, R. L. Jameson, and F. E. Allison, *Shock Hugoniot for Composition B,* BRL Report No. 1250, May 1964.

S. R. Brinkley, Jr., and J. G. Kirkwood, "Theory of the Propagation of Shock Waves", *The Physical Review,* 71, 9 (May 1947).

S. R. Brinkley, Jr., J G. Kirkwood, and J. M. Richardson, *Tables of Properties of Air Along the Hugoniot Curve and the Adiabatics and Terminating in the Hugoniot Curve,* ASRD Report No. 3550, April 1944.

H. L. Brode, "Blast Waves from a Spherical Charge", *Phys. of Fluids,* 2, 2, 217 (1959).

H. L. Brode, *The Blast Wave in Air Resulting from a High Temperature, High Pressure Sphere of Air,* RM-1825-AEC, The Rand Corp., Santa Monica, Calif., December 1956.

H. L. Brode, "A Calculation of the Blast Wave from a Spherical Charge of TNT", The Rand Corp., RM-1965, August 1957, AD-144 302.

H. L. Brode, "Numerical Solutions of Spherical Blast Waves", *Jour. of Appl. Phys.*, 26, 6, 766-775 (June 1955).

H. L. Brode, *Point Source Explosion in Air,* RM-1824-AEC, The Rand Corp., December 3, 1956.

H. L. Brode, *Theoretical Solutions of Spherical Shock Tube Blast,* RM-1974, The Rand Corp., September 1957.

J. N. Brooks, *DRI Blast Recording Equipment,* Phase Report No. 5, Contract N ORD 16009, Denver Research Institute, Denver, Colorado, March 27, 1957.

H. N. Brown, *Effects of Scaling on the Interaction Between Shock Waves and Structures,* Appendix I to BRL Report No. 1011, Aberdeen Proving Ground, Md., March 1957.

P. L. Browne and M. S. Hoyt, *HASTI, a Numerical Calculation of Two-Dimensional Lagrangian Hydrodynamics Utilizing the Concept of Space-Dependent Time Steps,* LA-3324-MS, May 1965.

E. J. Bryant, R. A. Eberhard, and C. N. Kingery, *Mach Reflection Over Hard Packed Dirt and Dry Sand,* BRL Report No. 809, July 1952.

E. J. Bryant, N. H. Ethridge, and J. H. Keefer, *Operation TEAPOT Project 1.14b, Measurements of Air-Blast Phenomena with Self-Recording Gauges,* WT-1155, July 1965.

A. E. Bryson and R. W. F. Gross, "Diffraction of Strong Shocks by Cones, Cylinders and

Spheres", *J. Fluid Mech.*, 10, I, 1-16 (Feb. 1961).

T. D. Butler, "Numerical Calculations of the Transient Loading of Blunt Obstacles by Shocks in Air", *AIAA Jour.*, 4, 3, 460-467 (March 1966).

S. Chandrasekhar, *The Normal Reflection of a Blast Wave*, BRL Report No. 439, Aberdeen Proving Ground, Md., December 1943.

T. S. Chang and O. Laporte, "Reflection of Strong Blast Waves", *Physics of Fluids*, 7, 8, 1225-1232 (Aug. 1964).

P. C. Chou and S. L. Huang, "Late-Stage Equivalence in Spherical Blasts as Calculated by the Method of Characteristics", *Jour. of Appl. Physics*, 40, 2, 752-759 (Feb. 1969).

P. C. Chou and R. R. Karpp, *Solution of the Blast Wave by the Method of Characteristics*, DIT Report No. 125-7, Contract No. DA-36-034-ORD-3672RD, Drexel Institute of Tech., September 1965.

P. C. Chou, R. R. Karpp, and S. L. Huang, "Numerical Calculation of Blast Waves by the Method of Characteristics", *AIAA Journal*, 5, 4, 618-623 (April 1967).

W. H. Chu and W. E. Baker, *Performance Analysis of a Helium-Air Shock Tube*, Final Report, SwRI Project 02-1974, Southwest Research Institute, San Antonio, Texas, December 1966.

R. H. Cole, *Underwater Explosions*, Dover Publications, Inc., N.Y., 1965.

M. Collins, *Use of the HYDRO I Code in the Analysis of Transient Axisymmetric Shock Hydrodynamics Problems*, Tech. Report 3251, Picatinny Arsenal, July 1965.

M. A. Cook, *The Science of High Explosives*, Reinhold, N.Y., 1958.

R. Courant and K. O. Friedrichs, *Supersonic Flow and Shock Waves*, Interscience Pub., Inc., N.Y., 1948.

B. K. Crowley, *A Comparison of Analytical and Numerical Solutions for the Shock Tube Problem*, UCRL-14198 preprint, Lawrence Radiation Lab., Univ. of Calif., Livermore, Calif., May 1965.

B. K. Crowley, *PUFL, An Almost-Lagrangian Gasdynamic Calculation for Pipe Flows With Mass Entrainment*, UCRL-14556, Lawrence Radiation Lab., Livermore, Calif., May 1966.

W. Curtis, *Free Air Blast Measurements on Spherical Pentolite*, BRL Memo Report No. 544, Aberdeen Proving Ground, Md., July 1951.

B. J. Daly, *The Bounding of Instabilities of the PIC Difference Equations*, Report No. LA 2414, Appendix I, Los Alamos Scientific Lab., 1962.

B. J. Daly, F. H. Harlow, J. E. Welch, et al., *Numerical Fluid Dynamics Using the Particle-and-Force Method*, LA 3144, Los Alamos Scientific Lab., September 1964.

C. W. Davis, Jr., *The AFWL ROC-VTS Computer Code*, AFWL-TR-65-74, July 1965.

V. D. D. Dawson, *Pressure-Gauge Design for the Measurement of Pressures in Shocktube Wind Tunnels, Shocktubes, and Guns.* Navweps Report 7326, U. S. Naval Ord. Lab., January 1961.

R. DeBar, *One Dimensional Eulerian Hydrodynamics Difference Equations*, UCRL-12238-T, Lawrence Radiation Lab., Livermore, Calif., October 1965.

J. H. deLeeuw, I. I. Glass and L. E. Heuckroth, *A High-Speed Multi-Source Spark Camera*, UTIA Tech. Note No. 26, 1960.

Jane M. Dewey, O. T. Johnson, and J. D. Patterson II, *Mechanical Impulse Measurements Close to Explosive Charges* BRL Report.

Jane Dewey and J. Sperrazza, *The Effect of Atmospheric Pressure and Temperature on Air Shock*, Ballistic Research Labs. Report

No. 721, Aberdeen Proving Ground, Md., 1950.

John M. Dewey, "The Air Velocity in Blast Waves from TNT Explosion", *Proc. of the Royal Soc.*, A 279, 366-385 (1964).

John M. Dewey, "Precursor Shocks Produced by a Large Field Chemical Explosion", *Nature*, 205, 1306.

John M. Dewey and W. A. Anson, "A Blast Wave Density Gage Using Beta-Radiation", *J. Sci. Instrum.* 46, 568-572 (1963).

W. Döering and G. Burkhardt, *Contributions to the Theory of Detonation*, TR No. F-TS-1227-1A, Wright-Patterson AFB, Ohio, May 1949, p. 307.

R. E. Duff, and R. N. Hollyer, *The Effect of Wall Boundary Layer on the Diffraction of Shock Waves Around Cylindrical and Rectangular Obstacles*, Univ. of Michigan, Ann Arbor, Michigan, June 21, 1950.

V. Ericsson and K. Edin, "On Complete Blast Scaling", *Jour. of the Physics of Fluids*, 3, 5, 893-895 (Sep - Oct 1960).

N. H. Ethridge, *A Procedure for Reading and Smoothing Pressure-Time Data from H. E. and Nuclear Explosions*, BRL Memo Report 1691, Aberdeen Proving Ground, Md., September 1965.

W. O. Ewing, Jr., and J. W. Hanna, *A Cantilever for Measuring Air Blast*, BRL Tech. Note No. 1139, August 1957.

W. J. Fader, *Amplifier Frequency Response Requirements for Recording Short Duration Air Blast Pressure Pulses*, BRL Memo Report No. 569, October 1951.

E. Fisher, *Air Blast Resulting From the Detonation of Small TNT Charges*, Report NAVORD 2890, U. S. Naval Ordnance Laboratory, July 27, 1953.

E. Fisher, *Spherical Cast TNT Charges: Air Blast Measurements on*, Report NOLM 10780, U. S. Naval Ordnance Laboratory, January 23, 1950.

J. W. Fitzgerald, *Design Considerations for Pencil Type Air Blast Gauges*, Contract No. DA-36-034-ORD-1860, Prepared for BRL by Atlantic Research Corporation, Alexandria, Va., November 1, 1955.

P. D. Flynn, *Elastic Response of Simple Structures to Pulse Loading*, BRL Memo Report No. 525, Aberdeen Proving Ground, Md., November 1950.

P. Fox and A. Ralston, "On the Solution of Equations for Spherical Waves of Finite Amplitude", *J. Math. and Phys.*, 36, 4 (Jan. 1958).

S. Fujiwhara, *Bull. Cent. Meteor. Obs. Japan*, 2, 1 (1912), and 2, 2 (1916).

W. R. Gage and C. L. Mader, *Three-Dimensional Cartesian Particle-In-Cell Calculations*, LA-3422, January 1966.

S. K. Garg and J. Siekman, "Approximate Solution of the Propagation of an Axisymmetric Blast Wave Generated by a Finite Spherical Charge", *ZAMP*, 17, 1, 108-121 (1966).

R. A. Gentry, R. E. Martin, and B. J. Daly, "An Eulerian Differencing Method for Unsteady Compressible Flow Problems", *J. of Computational Physics*, 1, 87-118 (1966).

N. Gerber and J. M. Bartos, *Tables of Cylindrical Blast Functions*, BRL Memo Report 1376, Aberdeen Proving Ground, Md., 1961.

L. Giglio-Tos and R. E. Reisler, *Air Blast Studies of Large Ammonium Nitrate/Fuel Oil Explosions*, BRL Memo Report No. 2057, August 1970.

I. I. Glass, *Aerodynamics of Blasts*, UTIA Review No. 17, Institute of Aerophysics, Univ. of Toronto, September 1960.

I. I. Glass, "Spherical Flows and Shock

Waves", *UTIA Decennial Symposium*, 3, 233 (1959).

I. I. Glass and J. H. Hall, "Shock Sphere – An Apparatus for Generating Spherical Flows", *Jour. Appl. Phys.*, 28, 424 (1957).

I. I. Glass and L. E. Heuckroth, "Head-on Collision of Spherical Shock Waves", Phys. of Fluids, 2, 5, 542 (1959).

S. Glasstone, Ed., *The Effects of Nuclear Weapons*, U. S. Atomic Energy Commission, Rev. Ed., April 1962.

H. Goldstein and A. Hoffman, *Preliminary Face-On Air Blast Measurements* BRL Technical Note No. 788, Aberdeen Proving Ground, Md., April 1953.

H. Goldstein and J. von Neumann, *Blast Wave Calculation*, Collected Work of J. von Neumann, Vol. VI, Pergamon Press, Oxford, England, 1963, pp. 386-412 (also McMillan, N.Y.).

H. J. Goodman, *Aerodynamic and Frequency Dependent Errors in an Air Blast Gauge*, BRL Report No. 1345, October 1966.

H. J. Goodman, *Compiled Free-Air Blast Data on Bare Spherical Pentolite*, BRL Report No. 1092, Feb. 1960.

H. J. Goodman and R. E. Shear, *Pressure, Density and Internal Energy of Pentolite Explosion Products*, BRL Report No. 1212.

J. W. Goresh and R. G. Dunn, *Tables of Blast Wave Parameters-1. Spherical Explosions*, ARL 69-0011, Aero Research Lab., Office of Aerospace Res., USAF, Jan. 1969.

B. A. Granath and G. A. Coulter, *BRL Shock Tube Piezo-Electric Blast Gauges*, BRL Technical Note No. 1478, Aberdeen Proving Ground, Md., August 1962

S. A. Gränstrom, "Loading Characteristics of Air Blasts from Detonating Charges", *Acta Polytechnica*, 196, (1956); also, *Trans. of the Royal Institute of Technology*, Stockholm, Sweden, No. 100 (1956).

W. Griffith, "Shock Tube Studies of Transonic Flow Over Wedge Profiles", *J. Aero. Sci.*, 19, 249 (1949).

T. K. Groves, "A Photo-Optical System of Recording Shock Profiles from Chemical Explosives", *Shock, Vibration, and Associated Environments*, Bulletin No. 28, Part III, 59-67 (Sept. 1960).

F. H. Harlow, "Hydrodynamic Problems Involving Large Fluid Dynamics", *J. Assn. Comp. Machinery*, 4, 2 (April 1957).

F. H. Harlow, "The Particle-In-Cell Method for Numerical Solution of Problems in Fluid Dynamics", *Symposia in Appl. Math., Proc.*, XV (1963).

F. H. Harlow, *Theory of Correspondence Between Fluid Dynamics and Particle and Force Models*, Report LA 2806, Los Alamos Scientific Lab., November 1962.

F. H. Harlow, et al., *Two-Dimensional Hydrodynamic Calculations*, LA-2301, Los Alamos Scientific Lab., Los Alamos, New Mexico, September 1959.

F. H. Harlow and B. D. Meixner, *The Particle-and-Force Computing Method in Fluid Dynamics*, Report LAMS-2567, Los Alamos Scientific Lab., June 1961.

D. R. Hartree, *Some Practical Methods of Using Method of Characteristics in the Calculation of Non-Steady Compressible Flows*, Report LA-HU-1, Los Alamos, 1952.

D. Hicks, *Hydrocode Test Problems*, AWL-TR-67-127, Air Force Weapons Laboratory, February 1968.

D. Hicks and R. Pelzl, *Comparison Between a von Neumann-Richtmyer Hydrocode (AFWL's PUFF) and a Lax-Wendroff Hydrocode*, AFWL-TR-68-112, Air Force Weapons Laboratory, October 1968.

J. Hilsenrath and M. Klein, *Tables of Thermodynamic Properties of Air in Chemical Equilibrium Including 2nd Virial Corrections from 1500°K to 15,000°K*, TDR-63-161, Arnold Engineering Dev. Center, 1963.

J. Hilsenrath, et al., *Thermodynamic Properties of Highly Ionized Air*, Air Force Special Weapons Center, AFSWC-TR-56-35, April 1957.

D. V. Ho, *Notes on Shock Propagation in a Non-Uniform Duct*, Tech. Report No. 4, Contract DA-19-020-ORD-5126, Div. of Appl. Math, Brown Univ., Providence, R. I., Nov. 1960.

A. J. Hoffman and S. N. Mills, Jr., *Air Blast Measurements About Explosive Charges at Side-On and Normal Incidence*, BRL Report No. 988, Aberdeen Proving Ground, Md., July 1956.

M. Holt, *Basic Developments in Fluid Dynamics*, Vol. I, Academic Press, N.Y., 1965.

M. Holt, "The Initial Behaviour of a Spherical Explosion", *Proc. Roy. Soc. (London)*, A234, 89 (1956).

B. Hopkinson, British Ordnance Board Minutes 13565, 1915.

S. L. Huang and P. C. Chou, *Calculations of Expanding Shock Waves and Late-Stage Equivalence*, Report 125-12, Contract DA-18-001-AMC-8X(x), Drexel Institute of Tech., Philadelphia, Penn., April 1968.

S. L. Huang and P. C. Chou., *Solution of Blast Waves by a Constant Time Scheme in the Method of Characteristics*, Report No. 125-9, Contract No. DA-18001-AMC-876(X), Drexel Institute of Tech., August 1966.

H. Hugoniot, "Mémoire sur la propagation du mouvement dans les Corps et specialement dans les gaz parfaits", *J. de l'école polytech. Paris*, 57 (1887), and 58 (1889).

W. G. Hyzer, *Engineering and Scientific High-Speed Photography*, The Macmillan Co., N.Y. 1962.

W. H. Jack, Jr., *Measurements of Normally Reflected Shock Waves from Explosive Charges*, BRL Memo Report No. 1499, July 1963.

W. H. Jack, Jr., and B. F. Armendt, Jr., *Measurements of Normally Reflected Shock Parameters from Explosive Charges Under Simulated High Altitude Conditions*, BRL Report No. 1280, Aberdeen Proving Ground, Md., April 1965.

K. J. Jarvis, *The Measurement of Air Blast*, Armament Research and Development Establishment, Ft. Halstead, Kent, England (undated).

R. L. Jarvis, et al., *A Program to Induce High Blast-Induced Airloads and Structural Response of Lifting Surfaces*, ASD-TDR-63-764, Vol. II, July 1964.

E. G. Johnson, *Propellant Hazards Research Facility*, Technical Report S-152, Rohm & Haas Co., Huntsville, Ala., Oct. 1967.

O. T. Johnson and W. O. Ewing, Jr., *An Omni-Directional Gauge for Measuring the Dynamic Pressure Behind a Shock Front*, BRL Memo Report No. 1324, March 1962.

O. T. Johnson, J. D. Patterson, II, and W. C. Olson, *A Simple Mechanical Method for Measuring the Reflected Impulse of Air Blast Waves*, BRL Memo Report No. 1088, July 1957, Also, *Proc. of 3rd U. S. Mat. Cong. of Appl. Mech.*, ASME, N. Y., 203-207 (June 1958).

W. E. Johnson, *OIL-a Continuous Two-Dimensional Eulerian Hydrodynamic Code*, GAMD-5580, October 1964.

D. L. Jones, "Blast Waves and Scaling Laws", *Physics of Fluids*, 13, 5, 1398-1399 (May 1970).

D. L. Jones, *Energy Parameter B for Strong*

Blast Waves, National Bureau Std. Tech. Note 155, 1962.

D. L. Jones, "Intermediate Strength Blast Wave", *The Physics of Fluids*, 11, 1664-1667 (Aug. 8, 1968).

D. L. Jones, "Strong Blast Waves in Spherical, Cylindrical and Plane Shocks", *Phys. Fluids*, 4, 1183 (Sept. 1961). Also see Erratum, *Phys. Fluids*, 5, 637 (May 1962).

D. M. Jones, P. M. Martin, and C. K. Thornhill, "A Note on the Pseudo-Stationary Flow Behind A Strong Shock Diffracted or Reflected at a Corner", *Proc. Royal Soc.*, A209 238 (1951).

G. A. Jones, *High Speed Photography*, John Wiley and Sons, Inc., N. Y., 1952.

M. A. Kaplan and R. A. Papetti, *An Analysis of the Two Dimensional Particle-In-Cell Method*, RM-4876-PR, September 1966.

W. D. Kennedy, "Explosions and Explosives in Air", *Chapter* 2, Vol. I, *Effects of Impact and Explosion*, Summary Tech Report of Division 2, NDRC, Washington, D. C., 1946.

C. N. Kingery, *Air Blast Parameters Versus Distance for Hemispherical TNT Surface Bursts*, BRL Report No. 1344, September 1966.

C. N. Kingery, *Parametric Analysis of Sub-Kiloton Nuclear and High Explosive Blast*, BRL Report No. 1393, February 1968.

C. N. Kingery, et al., *Surface Air Blast Measurements from a 100-Ton TNT Detonation*, BRL Memo Report No. 1410, Aberdeen Proving Ground, Md., June 1952.

G. F. Kinney, *Explosive Shocks in Air*, The MacMillan Co., N.Y., 1962.

J. G. Kirkwood and S. R. Brinkley, Jr., *Theory of the Propagation of Shock Waves from Explosive Sources in Air and Water*, OSRD Report 4814, 1945.

A. R. Kiwan, *Self Similar Flows Outside an Expanding Sphere*, BRL Report No. 1495, September 1970.

H. G. Kolsky, *A Method for the Numerical Solution of Transient Hydro-dynamic Shock Problems in Two Space Dimensions*, Report LA-1867, Los Alamos Scientific Lab., March 1955.

L. D. Landau and K. P. Stanyukovich, "On the Study of Detonation in Condensed Explosives", *Doklady Akad., Nauk SSSR*, 46, 399 (1945).

R. J. Larson and W. Olson, *Measurements of Air Blast Effects from Simulated Nuclear Reactor Core Excursions*, BRL Memo Report No. 1162, Aberdeen Proving Ground, Md., September 1957.

C. K. Law, *Diffraction of Strong Shock Waves by a Sharp Compressive Corner*, UTIAS Tech. Note No. 150, APOSR 70-0767TR, July 1970.

P. D. Lax and R. D. Ricktmyer, "Survey of Stability of Linear Finite Difference Equations", *Comm. Pure and Appl. Math.*, 9, 267-293 (1956)

J. H. Lee, R. Knystautas, and G. G. Glen, *Theory of Explosions*, Report No. MERL-69-10, McGill Univ., Montreal, Canada, Nov. 1969.

D. P. LeFevre, *Evaluation of New Self-Recording Air Blast Instrumentation: Project 1.36 Operation SNOWBALL*, BRL Memo Report No. 1815, January 1967.

D. L. Lehto and L. J. Belliveau, *The Treatment of Airblast Radius-Time and Pressure Distance Data by Use of Polynominal Approximations, with Applications to Pentolite Data*, NOLTR 62-85, DASA-1352, U.S. Naval Ord. Lab., White Oak, Md., March 1962.

D. L. Lehto and R. A. Larson, *Long Range Propagation of Spherical Shockwaves from Explosions in Air*, NOLTR 69-88, U. S. Naval Ord. Lab., White Oak, Md., July 1969.

D. Lehto and M. Lutzky. *One Dimensional Hydrodynamic Code for Nuclear Explosion Calculations*, NOLTR 62-168, DASA-1518, U. S. Naval Ordnance Lab., White Oak, Silver Spring, Md., March 1965.

D. Levine, *Acceleration-Compensating Pressure Transducers for Surface-Pressure Measurements*, NAVORD Report 6834, January 18, 1961.

P. Lieberman, *Ferris Wheel Series, Flat Top Event. Project Officers Report-Project 1.36. Close-In Pressure-Time Histories*, POR-3004, (WT-3004), IIT Research Institute Technology Center, Chicago, Ill., October 1966.

H. W. Liepmann and A. E. Puckett, *Introduction to Aerodynamics of a Compressible Fluid*, John Wiley & Sons, N. Y., 1947.

M. J. Lighthill, "On the Diffraction of Blast I", *Proc. Royal Soc.*, A 198, 454 (1949).

M. J. Lighthill, "On the Diffraction of Blast II", *Proc. Royal Soc.*, A 200, 554 (1950).

S. C. Lin, "Cylindrical Shock Waves Produced by an Instantaneous Energy Release", *J. Appl. Phys.*, 25, 1 (Jan. 1954).

H. E. Lindberg and R. D. Firth, *Structural Response of SPINE Vehicles, Vol. II, Simulation of Transient Surface Loads by Explosive Blast Waves*, Tech. Report AFWL-TR-66-163, Vol. II, Air Force Weapons Lab., Kirtland AFB, New Mexico, May 1967.

G. Ludford and R. J. Seeger, "An Unsteady Flow of Compressible Viscous Flow". *J. Appl. Phys.*, 24, 4, 490-495 (April 1953).

M. Lutzky, *Explosions in Vacuum*, NOLTR 62-19, U. S. Naval Ord. Lab., White Oak, Md., January 1962.

M. Lutzky, *The Flow Field Behind a Spherical Detonation in TNT Using the Landau-Stanyukovich Equation of State for Detonation Products*, NOLTR 64-40, U. S. Naval Ord. Lab., White Oak, Md., December 1964.

M. Lutzky, *Theoretical Versus Experimental Results for Air Blast from One-Pound Spherical TNT and Pentolite Charges at Sea Level Conditions*, NOLR 65-57, July 1965.

M. Lutzky and D. Lehto, *On the Scaling of Pressures from Nuclear Explosions with Some Observations on the Validity of the Point-Source Solution*, NOLTR 65-74, U. S. Naval Ordnance Laboratory, White Oak, Md., September 1965.

M. Lutzky and D. L. Lehto, "Scaling of Spherical Blast", *Jour. Appl. Physics*, 41, 2, 844-846 (Feb. 1970).

M. Lutzky and D. Lehto, *Shock Propagation in Nonhomogeneous Atmospheres and Modified Sachs Scaling. Part I: Exponential Ideal-Gas Atmospheres*, NOLTR 67-20, U. S. Naval Ord. Lab., White Oak, Md., June 1967.

M. Lutzky and D. Lehto, *Transformations for Scaling of Close-in Pressures from Nuclear Explosions*, NOLTR66-12, U. S. Naval Ord. Lab., March 1966.

E. Mach and J. Sommer, "Uber die Fortpflanzungsgeschwindigkeit von Explosionsschallwellen", *Akademie de Wisseschafter, Sitzangberichte der Wiener*, 74 (1877).

R. C. Makino, *The Kirkwood-Brinkley Theory of the Propagation of Spherical Shock Waves, and Its Comparison with Experiment*, BRL Report No. 750, Aberdeen Proving Ground, Maryland, April 1951.

R. C. Makino and R. E. Shear, *Estimation of Normally Reflected Impulse of Blast Waves*, BRL Technical Note No. 1010, Aberdeen Proving Ground, Maryland, May 1955.

R. C. Makino and R. E. Shear, *Unsteady Spherical Flow Behind a Known Shock Line*, BRL Report No. 1154, November 1961.

B. W. Marshner, *An Investigation of Detached Shock Waves*, M. S. Thesis, California Institute of Tech., 1948.

V. C. Martin, K. F. Mead, and J. E. Uppard, *Blast Loading of a Right Circular Cylinder*, AWRE Report No. 0-93/65, Atomic Weapons Research Establishment, Aldermaston, Berkshire, England, November 1965.

D. L. Merritt and P. M. Aronson, *Study of Blast-Bow Wave Intersections in a Wind Tunnel*, AIAA Paper No. 65-5 presented at the AIAA Second Aerospace Science Meeting, New York, January 1965. (Also, private communications with Gentry, et al.).

R. R. Mills, Jr., F. J. Fisch, B. W. Jezek and W. E. Baker, *Self-Consistent Blast Wave Parameters*, DASA-1559, Aircraft Armaments, Inc., Cockeysville, Md., October 1964.

E. A. Milne, *Phil. Mag. and Jour. of Science*, 42, 96-114 (1921).

R. A. Minzer, K. S. W. Champion, and H. L. Pond, *The ARDC Model Atmosphere, 1959*, AFCRC-TR-59-267, August 1969.

R. W. Morton and J. L. Patterson, *A Transient Pressure Measurement System for Blast Effect Research*, Paper 148-LA 61-1, Presented at 16th Annual ISA Instrument-Automation Conf., Los Angeles, California, September 1961.

J. C. Muirhead and W. M. McMurtry, "Surface Tension Gauges for the Measurement of Low Transient Pressures", *Review of Sci. Inst.*, 33, 12, 1473,1474 (Dec. 1962).

J. A. McFadden, *Initial Behavior of a Spherical Blast*, NAVORD Report No. 2378, 1952.

J. A. McFadden, "Initial Behavior of a Spherical Blast", *J. Appl. Phys.*, 1952.

G. E. Nevill, Jr., *Similitude Studies of Re-Entry Vehicle Response to Impulsive Loading*, AFWL TDR 63-1, Vol. 1, Kirtland Air Force Base, New Mexico, 1963.

C. H. Norris, R. J. Hansen, M. J. Holley, Jr., J. M. Biggs, S. Namyet, and J. K. Minami, *Structural Design for Dynamic Loads*, McGraw-Hill Book Co., N. Y., 1959, pp. 249-52.

W. C. Olson and H. Goldstein, *Air Blast Measurements Around Water-Filled Simulated Nuclear Reactor Core Vessels*, BRL Memorandum Report No. 1219, Aberdeen Proving Ground, Maryland, July 1959.

W. C. Olson, J. D. Patterson, II, and J. S. Williams, *The Effect of Atmospheric Pressure on the Reflected Impulse from Blast Waves*, BRL Memo Report No. 1241, Aberdeen Proving Ground, Md., January 1960.

W. Olson and J. Wenig, *A Double-Charge Technique to Measure Face-On Blast*, BRL Memo Report No. 1347, APG, Md., May 1961.

A. K. Oppenheim, *The No-Man's Land of Gas Dynamics of Explosions*, AIAA Paper No. 66-517, AIAA 6th Aerospace Sciences Meeting, Los Angeles, Calif., June 1966.

T. Orlow, et al., *A Computer Program for the Analysis of Transient Axially Symmetric Explosion and Shock Dynamics Problems*, USNOL Report NAVWEPS 7265, 1960.

K. Oshima, *Blast Waves Produced by Explosive Waves*, Report 358, Aeronautical Research Institute, Univ. of Tokyo, Tokyo, Japan, July 1960.

D. C. Pack, "The Reflection and Diffraction of Shock Waves", *J. Fluid Mech.*, 18, 549 (1964).

S. I. Pai, *Introduction to Theory of Compressible Flow*, D. Van Nostrand Co., N. Y. 1959.

W. O. Palmer and J. C. Muirhead, "A Squirt Gauge for Peak Blast Pressure Indication", *Review of Sci. Inst.*, 40, 12, 1637-1638 (Dec. 1969).

J. L. Patterson, *A Miniature Electrical Pressure Gage Utilizing a Stretched Flat Diaphragm*, NACA TN 2659, April 1962.

B. Perkins, Jr., P. H. Lorrain and W. H. Townsend, *Forecasting the Focus of Air Blasts due to Meteorological Conditions in the Lower Atmosphere*, BRL Report No. 1118, Aberdeen Proving Ground, Md., October 1960.

R. Piacesi, *Numerical Hydrodynamic Calculation of the Flow of the Detonation Products from a Point-Initiated Explosive Cylinder*, NOLTR 66-150, U. S. Naval Ordnance Lab., White Oak, Md., January 1967.

R. Piacesi, et al., *A Computer Analysis of the Two Stage Hypervelocity Model Launchers*, NOLTR-62-87, U. S. Naval Ordnance Lab., Feb. 1963.

H. B. Pierce and J. C. Manning, *Experimental Investigation of Blast Loading on an Airfoil in Mach Number 0.7 Airflow With Initial Angle-of-Attack Change of 20°*, NASA TN D-1603, February 1963.

K. D. Pyatt, *HECTIC-a Two-Dimensional Interaction Code*, AFWL-TR-65-90, Vol. II, Addendum, October 1965.

A. Ralson and H. S. Wilf, *Mathematical Methods for Digital Computers*, John Wiley & Sons, N. Y., 1960.

T. S. Rathke, *A System for Dynamic Calibration of Pressure Transducers* Inst. Soc. of Am. Preprint No. P19-2-PHYMMID-67, 22nd ISA Conference and Exhibit, Chicago, Ill., Sept. 1967.

R. E. Reisler, "The Mechanical Self-Recording Pressure-Time Gage – A Useful Instrument for the Acquisition of Air Blast Data from Nuclear and Large HE Detonations", *Shock, Vibration and Associated Environments*, Bulletin No. 28, Part III, 99-112 (Sept. 1960).

R. E. Reisler, J. H. Keefer, and L. Giglio-Tos, *Basic Air Blast Measurements from a 500-Ton TNT Detonation Project 1.1 Operation Snowball*, BRL Memo Report No. 818, December 1966.

R. E. Reisler, L. Giglio-Tos, and R. C. Kellner, *Ferris Wheel Series, Flat Top Event, Project Officers Report – Project 1.1, Airblast Phenomena*, POR-3001, October 1966.

R. E. Reisler, L. Giglio-Tos, G. D. Teel, and D. P. LeFevre, *Air Blast Parameters from Summer and Winter 20-Ton TNT Explosions, Operation Distant Plain, Events 3 and 5*, BRL Memo Report No. 1894, November 1967.

R. E. Reisler, N. H. Ethridge, D. P. LeFevre, and L. Giglio-Tos, *Air Blast Measurements From the Detonation of an Explosive Gas Contained in Hemispherical Balloon (Operation Distant Plain Event 2A)*, Ballistic Research Laboratories, Aberdeen Proving Ground, Maryland, July 1971.

M. Rich. *A Method for Eulerian Fluid Dynamics* Report No. LAMS-2826, Los Alamos Scientific Lab., 1963.

P. I. Richards, *Sharp Shock Lagrangian Hydrodynamics Code*, Report No. TO-B 66-74, BRL, Aberdeen Proving Ground, Md., October 1966.

E. H. Rogers, *Two-Numerical Methods for Calculating Axisymmetric Flow*, BRL MR 1745, Ballistic Research Lab., Aberdeen Proving Ground, Md., May 1966.

M. H. Rogers, "Similarity Flows Behind Strong Shock Waves", Quart. *J. Mech. Appl.* 8, 337-367 (1960).

J. Rosciszewski, "Calculations of the Motion of Non-Uniform Shock Waves", *J. Fluid Mech.*, 8, 337-367 (1960).

C. A. Rouse, "Theoretical Analysis of the Hydrodynamic Flow in Exploding Wire Phenomena", *Exploding Wires*, 227. Plenum Press, N.Y. (1959).

R. H. Rowland, *Blast and Shock Measurement, State-of-the-Art Review*, DASA 1986, November 1967.

G. Rudinger, *Wave Diagrams for Nonsteady Flow in Ducts*, D. Van Nostrand, Co., N. Y., 1955.

L. Rudlin, *On the Origin of Shockwaves from Condensed Explosions in Air. Part 2, Measurements of Airshock Pressures from 8-lb TNT Spheres of Various Densities at Ambient Pressures*, NOLTR 63-16, DASA-1360, U. S. Naval Ordnance Lab., October 1963.

L. Rudlin , *On the Origin of Shockwaves from Spherical Condensed Explosions in Air. Part I, Results of Photographic Observations of Pentolite Hemispheres at Ambient Conditions*, NOLTR 62-182, DASA-1360, U. S. Naval Ord. Lab., August 1963.

J. R. Ruetenik and S. D. Lewis, *Computation of Blast Properties for Spherical TNT or Pentolite from Measured Pressure Histories*, AFFDL-TR-66-47, October 1966.

J. R. Ruetenik and S. D. Lewis, *Pressure Probe and System for Measuring Large Blast Waves*, Tech. Report AFFDL-TR-65-35, A. F. Flight Dynamics Lab., Wright-Patterson AFB, Ohio, June 1965.

R. G. Sachs, *The Calibration of Paper Blast Meters*, BRL Report No. 472, Aberdeen Proving Ground, Md., June 1944.

R. G. Sachs, *The Dependence of Blast on Ambient Pressure and Temperature*, BRL Report No. 466, Aberdeen Proving Ground, Md., May 1944.

A. Sakurai, "On the Propagation of Structures of the Blast Wave, Part I", *J. of Phys. Soc. of Japan*, 8, 5, 662-669 (1953), also "Part II", *Jour. Phys. Soc. of Japan*, 9, 2, 256-266 (1954).

R. F. Saxe, *High-Speed Photography*, The Focal Press, London and N. Y., 1966.

H. Schardin, "Measurement of Spherical Waves", *Communs. Pure and Appl. Math.*, 7, 1, 223 (1954).

W. J. Schenck, "Kerr Cells for Ultrahighspeed Photography", *ISA Transactions*, 5, 1, 14-27 (1966).

S. D. Schleuter, R. G. Hippensteel, and B. F. Armendt, *Measurements of Air Blast Parameters Above a Reflecting Surface*, BRL Memo Report No. 1645, April 1965.

L. I. Sedov, *Similarity and Dimensional Methods in Mechanics*, Academic Press, N. Y., 1959, p. 210.

R. E. Shear, *Detonation Properties of Pentolite*, BRL Report No. 1159, December 1961.

R. E. Shear, *Incident and Reflected Blast Pressures for Pentolite*, BRL Report No. 1262, Aberdeen Proving Ground, Md., September 1964.

R. E. Shear and B. D. Day, *Tables of Thermodynamic and Shock Front Parameters for Air*, BRL Memo Report No. 1206, May 1959.

R. E. Shear and R. C. Makino, *Unsteady Spherical Flow Behind a Known Shock Line*, BRL Report No. 1154, BRL, Aberdeen Proving Ground, Md., November 1961.

R. E. Shear and P. McCane, *Normally Reflected Shock Front Parameters*, BRL Memo Report No. 1273, Aberdeen Proving Ground, Md., May 1960.

R. E. Shear and E. Q. Wright, *Calculated Peak Pressure-Distance Curves for Pentolite and TNT*, BRL Memo Report No. 1423, August 1962.

B. Soroka and G. T. Watson, *An Eight-Channel High-Performance Oscillograph Recording*

System, BRL Memo Report No. 1765, May 1966.

B. Soroka and J. Wenig, *High Impedance Cathode Followers for Piezoelectric Gage Recording in Air Blast Research*, BRL Memo Report No. 1474, April 1963.

J. Sperrazza, "Modeling of Air Blast", in *Use of Models and Scaling in Shock and Vibration*, W. E. Baker, Ed., ASME, N. Y., Nov. 1963, 65-78.

R. S. Srivastava, and M. G. Chopra, "Diffraction of Blast Wave for the Oblique Case", *J. Fluid Mech.*, 40, Part 4, 821-831 (1970).

K. P. Stanukovich, *Unsteady Motion of Continuous Media*, Pergamon Press, N.Y., 1960.

R. G. Stoner and W. Bleakney, "The Attenuation of Spherical Shock Waves in Air", *Journal of Appl. Physics*, 19, 7, 670-678 (July 1948).

M. Sultanoff, "A 100,000,000-frame-per-second Camera", *Rev. Sci. Instr.*, 21, 653-656 (July 1950).

M. Sultanoff and G. McVey, *Observations from Spherical Pentolite Charges*, BRL Report No. 984, Aberdeen Proving Ground, Md., July 1956.

M. Sultanoff and G. McVey, *Shock-Pressure at and Close to the Surface of Spherical Pentolite Charges Inferred from Optical Measurements*, BRL Report No. 917, Aberdeen Proving Ground, Md., August 1954.

M. Sultanoff and R. L. Jameson, "New Observations of Explosive Phenomena by Submicrosecond Color Photography", *J. SMPTE*, 69, (Feb. 1960).

A. H. Taub, "Refraction of Plane Shock Waves", *Phys. Rev.*, 72, 51 (1947).

G. I. Taylor, "The Air Wave Surrounding an Expanding Sphere", *Proc. Royal Soc.*, A, 186, 273-292 (1936).

G. I. Taylor, "The Formation of a Blast Wave by a Very Intense Explosion: II The Atomic Explosion of 1945", *Proc. Royal Soc.*, 201, 175-186 (1950).

G. I. Taylor, "The Formation of a Blast Wave by a Very Intense Explosion: I Theoretical Discussion", *Proc. Royal Soc.*, 201, 159-174 (1950).

G. I. Taylor, "The Propagation and Decay of Blast Waves", Paper 20 in *The Scientific Papers of Sir Geoffrey Ingram Taylor*, III, Cambridge Univ. Press, 221-235 (1963).

G. I. Taylor, "The Propagation of Blast Waves Over the Ground", Paper 29 in *The Scientific Papers of Sir Geoffrey Ingram Taylor*, III, Cambridge Univ. Press, 274-276 (1963).

G. I. Taylor, "Notes on the Dynamics of Shockwaves from Bare Explosive Charges", Paper 26 in *The Scientific Papers of Sir Geoffrey Ingram Taylor*, III Cambridge Univ. Press, 255-259 (1963).

G. I. Taylor, "Pressures on Solid Bodies Near an Explosion", Paper 27 in *The Scientific Papers of Sir Geoffrey Ingram Taylor*, III, Cambridge Univ. Press, 260-267 (1963).

G. I. Taylor and H. Jones, "Blast Impulse and Fragment Velocities from Cased Charges", Paper 40 in *The Scientific Papers of Sir Geoffrey Ingram Taylor*, III, Cambridge Univ. Press, 363-369 (1963).

G. I. Taylor and H. Jones, "The Bursting of Cylindrical Cased Charges", Paper 42 in *The Scientific Papers of Sir Geoffrey Ingram Taylor*, III, Cambridge Univ. Press, 379-382 (1963).

F. Theilheimer, *The Determination of the Time Constant of a Blast Wave from the Pressure-Distance Relation*, NAVORD Report 1734, U. S. Naval Ordnance Lab., December 1950.

L. Ting and H. F. Ludloff, "Aerodynamics of Blasts", *J. Aero Sci.*, 18 139 (1951).

G. Uhlenbeck, *Diffraction of Shock Waves Around Various Obstacles,* University of Michigan, Engineering Research Institute, Ann Arbor, Michigan, March 21, 1950.

J. J. Unwin, "The Production of Wave by the Sudden Release of a Spherical Distribution of Compressed Air in the Atmosphere", *Proc. Roy. Soc.*, A 178 (1941).

G. C. Vlases, and D. L. Jones, "Blast Waves from an Inverse Pinch Machine", *Phys. of Fluid*, 9, 3, 478-484 (March 1966).

J. von Neumann and R. D. Richtmyer, "A Method for the Numerical Calculation of Hydrodynamic Shocks", *J. Appl. Phys.*, 21, 233-237 (1950).

W. A. Walker, D. Piacesi, and H. M. Sternberg, *A Fortran Program for the Numerical Solution of Explosion and Shock Hydrodynamic Problems in One-Space Dimension,* NOLTR 64-114, U. S. Naval Ordnance Lab.

G. T. Watson and R. D. Wilson, *BRL Time-of-Arrival Blast Gage,* BRL Technical Note No. 1476, Aberdeen Proving Ground, Md., August 1962.

F. Wecken, "Les Lois de Similitude Dans Les Explosions A Symétrie Sphérique", *Mémorial De L'Artillerie Francaise Sciences et Techniques de l'Armement,* 35, 136 (1961).

W. Weibull, *Explosion of Spherical Charges in Air: Travel Time, Velocity of Front, and Duration of Shock Waves,* Report No. X-127, BRL, Aberdeen Proving Ground, Md., February 1950.

H. S. Wells, *Development and Test of Prototype Miniature, Rugged, Self-Recording Air Blast Instrumentation,* Report No. EIR 700, The Bendix Corp., Baltimore, Md., November 1966.

A. B. Wenzel and R. L. Bessey, *Barricaded and Unbarricaded Blast Measurements,* Contract No. DAHC04-69-C-0028, Subcontract 1-OU-431, Southwest Research Institute, October 1969.

W. A. Whitaker, E. A. Nawrocki, C. E. Needham, and W. W. Troutman, *Theoretical Calculations of the Phenomenology of Detonations,* Vol. 1 and 2, AFWL-TR 66-141, Vol. I, Air Force Weapons Lab., Res. and Tech. Div., Air Force Systems Command, Kirtland Air Force Base, New Mexico, November 1966.

D. R. White, D. K. Weimer, and W. Bleakney, *The Diffraction of Shock Waves Around Obstacles and the Transient Loading of Structures,* Tech. Report II-6 Princeton University, Dept. of Physics, August 1, 1950.

T. Whiteside, *Instrument Development Section Notes,* UKAEA, Atomic Weapons Research Establishment, AWRE, Foulness, January 1967.

G. B. Whitham, "A New Approach to Problems of Shock Dynamics, Part II, Three-Dimensional Problems", *J. Fluid Mechanics,* 5, Part 3, 369-386 (April 1959).

G. B. Whitham, "The Propagation of Weak Spherical Shocks in Stars", *Comm. Pure and Appl. Math.*, VI, 397-414 (1953).

M. Wilkins, et al., *A Computer Program for Calculating One-Dimensional Hydrodynamic Flow-Ko Code,* UCRL 6919, Univ. of Calif. Radiation Lab., July 1962.

F. A. Williams, *Combustion Theory*, Addison-Wesley Publishing Co., Inc., Reading, Mass., 1965.

J. S. Williams, *A High Intensity, Short Duration Photographic Light Source for Use at Low Ambient Pressure,* BRL Technical Note No. 1618, Aberdeen Proving Ground, Md., June 1966.

R. D. Wilson, *The Application of an Operational Amplifier to the Use of Piezoelectric Transducers,* BRL Memo Report No. 1646, April 1965.

C. Wilton and K. Kaplan, *Preliminary Investigation of Pulse Shapes from a Near-Simul-*

taneous Detonation of Two High-Explosive Charges in a Barricaded Enclosure, Final Report URS 649A-1, URS, Burlingame, Calif., April 1966.

I. O. Wolf, et al., *An Experimental Investigation of Blast-Induced Airloads and Response of Lifting Surfaces*, AFFDL-TR-64-176, March 1965.

Yu. S. Yakovlev, *The Hydrodynamics of an Explosion*, FTD-TT-63-381/1 + 2, Wright-Patterson Air Force Base, Dayton, Ohio, September 1963.

T. A. Zaker, *Blast Pressures from Sequential Explosions*, Final Report J6166, IITRI, October 1969.

E. A. Zeitlin, *The Blast Environment: Methodology and Instrumentation Techniques with Applications to New Facilities*, NAVWEPS Report 8782, U. S. Naval Ordnance Test Station, China Lake, Calif., August 1965.

Ia. B. Zeldovich and S. A. Kompaneets, *Theory of Detonation*, Academic Press, N. Y., 1960.

INDEX

A

Accuracy of measurement of blast waves, 5-18 through 5-19
Acoustic approximations
  for asymptotes for blast wave properties, 6-6, 6-9
  in long-range focusing, 1-19 through 1-21
  in reflection of weak shocks, 1-7, 1-9, 1-11, 1-12
Analytic solutions to blast wave equations
  for strong shocks, 2-6 through 2-9
  for weak shocks, 2-14 through 2-16
  time constant, 2-19 through 2-20
Arrival-time gages (*See:* Gages)

B

Basic equations (*See:* Equations)
Blast parameters, nondimensional
  arrival time, 6-5, 6-7, 6-8, 6-9
  density, 6-5 through 6-11
  durations, 6-5, 6-9 through 6-11
  impulses, 6-5, 69 through 6-11
  initial rate of decay of pressure, 6-5, 6-11, 6-13
  pressures, 6-5, 6-6, through 6-11
  scaled distance, 6-5, 6-8 through 6-14
  shock-front parameters, 6-5 through 6-11
  temperature, 6-5 through 6-11
  time constant, 6-5, 6-11
  velocities, 6-5 through 6-6, 6-8 through 6-9
Blast sources, 1-2
Blast wave
  diffraction
    about cylinders, 1-14 through 1-16
    about rectangular blocks, 1-12 through 1-14
  measurement
    accuracy (*See:* Accuracy of measurement of blast waves)
    dynamic pressures, 5-9, 5-11
  "free-air" waves, 5-2 through 5-6
  from sequential explosions, 5-16
  Mach waves, 5-10 through 5-12
  normally reflected waves, 5-4 through 5-5, 5-12 through 5-14, 5-17
  obliquely reflected waves, 5-10 through 5-12
  sources on or near the ground, 5-5 through 5-11
  under real and simulated altitude conditions, 5-13 through 5-17
physical properties (*See:* Blast parameters, nondimensional)
  arrival time, 1-2, 1-3, 5-6, 5-8, 5-10
  duration of positive phase, 5-5, 5-8, 5-11
  negative impulse, 1-3
  particle velocity, 5-10
  positive impulse, 1-3, 5-3, 5-7, 5-9, 5-11, 5-14, 5-15, 5-16
  pressure (*See:* Blast wave, pressure), 1-2, 1-3, 5-3, 5-4, 5-5, 5-7, 5-8, 5-11, 5-14
  shock velocity, 5-10
pressure
  dynamic pressure, 6-5, 6-7, 6-8, 6-14 through 6-16
  effect of ambient conditions, 3-13 through 3-14, 5-13 through 5-16
  overpressure, 1-3 through 1-4, 2-16, 2-8, 2-20, 5-2 through 5-10
  peak pressures, 1-2, 1-3, 6-6, 6-8
  reflected pressures, 1-7 through 1-11, 5-12, 5-13, 6-7, 6-10
  side-on pressure, 1-3, 2-19, 6-11, 6-12
scaling
  Hopkinson scaling
    definition and implications, 3-2 through 3-7
    experimental verification, 3-3 through 3-5
    proof, 3-7 through 3-9
  limitations of, 3-23 through 3-24
  Ivtzky and Lehto scaling, 3-15 through 3-17
  Sachs' scaling
    definition, 3-9
    experimental verification, 3-13 through 3-16
    proof, 3-11 through 3-13
    sample calculation, 3-9 through 3-11
  scaling of reflected impulse, through 3-18
  Wecken's laws, 3-18 through 3-20

C

Calibration techniques
  dynamic calibration, 8-21, 8-24, 8-25
  static calibration, 8-23 through 8-25
Cameras
  fast-shutter still cameras
    Kerr cell, 9-7, 9-8, 9-11
    magneto-optic effect, 9-7
  framing motion picture cameras
    Beckman and Whitley, 9-4
    Cordin, 9-4, 9-8
    drum, 9-2
    Dynafax, 9-2
    Eastman, 9-2
    Fastax, 9-2, 9-3
    Hycam, 9-2, 9-4
    intermittent, 9-1
    rotating mirror, 9-3 through 9-8
    rotating prism, 9-2 through 9-5

  image-converter cameras, 9-9 through 9-13
  image-dissector cameras, 9-4, 9-5, 9-6
  streak cameras, 9-6, 9-7, 9-8, 9-9
Cathode-ray tube (CRT) blast recorders, 8-1 through 8-6
Charts of compiled blast parameters, 6-9, 6-11, 6-13
Computational methods
  comparison of methods, 4-34, 4-35
  fluid in cell (FLIC) method, 4-29 through 4-33
  Gränstrom method, 4-5, 4-6
  Kirkwood and Brinkley method, 4-2 through 4-5
  methods of characteristics, 4-6 through 4-8
  particle and force (PAF) method, 4-16 through 4-24
  particle-in-cell (PIC) method, 4-24 through 4-29
  with fictitious viscosity
    Brode's method, 4-9 through 4-12
    von Neumann and Richtmyer method, 4-8, 4-9
    WUNDY code, 4-13 through 4-16
Corrections for gage size errors, 10-4 through 10-5

D-E

Density gage (*See:* Gages)
Diffraction (*See:* Blast wave, diffraction)
Effects of explosive composition, 1-21 through 1-23
Equations
  basic
    definitions of impulse, 1-3, 3-3
      in Eulerian form, 2-4, 2-5, 2-20, 2-21
      in Lagrangian form, 2-3, 2-4
      Rankine-Hugoniot equations, 2-4, 2-7 2-10, 2-21
  one-dimensional blast waves
    cylindrically symmetric flow, 2-5
    linear flow, 2-5
    spherically symmetric flow, 2-5, 2-21
  time histories of blast parameters, 1-3 through 1-5
Explosives, properties of, 6-4

F

Fluid in cell (FLIC) computational methods (*See:* Computational methods)
Focusing, long range, 1-18 through 1-22

G

Gages
  arrival-time
    blast switch, 7-14, 7-16
    piezoelectric, 7-15, 7-16
  density, 7-19 through 7-20
  mechanical
    burst diaphragm, 7-21 through 7-24
    cantilever beam, 7-22 through 7-23
    deformed disc, 7-22
    squirt, 7-24, 7-25
    surface tension, 7-24
    tin can, 7-22
  self-recording blast, 8-17 through 8-21
Galvanometer oscillograph instrumentation systems, 8-9 through 8-10
Gränstrom method (*See:* Computational methods)

H-L

Hopkinson's scaling law (*See:* Blast wave, scaling)
Image converter cameras (*See:* Cameras)
Image-dissector cameras (*See:* Cameras)
Impulse transducers (*See:* Transducers)
Instrumentation systems
  effect of nuclear weapons on, 8-10 through 8-13
  magnetic tape, 8-6
  hardened, 8-15 through 8-17
  laboratory, 8-6 through 8-9
  portable, 8-14 through 8-15
Kirkwood and Brinkley (*See:* Computational methods)
Lutzky and Lehto scaling (*See:* Blast wave, scaling)

M

Magnetic tape instrumentation systems (*See:* Instrumentation systems, magnetic tape)
Measurements of blast waves (*See:* Blast wave, measurement)
Mechanical gages (*See:* Gages)
Methods for accurate estimation of positive duration, 10-7 through 10-9
Methods of characteristics (*See:* Computational methods)

T-Z

Transducers
  impulse, 7-20
  pressure
    Atlantic Research Corp., 7-4, 7-10, 7-11, 7-26 through 7-28
    British, 7-4 through 7-6, 7-14 through 7-16
    BRL, 7-2, 7-3, 7-7 through 7-9
    drag, 7-17 through 7-19
    dynamic, 7-17 through 7-19
    Dynisco, 7-13, 7-14
    Kaman Nuclear, 7-10 through 7-12
    Kistler, 7-10, 7-12, 7-26 through 7-28
    miniature, 7-7 through 7-14
    NASA, 7-8 through 7-10
  zero-time, 7-14, 7-16
Wecken's laws (*See:* Blast wave, scaling)
Zero-time transducers (*See:* Transducers)

ENGINEERING DESIGN HANDBOOKS

Available to AMC activities, DOD agencies, and Government agencies from Letterkenny Army Depot, Chambersburg, PA 17201. Unclassified documents available to contractors and universities from National Technical Information Service (NTIS), Department of Commerce, Springfield, VA 22151.

No. AMCP 706-	Title
100	Design Guidance for Producibility
104	Value Engineering
106	Elements of Armament Engineering, Part One, Sources of Energy
107	Elements of Armament Engineering, Part Two, Ballistics
108	Elements of Armament Engineering, Part Three, Weapon Systems and Components
109	Tables of the Cumulative Binomial Probabilities
110	Experimental Statistics, Section 1, Basic Concepts and Analysis of Measurement Data
111	Experimental Statistics, Section 2, Analysis of Enumerative and Classificatory Data
112	Experimental Statistics, Section 3, Planning and Analysis of Comparative Experiments
113	Experimental Statistics, Section 4, Special Topics
114	Experimental Statistics, Section 5, Tables
115	**Environmental Series, Part One, Basic Environmental Concepts
116	**Environmental Series, Part Two, Natural Environmental Factors
117	*Environmental Series, Part Three, Induced Environmental Factors
118	*Environmental Series, Part Four, Life Cycle Environments
119	*Environmental Series, Part Five, Glossary of Environmental Terms
120	Criteria for Environmental Control of Mobile Systems
121	Packaging and Pack Engineering
123	Hydraulic Fluids
124	*Reliable Military Electronics
125	Electrical Wire and Cable
126(S)	*Vulnerability of Communication-Electronic (C-E) Systems to Electronic Countermeasures (U)
127	Infrared Military Systems, Part One
128(S)	Infrared Military Systems, Part Two (U)
129	*Electromagnetic Compatibility (EMC)
130	Design for Air Transport and Airdrop of Materiel
132	*Maintenance Engineering Techniques (MET)
133	*Maintainability Engineering Theory and Practice (METAP)
134	Maintainability Guide for Design
135	+Inventions, Patents, and Related Matters
136	**Servomechanisms, Section 1, Theory
137	**Servomechanisms, Section 2, Measurement and Signal Converters
138	**Servomechanisms, Section 3, Amplification
139	**Servomechanisms, Section 4, Power Elements and System Design
140	Trajectories, Differential Effects, and Data for Projectiles
150	Interior Ballistics of Guns
160(S)	Elements of Terminal Ballistics, Part One, Kill Mechanisms and Vulnerability (U)
161(S)	Elements of Terminal Ballistics, Part Two, Collection and Analysis of Data Concerning Targets (U)
162(SRD)	Elements of Terminal Ballistics, Part Three, Application to Missile and Space Targets(U)
165	Liquid-Filled Projectile Design
170(S)	Armor and Its Applications (U)
175	Solid Propellants, Part One
176(C)	+Solid Propellants, Part Two (U)
177	Properties of Explosives of Military Interest
178(C)	+Properties of Explosives of Military Interest, Section 2 (U) (*Replaced by -177*)
179	Explosive Trains
180	Principles of Explosive Behavior
181	Explosions in Air, Part One
182(S)	*Explosions in Air, Part Two (U)
185	Military Pyrotechnics, Part One, Theory and Application
186	Military Pyrotechnics, Part Two, Safety, Procedures and Glossary
187	Military Pyrotechnics, Part Three, Properties of Materials Used in Pyrotechnic Compositions
188	Military Pyrotechnics, Part Four, Design of Ammunition for Pyrotechnic Effects
189	Military Pyrotechnics, Part Five, Bibliography
190	*Army Weapon System Analysis
191	System Analysis and Cost-Effectiveness
192	Computer Aided Design of Mechanical Systems
195	*Development Guide for Reliability, Part One, Introduction, Background, and Planning for Army Materiel Requirements
196	*Development Guide for Reliability, Part Two, Design for Reliability
197	*Development Guide for Reliability, Part Three, Reliability Prediction
198	*Development Guide for Reliability, Part Four, Reliability Measurement
199	*Development Guide for Reliability, Part Five, Contracting for Reliability
200	*Development Guide for Reliability, Part Six, Mathematical Appendix and Glossary
201	*Helicopter Engineering, Part One, Preliminary Design
202	*Helicopter Engineering, Part Two, Detail Design
203	Helicopter Engineering, Part Three, Qualification Assurance
204	Helicopter Performance Testing
205	*Timing Systems and Components
210	Fuzes
211(C)	Fuzes, Proximity, Electrical, Part One (U)
212(S)	Fuzes, Proximity, Electrical, Part Two (U)
213(S)	Fuzes, Proximity, Electrical, Part Three (U)
214(S)	Fuzes, Proximity, Electrical, Part Four (U)
215(C)	Fuzes, Proximity, Electrical, Part Five (U)
235	Hardening Weapon Systems Against RF Energy
238	*Recoilless Rifle Weapon Systems
239	*Small Arms Weapon Systems
240(S)	Grenades (U)
242	Design for Control of Projectile Flight Characteristics (*Replaces -244*)
244	Ammunition, Section 1, Artillery Ammunition--General, with Table of Contents, Glossary, and Index for Series
245(C)	Ammunition, Section 2, Design for Terminal Effects (U)
246	+Ammunition, Section 3, Design for Control of Flight Characteristics (*Replaced by -242*)
247	Ammunition, Section 4, Design for Projection
248	+Ammunition, Section 5, Inspection Aspects of Artillery Ammunition Design
249	Ammunition, Section 6, Manufacture of Metallic Components of Artillery Ammunition
250	Guns--General
251	Muzzle Devices
252	**Gun Tubes
253	*Breech Mechanism Design
255	Spectral Characteristics of Muzzle Flash
260	Automatic Weapons
270	**Propellant Actuated Devices
280	Design of Aerodynamically Stabilized Free Rockets
281(SRD)	Weapon System Effectiveness (U)
282	+Propulsion and Propellants (*Replaced by -285*)
283	Aerodynamics
284(C)	Trajectories (U)
285	Elements of Aircraft and Missile Propulsion (*Replaces -282*)
286	Structures
290(C)	Warheads--General (U)
291	Surface-to-Air Missiles, Part One, System Integration
292	+Surface-to-Air Missiles, Part Two, Weapon Control
293	+Surface-to-Air Missiles, Part Three, Computers
294(S)	Surface-to-Air Missiles, Part Four, Missile Armament (U)
295(S)	Surface-to-Air Missiles, Part Five, Countermeasures (U)
296	+Surface-to-Air Missiles, Part Six, Structures and Power Sources
297(S)	+Surface-to-Air Missiles, Part Seven, Sample Problem (U)
300	Fabric Design
327	Fire Control Systems--General
329	Fire Control Computing Systems
331	Compensating Elements
335(SRD)	*Design Engineers' Nuclear Effects Manual (DENEM), Volume I, Munitions and Weapon Systems (U)
336(SRD)	*Design Engineers' Nuclear Effects Manual (DENEM), Volume II, Electronic Systems and Logistical Systems (U)
337(SRD)	*Design Engineers' Nuclear Effects Manual (DENEM), Volume III, Nuclear Environment (U)
338(SRD)	*Design Engineers' Nuclear Effects Manual (DENEM), Volume IV, Nuclear Effects (U)
340	Carriages and Mounts--General
341	Cradles
342	Recoil Systems
343	Top Carriages
344	Bottom Carriages
345	Equilibrators
346	Elevating Mechanisms
347	Traversing Mechanisms
350	Wheeled Amphibians
355	The Automotive Assembly
356	Automotive Suspensions
357	Automotive Bodies and Hulls
360	Military Vehicle Electrical Systems
361	*Military Vehicle Power Plant Cooling
445	Sabot Technology Engineering

*UNDER PREPARATION--not available
**REVISION UNDER PREPARATION
+OBSOLETE--out of stock

(AMCRD-TV)

FOR THE COMMANDER:

OFFICIAL:

JOSEPH W. PEZDIRTZ
Major General, USA
Chief of Staff

JOHN LYCAS
Colonel, GS
Chief, HQ Admin Mgt Ofc

DISTRIBUTION:
Special

* U.S. GOVERNMENT PRINTING OFFICE: 1974 O - 552-931